

https://dspace.org/

A parametric study of resin-gel synthesis to understand the formation mechanism of titanium-oxide nanoparticles

Narrandes, Ashvir Ashwin

2018

https://hdl.handle.net/10539/26059

Narrandes, Ashvir Ashwin (2018) A parametric study of resin-gel synthesis to understand the formation mechanism of titanium-oxide nanoparticles, University of the Witwatersrand, Johannesburg, <http://hdl.handle.net/10539/26059>

Downloaded from a DSpace repository. https://dspace.org/

A PARAMETRIC STUDY OF RESIN-GEL SYNTHESIS TO UNDERSTAND THE FORMATION MECHANISM OF TITANIUM–DIOXIDE NANOPARTICLES

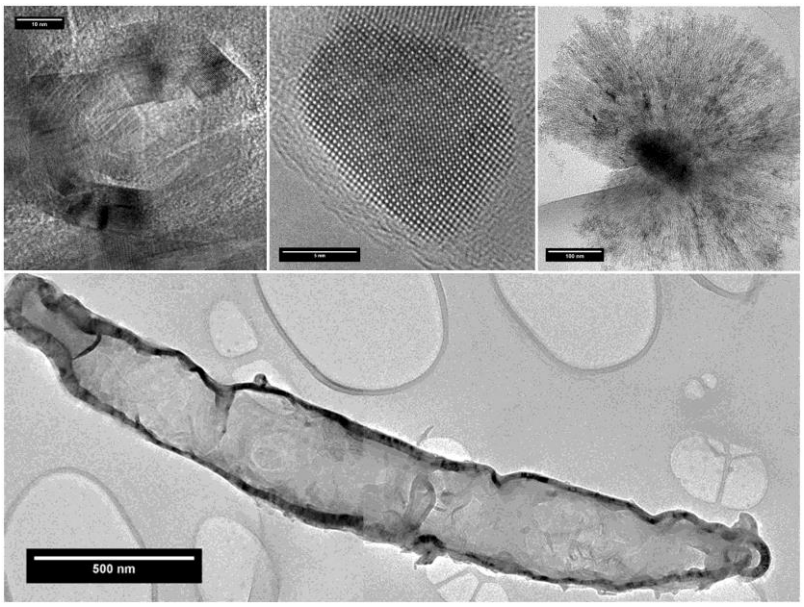

A Thesis submitted to the Faculty of Science,

University of the Witwatersrand, Johannesburg,

in fulfilment of the requirements for the degree of

Doctor of Philosophy

by

Ashvir Narrandes

Declaration



I declare that this Thesis is my own, unaided work.

It is being submitted for the Degree of

Doctor of Philosophy

at the University of the Witwatersrand, Johannesburg.

It has not been submitted before for any degree or examination

at any other University

	29 / 05 / 2018	Johannesburg
Candidate	**Date**	**Place**

(Ashvir Narrandes)

Abstract

The relatively unknown resin-gel synthesis technique has the potential to form multi-mode mixed metal oxide nanoparticles with differing stoichiometries. These oxides can be employed in a plethora of applications. In order to exploit these benefits, the mechanism of nanoparticle formation must be understood. To this end, this study embarked on a parametric investigation to gain insights on the formation of the less stable anatase and more stable rutile (titanium dioxide) using resin-gel synthesis. By adjusting parameters such as the type of polymer, solvent, acid, and metal ion precursor, and by varying other parameters such as the polymer chain length, polymer stoichiometry, and heating rate, a model for nanoparticle formation was developed and refined. This model considered the formation of hydroxylated metal ion species following the addition of a metal ion precursor to a hydroxyl-containing solvent. These species were protected and stabilised by the remaining fragments of solvent components. In addition, the size of the ligands attached to the metal ion precursor governed the amount of protection and stabilisation afforded to the hydroxylated species by the precursor. These complexes were coordinated to polymer chains that underwent degradation during the course of heating and ignition. Polymer degradation produced polymer reaction chambers. The formation, action, and interaction of these chambers with developing titania crystallites are a novel finding of this work. The sizes of these chambers were controlled largely by the quantity of polymer present in the reaction. The number of accessible oxygen sites on the precursor determined the degree of association between the metal ion complexes and the reaction chambers. If the association was intimate, the polymer reaction chambers served to stabilise and protect the newly nucleated anatase particles. If the combination of protection effects afforded by the solvent components, precursor ligands, and association of reaction chambers of appropriate sizes was insufficient to stabilise nucleated anatase, it readily converted into the rutile phase. Anisotropic growth along [0 0 1] then caused rutile to form nanorods. Rutile mesocrystals developed following sufficient polymer degradation. The association of nanoparticles with polymer fragments was viewed using TEM. Additionally, TEM investigations revealed the presence of polymer-derived superstructures containing reaction chambers. Reaction chambers presented with various morphologies and were composed of crystalline carbon.

Dedicated to my mother

Your strength and sacrifice knows no bounds.

Thank you, for everything.

Acknowledgements

A study of this magnitude is made feasible by the combined efforts of a number of individuals and institutions. It is my hope that our interactions were as enjoyable to you, as they were beneficial to me.

Dr. Paul Franklyn

My supervisor, mentor, and for all intents and purposes, my guru. Thank you for your selfless guidance throughout my academic career, and for imparting creative problem-solving, and critical thinking skills to me. I am also thankful for your intuition, compassion, empathy, and kindness – for pushing me when I needed to be pushed, and leaving me alone, when it was necessary. I will attempt to emulate your scientific and humanitarian prowess through the rest of my career. To paraphrase Sir Isaac Newton: any brilliance achieved through this work is only because it was standing on the shoulders of a giant.

Prof. Neil Coville

Thank you for your assistance with the final submission of this work. In particular, thank you for your warm, calming, and insightful demeanour leading by example and nurturing talent.

Mathias Kiefer

Thank for your assistance with high precision synthesis of precursor variation samples.

Prof. Alexander Ziegler, **Jacques Gerber**, **Deran Reddy**, **Manoko Maubane**, and **Zikhona Tetana (**Microscopy and Microanalysis Unit)

Thank you for your assistance in various ways with (HR)TEM and SEM investigations, problem diagnoses and correction, and training. Special thanks to Deran Reddy for assistance with sample preparation for ultramicrotomy.

Dr. David Jefferson

Thank you for your accommodation and supervision on HRTEM at the University of Cambridge. Thanks are extended to **Dr. Katharine Moore** for assistance with HRTEM.

Prof. Basil Julies

Thank you for your accommodation on HRTEM at the Electron Microscope Unit (University of the Western Cape).

Dr. James Wesley-Smith

Thank you for granting me access on the HRTEM at the CSIR.

Prof. Dave Billing

Thank you for permitting my overnight use of the D2. Thanks are also extended to **Dr. Wilson Mogodi** for assistance with PXRD.

Neo Phao and **Evah Phago**

Thank you for the swift TGA analysis.

Rudo Sithole

Thank you for assistance with setting up Schlenk experiments. Thanks are also extended to **Dr. Juanita van Wyk** for accommodating my O_2 deprived experiments in your lab.

Tapuwa Dzara

Thank you for the bespoke glassware that allowed me to conduct the Schlenk experiments.

Joyce Gama and **Ignatia Khumalo**

Thank you for accommodating some experiments in your labs'.

CATOMAT research group within the School of Chemistry

Thank you for providing a calm, welcoming environment for the mutual exchange of ideas.

Chemical Industries Education and Training Authority (contract 3417)

Thank you for funding the mature phase of this research. Special thanks are extended to **Prof. Dean Brady** and **Thulani Shabalala** for assistance with administration of these funds.

National Research Foundation (grant 86140)

Thank you for funding a significant portion of this research.

PetroSA

Thank you for funding the developmental stages of this research.

Awards, Publications, and Conferences

Awards

Microscopy Society of Southern Africa "Most Promising Microscopist" award (2013): Most prestigious microscopy student award in South Africa awarded for work on imaging resin-gel synthesised nanoparticles. The prize included a sponsored trip to present this work at a chosen international conference.

Publications

Franklyn, P. J. & Narrandes, A. Unlocking the Secrets Behind the Resin-Gel Synthesis for the Controlled Formation of Anatase and Rutile. in *Proceedings of The International Conference Nanomaterials: Applications And Properties* **1,** 01PCN40–1 – 01PCN40–4 (Sumy State University, 2012).

Conferences and Conclave

- Conference: **18th International Microscopy Conference** (Prague, Czech Republic – 2014).
    - Presentation: "HRTEM Studies of Crystalline Growth to Unlock the Formation Mechanisms of Titania Nanodandelions" (poster).
    - Presentation: "The Effect of Precursor Variation on the Formation of TiO_2 Synthesised by the Resin-Gel Method" (poster).
- Conference: **51st Microscopy Society of Southern Africa** (Pretoria, South Africa – 2013).
    - Presentation: "Intermittent Resin-gel Synthesis: Supporting the Proposed Hypothesis" (oral).
    - Presentation: "Optimal Conditions for Hydrothermal Synthesis of Nano-Rutile Dandelions" (oral).
- Conference: **Microscopy Conference** (Regensburg, Germany – 2013).
    - Presentation: "Investigating the Formation Mechanism of Three-dimensional Mesocrystalline Rutile Nanospheres Synthesised by the Resin-gel Method" (oral).
- Conclave: **6th International Science Conclave** (Allahabad, India – 2013).
    - Invited to attend.

- Conference: **50th Microscopy Society of Southern Africa** (Cape Town, South Africa – 2012).
    - Presentation: "Imaging 3D Mesocrystalline Rutile Nanoballs Synthesized by the Resin-gel Method" (oral).
    - Presentation: "Refining the Mechanistic Model Describing Titania Formation Using Resin-Gel Synthesis" (poster).
- Conference: **Nanomaterials: Applications and Properties** (Alushta, Ukraine – 2011).
    - Accepted: "Unlocking the Secrets behind the Resin-Gel Synthesis for the Controlled Formation of Anatase and Rutile" (oral).
- Conference: **49th Microscopy Society of Southern Africa** (Pretoria, South Africa).
    - Presentation: "Steps toward elucidating the mechanism of the resin-gel synthesis" (oral).

Table of Contents

Declaration ii

Abstract iii

Dedication iv

Acknowledgements v

Awards, Publications, and Conferences vii

Awards vii

Publications vii

Conferences and Conclave vii

Table of Contents ix

List of Figures xviii

List of Tables xliv

List of Equations xlvii

List of Abbreviations xlviii

List of Symbols l

List of Units li

Chapter 1: Introduction 1

1.1 Synthetic Descriptions 3

1.1.1 Pechini Method 3

1.1.2 Sol-Gel Synthesis 6

1.1.3 Sol Synthesis 10

1.1.4 Combustion Synthesis 11

1.1.5 Resin-Gel Synthesis 15

1.1.6 Hydrothermal Synthesis 17

1.2 Description of TiO_2 24

1.2.1 Origin and Discovery 24

1.2.2 Crystallography 25

1.2.3 Surface Energetics 29
1.2.4 Stability and Phase Transformations 33
1.2.4.1 Brookite to Rutile Transformation 34
1.2.4.2 Anatase to Rutile Transformation 35
1.2.4.2.1 Transformation dependence on Particle Size 37
1.2.4.3 Direct Rutile Formation 40
1.2.5 Transformation Mechanisms 41
1.2.6 Mesocrystalline TiO_2 47
1.2.6.1 Rutile Mesocrystals 47
1.2.6.2 Anatase Mesocrystals 52
1.2.7 Electronic Bonding Structure 56
1.3 Polyethylene Glycol 59
1.3.1 Description and Structure 59
1.3.2 Melting Characteristics 61
1.3.3 Solution Behaviour 63
1.3.4 PEG – biological particle Interactions 65
1.3.5 PEG-metal ion Interactions 66
1.3.6 TiO_2 Synthesis from Ethylene Glycol 67
1.4 Characterisation Techniques 69
1.4.1 Powder X-ray diffraction 69
1.4.1.1 Principles of PXRD 70
1.4.1.2 Data Analysis 72
1.4.1.2.1 Spurr and Myers equation 72
1.4.1.2.2 Scherrer Equation 73
1.4.2 Transmission Electron Microscopy 75
1.4.2.1 The need for Electrons 76
1.4.2.2 Principles of TEM 78

1.4.2.3 High Resolution Transmission Electron Microscopy 81
1.4.2.3.1 Data Analysis 81
1.4.3 Thermogravimetric Analysis 81
1.5 References 82
Chapter 2: Aims 105
Chapter 3: Experimental Overview 107
3.1 Parameter Variation 107
3.1.1 Polymer Type Variation 107
3.1.2 Solvent Variation 108
3.1.3 Polymer Chain Length Variation 108
3.1.4 PEG quantity variation 109
3.1.5 Acid Variation 109
3.1.6 Heating Rate Variation 109
3.1.7 Metal Ion Precursor Variation 110
3.2 Controlled Temporal Intermittent Resin-gel Synthesis 111
3.3 Characterisation and Data Analysis 112
3.4 References 112
Chapter 4: Preliminary Investigations 113
4.1 PEG Decomposition Temperature Range 113
4.2 Systematic O_2 Elimination 116
4.3 References 134
Chapter 5: Effects of Solvent and PEG Molecular Weight on Titania Polymorph and Crystallite Size Formation 135
5.1 Experimental Procedure 135
5.1.1 Ethanol Mediated Synthesis 135
5.1.2 Water containing HNO_3 Mediated Synthesis 136
5.1.3 Heat Treatments 136

5.1.4 Characterisation 137
5.1.5 Results and Discussion 138
5.1.6 Ethanol Mediated Synthesis 138
5.1.7 Water containing HNO_3 Mediated Synthesis 150
5.1.8 Comparison of the Effects of Ethanol and Water containing HNO_3 161
5.2 Conclusions 165
5.3 References 167
Chapter 6: Effects of an Enhanced Heating Rate on Titania Polymorph and Crystallite Size Formation 169
6.1 Experimental Procedure 169
6.1.1 Ethanol Mediated Synthesis 169
6.1.2 Water containing HNO_3 Mediated Synthesis 170
6.1.3 Heat Treatments 170
6.1.4 Characterisation 170
6.2 Results and Discussion 171
6.2.1 Ethanol Mediated Synthesis 171
6.2.2 Conventional and Forced Heating using an Ethanol Solvent 179
6.2.3 Water containing HNO_3 Mediated Synthesis 181
6.2.4 Conventional and Forced Heating using a Water containing HNO_3 Solvent 193
6.3 Conclusions 196
6.4 References 197
Chapter 7: Effects of Citric Acid on Titania Polymorph and Crystallite Size Formation 199
7.1 Experimental Procedure 200
7.1.1 Addition of Ti^+ ions to PEG in a (1 : 1) Ratio 200
7.1.2 Heat Treatments 201
7.1.3 Characterisation 202
7.2 Results and Discussion 202

7.2.1 Effects of Citric Acid 202
7.2.2 Comparison of the Effects of Citric Acid 210
7.3 Conclusions 213
7.4 References 214
Chapter 8: Effects of Polyethylene Glycol Molecular Weight and Stoichiometry on Titania Polymorph and Crystallite Size Formation 215
8.1 Experimental Procedure 215
8.1.1 Addition of Ti ions to PEG in a (1 : 1) Ratio 216
8.1.2 Addition of Ti ions to PEG in a (1 : 0.5) Ratio 217
8.1.3 Addition of Ti ions to PEG in a (1 : 0.1) Ratio 218
8.1.4 Heat Treatments 219
8.1.5 Characterisation 219
8.2 Results and Discussion 220
8.2.1 Addition of Ti ions to PEG in a (1 : 1) Ratio 220
8.2.2 Addition of Ti ions to PEG in a (1 : 0.5) Ratio 237
8.2.3 Addition of Ti ions to PEG in a (1 : 0.1) Ratio 252
8.2.4 Comparison of the Effects of PEG Stoichiometry 259
8.3 Conclusions 263
8.4 References 264
Chapter 9: Effects of Rapid Heating on Titania Polymorph and Crystallite Size Formation 265
9.1 Experimental Procedure 265
9.1.1 Heat Treatments 265
9.1.2 Characterisation 267
9.2 Results and Discussion 269
9.2.1 Rapid heating samples prepared in a (1 : 1) ratio 269
9.2.2 Addition of Ti ions to PEG in a (1 : 0.5) Ratio 282
9.2.3 Comparison of the Effects of Rapid Heating 292

9.3 Conclusions 297

9.4 References 298

Chapter 10: Effects of Precursor Variation on Titania Polymorph and Crystallite Size Formation 300

10.1 Experimental Procedure 300

10.1.1 Titanium (IV) oxysulfate synthesis 301

10.1.2 Titanium (IV) isopropoxide synthesis 302

10.1.3 Titanium (IV) 2-ethylhexyloxide synthesis 303

10.1.4 Titanium diisopropoxide bis(acetylacetonate) synthesis 304

10.1.5 Titanium (IV) bis (ammonium lactato) dihydroxide solution synthesis 305

10.1.6 Titanium (IV) (triethanolaminato) isopropoxide synthesis 306

10.1.7 Heat Treatments 307

10.1.8 Characterisation 307

10.2 Results and Discussion 307

10.2.1 Titanium (IV) oxysulfate 308

10.2.2 Titanium (IV) isopropoxide 327

10.2.3 Titanium (IV) 2-ethylhexyloxide 335

10.2.4 Titanium diisopropoxide bis(acetylacetonate) 343

10.2.5 Titanium (IV) bis (ammonium lactato) dihydroxide solution 348

10.2.6 Titanium (IV) (triethanolaminato) isopropoxide 354

10.3 Conclusions 362

10.4 References 366

Chapter 11: Attempts at Directly Observing Titanium Dioxide Formation Using Controlled Temporal Intermittent Resin-gel Synthesis 368

11.1 Experimental Procedure 368

11.1.1 Liquid N_2 induced quenching 368

11.1.2 Aluminium rod generated molten drops 368

11.2 Results and Discussion 371

11.2.1 Liquid N_2 induced quenching 371
11.2.2 Aluminium rod generated molten drops 383
11.3 Conclusions 399
11.4 References 399
Chapter 12: Conclusions 401
12.1 Conclusion 1 401
12.2 Conclusion 2 402
12.3 Conclusion 3 402
12.4 Conclusion 4 403
12.5 Conclusion 5 403
12.6 Conclusion 6 404
12.7 Conclusion 7 404
12.8 Conclusion 8 405
12.9 Conclusion 9 406
12.10 Conclusion 10 407
Chapter 13: Proposals for Further Studies Related to Resin-gel Synthesis 408
13.1 Parameter Variation Studies 408
13.2 Quantitative Studies 409
13.3 Applications of Resin-gel Synthesis 410
Appendix A. JCPDS Powder Patterns and PXRD and (HR)TEM Components 411
A.1. JCPDS Powder Patterns for Titanium Dioxide Polymorphs 411
A.2. Powder X-ray Diffraction 413
A.2.1. Components of a PXRD 413
A.2.1.1. X-ray Source 413
A.2.1.2. Filters 415
A.2.1.3. Slits 415
A.2.1.4. Sample Holders 416

A.2.1.5. Monochromators 417

A.2.1.6. Detectors 417

A.2.1.7. Goniometers 418

A.2.2. PXRD Geometry 419

A.3. Transmission Electron Microscopy 420

A.3.1 Components of a TEM 420

6.4.1.1 A.3.1.1 Electron Source 422

6.4.1.2 A.3.1.2 Lenses 425

6.4.1.3 A.3.1.3 Apertures 425

A.4. References 426

Appendix B. XRD Analysis of Control Samples 427

B.1 Unloaded PEG 427

B.2 PEG loaded with a $TiCl_4$ Solution 428

B.3 Homogenised PEG 434

B.4 Homogenised PEG with Excess Distilled H_2O 435

B.5 Empty Zero-background Sample Holder 436

Appendix C. Effects of Solvent and PEG Molecular Weight on Titania Polymorph and Crystallite Size Formation 437

Appendix D. Effects of an Enhanced Heating Rate on Titania Polymorph and Crystallite Size Formation 440

Appendix E. Effects of Citric Acid on Titania Polymorph and Crystallite Size Formation 443

Appendix F. Effects of Polyethylene Glycol Molecular Weight and Stoichiometry on Titania Polymorph and Crystallite Size Formation 445

Appendix G. Effects of Rapid Heating on Titania Polymorph and Crystallite Size Formation 449

Appendix H. Effects of Precursor Variation on Titania Polymorph and Crystallite Size Formation 451

Appendix I. Attempts at Directly Observing Titanium Dioxide Formation Using Resin-gel Synthesis 458

Appendix J. Inference Based on Findings 460

Conclusion 2 460

Conclusion 3 460

Conclusion 4 461

Conclusion 5 462

Conclusion 6 462

Conclusion 8 463

Conclusion 10 463

The Grand Resin-gel Synthesis TiO_2 Particle Formation Hypothesis 464

List of Figures

Figure 1.1: Esterification process and network formation during the early stages of the Pechini synthesis[9]. 5

Figure 1.2: Shape and size dependence of anatase nanoparticles on various amine-based shape controllers at constant pH. (a) ethylenediamine, (b) trimethylenediamine, (c) diethylenetriamine, (d) triethylenetetramine, (e) diethylamine, (f) trimethylamine, and (g) triethylamine[21]. 9

Figure 1.3: TEM micrograph showing exclusive anatase formation. (b) Represents a higher magnification image of (a)[23]. 10

Figure 1.4: Formation of voluminous (left) $Li_4Ti_5O_{12}$ and (right) ZrO_2 by solution combustion[32, 34]. 12

Figure 1.5: Schematic representation of ignition induced polymer degradation leading to nanoparticle formation using resin-gel synthesis. 15

Figure 1.6: Increase in the number of publications on the use of hydrothermal syntheses, especially for powder fabrication[42]. 18

Figure 1.7: Natural and synthetic applications of hydrothermal technology[41]. 18

Figure 1.8: Unit cells of (a) rutile, (b) anatase and (c) brookite. Each octahedron has a titanium (IV) ion at the centre and oxygen atoms at each apex[58]. 25

Figure 1.9: Lattice illustrations of (a) TiO_2 (B), (b) TiO_2 (H), and (c) TiO_2 (R). TiO_2 (H) is illustrated with K^+ counter ions[54, 55, 56]. 27

Figure 1.10: Unit cells of (a) columbite, (b) baddeleyite, (c) fluorite, (d) pyrite, and (f) cotunnite. O and Ti ions are represented by large and small spheres respectively[57]. 28

Figure 1.11: Equilibrium shapes of (a – b) rutile and (c – d) anatase crystals[62, 63, 65]. Ramamoorthy et al., and Lazzeri et al., generated (a) and (c) respectively[62, 65]. Oliver et al., generated (b) and (d) using the rutile {1 1 0}, {0 1 1}, {2 2 1} and {1 0 0} faces, and the anatase {0 0 1} and {0 1 1} faces respectively[63]. 32

Figure 1.12: Side and top views of relaxed surfaces of rutile (a) {1 1 0} and (b) {0 1 1}, and anatase (c) {0 0 1} and (d) {0 1 1} surfaces. Surface oxygen's are yellow, bulk oxygen's red, second layer oxygen ions green, and titanium ions are blue[63]. 32

Figure 1.13: Enthalpy of rutile, anatase and brookite as a function of (a) particle size[68] and (b) surface area[67]. The darkened line in (b) represents the energetically stable phases[67]. 33

Figure 1.14: Unsaturated charge densities on different faces of (a) anatase and (b) rutile[85]. Greater unsaturated charge density on rutile surfaces make it unstable. 38

Figure 1.15: (a – e) Process of coalescence by movement of a grain boundary. Notice that the barrier to coalescence is associated with the smaller crystallite[86]. 40

Figure 1.16: Anatase and rutile formation mechanism. (a) Free octahedra in solution. Condensation between two octahedra results in (b) corner sharing followed by (c) edge sharing. (d) Third octahedron joins the forming chain at a corner. If the final condensation causes (e) linear edge sharing, thermodynamically favoured rutile is formed or (f) right angle edge sharing, statistically favoured anatase is formed[88]. 41

Figure 1.17: Transformation of anatase to rutile via (a) shorter and (b) longer reaction times[89]. Nuclei growth rate is represented by g. Step (i): rutile nucleation occurs at the interface between two anatase particles in contact. Step (ii): growth of rutile nuclei is rapid from smaller anatase particles (a) but extended for larger anatase particles (b). Step (iii): formation of a rutile particle from the particle-particle neck occurring simultaneously with step (ii). 42

Figure 1.18: (a) Particles self-organising to attach at specific surfaces. (b) Formation of a twinned crystal from the mismatched interfaces. (c) Formation of a new phase from the twin surface, intergrown in the particle[93]. 44

Figure 1.19: Apparent inverse relationship between the amount of brookite and respective particle size as a function of hydrothermal treatment time at 250 °C[93]. 44

Figure 1.20: (a) FE-SEM image of self-assembled rutile showing pyramidal tips. (b) TEM image of a single rutile nanorod showing orientation of the tip in relation to the surface of the rod[109]. 48

Figure 1.21: (a) Radial growth of rutile crystals comprising the superstructure. (b) Needle-like nature of rutile, appearing as single crystals[97]. 49

Figure 1.22: Mechanism of rutile mesocrystal formation based on the distribution of $TiOH^{3+}$ in solution[102]. 50

Figure 1.23: Formation of hollow rutile mesocrystals after ultra-sonication[114]. 51

Figure 1.24: Mechanism of hollow rutile mesocrystal formation[114]. Step A illustrates ligand exchange. Step B shows formation of TiO_2 by O_2 elimination from decomposition. Step C shows the formation of anisotropic rutile. Step D illustrates the effects of bubbles as a template. Step E shows the formation of a hollow sphere[114]. 52

Figure 1.25: Anatase mesocrystals composed of spherical anatase single crystals[111]. 52

Figure 1.26: Anatase mesocrystals synthesised with a reaction time of (a) 2 hours forming structures with solid cores and (b) 20 hours forming structures with hollowed cores[115]. Scale bars = 200 nm. 53

Figure 1.27: Cross-sectional TEM image of microtomed anatase[99]. This image suggests that the structure contains a hollow core[99]. 54

Figure 1.28: HRTEM images of anatase superstructures showing (a) complete mesocrystal comprising non-uniform 1D nanostructures and (b) individual 1D nanostructures with growth along [1 0 1]. Note the lack of pyramidal or rounded tip nanostructures. Insert in (a) shows the SAED pattern with four indexed rings. Insert in (b) shows the lattice spacing between (1 0 1) planes[99]. 54

Figure 1.29: SEM images of anatase (A) nanowires and (B) mesocrystals. Inserts show schematics of anatase nanowires and superstructures. 55

Figure 1.30: Local orbital bonding structure of titanium dioxide. (a) Atomic levels. (b) Crystal field splitting levels. (c) Final interaction states. Solid and dashed lines represent large and small contributions respectively[121]. 57

Figure 1.31: Total and angular momentum decomposed densities of states for rutile (left) and anatase (right). The contributions to the local densities of states from $O_{2s,}$ O_{2p} and Ti_{3d} are shown[120]. 57

Figure 1.32: Schematic energy levels diagram of the lowest unoccupied local orbital structure of a $[TiO_6]^{8-}$ cluster with O_h, D_{2h} (rutile) and D_{2d} anatase symmetry[123]. 58

Figure 1.33: Basic linear structure of Polyethylene glycol. 59

Figure 1.34: Typical 7_2 helical conformation of PEO. (a) Lateral view, (b) axial view, and (c) gauche and trans configurations[134]. 60

Figure 1.35: Schematic of a single crystal polymer exhibiting regular chain folding into sheets on the order of 10 nm[135]. Random coil conformations ensue after melting[135]. 60

Figure 1.36: Change of PEO from a hydrated coil to a collapsed globule under the action of heating at the low critical solution temperature[135]. Red spheres represent ethylene oxide; blue spheres represent water molecules[135]. 61

Figure 1.37: Melting point and heat of melting dependence on PEG molecular weight[136]. 62

Figure 1.38: Optical micrographs showing the solidification process for PEG with a molecular weight of 10000 g/mol[136]. Notice how the spherulites grow to eventually impinge on each other and decrease the growth rate. 62

Figure 1.39: (a) End and (b) side view of a PEG tri-hydrate complex model[142]. 64

Figure 1.40: Interference of a wave scattering from two different planes of a crystal separated by a distance, d. The dashed lines run parallel to the crests or troughs of the incident and diffracted wavefronts. BAE represents the additional distance that must be covered by the second wave before and after reflection[162]. 71

Figure 1.41: Comparison of scattered beams after interacting with (top) a single crystal and (bottom) a powder consisting of many randomly oriented crystallites[161]. 72

Figure 1.42: Various signals generated from a high-energy incident beam of electrons interacting with a thin specimen. The arrows indicate approximate areas where the signals can be detected[170]. 79

Figure 1.43: The two basic operating modes of the TEM illustrated schematically using only three lenses. The intermediate lens selects either the back focal plane (bfp) (A) or the image

plane (B) of the objective lens as its object. Note the positions of the selected area diffraction (SAD) and objective apertures in (A) diffraction and (B) imaging modes[170]. 80

Figure 1.44: PerkinElmer STA 6000 analyser used for TGA analysis in this study. 82

Figure 3.1: (a) Oxygen containing PEG and (b) oxygen free PEI. 107

Figure 4.1: TGA of unloaded PEG of various molecular weights. 114

Figure 4.2: TGA and 1st derivatives of unloaded and loaded PEG 3000 g/mol. 115

Figure 4.3: TGA and 1st derivatives of unloaded and loaded PEG 10000 g/mol. 115

Figure 4.4: XRD of samples synthesised using systematic O_2 elimination. 119

Figure 4.5: Sample 1 showing the formation of anatase crystallites using PEI. 121

Figure 4.6: Sample 2 produced a mixture of isotropic and anisotropic nanoparticles. 122

Figure 4.7: Closer inspection of the anisotropic crystallites found in sample 2 revealed the presence of rutile aligned along [1 1 1]. 123

Figure 4.8: Generated from sample 3 before calcination. Nanoparticles composed of TiO_2 were present in this sample. 124

Figure 4.9: Sample 3 also revealed the presence of large structures that were most likely a form of carbon generated from PEI. This structure appears to loop back on itself forming possible cavities for titania nucleation. 125

Figure 4.10: Closer inspection of the structure (most likely a form of carbon) in figure 4.9 revealed crystalline features. 126

Figure 4.11: Sample 4 produced nearly phase pure anatase as ascertained from XRD. 127

Figure 4.12: Sample 5 produced phase pure anatase crystallites as evidenced from XRD. In this TEM image, the TiO_2 crystallites appear to have well-defined edges. 128

Figure 4.13: Sample 5 produced a structure likely generated from the degradation of PEG. Loops and folds are evident within this structure and are likely areas for TiO_2 nucleation. EDS analysis reveals the structure to be composed of carbon and oxygen – consistent with

the decomposition products of PEG. The Cu peaks in the EDS were generated from the TEM grid. 129

Figure 4.14: Sample 6 shows the presence of numerous well-defined crystallites. From XRD, this sample produced a mixture of anatase and rutile. High aspect ratio rutile nanorods were not evident from this sample. 130

Figure 4.15: Sample 7 (complete O_2 removal) produced these hollow shell superstructures of unknown composition measuring between 650 – 800 nm across its diameters. Expectedly, no TiO_2 nanoparticles were formed. 131

Figure 4.16: Calcination of sample 7 produced titania nanoparticles. This implies that unstable Ti containing species were present in the sample before calcination. These species subsequently reacted with atmospheric O_2 to form TiO_2. 132

Figure 4.17: Sample 8 produced nearly phase pure rutile according to XRD. This image shows a well-defined rutile crystallite in the [1 1 1] orientation. 133

Figure 5.1: Progression of ignition. (a) Appearance of samples a short while after heating had commenced. (b) Sample colour change characteristic of polymer degradation owing to increased temperatures. (c) Pyrolysis after having reached the respective flash temperatures. (d) Black appearance of samples after ignition before calcination. 137

Figure 5.2: PXRD patterns of samples synthesised using ethanol pre-calcination. 138

Figure 5.3: PXRD patterns of replicate samples synthesised using ethanol pre-calcination. 138

Figure 5.4: PXRD patterns of calcined samples formed from ethanol. 139

Figure 5.5: PXRD patterns of replicate calcined samples formed from ethanol. 140

Figure 5.6: Average amount of anatase formed in ethanol pre- and post-calcination. 141

Figure 5.7: Average anatase crystallite size formed in ethanol pre- and post-calcination. 141

Figure 5.8: Average amount of anatase with associated average crystallite size formed in ethanol pre-calcination. 144

Figure 5.9: Average amount of anatase with associated average crystallite size formed in ethanol post-calcination. 144

Figure 5.10: (PEG 4000 in ethanol pre-calcination) Distribution of fine anatase particles within the carbon film of the TEM grid. 145

Figure 5.11: (PEG 4000 in ethanol pre-calcination). Agglomeration of anatase particles. The difficulty in distinguishing individual particles is likely due to the presence of carbon on the sample, left over from the ignition of PEG. 146

Figure 5.12: (PEG 4000 in ethanol post-calcination). This area shows particles that are nicely separated, in a region of particles that have agglomerated. 147

Figure 5.13: (PEG 4000 in ethanol post-calcination). Crystallites appear to have well-defined geometric shapes. Crystallites measure between 10 – 14 nm. 148

Figure 5.14: (PEG 4000 in ethanol post-calcination). Particles appear to be aggregating around a common point to form a spherical aggregation. 149

Figure 5.15: PXRD patterns of samples formed from water containing HNO_3 pre-calcination. 150

Figure 5.16: PXRD patterns of replicate samples formed from water containing HNO_3 pre-calcination. 150

Figure 5.17: PXRD patterns of calcined samples formed from water containing HNO_3. 151

Figure 5.18: PXRD patterns of replicate calcined samples formed from water containing HNO_3. 152

Figure 5.19: Average amount of rutile formed in water containing HNO_3 pre- and post-calcination. 153

Figure 5.20: Average rutile crystallite size formed in water containing HNO_3 pre- and post-calcination. 153

Figure 5.21: Average amount of rutile with associated average crystallite size formed in water containing HNO_3 pre-calcination. 155

Figure 5.22: Average amount of rutile with associated average crystallite size formed in water containing HNO_3 post-calcination. 157

Figure 5.23: (PEG 4000 in water containing HNO_3 pre-calcination). The particles display anisotropic growth, being longer than they are wider and suggesting the formation of rutile nanorods. 159

Figure 5.24: (PEG 4000 in water containing HNO_3 pre-calcination). The rutile nanorods appear to aggregate from a common point (or set of common points) forming a superstructure. The length of the rutile nanorods is consistent with crystallite size data obtained via PXRD analysis of the sample. Platelet like particles were also formed. 160

Figure 5.25: Amount of anatase and rutile formed in ethanol and water containing HNO_3 respectively, as a function of increasing PEG molecular weight pre-calcination. 161

Figure 5.26: Amount of anatase and rutile formed in ethanol and water containing HNO_3 respectively, as a function of increasing PEG molecular weight post-calcination. 161

Figure 5.27: Anatase and rutile crystallite size formed in ethanol and water containing HNO_3 respectively, as a function of increasing PEG molecular weight pre-calcination. 164

Figure 5.28: Anatase and rutile crystallite size formed in ethanol and water containing HNO_3 respectively, as a function of increasing PEG molecular weight post-calcination. 165

Figure 5.29: Proposed mechanism reflecting effects of polymer chain length and remaining matrix components. (a) Longer and (b) shorter polymer fragments with associated hydroxylated metal ions form larger (c, e) and smaller (d, f) reaction chambers after scission respectively. Smaller chambers better stabilise and cap the nucleating anatase phase. Larger remaining matrix components (c, d) stabilise the nucleated anatase phase better than smaller remaining matrix components (e, f). 167

Figure 6.1: PXRD patterns of samples synthesised using ethanol pre-calcination. 171

Figure 6.2: PXRD patterns of samples synthesised using ethanol post-calcination. 172

Figure 6.3: Average amount of anatase formed in ethanol pre- and post-calcination. 173

Figure 6.4: Average anatase crystallite size formed in ethanol pre- and post-calcination. 174

Figure 6.5: Average amount of anatase with associated crystallite size formed from ethanol pre-calcination. 175

Figure 6.6: Average amount of anatase with associated crystallite size formed from ethanol post-calcination. 176

Figure 6.7: Well defined, seemingly elongated cubic anatase crystallites exhibited by PEG 8000 + EtOH under enhanced heating conditions. 177

Figure 6.8: (PEG 8000 + EtOH post-calcination). Anatase is visible with a degree of agglomeration in some parts of the sample. Calcination caused particle sintering. 178

Figure 6.9: Comparison of average amount of anatase formed in ethanol under conventional and enhanced heating methods. 179

Figure 6.10: Comparison of average anatase crystallite size formed in ethanol under conventional and enhanced heating methods. 179

Figure 6.11: PXRD patterns of samples synthesised using water containing HNO_3 pre-calcination. 182

Figure 6.12: PXRD patterns of samples synthesised using ethanol post-calcination. 182

Figure 6.13: Average amount of rutile formed in water containing HNO_3 pre- and post-calcination. 183

Figure 6.14: Average rutile crystallite size formed in water containing HNO_3 pre- and post-calcination. 183

Figure 6.15: Average amount of rutile with associated average crystallite size formed in water containing HNO_3 pre-calcination. 185

Figure 6.16: Average amount of rutile with associated average crystallite size formed in water containing HNO_3 post-calcination. 185

Figure 6.17: Agglomerated anatase crystallites observed from sample OPEG 200 + H_2O. This image shows a variety of crystallites of different sizes. Some crystallites exhibit anisotropic growth. 189

Figure 6.18: Well-defined anatase crystallites formed from sample OPEG 1000 + H_2O. One-dimensional lattice fringes are visible for most crystals. Moiré fringe artefacts are evident. 190

Figure 6.19: Anatase crystallites of various sizes and shapes from OPEG 4000 + H_2O. 191

Figure 6.20: An area of sample OPEG 6000 + H_2O containing a mixture of rutile and anatase crystallites. 192

Figure 6.21: Comparison of average amount of rutile formed in water containing HNO_3 under conventional and enhanced heating methods. 193

Figure 6.22: Comparison of average rutile crystallite size formed in water containing HNO_3 under conventional and enhanced heating methods. 195

Figure 7.1: Structural formula of citric acid monohydrate. 199

Figure 7.2: PXRD patterns of samples pre-calcination. 202

Figure 7.3: PXRD patterns of replicate samples pre-calcination. 203

Figure 7.4: PXRD patterns of calcined samples. 204

Figure 7.5: PXRD patterns of replicate calcined samples. 204

Figure 7.6: Average amount of anatase formed pre- and post-calcination. 206

Figure 7.7: Average anatase crystallite size formed pre- and post-calcination. 207

Figure 7.8: Average amount of anatase with associated crystallite size formed pre-calcination. 208

Figure 7.9: Average amount of anatase with associated crystallite size formed post-calcination. 208

Figure 7.10: (PEG 1000 g/mol). Anatase crystallites measuring between 9 – 12 nm. The line profile of the large crystal on the right of the image confirms the presence of anatase as the lattice spacing measures 0.35 nm. This is consistent for anatase in the (1 0 1) orientation[5]. 209

Figure 7.11: Variation in the amount of anatase formed in different experiments. 210

Figure 7.12: Variation anatase crystallite size formed in different experiments. 212

Figure 8.1: PXRD patterns of samples synthesised in a (1 : 1) ratio pre-calcination. 220

Figure 8.2: PXRD patterns of replicate samples synthesised in a (1 : 1) ratio pre-calcination. 220

Figure 8.3: PXRD patterns of calcined samples synthesised in a (1 : 1) ratio. 222

Figure 8.4: PXRD patterns of replicate calcined samples synthesised in a (1 : 1) ratio. 222

Figure 8.5: Average amount of rutile formed from a (1 : 1) ratio pre- and post-calcination. 224

Figure 8.6: Average rutile crystallite size formed from a (1 : 1) ratio pre- and post-calcination. 224

Figure 8.7: Average amount of rutile with associated crystallite size formed in a (1 : 1) synthesis pre-calcination. 226

Figure 8.8: Average amount of rutile with associated crystallite size formed in a (1 : 1) synthesis post-calcination. 226

Figure 8.9: (PEG 6000 g/mol in a Ti^{+} : PEG ratio of (1 : 1)). This region of the sample showed a mixture of crystals of different sizes. Larger crystals measure ~ 25 – 30 nm. Smaller crystals measure ~ 2 – 7 nm. Also visible are large amounts of amorphous material that is most likely carbon. The insert compares the experimental and simulated FFT's (experimental FFT obtained from area delineated within the square). The selected crystal is rutile in the (0 1 0) or (1 0 0) orientation. 229

Figure 8.10: (PEG 6000 g/mol in a Ti^{+} : PEG ratio of (1 : 1)). Appearance of a twinned rutile crystal in the (0 0 1) orientation. This crystal measures approximately 10 nm across. The insert is a magnified version of the crystal showing a lattice spacing of 0.33 nm. The arrow indicates an imperfection in the lattice. 230

Figure 8.11: (PEG 6000 g/mol in a Ti^{+} : PEG ratio of (1 : 1)). In addition to forming small crystals, the sample synthesised from PEG 6000 also exhibited rutile mesocrystals. This mesocrystal measured approximately 270 nm end to end. It also appeared to consist of 6 distinct sections (separated by lines). 231

Figure 8.12: (PEG 6000 g/mol in a Ti^{+} : PEG ratio of (1 : 1)). A magnified portion of the rutile dandelion in figure 8.11. Rutile crystallites exhibit anisotropic growth to form nanorods. If the nanorods are assumed to be continuous particles, they measure approximately 50 nm from the bottom left corner of the image to the tips of the rods. The lattice spacing measures 0.33 nm. The amorphous content is part of the holey carbon film.232

Figure 8.13: (PEG 12000 g/mol in a Ti^{+} : PEG ratio of (1 : 1)). Single crystal anatase in the (0 0 1) orientation. This crystal measures approximately 6.4 nm across with a lattice spacing of 0.36 nm. The arrow indicates a potential high energy surface. 233

Figure 8.14: (PEG 12000 g/mol in a Ti^{+} : PEG ratio of (1 : 1)). Appearance of a fragment of assembled titania measuring 218 nm and 175 nm across the length and width respectively. This assembly resembles a fragment of the superstructure present in figure 8.11. 234

Figure 8.15: (PEG 12000 g/mol in a Ti^{+} : PEG ratio of (1 : 1)). Based on the lattice spacing of 0.33 nm, the fragment presented in figure 8.14 is likely composed of high aspect ratio rutile crystals. The width of the discernible rutile nanorod (highlighted with a double headed arrow) measured approximately 10 nm. 235

Figure 8.16: (PEG 12000 g/mol in a Ti^{+} : PEG ratio of (1 : 1)). The size of this structure suggests that it is undecomposed polymer remaining in the sample after pyrolysis. This conjecture is further supported by the observation that no lattice fringes were obtained from this structure. 236

Figure 8.17: PXRD patterns of samples synthesised in a (1 : 0.5) ratio pre-calcination. 237

Figure 8.18: PXRD patterns of replicate samples synthesised in a (1 : 0.5) ratio pre-calcination. 237

Figure 8.19 PXRD patterns of samples synthesised in a (1 : 0.5) ratio post-calcination. 239

Figure 8.20: PXRD patterns of replicate samples synthesised in a (1 : 0.5) ratio post-calcination. 239

Figure 8.21: Average amount of rutile formed from a (1 : 0.5) ratio pre- and post-calcination. 240

Figure 8.22: Average rutile crystallite size formed from a (1 : 0.5) ratio pre- and post-calcination. 240

Figure 8.23: Average amount of rutile with associated crystallite size formed in a (1 : 0.5) synthesis pre-calcination. 243

Figure 8.24: Average amount of rutile with associated crystallite size formed in a (1 : 0.5) synthesis post-calcination. 243

Figure 8.25: (PEG 6000 in a (1 : 0.5) ratio post-calcination). Single rutile crystal in the (1 1 1) orientation. This crystal measured ~ 9 nm top to bottom and ~ 7 nm across. Morphologically, it appeared to occur as a pentagon. Arrows indicate steps along the crystal. 248

Figure 8.26: (PEG 6000 in a (1 : 0.5) ratio post-calcination). Anisotropic rutile crystal in the (0 1 0) or (1 0 0) orientation. This crystal measures approximately 15.5 nm across its length and 8.5 nm across its width. 249

Figure 8.27: (PEG 6000 in a (1 : 0.5) ratio pre-calcination). This sample produced rutile superstructures. Arrows in the image indicate carbon deposited on the surface of the superstructure. This radius of this superstructure measured approximately 500 nm. 250

Figure 8.28: (PEG 6000 in a (1 : 0.5) ratio pre-calcination). Appearance of the ends of the superstructure imaged in figure 8.27. The rutile nanorod in the upper part of the image is pyramidically capped, occurs along (0 0 1) and measures approximately 8 nm across its width. From this image it appears that the nanorod is a continuous single crystal that extends far into the superstructure. 251

Figure 8.29: PXRD patterns of samples synthesised in a (1 : 0.1) ratio pre-calcination. 252

Figure 8.30: PXRD patterns of replicate samples synthesised in a (1 : 0.1) ratio pre-calcination. 252

Figure 8.31: PXRD patterns of samples synthesised in a (1 : 0.1) ratio post-calcination. 254

Figure 8.32: PXRD patterns of replicate samples synthesised in a (1 : 0.1) ratio post-calcination. 254

Figure 8.33: Average amount of rutile formed from a (1 : 0.1) ratio pre- and post-calcination. 255

Figure 8.34: Average amount of anatase with associated crystallite size formed in a (1 : 0.1) synthesis pre-calcination. 256

Figure 8.35: Average amount of anatase with associated crystallite size formed in a (1 : 0.1) synthesis post-calcination. 256

Figure 8.36: (PEG 4000 g/mol in a (1 : 0.1) ratio post-calcination) showing well-defined anatase crystallites. The crystal appearing in the lower right part of the image measures ~ 20 nm top to bottom and ~ 22 nm left to right. This is consistent with PXRD findings. 258

Figure 8.37: Effects of different PEG stoichiometries on the amount of rutile formed pre-calcination. 259

Figure 8.38: Effects of different PEG stoichiometries on rutile crystallite size formed pre-calcination. 262

Figure 9.1: Cast iron jaffle maker employed as the heating vessel for the rapid heat synthesis experiments. The inside surfaces of the vessel were used to heat the resin-gels. 266

Figure 9.2: Progression of rapid heat synthesis. (a) Initial addition of molten resin-gel to the vessel. (b) After a few seconds, the mixture moved to fill the area of the vessel accompanied by bubbling and sputtering. (c) Toward the end of the ignition, vapour was emitted with an audible hissing sound. (d) A thin film of black powder was formed post-ignition that was (e) calcined after a few seconds. The yellow appearance of the sample gave way to white after the powder was cooled to room temperature. 268

Figure 9.3: PXRD patterns of calcined samples synthesised in a (1 : 1) ratio. 269

Figure 9.4: PXRD patterns of replicate calcined samples synthesised in a (1 : 1) ratio. 269

Figure 9.5: Average amount of rutile with associated crystallite size formed in a (1 : 1) synthesis. 272

Figure 9.6: Average amount of anatase with associated crystallite size formed in a (1 : 1) synthesis. 274

Figure 9.7: Comparison between the size of anatase and rutile crystallites formed in a (1 : 1) synthesis. 276

Figure 9.8: (PEG 3000 g/mol in a Ti^{+} : PEG ratio of (1 : 1)). Single rutile crystallite in the (0 0 1) orientation. The short arrows on the right indicates the position of steps on the right side of the crystal. This crystal measures 15.69 nm down its length and 11.87 nm across its width. Long arrows toward the top of the image point to the position of oriented attachment. This is especially visible on the left side of the image where the 2D lattice fringes appear to merge with the 1D fringes from another crystal. 277

Figure 9.9: (PEG 3000 g/mol in a Ti^{+} : PEG ratio of (1 : 1)). Single rutile crystal in the (0 1 0) or (1 0 0) orientation. Notice the inconsistent shape of this anisotropic shaped crystal. It measures ~ 23 nm top to bottom and ~ 15 nm along its width. The semi-amorphous ring may be attributed to residual carbon or polymer components. 278

Figure 9.10: (PEG 3000 g/mol in a Ti^{+} : PEG ratio of (1 : 1)). Rutile mesocrystals were evident in this sample. This superstructure appears to be slightly fragmented along its centre. It has a diameter of ~ 500 nm. 279

Figure 9.11: (PEG 3000 g/mol in a Ti^{+} : PEG ratio of (1 : 1)). The tip of a rutile mesocrystal measuring ~ 16 nm across its width and more than 23 nm across its length. Rutile was confirmed by measuring the distance between peaks (0.33 nm) generated in the line profile. The tip of this crystal is inconsistent and shows a degree of tapering. 280

Figure 9.12: (PEG 3000 g/mol in a Ti^{+} : PEG ratio of (1 : 1)). Well-defined rutile nanorod imaged at the tip of a mesocrystal. This crystal was aligned along (1 1 1) and measured ~ 18 nm across its width and over 22 nm down its length. The tip is also curved rather than flat as previously described[7]. From this image, it appears that the nanorod is made up of a single anisotropic crystal. 281

Figure 9.13: PXRD patterns of calcined samples synthesised in a (1 : 0.5). 282

Figure 9.14: PXRD patterns of replicate calcined samples synthesised in a (1 : 0.5) ratio. 283

Figure 9.15: Average amount of rutile with associated crystallite size formed in a (1 : 0.5) synthesis. 284

Figure 9.16: Average amount of anatase with associated crystallite size formed in a (1 : 0.5) synthesis. 286

Figure 9.17: Comparison between the size of anatase and rutile crystallites formed in a (1 : 0.5) synthesis. 287

Figure 9.18: (PEG 1500 g/mol in a Ti+ : PEG ratio of (1 : 0.5)). Well-defined single crystal. This crystal measured ~ 30 nm across its width and ~ 27 nm top to bottom. 2D lattice fringes were not obtained from this crystal, however, a line profile revealed the lattice spacing to be 0.35 nm and is consistent with anatase in the (1 0 1) orientation[7]. 288

Figure 9.19: (PEG 1500 g/mol in a Ti+ : PEG ratio of (1 : 0.5)). Rutile crystallite in the (1 1 1) orientation. This crystallite measured ~ 34 nm top to bottom and ~ 30 nm across its width. The crystal appears to be tapered toward the tip and is characteristic of rutile nanorods comprising mesocrystals. 289

Figure 9.20: (PEG 6000 g/mol in a Ti+ : PEG ratio of (1 : 0.5)). Rutile crystal presenting with a tapered tip. Interestingly, this particular crystal did not form part of a mesocrystal. This crystal measured ~ 23 nm across its width and over 27 nm down its length. Rutile was confirmed by measuring the distance between peaks in the line profile. 290

Figure 9.21: (PEG 6000 g/mol in a Ti+ : PEG ratio of (1 : 0.5)). Tapered tip of a rutile crystal along (1 1 1). The insert shows the crystal at lower magnification in relation to other crystals. This crystal did not form part of a mesocrystal despite possessing the characteristics of a rutile nanorod in a mesocrystal. The crystal measured ~ 20 nm across its width and at least 18 nm from top to bottom. Amorphous material surrounded the crystal. 291

Figure 9.22: Effects of different heating rates on the mass percentage of rutile formed in different experiments. 292

Figure 9.23: Effects of different heating rates on rutile crystallite size formed in different experiments. 295

Figure 9.24: Effects of rapid heating on anatase crystallite size formed in a (1 : 1) and (1 : 0.5) synthesis. 296

Figure 10.1: Structural representation of titanium (IV) oxysulfate. 301

Figure 10.2: Structural representation of titanium (IV) isopropoxide. 302

Figure 10.3: Structural representation of titanium (IV) 2-ethylhexyloxide. 303

Figure 10.4: Structural representation of titanium diisopropoxide bis(acetylacetonate). 304

Figure 10.5: Structural representation of titanium (IV) bis (ammonium lactato) dihydroxide solution. 305

Figure 10.6: Structural representation of titanium (IV) (triethanolaminato) isopropoxide. 306

Figure 10.7: PXRD patterns of TiOxS generated samples. 308

Figure 10.8: Average amount of anatase with associated crystallite size formed using TiOxS. 308

Figure 10.9: PXRD patterns of $OTiCl_x$ generated samples. 314

Figure 10.10: (PEG 1500 g/mol). An imperfect spherical aggregation of anatase crystallites distended toward the left side of the image. The vertical and horizontal diameters measured ~ 320 nm and 360 nm respectively. Crystallites contained within the circle were imaged further, and represented in the following image. 316

Figure 10.11: (PEG 1500 g/mol). A magnified portion of crystals occurring at the edge of the anatase mesocrystal. Anatase crystallites measured between ~ 5.5 – 8.5 nm. The highlighted crystal presented along (0 0 1). 317

Figure 10.12: (PEG 3000 g/mol). Anatase mesocrystals appeared to fuse together via irregularly aggregated anatase crystallites. Additionally, the anatase mesocrystals displayed an imperfect spherical shape. 318

Figure 10.13: (PEG 3000 g/mol). This anatase mesocrystal appeared to be flattened on one side and had a more rounded appearance on the opposite side. The flattened shape was validated by it measuring ~ 240 nm across its width and ~ 190 nm across its length. Due to the differences in amplitude contrast, it appeared that the anatase crystallites comprising the ‘bridge’ between two mesocrystals were not as concentrated as the mesocrystals themselves. 319

Figure 10.14: (PEG 3000 g/mol). Anatase crystals with well-defined edges. The highlighted anatase crystal measured 8.1 nm across its width and 11.2 nm across its length and was in the (0 0 1) orientation. 320

Figure 10.15: (PEG 3000 g/mol). The highlighted rutile crystal was oriented along (1 1 1). This crystal did not have well-defined edges as observed for anatase single crystals formed in this sample. 321

Figure 10.16: (PEG 4000 g/mol). Formation of two anatase mesocrystals (arrows) in a region of sample dominated by agglomerated anatase crystallites. 322

Figure 10.17: ($OTiCl_x$, PEG 400 g/mol). Evidence of superstructures was obtained when $BaCl_2$ was employed in the synthesis. According to the EDS spectrum, the highlighted area of the superstructure (yellow circle) consisted of Ti^+ and O^- exclusively. Cu signals observed in the EDS spectrum as likely generated from the TEM grid. This mesocrystal measured ~ 280 nm across its width. 323

Figure 10.18: ($OTiCl_x$, PEG 400 g/mol). This area of the sample revealed an aggregation of particles with an elemental composition of Ba, S, C, and O. 324

Figure 10.19: ($OTiCl_x$, PEG 400 g/mol). The highlighted structure measured ~ 700 nm across its width and had an elemental composition of Ba, S, O, and Cl. 325

Figure 10.20: ($OTiCl_x$, PEG 400 g/mol). These particles were composed of Ti, O, Ba, S, and Cl. It is unclear whether these elements formed a unique crystal structure or existed separately as TiO_2 and Ba containing crystals, in the same part of the sample. The arrow indicates crystals that appear to be TiO_2. 326

Figure 10.21: PXRD patterns of Ti-isopro generated samples. 327

Figure 10.22: Average amount of anatase with associated crystallite size formed using Ti-isopro. 328

Figure 10.23: Post-calcination comparison of the average amount of anatase formed using $TiCl_4$ in ethanol with Ti-isopro in water containing HNO_3. 330

Figure 10.24: Post-calcination comparison of the average anatase crystallite size obtained using $TiCl_4$ in ethanol with Ti-isopro in water containing HNO_3. 330

Figure 10.25: (PEG 400 g/mol). Anatase crystallites consistent in shape and size when Ti-isopro was employed as the precursor. 332

Figure 10.26: (PEG 400 g/mol). Well defined cubic shape of an anatase crystal. This crystal measured ~ 22 nm and ~ 28 nm across its width and length respectively. 333

Figure 10.27: (PEG 4000 g/mol). Anatase crystallites exhibiting various shapes, as documented previously. 334

Figure 10.28: PXRD patterns of Ti-EHOx generated samples. 335

Figure 10.29: Average amount of anatase with associated crystallite size formed using Ti-EHOx. 336

Figure 10.30: (PEG 3000 g/mol). Anatase crystallites consistent in appearance to that previously observed in this study. 339

Figure 10.31: (PEG 3000 g/mol). The highlighted anatase crystal measured approximately 15 nm across its length and width. This crystal was aligned along (0 0 1) as evidenced by a comparison of the generated and simulated FFT's. Note that this crystal does not have well defined edges. 340

Figure 10.32: (PEG 20000 g/mol). The arrows indicate tapered, pyramidically capped ends of rutile crystallites. This is characteristic of rutile crystals[7]. The white lines denote an anisotropic rutile crystal measuring > 48 nm in length and approximately 22 nm across its width. 341

Figure 10.33: (PEG 20000 g/mol). Further confirmation of anisotropic rutile crystals. The arrow indicates the tapered end of a rutile crystal. An interesting note is that rutile mesocrystal formation was not observed, despite the formation of anisotropic rutile crystals. 342

Figure 10.34: PXRD patterns of Ti-AcAc generated samples. 343

Figure 10.35: Average amount of anatase with associated crystallite size formed using Ti-AcAc. 344

Figure 10.36: (PEG 10000 g/mol). Anatase crystals seemingly hexagonal in shape. 346

Figure 10.37: (PEG 20000 g/mol). The image reveals variation in crystal shape. The black arrow points to an anisotropic crystal with a tapered tip that is characteristic of rutile. This is in contrast to the square crystal with rounded edges pointed to by the white arrow. The shape of that crystal is characteristic of anatase. 347

Figure 10.38: PXRD patterns of Ti-AmOH generated samples. 348

Figure 10.39: Average amount of anatase with associated crystallite size formed using Ti-AmOH. 349

Figure 10.40: (PEG 12000 g/mol). Appearance of anatase crystals composed of various shapes including characteristic oblate habitus. 351

Figure 10.41: (PEG 12000 g/mol). Anatase crystals depicting various shapes were synthesised as evidenced in this TEM image. These crystals have well-defined edges and appear to pack together in a distinct manner. Unequal hexagonally shaped anatase crystals have been previously documented in this study. 352

Figure 10.42: (PEG 12000 g/mol). This TEM image reveals the presence of anatase crystals comprising distinct and indistinct edges. The highlighted anatase crystal occurs along (0 1 0) and has distinct edges. The generated FFT was magnified for clarity. This was to compensate for the limited resolving power of the low resolution TEM. 353

Figure 10.43: PXRD patterns of Ti-EApro generated samples. 354

Figure 10.44: Average amount of anatase with associated crystallite size formed using Ti-EApro. 356

Figure 10.45: Post-calcination comparison of the average amount of anatase formed using TiOxS and Ti-EApro. 357

Figure 10.46: Post-calcination comparison of the average anatase crystallite size obtained using TiOxS and Ti-EApro. 358

Figure 10.47: (PEG 200 g/mol). Anatase crystals with various sizes. This is consistent with previously observed anatase crystals. 360

Figure 10.48: (PEG 20000 g/mol). A mixture of anatase and rutile crystallites (highlighted in white). 361

Figure 10.49: Effects of different Ti precursors on the mass percentage of anatase formed. 364

Figure 10.50: Effects of different Ti precursors on anatase crystallite size. 365

Figure 11.1: Appearance of specimens collected on aluminium sheets prior to being transferred to holey carbon TEM grids. Samples were synthesised using PEG (a) 3000 g/mol, (b) 4000 g/mol, (c) 6000 g/mol, (d) 8000 g/mol, (e) 10000 g/mol, and (f) 12000 g/mol. 370

Figure 11.2: PXRD patterns showing the evolution of an anatase peak as the reaction proceeded. 371

Figure 11.3: PXRD patterns of replicate samples showing the evolution of an anatase peak as the reaction proceeded. 371

Figure 11.4: (before heating). This image was generated from the sample after solvent evaporation and before heating. The darker regions within this image represent crystallite ordering. 374

Figure 11.5: (before heating). By adjusting focus to minimum contrast focus, the above region of the sample revealed the presence of faint 1D lattice fringes (highlighted by the arrow). 375

Figure 11.6: (during heating (dark brown)). A region of the sample containing a sheet of PEG. This structure measured > 0.45 μm in width and > 1.1 μm in length. 376

Figure 11.7: (during heating (dark brown)). Adjusting focus to near minimum contrast focus revealed the presence of large PEG sheets. These sheets contained material represented by the darker areas within the sheet in this image. The size of these darker regions implied that it was unlikely TiO_2 nanoparticles. The upper darker region within this PEG sheet was imaged and is represented in the next image. 377

Figure 11.8: (during heating (dark brown)). This large structure corresponded to PEG and measured ~ 350 nm in width and ~ 400 nm in length. 378

Figure 11.9: (during heating (dark brown)). Interestingly, some regions of the sample revealed the presence of crystalline material associated with PEG superstructures. Based on the anisotropic characteristics of these crystallites, they were most likely rutile aligned along [0 0 1]. 379

Figure 11.10: (during heating (dark brown)). Confirmation of the presence of anisotropic rutile in the sample. As confirmed by FFT, this crystal was aligned along [0 0 1]. It measured 14 nm across its width and > 20 nm across its length. The tip of the nanorod was tapered as previously documented[6]. No rutile mesocrystals were observed in this sample. 380

Figure 11.11: (during heating (black)). Interestingly, large PEG sheets were observed later on in the reaction. These sheets measured ~ 0.6 – 0.9 μm in length. The width of the sheets appeared to vary depending on visible fragmentation. 381

Figure 11.12: (during heating (black)). Most of the sample contained crystalline material. This image contains an interestingly shaped crystal in the (0 0 1) orientation. 382

Figure 11.13: (during heating (black)). Anisotropic rutile crystals with tapered ends along [0 0 1] were observed. The lattice spacing of 0.33 nm is consistent with that previously observed for rutile crystals. 383

Figure 11.14: (PEG 3000 g/mol after 1 hour). A polymer fragment likely containing many small nanoparticles (represented by the darker dots within the polymer). The fragment measured ~ 130 nm across its width and > 200 nm in length. 384

Figure 11.15: (PEG 3000 g/mol after 1 hour). Nearly spherical polymer fragment formations were observed. The structures measured ~ 80 nm in diameter. Darker regions within the polymer spheres (represented by dots) are indicative of the presence of titania nanoparticles. 385

Figure 11.16: (PEG 3000 g/mol after 1 hour). Individual nanoparticles measured between 3 – 7 nm. Interestingly, some particles appeared to aggregate into a structure measuring > 60 nm across its width and length (contained within the circle). Distinct particles were observed at the edges of the structure, in contrast to the centre region of the structure that appeared to contain larger particles. 386

Figure 11.17: (PEG 3000 g/mol after 1 hour). “Tuning-fork shaped structures”. 387

Figure 11.18: (PEG 6000 g/mol after 1 hour). Imaging this sample also revealed the presence of nanoparticles contained within polymer fragments after 1 hour of heating. 388

Figure 11.19: (PEG 6000 g/mol after 1 hour). The superstructure within the polymer (darker region of the image) is consistent with the formation of a rutile mesocrystal. The structure measured ~ 500 nm across its width and ~ 400 nm from top to bottom. 389

Figure 11.20: (PEG 12000 g/mol after 1 hour). This image shows the presence of nanoparticles (highlighted with arrows) associated with polymer fragments. 390

Figure 11.21: (PEG 4000 g/mol after 3.5 hours). The structure contained within the image measured ~ 1.2 μm across its length and width and is indicative of PEG (or carbon generated from PEG) aggregation. 391

Figure 11.22: (PEG 4000 g/mol after 3.5 hours). This image represents PEG sheets (or carbon material generated from PEG) folding back on itself to create non-spherical reaction chambers. The light contrast of the central region of the chambers suggests that they are hollow or nearly hollow. As highlighted by arrows, the central hollow region of the chambers measured between 3 – 7 nm in width. The region contained with the circle was magnified and imaged. This image follows. 392

Figure 11.23: (PEG 4000 g/mol after 3.5 hours). Apparent formation of a circular reaction chamber. The intershell spacing measured 0.326 nm. 393

Figure 11.24: (PEG 10000 g/mol during ignition). This sample produced titania that aggregated into anisotropic rods (highlighted by arrows). Some of these rods arranged into hierarchical superstructures (highlighted by white circles). Black circles are indicative of smaller, more densely packed nanoparticles. 394

Figure 11.25: (PEG 10000 g/mol during ignition). Sparsely grown mesocrystal most likely comprised of rutile. The central region of this assembly is significantly denser than the outer rim. Additionally, the mesocrystal is imperfect as evidenced by the lack of nanorods present in the lower left part of the image. 395

Figure 11.26: (PEG 10000 g/mol during ignition). A large polymer structure was observed in this sample. An interesting feature of this structure is the boundary that encloses it. Within

the polymer, many different structures can be observed. The following images represent magnified sections of this structure. 396

Figure 11.27: (PEG 10000 g/mol during ignition). A magnified image of the right hand side of the structure observed in figure 11.26. The outside boundary appears to loop causing the internal structure to change, and may be indicative of a polymer reaction chamber. 397

Figure 11.28: (PEG 10000 g/mol during ignition). The internal components of this portion of the superstructure are similar to that observed in figure 11.21. 398

Figure A.1: JCPDS card for rutile. 411

Figure A.2: JCPDS card for anatase. 411

Figure A.3: JCPDS card for brookite. 412

Figure A.4: (left) Bruker D2 Phaser diffractometer. (right) Internal mechanics of the D2 showing X-ray source, sample loading assembly and detector[4]. The source and detector rotate along the θ-θ goniometer respectively. 413

Figure A.5: (left) Schematic of a sealed X-ray tube. (right) Photograph of an actual X-ray tube[2]. 414

Figure A.6: (left) A typical X-ray slit that is 0.3° in size. (right) Söller slits are composed of fine parallel foils[2]. 415

Figure A.7: Components of a powder diffractometer showing positions of the slits, sample and monochromator and detector in the beam path[6]. 416

Figure A.8: Flat-plate, shallow-well sample holders. (left) Filled and unfilled Si zero-background sample holders used in the D2 Phaser. (right) Non-rotating sample holder used in the forty-position sample changer of the D5000. 417

Figure A.9 Diagram of the goniometer path (defined by the circumference of the circle centred on the flat sample) in relation to some of the components of a θ-2θ diffractometer in Bragg-Brentano geometry[3]. 418

Figure A.10: FEI Tecnai T12 TEM based at the University of the Witwatersrand. 420

Figure A.11: JEOL 3011 HRTEM based at the University of Cambridge. 421

Figure A.12: Cross-section schematic of a typical TEM showing the major components in appropriate positions[3]. 422

Figure A.13: Schematic of a thermionic emission gun. The convergence/divergence angle is given by α_0 and this is the true source for the lenses in the TEM[8]. 424

Figure A.14: Schematic of a field-emission gun. Notice how the two anode geometry creates a crossover point[8]. 424

Figure A.15: Cross-section schematic of a TEM lens consisting of Fe polepieces surrounded by Cu coils[8]. 425

Figure B.1: XRD of unloaded PEG of various molecular weights. 427

Figure B.2: XRD of loaded PEG of various molecular weights. 428

Figure B.3: XRD patterns for unloaded and loaded PEG 400 g/mol. 429

Figure B.4: XRD patterns for unloaded and loaded PEG 1500 g/mol. 429

Figure B.5: XRD patterns for unloaded and loaded PEG 3000 g/mol. 430

Figure B.6: XRD patterns for unloaded and loaded PEG 4000 g/mol. 430

Figure B.7: XRD patterns for unloaded and loaded PEG 6000 g/mol. 431

Figure B.8: XRD patterns for unloaded and loaded PEG 8000 g/mol. 431

Figure B.9: XRD patterns for unloaded and loaded PEG 10000 g/mol. 432

Figure B.10: XRD patterns for unloaded and loaded PEG 12000 g/mol. 432

Figure B.11: XRD patterns for unloaded and loaded PEG 20000 g/mol. 433

Figure B.12: Comparison of XRD patterns generated for as received and homogenised PEG 6000 g/mol. 434

Figure B.13: Comparison of XRD patterns generated for as received, homogenised without water, and homogenised with water PEG 6000 g/mol. 435

Figure B.14: XRD pattern generated from an empty Si zero-background sample holder. 436

Figure I.1: This TEM image was obtained from a sample synthesised without any polymer. The wrapping effect of the holey carbon film is evident in the formation of this pseudo-superstructure. 458

Figure I.2: Side profile view of the formation of a pseudo-superstructure. This structure was obtained from a sample synthesised without PEG and shows associated nanoparticles with the wrapped holey carbon film. Note that these structures occurred as a doublet giving rise to a ‘tuning-fork’ structure or individually as represented in this image. 459

List of Tables

Table 1.1: Various oxides formed using the Pechini method[4]. 6

Table 1.2: Various oxides formed using gel combustion synthesis[31]. 13

Table 1.3: Oxides formed using the hydrothermal batch reaction method above supercritical conditions[44]. 20

Table 1.4 (1): Oxides formed using the hydrothermal flow reaction method above supercritical conditions[44]. 21

Table 1.5: Crystallography and physical properties of naturally occurring TiO_2. 26

Table 1.6: Crystallography of metastable phases of TiO_2. 27

Table 1.7: Crystallography of high pressure phases of TiO_2. 28

Table 1.8: Surface energetics of different rutile surfaces[63]. 30

Table 1.9: Surface energetics of different anatase surfaces[63]. 31

Table 1.10: Variations in the anatase to rutile transformation temperature[69]. 36

Table 1.11: Displacements of oxygen and titanium ions during transformation propagation to rutile[94]. 45

Table 1.12: Electron properties as a function of increasing accelerating voltage[170]. 78

Table 3.1: Average PEG molecular weights used in this study with associated average number of monomers per chain. 108

Table 3.2: Various titanium ion containing precursors used in this study. 110

Table 4.1: O_2 containing and O_2 free components with quantities employed in this study. 116

Table 4.2: Variation in the amount and size of anatase and rutile crystallites formed using various O_2 deprivation experiments. 119

Table 5.1: Average anatase crystallite size formed in ethanol and water containing HNO3. 158

Table 5.2: Average rutile crystallite size formed in ethanol and water containing HNO_3. 158

Table 6.1: Average anatase crystallite size formed in ethanol and water containing HNO_3. 187

Table 6.2: Increase in anatase crystallite size from samples synthesised using water containing HNO_3 and enhanced heating. 188

Table 7.1: Quantities of Ti ions and PEG added to achieve a (1 : 1) stoichiometry. 201

Table 8.1: Quantities of Ti ions and PEG added to achieve a (1 : 1) stoichiometry. 217

Table 8.2: Quantities of Ti ions and PEG added to achieve a (1 : 0.5) stoichiometry. 218

Table 8.3: Quantities of Ti ions and PEG added to achieve a (1 : 0.1) stoichiometry. 219

Table 8.4: Average amount of anatase and respective crystallite size formed in a (1 : 1) synthesis, post-calcination. 227

Table 8.5: Average amount of anatase and respective crystallite size formed in a (1 : 0.5) synthesis, pre-calcination. 244

Table 8.6: Average amount of anatase and respective crystallite size formed in a (1 : 0.5) synthesis, post-calcination. 244

Table 8.7: Comparison of anatase formation using (1 : 1) and (1 : 0.5) synthesis conditions, pre-calcination. 245

Table 8.8: Comparison of anatase formation using (1 : 1) and (1 : 0.5) synthesis conditions, post-calcination. 246

Table 8.9: Variation in anatase formation using different PEG stoichiometries. 257

Table 10.1: TiOxS and PEG added to achieve a (1 : 0.5) stoichiometry. 301

Table 10.2: Ti-isopro and PEG added to achieve a (1 : 0.5) stoichiometry. 302

Table 10.3: Ti-EHOx and PEG added to achieve a (1 : 0.5) stoichiometry. 303

Table 10.4: Ti-AcAc and PEG added to achieve a (1 : 0.5) stoichiometry. 304

Table 10.5: Ti-AmOH and PEG added to achieve a (1 : 0.5) stoichiometry. 305

Table 10.6: Ti-EApro and PEG added to achieve a (1 : 0.5) stoichiometry. 306

Table 10.7: Variation in the amount and size of anatase formed using different Ti^{+} precursors. 315

Table 11.1: $TiCl_4$ and PEG added to achieve a (1 : 1) stoichiometry. 369

List of Equations

(1.1) $SiCl_4 + ROH \rightarrow Si(OR)_4 + 4HCl$ 7

(1.2) $Si(OR)_4 + nH_2O \rightarrow Si(OR)_{4-n}(OH)_n + nROH$ 7

(1.3) $TiX_4 + Ti(OR)_4 \rightarrow 2TiO_2 + 4RX$ 10

(1.4) $TiX_4 + 2ROR \rightarrow TiO_2 + 4RX$ 10

(1.5) $BA = AE = d \sin \theta$ 70

(1.6) $BAE = 2d \sin \theta$ 70

(1.7) $BAE = n\lambda$ 70

(1.8) $2d \sin \theta = n\lambda$ 70

(1.9) $xA = 1/(1 + 1.26\ IR/IA)$ 72

(1.10) $xR = 1/(1 + 0.79\ IA/IR)$ 73

(1.11) $xA = 1/(1 + 1.47\ IR/IA)$ 73

(1.12) $xR = 1/(1 + 0.68\ IA/IR)$ 73

(1.13) $L = K\lambda/\beta \cos \vartheta$ 74

(1.14) $\delta = 0.61\lambda/\mu \cos \beta$ 76

(1.15) $\lambda = hp$ 77

(1.16) $\lambda = h/(2meeV)E0.5$ 77

(1.17) $\lambda = h/[2meeV\ 1 + eV2mec2]E0.5$ 77

(1.18) $Ti^+ + Polymer + Solvent \rightarrow TiO_2$ 107

(10.1) $TiOSO_4 + BaCl_2 \rightarrow OTiCl_2 + BaSO_4$ 313

List of Abbreviations

In Alphabetical Order

3D	–	Three-Dimensional
AEM	–	Analytical Electron Microscope/y
AFM	–	Atomic Force Microscope/y
BCE	–	Before Common Era
CBED	–	Convergent-Beam Electron Diffraction
Cc	–	Chromatic Aberration
Cs	–	Spherical Aberration
D2	–	Bruker D2 Phaser Diffractometer
D5000	–	Siemens D5000 Diffractometer
DFT	–	Density Functional Theory
DOS	–	Density of States
DTA	–	Differential Thermal Analysis
EDS	–	Energy Dispersive Spectroscopy
EDTA	–	Ethylenediaminetetraacetate
EELS	–	Electron Energy Loss Spectroscopy
et al.	–	et alia
FE-SEM	–	Field-Emission Scanning Electron Microscope/y
F20	–	FEI Tecnai F20 Transmission Electron Microscope
FWHM	–	Full Width at Half Maximum height
HOMO	–	Highest Occupied Molecular Orbital
LPG	–	Liquefied Petroleum Gas
HRTEM	–	High Resolution Transmission Electron Microscope/y
LUMO	–	Lowest Unoccupied Molecular Orbital
PBE	–	Perdew-Burke-Ernzerhof
PEG	–	Polyethylene Glycol
PEI	–	Polyethyleneimine

PEO	–	Polyethylene Oxide
PJF	–	Paul John Franklyn
PXRD	–	Powder X-ray Diffraction
SCS	–	Solution Combustion Synthesis
SHS	–	Self-propagating High-temperature Synthesis
Sol-gel	–	Solution-gel
STEM	–	Scanning Transmission Electron Microscope/y
T12	–	FEI Tecnai T12 Transmission Electron Microscope
TEM	–	Transmission Electron Microscope/y
TGA	–	Thermogravimetric Analysis
Ti-AcAc	–	Titanium (IV) diisopropoxide bis(acetylacetonate)
Ti-AmOH	–	Titanium (IV) bis (ammonium lactato) dihydroxide
Ti-EApro	–	Titanium (IV) (triethanolaminato) isopropoxide
Ti-EHOx	–	Titanium (IV) 2-ethylhexyloxide
Ti-isopro	–	Titanium (IV) isopropoxide
TiOxS	–	Titanium (IV) oxysulfate
Titania	–	Titanium dioxide
USSR	–	Union of Soviet Socialist Republics
VCS	–	Volume Combustion Synthesis
XRD	–	X-ray Diffraction

List of Symbols

ρ	–	Density
$\Delta H_f°$	–	Standard change in enthalpy of formation
S°	–	Standard entropy
n	–	Refractive index
D_{hkl}	–	d-spacing
d	–	Interplanar spacing
Z	–	Atomic number
a, b, c, α, β, γ	–	Lattice parameters
(*hkl*)	–	Specific Miller plane
{*hkl*}	–	Set of Miller planes related by symmetry
[*hkl*]	–	Direction in the crystal
<*hkl*>	–	Symmetrically equivalent directions within the lattice
||	–	Parallel
~	–	Approximately
λ	–	Wavelength
X_A	–	Weight fraction of anatase
X_R	–	Weight fraction of rutile
I_A	–	Maximum intensity of the anatase (101) peak
I_R	–	Maximum intensity of the rutile (110) peak
K	–	Scherrer constant
h	–	Planck's constant

List of Units

Å	–	Ångström*
°	–	Degrees
°C	–	Degrees Celsius
g	–	Gramme
h	–	Hour
J	–	Joules
kJ	–	Kilojoules
K	–	Kelvin
MPa	–	Megapascal
GPa	–	Gigapascal
M	–	Molar
Min	–	Minute
s	–	Second
ms	–	Millisecond
Mol	–	Mole
m	–	Metre
cm	–	Centimetre
mm	–	Millimetre
µm	–	Micrometre
nm	–	Nanometre
kcal	–	kilocalorie
eV	–	Electron Volt
Kα	–	K-alpha emission line
Kβ	–	K-beta emission line
W	–	Watt

* Ångström (Å) is used throughout this thesis, (as opposed to Angstrom - A) as the former was adopted by the International Union of Pure and Applied Chemistry in 1949. This despite the International Astronomical Union adopting the use of Angstrom (A) in 1938[1].

1. Dingle, H. Angstrom (A) or Ångström (Å)? *Nature* **167,** 908–908 (1951).

Chapter 1: Introduction

Consider the synthesis of a hypothetical oxide or nitride material from any chosen subset of elements in the d-block of the periodic table. Imagine that this material is stable under, at minimum, normal working conditions and is synthesised at the nanoscale with a degree of control over particle size, shape and morphology. This material now incorporates all of the properties associated with nanoscale confinement of all the elements it comprises in strange, wonderful and exciting combinations. Now ponder over the seemingly endless probabilities of the wide range of exotic properties and uses of such a complicated material.

In the field of solid state science and materials chemistry, a fabrication method offering non-stoichiometric multi-mode mixed metal oxide nanomaterials with controlled morphologies appears to be far-fetched. Techniques such as sol-gel synthesis and solvothermal syntheses serve as excellent routes for the formation of oxide nanoparticles with strongly controlled properties[1] but lack the ability to combine materials that will possess advanced functional properties. The Pechini method has become well established for the fabrication of mixed metal oxide nanoparticles with the inconvenience of poor control over particle morphology[2]. It stands to reason that a synthetic technique based on the advances of endorsed nanomaterial syntheses is necessary to achieve the abovementioned targeted materials.

Nanomaterials have been part of recorded human history since as early as 15000 BCE[3]. Early records show of their use in clays and as decorative substances in glasses and paintings[3]. In the half century since Feynman's "There's plenty of room at the bottom" speech,[4] significant progress has been made in the synthesis and applications of nanomaterials and they have become useful in diverse disciplines as stated by Cushing *et al*: automotive technology, medical applications, earth science and chemistry[2], among others. The formation of new nanoparticles has largely been a series of methodical experiments in an attempt to synthesise the target material related to a specific function.

It is believed that the next phase of the nanotechnology evolution is to take currently available nanomaterials (especially those containing metal ions) and combine them in

various ways with differing stoichiometries in the hope of producing advanced materials that possess peculiar properties and that are be able to perform functions that we cannot, for the moment, fathom.

It is with this rationale that the idea of resin-gel synthesis[5] was developed in this study. As a relatively unknown synthetic procedure, resin-gel synthesis has the potential to form multi-mode non-stoichiometric mixed metal oxide nanoparticles. Due to the perceived mechanism of particle formation, it has the ability to form two or more separate products within the same reaction mixture that do not necessarily correspond to the energy minima of the system. To utilize its full potential the mechanism of nanoparticle formation must be fully understood. An understanding of this mechanism was achieved in this study by varying several parameters involved in the synthesis and observing changes to the synthesised products. As a result of the nature of the experimentation, it was concluded that a suitable reference material was required on which to base the results of each experiment.

To this end, titanium dioxide (titania) was selected as the choice of reference material given that it has been extensively studied in the literature and can be synthesised from relatively inexpensive precursors. The transition temperatures from brookite and anatase to rutile have been thoroughly explored. The dependence of these transitions on particle size has also been described[6]. This would assist in the elucidation of the mechanism of particle formation under resin-gel synthesis conditions.

A coordinating polymer is an important tuneable parameter in the resin-gel synthesis method. Polyethylene glycol (PEG) was selected as the polymer for most of the experiments in this study.

The literature review of this thesis will primarily focus on a few synthesis techniques for the formation of oxide nanoparticles, including how they compare and contrast to the currently accepted working theory of rein-gel synthesis. It will also reflect on how titania makes a good reference material on which to model the resin-gel synthesis mode of nanoparticle formation. Additionally, the chemistry of PEG will be discussed. Finally, this literature review will touch on some important materials characterisation techniques that were used in this study.

1.1 Synthetic Descriptions

This section will focus on describing resin-gel synthesis and other, more established methods for the synthesis of mainly oxide nanoparticles. These techniques do not correspond to the exclusive formation of oxides but have been prepared in such a manner to highlight the principles of each technique as it applies to oxide formation, provide some information on the type of particles formed, and compare and contrast these methods with resin-gel synthesis.

1.1.1 Pechini Method

In 1967 Alfred L. Leavitt and William L. Jarvis examined a patent filed at the United States Patent Office about a method to prepare lead and alkaline titanates and niobates in any proportion using resin intermediates[7]. This method was created by Maggio Pechini and forms the foundation for resin-gel synthesis. Pechini developed this technique as a modified sol-gel-combustion synthesis to address the synthesis problems with metals that possess poor hydrolysis equilibria[8]. Using the Pechini method, reactant metals do not require the ability to form suitable hydroxo complexes[8]. Because chelates have the ability to form complexes with a wide range of metals over a large pH range, this technique has the ability to form oxides of vast complexity[8]. According to Roque-Malherbe, this technique is well known for its ability to form homogenous, multi-component metal oxides[8]. This synthesis was initially developed for the preparation of thin films but has been adapted for the formation of powders.

The basic principle of the Pechini method is illustrated conceptually in figure 1.1. It involves the addition of alpha-hydroxycarboxylic acids to form chelates with hydrated oxides and alkoxides of titanium, zirconium and niobium[7]. A stoichiometric amount of a basic metal compound such as lead and alkaline earth metal oxides, hydroxides, alkoxides and carbonates is then added to this mixture. When heated with a polyhydroxy alcohol such as ethylene glycol, the chelates undergo polyesterification[7] and gelation[8]; a process that serves to connect the chelates[7]. The solvent is removed by heating but no crystallisation occurs. Rather, a solid resin containing the metal ion precursors in solid solution is formed[7]. This is due to the manner in which the metal solutions are mixed in the resin intermediate: the metal atoms are bonded through oxygen to organic radicals that comprise the cross-linked network[7]. The segregation of metal ions by the immobilisation of metal complexes through the organic polymer

network ensures compositional homogeneity[8]. This intimate atomic scale metal ion mixing lowers the synthesis temperature and increases the rate of reaction. Following gelation and drying, the solid intermediate is heated to begin pyrolysis. As a result sub-micron pure phase multi-component metal oxides are formed[8].

Since the ratio of different metal oxides in the resin intermediate is uniform in both the solid and liquid phases, by adding known compositions and concentrations of the metal ions, any ratio and combination of metal oxide can be tailored into the resin intermediate[7]. These tuneable ratios are a powerful consequence of the Pechini method and are carried into this adaptation of the Pechini method: resin-gel synthesis. Compounds that are insoluble in the presence of desired metal ion precursors or compounds that are soluble in the liquid but not solid phase are incompatible for use in this synthesis[7] as it may lead to phase separation in the final product.

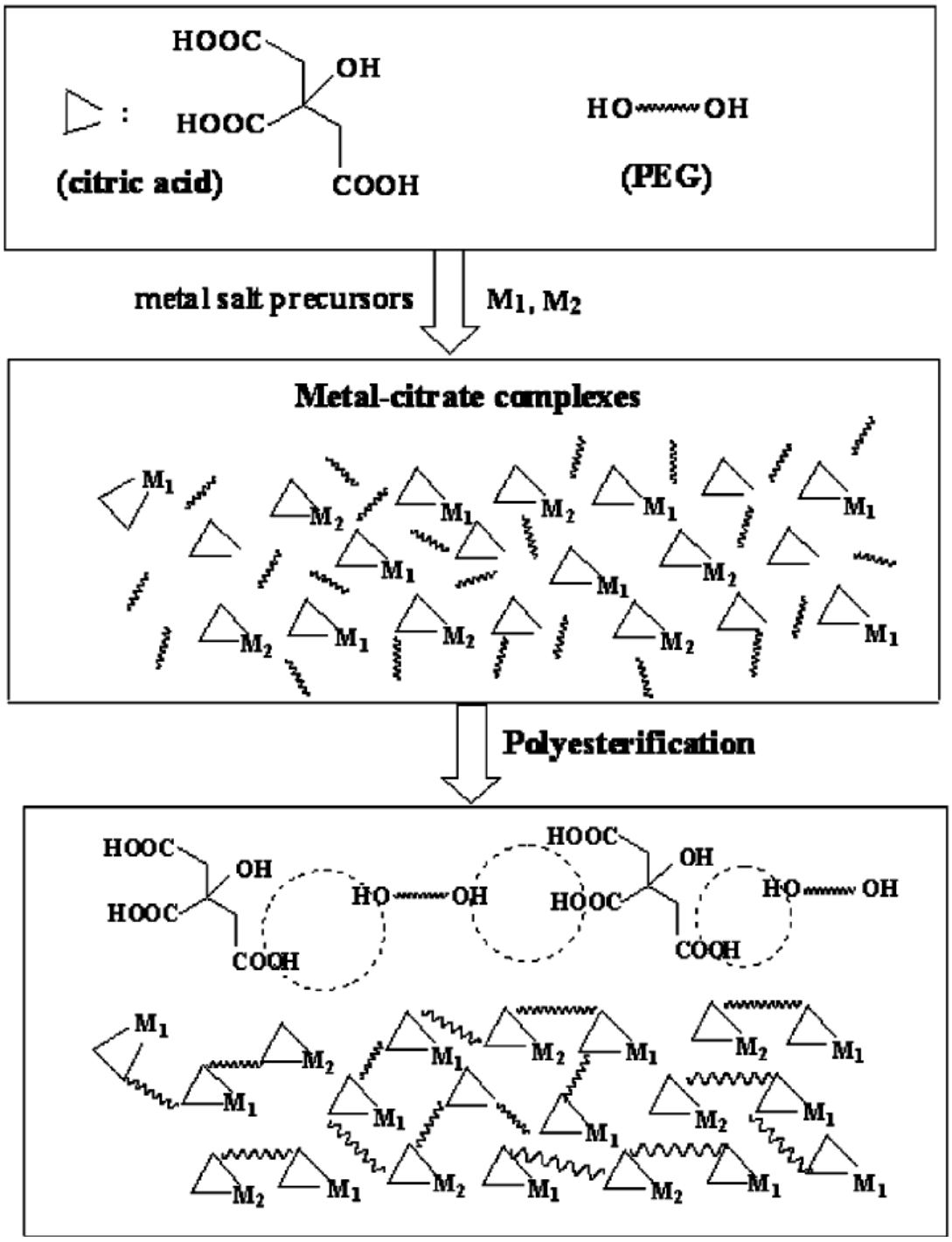

Figure 1.1: Esterification process and network formation during the early stages of the Pechini synthesis[9].

The Pechini method has been used to synthesise a variety of different materials with various metal precursors and a range of different chelating agents such as ehtylenediaminetetraacetate (EDTA)[2]. Table 1.1 shows a representative view of the various materials prepared using the Pechini method. A number of these syntheses deviate from the polyesterification step by the omission of a polyol due to the use of a

polymer based chelating agent that coordinates directly with the metal ions[2]. As such, it is difficult to achieve tailored particle sizes and regular particle morphology[2].

Table 1.1: Various oxides formed using the Pechini method[4].

compd	starting material	chelating agent	polymerization agent	calcination temp (°C)	product size (nm)
$ZnTiO_3$	$Zn(OAc)_2$ $Ti(OBu)_4$	CA	EG	500−1000	18−31
$SrTiO_3$	$Ti(OBu)_4$	CA + PAA	EG	550−700	<500
$YNi_{0.33}Mn_{0.67}O_3$	$Y(NO_3)_3$ $Ni(NO_3)_2$ $Mn(NO_3)_2$	CA	EG	750−800	17
$YBa_2Cu_3O_{7-\delta}$	$Y(NO_3)_3$ $BaCO_3$ $CuCO_3$	CA	EG	920	not stated
$Y_xZr_{1-x}O_{2-x/2}$	$Y(NO_3)_3$ $ZrCl_4$	CA	EG	600−1000	~20
$Zr_xCe_{1-x}O_2$ ($x = 0.35$)	$ZrOCl_2$ $(NH_4)_2Ce(NO_3)_6$	glycine	none	600	13
$BaTiO_3$	$BaCO_3$ $Ti(O^iPr)_4$	CA	EG	700−1100	50−340
$BaCeO_3$	$BaCO_3$ $Ce(NO_3)_3$	CA	EG	800−1000	~100
$LaCoO_3$	$La(NO_3)_3$ $Co(NO_3)_2$	glycine	none	800	35
$RE_xLi_{1-x}NbO_3$ (RE = La, Pr, Sm, Er)	Li_2CO_3 Nb-ammonium complex La_2O_3 $Pr_2(CO_3)_3$ $Sm_2(CO_3)_3$ $Er_2(CO_3)_3$	CA	EG	500−900	40−60
$La_{1.85}Sr_{0.15}CuO_4$	$La(NO_3)_3$ $SrCO_3$ $Cu(NO_3)_2$	CA	EG	900	<1 μm
$Pb_3MgNb_2O_9$	$PbCO_3$ $MgCO_3$ $Nb(OEt)_5$	CA	EG	400−800	~50
$Bi_2Sr_2Ca_{n-1}Cu_nO_{4+2n+\delta}$ ($n = 1, 2, 3$)	$Bi(NO_3)_3$	EDTA	none	700	not stated

The Pechini method inherently offers a double edged sword: having various metal ions stuck in the organic matrix assists in multi-component metal oxide formation however, since the metal ions do not play a role in forming the network (unlike sol-gel syntheses), it is difficult to attain control of particle size, shape and morphology[2]. Post-calcination particles are spherical and no specific particle shapes have been reported[2]. Due to a lack of obtainable data, it was believed that the Pechini method favoured the exclusive formation of oxides[2], however, recent studies have shown that they may be used for the synthesis of nitrides[10].

1.1.2 Sol-Gel Synthesis

The sol-gel synthesis procedure is a well-known technique for the fabrication of metal oxides. Its use dates back to as far as 1846 when Ebelmen hydrolysed $SiCl_4$ and formed complexes with alcohol[2, 11, 12]. Traditionally, sol-gel synthesis is a method for preparing oxide particles of silicon and titanium by the hydrolysis and condensation of alkoxide based precursors[13], although other inorganic metal salts and metal organic compounds may be used[1, 2].

In a review of sol-gel preparation of high temperature oxides, Masato Kakihana defined sol-gel processing as the conversion of a colloidal solution of monomers (sol) into a solid matter (gel) without the formation of a precipitate[14]. This solid matter may or may not form an infinite, rigid, three-dimensional network to be classified as a gel[14]. Depending on a number of factors such as treatments of precursors, heat treatments, etc., sol-gel synthesis may be used to form thin films, aerogels, ceramic fibres and ultrafine and uniform powders,[1, 12]. A sol-gel synthesised sample may be handled using two different routes[14]:

a. Network formation route

   This route is based on the destabilisation of a sol to form a gel. Heat treatments at various temperatures control the formation of glasses or polycrystalline samples.

b. Molecular route

   This route is based on the hydrolysis and polycondensation of organic or inorganic metal ion precursors. The specific reactions pertaining to the hydrolysis and condensation steps vary according to the precursor employed in the synthesis. The general steps involved in the sol-gel process mainly pertain to the use of an alkoxide precursor[2] such as $Si(OR)_4$ and are as follows:

   1. Sol formation

      A precursor such as $SiCl_4$ forms a stable solution of $Si(OR)_4$ when added to an alcohol in the absence of water:

      $$\mathbf{SiCl_4 + ROH \rightarrow Si(OR)_4 + 4HCl} \qquad \mathbf{(1.1)}$$

      In the presence of water, hydrolysis is initiated and the ratio of Si/H_2O governs the number of alkoxy groups that can be substituted:

      $$\mathbf{Si(OR)_4 + \mathit{n}H_2O \rightarrow Si(OR)_{4-n}(OH)_n + \mathit{n}ROH} \qquad \mathbf{(1.2)}$$

      Variation of the number of available water molecules strongly influences the condition of the gel. The degree of OH^- substituted on the parent Si group controls whether the gel will be composed of chains, rings or branched, three-dimensional agglomerates.

2. Gelation

   A polycondensation or polyesterification reaction results in the formation of an alcohol bridged network:

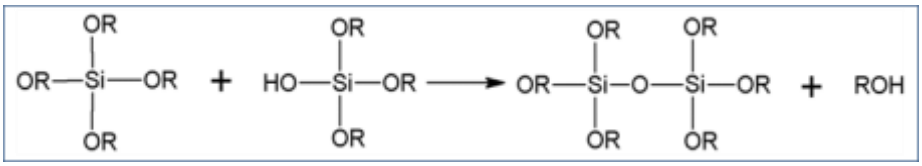

   This condensation reaction allows for the formation of a large three-dimensional network that forms over time governed by the temperature, pH and rate of solvent removal. The gel may be cast into a mould to obtain a desired shape.

3. Syneresis

   The gel is aged. Polycondensation reactions continue to remove liquid from the pores. The resulting effect is strengthening of the gel into a solid.

4. Drying

   Water and other liquids are removed from the pore network by thermal evaporation or under supercritical conditions. This forms either a xerogel or aerogel respectively.

5. Dehydration

   High temperature gel calcination is performed to remove unwanted groups such as surface-bound M-OH. This procedure prevents rehydration and allows the gel to be chemically stable.

6. Densification

   This is the last procedure in the treatment of formed gels. Heating the gel at high temperatures breaks down the pore network and causes the gel density to increase.

Sol-gel processing has been used in the synthesis of nano-oxide materials from various starting materials. The control of particle size is achieved through the combined efforts of precursor concentration variation, reactant feed rate, pH control and calcination temperatures[2]. Although it has been reported[15], the sol-gel synthesis

technique is not popular for the formation of mixed metal oxides. Since metal ions play an active role in comprising the gel network, it is possible to achieve a degree of control of particle size and shape but limits the ability to form mixed metal oxide nanoparticles. Sol-gel syntheses allow for the formation of homogeneous intermediates and pure sample formation. A disadvantage of oxide preparation by sol-gel synthesis is that high temperature heat treatments are necessary to cause surface dehydroxylation to occur[12].

Much work has been done in the formation of shaped titania nanoparticles using the sol-gel method[16, 17, 18, 19, 20, 21]. Sugimoto *et al.*[16 – 20] have shown that varying reaction parameters led to the formation of anatase nanoparticles with controlled sizes and shapes. Amines were used as shape controllers to cap and protect developing anatase particles and inhibit their transformation into rutile. Solution pH was adjusted using $HClO_4$ or NaOH and it was found that nanoparticles change from cuboidal to ellipsoidal above a pH of 11 when triethanolamine was employed in the synthesis. Figure 1.2 shows the effect of various amines on the formation of ellipsoidal particles with different aspect ratios at the same pH. Shape controllers work by adsorbing to specific crystal planes on the developing crystal and this in turn adjusts the growth rate of these planes[16 – 20].

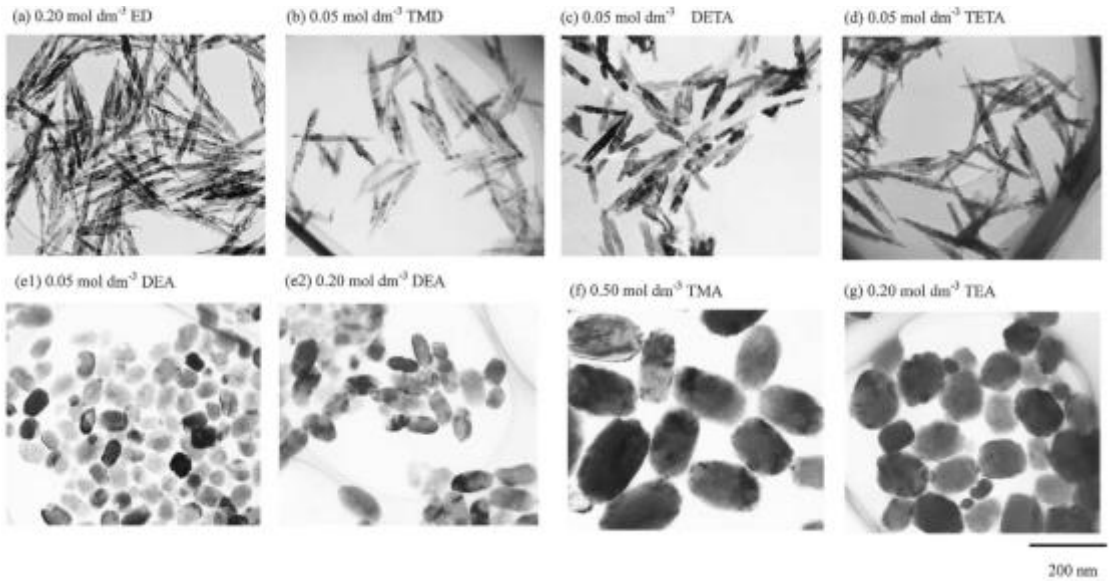

Figure 1.2: Shape and size dependence of anatase nanoparticles on various amine-based shape controllers at constant pH. (a) ethylenediamine, (b) trimethylenediamine, (c) diethylenetriamine, (d) triethylenetetramine, (e) diethylamine, (f) trimethylamine, and (g) triethylamine[21].

1.1.3 Sol Synthesis

As mentioned previously, a disadvantage of oxide formation by sol-gel synthesis is surface bound hydroxyl groups that must be removed by chemical or heat treatments[12]. These hydroxyls affect the properties of some materials such as titanium dioxide: hydroxylated titania provides a weaker reducing surface than dehydroxylated titania surfaces[22]. Surface-bound water and hydroxyl groups also affect sintering rates[12]. According to Niederberger *et al*., sol-gel synthesis struggles to produce phase pure oxide materials with high crystallinity[23]. One method to address these issues is in the form of the sol synthesis. This method is based on the non-hydrolytic equivalent of the sol-gel method for the fabrication of metal oxides[24]. It typically involves the addition of a metal halide to an oxygen donor molecule. This may be in the form of a metal alkoxide or organic ether etc[24]. Reactions typically proceed in the following manner:

$$TiX_4 + Ti(OR)_4 \rightarrow 2TiO_2 + 4RX \quad (1.3)$$

$$TiX_4 + 2ROR \rightarrow TiO_2 + 4RX \quad (1.4)$$

A condensation reaction between the halide and oxygen containing species allows for the formation of Ti-O-Ti bridges with the elimination of alkyl halides. Trentler *et al*. have demonstrated control over average particle size by reactant variation[24]. The sol synthesis has proven useful for the formation of phase pure anatase of uniform size and shape with little agglomeration at synthesis temperatures as low as 40 °C as shown in figure 1.3[23]. Niederberger *et al*. have also demonstrated the ability to tailor particle size within the range of 4 – 8 nm in increments of 0.5 nm using the sol method by decreasing the concentration of the titanium tetrachloride precursor[23].

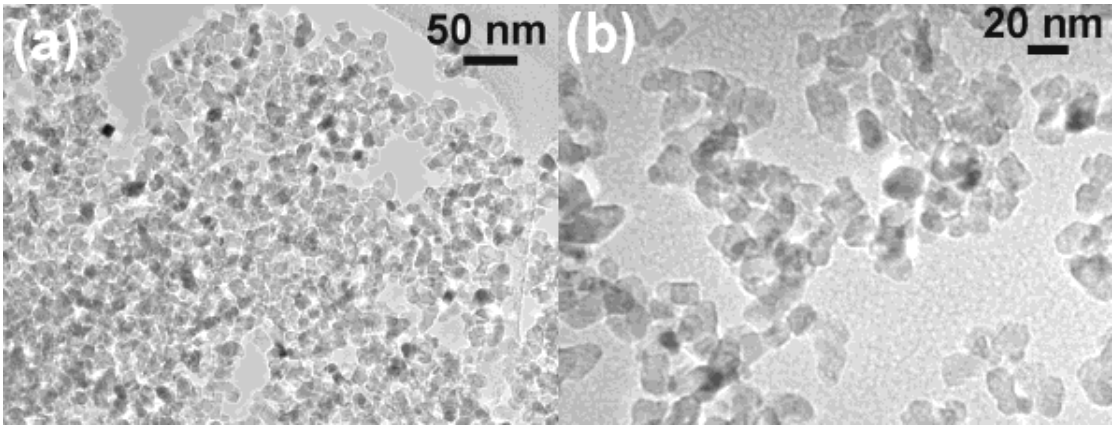

Figure 1.3: TEM micrograph showing exclusive anatase formation. (b) Represents a higher magnification image of (a)[23].

1.1.4 Combustion Synthesis

Formation of solids with controlled structures, compositions and properties by the ceramic route affords the inherent difficulty of requiring atomic and ionic species to diffuse through reactants and products[25]. For the diffusion process to occur, multiple mechanical procedures must be performed at elevated temperatures for a duration of time[25]. Combustion synthesis is a synthetic technique that eliminates diffusion control problems[25].

Combustion synthesis may be defined as an exothermic redox reaction where a fuel is oxidised in the presence of an oxidising agent[25, 26]. As stated by Rajeshwar and de Tacconi[27]: "Combustion synthesis is essentially a controlled explosion carried out in a synthetic context". Oxygen serves as a good oxidising agent due to its high electronegativity and atmospheric abundance[27]. Although combustion synthesis was initially used by humans to produce carbon black for cave paintings, the first literature entry for the use of combustion synthesis for the formation of a ceramic refractory material dates back to 1825 when zirconium metal was heated to produce the oxide form[28]. Nonetheless, the Pechini method – a close cousin of combustion synthesis[27] – is regarded as the first real use of combustion synthesis[7, 26]. Combustion synthesis or Self-Propagating High-Temperature Synthesis (SHS), as it has been defined in the literature, is a simple, swift, low cost, non-capital-intensive and energy efficient manner for the preparation of high purity materials and nanomaterials with unique properties to withstand extreme conditions[25, 26, 27, 28, 29, 30]. This method may also be used for the formation of metastable phases[29]. SHS was developed by Merzhanov, Borovinsky and Skhiro at the Institute for Chemical Physics of the former Union of Soviet Socialist Republics (USSR) Academy of Sciences in the late 1960's and early 1970's after discovering that solid combustion products had formed from solid reactants[26, 28, 29]. According to Lackner *et al.*, the future of nanomaterial synthesis will be developed around SHS[26].

Although ubiquitously referred to as SHS in the solid state, the combustion process may be defined according to the state of matter of the reactants involved[26, 30]:

a. Gas phase combustion synthesis: is known as flame synthesis and is responsible for the formation of non-agglomerated nanomaterials.

b. Liquid phase combustion synthesis: is known as solution combustion synthesis (SCS) and occurs from a metal salt in aqueous solution in the presence of an

organic fuel. A high degree of homogeneity is achieved through molecular mixing[25]. Solid state synthesis tends to produce particles that are more coarse compared with those formed from liquid phase combustion[30].

c. Solid phase combustion synthesis: is known as gasless combustion or solid flame synthesis and may occur as either SHS reactions or Volume Combustion Synthesis (VCS). In the former, combustion propagates through the reaction mixture whereas in the latter, combustion occurs simultaneously throughout the volume of the material or as explosions.

This sub-section will continue to describe gel combustion synthesis – a branch of liquid phase combustion – as synthesis of nanoparticles throughout this study was based on this type of combustion reaction.

Gel combustion synthesis is based on the paradigm that once a reaction has been initiated under the action of heating, a self-sustaining exothermic reaction occurs that produces a powder as a final product[27, 31]. It involves dissolving metal salts with an organic complexing agent followed by solvent evaporation. The resultant homogenous gel is heated to ignition to remove the organic matter[26]. Due to the mechanism of operation, gel combustion characteristically allows for the formation of fine, homogeneous powders, of high purity.[31] The final product usually represents a froth-like voluminous powder[32, 33, 34] as seen in figure 1.4.

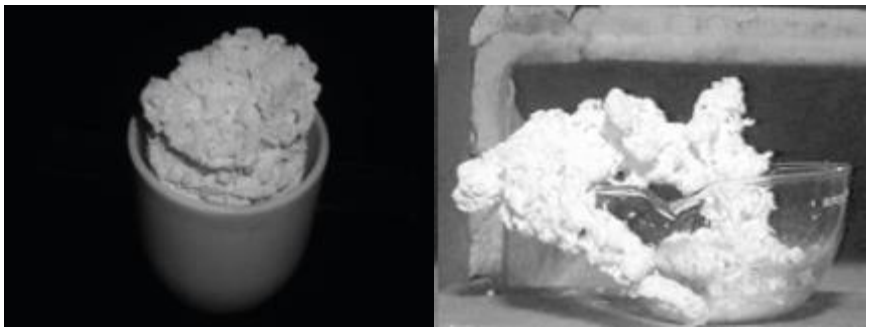

Figure 1.4: Formation of voluminous (left) $Li_4Ti_5O_{12}$ and (right) ZrO_2 by solution combustion[32, 34].

As evidenced in table 1.2, gel combustion produces a wide array of different metal containing oxide nanomaterials. It serves as an excellent alternative to traditional sol-gel processing as it makes use of cheaper, environmentally benign precursors, is energy and time efficient, and allows for doping by ionic substituiton[26, 27, 30, 31].

Table 1.2: Various oxides formed using gel combustion synthesis[31].

Material	Fuel[a]	Particle size	Application
Al_2O_3	U	4 μm	Abrasive
MAl_2O_4 (M = Mn e Zn)	AM + U/CH/ODH/GLI	15–28 nm	Catalyst support
$M/MgAl_2O_4$, M = Fe-Co/Ni	U	10 nm	Catalyst
Co^{+2}/Al_2O_3	U	0.2–0.3 μm	Pigment
$Eu^{+3}/Y_3Al_5O_{12}$	U	60–90 nm	Red phosphorus
$Ce_{1-x}Tb_xMgAl_{11}O_{19}$	CH	10–20 μm	Green phosphorus
M/Al_2O_3, M = Pt, Pd, Ag	U	7–10 nm	Catalyst
Pd/Al_2O_3	U	10–18 nm	Catalyst
CeO_2-ZrO_2	ODH	18 nm	Oxigen storage
	GLI	100 μm	Capasitor
M/CeO_2, M = Pt, Pd, Ag	ODH	1–2 nm	Catalyst
$Ce_{1-x}Pt_xO_2$	CH	4–6 nm	H_2-O_2 combination catalyst
Ni-YSZ, (Ni,Co/Fe/Cu) -YSZ	U	~40 nm	Combustion cell anode (SOFC)
$LaSrFeO_3$	CH/ODH	20–30 nm	SOFC cathode
$LaCrO_3$	U	20 nm	Interconnection for SOFC
$LiCo_{0.5}M_{0.5}O_2$	U	5–10 μm	Lithium battery
$MFe_2O_4/BaFe_{12}O_{19}$	ODH	60–100 nm	Magnetic oxide
$BaTiO_3$	GLI/AC	18–25 nm	Dielectric material
$Pb(Zr,Ti)O_3$	AC	60 nm	Piezoelectric material
ZnO	U	<100 nm	Varistor

[a]*U* urea, *CH* carbohydrazides, *ODH* oxalildihidrazida, *GLI* glycine, *AC* citric acid, *AM* metal acetate

Ionic substitution is a powerful consequence of combustion synthesis for solar energy and environmental remediation applications as it allows for desired products to be chemically modified *in situ* by varying the metal ion and precursor chemistry[27]. The disadvantages are formation of a precipitate before complete gelation has occurred and evaporation or decomposition of the reaction components before the polymer has been completely degraded[26]. These disadvantages are mainly reaction component specific and can be circumvented by careful selection of different precursor materials.

Other, more general disadvantages of using gel combustion synthesis include a lengthy precursor preparation time (several days to weeks), a low yield and the inability of some metals to form complexes with combustible ligands[25].

Although gel combustion is fairly robust with respect to parameter variation, the mechanism of combustion is complex and depending on the system, not always fully understood[31]. To assess feasibility of a combustion reaction to synthesise a desired product, thermodynamic analysis such as calculation of the adiabatic temperature, must be performed[29]. A reaction will only be self-propagating in the solid state if the adiabatic temperature is achieved[35]. This is not a requirement for liquid phase combustion hence reaction and flame temperatures may be significantly lower[35].

Parameters such as type of metal precursor anion[27], type of metal precursor[27], use of metal or non-metal based dopant[27], type of fuel, type of flame, air-fuel-oxidiser ratio, excess oxidiser, generated gasses, ignition temperature, atmospheric conditions, fuel solubility, and the amount of water contained in the gel have the ability to influence the combustion process[31].

A study conducted by Nagaveni *et al*. demonstrated the effect of different fuels on the particle size and photocatalytic activity of formed titania[36]. In the study, glycine (G), hexamethylenetetramine (H), and oxalyldihydrazide (O) were employed as fuels with a titanyl nitrate precursor. It was shown by PXRD and TEM that titania particle size increased in the order: G < H < O. Particle size displayed an inversely proportional relationship to the initial rate of phenol decomposition.

The type of fuel/oxidant mixture used in the synthesis affects the reaction enthalpy and temperature and this in turn affects the crystallite size, surface area and degree of agglomeration of formed products[27, 31]. Gas evolution during combustion dissipates generated heat thereby lowering reaction temperature and inhibiting sintering. The evolution of gas is also responsible for breaking large clusters and creating pores between particles. This has the effect of decreasing particle size and limiting the amount of agglomeration. It has been shown that the mixture mass to combustion-container ratio is critical to allow or deny the combustion process to occur[37].

Atmospheric composition and temperature affect the combustion process and result in incomplete combustion products, metastable phases or a mixture of two or more phases[31].

1.1.5 Resin-Gel Synthesis

Resin-gel synthesis (chronological ordering of the technique demands that the nomenclature exist as Gel-resin synthesis, however, by the English language rule of ablaut reduplication, the technique is correctly called Resin-gel synthesis) is a relatively unknown hypothermal combustion synthesis technique based on the Pechini method for the fabrication of mixed metal oxide nanoparticles[5]. This technique is based on thermodynamic control in the sense that the system is allowed to attain equilibrium and is then disrupted to form nanoparticles. As stated previously, resin-gel synthesis has the potential to become a powerful tool for the fabrication of multi-mode mixed metal oxide nanoparticles with various stoichiometries. This method involves forming a solution of metal ions by addition of a metal compound precursor in an appropriate solvent. A titanium tetrachloride precursor in water will form the following hydroxylated species:

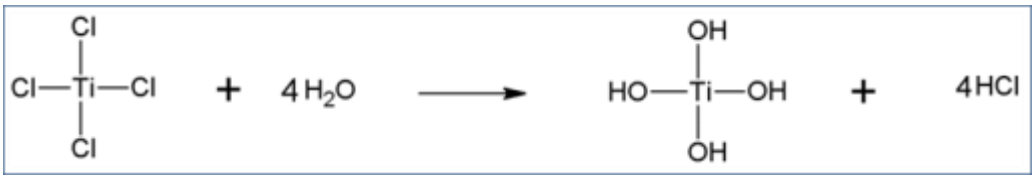

A long chain coordinating polymer (such as polyethylene glycol) is then added to this solution[5]. The mixture is stirred and heated until a homogeneous gel is formed[5]. A hard resin is formed by removing excess solvent through evaporation[5, 38]. It is assumed that the polymer chains coordinate to and immobilise the metal ions therefore preventing segregation and precipitation[38]. Following polymer degradation resulting from sample ignition, the metal ions are forced closer together to form oxide nanoparticles[38]. A facile representation of this process is given in figure 1.5.

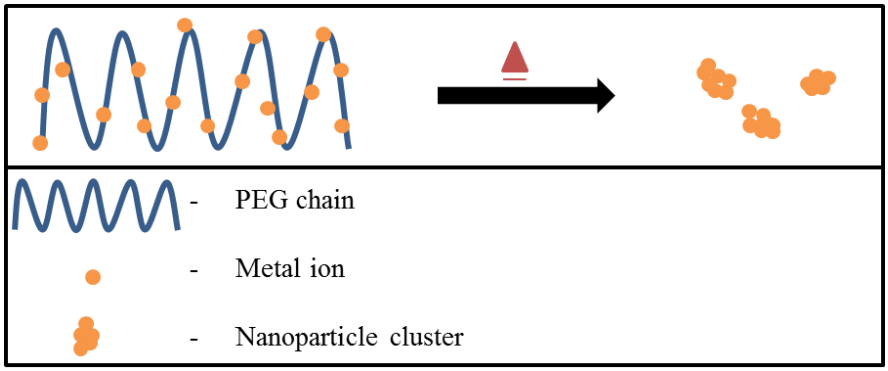

Figure 1.5: Schematic representation of ignition induced polymer degradation leading to nanoparticle formation using resin-gel synthesis.

Resin-gel synthesis and the Pechini method have the capability of forming mixed metal oxide nanoparticles[5]. It differs from the Pechini method in that it eliminates the need for a complexing agent such as citric acid. Since the polymer is added directly to the metal ion solution, no polyesterification occurs making this synthesis more robust than the Pechini method[5]. Using the Pechini method, modest control over particle morphology is achieved by varying the ratio of the alpha-hydroxycarboxylic acid to polyhydroxy alcohol[5]. Because of the number of variables in resin-gel synthesis, adjusting parameters such as polymer chain length has the potential to control the size of formed nanoparticles. In addition, changing the type and length of polymer chains used in the synthesis will serve to adjust the fuel to metal ion ratio resulting in a change in the combustion properties[31]. As discussed previously, this affects particle size, shape, purity, morphology, and phase composition[27, 31].

The resin-gel method has successfully prepared phase pure mixed metal oxides of the form $Cu_xTi_yO_z$ with various stoichiometries in the 5 – 45 nm range[5]. Phase pure material was obtained by adjusting the solvent to polymer ratio and calcining between 300 – 900 °C[5]. Post synthesis calcination was performed at lower temperatures for shorter periods of time as compared with other synthetic procedures[5]. The use of ethanol as a solvent promoted the formation of smaller crystallites compared with water. This is likely due in part to the higher dielectric constant of ethanol[5].

The chemistry governing nanoparticle formation is currently unknown. Critical to harnessing the power of this technique is to understand the mechanism of nanoparticle formation. The effect of various reaction parameters such as choice of solvent and coordinating polymer, polymer chain length, the inclusion of a coordinating organic acid, heating rates, synthesis temperatures, ignition temperatures and choice of metal ion precursor must be investigated in order to begin understanding the mechanism. Once understood, these tuneable parameters will allow the resin-gel method to become a juggernaut in the field of mixed metal oxide synthesis. Although not reported, this technique may theoretically be used for the synthesis of nitrides and carbides provided suitable solvents and polymers are used, and the source of oxygen responsible for oxide formation is diagnosed (i.e.: atmospheric or reaction component based).

1.1.6 Hydrothermal Synthesis

Hydrothermal synthesis is a useful tool for the fabrication of nanostructured materials in the field of electronics, catalysis and ceramics[39, 40]. Due to the number of publications and variations in conditions such as temperature and pressure, it is difficult to provide an exact, all-encompassing definition of the hydrothermal process. An attempt to include the traditional definition and the latest variations of the process parameters has been made by Byrappa and Yoshimura[41]: "Any heterogeneous chemical reaction in the presence of a solvent (whether aqueous or nonaqueous) above room temperature and at pressure greater than 1 atm in a closed system". This definition is considered to be most correct according to Wang *et al*[40]. Strictly, the hydrothermal process is one that occurs in water as the term solvothermal has been used to describe hydrothermal-like reactions using a solvent other than water[1]. Although it has become a well-known and well-studied technique for the fabrication of oxide nanoparticles, this method has its origins in the field of geology.

In the mid 1800's Sir Roderick Murchison, a Scottish geologist, coined the term hydrothermal to describe the method by which water at elevated temperature and pressure causes changes in the earth's crust resulting in the formation of various rocks and minerals[41]. The primary application of the hydrothermal method by geologists was to simulate natural hydrothermal phenomena in a laboratory[42]. In 1845 Emil von Schäfhautl made the first laboratory based use of the hydrothermal method when he successfully grew quartz crystals from precipitated silicic acid in a steam digester[41]. The first successful commercial application of the hydrothermal method was to use NaOH to leach bauxite and obtain Al_2O_3[41]. The aluminium oxide could then be processed into the metallic form. Karl Josef Bayer pioneered this method in 1892 and it is still in use today[41]. In addition, the hydrothermal method is used to extract metal from, as stated by Byrappa and Yoshimura[41]: ilmenite, wolframite, cassiterite, laterites, uranium ores, sulphides of gold, copper, nickel, zinc, arsenic, antimony, etc.

Since the mid 1970's Japanese researchers began a series of experiments to determine other uses for the hydrothermal synthesis technique than for hydrometallurgical and single crystal growth[41]. This is largely due to the discovery of ceramics that can be synthesised under mild conditions of temperature and pressure[42]. Figure 1.6 shows the increase in quantity of published material on the use of hydrothermal synthesis and figure 1.7 illustrates the interdisciplinary nature of the hydrothermal technique.

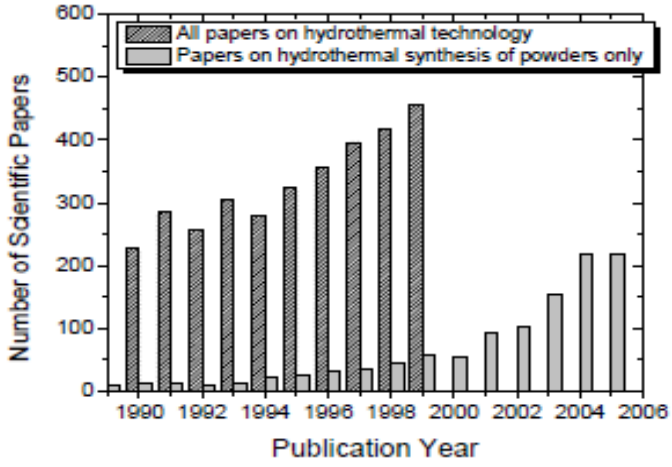

Figure 1.6: Increase in the number of publications on the use of hydrothermal syntheses, especially for powder fabrication[42].

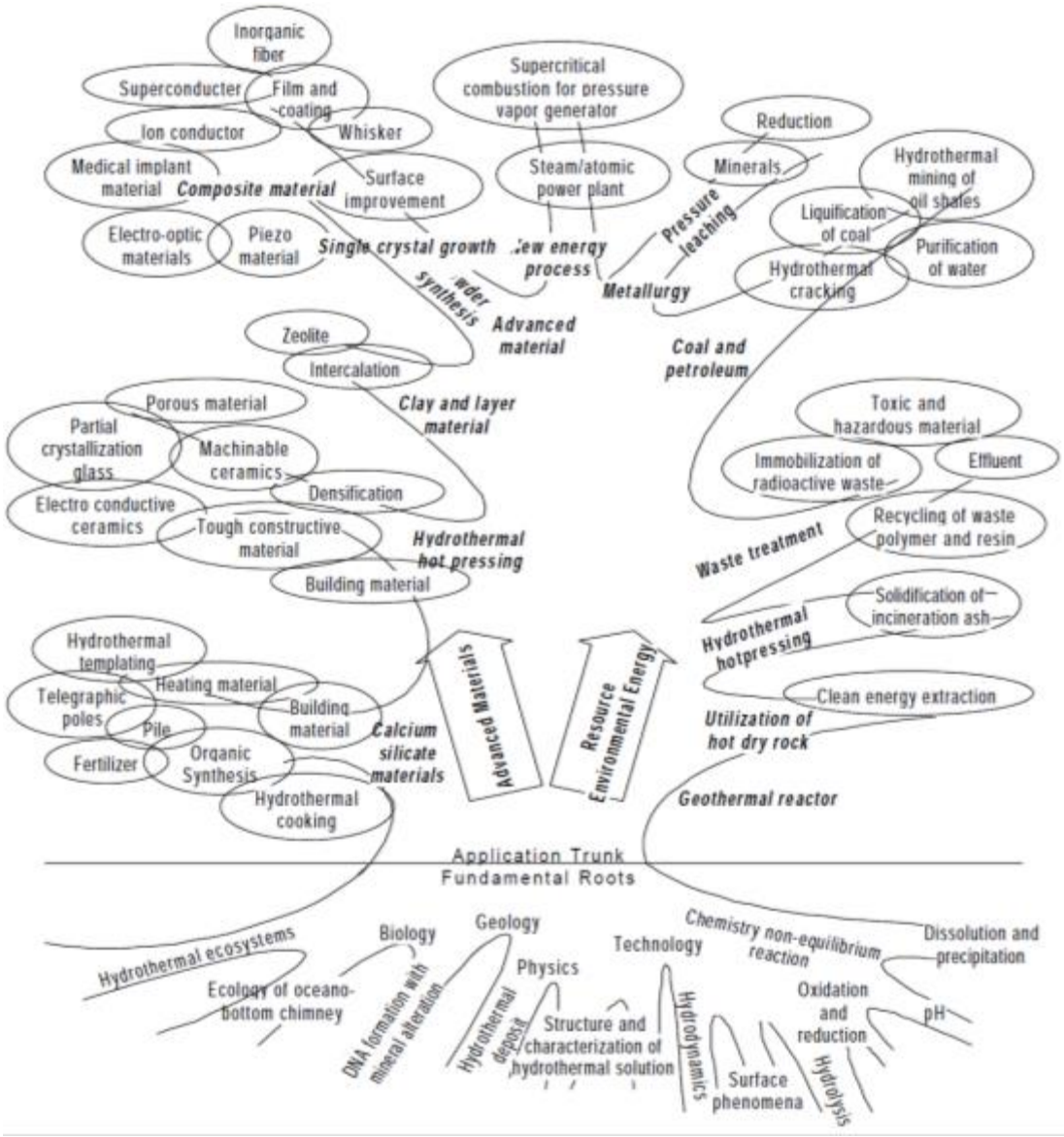

Figure 1.7: Natural and synthetic applications of hydrothermal technology[41].

The traditional synthesis procedure is usually conducted in a Teflon lined steel autoclave under conditions of controlled temperatures and pressures[1, 39, 40, 41]. Reaction conditions can be tuned to obtain subcritical or supercritical water[43]. Surpassing the critical temperature and pressure of water (374 °C and 22.1 MPa respectively) changes properties such as density, solubility and the dielectric constant[44]. The dielectric constant for water is 78 at room temperature[44]. This allows for the dissolution of polar inorganic salts. Increasing temperature and decreasing pressure serves to decrease the dielectric constant favouring dissolution of organic compounds[44]. A dielectric constant below 10 magnifies the effect of the dielectric constant on the reaction rate according to electrostatic theory[44]. Since solubility is lowered, super saturation occurs in accordance with nucleation theory[44]. These combined effects allow water to form an advantageous medium for particle formation[44]. Supercritical solvents have the effect of promoting the formation of multi metal oxides[44]. Tables 1.3 and 1.4 provide a subset of formed oxides from batch and flow hydrothermal syntheses above supercritical conditions.

The hydrothermal synthesis has the advantage of forming products with high degrees of crystallinity, in addition to affording control over particle size, shape, morphology[42] and crystal phase[41, 44]. This is because crystallised powders are precipitated directly from solution which serves to control the rate and uniformity of nucleation, growth and aging[42]. Particles formed under hydrothermal conditions are intrinsically pure due to the process of crystal growth that tends to reject impurities[42]. All ceramics (powders, fibres, single crystals, monolithic ceramic bodies, metal coatings and polymers) can be produced by the hydrothermal method[42]. Other advantages of the hydrothermal technique include high particle surface area or the formation of dense sintered powders, a continuous reaction with short reaction times requiring no milling or calcination and lower energy requirements[41]. The disadvantages are that moderate temperatures (100 – 400 °C)[44] and pressures (3 – 44 MPa)[44] may perturb the desired crystal structure[41]. Some products require high purity seed particles to initiate nucleation[41]. Surface treatments are necessary to remove unreacted reaction matrix components[41]. It differs from the resin-gel method in its inability to form non-stoichiometric multi mixed metal oxide nanoparticles, requires the use of specialised equipment in terms of an autoclave and requires longer synthesis times under mild conditions to obtain a high yield.

Table 1.3: Oxides formed using the hydrothermal batch reaction method above supercritical conditions[44].

Starting Materials	Conditions	Products	Particle size (nm)
$Ti(OC_3H_7)_4$	100–400 °C, 24 h	TiO_2	20–115
$Ti(OC_3H_7)_4$, KOH	350–450 °C, 14–44 MPa, 2–25 h	$K_2Ti_6O_{13}$	12.5–20.1
Nb_2O_5, KOH	200–400 °C, 2–72 h	$K_4Nb_6O_{19}$, $KNbO_3$	7–19
Nb_2O_5, KOH	400 °C, 24 MPa, 2–24 h	$KNbO_3$	15.2–42.1
$Ti(OC_3H_7)_4$, Nb_2O_5, KOH	300–400 °C, 3–25 MPa, 2–24 h	$KTiNbO_5$	1000–3000
Ta_2O_5, KOH	400 °C, 25 MPa, 2–48 h	$KTaO_3$	1000–10000
$Zn(NO_3)_2$, $Mn(NO_3)_2$ SiO_2, KOH	400 °C, 29 MPa, 0.5–1.5 h	Zn_2SiO_4:Mn	Several μm in length (rod-like)
$Fe(NO_3)_39H_2O$, $In(NO_3)_35H_2O$	400 °C, 30 MPa, 4 h	-$(Fe_{1-x}In_x)_2O_3$ c-$(Fe_{1-x}In_x)_2O_3$	30–40
$FeSO_47H_2O$, LiOH	121–388 °C, <33.5 MPa, 10 min–1 h	$LiFePO_4$	1000–2000
$Ce(NO_3)_3$, lignosulfate	250 °C, 10 min	CeO_2	5–20
V_2O_5,$Y(NO_3)_3$, KOH	200–380 °C, 1–10 h	YVO_4	50–200
$Co(NO_3)_26H_2O$, $Fe(NO_3)_39H_2O$, (Li, Na,K)OH	390 °C, pH 12 <6 h	$CoFe_2O_4$	5
$Fe(NO_3)_39H_2O$	394 °C, 5–30 d	Fe_2O_3	16–36
$Y(NO_3)_36H_2O$, $Al(NO_3)_39H_2O$, $Eu(NO_3)_36H_2O$, KOH	400 °C, 30 MPa, 2 h, pH 7–11	$Y_3Al_5O_{12}$ (YAG):Eu	<3000 in length(rod-like)
$Ce(NO_3)_36H_2O$, NaOH	390 °C, pH 7–9 2 h	CeO_2	3–8
Er_2O_3, NaOH	300 °C, 25 MPa 2–22 h	ErOOH, $Er_2OCO_3(OH)_2$	6000–12000 (rod-like)
$MgCl_26H_2O$, $K_4P_2O_7$, HCl	400–450 °C, 25–32 MPa, 5–120 min	$Mg_{3.5}H_2(PO_4)_3$	20–500
$Cu(NO_3)_23H_2O$, $Al(NO_3)_39H_2O$, HCOOH, NaOH	400 °C, 30 MPa, 10–30 min	$CuAlO_2$	2000–5000

Table 1.4 (1): Oxides formed using the hydrothermal flow reaction method above supercritical conditions[44].

Starting Materials	Conditions	Products	Particle size (nm)
TiO_2 sol, KOH	350–420 °C, 30 MPa, 2–3 s	$K_2Ti_6O_{13}$, TiO_2	10 (width), 500–1000 (length)
$ZrO(NO_3)_2$, $ZrO(Ac)_2$	400 °C, 30 MPa, 1.8 s	ZrO_2	6.8–7
$Al(NO_3)_3$	350–400 °C, 25–40 MPa, 2–64 s	γ-AlOOH	63–473
$Al(NO_3)_3$	400–500 °C, 25–35 MPa, 0.063–3 s	γ-AlOOH, γ-Al_2O_3	3.9–6.4
$Ba(OH)_2$, TiO_2 sol	300–420 °C, 30 MPa, 0.1–40 s	$BaTiO_3$	13–48.4
$Ba(OH)_2$, TiO_2 sol	300–420 °C, 20–40 MPa, 0.7–5.1 s	Tetragonal/ Cubic $BaTiO_3$	10–100
$Ba(OH)_2$, TiO_2 sol	400 °C, 30 MPa, 7 ms–2 s	Tetragonal/ Cubic $BaTiO_3$	9–32
$Ca(NO_3)_2$, $Sr(NO_3)_2$, $Fe(NO_3)_3$, TiO_2 sol	300–400 °C, 30 MPa, 10 s	$Ca_{0.8}Sr_{0.2}Ti_{1x}Fe_xO_{3-}$	20–27
$ZrO(NO_3)_2$, $Y(NO_3)_3$	300–400 °C, 30 MPa, 0.17–0.35 s	YSZ	4–6
$Zn(CH_3CO_2)_2$, H_2O_2	400 °C, 245atm, 8.9–16.3 s	ZnO	39–320
$Fe(NO_3)_3$, $Co(NO_3)_2$, NaOH	475–675K, 25 MPa, 11–23 s	$CoFe_2O_4$	13–23
$Al(NO_3)_3$ $Y(NO_3)_3$ $Tb(NO_3)_3$, KOH	400 °C, 30 MPa, 2.5 s	$(Y_{2.7}Tb_{0.3})Al_5O_{12}$	14–152
$Zn(NO_3)_26H_2O$	390 °C, 30MPa, 22 s	ZnO	<10000 (whisker)
$Zn(NO_3)_26H_2O$, LiOH	390 °C, 30MPa, 0.7 s	ZnO	16–57
$Zn(NO_3)_26H_2O$, LiOH	400 °C, 30MPa, 0.03 s	ZnO(nanorod)	38 (width), 230 (length)
$Ba(OiPr)_2$, $Ti(OiPr)_4$, EtOH	330–380 °C, 16 MPa, 119–166 s	Cubic $BaTiO_3$	15–36
$(Ba,Sr)(OiPr)_2$, Ti(OiPr), EtOH	380 °C, 26 MPa, 119–166 s	Cubic $BaTiO_3$	<50
$Mn(NO_3)_26H_2O$, LiOH, $LiNO_3$	400–420 °C, 30 MPa, 10–40 s	$LiMn_2O_4$	<100

Table 1.4 (2): Oxides formed using the hydrothermal flow reaction method above supercritical conditions[44].

Starting Materials	Conditions	Products	Particle Size (nm)
$SnCl_2$ $InCl_3$	350–380 °C, 30 MPa	Cubic/Tetragonal In_2O_3, SnO_2, ITO	<10
Al(AcAc)/$Al(NO_3)_3$, Y acetate/$Y(NO_3)_3$	260–385 °C, 24 MPa	Cubic $Y_2Al_5O_{12}$	<150
$Al(NO_3)_3$, $Y(NO_3)_3$, $Eu(NO_3)_3$, KOH	400 °C, 28 MPa	Cubic $(Y,Eu)_2Al_5O_{12}$	<100
$La(NO_3)_3$, $Ni(NO_3)_2$, KOH	400°C, 24 MPa	Rhombohedral $La_{n+1}Ni_nO_{3n+1}$	<430
$Zr(CH_3COO)_4$/ $Zr(CH_3CH_2O)$	300–450 °C, 10–45 MPa	Tetragonal/ monoclinic ZrO_2	<10
$SnCl_2$	385–415 °C, 30 MPa	Tetragonal/ SnO_2	<10
$Al(NO_3)_3$, KOH	400 °C, 30–40 MPa	γ-AlOOH, γ-Al_2O_3	<20
$Fe(NO_3)_3$, PVA	487–648 K, 21.7–23 MPa	α-Fe_2O_3	<23
$FeSO_4$, H_3PO_4, LiOH	573–658 K	Orthorhombic $LiFePO_4$	<130
TiO_2 sol, $Ba(OH)_2$	400 °C, 30 MPa	Tetragonal $BaTiO_3$	<20
$ZrO(NO_3)_2$, $Ba(OH)_2$/ $Ba(NO_3)_2$/$Ba(CH_3CO_2)_2$, NaOH	450–485 °C, 30 MPa	Cubic $BaZrO_3$	<100
$Fe(NO_3)_3$, $Ni(NO_3)_2$, $Cu(NO_3)_2$, $Zn(NO_3)_2$, KOH	400 °C, 30 MPa	Rhombohedral/Cubic, Tetragonal (Ni, Cu,Zn)Fe_2O_4	<22
$Ca(NO_3)_2$, $Mg(NO_3)_2$, $(NH_4)_2HPO_4$	400 °C, 30 MPa	$Ca_{10-x}Mg_x(PO_4)_6(OH)_2$/ $Ca_{3-y}Mg_y(HPO_4)_2$ $(PO_4)_{2-2x/3}$	<80
$ZrO(NO_3)_2$, $Ce(NO_3)_3$, NH_4OH	Supercritical Conditions	Cubic/Tetragonal $Ce_xZr_{1-x}O_2$	7–16
$Co(NO_3)_2$, KOH, $Ni(NO_3)_2$/ $Ni(CH_3CO_2)_2H_2O_2$	90–310 °C, 24.1 MPa	Hexagonal, Cubic $Ni(OH)_2Co_xNi_{1-x}(OH)_2$, $NiCo_2O_4$	<100
$Zn(NO_3)_2$, KOH, hexylamine	400 °C, 30 MPa	Hexagonal ZnO	<150×600 (rod)
$Ce(NO_3)_3$, Hexanoic acid	250 °C, 25 MPa	Cubic CeO_2	<60

The physical chemistry describing crystal growth under hydrothermal conditions consists of understanding the physico-chemical and hydrodynamic principles, phase formations, solutions, solubility, phase equilibria, thermodynamics and kinetics of the reaction system[41]. Understanding the physical chemistry processes occurring in the aqueous solution is critical to manipulating the crystallisation process[42]. Since the hydrothermal method is not the primary synthetic technique in this study, it shall only be discussed further in its capacity to form titania nanoparticles.

The hydrothermal technique has become one of the best methods for the preparation of titania nanoparticles due to its ability to obtain highly homogeneous, crystalline material with good control over particle size and shape, from relatively low reaction temperatures (~ 150 °C)[41]. Additionally, particle agglomeration and size distribution is limited[41]. Mild condition titania syntheses typically occur in small, Teflon lined autoclaves at temperatures lower than 200 °C and pressures lower than 10 MPa[40, 41]. Kasuga *et al.* conducted the initial study on the use of hydrothermal synthesis for the formation of anatase nanotubes from sol-gel synthesis derived fine titania powders[45]. In the study, titania powder (< 45 μm) was introduced into a Teflon lined autoclave with 20 ml of NaOH at concentrations of 2.5, 5, 10, or 20 M. The vessel was kept at 20, 60 or 110 °C for 20 hours. Formed products were washed with 0.1 M HCl and distilled water, and separated from the solution by centrifugation. Samples prepared with 10 M NaOH at 110 °C produced powders with a specific surface area of ~ 400 m^2/g. This treatment resulted in the formation of anatase nanotubes that were ~ 100 nm long and ~ 8 nm wide. TiO_2 morphology can be tuned by adjusting the source of titanium dioxide (i.e.: seed crystals or a titanium ion precursor), the concentration of the base, reaction temperature and duration, acid washing the products[40]. Tailoring these parameters allows for the formation of nanotubes, nanoribbons, and nanowires. Adjusting the solution pH has the effect of changing the charge state and adsorption properties of the surfactant on the TiO_2 surface[40]. As a result, TiO_2 nanosheets, nanorods, nanotubes, and nanoflowers may be obtained[40].

The use of an organic based solvent such as alcohol or toluene[46] in place of water promotes the formation of smaller TiO_2 crystals as a result of a lower dielectric constant reducing the solubility of TiO_2. Additionally, an organic solvent allows for the formation of products that are free from foreign anions owing to the low relative permittivity of the solvent[46].

1.2 Description of TiO_2

The purpose of this study was to understand the mechanism by which resin-gel synthesis forms nanoparticles. Therefore, a suitable material was required to serve as a reference material on which to understand the effects of varying parameters in the synthetic procedure. The desired material had to be well understood and well-studied. Furthermore, the material had to be cheap to produce, environmentally benign and non-toxic in the bulk and sub-micron phase. It is with these considerations that titanium dioxide was selected as a suitable reference material on which to understand the resin-gel synthesis technique. The following sub-sections will describe the origin, discovery, crystallography, surface energetics, stability, phase transformations, transformation mechanisms, and electronic bonding structure of nanoscale titanium dioxide to better understand the properties of this material and how it relates to parameter variation during resin-gel synthesis.

1.2.1 Origin and Discovery

"If you wish to make an apple pie from scratch, you must first invent the universe" – Carl Sagan.

The chain of events that led to the origin of titanium dioxide began ~ 13.82 billion years ago when the universe had begun according to the prevailing big bang theory[47]. Approximately 10^{-34} seconds after the start of the big bang, the entire spatial extent of the universe had expanded by a factor of 10^{30} from smaller than the size of a proton[48]. A temperature of ~ 10^{27} K allowed for the formation of photons, leptons and quarks but not neutrons or protons[48]. After ~ 10^{-4} seconds, quarks had combined to form protons and neutrons due to universe expansion induced cooling[48]. Further cooling reduced the kinetic energy of protons and neutrons[49] to the extent that any collisions allowed these particles to adhere under the action of the strong force. Hence, low mass nuclei were formed: ^{2}He, ^{3}He, ^{4}He, and ^{4}Li[48]. Further cooling allowed electrons to bind to nuclei under the electromagnetic force[49]. Gravitational condensation of clouds of H and He atoms gave rise to high temperatures and densities within the clouds[49]. Consequently, nuclear fusion reactions occurred inside stars to form the light elements (up to Z = 26)[49]. The first formed stars were too hot to support the formation of solid crystals[50]. Following supernovae millions of years after the big bang, the remains cooled and condensed into minerals[50]. It is believed that solar flares caused the initially formed minerals to melt and mix to form new minerals on primitive

earth[50]. Heat, pressure, tectonic activity and water would have then transformed these minerals into different forms and resulted in the formation of new minerals[50]. According to Hazen there is a co-evolutionary relationship between biological processes and mineral diversity on earth[51]. The combination of these events would have led to the formation of rutile, anatase and brookite minerals.

Menacchanine was discovered in 1791 after the English chemist, William Gregor, analysed a sample of black sand in Menaccan, Cornwall[51]. In 1975, German chemist, Martin Heinrich Klaproth discovered the same material in Hungary[51, 52]. Klaproth realised the discovery was of a metal oxide and named the new metal titanium[51] after the Titans of Greek Mythology. Titanium dioxide was found in rocks obtained during the Apollo 17 lunar mission and is present in the spectra of M-type stars[52].

1.2.2 Crystallography

TiO_2 occurs naturally in three different polymorphs: rutile, anatase and brookite[53]. Three synthetic, metastable phases were also discovered: TiO_2 (B)[54], TiO_2 (H)[55], and TiO_2 (R)[56]. Five high pressure forms of TiO_2 exist[57]: columbite, baddeleyite, fluorite, pyrite and cotunnite. These structures are obtained by applying varying amounts of pressure on either anatase or rutile. The crystalline properties of all 11 polymorphs of titania, grouped according to naturally occurring, metastable and high pressure phases, are represented in tables 1.5, 1.6, and 1.7 respectively. Figures 1.8 – 1.10 illustrate the structures of all 11 polymorphs, grouped appropriately. Owing to this study focussing on rutile and anatase formation (and because brookite readily converts to rutile and anatase) these two polymorphs shall be discussed further.

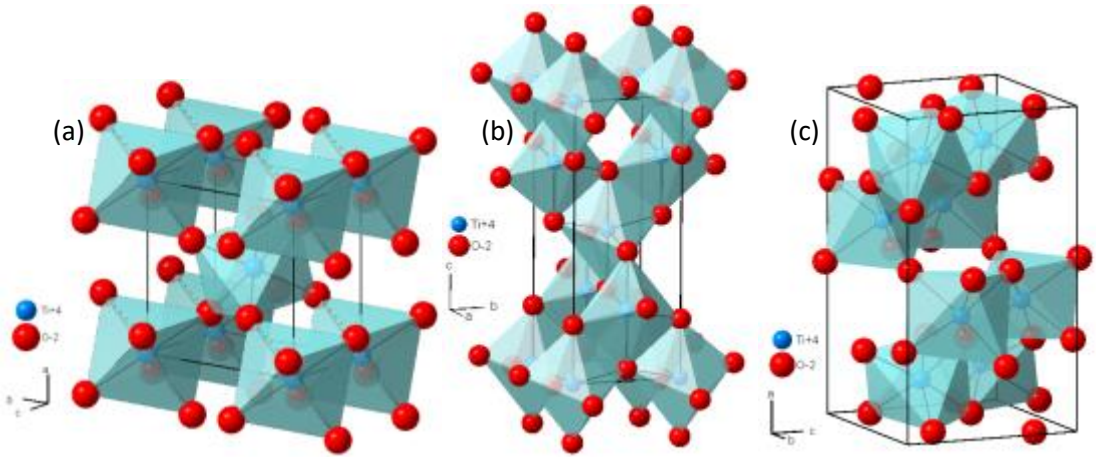

Figure 1.8: Unit cells of (a) rutile, (b) anatase and (c) brookite. Each octahedron has a titanium (IV) ion at the centre and oxygen atoms at each apex[58].

Table 1.5: Crystallography and physical properties of naturally occurring TiO_2.

		Rutile	Anatase	Brookite
Number of atoms in unit cell		2	4	8
Crystal system		Tetragonal	Tetragonal	Orthorhombic
Space group		$P4_2/mnm$	$I4_1/amd$	$Pbca$
Lattice Parameters	**a (Å)**	4.5937	3.785	5.456
	b (Å)	4.5937	3.785	9.182
	c (Å)	2.9618	9.514	5.143
Unit Cell Volume (Å)		62.5001	136.300	257.649
$\rho_{(bulk)}$ **(g.cm^{-3})**		4.250	3.894	4.23
Relative Abundance		Most	Intermediate	Least
Relative Octahedron Distortion		Least	Most	Incomparable*
Relative Ti-Ti bond distance		Shorter	Longer	Incomparable*
Relative Ti-O bond length		Longer	Shorter	Incomparable*
Mohs Hardness		6.2	5.8	5.8
$\Delta H_f°$ (298.15 K) (kJ.mol^{-1})		-944.0 $\pm$ 0.8	-224.6	-941.8
S° (298.15 K) (J.K^{-1}.mol^{-1})		50.62 $\pm$ 0.3	49.92	N/A
Madelung Constant		2.408	2.400	N/A
Index of Refraction (n_α, n_β, n_γ)		2.609, 2.900	2.488, 2.561	2.583, 2.584, 2.700
References		(52, 59)	(52, 58, 59)	(52, 58)

*Brookite forms part of a different crystal system

Table 1.6: Crystallography of metastable phases of TiO_2.

		TiO_2 (B)	TiO_2 (H) Hollandite-type	TiO_2 (R) Ramsdellite-type
Source		Hydrolysis of $K_2Ti_4O_9$	Topotactic oxidation of K_xTiO_2 (x ~ 0.25)	Topotactic oxidation of $Li_{0.5}TiO_2$
Number of atoms in unit cell		4	8	4
Crystal system		Monoclinic	Tetragonal	Orthorhombic
Space group		N/A	I4/*m*	P*bnm*
Lattice Parameters	**a (Å)**	12.146	10.161 (3)	4.9022 (14)
	b (Å)	3.862	10.161 (3)	9.4590 (12)
	c (Å)	6.451	2.970 (1)	2.9585 (14)
	β	106.8°	N/A	N/A
Unit Cell Volume (Å)		289.7	306.640	137.18 (7)
References		(54)	(55)	(56)

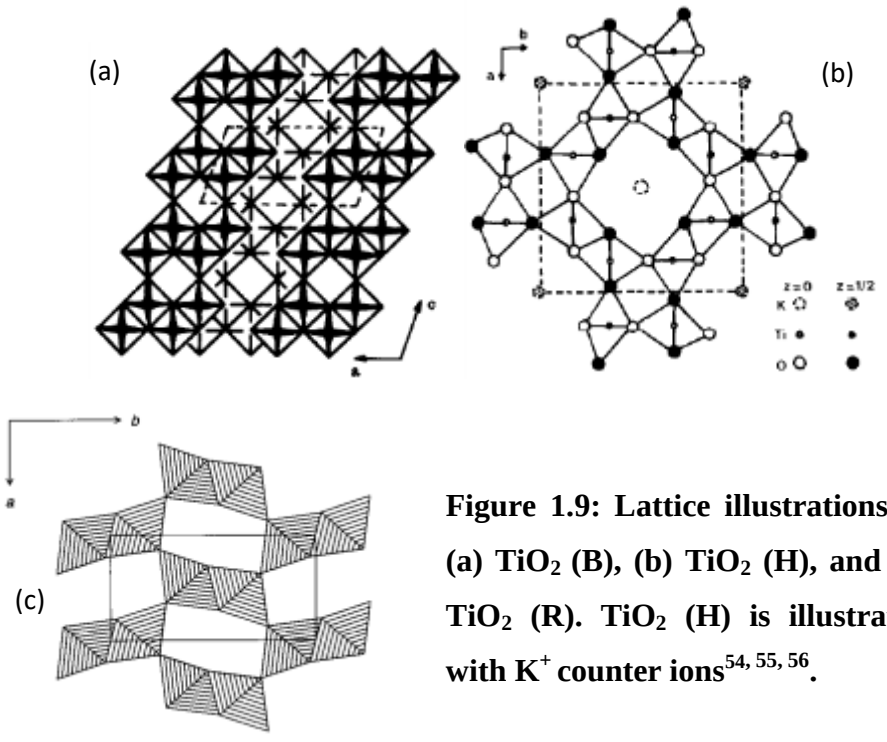

Figure 1.9: Lattice illustrations of (a) TiO_2 (B), (b) TiO_2 (H), and (c) TiO_2 (R). TiO_2 (H) is illustrated with K^+ counter ions[54, 55, 56].

Table 1.7: Crystallography of high pressure phases of TiO_2.

		Columbite	Baddeleyite	Fluorite	Pyrite	Cotunnite
Source (GPa)		4 – 10	20	60	60	> 60
Number of atoms in unit cell		4	4	1	Not Available	4
Crystal system		Orthorhombic	Monoclinic	Cubic	Cubic	Orthorhombic
Space group		P*bcn*	$P2_1/c$	F*m*3*m*	$Pa\overline{3}$	P*nma*
Lattice Parameters	**a(Å)**	4.541	4.662	Not Available	Not Available	5.136
	b(Å)	5.493	4.969	Not Available	Not Available	2.989
	c(Å)	4.906	4.911	Not Available	Not Available	5.966
	β	Not Available	99.4°	Not Available	Not Available	Not Available
Unit Cell Volume (Å)		122.374	112.2	Not Available	Not Available	91.587
References		(57)	(57)	(57)	(57)	(57)

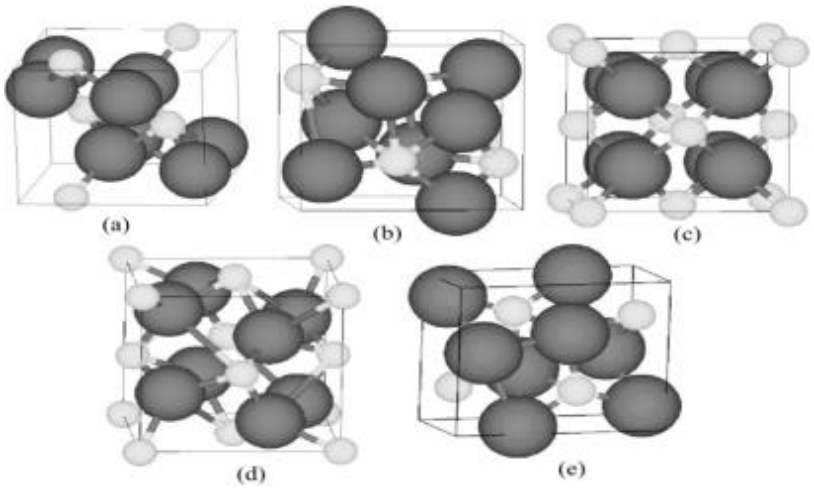

Figure 1.10: Unit cells of (a) columbite, (b) baddeleyite, (c) fluorite, (d) pyrite, and (f) cotunnite. O and Ti ions are represented by large and small spheres respectively[57].

TiO_2 is described as a covalent oxide[53, 60]. Rutile and anatase polymorphs may be described as chains of corner or edge sharing TiO_6 octahedra[61]. Each octahedron contains a Ti^{4+} ion at the centre coordinated to two axial and four equatorial O^{2-} ions[61]. Each O^{2-} ion is coordinated to three Ti^{4+} ions. The polymorphs differ by the degree of distortion and orientation of the octahedra[61]. Rutile can be considered as a tetragonal version of the $CaCl_2$ orthorhombic structure[59]. Each octahedron shares two edges, forming chains along [0 0 1] and octahedra chains are linked to each other by sharing vertices[59]. Anatase octahedra share four edges forming zigzag chains along [2 2 1][59]. In the rutile structure, each octahedron is in contact with ten neighbouring octahedra (two edge sharing and eight corner sharing) in comparison to anatase where each octahedron is in contact with eight neighbouring octahedra (four edge and four corner sharing)[61]. The octahedral in rutile are less distorted than those in anatase[61]. The octahedra of both rutile and anatase exhibit two long and four short Ti-O bonds[59]. In anatase, the Ti-Ti bond separation is longer and the Ti-O bond lengths are shorter than rutile[61]. The difference in density between the two polymorphs is due to the differences between the two lattice structures[61]. It has been shown that distortions in the lattice causes the lattice geometry to change[1].

1.2.3 Surface Energetics

For relaxed surfaces, Ramamoorthy *et al.,* found that on the basis of dangling bonds and according to self-consistent *ab initio* calculations, rutile surfaces were ordered in terms of increasing surface energy in the following way: (1 1 0) < (1 0 0) < (0 1 1) < (0 0 1)[62]. Oliver *et al.,* used atomistic simulations based on equilibrium and pseudo-kinetic methodologies to determine the energetics of rutile surfaces. The four expressed surfaces in the relaxed equilibrium morphology of rutile appear in the following order of increasing energy: {1 1 0} < {0 1 1} < {2 2 1} < {1 0 0}[63]. Thus both methods establish the rutile {1 1 0} surface as being the most stable[62, 63, 64]. Since the {2 2 1} and {1 1 1} rutile surfaces are both first-order dipyramids of the tetragonal system, and since the faces are present with small surface areas, the two surfaces would appear to be similar[63]. The rutile {1 1 0} surface contained five and six coordinate species[63]. Table 1.8 (adapted from reference 64) compares the surface energy of various relaxed and unrelaxed rutile surfaces.

Lazzeri *et al.,* used a*b initio* density functional theory (DFT) calculations based on the Perdew-Burke-Ernzerhof (PBE) approximation to determine the surface energetics of

anatase[65, 66]. Surfaces containing fourfold coordinated Ti atoms were found to be more energetic than surfaces containing fivefold coordinated Ti atoms[65]. For relaxed anatase, surfaces were ordered in terms of increasing surface energy in the following way: (1 0 1) < (1 0 0) < (0 0 1) < (1 1 0)[65, 66]. Atomistic modelling used by Oliver *at al.,* showed that the two expressed surfaces in the relaxed equilibrium morphology of anatase appear in the following order of increasing energy: {0 0 1} < {0 1 1}[63]. The anatase {0 0 1} surface contained five coordinate species[63].

Table 1.8: Surface energetics of different rutile surfaces[63].

{hkl}	**Area (Å)**	**D_{hkl} (Å)**	**$E_{unrelaxed}$ ($J.m^{-2}$)**	**$E_{relaxed}$ ($J.m^{-2}$)**
{1 1 0}*	19.12	3.18	2.05	1.78
{0 1 1}*	24.30	2.50	2.06	1.85
{2 2 1a}*	43.24	1.4	3.83	2.02
{1 0 0}*	13.52	2.25	2.40	2.08
{1 2 1}	36.35	1.67	2.67	2.16
{0 2 1}	33.75	0.90	2.85	2.28
{0 0 1}	20.19	1.50	2.81	2.40
{1 2 2b}	50.44	1.20	4.01	2.52
{1 1 1b}	27.81	2.18	3.95	2.60
{1 2 0b}	30.23	2.01	6.13	2.62
{1 2 2a}	50.44	1.20	4.01	2.82
{1 1 1a}	27.81	2.18	3.95	2.91
{0 1 2}	42.58	0.72	6.06	2.95
{2 2 1b}	43.24	1.4	3.83	3.29
{1 2 0a}	30.23	2.01	6.13	3.66
{1 1 2}	44.68	1.36	4.88	4.01

* Rows indicate energetics of surfaces expressed in the relaxed equilibrium morphology of rutile.

The surface energies of various relaxed and unrelaxed anatase surfaces are given in table 1.9 (adapted from reference 64). From this table it can be seen that the surface energy of anatase {0 0 1} is lower than the surface energy of any rutile surface (table 1.8). Figure 1.11 compares the equilibrium morphology of anatase and rutile as determined by Oliver *et al*., with the equilibrium shape of a macroscopic rutile and anatase crystal based on a Wulff construction as determined by Ramamoorthy *et al.* and Lazzeri *et al.* respectively. Figure 1.12 shows the top and side views of the {1 1 0} and {0 1 1} surfaces of rutile and the {0 0 1} and {0 1 1} surfaces of anatase.

Table 1.9: Surface energetics of different anatase surfaces[63].

{hkl}	**Area (Å)**	**D_{hkl} (Å)**	**$E_{unrelaxed}$ ($J.m^{-2}$)**	**$E_{relaxed}$ ($J.m^{-2}$)**
{0 0 1}*	14.22	2.39	1.28	1.28
{0 1 1a}*	38.79	3.51	1.60	1.40
{1 0 0}	36.09	1.89	2.26	1.68
{1 1 2}	58.44	2.33	2.05	1.81
{0 2 1b}	73.56	0.93	2.36	1.81
{1 2 1b}	81.94	1.66	2.42	1.94
{1 2 0}	80.69	0.84	2.54	1.98
{1 2 2}	85.56	0.79	4.98	2.05
{0 1 1b}	38.79	3.51	2.71	2.18
{1 1 0}	51.03	1.34	2.65	2.19
{0 1 2}	45.94	1.48	4.76	2.42
{2 2 1}	103.05	0.33	4.89	2.69
{1 1 1}	52.98	0.64	5.75	2.87
{0 2 1a}	73.56	0.93	5.91	2.97
{1 2 1a}	81.94	1.66	4.96	3.05

* Rows indicate energetics of surfaces expressed in the relaxed equilibrium morphology of anatase.

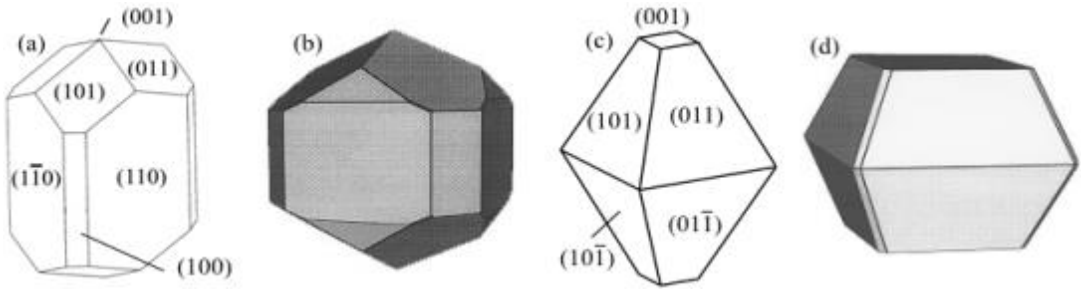

Figure 1.11: Equilibrium shapes of (a – b) rutile and (c – d) anatase crystals[62, 63, 65]. Ramamoorthy *et al.*, and Lazzeri *et al.*, generated (a) and (c) respectively[62, 65]. Oliver *et al.*, generated (b) and (d) using the rutile {1 1 0}, {0 1 1}, {2 2 1} and {1 0 0} faces, and the anatase {0 0 1} and {0 1 1} faces respectively[63].

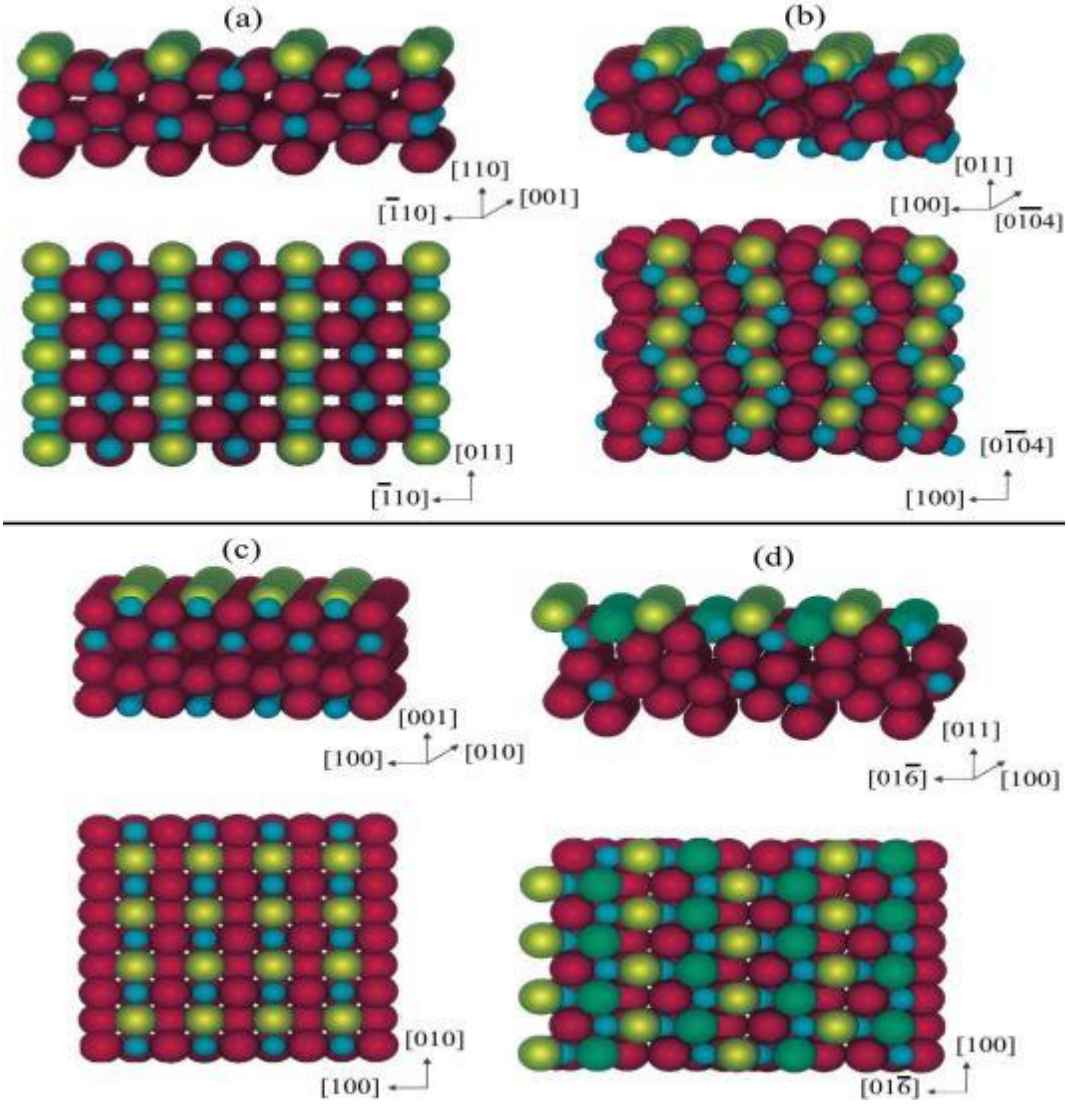

Figure 1.12: Side and top views of relaxed surfaces of rutile (a) {1 1 0} and (b) {0 1 1}, and anatase (c) {0 0 1} and (d) {0 1 1} surfaces. Surface oxygen's are yellow, bulk oxygen's red, second layer oxygen ions green, and titanium ions are blue[63].

1.2.4 Stability and Phase Transformations

Rutile is considered to be the most stable phase under ambient conditions in the bulk phase[53]. At the nanoscale, due to small differences in surface enthalpies, a strong correlation exists between the size of particles and the phase that presents with greatest stability[53, 67]. Zhang and Banfield analysed phase stability at the nanoscale by considering the contribution to surface free energy, from surface enthalpy data, of all three polymorphs[68]. Their model showed that each phase of titania is most thermodynamically stable at different particle sizes evident in figure 1.13 (a). For particles less than 11 nm in size, anatase is the most stable phase; for particles between 11 and 35 nm, brookite is the most stable; and for particles greater than 35 nm, rutile presents with greatest stability[68]. From figure 1.13 (a) it can be seen that anatase becomes more stable than rutile at ~ 16 nm. The transformation dependence on particle size will be discussed later. Ranade *et al*. used high temperature oxide melt drop solution calorimetry to calculate the surface enthalpies of rutile, brookite and anatase to be 2.2 $\pm$ 0.2 J/m^2, 1.0 $\pm$ 0.2 J/m^2, and 0.4 $\pm$ 0.1 J/m^2 respectively[67]. The uncertainty in the brookite surface enthalpy value is an estimate as it was generated using two data points. The values obtained using this method are for samples with an averaged number of different crystal faces. Figure 1.13 (b) shows the enthalpies of all three polymorphs of titania relative to bulk rutile as a function of surface area.

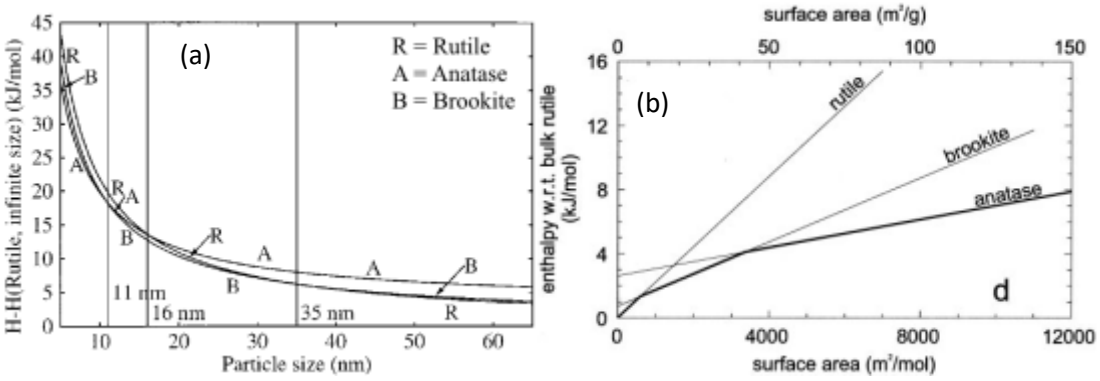

Figure 1.13: Enthalpy of rutile, anatase and brookite as a function of (a) particle size[68] and (b) surface area[67]. The darkened line in (b) represents the energetically stable phases[67].

According to figure 1.13 (b), rutile is the most stable phase when the surface area is less than 592 m^2/mol (7 m^2/g), brookite is preferred when the surface area is between 592 – 3174 m^2/mol (7 – 40 m^2/g) and anatase is most thermodynamically stable for surface areas greater than 3174 m^2/mol (40 m^2/g)[67].

Upon heating, all polymorphs undergo an irreversible transformation into rutile: brookite to anatase to rutile, anatase to brookite to rutile, brookite to rutile and anatase to rutile[67]. All transformations terminating as rutile are irreversible due to rutile having a lower Gibbs free energy than anatase at all temperatures above 0 K and all positive pressures[69]. It must be noted that these transitions and corresponding transition temperatures have been debated in the literature. The terms transformation and transition have been used interchangeably throughout this section. Titania phase transformations are dependent on thermodynamics and kinetics, and are therefore discussed concurrently in this subsection. The anatase to brookite transformation is not discussed further as brookite and anatase are described as having a polytypic structural relationship with their interconversion requiring simple atom displacement on either two or four Ti planes[68, 70].

1.2.4.1 Brookite to Rutile Transformation

Ye *et al.* found that for a sample containing all three polymorphs, at temperatures lower than 780 °C, grain growth for rutile, anatase and brookite was slow[71]. Additionally, there was a slight decrease in the quantity of the brookite phase with a corresponding increase in the anatase phase. The quantity of the rutile phase remained unchanged in this temperature range. It was concluded that below 780 °C, brookite transformed into anatase and no anatase to rutile or brookite to rutile phase transformations occurred. Between 780 °C and 850 °C, brookite transformed into anatase and anatase transformed into rutile. Dramatic grain growth was found above 818 °C for all phases and was attributed to phase transformations occurring within this temperature range. According to the authors, brookite cannot transform directly into rutile. This claim was verified from a sample containing 100% brookite heated to induce phase transformations in a study by Bakardjieva *et al.* [72] It was also shown by Bakardjieva *et al.* that larger anatase crystals rather than smaller crystals readily transform into rutile[72].

Contradictory to the studies by Ye *et al.* and Bakardjieva *et al.,* Kominami *et al.* revealed that brookite transformed directly into rutile upon calcination at 700 °C and was completely transformed at 900 °C [73]. Hu *et al.*, have shown that brookite may transform directly into rutile[74]. The attachment of brookite on anatase is thought to increase the rate and lower the transition temperature of the anatase to rutile transition by increasing the number of nucleation sites at the interface[74]. Brookite crystals (~ 25

nm) occurring in monodispersed spheres (~ 125 nm) were found to be stable up to ~ 500 °C, above which occurred a direct transition to rutile[75].

1.2.4.2 Anatase to Rutile Transformation

Brookite synthesis is difficult as, being a metastable phase, it readily converts to either anatase or rutile[69]. Therefore, for titania synthesis, the first formed phase is generally anatase (there are exceptions to this generalisation)[69]. This is due to two reasons[69]: structurally, it is easier for the less constrained molecular structure of anatase to arrange into long range ordered octahedra from short range ordered TiO_2. Thermodynamically, anatase possesses lower surface energy compared with rutile and this facilitates a greater rate of recrystallisation[76]. The anatase to rutile phase transformation is greatly dependent on the synthesis parameters[69]. Anatase does not instantaneously transform into rutile. Transformation is a reconstructive process that depends on time and temperature[69]. This reconstructive transformation causes a volumetric decrease of ~ 8% and contraction of the c-axis[69]. During the course of transformation to rutile, the anatase (1 1 2) planes are retained as the rutile (1 1 0) planes[69]. Some of the factors that affect the transition of undoped anatase to rutile include[69]: particle size, shape, surface area, atmospheric conditions, sample volume, type of sample container, heating rate, soaking time, impurities, and measurement technique.

Rao found the temperature of transformation of anatase into rutile to be 610 $\pm$ 10 °C. Below this temperature, the transformation was immeasurably slow[77]. An analysis of Rao's data by Banfield *et al.* revealed that at 510 °C, 5% transformation would occur after more than 41 days and 95% transformation will be achieved in < 7 years[78]. According to Hwu *et al*., anatase transformed into rutile at temperatures greater than 700 °C and was more stable than rutile for particles smaller than 50 nm[79]. Zhang *et al*. have demonstrated that TiO_2 prepared by calcining $Ti(OH)_4$ in air at 500 °C, exists as pure anatase[80]. Heating to 550 – 680 °C caused anatase in the bulk to begin to transform into rutile, leaving the surface unaltered as anatase. At 700 °C all bulk TiO_2 was transformed into rutile leaving 44% of the surface remaining as anatase. Surface anatase completely transformed into rutile at 800 °C. Adjusting the surface chemistry of developing titania nanoparticles served to control morphology and impacted the particle size at which anatase transformed into rutile[81]. Rutile crystallites were found to be larger than the average respective precursor anatase crystallites during the initial

stages of transformation[82]. Table 1.10 shows the variation in the anatase to rutile phase transformation temperature dependent on the method of fabrication and source of data.

Table 1.10: Variations in the anatase to rutile transformation temperature[69].

Year	Temp. (°C)*	Fabrication Details	Data Source
1961	610	Highly pure powder	Onset temperature observed by XRD after firing for 24 h
1965	(1190) (1138) (1115)	Powders from three different suppliers	Apices of DTA peaks
1968	610	Commercially available reagent grade powder	Onset temperature observed by XRD after extended firing (1–5 days)
1995	390	Sol–gel synthesised powder	Appearance of detectable rutile peak by XRD after 1 week
1996	675	Sol–gel synthesised powder	Appearance of detectable rutile peak by XRD after 4 min
1997	(787)	Sol–gel synthesised powder	Reported value: apex of DTA peak
	720		Corrected value: onset of DTA peak
1997	465	4-6 nm particles prepared through a sol–gel method	Appearance of detectable rutile peak by XRD
1999	(616)	Sol–gel synthesised powder	Reported value: 50% transformation observed by XRD
2001	(680)	Sol–gel synthesised powder	Reported value: 50% transformation observed by XRD
	600		Onset temperature from graph
2001	600	Sol–gel synthesised powder	Appearance of detectable rutile peak by XRD
2002	(700)	Sol–gel synthesised powder	50% transformation observed by XRD
	600		Appearance of detectable rutile peak by XRD
2005	600 – 700	Highly pure nanocrystals synthesised from$TiCl_4$ Sol–Gel	Appearance of detectable rutile peak by XRD
2007	(900)	Sol–gel synthesised powder	Apex of broad DTA peak

* Data in parenthesis do not correspond to the onset of the transformation

It is interesting to note that data sourced using Differential Thermal Analysis (DTA) gave greater phase transition temperatures. This is due to the sigmoidal nature of the DTA curve with the apex of the curve corresponding to the greatest rate of transformation and not the onset of transformation[69].

By altering the number of vacancies in the oxygen sub-lattice[69], dopants, defects and impurities can either enhance or impede anatase transforming into rutile[83, 84]. The number of oxygen vacancies is proportional to the ease of transformation as they allow for enhanced lattice relaxation and the subsequent rearrangement of atoms upon heating, into the rutile form[69].

1.2.4.2.1 Transformation dependence on Particle Size

The work by Banfield was conducted on solid titania in a gaseous environment. Other mechanisms may play a role in the liquid phase.

Banfield *et al.* showed that the anatase to rutile transformation is strongly dependent on crystallite size[78]. According to the study, enhanced anatase to rutile transformation rates were obtained when anatase existed as fine crystallites. Rapid transformation was attributed to low activation energy (267.8 $kJ.mol^{-1}$). Because the initially formed rutile crystals displayed a significant volume change compared with that of coexisting anatase, the authors suggested that anatase grew to a critical size before transforming into rutile. In a later study, anatase was deduced as having a smaller critical radius than rutile[76].

Gribb and Banfield discovered that coarsening of reactant anatase and product rutile occurred simultaneously with transformation, and smaller anatase crystallites enhanced the rate of transformation[76]. Once rutile was formed, it coarsened much faster than anatase. Based on coarsening kinetics of anatase and rutile, the authors were able to predict that anatase was more stable than rutile at small crystallite sizes[76]. This is due to rutile theoretically having a 15% greater surface energy than anatase resulting in the total free energy of rutile being greater than that of anatase for crystallites in the nanometer range[76]. Since the smallest detected rutile crystallite was 13 nm, the authors suggested that the smallest formed stable anatase crystallite would also be 13 nm. The surface energy of this particle was theoretically estimated as having 85% of the total surface energy of a similar rutile particle. Additionally, a TEM investigation of partly transformed samples revealed that crystallites were either completely anatase or completely rutile, with no partially transformed crystals

observed; suggesting that once transformation was initiated within an anatase crystal, it proceeded swiftly throughout the crystal[76]. This led to the assumption that the rate of nucleation was the rate limiting step[76]. For larger particles, rutile coarsened at the expense of anatase[69, 76].

Zhang and Banfield proved by experimental and theoretical analysis that anatase particles smaller than 14 nm are more thermodynamically stable than rutile[85]. The researchers found that under standard pressure and in the temperature range of 300 – 1000 K, anatase was more stable than rutile up to a size of 8 nm when the effect of surface stress was not considered. Including surface stress effects increased the size up to which anatase was stable, to 14 nm. The relative stabilities were established from a model to calculate the surface free energies of anatase and rutile based on the surface enthalpies and surface heat capacities of each polymorph. It was also assumed that surface stress equals surface free energy in value. The result was verified by a structure based analysis of free energy: surface free energy is defined as the amount of reversible work per unit area required to form a new surface[85]. TiO_2 surfaces have ions with unsaturated coordination and hence unbalanced electric charges. More work is required to form a new surface from a surface that has a greater number of unsaturated charges[85]. If more work is required to form a new surface, the implication is that that surface has greater surface energy and hence greater surface free energy[85]. Figure 1.14 illustrates the number of unsaturated charges associated with oxygen on different faces of anatase and rutile per unit area. From this figure it is evident that rutile has higher unsaturated charge densities and hence higher surface free energy than anatase.

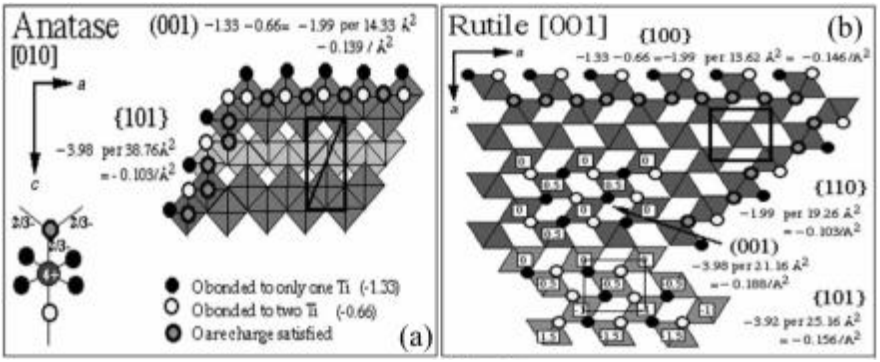

Figure 1.14: Unsaturated charge densities on different faces of (a) anatase and (b) rutile[85]. Greater unsaturated charge density on rutile surfaces make it unstable.

Ding and Liu also found that smaller anatase grains transformed into rutile at lower temperatures than larger grains[86]. Temperatures employed in this study were 650 °C or higher. Additionally, the transformation of smaller grains occurred over a greater temperature range than for larger grains. The study showed that smaller anatase grains transformed into larger rutile grains (and vice versa) after heat treatment. The researchers discovered that the anatase to rutile phase transformation dramatically enhanced grain growth.

Intuitively, smaller anatase particles would be expected to transform into larger rutile particles as larger particles are more thermodynamically favoured than smaller particles[87]. As a result, material flows from smaller to larger crystallites on the basis of larger crystallites having a lower volume potential[76]. Transformation follows a two stage process involving nucleation and growth[76, 86].

Since nanocrystalline materials have a large fraction of atoms situated on the surface, it is reasonable to deduce that nucleation occurs on crystallite surfaces[86]. Given that grain size is inversely proportional to the specific surface area, decreasing grain size serves to increase the surface area and hence the number of nucleation sites on which transformation may occur[76, 86].

Moreover, the thermodynamic driving force of grain growth can be attributed to the high free energy of the specific surface areas. Therefore, decreasing grain size causes an increase in the specific surface area and consequently enhances the rate of grain growth[76, 86].

The strain energy associated with nucleus formation is a size dependent parameter that is a fundamental factor in influencing the rate of transformation[76]. Due to surface tension and surface curvature, small anatase crystallites are subjected to pressure[76]. This pressure promotes the rate of transformation by reducing the strain energy associated with the formation of a rutile nucleus[76]. The strain energy concerned with the formation of a rutile nucleus was found to be significant as the molar volume of rutile is approximately 10% less than that of anatase[76]. In a later study, Zhang and Banfield modelled the effect of surface stress on phase stability[85].

From a kinetics perspective[86], grain growth will occur when smaller grains coalesce into larger grains by atomic diffusion, rearrangement or movement of grain boundaries as illustrated schematically in figure 1.15. According to this model, to

increase grain size from smaller grains, a barrier to coalescence must be overcome. The height of this barrier is related to the size of the smaller crystallite which is consumed by the larger crystallite during coalescence. Therefore, smaller crystallites will have smaller associated barriers and this will in turn facilitate easier grain boundary movement resulting in easier grain growth.

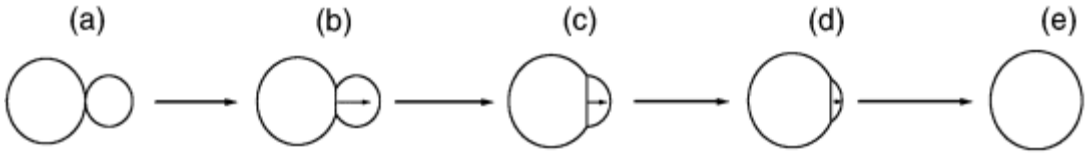

Figure 1.15: (a – e) Process of coalescence by movement of a grain boundary. Notice that the barrier to coalescence is associated with the smaller crystallite[86].

The anatase to rutile phase transformation and grain growth are competing processes in the sense that some small grain anatase particles will immediately transform into rutile (thermodynamics), whereas other grains will grow rapidly (kinetics). Larger grains will then transform into rutile at a slower rate[86]. Due to the high mobility of atoms during phase transition, atomic diffusion, rearrangement, and movement of the grain boundary is enhanced and grain growth is favoured[86]. Increasing temperature provides the system with sufficient energy for anatase to rutile transformations to take place without concern for the incentives afforded by small crystallites[76].

1.2.4.3 Direct Rutile Formation

It is possible to form rutile directly from solution without first going through an anatase or brookite phase. This can only occur under specific synthesis conditions. For example, in the sol-gel synthesis of TiO_2 starting from a titanium isopropoxide precursor, Gopal *et al*. have shown that the heating rate of the sol affected the formed polymorph in the following way[88]: slow heating (0.5 °C min^{-1}) produced rutile exclusively; intermediate heating (2 °C min^{-1}) produced a mixture of anatase and rutile and fast heating (5 °C min^{-1}) produced anatase exclusively. All samples were heated to a maximum temperature of < 100 °C.

To explain this observation, the authors argued that in a simple nucleation model, the greater thermodynamic stability of rutile will result in lower activation energy for its formation[88]. Therefore, the nucleation activation energy, Q, will order in the following way: $Q_{rutile} < Q_{anatase} < Q_{amorphous}$. As a result, lower synthesis temperatures will favour the formation of rutile. A schematic describing a plausible mechanism for direct rutile

formation is illustrated in figure 1.16. This mechanism considers three crystallised octahedra that are free in solution. A condensation reaction between two of the octahedra will result in the sharing of a corner; a second condensation will result in edge sharing and begin forming a chain. Cation-cation repulsion will cause the centres of each octahedra to pull apart causing the shared edge to shorten. A condensation reaction between the third octahedra and the developing chain will occur by sharing a corner. A final condensation will cause the third octahedra to join the chain linearly (forming rutile) or at right angles (forming anatase). According to the authors, the linear formation is more thermodynamically stable as it allows the cations to exist at greatest distances apart from each other. The right angle formation is statistically favoured as there are two edges available for anatase formation and one edge available for rutile formation. Therefore, faster reaction rates favour the formation of anatase.

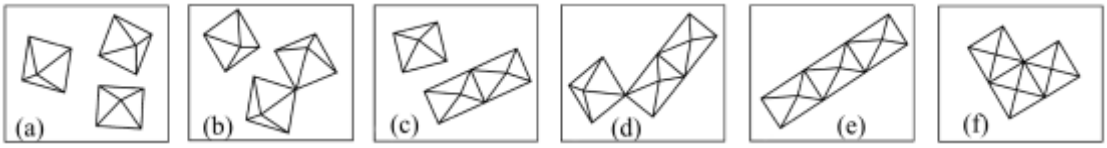

Figure 1.16: Anatase and rutile formation mechanism. (a) Free octahedra in solution. Condensation between two octahedra results in (b) corner sharing followed by (c) edge sharing. (d) Third octahedron joins the forming chain at a corner. If the final condensation causes (e) linear edge sharing, thermodynamically favoured rutile is formed or (f) right angle edge sharing, statistically favoured anatase is formed[88].

1.2.5 Transformation Mechanisms

On the analysis of the kinetics of the anatase to rutile phase transformation, Zhang and Banfield proposed a model that combined interface nucleation and constant growth[89]. The authors suggested that the rate of transformation was proportional to the number of anatase particles in a given volume. Based on the data obtained from Gribb and Banfield[76], the rate of transformation was found to be 2nd order with respect to the number of anatase particles[89]. The 2nd order phase transformation indicated that, over shorter reaction times, the net transformation rate was limited by rutile nucleation in the contact area between two anatase particles; the nucleation rate was determined by the probability of contact between two anatase particles. Over longer reaction times, nuclei growth contributed to the overall rate of transformation in addition to interface

nucleation. The steps involved in phase transformation over shorter and longer reaction times are given in figure 1.17.

As mentioned previously, Gribb and Banfield found formed crystals to be either anatase or rutile with no combination within a crystallite[76]. This may be understood in terms of figure 1.17 in the following way: during short reaction times rutile nuclei on the interface grow swiftly to exhaust the two in-contact anatase particles; during long reaction times, partially formed anatase particles are not detected due to a decrease in the number (and implied increase in particle size) of anatase particles[89]. In section 1.2.4.2.1 smaller anatase particles were shown to transform into rutile more readily than larger particles. This can be attributed to smaller particles increasing the number of particle-particle contacts per unit volume[90].

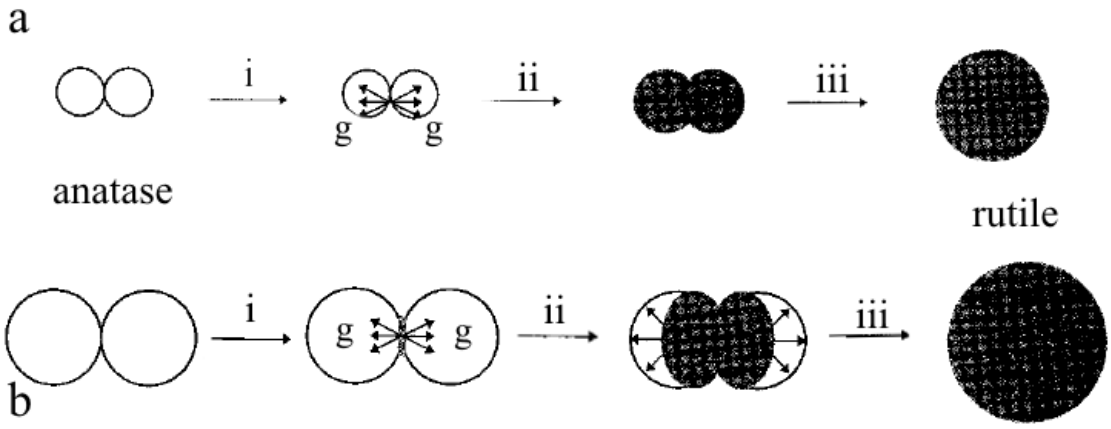

Figure 1.17: Transformation of anatase to rutile via (a) shorter and (b) longer reaction times[89]. Nuclei growth rate is represented by g. Step (i): rutile nucleation occurs at the interface between two anatase particles in contact. Step (ii): growth of rutile nuclei is rapid from smaller anatase particles (a) but extended for larger anatase particles (b). Step (iii): formation of a rutile particle from the particle-particle neck occurring simultaneously with step (ii).

Different synthesis pathways tend to affect the rate of transformation[89]. Given that alternate pathways can produce aggregates with different nanocrystal packing arrangements, it is feasible that structural elements found at the particle-particle interface will vary. This variation can promote or hinder rutile nucleation by interfering with the number of favourable rutile nucleation sites[89].

Interface nucleation activation energy was found to be 165.6 $\pm$ 1.1 (1.7) kJ/mol; the apparent activation energy was calculated as 100.0 $\pm$ 0.9 (0.9) kJ/mol; the coarsening

of anatase particles activation energy was 68.6 ± 0.3 (0.4) kJ/mol[89]. The activation energy of nuclei growth was nearly zero indicating that the rate of nuclei growth was constant and independent of temperature[89].

Oriented attachment is an important growth mechanism for nanocrystalline particles and may be used to explain phase transformations and growth in titania[91]. Adjacent particles undergo oriented attachment by spontaneously self-organising along common crystallographic directions. Bonding between particles at these planar interfaces reduces the number of unsatisfied bonds thereby lowering total energy by reducing surface energy. Therefore, a strong driving force exists for particle orientation. Despite synthesis occurring under hydrothermal conditions, this mechanism can apply in any solution based synthesis due to the high mobility of particles and probability of re-orientation[92]. The mechanism may also dominate when particles nucleate beside each other on a substrate and coalescence occurs during growth.

Oriented attachment is capable of forming homogeneous single crystals or crystals separated by twin boundaries (twin boundaries are formed when two crystals exist coherently in the plane of the interface but the crystallographic axes on either side of the interface are related by symmetry conditions not present in the untwinned crystal)[91]. Twin boundaries can have atomic arrangements dissimilar to the bulk material but similar to a polymorph[93]. Therefore, twin boundaries can serve as nucleation sites for phase transformations. Anatase {1 1 2} twin surfaces can be defined as a brookite unit cell and atomic displacements within the twin interface serves to nucleate brookite[93]. For anatase, attachment generally occurs between high surface energy planes[91]. Figure 1.18 shows particles attaching at specific surfaces in an oriented way, forming twinned and intergrown crystals[93].

Penn and Banfield found an interesting relationship between the amount of brookite and respective particle size formed during the course of a hydrothermal treatment at a constant temperature of 250 °C, as given in figure 1.19[93]. Brookite had converted to anatase over time as evidenced by XRD analysis. There appears to be an inverse relationship between the amount of brookite and respective particle size, implying brookite coarsened while concurrently decreasing in content. The authors suggested a combination of three processes to describe this behaviour[93]:

(1) Oriented attachment occurred between brookite and anatase crystals allowing brookite to coarsen by addition of material from solution or anatase transformation.

(2) Brookite crystals trapped between oriented anatase crystals were eventually utilised by transformation into anatase.

(3) Twin surfaces between anatase particles nucleated brookite.

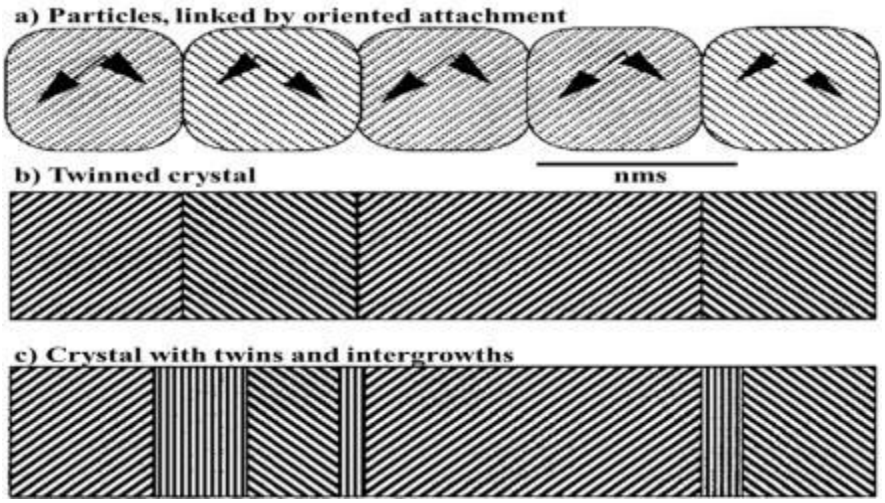

Figure 1.18: (a) Particles self-organising to attach at specific surfaces. (b) Formation of a twinned crystal from the mismatched interfaces. (c) Formation of a new phase from the twin surface, intergrown in the particle[93].

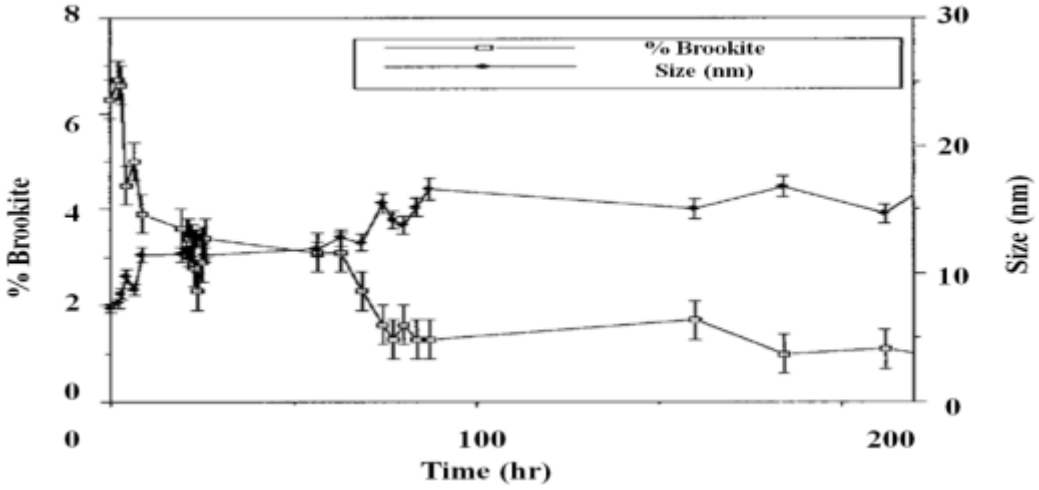

Figure 1.19: Apparent inverse relationship between the amount of brookite and respective particle size as a function of hydrothermal treatment time at 250 °C[93].

Figure 1.19 favours processes (1) and (2), however brookite is less dense than anatase and as a result may possess lower surface energy than anatase. Therefore, at small particle sizes – when surface energy contributes significantly to total free energy – brookite can be more thermodynamically favoured than anatase[93]. When the structural energies of brookite and anatase are similar, random thermal fluctuations may favour brookite transformation from anatase[93].

In a separate study, Penn and Banfield found that rutile was nucleated at anatase {1 1 2} twin boundaries created by oriented attachment[94]. The anatase {1 1 2} twin interface was found to be structurally similar to rutile. Rutile-like structures at twin interfaces caused a reduction in the activation energy of transformation. Transformation of the twin interface into rutile involved displacement of half of the Ti octahedra and retention of the other half. Displacements were found to be 2.7 Å along anatase [1 1 0]. A chain-like transformation occurred from rutile formed at the interface into surrounding anatase. This propagation reaction involved joint displacement of oxygen anions and titanium cations as given in table 1.11[94]. Bulk anatase transformation required 7 out of 24 Ti-O bonds per unit cell to be broken.

Table 1.11: Displacements of oxygen and titanium ions during transformation propagation to rutile[94].

Atom	Displacements	Bonds broken
Ti	½ inherited, ½ displaced (2.7 Å || <1 1 0>)	0, 8
O	distortions	
Ti	all displaced (1.2 Å || <1 1 1> + 1.3 Å || <1 1 0>) = 1.8Å || ~ <3 3 1>	8
O	all displaced (1/2 Å || <1 1 1> + 1.3 Å || <1 1 0>) = 1.4 Å || ~ <2 2 1>	
Ti	all displaced (1.3 Å || <1 1 0>)	4
O	all displaced (1/2 Å || <1 1 1> + 1.3 Å || <1 1 0>) = 1.4 Å || ~ <2 2 1>	
Ti	all displaced (-1.2 Å || <1 1 1> + 1.3 Å || <1 1 0>) = 1.8Å || ~ $<\bar{3}\,\bar{3}\,\bar{1}>$	8 Total = 28 / 96

Transformation occurred in slabs in order from the propagation leading edge (i.e.: the first displaced Ti ions caused distortion of O ions which in turn caused a 1.8 Å displacement of the next plane of Ti ions etc., until the mechanism repeated causing half of the Ti octahedra to be inherited in the next slab of transformed material)[94]. Rutile particles were found to be either single crystals or singly twinned on (0 1 0). A lack of observable complex twinning and symmetry-related intergrowths on rutile crystals led the researchers to infer that nucleation occurred at a single site within a transforming particle. The proposed mechanism is valid for both nano-scale and macroscopic material suggesting that this mechanism is independent of particle size[94].

Although not mentioned previously, nano-amorphous titania can be formed by allowing rapid formation of titania nuclei while inhibiting re-crystallisation by reducing reaction temperature and time[95]. Heating amorphous titania caused transformation into anatase and then rutile if sufficient energy was supplied to the system[95]. Since no incubation period was observed before transformation of amorphous titania to anatase, the transformation occurred via interface nucleation as opposed to bulk nucleation.

Zhang and Banfield proposed a kinetic model based on the Smoluchowski coagulation formulation, to describe the kinetics of transformation of amorphous titania into anatase in air[95]. The authors showed that small amorphous titania particles (2.5 – 3 nm) were more stable than anatase and that amorphous particles readily converted to anatase in air at relatively low temperatures (300 – 400 °C). Using molecular dynamics simulations, the crossover particle size range for phase stability reversal between amorphous titania and anatase was determined as being 3 – 3.5 nm. It was assumed that interface nucleation controlled the rate of two amorphous particles merging to form an anatase particle. Following anatase formation by interface nucleation, amorphous particles crystallised onto formed anatase by atomic diffusion, increasing the size of anatase particles. It was also possible for two anatase particles to merge to form a larger anatase particle by atomic diffusion. Amorphous particles coarsened when thermal fluctuations at the interface were not high enough to allow for phase transformation. The larger amorphous cluster was less stable than anatase of the same size and would readily convert to anatase as the reaction proceeded.

1.2.6 Mesocrystalline TiO_2

Mesocrystalline materials typically refer to controlled self-organisation of nanoparticles, and are observed for many different systems[96]. In literature, mesocrystals are described as three dimensional hierarchical arrangement of crystals forming oriented superstructures[97]. Dendritic in nature, TiO_2 rutile superstructures align in a common crystallographic manner and are called by many names: chrysanthemums, dandelions, sea-urchins, nanodandelions, nanourchins flower-like, pinecone-like and star-like[98, 99, 100, 101, 102, 103, 104]. Due to the variation in naming, some studies have incorrectly reported novelty or rarity of self-assembled titania using the hydrothermal method[105, 106]. This despite the hydrothermal method successfully preparing TiO_2 superstructures previously[107, 108, 109, 58]. Both anatase and rutile mesocrystals have been documented[108, 109, 110, 111]. Rutile crystals comprising superstructures are referred to as rods or wires[97, 109, 103]. It is unlikely that these assemblies occur as a result of agglomeration as ultrasonic treatment was found to be ineffective at destroying the superstructures[102].

1.2.6.1 Rutile Mesocrystals

Using low temperature hydrothermal synthesis based on $TiCl_3$, Hosono *et al*., discovered that synthesised TiO_2 films consisted of aggregated superstructures. These superstructures were composed of highly crystalline rectangular parallelepiped rutile crystals[108]. According to FE-SEM images, the crystals were found to be 150 – 250 nm in width and 3 – 4 μm in length growing along [0 0 1][108]. Rutile crystal anisotropy was attributed to adsorption of Cl^- species onto the (1 1 0) plane[108]. This adsorption impeded growth along [1 1 0] while promoting growth along [0 0 1][108]. Interestingly, nitrogen saturated solutions did not promote the formation of rutile films. This was in contrast to oxygen saturated solutions that promoted the formation of rutile films. The researchers deduced that film deposition was dependent on heterogeneous nucleation driven by a slow oxidation process consuming dissolved oxygen.

Kakiuchi *et al*., used low temperature heterogeneous nucleation to infer that the formation of self-assembled rutile nanorods were likely preceded by the formation of tetratitanate species[109]. Higher temperature synthesis produced self-assembled rutile nanorods that possessed lateral surfaces corresponding to the {1 1 0} plane[109]. The growth direction of these rutile nanorods were along the [0 0 1] axis[109]. Interestingly, the researchers found that after 24 hours of heating the reaction solution, the tops of

all rods were pyramidically capped (figure 1.20)[109]. A contact angle of ~ 130° was evident between the pyramid plane {1 1 1} and the lateral plane {1 1 0}[109].

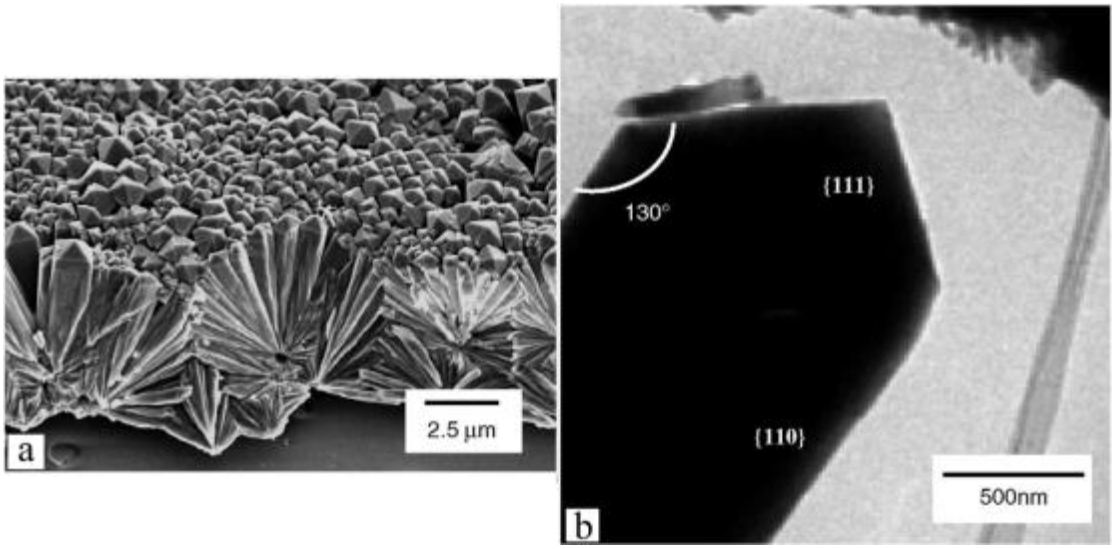

Figure 1.20: (a) FE-SEM image of self-assembled rutile showing pyramidal tips. (b) TEM image of a single rutile nanorod showing orientation of the tip in relation to the surface of the rod[109].

Hydrothermal synthesis was responsible for the fabrication of rutile nanorods that measured 300 – 400 nm in length and 60 – 100 nm in diameter[112]. The study conducted by Bae *et al.,* revealed that the rods exhibited either symmetrical or asymmetrical triangular tips depending on the concentration of NaCl used in the synthesis[112]. As described above, these rods grew anisotropically along [0 0 1]. Side surfaces were assigned to (1 1 0), with triangular tips manifesting on the (1 1 1) plane[112].

In the microwave assisted hydrothermal synthesis of rutile mesocrystals, Zhang *et al.*, proposed that rutile nanowires comprising self-assembled superstructures grow radially (figure 1.21)[97]. These nanowires were found to be single-crystalline in nature with an approximate length and diameter of 2 µm and 7.5 nm respectively[97]. The researchers concluded that growth occurred along [0 0 1]. The structure was found to contain pores arising from intra-agglomerated primary particles and inter-aggregated secondary particles[97].

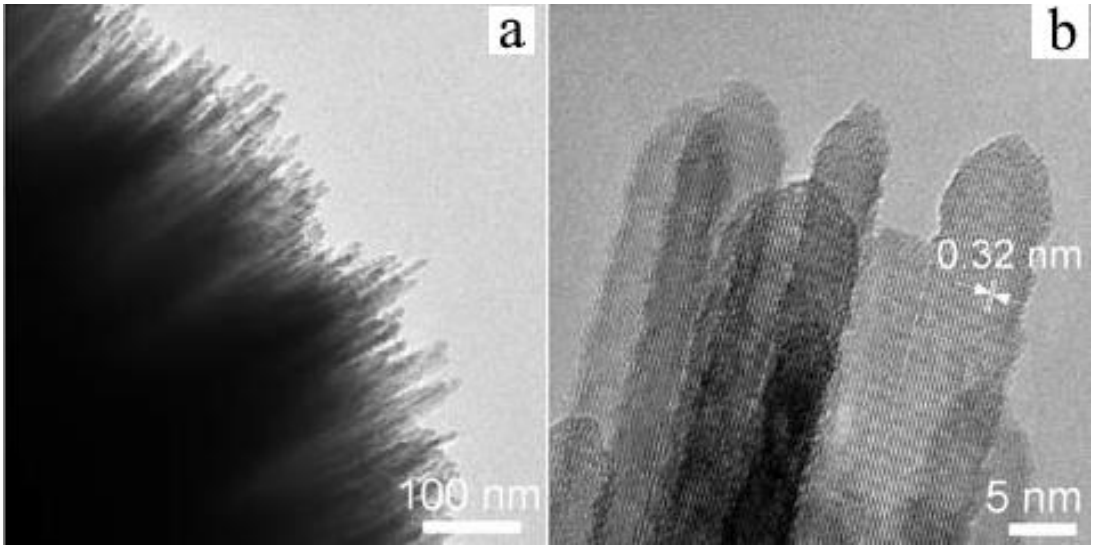

Figure 1.21: (a) Radial growth of rutile crystals comprising the superstructure. (b) Needle-like nature of rutile, appearing as single crystals[97].

Karim *et al*., used low temperature dissolution re-precipitation to grow anisotropic rutile that self-assembled after aging[113]. Rutile crystallites comprising mesocrystals were found to be discontinuous[113] – in contrast to the findings by Zhang *et al*[97]. This discovery was based on a correlation between mean crystallite size obtained from the Scherrer equation and observations of crystallite size using HRTEM[113].

Yang *et al*., synthesised rutile mesocrystals by a sonochemical method in a $TiCl_4$/HCl solution[103]. Multiple crystal twinning along the {1 0 1} association plane was proposed as the reason for the formation of 'star-like structures'. The authors suggested that the sonochemical method likely provided an environment conducive to twinning[103]. Thermal gradients within the solution have the propensity for causing localised stress within developing crystals. This phenomenon is beneficial for the formation of crystal twins[103].

By monitoring the formation of rutile mesocrystals using low temperature aqueous-phase synthesis as a function of changing $TiCl_4$ concentration, Li *et al.*, suggested the following mechanism to explain superstructure formation[102]: a 3D cluster (nucleus) of critical size formed initially in solution. This cluster served to nucleate rutile crystallites under the action of stirring. Since rutile is the preferred phase, crystallites had a propensity for growing anisotropically along [0 0 1].

A lower added $TiCl_4$ concentration implied fewer $TiOH^{3+}$ ions in solution and hence a low-density distribution of these ions around the developing clusters[102]. Accordingly,

the low ion distribution favoured anisotropic growth resulting in the formation of needle-like structures (figure 1.22)[102]. The distribution density of $TiOH^{3+}$ increased with increasing $TiCl_4$ concentration[102]. This caused attachment of $TiOH^{3+}$ to occur with equal probability all around the cluster[102]. Anisotropic growth in multiple directions – nucleated from the active sites on the cluster – would then form 'flower-like' structures (figure 1.22)[102]. High $TiCl_4$ concentrations increased the amount of $TiOH^{3+}$ surrounding the cluster[102]. As a result, the cluster aggregated and increased in size[102]. Consequently, the remaining $TiOH^{3+}$ displayed an asymmetric distribution around the cluster, blocking the anisotropic growth process and favouring the formation of 'pinecone-like' structures (figure 1.22)[102].

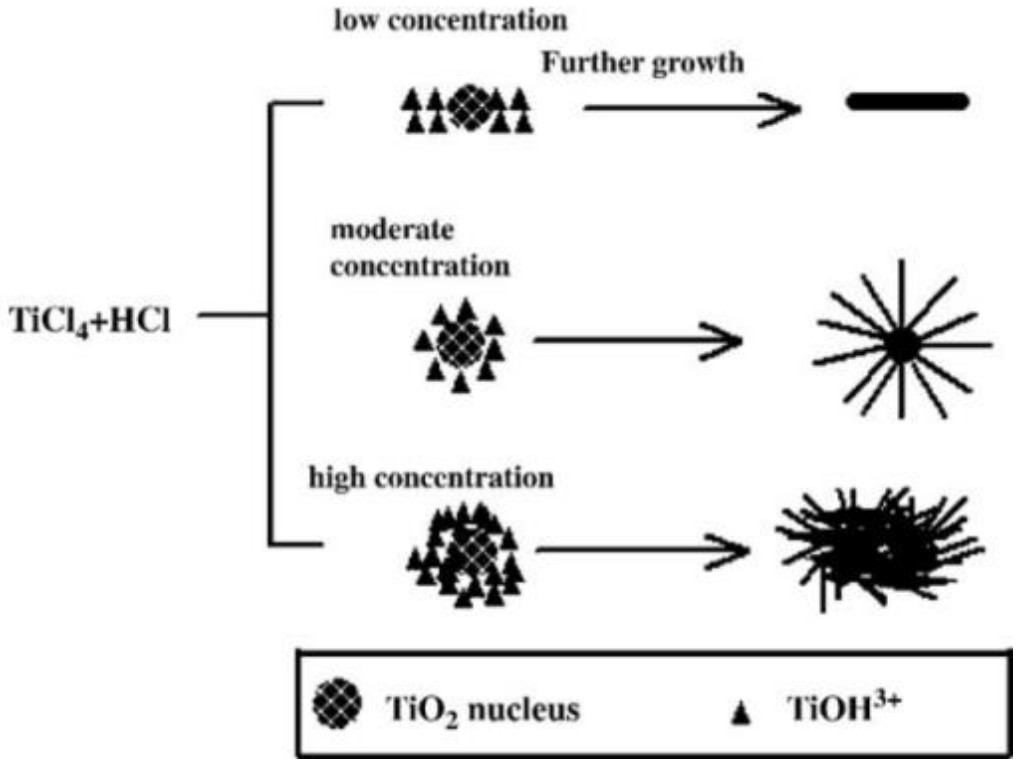

Figure 1.22: Mechanism of rutile mesocrystal formation based on the distribution of $TiOH^{3+}$ in solution[102].

Yi *et al.*, have considered a mechanism of rutile mesocrystal formation that suggests the superstructures do not possess a hollowed centre[106]. Based on a hydrothermal synthesis involving hollow, spherical SnO_2 templates, the authors suggested that the Ti^{4+} precursor moved toward the high energy interface between HCl and toluene. Hydrolysis of the Ti^{4+} precursor nucleated TiO_2 on the surface of SnO_2. TiO_2 then grew toward the centre of the sphere, with the associated dissolution of the template, to form 'dandelions'.

A separate study claimed that the rutile superstructures are hollow[114], in contrast to the abovementioned study by Li *et al*. and Yi *et al.* The study employed the use of potassium titanium oxalate, distilled water, H_2O_2, and HCl in an autoclave. Post ultra-sonication SEM analysis revealed the apparent presence of hollow rutile mesocrystals[114] (figure 1.23).

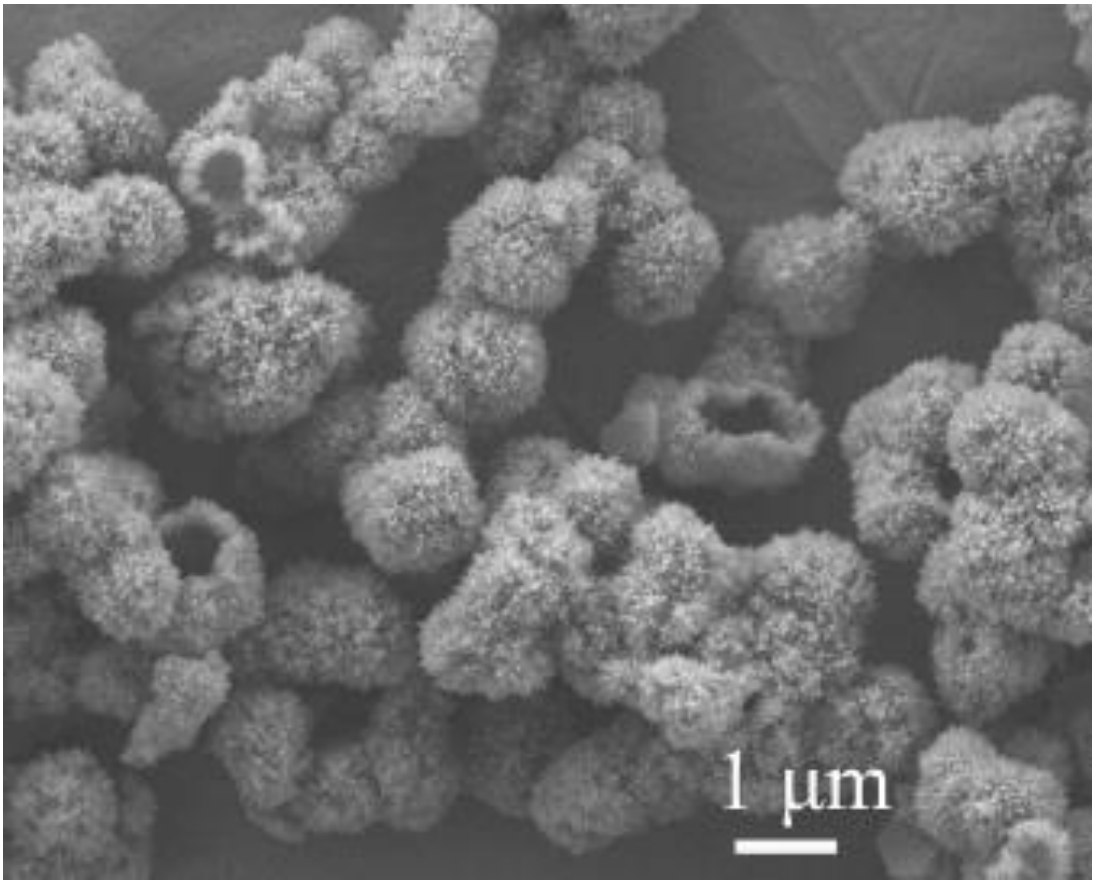

Figure 1.23: Formation of hollow rutile mesocrystals after ultra-sonication[114].

The researchers claimed that the large titanium ion precursor provided the starting material for the formation of organised 3D architectures[114]. Acidic hydrothermal conditions promoted the exchange of $[C_2O_4]^{2-}$ with O_2^{2-} ions[114]. Decomposition led to the release of O_2 to form rutile[114]. As discussed previously, an intrinsic property of rutile is its anisotropic growth along [0 0 1] to form nanorods. H_2O_2 decomposition formed bubbles that served as templates for the self-assembly of rutile nanorods[114]. Interfacial energy minimisation was responsible for driving the formation of hollow spheres[114]. This mechanism is illustrated in figure 1.24.

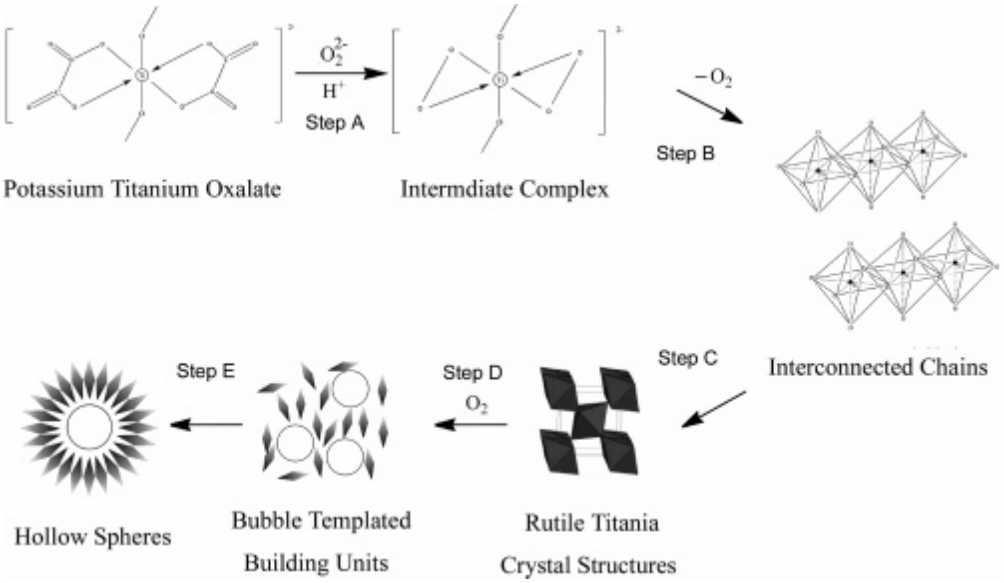

Figure 1.24: Mechanism of hollow rutile mesocrystal formation[114]. Step A illustrates ligand exchange. Step B shows formation of TiO_2 by O_2 elimination from decomposition. Step C shows the formation of anisotropic rutile. Step D illustrates the effects of bubbles as a template. Step E shows the formation of a hollow sphere[114].

1.2.6.2 Anatase Mesocrystals

Tartaj manipulated thermal destabilisation of inverse microemulsions to form kinetically stable self-assembled nanomicellar anatase structures[111]. This method resulted in the formation of anatase superstructures smaller than 100 nm[111]. Anatase mesocrystals comprised spherical assemblies of anatase crystals (measuring approximately 7 nm) oriented along {1 0 1} surfaces (figure 1.25)[111]. This is in contrast to the needle-like rutile crystals found in rutile superstructures.

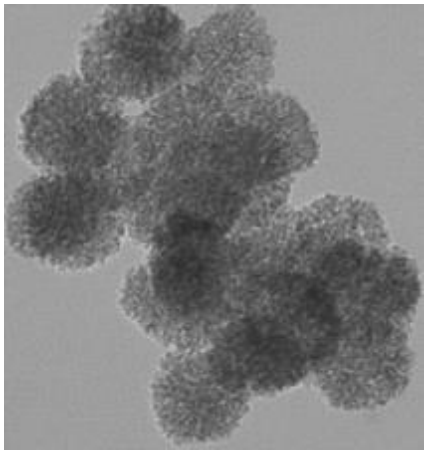

Figure 1.25: Anatase mesocrystals composed of spherical anatase single crystals[111].

Yang and Zeng prepared hollow anatase TiO_2 mesocrystals using a simple one pot hydrothermal process and TiF_4 as a starting material[115]. Reaction time controlled the formation of hollow spheres (figure 1.26)[115]. This observation led the researchers to postulate that Ostwald ripening was an underlying mechanism governing the hollowing process[115].

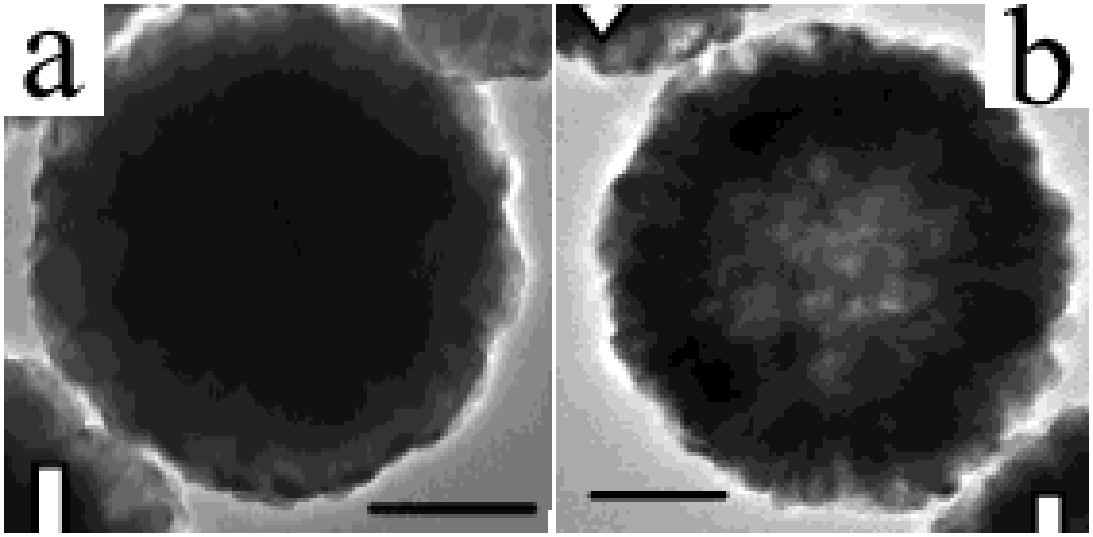

Figure 1.26: Anatase mesocrystals synthesised with a reaction time of (a) 2 hours forming structures with solid cores and (b) 20 hours forming structures with hollowed cores[115]. Scale bars = 200 nm.

Mao *et al*., synthesised 3D anatase mesocrystals composed of 1D nanostructures using a one-pot process sans sacrificial template[99]. H_2O_2 was added with NaOH or KOH to Ti foil. This formed either sodium or potassium hydrogen titanate. Hydrogen titanate was formed by neutralising the formed product with HCl. Anatase mesocrystals were then formed by annealing the titanate product[99].

Curiously, the researchers referred to their superstructures as agglomerates even though sonication for up to one hour did not destroy the assemblies[99]. TEM analysis on microtomed sections (figure 1.27) revealed that the anatase mesocrystals consisted of 1D nanostructures, existing perpendicularly to a central hollow core[99]. The study did not mention if the sections contained the central region of the superstructures, or regions above or below the centre. It is theoretically possible to image hollowed assemblies if microtomed sections contained non-central regions of the structures. This is due to the effects of the cured epoxy resin that allows for the observation of slices containing anatase with pseudo-structural integrity.

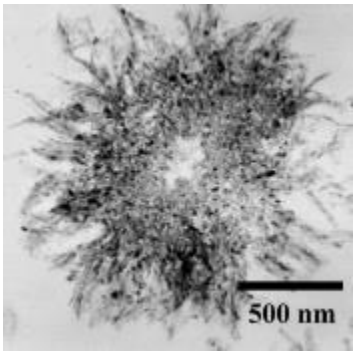

Figure 1.27: Cross-sectional TEM image of microtomed anatase[99]. This image suggests that the structure contains a hollow core[99].

HRTEM imaging of anatase mesocrystals revealed that the individual 1D nanostructures (figure 1.28a) were not as dense or uniform as for those seen in rutile mesocrystals. Additionally, 1D anatase nanostructures possessed tips that were not pyramidal or rounded (figure 1.28b). Lastly, the lattice spacings between the (1 0 1) planes were measured to be 0.352 nm. These observations were confirmed in a separate study by Zhou *et al*[116].

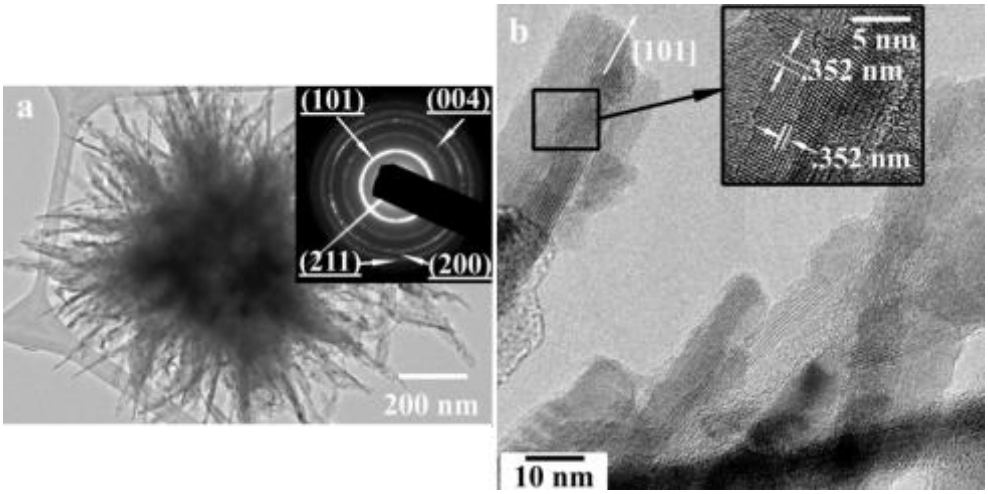

Figure 1.28: HRTEM images of anatase superstructures showing (a) complete mesocrystal comprising non-uniform 1D nanostructures and (b) individual 1D nanostructures with growth along [1 0 1]. Note the lack of pyramidal or rounded tip nanostructures. Insert in (a) shows the SAED pattern with four indexed rings. Insert in (b) shows the lattice spacing between (1 0 1) planes[99].

Based on AFM measurements of surface roughness, SEM images taken at different times during the reaction, and measurements of the temporal evolution of titanium concentrations, the researchers were able to postulate the formation mechanism of 3D

anatase mesocrystals as consisting of two parts: (1) growth of 1D nanostructures and (2) self-assembly[99]. A redox reaction between H_2O_2 and Ti foil caused the Ti foil surface to roughen. The formed 2D nanosheets then rolled up under high temperature conditions. These rolled sheets led to the formation of 1D nanostructures (nanowires). It has been suggested that the interface between the Ti surface and peroxide afforded a distinctive micro-environment for the rolling up of nanosheets into nanowires[99]. Following growth, the 1D nanostructures began to self-assemble into 3D spheres. This effect was likely driven by interfacial tension, van der Waals forces and hydrophilicity of adjacent surfaces[99]. The suggested mechanism does not explain the existence of hollowed spheres.

Park *et* al. used drop solution calorimetry in a molten sodium molybdate solvent at 702 °C to show that anatase structures with complex morphologies possessed greater surface energies[98]. In contrast to the study by Tartaj, anatase superstructures formed in this study were composed of nanowires measuring ~ 10 nm in diameter (figure 1.29)[98]. Non-assembled nanowires were larger than nanowires comprising 3D assemblies[98]. Based on the heat of water absorption, it was found that water molecules were chemisorbed on the anatase surfaces at low water coverage[98]. At high coverage, additional water molecules were physisorbed[98]. This trend was present regardless of crystallite morphology. The researchers found that surface enthalpies of hydrated surfaces of anatase nanoparticles, 'nanowires', and 'sea-urchin assemblies' measured 0.51 ± 0.05, 1.07 ± 0.28, and 1.29 ± 0.16 J m^{-2} respectively[98]. In contrast, respective anhydrous surfaces measured[98] 0.74 ± 0.04, 1.24 ± 0.28, and 1.41 ± 0.16 J m^{-2}. Lower surface enthalpies for hydrated surfaces corresponds to the stabilisation effect afforded by surface hydration[98].

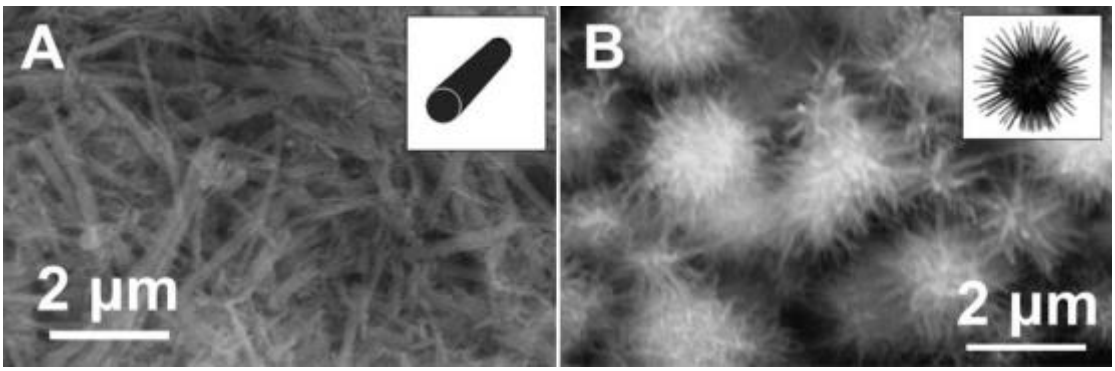

Figure 1.29: SEM images of anatase (A) nanowires and (B) mesocrystals. Inserts show schematics of anatase nanowires and superstructures.

1.2.7 Electronic Bonding Structure

A complete discussion on the electronic properties of titanium dioxide will involve descriptions of electron and charge carrier mobility, resistivity, and thermoelectric power in bulk and nano-samples accounting for anisotropy[117]. These discussions are of paramount importance to work concerned with the application of titania as semi-conducting materials and shall therefore, not be discussed further. The purpose of this section is to discuss the bonding structure of titanium dioxide. The electrical properties of anatase and rutile vary significantly[118].

As would be expected, the oxygen *p*-orbitals and the titanium *d*-orbitals each contribute to both the bonding (HOMO) and anti-bonding orbitals (LUMO)[119] as evidenced in figure 1.30. In an octahedral-type crystal field, there are five unoccupied *d*-states of the central Ti ion. These five states are split into the energetically higher lying twofold-degenerate e_g-like states possessing $d_{x^2-y^2}$ and d_{z^2} character and the energetically lower lying threefold-degenerate t_{2g}-like d_{xy}, d_{yz} and d_{xz} type states.[120]

According to Asahi *et al.,* a noteworthy feature in the local orbital structure diagram is the p_π orbital and the d_{xy} states at the top of the valence and bottom of the conduction bands respectively[121]. This feature is present in both anatase and rutile but is less significant in rutile. This difference is attributed to rutile being denser than anatase. It is also due to the different metal-metal bond lengths exhibited by the two polymorphs: the larger metal-metal bond distance of 5.35 Å in anatase implies that the Ti d_{xy} orbitals at the bottom of the conduction band must be isolated whereas the smaller metal-metal bond distance of 2.96 Å in rutile implies that the t_{2g} orbitals at the bottom of the conduction band need not be as isolated.

Anatase has a bandgap of 3.2 eV as opposed to the bandgap of rutile which is 3.0 eV[119]. According to Diebold, the surface electronic structure of stoichiometric titanium dioxide is similar to that of bulk titania in the sense that there are no observed or predicted surface states[64]. Despite this, by considering a mathematical, quantum mechanical approach to calculating the bandgap shift in quantum materials, the bandgap of a 1.2 nm anatase particle was found to be greater than that of the bulk by 0.15 eV (i.e.: nano-anatase had a bandgap of 3.35 eV)[122].

The total and angular momentum decomposed densities of states (DOS) for anatase and rutile are given in figure 1.31.

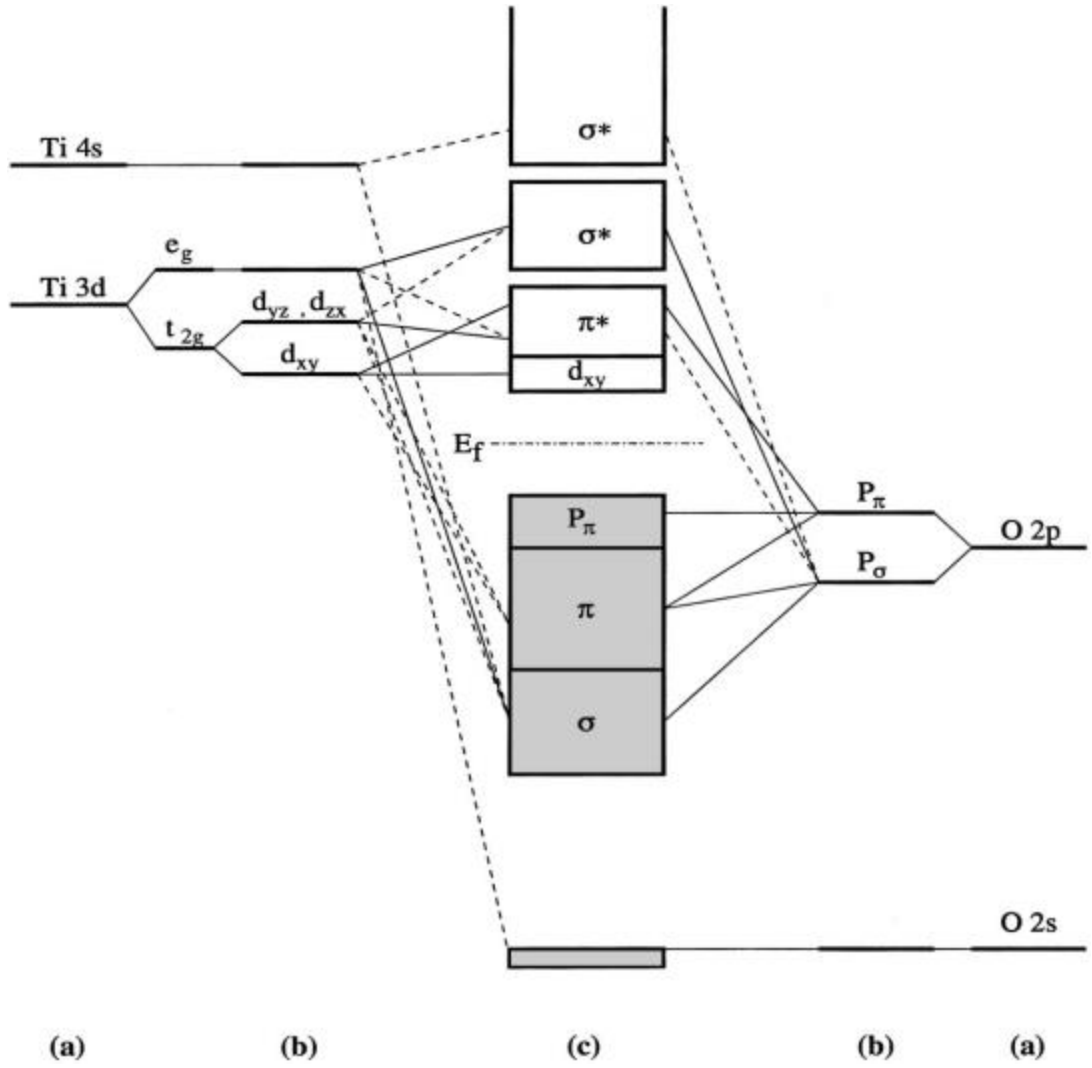

Figure 1.30: Local orbital bonding structure of titanium dioxide. (a) Atomic levels. (b) Crystal field splitting levels. (c) Final interaction states. Solid and dashed lines represent large and small contributions respectively[121].

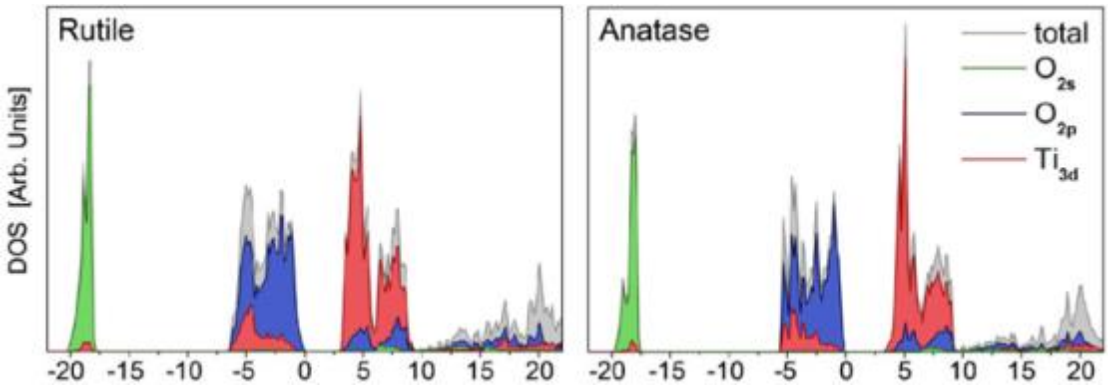

Figure 1.31: Total and angular momentum decomposed densities of states for rutile (left) and anatase (right). The contributions to the local densities of states from $O_{2s,}$ O_{2p} and Ti_{3d} are shown[120].

An analysis of the DOS by Landmann *et al.*, revealed mainly O_{2p}-like valence band states and Ti_{3d}-like conduction band states around the band edges for both anatase and rutile[120].Two sub-bands are formed from the separation of the Ti_{3d}-like bands. The inner conduction band structure is connected to the "distorted-octahedron-type short-range-order"[120]. In the O_{2p}-like valence band, rutile presents with a weak two-peak separation. This separation is weaker for anatase. The O_{2p} band in rutile splits as a result of the sp^2-like hybridisation in the planar (Y-shaped) OTi_3 building blocks. Bonding σ-hybrid states are formed between the p_x and p_y states of the oxygen ion and the central titanium ion[120]. These σ states form the lower edge of the O_{2p}-like valence band. Lone pair π states are formed from p_z-type states. These π states comprise the uppermost valence band edge and are higher in energy than the sp^2-like hybrid states[120]. Anatase differs from rutile as the (T-shaped) OTi_3 building blocks result in greater deviations from the ideal sp^2 hybrid states than for rutile[120].

A schematic energy level diagram of the lowest unoccupied local orbital structure of a $[TiO_6]^{8-}$ cluster with O_h, D_{2h} and D_{2d} symmetry is provided in figure 1.32. D_{2d} anatase is an octahedral structure that has been tetragonally distorted such that every titanium cation is surrounded by six oxygen atoms in an elongated octahedral geometry[1].

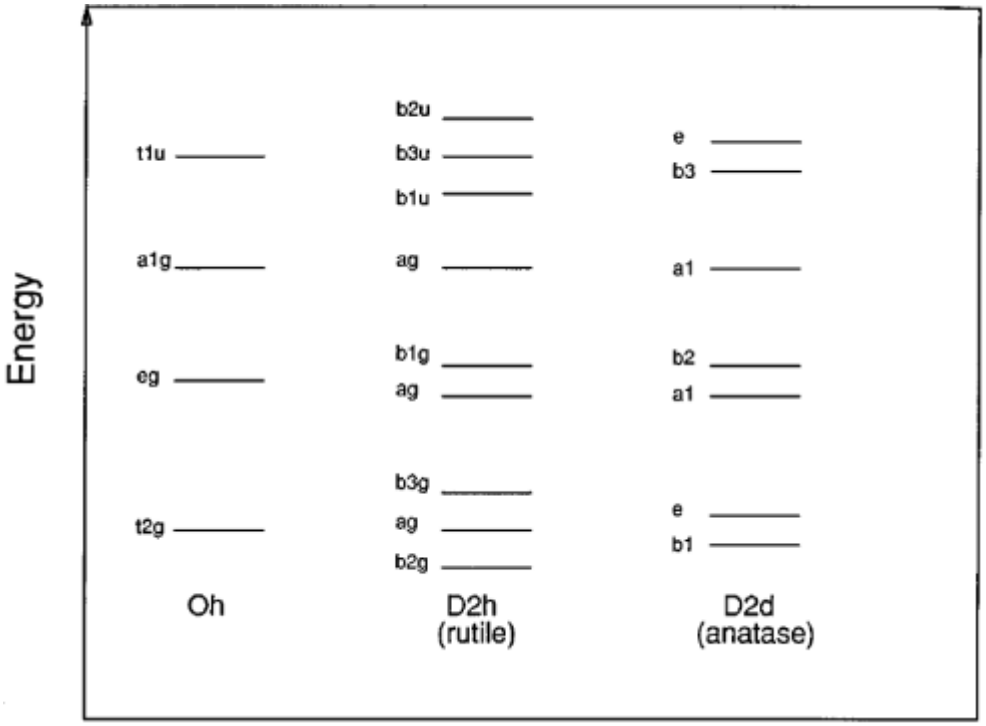

Figure 1.32: Schematic energy levels diagram of the lowest unoccupied local orbital structure of a $[TiO_6]^{8-}$ cluster with O_h, D_{2h} (rutile) and D_{2d} anatase symmetry[123].

1.3 Polyethylene Glycol

The role of the polymer in a typical resin-gel synthesis experiment is to coordinate the metal ions and force them into nanoparticle clusters under the action of intimate atomic scale mixing. PEG was selected as the coordinating polymer for most experiments in this study. The importance of PEG towards understanding the mechanism of nanoparticle formation warranted a discussion of the following subsections: description, structure, melting characteristics, solution behaviour, interactions with biological particles and metal ions, and the synthesis of TiO_2 from ethylene glycol.

1.3.1 Description and Structure

PEG is an uncharged, inert, amphiphilic, linear polymer[124, 125, 126, 127] that is soluble in aqueous solutions[128]. Because PEG consists of alternating parts that are hydrophilic and hydrophobic, it is possible that PEG can behave as an internal, pseudo-block-copolymer in solution. Miyazawa described PEG as a special case of a helical polymer composed of planar zigzag chains[129]. Opschoor considered PEG chains to be kinked, irregularly shaped helical structures[130]. The basic, linear structure is represented in figure 1.33.

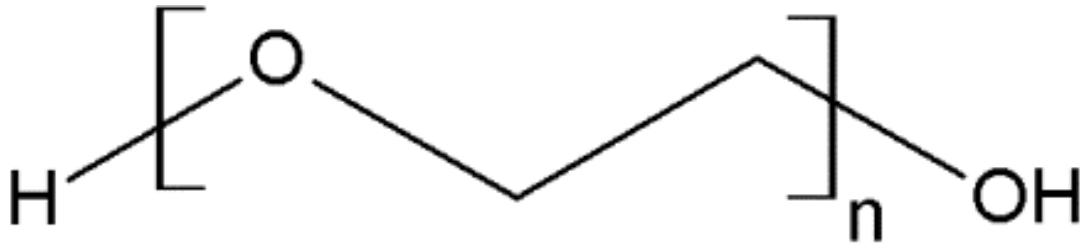

Figure 1.33: Basic linear structure of Polyethylene glycol.

According to the most likely model proposed by Miyazawa[131], highly oriented crystalline films of PEG contain seven repeating units and two helical turns per fibre period of 19.25 Å. The internal rotation angles for the C-C and C-O bond were found to be 60° and 191.5° respectively[131]. Polyethylene oxide (PEO) is analogous to PEG but refers to polymers with a molecular weight of > 100000. The symmetry of PEO is isomorphous with the D(4π/7) factor group[132]. PEO has a 7_2 helical form constructed with successive *trans* (CCOC), *gauche* (OCCO), and *trans* (COCC) conformers with associated bond angles of 192°, 60°, and 192° along the chain, respectively (figure 1.34)[132]. The *trans-gauche-trans* conformation is the most energetically stable[133].

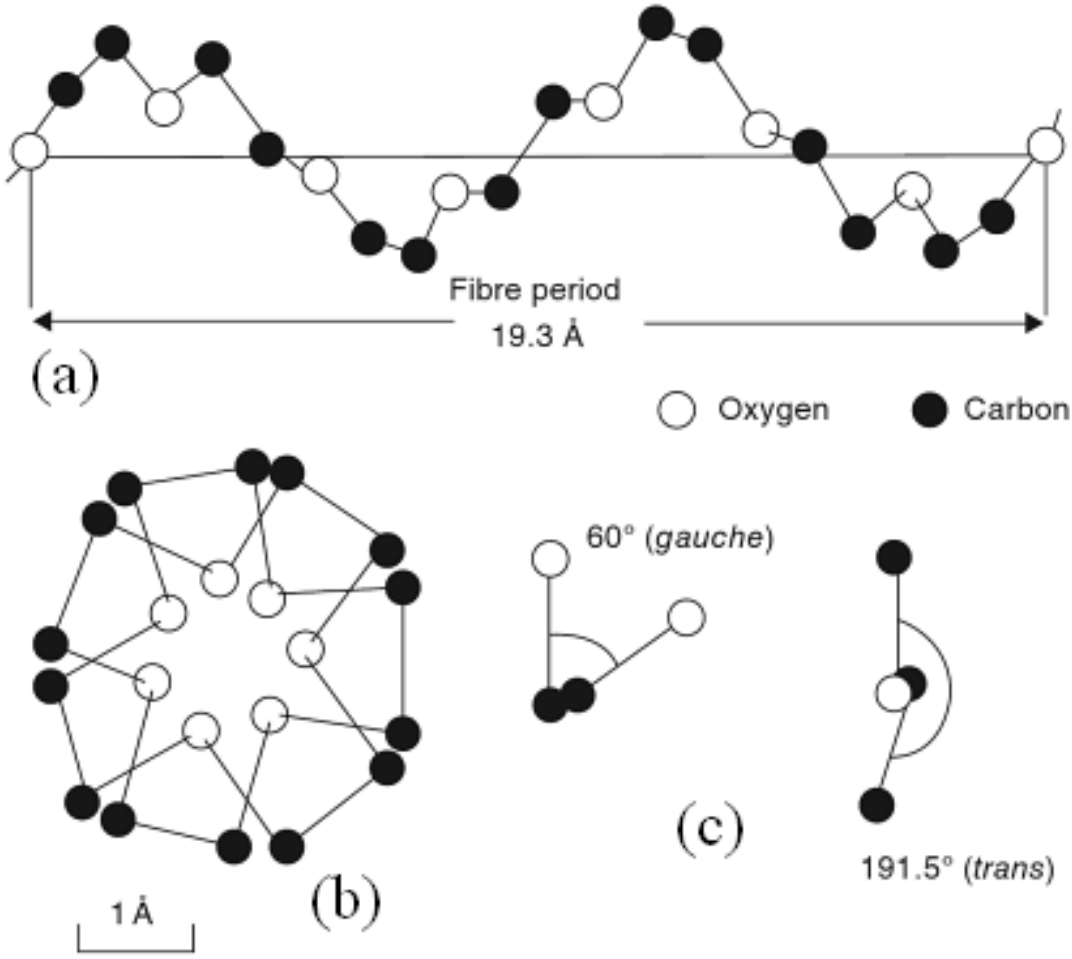

Figure 1.34: Typical 7_2 helical conformation of PEO. (a) Lateral view, (b) axial view, and (c) *gauche* and *trans* configurations[134].

Polyethylene crystals have a lamellar shape in accordance with a chain folding conformation model, given in figure 1.35[135]. According to the model, chains arrange in sheets with a thickness of ~ 10 nm. Sheets can be larger in perpendicular directions[135].

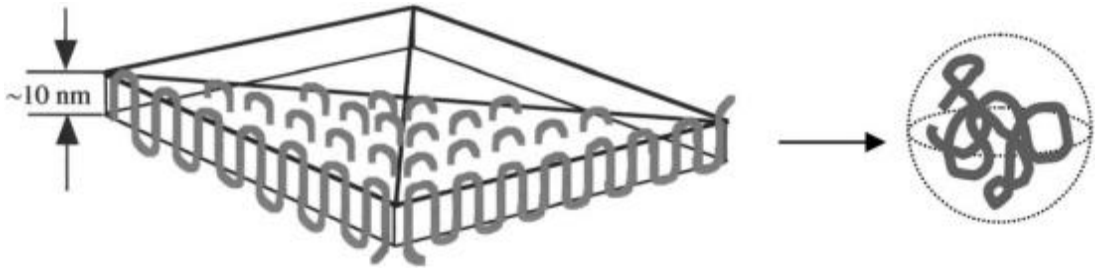

Figure 1.35: Schematic of a single crystal polymer exhibiting regular chain folding into sheets on the order of 10 nm[135]. Random coil conformations ensue after melting[135].

1.3.2 Melting Characteristics

PEO goes through a helix-coil transition when melted[132]. Above the upper critical solution temperature, the homogenous state of PEO becomes stable again causing the amorphous polymer state to form random coil conformations[135]. In solution, water solubility of PEO decreases with increasing temperature[135]. This behaviour is characterised by the low critical solution temperature[135]. In highly diluted solutions, at the low critical solution temperature, hydrated coils collapse into globules[135] as evidenced in figure 1.36.

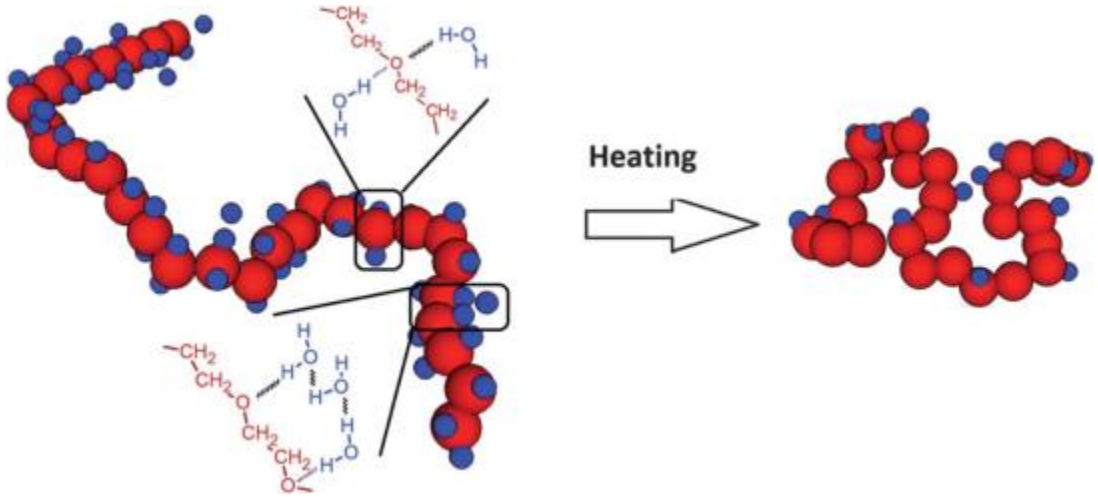

Figure 1.36: Change of PEO from a hydrated coil to a collapsed globule under the action of heating at the low critical solution temperature[135]. Red spheres represent ethylene oxide; blue spheres represent water molecules[135].

PEG exhibits congruent melting behaviour[136] thus favouring compositional homogeneity in the resin and in the final product. It was shown that the melting temperature and heat of melting of PEG increased with increasing molecular weight (figure 1.37)[136]. PEG molecular weight affects its melting and crystallisation behaviour in the following way: higher molecular weight PEG chains favour the formation of a crystalline phase on account of lower segmental mobility, and appropriate geometrical alignment of the chains[136]. PEG chains with higher molecular weights solidify at higher temperatures than lower molecular weight chains[136]. This relationship was attributed to the formation of a multi-layered lamellar structure from many small crystalline structures joining together as PEG was cooled to a solid, as revealed by optical microscopy (figure 1.38)[136]. The growth rate of spherulites decreased when impingement with other growing spherulties occurred.

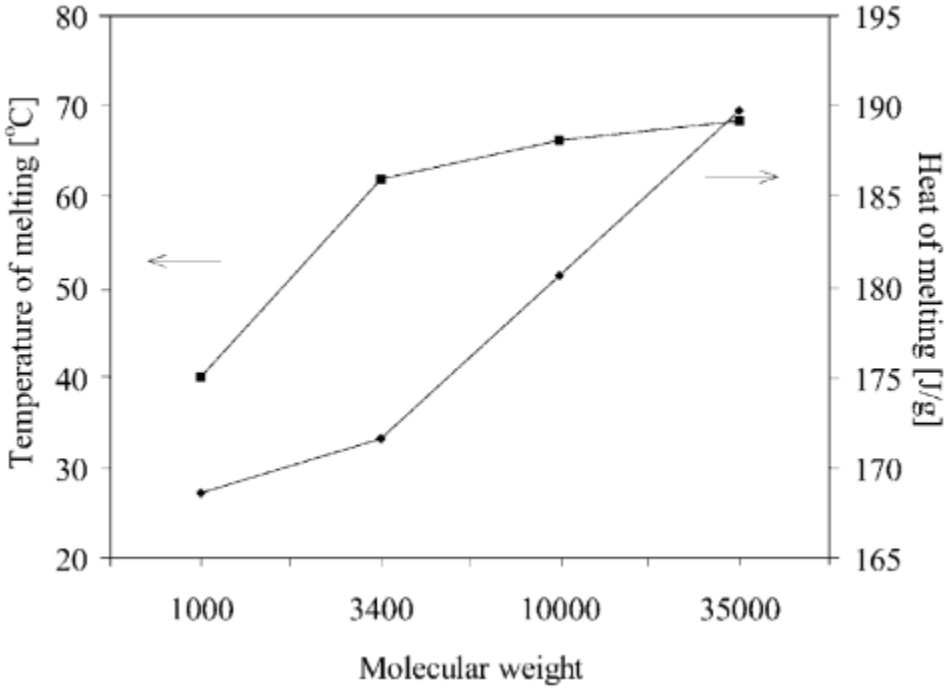

Figure 1.37: Melting point and heat of melting dependence on PEG molecular weight[136].

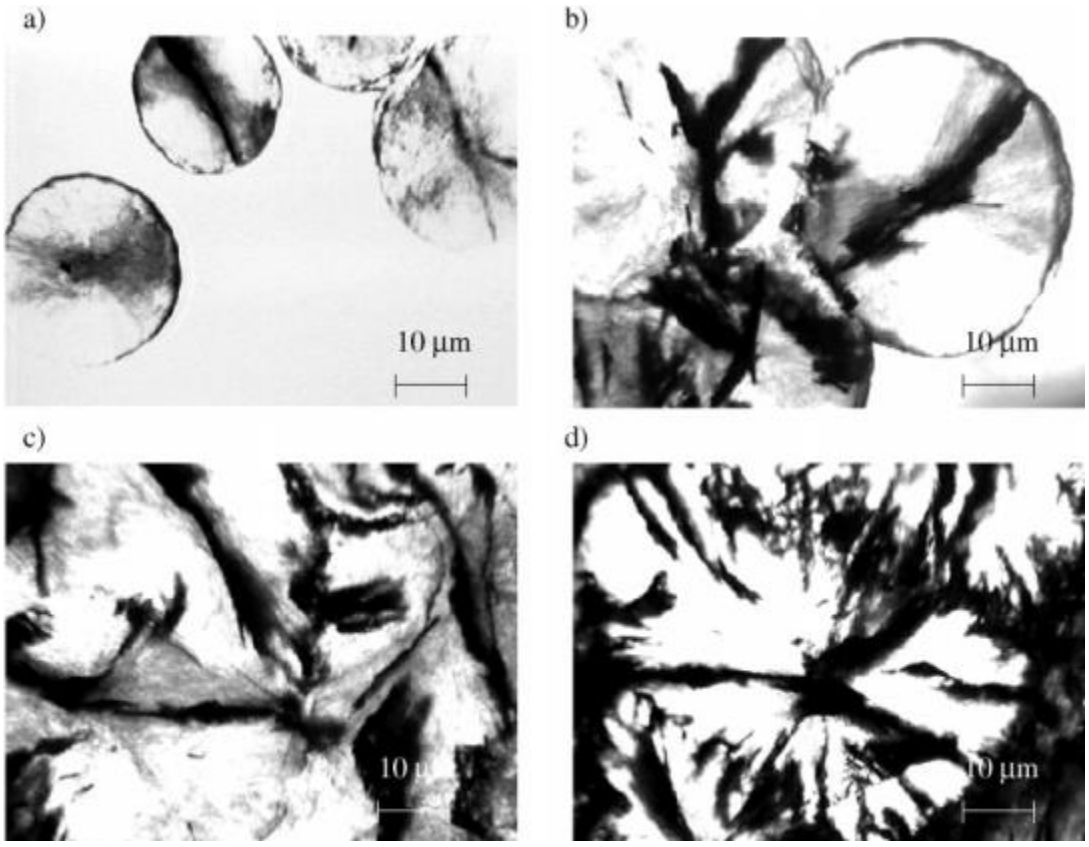

Figure 1.38: Optical micrographs showing the solidification process for PEG with a molecular weight of 10000 g/mol[136]. Notice how the spherulites grow to eventually impinge on each other and decrease the growth rate.

1.3.3 Solution Behaviour

Raman analysis revealed that the crystallinity of PEO was lost when its concentration in aqueous and chloroform solutions reached approximately 50% by weight, suggesting that solutions of PEG retain some crystalline characteristics as a helix[132]. Crystallinity retention in solution may be attributed to PEG's hydrogen-bond acceptor character. Additionally, size compatibility of ethylene glycol monomers in a network of hydrogen-bonded water causes a higher-order interchain structure of PEG in solution[137]. Simulations showed the existence of a helix in solution and experimental data showed that the helix had a greater diameter in solution than in the crystal form[133]. Complex formation between PEG and water occurred as a result of hydrogen bonding between water molecules and oxygen atoms along the chain[132]. Hydrogen bonding was altered by hydrophobic interactions between water clusters and hydrophobic groups of the polymer[132]. The hydrogen bonded complex consisted of three water molecules per monomer unit that was destroyed when the solution temperature was increased above the melting point of PEG[132].

Graham *et al*., found that PEO displayed dramatic syneresis between 0 and 100 °C but retained approximately three water molecules per ether oxygen above 100 °C[138]. The association of PEO with three moles of water per monomer unit was found to be exothermic and this negative enthalpy change provided the driving force for the formation of tri-hydrated complexes[139]. Additionally, the researchers concluded that water promoted significant ordering on admixture with the polymer to which it was bound[138]. Water acts as an anti-plasticizer, increasing the glass transition temperature as the number of moles of water to ether group are increased[139]. Above 373 K, PEO was found to exist as a highly hydrated complex as opposed to an anhydrous polymer[138].

The interaction of PEG with water depends on the chain length[140]. It was found that low molecular weight polymers (< 600) form tetra-hydrate complexes compared to higher molecular weight polymers that formed tri- and hexa-hydrate complexes[140]. Other studies revealed the formation of mono-, tri-, tetra-, and hexa-hydrate complexes[139, 141]. For PEG 5700, monohydrate complexes were shown to form when up to two moles of water were present in solution; tri-hydrate complexes were stable up to forty-two moles of water in solution[139]. Tri-hydrates of PEG 440 and PEG 560 decomposed after five moles of water were added to the solution[139]. This is contrast to

PEG 950 that retained its tri-hydrate complexes after further dilution[139]. The dependence of complex formation in water with chain length can be explained qualitatively in terms of the size and number of loops in a helix required to form a stable structure[139]. Two to four loops are required to generate a helical structure containing sufficient water to form a tri-hydrate complex[139]. It is theoretically possible to have mono- and tri-hydrated complexes coexisting in a linear PEG chain[142]. The currently accepted theory of tri-hydrate complex formation is that the ether oxygen atom in the polymer attaches to a water molecule through a hydrogen bond, then takes up a further two water molecules[142]. A postulated plausible structure corresponding to the tri-hydrated complex is given in figure 1.39. This structure maintains a helix of seven repeating units per fibre period presenting a hydrophobic surface to the bulk water and an interior hydrophilic channel[142].

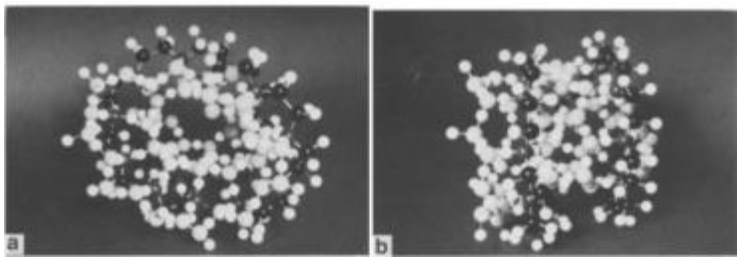

Figure 1.39: (a) End and (b) side view of a PEG tri-hydrate complex model[142].

The inner hydration results from the formation of a net due to: hydrogen bonding between ethoxy groups within the helix and one hydrogen atom from water, and hydrogen bonds between inner water molecules[133]. Solution concentration, temperature, chain-length, and chain-termination influence the type of formed net[133]. Helix formation in solution has been proposed as the driving force for aggregation[143].

Interfacial water around the chain does not play a significant role when PEG is introduced in solution[142]. Any effects caused by interfacial water are suppressed by hydrogen bonding between the ether oxygen and water molecules[142].

Money found that a complex relationship existed between PEG concentration and average relative molecular weight on the osmotic pressure of aqueous solutions[144]. Long chain polymers did not behave as a number of individual units causing osmotic pressure results to vary significantly for high molecular weight PEG[144]. Based on PEG 6000, it has been suggested that the configuration of PEG changes with changing concentration in the following way: at higher concentrations, the configuration is folding; at lower concentrations, the configuration is extended[144]. Since PEG 6000

exists as rigid, helical segments in aqueous solutions, a substantial amount of hydrogen bonding occurs on the exposed oxygen along the disordered helix. It is possible that disorder and water binding increases with increasing PEG concentrations causing suppression of the thermodynamic activity of water[144].

It is possible for PEG chains to fold upon themselves in solution[133]. This occurs with the assistance of inner water molecules linked to oxygen bridges that create a hydrophobic body with carbon on the outside of the helix[133]. Hydrophilic –OH groups on either side of the chain give the folded polymer amphiphilic characteristics[133].

Steuter *et al.*, suggested that the total mass or total number of molecular subunits may be a more important controlling factor of water potential than the total number of polymer chains[127]. Higher molecular weight polymers have longer but fewer chains per gram of polymer. It is also possible that a long-chain polymer can coil back on itself[127]. The entropy change associated with coiling would be dependent on chain flexibility[127]. Excess solvent is absorbed by PEG in solution until equilibrium is reached between interaction of the solvent with polymer chain segments and the forces resulting from expansion of the network structure[127]. PEG concentration is also directly proportional to the probability of polymer-polymer interactions, that serve to increase entropy[127]. It has been reported that some ethylene oxide adducts form micellar structures in aqueous solutions. Micelles formed as a result of hydrogen bonding between ethylene oxide subunits and H_2O molecules[127]. PEG concentration was found to be directly proportional to the number of formed micelles[127].

1.3.4 PEG – biological particle Interactions

PEG is used as a carrier in various pharmaceutical formulations, foods, and cosmetics[124,]. Since it possess low immunogenicity and antigenicity properties, and has a low order of toxicity[145, 137], PEG has been extensively studied for the conjugation of biologically active molecules such as liposomes and proteins[124, 128, 137]. To this end, interactions of the PEG chain architecture with contained biological molecules are important to the efficacy of the polymer as a carrier. Additionally, the surface structure of PEG chains at cellular receptor interfaces is important[146]. PEG protection of liposomes has been documented[126]. The accepted mechanism of operation is that liposomes coated with PEG sterically hinders interactions between blood components and the liposome surface[126]. PEG is useful in the biomedical field owing to the high mobility associated with conformational flexibility of its chains and

water-binding capabilities[128, 137]. These characteristics cause a steric exclusion effect between PEG chains in water[137]. Flexibility is described as free rotation of individual polymer units around inter-unit linkages[126]. Therefore, greater polymer flexibility implies more independent motion of polymeric units relative to neighbouring units and a greater number of possible conformations with the biological molecule.

PEG protection of nanoparticles operates on a similar basis, except either physical adsorption or chemical grafting of the polymer onto the particles is necessary[126]. The endocytic process involves the adherence of a particle onto the surface of the polymer formed membrane[147]. Particles enter the polymer through invagination of the fluid bilayer causing complete wrapping of the particles[147]. This causes membrane coated particles to become completely detached from the outer membrane[147]. For particles that are larger than the membrane thickness, membranes wrap around and engulf particles[148]. Wrapping will only occur around particles if the interaction energy between the membrane and particle is greater than the energy cost of membrane bending[148, 149]. Successful wrapping depends on the interaction range of the particle-membrane adhesion potential, nanoparticle shape, size, elasticity, and surface properties, and the change of shape of membranes during wrapping[148, 150].

Some of the many other uses in the biomedical sphere include tissue engineering scaffolding, drug delivery, and surface functionalization. Concepts of PEG-biological-molecule interaction, focussing on particle protection and wrapping, will be applied to the PEG-metal ion system employed in this study with the understanding that metal ions were added to the polymer before any wrapping processes were induced. Therefore, the mechanism of particle-polymer interaction will not be an exact mirror of that occurring in biological systems.

1.3.5 PEG-metal ion Interactions

When PEG acts as a phase transfer catalyst, factors such as molecular weight, chain terminating group, and characteristics of the associated cations and anions influence its activity[151]. Many catalytic centres exist per PEG molecule for alkoxylation reactions[151]. Single crystal complexes are formed between low molecular weight PEG and metal cations in acetonitrile, methanol, and their mixtures[151]. Using a combination of X-ray crystal structure and NMR analyses, ultra-low molecular weight PEG (i.e.: 3 – 4 repeating units per chain) was found to complex metal ions in a stoichiometric manner (PEG : Sr^{2+} = 2 : 1). Higher molecular weight polymers (9 – 10 repeating

units per chain) were found to helically wrap the Sr^{2+} ion[151]. The latter gave the complex a hydrophobic exterior, dehydrating the metal ion[151]. PEG also has the ability to complex several metal ions of different sizes[151].

Rogers *et al.*, prepared a series of various lanthanide containing PEG complexes with a variety of different chain lengths[152]. The results showed that the primary coordination sphere was dominated by steric effects within the complexes[152]. The choice of anion affected the coordination sphere and changed the mode of polymer wrapping. This caused structural changes to the PEG chains that encircled the metal ions[152]. PEG chain length was found to affect coordination number[152]. Hydrogen bonding in the metal/polyether complexes influenced crystallisation and contributed to the formation of surpramolecular structures[152]. Bonding complexity was increased when water was present in the inner or outer coordination spheres[152]. A separate study revealed that Li^+ was contained inside a helical arrangement of PEG consisting of six repeating units per chain[151].

Based on investigations of morphology and conductivity, a double helical model was proposed for the interaction between PEO and alkali metal complexes[153]. PEO-alkali-metal-complexes form with a stoichiometry of 1 mol of cations for every four mols of ethylene oxide units[153]. The unit cell compositions requires either two chains, each with with four ethylene oxide units or four chains, each with two ethylene oxide units[153]. Based on the geometry of the fully extended conformation, it is not possible to have the latter orientation[153]. A double helix conformation provided a cylindrical structure such that the anions occupied spaces between cylinders[153]. Cations were encapsulated within the tubes.

1.3.6 TiO_2 Synthesis from Ethylene Glycol

The interaction of ethylene glycol with Ti has been documented[154]. Raja *et al.*, found that varying water content in an ethylene glycol electrolyte had a profound effect on the TiO_2 nanotubular arrays formed form anodisation of Ti. An accurate account of the mechanism governing this phenomenon was not made[154].

An ethylene glycol-mediated TiO_2 synthesis has been reported[155]. According to Lee and Lee, ethylene glycol serves as a polymerisation agent, capturing metal ions via a polymerisation-complexation mechanism[155]. This causes a decrease in the mobility of metal ions, preventing precipitation and agglomeration of the cation species[155]. Constraining the system involves mechanical, steric entrapment and not just chemical

chelation[155]. Ethylene glycol forms a homogenous polymeric network with the metal ions and is an easier and cheaper synthesis route for nanoparticle formation than sol-gel synthesis[155]. In accordance with this method, prepared gels needed to be calcined in order to obtain powder samples[155]. After calcination at 800 °C, powder diffraction revealed that samples synthesised from a 1 : 1 weight ratio of metal ions to ethylene glycol consisted of both anatase and rutile[155]. Any higher ratios of ethylene glycol (i.e.: 1 : 3, 1 : 5, 1 : 7) formed rutile exclusively[155]. The researchers postulated that insufficient ethylene glycol caused the distribution of cations to lack homogeneity owing to a deficiency of steric entrapment[155]. TEM analysis revealed large agglomerated particles, however there was no evidence of dandelion formation[155].

Ethylene glycol is an attractive medium for the formation of metal oxides due to its relatively high boiling point[156]. According to Li *et al*., metal oxide morphology variation was possible by varying the metal salt in ethylene glycol[156]. Anatase nanorods and rutile dandelions (chrysanthemums) were evidenced from the synthesis of titanium butoxide in ethylene glycol after the initially synthesised products were heated at 400 °C in air or under vacuum respectively[156]. Interestingly, from SEM imaging alone, the researchers were able to deduce that the dandelion rods connected to a single root at the centre of the dandelion. Additionally, the researchers suggested that the rutile tended to transform into chrysanthemums owing to the presence of alkoxide generated carbon in the crystal. These deductions were made without any powder diffraction or high resolution transmission electron microscopy analyses.

Initial polyol mediated metal oxide syntheses formed amorphous powders with post-reaction calcination procedures resulting in aggregation and crystal growth[157]. Tripathy *et al*., confirmed that the as-prepared titanium dioxide particles from the polyol technique using a titanium iso-propoxide precursor in acetone and ethylene glycol, were amorphous[157]. Polyol syntheses appear to require the assistance of vacuum conditions[156, 157]. The accepted mechanism of particle formation is that acetone acts as the oil phase stabilised by ethylene glycol[157]. The water-in-oil emulsion serves as a micro-reactor controlling particle size distribution[157].

The polyol synthesis method has also been employed for the formation of highly dispersed, homogenous TiO_2-SnO_2 nanoparticles of different compositions by weight[158].

1.4 Characterisation Techniques

Many techniques are available for the characterisation of different properties of various materials. The two techniques paramount to this study were powder X-ray diffraction and (high resolution) transmission electron microscopy. These techniques are vital to elucidating atomic scale structure and hence form the backbone of all materials research. In this study, the chosen characterisation techniques were used to obtain particle size, composition and orientation information. These techniques shall be discussed in greater detail focusing on the principles, mode of operation and the information that can be obtained from the correct use of the chosen technique. A discussion on the components of each instrument is given in appendix A. A brief discussion on the principles of thermogravimetric analysis is also included.

1.4.1 Powder X-ray diffraction

According to Dinnebier and Billinge, single crystal analysis is the most frequently used technique for the determination of crystal structures[159]. Single crystal analysis is a non-destructive technique limited to providing specific information not concerned with bulk material. Is it also not always possible to fabricate high quality single crystals of certain materials synthesised under specific conditions.

The PXRD method remained a qualitative and semi-quantitative phase analysis and macroscopic stress measurement technique for nearly 50 years owing to the intrinsic problem possessed by this technique[159]. The problem of peak overlap results from projecting a three-dimensional reciprocal space lattice onto a one-dimensional 2θ axis[159]. Despite this intrinsic issue, it is nevertheless possible to extract a plethora of structural and quantitative information from a one-dimensional projection such as[159, 160]: lattice dynamics, local structure, imperfections, dislocations, crystal structure, micro-strain, domain size, preferred orientation, qualitative and quantitative phase analysis. Although materials with any elemental composition may be studied using PXRD, the technique is better suited to heavier elements as these elements provide for better diffraction intensities[160]. Electrons produce greater diffraction intensities compared with X-rays and this shortcoming is highlighted for lighter elements[160]. The intensity of the diffracted beam also decreases for nanomaterial analyses. This is due to a decrease in the number of diffraction centres[160]. Finite size crystallite analyses causes an intensity distribution over a small angular range producing a peak broadening effect[161].

1.4.1.1 Principles of PXRD

In a typical diffraction experiment, an incident wave of radiation – that has a wavelength comparable to the spacing between atoms of the lattice – is directed into a material where it interacts, diffracts and scatters. Different types and positions of atoms emit scattered waves and cause interference along different directions[162]. There is a distinct geometric relationship between the waves that exhibit constructive interference and crystal structure of the material[162]. Diffraction patterns are composed of all the waves that interfered constructively. The use of X-rays for crystal diffraction is credited to Max von Laue (awarded the Nobel Prize in physics in 1914)[163], W. L Bragg, and W. H. Bragg (jointly awarded the Nobel Prize in physics in 1915)[163]. X-ray diffraction consists of measuring the intensity of the X-rays scattered by electrons associated with atoms[161]. The Fraunhofer approximation is used to calculate the detected intensities[161].

Structural elucidation from a PXRD pattern is possible due to the Bragg equation. This equation describes the principle of X-ray diffraction by sets of lattice planes. The Bragg approach is to consider X-rays as visible light that is reflected of lattice planes[161, 164]. Some X-rays are reflected of a plane such that the angle of incidence equals the angle of reflection whereas others are transmitted through the sample to be reflected by different planes[164]. Reflected waves from planes lying further into the material must travel a greater distance than those reflected from planes located closer to the material surface,[161] as evidence in figure 1.40. For constructive interference to occur, the additional distance, BAE, covered by the second beam in figure 1.40, must equal to a whole number multiple, n, of the wavelength λ[161]. The relationship between the interplanar *d-spacing, d,* and the incident angle (Bragg angle), θ, is related to the distance BA by:

$$\mathbf{BA = AE = } d \mathbf{\sin \theta} \qquad \mathbf{(1.5)}$$

And

$$\mathbf{BAE = 2}d \mathbf{\sin \theta} \qquad \mathbf{(1.6)}$$

But

$$\mathbf{BAE = n\lambda} \qquad \mathbf{(1.7)}$$

Therefore

$$\mathbf{2}d \mathbf{\sin \theta = n\lambda} \qquad \mathbf{(1.8)}$$

Equation (1.8) is the Bragg equation[164]. It should be noted that the above derivation stems from a conceptual argument as realistically, X-rays are diffracted from electrons bound to discrete atoms as opposed to reflected of planes. The result of this simplified, conceptual approach is the same as would be obtained from a thorough mathematical treatment[164].

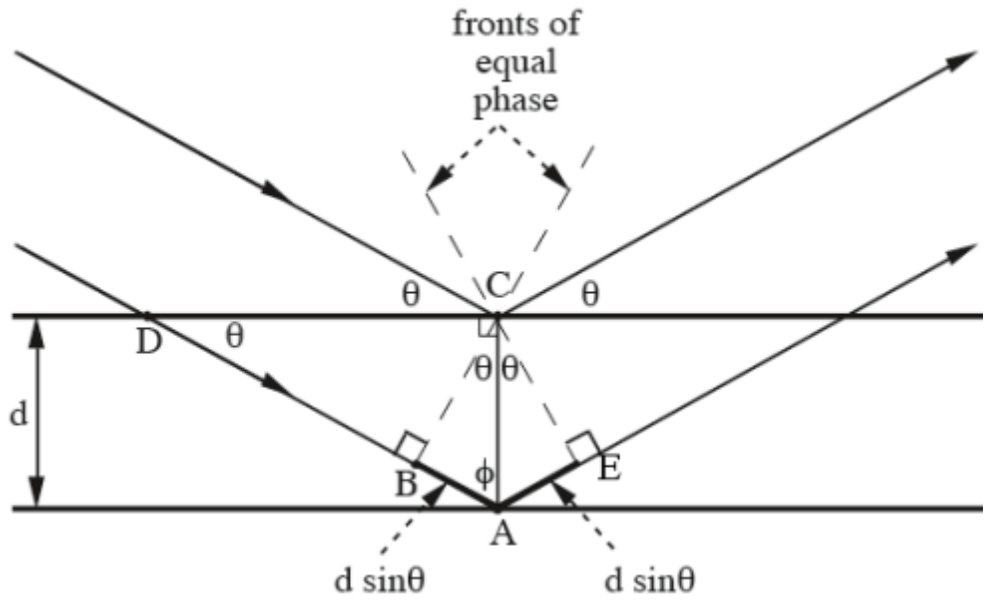

Figure 1.40: Interference of a wave scattering from two different planes of a crystal separated by a distance, *d.* The dashed lines run parallel to the crests or troughs of the incident and diffracted wavefronts. BAE represents the additional distance that must be covered by the second wave before and after reflection[162].

Figure 1.40 shows a simplified two-wave, two-plane interaction. In a real powder, polycrystalline sample, many beams are scattered by many planes of many crystallites. If preferred orientation is mitigated and the crystallites are randomly distributed within the sample, a cone of diffraction should be expected when using monochromatic radiation in accordance with the Debye-Scherrer method as seen in figure 1.41. A two-dimensional detector will reveal these cones as diffraction circles[161]. Diffractometers set up with Bragg-Brentano geometry make either horizontal or vertical one-dimensional cuts through the rings to produce line diffraction patterns consisting of peaks wherever the cut intersected with part of the circle[161]. Therefore, it is imperative that the powder sample consists of fine grains as a coarse sample will produce anisotropic intensities in the diffraction pattern[161]. A complete discussion on the intensities of powder diffraction peaks shall not be discussed for brevity, but is discussed thoroughly in the literature[162, 165.]

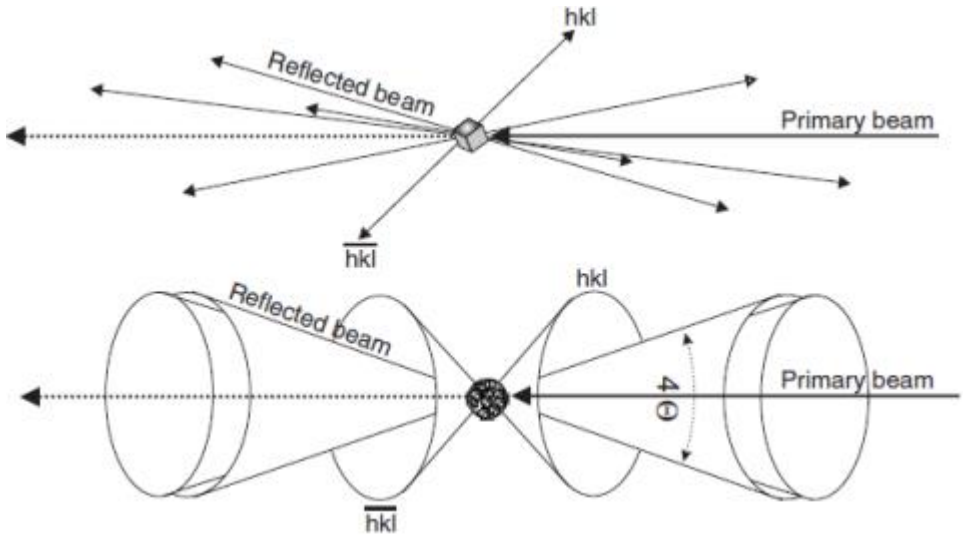

Figure 1.41: Comparison of scattered beams after interacting with (top) a single crystal and (bottom) a powder consisting of many randomly oriented crystallites[161].

1.4.1.2 Data Analysis

Powder diffraction was used in this study to obtain two different pieces of information from generated powder patterns: 1) relative amounts of each phase (rutile and anatase) present in each sample and 2) crystallite size of each phase present in each sample. Generated powder patterns were compared with previously obtained powder patterns from the JCPDS database (Appendix A)[58]. Bespoke software based on the Spurr and Myers equation, and instrumentally corrected Scherrer equation (including baseline and intensity corrections with K = 0.91) was employed to determine the relative amounts of each phase and crystallite size in each sample respectively. The source code for the peak fitting routine and particle size calculations can be found elsewhere[58]. A discussion on the application of these equations follows.

1.4.1.2.1 Spurr and Myers equation

The Spurr and Myers equation enables determination of the relative amounts of anatase and rutile in a mixed sample. It is based on the relationship between the weight ratio and intensity ratio for a given sample containing a mixture of allotropes: the scattering intensity of each component in a mixture of allotropes is proportional to its weight fraction[166].

$$\mathbf{x_A} = \frac{\mathbf{1}}{\mathbf{1 + 1.26\ \frac{I_R}{I_A}}} \qquad (1.9)$$

Equation 1.9 is the Spurr and Myers equation where X_A is the weight fraction of anatase in a sample; I_R and I_A are the maximum intensities of the rutile (1 1 0) and anatase (1 0 1) peaks respectively. This equation may be rearranged to obtain the weight fraction of rutile in a sample as given in equation 1.10:

$$\mathbf{x_R} = \frac{\mathbf{1}}{\mathbf{1 + 0.79\ \frac{I_A}{I_R}}} \qquad (1.10)$$

Where X_R is the weight fraction of rutile; I_R and I_A are the same as described above. It has been recommended by Spurr and Myers that equation 1.9 changes to equation 1.11 when I_A approaches zero.

$$\mathbf{x_A} = \frac{\mathbf{1}}{\mathbf{1 + 1.47\ \frac{I_R}{I_A}}} \qquad (1.11)$$

By inference, when I_R approaches zero equation 1.10 becomes:

$$\mathbf{x_R} = \frac{\mathbf{1}}{\mathbf{1 + 0.68\ \frac{I_A}{I_R}}} \qquad (1.12)$$

The standard error in X_A or X_R is 3 – 4 %.

1.4.1.2.2 Scherrer Equation

Many factors contribute to peak broadening in a diffraction pattern. These factors may be grouped as either instrumental or specimen broadening. Specimen broadening occurs as a result of temperature factors, different types of crystal macro- and micro-strain, and crystallite size[167]. Crystallite strain and size affect diffraction peaks in the following way:

Macroscopic strains change the interplanar *d*-spacing and cause a shift in the average position of the diffraction peak. Microscopic strains such as non-uniform lattice distortions, dislocations, and grain surface relaxations, produce a distribution of *d*-spacings causing peak broadening[161]. A distribution of strains in a polycrystalline sample as a result of variable compression and tension, changes the lattice parameters of individual crystallites slightly[162]. This has the effect of changing the peak position and causes peak broadening[162].

Diffraction peak widths are also affected by crystallite size[161]. Larger crystallites have many crystallographic planes contributing to diffraction compared to smaller

crystallites[161]. Therefore, small errors in phase in larger crystallites will eventually result in destructive interference (owing to the probability of a beam diffracting from a crystallographic plane causing destructive interference)[161]. Since there are fewer crystallographic planes available for diffraction in small crystallites, small phase errors do not result in destructive interference but rather contribute to peak broadening[161].

The Scherrer equation is used to calculate crystal grain size by measuring peak broadening in a diffraction pattern. Crystallite size is inversely related to the full width at half maximum (FWHM) height of a particular peak such that narrower peaks correspond to larger crystallite sizes.

$$\mathbf{L} = \frac{\mathbf{K\lambda}}{\boldsymbol{\beta} \cos \boldsymbol{\vartheta}} \qquad (1.13)$$

Equation 1.13 is the uncorrected Scherrer equation where L is the average crystallite size, λ is the wavelength of X-radiation used, β is the peak width of the peak profile at half maximum height in radians, θ is the peak position and K is the Scherrer constant[168]. The value of K used in each calculation depends on the shape of different crystallites (K = 0.94 was used in this experiment).

Crystallites that grow anisotropically produce anisotropic peak broadening. Therefore, a non-spherical crystallite will cause sharp diffraction peaks corresponding to the direction of preferred growth and broad diffraction peaks corresponding to all other directions as proven in a study by Zhang *et al*. In the study, the researchers found that the (0 0 4) Bragg peak corresponding to 30 nm anatase nanorods was narrower and displayed stronger peak intensity compared with the (0 0 4) peak corresponding to 16 nm anatase nanorods[169]. This was due to the nanorods exhibiting preferential growth along the c-axis[169]. The (0 0 4) Bragg peak corresponding to spherical particles displayed the greatest width and poorest intensity of all three particle types. Other peaks remained similar in shape and intensity[169].

It is therefore necessary to use different values of K in equation 1.13 for different particle shapes. This was not done in this study as it was previously shown that the change in particle size was smaller than an error of 1 nm associated with equation 1.13.

1.4.2 Transmission Electron Microscopy

The optical microscope suffers from the inherent problem of limited resolution due to the wavelength of visible light. In 1932, Knoll and Ruska proposed the idea of an electron microscope[170]. This, seven years after de Broglie posited the wave-like characteristics of the electron and five years after Davisson and Germer, and Thomson and Reid demonstrated the wave nature of electrons experimentally[170]. Over the decades with ever improving TEM's, this instrument has become central to the complete microstructural characterisation of materials and devices[162]. As stated by Williams and Carter, referring to the TEM[170]: "No other scientific instrument exists which can offer such a broad range of characterisation techniques with such high spatial and analytical resolution, coupled with a completely quantitative understanding of the various techniques".

The primary advantage that electrons possess over X-rays is that they can be easily focussed[162]. While X-ray diffraction serves as a more powerful technique for bulk material quantification, TEM affords the ability to image (spatial imaging) and select a single crystallite for a diffraction experiment (diffraction imaging)[162]. Additionally, spectroscopic studies (analytical electron microscopy – AEM) – based on the principle of a generated electron in the beam causing electronic excitations within the atoms of the sample – are also possible[162]. These include techniques such as energy dispersive spectroscopy (EDS) and electron energy loss spectroscopy (EELS). It is therefore possible to obtain spectroscopic, crystallographic, and imaging information from a single small area within the specimen. Depending on the type of TEM available, it may be possible to obtain all of this information during a single analysis session.

As with all analysis techniques, the TEM is not without its disadvantages. The major issue with TEM generated images is that it is a two-dimensional image of a three-dimensional specimen. Provided that the entire specimen is electron transparent, the depth of field in a TEM allows for the top and bottom surfaces of the specimen to be in focus simultaneously. Depth of field coupled with two-dimensional projection can result in TEM images possessing artefacts. Samples can only be analysed in a vacuum therefore limiting sample analysis in ambient or natural environment conditions. The limitations placed on specimen thinness ensure that any single specimen is usually not representative of the sample. Only a small amount of the specimen can be analysed at

a time making TEM a time consuming technique (relative to powder diffractometry). In 2009, it was estimated that no more than 1 cm^3 of material had been analysed by all TEM's ever[170]. High throughput sample analysis is not yet practical due to the need to manually align the microscope before all specimen analyses, further increasing the time required for analysis per sample. Additionally, specimens must be sufficiently thin to allow electrons to pass through – this places limitations on the specimen types that can be imaged using TEM. The capital and running costs of a TEM increase the cost of per-sample analysis.

Specimen damage is a key disadvantage in the present study as partially synthesized specimens containing polymers were analysed. Polymers are sensitive to ionising radiation and are prone to beam damage making TEM a destructive technique. Incident electrons can cause scission in the main chain, changing the basic structure of the polymer. It can also cause side groups to be removed from the parent chain. This causes cross-linking between different polymer chains. The available method to mitigate this issue in this study was to operate under low dose conditions.

This section shall discuss conventional and phase contrast imaging in the transmission electron microscope and high-resolution transmission electron microscope. These have been employed in this work to study the structural relationships between polymorphs post-synthesis and during incomplete syntheses on the nanoscale. Other transmission electron microscopy instruments/techniques such as scanning transmission electron microscopy (STEM), analytical electron microscopy (AEM), convergent-beam electron diffraction (CBED), Z-contrast imaging, Lorentz microscopy, *in-situ* techniques, and holography will not be discussed. Much of this section has been adapted from Transmission Electron Microscopy: A Textbook for Materials Science by D. B. Williams and C. Barry Carter[170] and Transmission Electron Microscopy and Diffractometry by B. Fultz and J. M. Howe[162].

1.4.2.1 The need for Electrons

The resolution of microscopes is on the order of the wavelength of light used as a probe[171]. The Rayleigh criterion (equation 1.14) states that the smallest detail that may be resolved in a light microscope is approximately equal to half the wavelength of light used[170].

$$\boldsymbol{\delta = \frac{0.61\lambda}{\mu \cos \beta}} \qquad (1.14)$$

Where δ is the resolution limit, λ is the wavelength of radiation, μ is the refractive index of the viewing material and β is the semi-angle of collection of the magnifying glass. Therefore, it is not possible to use light based microscopes to image features on the nano-scale. The de Broglie relation (equation 1.15) shows a relationship between the linear momentum, *p*, of a particle and its wavelength, λ (*h* is Planck's constant)[171].

$$\boldsymbol{\lambda} = \frac{\boldsymbol{h}}{\boldsymbol{p}} \qquad (1.15)$$

From equation 1.15 it can be seen that particles with higher linear momenta possess shorter wavelengths. Once accelerated through a potential difference, V, the energy gained by the electrons is *e*V where *e* is the magnitude of its charge. Following acceleration, all the acquired energy is in the form of kinetic energy[171]. Accounting for the energy equivalency, equation 1.15 can be expressed as equation 1.16, where m_e is the mass of an electron.

$$\boldsymbol{\lambda} = \frac{\boldsymbol{h}}{(\boldsymbol{2m_e eV})^{1/2}} \qquad (1.16)$$

Equation 1.16 is a non-relativistic expression that shows by increasing the accelerating voltage, the wavelength of electrons can be decreased. Therefore, the resolution of a microscope can be improved by increasing the energy of the radiation source. For electron energies greater than 100 keV, relativistic effects must be considered as given in equation 1.17.

$$\boldsymbol{\lambda} = \frac{\boldsymbol{h}}{[\boldsymbol{2m_e eV}\left(\boldsymbol{1} + \frac{\boldsymbol{eV}}{\boldsymbol{2m_e c^2}}\right)]^{1/2}} \qquad (1.17)$$

Electrons possessing 100 keV energy spiral through the TEM column relativistically at $\sim 1.6 \times 10^8$ m/s such that there is never more than one electron interacting with the specimen at any given time. Electron properties as a function of increasing accelerating voltage are given in table 1.12.

The principles of X-ray and electron scattering are different. In X-ray diffraction, the negatively charged electron cloud of the specimen interacts with the electromagnetic field of the incident X-rays. Specimen electrons then oscillate with the period of the applied X-ray beam. As is typical of accelerated charged particles, the electrons subsequently emit their own electromagnetic field that is consistent in wavelength and

phase with the incident X-radiation. The ensuing field propagates radially from all scattering sources. In electron scattering, electrons interact with the local electromagnetic fields of the specimen as they are scattered by both the nuclei and electron cloud in the material. There is no field-to-field exchange as is the case for X-ray scattering. This makes electron scattering a more complex process than X-ray scattering.

Table 1.12: Electron properties as a function of increasing accelerating voltage[170].

Accelerating Voltage (kV)	Non-relativistic wavelength (nm)	Relativistic wavelength (nm)	Mass ($\times m_e$)	Velocity ($\times 10^8 \mathrm{m/s}$)
100	0.00386	0.00370	1.196	1.644
120	0.00352	0.00335	1.253	1.759
200	0.00273	0.00251	1.391	2.086
300	0.00223	0.00197	1.587	2.330
400	0.00193	0.00164	1.783	2.484
1000	0.00122	0.00087	2.957	2.823

1.4.2.2 Principles of TEM

An electron gun emits a beam of electrons with a well-defined de Broglie wavelength. Magnetic fields in various electromagnetic lenses focus the electron beam of uniform intensity onto the specimen. The electrons in the beam interact with matter in the specimen, exploiting the wave-particle duality of electrons in the beam. After interacting with the specimen, transmitted electrons have a non-uniform distribution. The specimen can be imaged with spatial distribution observed as contrast in the images; angular distribution of scattering can be observed as diffraction patterns from the specimen. A restricting aperture allows for electrons that have gone through a specific type of interaction to be selected to reach the detector. The type of information obtained is dependent on the type of electron beam interaction monitored (figure 1.42).

Central to obtaining any information from a TEM, are electrostatic interactions that cause electron scattering. Electrons can be forward-scattered or back-scattered depending on the thickness of the specimen. Forward-scattering can be grouped according to electron energy loss (i.e.: elastic or inelastic) and electron wave phase

shifts (i.e.: coherent or incoherent). Different types of scattering occur depending on the angle at which transmitted electrons are scattered. The characteristics of the scattering event are governed by the incident electron energy, atomic weight of the scattering atom, the specimen thickness, density, crystallinity, and angle of the specimen to the incident beam. The probability of an incident electron interacting with an atom within the specimen is given by the interaction cross section and intuitively, a larger cross section increases the chances of scattering. Interestingly, higher incident electron energies decrease the interaction cross section.

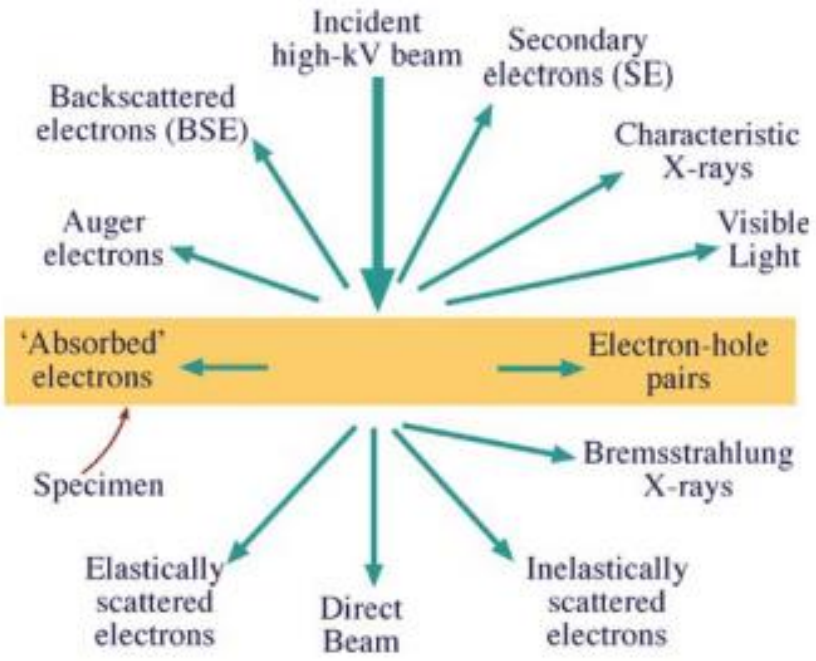

Figure 1.42: Various signals generated from a high-energy incident beam of electrons interacting with a thin specimen. The arrows indicate approximate areas where the signals can be detected[170].

Imaging and diffraction are the two primary modes in a TEM. To see a diffraction pattern, the imaging system lenses have to be adjusted such that the back focal plane of the objective lens becomes the object plane for the intermediate lens. Additionally, the objective aperture must be removed from the back focal plane and the selected area diffraction aperture must be inserted into the image plane. To operate in imaging mode, the intermediate lens is adjusted such that its object plane is the imaging plane of the objective lens. The objective aperture must be inserted into the back focal plane of the objective lens and the selected area diffraction aperture must be removed from the image plane. These two operations are illustrated schematically in figure 1.43.

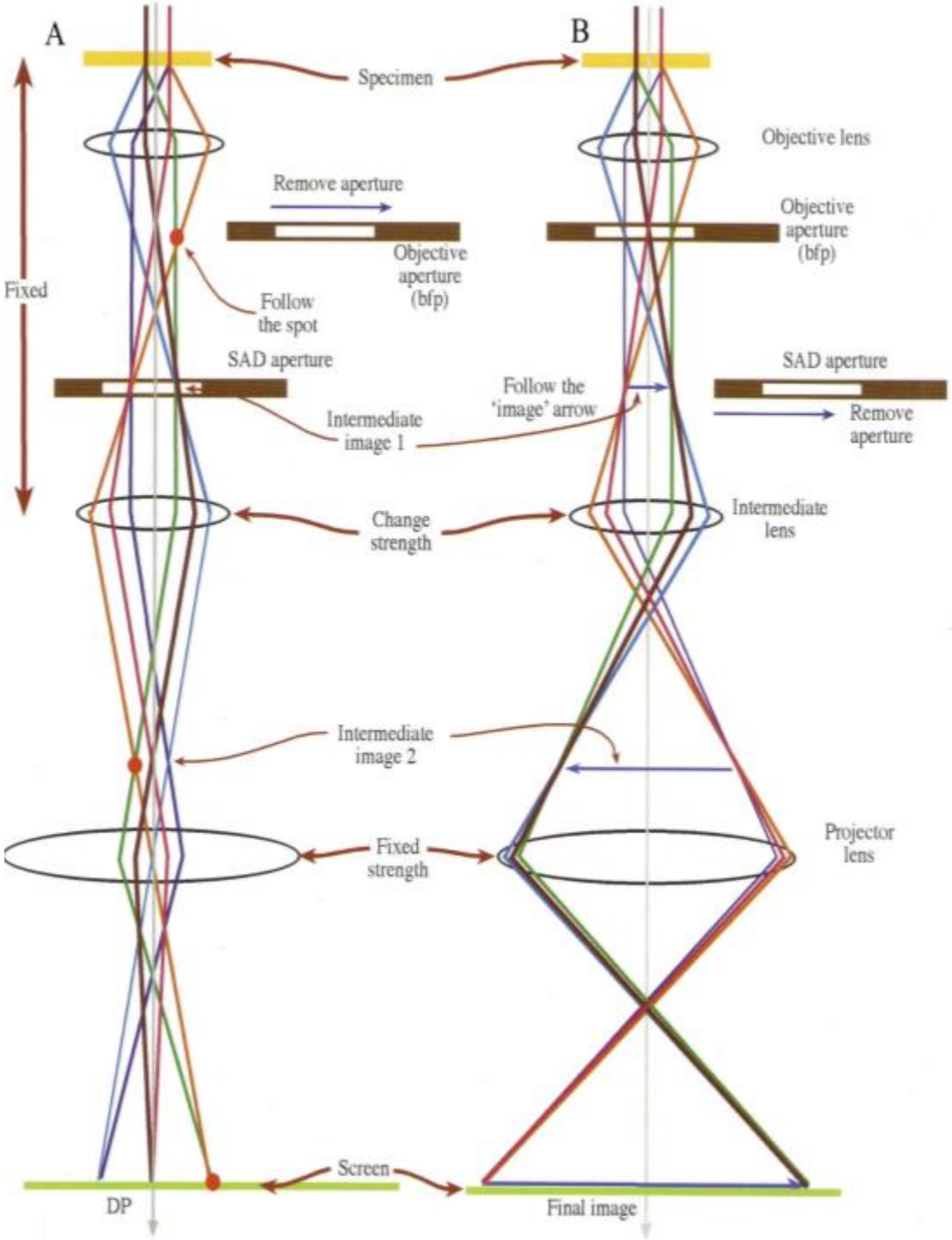

Figure 1.43: The two basic operating modes of the TEM illustrated schematically using only three lenses. The intermediate lens selects either the back focal plane (bfp) (A) or the image plane (B) of the objective lens as its object. Note the positions of the selected area diffraction (SAD) and objective apertures in (A) diffraction and (B) imaging modes[170].

1.4.2.3 High Resolution Transmission Electron Microscopy

Implicit in the name, HRTEM is capable of resolving lattice fringes in appropriate specimens. This is achieved by exploiting phase contrast imaging in the instrument: the phase of diffracted electron waves interfere with the phase of transmitted waves[162]. Fourier transforms are used to understand atomic resolution images generated in the HRTEM.

HRTEM image interpretation requires matching experimentally obtained images with computed image simulations of model structures using for example, the multislice algorithm[162]. The multislice approach is two-fold[162]: images are simulated considering 1) beam-specimen interaction and 2) modifying the electron wavefunction based on the effects of the instrument – primarily the effects of the objective lens. Initially, the specimen is divided into many slices of a specific thickness. The crystal potential of each slice is considered as a two-dimensional projected potential. Once the effect of the first slice on the phase of the incident wavefront has been ascertained, the ensuing wavefunction is propagated to the next slice. This procedure is repeated, slice by slice, until the sample thickness has been achieved. Accelerating voltage is the only microscope parameter considered in the beam-specimen calculation.

1.4.2.3.1 Data Analysis

In the present study an open source image processing program, ImageJ, was employed to obtain image simulations based on experimentally obtained images. ImageJ makes use of fast Fourier transforms to obtain frequency domain images. The calculation is based on an implementation of the Fourier-related two-dimensional fast Hartley Transform[172]. Calculated image simulations were then compared with theoretically obtained simulations so that comments on atomic structure could be made.

1.4.3 Thermogravimetric Analysis

Thermogravimetric analysis (TGA) involves measuring the change in mass of a sample as a function of increasing temperature[164]. The sample is heated at a constant rate until it begins to decompose at a specific temperature. Decomposition can occur over a range of temperatures. The change in mass can be used to make quantitative calculations of compositional changes[164]. The temperature at which decomposition begins and ends is not a fundamental property of the sample. Decomposition temperatures depend on heating rate, nature of the solid, and atmosphere above the

sample, and as a result, do not represent the equilibrium decomposition temperature[164]. Figure 1.44 shows a PerkinElmer STA 6000 analyser.



Figure 1.44: PerkinElmer STA 6000 analyser used for TGA analysis in this study.

1.5 References

1. Chen, X. & Mao, S. S. Titanium Dioxide Nanomaterials: Synthesis, Properties, Modifications, and Applications. *Chemical Reviews* **107,** 2891 – 2959 (2007).

2. Cushing, B. L., Kolesnichenko, V. L. & O'Connor, C. J. Recent Advances in the Liquid-Phase Syntheses of Inorganic Nanoparticles. *Chemical Reviews* **104,** 3893 – 3946 (2004).

3. Colomban, P. The use of metal nanoparticles to produce yellow, red and iridescent colour, from Bronze Age to Present Times in lustre pottery and glass: Solid state chemistry, spectroscopy and nanostructure. *Journal of Nano Research* **8,** 109 –132 (2009).

4. Feynman, R. There's plenty of room at the bottom. *Engineering and Science* **23,** 22 – 36 (1960).

5. Dziike Mutambara, F. Resin-gel synthesis and characterisation of copper and titanium mixed metal oxides nanoparticles. (University of the Witwatersrand, 2014).

6. Navrotsky, A. Energetics of nanoparticle oxides: interplay between surface energy and polymorphism. *Geochemical Transactions* **4,** 34 – 37 (2003).

7. Pechini, M. P. Method of preparing lead and earth titanates and niobates and coating method using the same to form a capacitor. (1967).

8. Roque-Malherbe, R. M. A. *The Physical Chemistry of Materials: Energy and Environmental Applications*. (CRC Press, Taylor Francis Group, 2010).

9. Lin, J., Yu, M., Lin, C. & Liu, X. Multiform Oxide Optical Materials via the Versatile Pechini-Type Sol-Gel Process: Synthesis and Characteristics. *Journal of Physical Chemistry C* **111,** 5835 – 5845 (2007).

10. Hassanzadeh-Tabrizi, S. A. Synthesis and luminescence properties of YAG:Ce nanopowder prepared by the Pechini method. *Advanced Powder Technology* **23,** 324 – 327 (2012).

11. Ebelmen, M. Recherches sur les combinaisons des acides borique et silicique avec les e´thers. *Annales de chimie et de physique* **16,** 129 – 166 (1846).

12. Brinker, C. J. & Scherer, G. W. *Sol-Gel Science: The Physics and Chemistry of Sol-Gel Processing*. (Academic Press, Inc, 1990).

13. Wright, J. D. & Sommerdijk, N. A. J. M. *Sol-Gel Materials: Chemistry and Applications*. (CRC Press, 2001).

14. Kakihana, M. Invited review 'sol-gel' preparation of high temperature superconducting oxides. *Journal of Sol-Gel Science and Technology* **6,** 7 – 55 (1996).

15. Oliveira, M. M., Schnitzler, D. C. & Zarbin, A. J. G. (Ti,Sn)O2 Mixed Oxides Nanoparticles Obtained by the Sol−Gel Route. *Chemistry of Materials* **15,** 1903 – 1909 (2003).

16. Chemseddine, A. & Moritz, T. Nanostructuring Titania: Control over Nanocrystal Structure, Size, Shape, and Organization. *European Journal of Inorganic Chemistry* **1999,** 235 – 245 (1999).

17. Sugimoto, T., Okada, K. & Itoh, H. Synthesis of Uniform Spindle-Type Titania Particles by the Gel–Sol Method. *Journal of Colloid and Interface Science* **193,** 140 – 143 (1997).

18. Sugimoto, T., Zhou, X. & Muramatsu, A. Synthesis of Uniform Anatase TiO2 Nanoparticles by Gel–Sol Method 1. Solution Chemistry of Ti(OH)(4−n)+ n Complexes. *Journal of Colloid and Interface Science* **252,** 339 – 346 (2002).

19. Sugimoto, T. & Zhou, X. Synthesis of Uniform Anatase TiO2 Nanoparticles by the Gel–Sol Method 2. Adsorption of OH− Ions to Ti(OH)4 Gel and TiO2 Particles. *Journal of Colloid and Interface Science* **252,** 347 – 353 (2002).

20. Sugimoto, T., Zhou, X. & Muramatsu, A. Synthesis of uniform anatase TiO2 nanoparticles by gel–sol method 3. Formation process and size control. *Journal of Colloid and Interface Science* **259,** 43 – 52 (2003).

21. Sugimoto, T., Zhou, X. & Muramatsu, A. Synthesis of uniform anatase TiO2 nanoparticles by gel–sol method 4. Shape control. *Journal of Colloid and Interface Science* **259,** 53 – 61 (2003).

22. Che, M., Nacgache, C. & Imelik, B. Electron Spin Resonance Studies on Titanium Dioxide and Magnesium Oxide-Electron Donor Properties. *Journal of Catalysis* **24,** 328 – 335 (1972).

23. Niederberger, M., Bartl, M. H. & Stucky, G. D. Benzyl Alcohol and Titanium TetrachloridesA Versatile Reaction System for the Nonaqueous and Low-Temperature Preparation of Crystalline and Luminescent Titania Nanoparticles. *Chemistry of Materials* **14,** 4364 – 4370 (2002).

24. Trentler, T. J., Denler, T. E., Bertone, J. F., Agrawal, A. & Colvin, V. L. Synthesis of TiO2 Nanocrystals by Nonhydrolytic Solution-Based Reactions. *Journal of the American Chemical Society* **121,** 1613 – 1614 (1999).

25. Patil, K. C., Singanahally, T. A. & Ekambaram, S. Combustion synthesis. *Current opinion in solid state and materials science* **2,** 158 – 165 (1997).

26. *Combustion Synthesis: Novel Routes to Novel Materials*. (Bentham Science Publishers Ltd., 2010).

27. Rajeshwar, K. & de Tacconi, N. R. Solution combustion synthesis of oxide semiconductors for solar energy conversion and environmental remediation. *Chemical Society Reviews* **38,** 1984 – 1998 (2009).

28. Moore, J. J. & Feng, H. J. Combustion synthesis of advanced materials: part 1. Reaction Parameters. *Progress in Materials Science* **39,** 243 – 273 (1995).

29. Varma, A. & Lebrat, J. Combustion Synthesis of Advanced Materials. *Chemical Engineering Science* **47,** 2179 – 2194 (1992).

30. Aruna, S. T. & Mukasyan, A. S. Combustion synthesis and nanomaterials. *Current Opinion in Solid State and Materials Science* **12,** 44 – 50 (2008).

31. Alves, A. K., Bergmann, C. P. & Berutti, F. A. *Novel Synthesis and Characterization of Nanostructured Materials*. (Springer-Verlag, 2013).

32. Prakash, A. S. *et al.* Solution-Combustion Synthesized Nanocrystalline Li4Ti5O12 As High-Rate Performance Li-Ion Battery Anode. *Chemistry of Materials* **22,** 2857 – 2863 (2010).

33. Nagaveni, K., Hegde, M. S. & Madras, G. Structure and Photocatalytic Activity of Ti1-xMxO2(ä (M) W, V, Ce, Zr, Fe, and Cu) Synthesized by Solution Combustion Method. *Journal of Physical Chemistry B* **108,** 20204 – 20212 (2004).

34. Mimani, T. & Patil, K. C. Solution combustion syntesis of nanoscale oxides and their composites. *Materials Physics and Mechanics* **4,** 134 – 137 (2001).

35. Patil, K. C. Advanced ceramics: Combustion synthesis and properties. *Bulletin of Materials Science* **16,** 533 – 541 (1993).

36. Nagaveni, K., Hegde, M. S., Ravishankar, N., Subbanna, G. N. & Madras, G. Synthesis and Structure of Nanocrystalline TiO2 with Lower Band Gap Showing High Photocatalytic Activity. *Langmuir* **20,** 2900 –2907 (2004).

37. Kingsley, J. J. & Patil, K. C. A novel combustion process for the synthesis of fine particle a-alumina and related oxide materials. *Materials Letters* **6,** 427 – 432 (1988).

38. Franklyn, P. J. & Narrandes, A. Unlocking the Secrets Behind the Resin-Gel Synthesis for the Controlled Formation of Anatase and Rutile. in *Proceedings of The International Conference Nanomaterials: Applications And Properties* **1,** 01PCN40–1 – 01PCN40–4 (Sumy State University, 2012).

39. Somiya, S. & Roy, R. Hydrothermal synthesis of fine oxide powders. *Bulletin of Materials Science* **23,** 453 – 460 (2000).

40. Wang, Y., He, Y., Lai, Q. & Fan, M. Review of the progress in preparing nano TiO2: An important environmental engineering material. *Journal of Environmental Sciences* **26,** 2139 – 2177 (2014).

41. Byrappa, K. & Yoshimura, M. *Handbook of Hydrothermal Technology: A Technology for Crystal Growth and Materials Processing*. (Noyes Publications / William Andrew Publishing, LLC, 2001).

42. Suchanek, W. L. & Riman, R. E. Hydrothermal Synthesis of Advanced Ceramic Powders. *Advances in Science and Technology* **45,** 184 – 193 (2006).

43. Hayashi, H. & Torii, K. Hydrothermal synthesis of titania photocatalyst under subcritical and supercritical water conditions. *Journal of Materials Chemistry* **12,** 3671 – 3676 (2002).

44. Hayashi, H. & Hakuta, Y. Hydrothermal Synthesis of Metal Oxide Nanoparticles in Supercritical Water. *Materials* **3,** 3794 – 3817 (2010).

45. Kasuga, T., Hiramatsu, M., Hoson, A., Sekino, T. & Niihara, K. Formation of Titanium Oxide Nanotube. *Langmuir* **14,** 3160 (1998).

46. Gupta, S. M. & Tripathi, M. A review on the synthesis of TiO2 nanoparticles by solution route. *Central European Journal of Chemistry* **10,** 279 – 294 (2012).

47. Landau, E. Better 'baby picture' of universe emerges. *CNN International Edition* (2013).

48. Halliday, D., Resnick, R. & Walker, J. *Fundamentals of Physics*. (Wiley International, 2005).

49. Shriver, D. F. *et al. Inorganic Chemistry*. (Oxford University Press, 2006).

50. Hazen, R. M. Evolution of Minerals. *Scientific American - Geology* **302,** 58 – 65 (2010).

51. Woodford, C. *The Eements: Titanium*. (Marshall Cavendish, 2003).

52. *CRC Handbook of Chemistry and Physics*. (CRC Press, Boca Raton, FL, 2005).

53. Fernández-García, M., Martínez-Arias, A., Hanson, J. C. & Rodriguez, J. A. Nanostructured Oxides in Chemistry: Characterization and Properties. *Chemical Reviews* **104,** 4063 – 4104 (2004).

54. Marchand, R., Brohan, L. & Tournoux, M. TiO2(B) A New Form of Titanium Dioxide and the Potassium Octatitanate K2Ti8O17. *Materials Research Bulletin* **15,** 1129 – 1133 (1980).

55. Latroche, M., Brohan, L., Marchand, R. & Tournoux, M. New Hollandite Oxides: TiO2(H) and K0.06TiO2. *Journal of solid state chemistry* **81,** 78 – 82 (1989).

56. Akimoto, J. *et al.* Topotactic Oxidation of Ramsdellite-Type Li0.5TiO2, A New Polymorph of Titanium Dioxide: TiO2 (R). *Journal of Solid State Chemistry* **113,** 27 – 36 (1994).

57. Muscat, J., Swamy, V. & Harrison, N. M. First-principles calculations of the phase stability of TiO2. *Physical Review B* **6,** 224112 (2002).

58. Franklyn, P. J. Hydrothermal Synthesis and Characterisation of Titania Nanoparticles. (University of the Witwatersrand, 2004).

59. Burdett, J. K., Hughbanks, T., Miller, G. J., Richadson, J. W. & Smith, J. V. Structural-Electronic Relationships in Inorganic Solids: Powder Neutron Diffraction Studies of the Rutile and Anatase Polymorphs of Titanium Dioxide at 15 and 295 K. *Journal of the American Chemical Society* **109,** 3639 – 3646 (1987).

60. Sousa, C. & Illas, F. Ionic-covalent transition in titanium oxides. *Physical Review B* **50,** 974 – 980 (1994).

61. Linsebigler, A. L., Lu, G. & Yates, Jr, J. T. Photocatalysis on TiO2 Surfaces: Principles, Mechanisms, and Selected Results. *Chemical Reviews* **95,** 735 – 758 (1995).

62. Ramamoorthy, M., Vanderbilt, D. & King-Smith, R. D. First-principles calculations of the energetics of stoichiometric TiO2 surfaces. *Physical Review B* **49,** 16721 – 16727 (1994).

63. Oliver, P. M., Watson, G. W., Kelsey, E. T. & Parker, S. C. Atomistic simulation of the surface structure of the TiO2 polymorphs rutile and anatase. *Journal of Materials Chemistry* **7,** 563 – 568 (1997).

64. Diebold, U. The surface science of titanium dioxide. *Surface Science Reports* **48,** 53 – 229 (2003).

65. Lazzeri, M., Vittadini, A. & Selloni, A. Structure and energetics of stoichiometric TiO2 anatase surfaces. *Physical Review B* **63,** 155409 (2001).

66. Lazzeri, M., Vittadini, A. & Selloni, A. Erratum: Structure and energetics of stoichiometric TiO2 anatase surfaces [Phys. Rev. B 63, 155409 (2001)]. *Physical Review B* **65,** 119901(E) (2002).

67. Ranade, M. R. *et al.* Energetics of nanocrystalline TiO2. *Proceedings of the National Academy of Sciences of the United States of America* **99,** 6476 – 6481 (2002).

68. Zhang, H. & Banfield, J. F. Understanding Polymorphic Phase Transformation Behavior during Growth of Nanocrystalline Aggregates: Insights from TiO2. *Journal of Physical Chemistry B* **104,** 3481 – 3487 (2000).

69. Hanaor, D. A. & Sorrell, C. C. Review of the anatase to rutile phase transformation. *Journal of Materials Science* **46,** 855 – 874 (2011).

70. Banfield, J. F. & Veblen, D. R. Conversion of perovskite to anatase and TiO2 (B): A TEM study and the use of fundamental building blocks for understanding relationships among the TiO, minerals. *American Mineralogist* **77,** 545 – 557 (1992).

71. Ye, X., Sha, J., Jiao, Z. & Zhang, L. Thermoanalytical Characteristic of Nanocrystalline Brookite-based Titanium Dioxide. *Nanostructured Materials* **8,** (1997).

72. Bakardjieva, S. *et al.* Transformation of brookite-type TiO2 nanocrystals to rutile: Correlation between microstructure and photoactivity. *Journal of Materials Chemistry* **16,** 1709 – 1716 (2006).

73. Kominami, H., Kohno, M. & Kera, Y. Synthesis of brookite-type titanium oxide nano-crystals in organic media. *Journal of Materials Chemistry* **10,** 1151 – 1156 (2000).

74. Hu, Y., Tsai, H. L. & Huang, C. L. Effect of brookite phase on the anatase–rutile transition in titania nanoparticles. *Journal of the European Ceramic Society* **23,** 691 – 696 (2003).

75. Li, J.-G., Tang, C., Li, D., Haneda, H. & Ishigaki, T. Monodispersed Spherical Particles of Brookite-type TiO2: Synthesis, Characterization, and Photocatalytic Property. *Journal of the American Ceramic Society* **87,** 1358 – 1361 (2004).

76. Gribb, A. A. & Banfield, J. F. Particle size effects on transformation kinetics and phase stability in nanocrystalline TiO2. *American Mineralogist* **82,** 717 – 728 (1997).

77. Rao, C. N. R. Kinetics and Thermodynamics of the Crystal Structure Transformation of Spectroscopically Pure Anatase to Rutile. *Canadian Journal of Chemistry* **39,** 498 – 500 (1961).

78. Banfield, J. F., Bischoff, B. L. & Anderson, M. A. TiO2 accessory minerals: coarsening, and transformation kinetics in pure and doped synthetic nanocrystalline materials. *Chemical Geology* **110,** 211 – 231 (1993).

79. Hwu, Y., Yao, Y. D., Cheng, N. F., Tung, C. Y. & Lin, H. M. X-Ray absorption of nanocrystal TiO2. *Nanostructured Materials* **9,** 355 – 358 (1997).

80. Zhang, J., Xu, Q., Feng, Z., Li, M. & Li, C. Importance of the Relationship between Surface Phases and Photocatalytic Activity of TiO2. *Angewandte Chemie International Edition* **47,** 1766 – 1769 (2008).

81. Barnard, A. S. & Curtiss, L. A. Prediction of TiO2 Nanoparticle Phase and Shape Transitions Controlled by Surface Chemistry. *Nano letters* **5,** 1261 – 1266 (2005).

82. Kumar, K.-N. P. Growth of Rutile Crystallites During the Initial Stage of Anatase-to-Rutile Transformation in Pure Titania and in Titania-Alumina Nanocomposites. *Scripta Metallurgica et Materialia* **32,** 873 – 877 (1995).

83. Hirano, M., Nakahara, C., Ota, K., Tanaike, O. & Inagaki, M. Photoactivity and phase stability of ZrO2-doped anatase-type TiO2 directly formed as nanometer-sized particles by hydrolysis under hydrothermal conditions. *Journal of Solid State Chemistry* **170,** 39 – 47 (2003).

84. Riyas, S., Krishnan, G. & Das, P. N. M. Anatase–rutile transformation in doped titania under argon and hydrogen atmospheres. *Advances in Applied Ceramics* **106,** 255 – 264 (2007).

85. Zhang, H. & Banfield, J. F. Thermodynamic analysis of phase stability of nanocrystalline titania. *Journal of Materials Chemistry* **8,** 2073 – 2076 (1998).

86. Ding, X. & Liu, X. Correlation between anatase-to-rutile transformation and grain growth in nanocrystalline titania powders. *Journal of Materials Research* **13,** 2556 – 2559 (1998).

87. Lorenz, R. & Voorhees, P. W. *Growth and Coarsening: Ostwald Ripening in Material Processing*. (Springer-Verlag, 2002).

88. Gopal, M., Chan, W. J. M. & De Jonghe, L. C. Room temperature synthesis of crystalline metal oxides. *Journal of Materials Science* **32,** 6001 – 6008 (1997).

89. Zhang, H. & Banfield, J. F. New kinetic model for the nanocrystalline anatase-to-rutile transformation revealing rate dependence on number of particles. *American Mineralogist* **84,** 528 – 535 (1999).

90. Zhang, H. & Banfield, J. F. Size Dependence of the Kinetic Rate Constant for Phase Transformation in TiO2 Nanoparticles. *Chemistry of Materials* **17,** 3421 – 3425 (2005).

91. Penn, R. L. & Banfield, J. F. Imperfect Oriented Attachment: Dislocation Generation in Defect-Free Nanocrystals. *Science* **281,** 969 – 971 (1998).

92. Zhang, H., Finnegan, M. & Banfield, J. F. Preparing Single-Phase Nanocrystalline Anatase from Amorphous Titania with Particle Sizes Tailored by Temperature. *Nano letters* **1,** 81 – 85 (2001).

93. Penn, R. L. & Banfield, J. F. Oriented attachment and growth, twinning, polytypism, and formation of metastable phases: Insights from nanocrystalline TiO2. *American Mineralogist* **83,** 1077 – 1082 (1998).

94. Penn, R. L. & Banfield, J. F. Formation of rutile nuclei at anatase {112} twin interfaces and the phase transformation mechanism in nanocrystalline titania. *American Mineralogist* **84,** 871 – 876 (1999).

95. Zhang, H. & Banfield, J. F. Kinetics of Crystallization and Crystal Growth of Nanocrystalline Anatase in Nanometer-Sized Amorphous Titania. *Chemistry of Materials* **14,** 4145 – 4154 (2002).

96. Cölfen, H. & Antonietti, M. Mesocrystals: Inorganic Superstructures Made by Highly Parallel Crystallization and Controlled Alignment. *Angewandte Chemie International Edition* **44,** 5576 – 5591 (2005).

97. Zhang, D., Li, G., Wang, F. & Yu, J. C. Green synthesis of a self-assembled rutile mesocrystalline photocatalyst. *CrystEngComm* **12,** 1759 – 1763 (2010).

98. Park, T., Levchenko, A. A., Zhou, H., Wong, S. S. & Navrotsky, A. Shape-dependent surface energetics of nanocrystalline TiO2. *Journal of Materials Chemistry* **20,** 8639 – 8645 (2010).

99. Mao, Y., Kanungo, M., Hemraj-Benny, T. & Wong, S. S. Synthesis and Growth Mechanism of Titanate and Titania One-Dimensional Nanostructures Self-Assembled into Hollow Micrometer-Scale Spherical Aggregates. *Journal of Physical Chemistry B* **110,** 702 – 710 (2006).

100. Song, W. *et al.* Dandelion-shaped TiO2/multi-layer graphene composed of TiO2(B) fibrils and anatase TiO2 pappi utilizing triphase boundaries for lithium storage. *Journal of Materials Chemistry A* **4,** 8762 – 8768 (2016).

101. Kharisov, B. I., Kharissova, O. V. & Ortiz-Mendez, U. *Handbook of Less-Common Nanostructures*. (CRC Press, 2012).

102. Li, Y., Liu, J. & Jia, Z. Morphological control and photodegradation behavior of rutile TiO2 prepared by a low-temperature process. *Materials Letters* **60,** 1753 – 1757 (2006).

103. Yang, K., Zhu, J., Huang, S., Zhu, X. & Ma, G. Sonochemical synthesis and microstructure investigation of rod-like nanocrystalline rutile titania. *Materials Letters* **57,** 4639 – 4642 (2003).

104. Bai, X., Xie, B., Pan, N., Wang, X. & Wang, H. Novel three-dimensional dandelion-like TiO2 structure with high photocatalytic activity. *Journal of Solid State Chemistry* **181,** 450 – 456 (2008).

105. Baloyi, J., Seadira, T., Raphulu, M. & Ochieng, A. Synthesis and Characterisation of Dandelion like TiO2 Structure as Photocatalyst for Industrial Wastewater Treatment Containing Toxic Metal Hg(II). in *Planetary Scientific Research Center Proceeding* **41,** 138 – 145 (Planetary Scientific Research Center (PSRC), 2014).

106. Yi, J. *et al.* Synthesis of dandelion-like TiO2 microspheres as anode materials for lithium ion batteries with enhanced rate capacity and cyclic performances. *International Journal of Minerals, Metallurgy and Materials* **19,** 1058 – 1062 (2012).

107. Yamabi, S. & Imai, H. Crystal Phase Control for Titanium Dioxide Films by Direct Deposition in Aqueous Solutions. *Chemistry of Materials* **14,** 609 – 614 (2002).

108. Hosono, E., Fujihara, S., Kakiuchi, K. & Imai, H. Growth of Submicrometer-Scale Rectangular Parallelepiped Rutile TiO2 Films in Aqueous TiCl3 Solutions under Hydrothermal Conditions. *Journal of the American Chemical Society* **126,** 7790 – 7791 (2004).

109. Kakiuchi, K., Hosono, E., Imai, H., Kimura, T. & Fujihara, S. {1 1 1}-faceting of low-temperature processed rutile TiO2 rods. *Journal of Crystal Growth* **293,** 541 – 545 (2006).

110. Liu, B. & Zeng, C. Carbon Nanotubes Supported Mesoporous Mesocrystals of Anatase TiO2. *Chemistry of Materials* **20,** 2711 – 2718 (2008).

111. Tartaj, P. Sub-100 nm TiO2 mesocrystalline assemblies with mesopores: preparation, characterization, enzyme immobilization and photocatalytic propertieswz. *Chemical Communications* **47,** 256 – 258 (2011).

112. Bae, E., Murakami, N. & Ohno, T. Exposed crystal surface-controlled TiO2 nanorods having rutile phase from TiCl3 under hydrothermal conditions. *Journal of Molecular Catalysis A: Chemical* **300,** 72 – 79 (2009).

113. Karim, M. R. *et al.* Synthesis and characterization of highly organized crystalline rutile nanoparticles by low-temperature dissolution-reprecipitation process. *Journal of Materials Research* **30,** 1887 – 1893 (2015).

114. Li, X., Xiong, Y., Li, Z. & Xie, Y. Large-Scale Fabrication of TiO2 Hierarchical Hollow Spheres. *Inorganic Chemistry* **45,** 3493 – 3495 (2006).

115. Yang, H. G. & Zeng, H. C. Preparation of Hollow Anatase TiO2 Nanospheres via Ostwald Ripening. *Journal of Physical Chemistry B* **108,** 3492 – 3495 (2004).

116. Zhou, Y., Huang, Y., Li, D. & He, W. Three-dimensional sea-urchin-like hierarchical TiO2 microspheres synthesized by a one-pot hydrothermal method and their enhanced photocatalytic activity. *Materials Research Bulletin* **48,** 2420 – 2425 (2013).

117. Forro, L. *et al.* High mobility n-type charge carriers in large single crystals of anatase (TiO2). *Journal of Applied Physics* **75,** 633 – 635 (1994).

118. Tang, H., Prasad, K., Sanjinés, R., Schmid, P. E. & Lévy, F. Electrical and optical properties of TiO2 anatase thin films. *Journal of Applied Physics* **75,** 2042 – 2047 (1994).

119. Agrawal, S., English, N. J., Ravindranathan, T. & MacElroy, J. M. D. Perspectives on ab initio molecular simulation of excited-state properties of organic dye molecules in dye-sensitised solar cells. *Physical Chemistry Chemical Physics* **14,** 12044 – 12056 (2012).

120. Landmann, M., Rauls, E. & Schmidt, W. G. The electronic structure and optical response of rutile, anatase and brookite TiO2. *Journal of Physics: Condensed Matter* **24,** 195503 – 195509 (2012).

121. Asahi, R., Taga, Y., Mannstadt, W. & Freeman, A. J. Electronic and optical properties of anatase TiO2. *Physical Review B* **61,** 7459 – 7465 (2000).

122. Kormann, C., Bahnemann, D. W. & Hoffmann, M. Preparation and Characterization of Quantum-Size Titanium Dioxide. *The Journal of Physical Chemistry* **92,** 5196 – 5201 (1988).

123. Wu, Z. Y., Ouvrard, G., Gressier, P. & Natoli, C. R. Ti and O K edges for titanium oxides by multiple scattering calculations: Comparison to XAS and EELS spectra. *Physical Review B* **55,** 10382 – 10391 (1997).

124. Fuertges, F. & Abuchowski, A. The Clinical Efficacy Of Poly(Ethylene Glycol)-Modified Proteins. *Journal of Controlled Release* **11,** 139 – 148

125. Wunderlich, B. Motion in Polyethylene. II. Vibrations in Crystalline Polyethylene. *The Journal of Chemical Physics* **37,** (1962).

126. Torchilin, V. P. & Trubetskoy, V. S. Which polymers can make nanoparticulate drug carriers long-circulating? *Advanced Drug Reviews* **16,** 141 – 155 (1995).

127. Steuter, A., Mozafar, A. & Goodin, J. R. Water Potential of Aqueous Polyethylene Glycol. *Plant Physiology* **67,** 64 – 67 (1981).

128. Zalipsky, S. Chemistry of polyethylene glycol conjugates with biologically active molecules. *Advanced Drug Reviews* **16,** 157 – 182 (1995).

129. Miyazawa, T. Molecular Vibrations and Structures of High Polymers. I. General Method of Normal Coordinate Treatment by Internal Coordinates and Infrared Frequencies and Conformations of (-CH2-)n, (-CH2-O-)n, and (-CH2-O-CH2-)n. *The Journal of Chemical Physics* **35,** 693 – 713 (1961).

130. Opschoor, A. Unperturbed Dimensions of Polyethylene Chain Molecules. *Die Makromolekulare Chemie* **85,** 249 – 260 (1965).

131. Miyazawa, T., Fukushima, K. & Ideguchi, Y. Molecular Vibrations and Structure of High Polymers. ITI. Polarized Infrared Spectra, Normal Vibrations, and Helical Conformation of Polyethylene Glycol. *The Journal of Chemical Physics* **37,** 2764 – 2776 (1962).

132. Maxfield, J. & Shepherd, I. W. Conformation of poly(ethylene oxide) in the solid state, melt and solution measured by Raman scattering. *Polymer* **16,** 505 – 509 (1975).

133. Azri, A., Giamarchi, P., Grohens, Y., Olier, R. & Privat, M. Polyethylene glycol aggregates in water formed through hydrophobic helical structures. *Journal of Colloid and Interface Science* **379,** 14 – 19 (2012).

134. Sequeira, C. & Santos, D. *Polymer Electrolytes: Fundamentals and Applications*. (Woodhead Publishing Limited, 2010).

135. Hocine, S. & Li, M.-H. Thermoresponsive self-assembled polymer colloids in water. *Soft Matter* **9,** 5839 – 5861 (2013).

136. Pielichowski, K. & Fleituch, K. Differential Scanning Calorimetry Studies On Poly(ethylene Glycol) with Different Molecular Weights For Their Energy Storage. *Polymers For Advanced Technologies* **13,** 690 – 696 (2002).

137. Pasche, S., De Paul, S. M., Vörös, J., Spencer, N. D. & Textor, M. Poly(L-lysine)-graft-poly(ethylene glycol) Assembled Monolayers on Niobium Oxide Surfaces: A Quantitative Study of the Influence of Polymer Interfacial

Architecture on Resistance to Protein Adsorption by ToF-SIMS and in Situ OWLS. *Langmuir* **19,** 9216 – 9225 (2003).

138. Graham, N. B., Nwachuku, N. E. & Walsh, D. J. Interaction of poly(ethylene oxide) with solvents: 1. Preparation and swelling of a crosslinked poly(ethylene oxide) hydrogel. *Polymer* **23,** 1345 – 1349 (1982).

139. Graham, N. B., Zulfiqar, M., Nwachuku, N. E. & Rashid, A. Interaction of poly(ethylene oxide) with solvents: 2. Water-poly(ethylene glycol). *Polymer* **30,** 528 – 533 (1989).

140. Rajulu, A. V. & Sab, P. M. Ultrasonic Studies of Water/Poly(Ethylene Glycol) Mixtures. *European Polymer Journal* **32,** 267 – 268 (1996).

141. Graham, N. B. & Chen, C. F. Interaction of Poly(Ethylene Oxide) With Solvent: 5. The Densities of Water/Poly(Ethylene Glycol) Mixtures. *European Polymer Journal* **29,** 149 – 151 (1993).

142. Graham, N. B., Zulfiqar, M., Nwachuku, N. E. & Rashid, A. Interaction of poly(ethylene oxide) with solvents: 4. Interaction of water with poly(ethylene oxide) crosslinked hydrogels. *Polymer* **31,** 909 – 916 (1990).

143. Derkaoui, N., Said, S., Grohens, Y., Olier, R. & Privat, M. PEG400 Novel Phase Description in Water. *Journal of Colloid and Interface Science* **305,** 330 – 338 (2007).

144. Money, N. P. Osmotic Pressure of Aqueous Polyethylene Glycols. *Plant Physiology* **91,** 766 – 769 (1989).

145. Myers, B. K., Lapucha, J. E. & Grayson, S. M. Synthesis and MALDI-ToF characterization of dendronized poly(ethylene glycol)s. *Brazilian Journal of Pharmaceutical Sciences* **49,** 45 – 55 (2013).

146. Essa, S., Rabanel, J. M. & Hildgen, P. Effect of polyethylene glycol (PEG) chain organization on the physicochemical properties of poly(D, L-lactide) (PLA) based nanoparticles. *European Journal of Pharmaceutics and Biopharmaceutics* **75,** 96 – 106 (2010).

147. Jaskiewicz, K. *et al.* Incorporation of Nanoparticles into Polymersomes: Size and Concentration Effects. *ACS Nano* **6,** 7254 – 7262 (2012).

148. Bahrami, A. H. *et al.* Wrapping of nanoparticles by membranes. *Advances in Colloid and Interface Science* **208,** 214 – 224 (2014).

149. Raatz, M., Lipowski, R. & Weikl, T. R. Cooperative wrapping of nanoparticles by membrane tubes. *Soft Matter* **10,** 3570 – 3577 (2014).

150. Yue, T., Wang, X., Huang, F. & Zhang, X. An unusual pathway for the membrane wrapping of rodlike nanoparticles and the orientation- and membrane wrapping-dependent nanoparticle interaction†. *Nanoscale* **5,** 9888 – 9896 (2013).

151. Chen, J., Spear, S. K., Huddleston, J. G. & Rogers, R. D. Polyethylene glycol and solutions of polyethylene glycol as green reaction media. *Green Chemistry* **7,** 64 – 82 (2005).

152. Rogers, R. D., Zhang, J. & Bauer, C. B. The effects of choice of anion (X=Cl-, SCN-, NO-) and polyethylene glycol (PEG) chain length on the local and

supramolecular structures of LnX, /PEG complexes. *Journal of Alloys and Compounds* **249,** 41 – 48 (1997).

153. Parker, J. M., Wright, P. V. & Lee, C. C. A double helical model for some alkali metal ion-poly(ethylene oxide) complexes. *Polymer* **22,** 1305 – 1307 (1981).

154. Raja, K. S., Gandhi, T. & Misra, M. Effect of water content of ethylene glycol as electrolyte for synthesis of ordered titania nanotubes. *Electrochemistry Communications* **9,** 1069 – 1076 (2007).

155. Lee, S. J. & Lee, C. H. Fabrication of nano-sized TiO2 powder via an ethylene glycol entrapment route. *Materials Letters* **56,** 705 – 708 (2002).

156. Li, Q. *et al.* Ethylene glycol-mediated synthesis of nanoporous anatase TiO2 rods and rutile TiO2 self-assembly chrysanthemums. *Journal of Alloys and Compounds* **471,** 477 – 480 (2009).

157. Tripathy, S. K., Sahoo, T., Mohapatra, M., Anand, S. & Yu, Y.-T. Polyol-assisted synthesis of TiO2 nanoparticles in a semi-aqueous solvent. *Journal of Physics and Chemistry of Solids* **70,** 147 – 152 (2009).

158. Sasikala, R. *et al.* Highly dispersed phase of SnO2 on TiO2 nanoparticles synthesized by polyol-mediated route: Photocatalytic activity for hydrogen generation. *Internatinal Journal of Hydrogen Energy* **34,** 3621 – 3630 (2009).

159. *Powder Diffraction: Theory and Practice*. (The Royal Society of Chemistry, 2008).

160. Barrett, D. H. A Stable High Temperature Gold Nano-Catalyst: Synthesis, Characterization and Application. (University of the Witwatersrand, 2012).

161. Dinnebier, R. E. & Billinge, S. J. L. Principles of Powder Diffraction. in *Powder Diffraction: Theory and Practice* (eds. Dinnebier, R. E. & Billinge, S. J. L.) 1 – 19 (The Royal Society of Chemistry, 2008).

162. Fultz, B. & Howe, J. M. *Transmission Electron Microscopy and Diffraction of Materials*. (Springer-Verlag, 2008).

163. The Editors of Encyclopædia Britannica. Winners of the Nobel Prize for Physics. *Encyclopædia Britannica* (2016).

164. West, A. R. *Basic Solid State Chemistry*. (John Wiley and Sons Ltd, 1999).

165. Von Dreele, R. B. & Rodriguez-Carvajal, J. The Intensity of a Bragg Reflection. in *Powder Diffraction: Theory and Practice* (eds. Dinnebier, R. E. & Billinge, S. J. L.) 58 – 88 (The Royal Society of Chemistry, 2008).

166. Spurr, R. A. & Myers, H. Quantitative Analysis of Anatase-Rutile Mixtures with an X-Ray Diffractometer. *Analytical Chemistry* **29,** 760 – 762 (1957).

167. Scardi, P. Microstructural Properties: Lattice Defects and Domain Size Effects. in *Powder Diffraction: Theory and Practice* (eds. Dinnebier, R. E. & Billinge, S. J. L.) 376 – 413 (The Royal Society of Chemistry, 2008).

168. Monshi, A., Foroughi, M. R. & Monshi, M. R. Modified Scherrer Equation to Estimate More Accurately Nano-Crystallite Size Using XRD. *World Journal of Nano Science and Engineering* **2,** 154 – 160 (2012).

169. Zhang, Z., Zhong, X., Liu, S., Li, D. & Han, M. Aminolysis Route to Monodisperse Titania Nanorods with Tunable Aspect Ratio. *Angewandte Chemie International Edition* **44,** 3466 – 3470 (2005).

170. Williams, D. B. & Carter, C. B. *Transmission Electron Microscopy: A Textbook For Materials Science*. (Springer Science+Business Media, LLC, 2009).

171. Atkins, P. & De Paula, J. *Atkins' Physical Chemistry*. (Oxford University Press, 2006).

172. Ferreira, T. & Rasband, W. ImageJ User Guide: IJ 1.45m. (2011).

Chapter 2: Aims

The overriding aim of this work was to take steps towards understanding the mechanism of nanoparticle formation using the resin-gel synthesis technique. The current working theory of resin-gel synthesis describes the process as a metal ion solution coordinating to a polymer. Evaporation of excess solvent produces a hardened wax which is heated to combustion producing nanoparticles. Since it is possible to form a plethora of homogeneous, non-stoichiometric, mixed metal oxide nanoparticles, and even potentially non-oxide materials, it is necessary to understand how the technique operates before it may be manipulated to form nanoparticles of controlled size, shape, morphology, and composition. Metal ion precursors tailored towards the formation of TiO_2 were selected in all syntheses. Conditions that permit the formation of different TiO_2 -polymorphs (or combinations of polymorphs) of various sizes are well established in the literature. Therefore the aim was to analyse the formed products for crystalline phases and crystallite sizes in order to gather information concerning the reaction conditions that were present during synthesis.

To achieve the primary aim, the approach used in this work was divided broadly into two categories: 1) parameter variation studies to deduce the effects of various reaction components on the formed products and 2) conducting temporally controlled intermittent resin-gel syntheses to form ‘snapshots’ of the reaction as it progressed to completion.

Basic resin-gel synthesis involves a few necessary reaction components: solvent, coordinating polymer, metal ion precursor, acid if necessary to aid solubility, and heat. For the parameter variation work, all of these components were adjusted accordingly in turn to satisfy various sub-aims. These included investigating the effects of changing the solvent, polymer, acid, and Ti ion containing precursor. Additionally, changing the polymer chain length and stoichiometry, and employing different heating rates in the synthesis.

‘Snapshots’ were obtained by allowing the reaction to proceed for a given amount of time and then freezing the process before completion. Generated samples were then

imaged using TEM to observe partially formed products with the aim of making comments on the reaction mechanism causing specific structure formation.

All fully formed products were analysed quantitatively for phase composition using PXRD. Crystallite size was also deduced from powder diffractometry. Fully synthesised and partially synthesised products were analysed using TEM and selected samples were analysed using HRTEM.

Cursory evaluation of initial results revealed the presence of rutile mesocrystal formation in most rutile containing samples. Therefore, an adjunct aim of this work was to describe the formation of rutile mesocrystals under resin-gel synthesis conditions.

Chapter 3: Experimental Overview

The primary purpose of this chapter is to highlight the general workflow process used throughout this research. Experimental setups for these works (as given in chapter 2) are mostly similar given that they follow the general equation 3.1:

$$\mathbf{Ti^{+} + Polymer + Solvent \xrightarrow{\Delta} TiO_2} \qquad \mathbf{(2.1)}$$

3.1 Parameter Variation

A bulk solution of Ti^{+} ions containing excess solvent was divided to generate an appropriate number of samples per experiment. A polymer with varying chain lengths was added to each solution in a volumetric equivalent or stoichiometric equivalent manner. The mixtures were stirred using a glass rod by hand and heated to an appropriate temperature to allow for the formation of homogeneous gels. Following complete solvent evaporation under infrared lamps, the hardened resins were divided equally to introduce a replicate. Resins were heated to their flash point using different heating rates. When necessary to remove carbon residue, samples were calcined in a muffle furnace. The various parameters and methods of variation follow.

3.1.1 Polymer Type Variation

Two types of polymer were employed in this study: polyethylene glycol (PEG) and polyethylenimine (PEI), as given in figure 3.1.

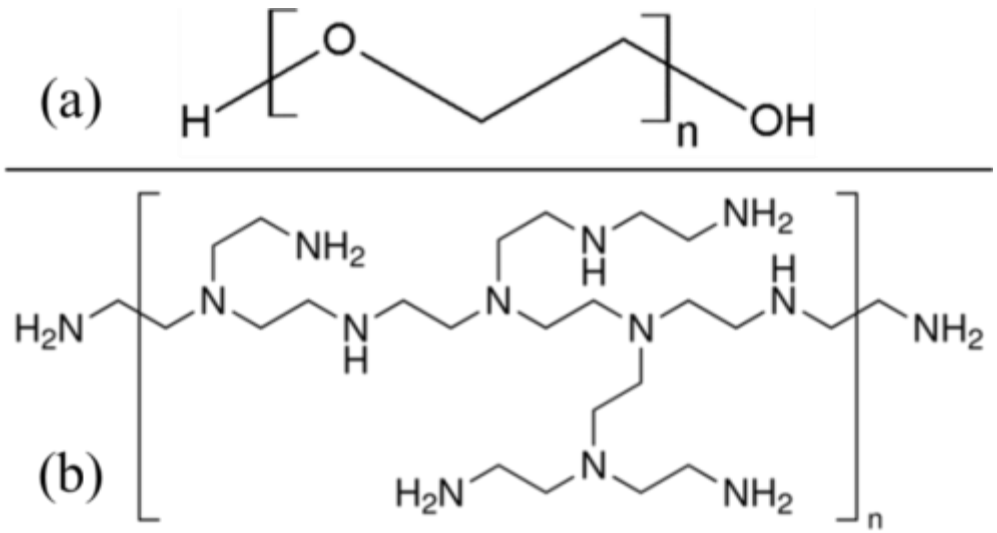

Figure 2.1: (a) Oxygen containing PEG and (b) oxygen free PEI.

3.1.2 Solvent Variation

Two solvents were employed in this study:

- ethanol
- water diluting HNO_3

3.1.3 Polymer Chain Length Variation

Polyethylene glycol (PEG) was used for the polymer chain length variation studies. Since there is only a single type of monomer present in this polymer, the number average molecular weight (M_n) and weight average molecular weight (M_w) are equal. The monomer unit ($-CH_2CH_2O-$) has a molecular weight of 44.05 g/mol. The approximate number of monomer units per polymer is obtained by dividing the average molecular weight of the polymer chain by the molecular weight of a single monomer. Table 3.1 lists all the chain lengths used in this study.

Table 2.1: Average PEG molecular weights used in this study with associated average number of monomers per chain.

Average PEG molecular weight (g/mol)	Average number of monomers per chain	Average number of fibre periods per chain
200	4.5	0.65
400	9.1	1.3
1000	22.7	3.2
1500	34.1	4.9
3000	68.1	9.7
4000	90.8	13.0
6000	136.2	19.8
8000	181.8	26.0
10000	227.2	32.5
12000	272.7	39.0
20000	454.4	65.0
35000	795.3	113.6

3.1.4 PEG quantity variation

The amount of polyethylene glycol was varied in two ways:

- volumetric variation – a volume equivalent amount of PEG was added to the metal ion solution
- stoichiometric variation – three ratios of the number of PEG chains of different molecular weights to metal ion precursor were selected –
  (Ti^{+} precursor : number of PEG chains):
  - 1 : 1
  - 1 : 0.5
  - 1 : 0.1

3.1.5 Acid Variation

Acid was added to reactions carried out in water. The two types selected were:

- nitric acid
- citric acid

3.1.6 Heating Rate Variation

Three different heating rates were selected (the nomenclature is specific to this investigation):

- conventional heating – resins were heated in a sand bath and ignited using a flame once they had reached their flash point.
- forced heating – resins were heated in a sand bath from below while concurrently being subjected to a blue flame generated using a Bunsen burner from above until ignition had occurred.
- rapid heating – Resins were poured onto a cast iron vessel pre-heated in a muffle furnace to 900 °C. This caused almost instantaneous resin ignition.

3.1.7 Metal Ion Precursor Variation

Seven different Ti^{+} containing precursors were used as given in table 3.2.

Table 2.2: Various titanium ion containing precursors used in this study.

Name, linear formula	Structure
Titanium (IV) chloride, **$TiCl_4$**	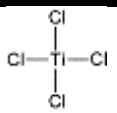
Titanium (IV) oxysulfate, **$TiOSO_4$**	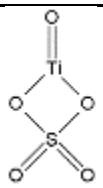
Titanium (IV) isopropoxide, **$Ti[OCH(CH_3)_2]_4$**	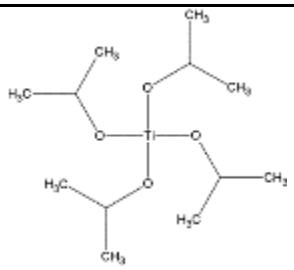
Titanium (IV) 2-ethylhexyloxide, **$Ti[OCH_2CH(C_2H_5)(CH_2)_3CH_3]_4$**	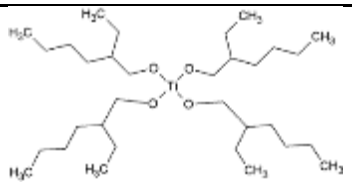
Titanium diisopropoxide bis(acetylacetonate), **$[(CH_3)_2CHO]_2Ti(C_5H_7O_2)_2$**	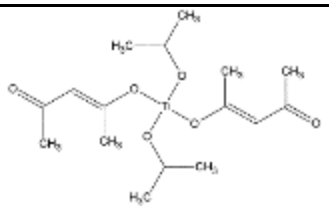
Titanium (IV) bis(ammonium lactato)dihydroxide solution, **$[CH_3CH(O\text{-})CO_2NH_4]_2Ti(OH)_2$**	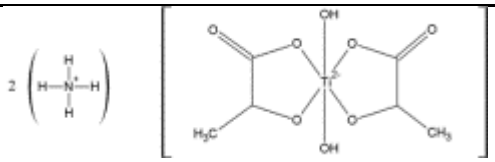
Titanium (IV) (triethanolaminato)isopropoxide, **$C_9H_{19}NO_4Ti$**	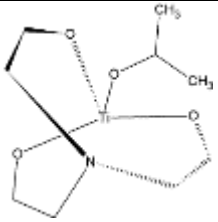

3.2 Controlled Temporal Intermittent Resin-gel Synthesis

Samples were generated according to equation (3.1) using water containing HNO_3 as the solvent and varying only the PEG chain length and stoichiometric ratio to the amount of added metal ions. Gel homogenisation and solvent evaporation were conducted as previously described. The conventional heating method was employed to initiate the process of polymer degradation to ignition. At various points during the degradation and ignition process, either:

- liquid N_2 was used to freeze the sample, generating an incompletely synthesised product, or
- a metal rod was dipped into the sample to obtain a specimen

XRD analysis was then attempted on suitable specimens. TEM analysis was performed on all specimens generated using the dipped metal rod technique.

3.3 Characterisation and Data Analysis

For PXRD analysis all samples were ground to a fine, consistent powder using an agate mortar and pestle.

PXRD analysis was achieved using either a Bruker D2 Phaser diffractometer or a Siemens D5000 diffractometer. The Bruker D2 instrument employed the Bragg-Brentano geometry with a θ-θ goniometer. Cu Kα or Co Kα radiation was used with a Ni Kβ filter. A 0.6 mm slit was used with secondary Söller slits at 2.5° and a LYNXEYE™ linear detector.

The Siemens D5000 employed the Bragg-Brentano geometry with a θ-2θ goniometer. Cu Kα radiation was used with a scintillation counter and Söller slits at 2°. This diffractometer possessed a forty-position sample changer containing flat-plate, shallow-well sample holders. Due to the lack of compatible zero-background sample holders, the present sample holders had to be completely filled with sample and then adjusted to a uniform sample height.

Data Manager (PJF shareware programs) and XRD Analyser (PJF shareware programs) were used to determine phase purity (mass % of each phase) and crystallite size respectively. Data Manager and XRD Analyser are bespoke peak analysis programs based on the Spurr and Myers, and instrumentally corrected Scherrer equations (K = 0.91) respectively[1].

TEM analysis was achieved using either an FEI Tecnai T12 TEM at 120 kV employing a LaB_6 source. High resolution imaging was conducted using an FEI Tecnai F20 at 200 kV with a field-emission gun, a JEOL JEM 2100 at 200 kV with a LaB_6 source, and a JEOL 3011 at 300 kV, LaB_6 source with Cs = 0.6 mm and Cc = 1.1 mm, and a 1 K camera.

3.4 References

1. Vrandečić, N. S., Erceg, M., Jakić, M. & Klarić, I. Kinetic analysis of thermal degradation of poly(ethylene glycol) and poly(ethylene oxide)s of different molecular weight. *Thermochimica Acta* **498,** 71 – 80 (2010).

Chapter 4: Preliminary Investigations

The aim of this chapter is to describe the preliminary investigations that were conducted to determine the required reaction temperatures and conditions for resin-gel synthesis. Other preliminary investigations included XRD analysis of control samples. Two primary preliminary investigations were conducted. The first investigation involved determining the temperature range for the decomposition of PEG of various molecular weights. The second investigation involved systematically removing O_2 from the system. Appendix B contains XRD analyses of control samples.

4.1 PEG Decomposition Temperature Range

During resin-gel synthesis, the metal ion/polymer mixture must be heated to ignition. For this to occur, the polymer within the sample must first decompose. Therefore, the purpose of this investigation was to ascertain the heating requirements for PEG decomposition. TGA was employed to determine the decomposition temperature range of PEG of various molecular weights. Decomposition effected by TGA is not a fundamental property of a material since factors such as heating rate and atmospheric contents above the sample influence decomposition[1]. Therefore, the decomposition temperature ranges obtained from this investigation will be used as a vague mark to determine the amount of heat required for resin-gel syntheses.

Analyses were completed using a PerkinElmer STA 6000 analyser. Between 5 – 10 mg of PEG was added to a ceramic pan and placed in the instrument furnace. The sample temperature was increased from room temperature to 900 °C at a rate of 10 °C/min under an oxidative atmosphere (air, 50 ml/min). Figure 4.1 shows the data collected from TGA for unloaded PEG samples.

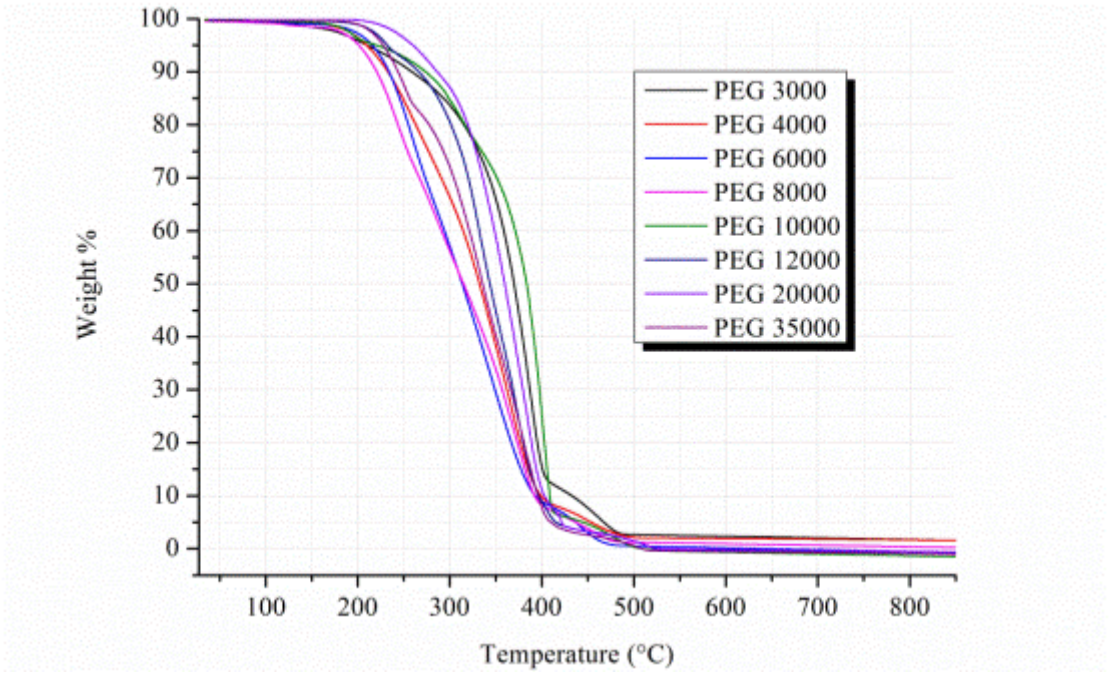

Figure 4.1: **TGA of unloaded PEG of various molecular weights.**

Figure 4.1 shows that for all represented samples, the onset of decomposition occurred ≥ 175 °C. PEG 200 – 1500 g/mol were not included in figure 4.1 as they existed as viscous liquids or waxes. As expected, the start of decomposition was delayed as the molecular weight of the polymer increased. In accordance with this result, Vradenčić *et al*., found that the melting temperature of PEG increased with increasing molecular weight[2]. This result confirms that during resin-gel synthesis, samples synthesised using longer chain polymers have to be heated for a longer period. At ≤ 500 °C, all samples had completely decomposed. This implies that a calcination temperature of 500 °C is sufficient to remove all residues remaining from ignition. Interestingly, the data suggests that higher molecular weight polymers produce fewer residues after decomposition than lower molecular weight polymers. Although the TGA shows a single degradation step for all samples, specific decomposition profiles appear to be independent of polymer chain length. This observation was made previously[2] and may result from the nature of PEG that undergoes random scission during oxidative degradation[3, 4].

A lower molecular weight PEG (3000 g/mol) and higher molecular weight PEG (10000 g/mol) were each loaded with a stoichiometric amount of $TiCl_4$ (Ti^{4+} : PEG = 1 : 0.5). TG analysis was performed on these samples and compared with the results obtained from unloaded PEG of the same molecular weight. These results are

represented in figures 4.2 and 4.3 respectively. As observed from figures 4.2 and 4.3, the degradation profile of the loaded and unloaded samples are similar. This implies that metal loading does not significantly interfere with the degradation procedure. Additionally, all resin-gel syntheses can be conducted in a medium that allows for uniform heating to ca. 200 °C – which represents the onset of thermal degradation.

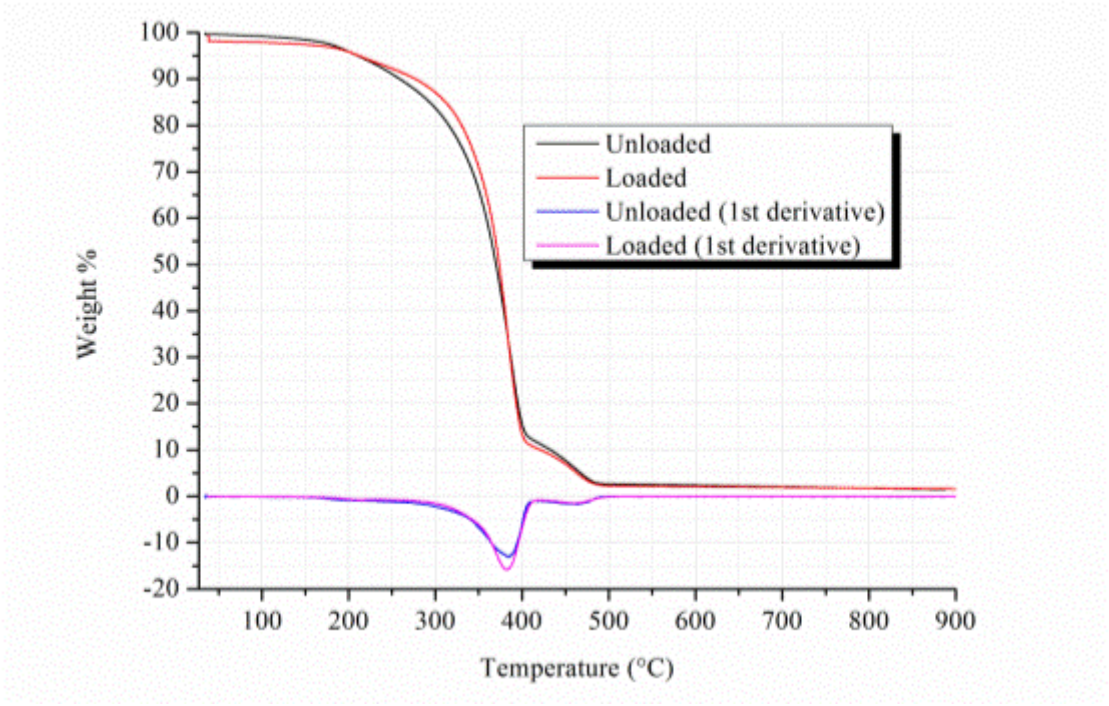

Figure 4.2: TGA and 1st derivatives of unloaded and loaded PEG 3000 g/mol.

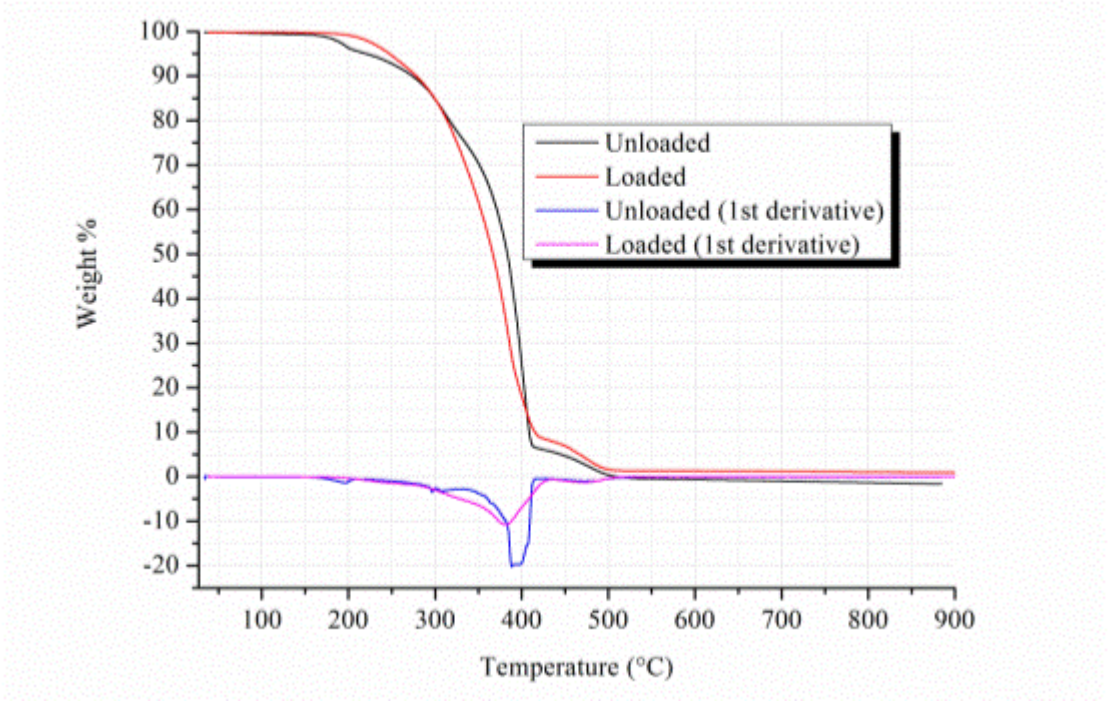

Figure 4.3: TGA and 1st derivatives of unloaded and loaded PEG 10000 g/mol.

4.2 Systematic O_2 Elimination

The purpose of this experiment was to observe changes in the products formed from resin-gel synthesis when the source of oxygen in the system was altered. This will allow for the determination of ideal synthesis conditions. Samples were synthesised in accordance with equation (3.1) with the exception that reaction components containing O_2 were systematically substituted for O_2-free components. Additionally, atmospheric O_2 was excluded from the reaction by conducting the component addition and polymer degradation steps under N_2 in a Schlenk line. The source of metal ions ($TiCl_4$) was not varied. Table 4.1 shows the O_2 containing and O_2 free components with quantities used in this study.

Table 4.1: O_2 containing and O_2 free components with quantities employed in this study.

	Polymer [quantity]	Solvent [quantity]	Atmosphere
O_2 containing	Polyethylene glycol (PEG), 10000 g/mol (Aldrich), [22.7474 g]	Distilled H_2O [12.0 ml] containing 1.0 ml HNO_3	Ambient
O_2 free	Polyethyleneimine (PEI), M_n ~ 10000 g/mol (Aldrich), [7.5824 g]	CH_2Cl_2 (99%, Merck), [12.0 ml]	N_2

Samples were synthesised using two different methods depending on whether the reaction was carried out in an oxidative atmosphere or under N_2. Under oxidative conditions, 0.5 ml (0.0045 mol) $TiCl_4$ (98%, Fluka) was added to 12.0 ml of a chosen solvent. This solution was then introduced into a calculated quantity of a chosen polymer. After homogenising using a combination of heating and stirring, the samples were placed approximately 30 cm under 2 commercially available 250 W infrared spotlights for 2 weeks. Following complete solvent evaporation, the samples were introduced into alumina-glazed crucibles in a sand bath. All samples were heated to their flash point and ignited using a Bunsen burner.

For synthesis under N_2, a three-neck round bottom flask was set atop a heater/stirrer containing a paraffin oil vessel and connected to a Schlenk line. A stopper was

inserted into the right opening of the round bottom flask. The remaining opening contained bespoke metal ion solution delivery glassware (made by inserting a flow control tap into the tapered midpoint of a cylinder, with a ground glass joint on one end, and a rubber septum covering on the other end).

A calculated quantity of a chosen polymer was added to this round bottom flask. The system was purged for 15 minutes with N_2. Thereafter, a syringe containing 0.5 ml (0.0045 mol) $TiCl_4$ (98%, Fluka) was inserted into the septum covering the bespoke glassware containing 12.0 ml of a chosen solvent. The flow control tap was opened to allow the solution to mix with the polymer. Thereafter, the system was purged for an additional 15 minutes. Following this time, the mixture was heated at a rate of 200 °C / hour for 1 hour and maintained for a further 3 hours (all under the flow of N_2). Ignition did not occur under N_2. The mixture was then allowed to cool overnight while still connected to the Schlenk line (no gas was flowing over the mixture). Using both synthesis methods, eight samples were synthesised as follows:

- sample 1 – oxygen free polymer
    - PEI, H_2O, oxidative atmosphere (O_2)
- sample 2 – oxygen free polymer and oxygen free solvent
    - PEI, CH_2Cl_2, oxidative atmosphere (O_2)
- sample 3 – oxygen free polymer and atmosphere
    - PEI, H_2O, inert atmosphere (N_2)
- sample 4 – oxygen free solvent
    - PEG, CH_2Cl_2, oxidative atmosphere (O_2)
- sample 5 – oxygen free solvent and atmosphere
    - PEG, CH_2Cl_2, inert atmosphere (N_2)
- sample 6 – oxygen free atmosphere
    - PEG, H_2O, inert atmosphere (N_2)
- sample 7 – oxygen free polymer, solvent, and atmosphere
    - PEI, CH_2Cl_2, inert atmosphere (N_2)
- sample 8 – complete presence of oxygen
    - PEG, H_2O, oxidative atmosphere (O_2)

XRD analysis of samples obtained directly after Schlenk synthesis did not reveal the presence of titania. It is believed that polymer degradation during heating under N_2 caused the polymers to become amorphous. The presence of amorphous polymers in the samples likely masked the presence of TiO_2 nanoparticles – as proven with TEM images later.

Therefore, all synthesised samples were placed in alumina crucibles and calcined in a muffle furnace (oxidative conditions) at 500 °C for 1 hour. The white powders were analysed using a Bruker D2 Phaser diffractometer employing Co Kα radiation between 20° – 40° 2θ. TEM analysis was achieved using an FEI Tecnai T12 TEM.

Figure 4.4 contains the XRD patterns for the abovementioned 8 samples synthesised using systematic O_2 elimination. The mass % of anatase and rutile with respective crystallite size formed per sample is quantified in table 4.2. Immediately obvious from figure 4.4 and table 4.2 is that all samples produced TiO_2. Samples 1 – 7 favoured the formation of anatase, compared to sample 8 that favoured the formation of rutile. Despite this, samples 3 and 6 showed a significant mixture of anatase and rutile. The largest rutile crystallites were formed from samples 3 and 6 suggesting that a mixture of phases within a sample encouraged rutile coarsening.

Comparing samples 1, 2, 4, and 8 (all synthesised in an oxidising atmosphere), it is clear that limiting oxygen in the system tends to form anatase. When oxygen was included in all components, rutile was the favoured phase.

Comparing samples 3, 5, 6, and 7 (all synthesised under N_2), samples synthesised using H_2O containing HNO_3 as a solvent produced a mixture of both anatase and rutile, compared with CH_2Cl_2 that favoured anatase formation. This indicates a dependency on the solvent more than the polymer used in an O_2 deprived system.

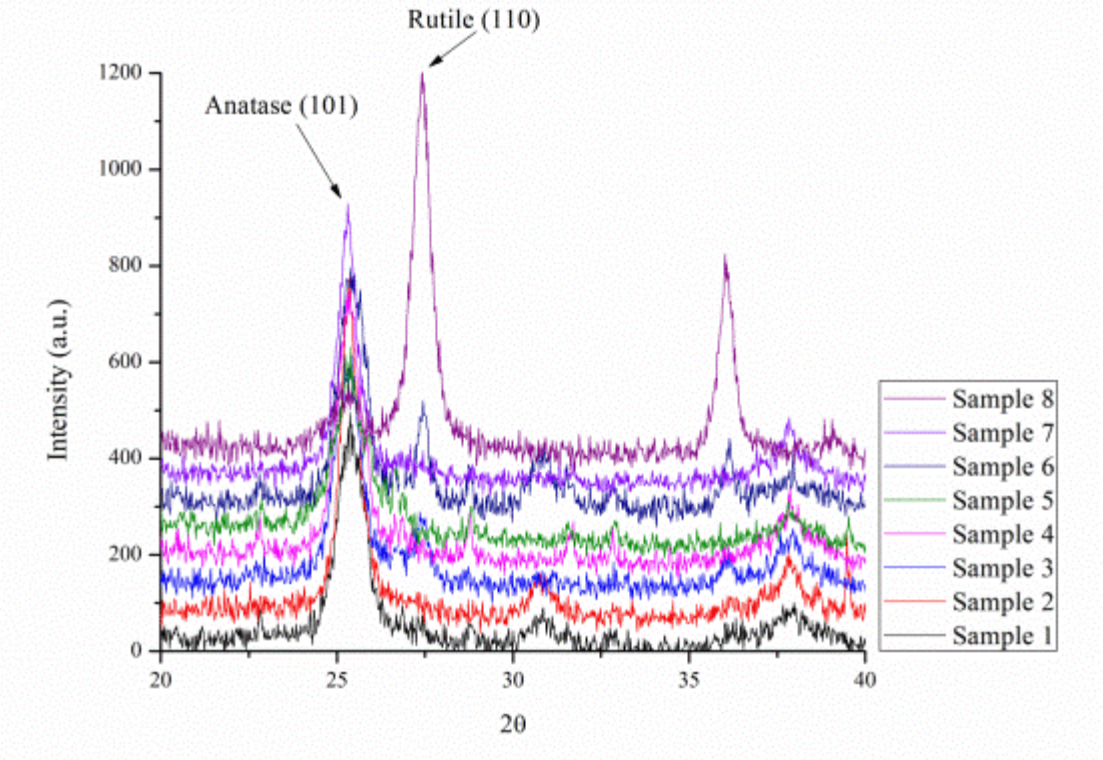

Figure 4.4: XRD of samples synthesised using systematic O_2 elimination.

Table 4.2: Variation in the amount and size of anatase and rutile crystallites formed using various O_2 deprivation experiments.

Sample	Average %Anatase	Average anatase crystallite size (nm)	Average rutile crystallite size (nm)
1 – PEI, H_2O, O_2	96.9 ± 3.9	10.6	
2 – PEI, CH_2Cl_2, O_2	94.8 ± 3.8	17.4	
3 – PEI, H_2O, N_2	76.5 ± 3.1	10.0	35.5
4 – PEG, CH_2Cl_2, O_2	99.7 ± 4.0	12.3	
5 – PEG, CH_2Cl_2, N_2	100.0 ± 4.0	8.8	
6 – PEG, H_2O, N_2	66.7 ± 2.7	11.2	35.6
7 – PEI, CH_2Cl_2, N_2	96.3 ± 3.9	16.6	
8 – PEG, H_2O, O_2	9.2 ± 0.4	11.9	17.5

Data obtained from samples 1 and 8 provide a comparison of the effects of an oxygen containing with an oxygen free polymer (PEG with PEI). Under the same conditions, PEI favoured the formation of anatase compared with PEG that favoured the formation of rutile. This may be due to the branched nature of PEI. It is expected that during synthesis, as PEI degrades, these branches better encapsulate the metal ions and afford a protecting effect on nucleating anatase crystallites. This is an interesting finding as it was believed that a coordinating polymer was necessary for the formation of nanoparticles in resin-gel synthesis. Ti_xN_y species were not discovered suggesting that PEI does not coordinate to metal ions.

Figures 4.5 – 4.17 represent TEM images collected for samples synthesised in this study. For samples 3, 4, and 5 (all synthesised under N_2), TEM images were obtained after synthesis but before calcination. For sample 7, TEM images were obtained before and after calcination.

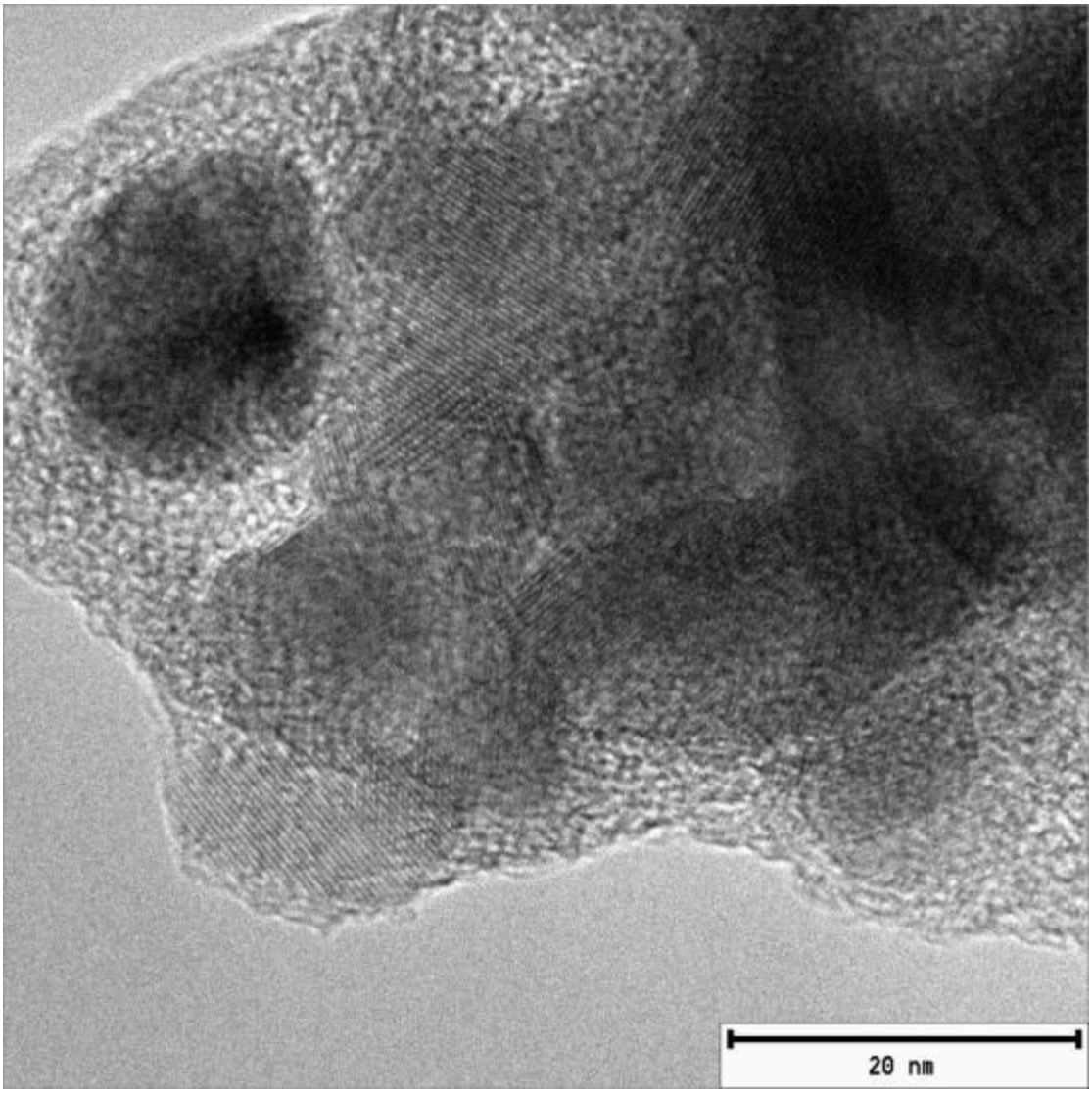

Figure 4.5: Sample 1 showing the formation of anatase crystallites using PEI.

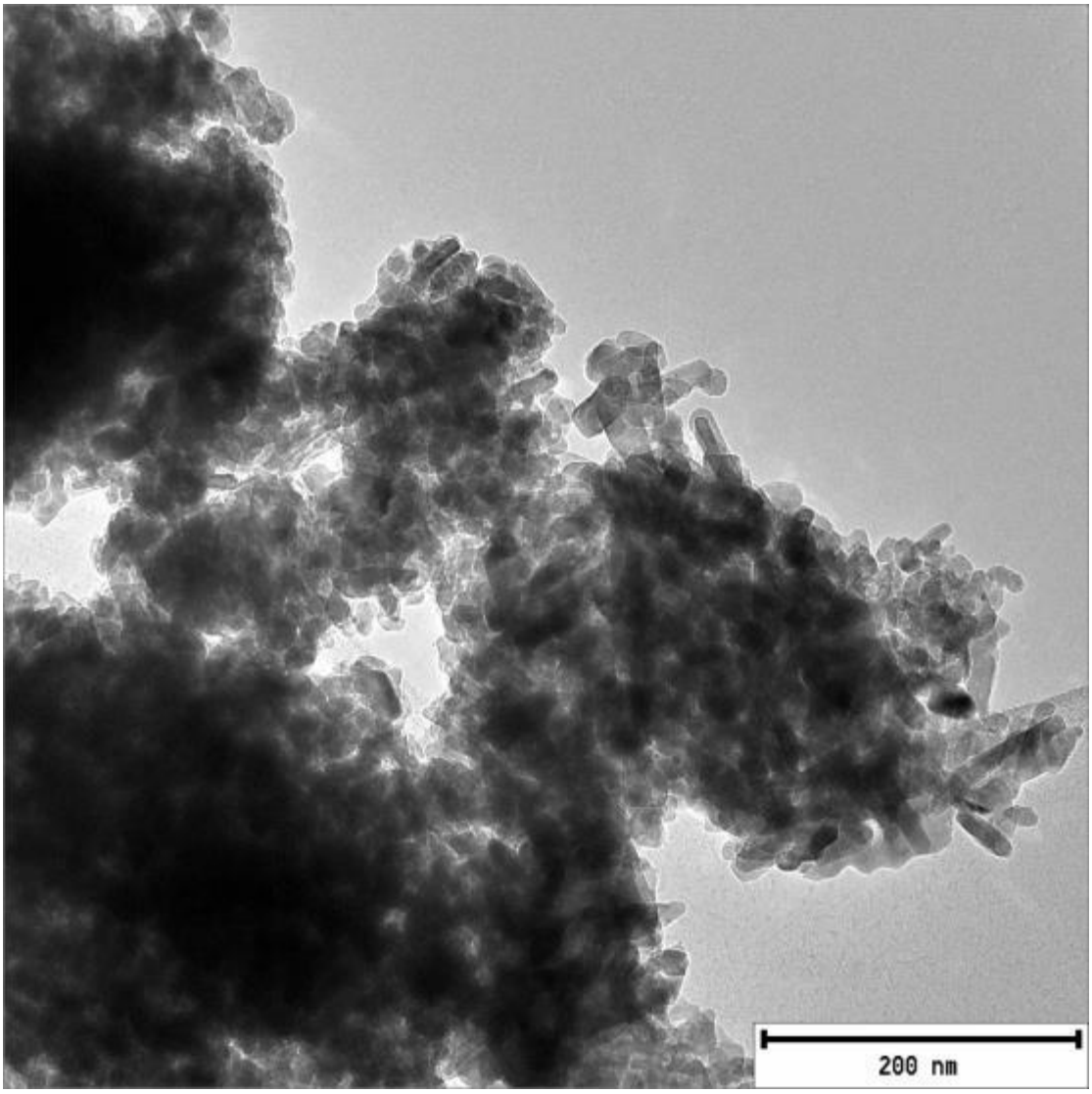

Figure 4.6: Sample 2 produced a mixture of isotropic and anisotropic nanoparticles.

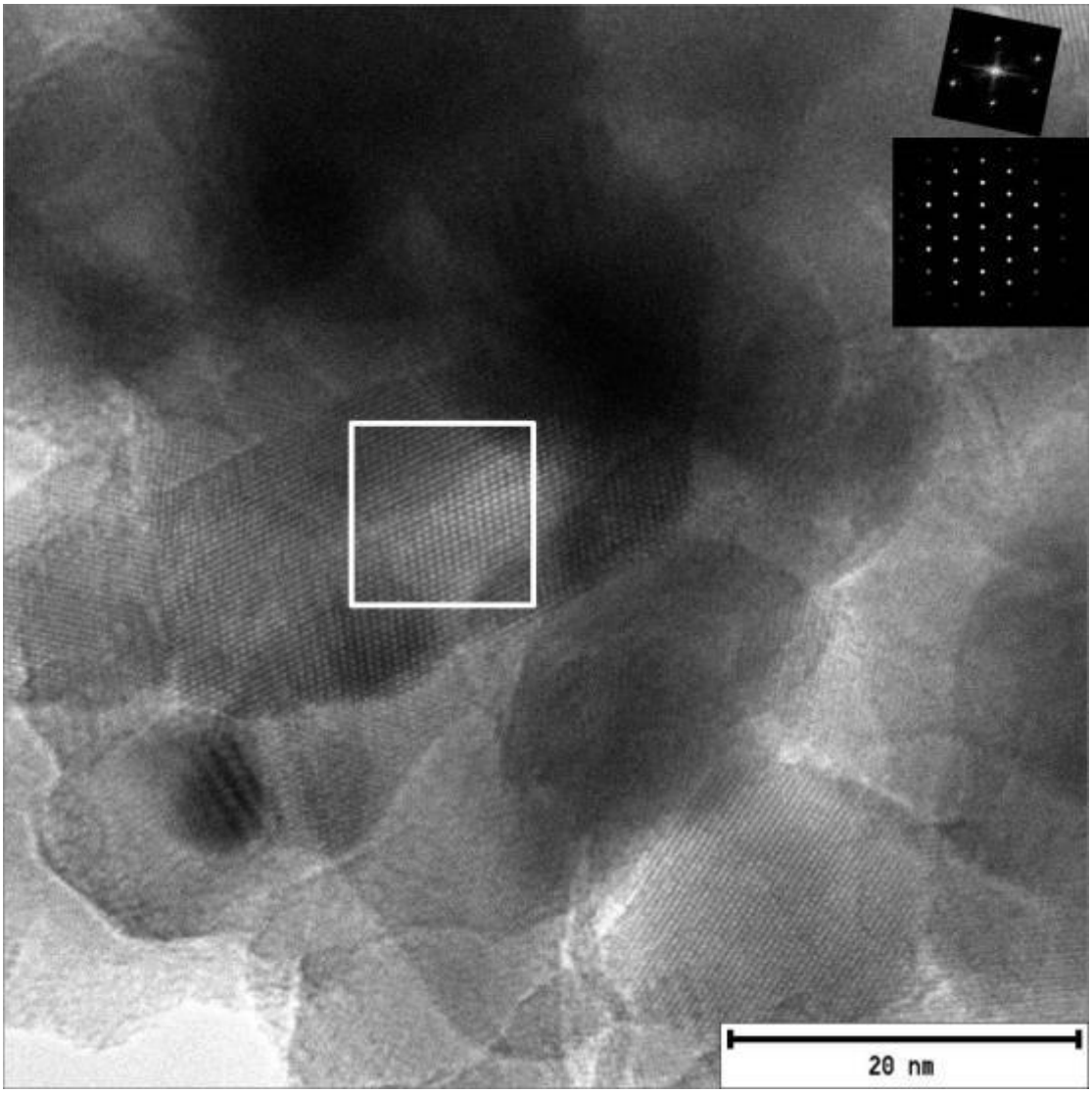

Figure 4.7: Closer inspection of the anisotropic crystallites found in sample 2 revealed the presence of rutile aligned along [1 1 1].

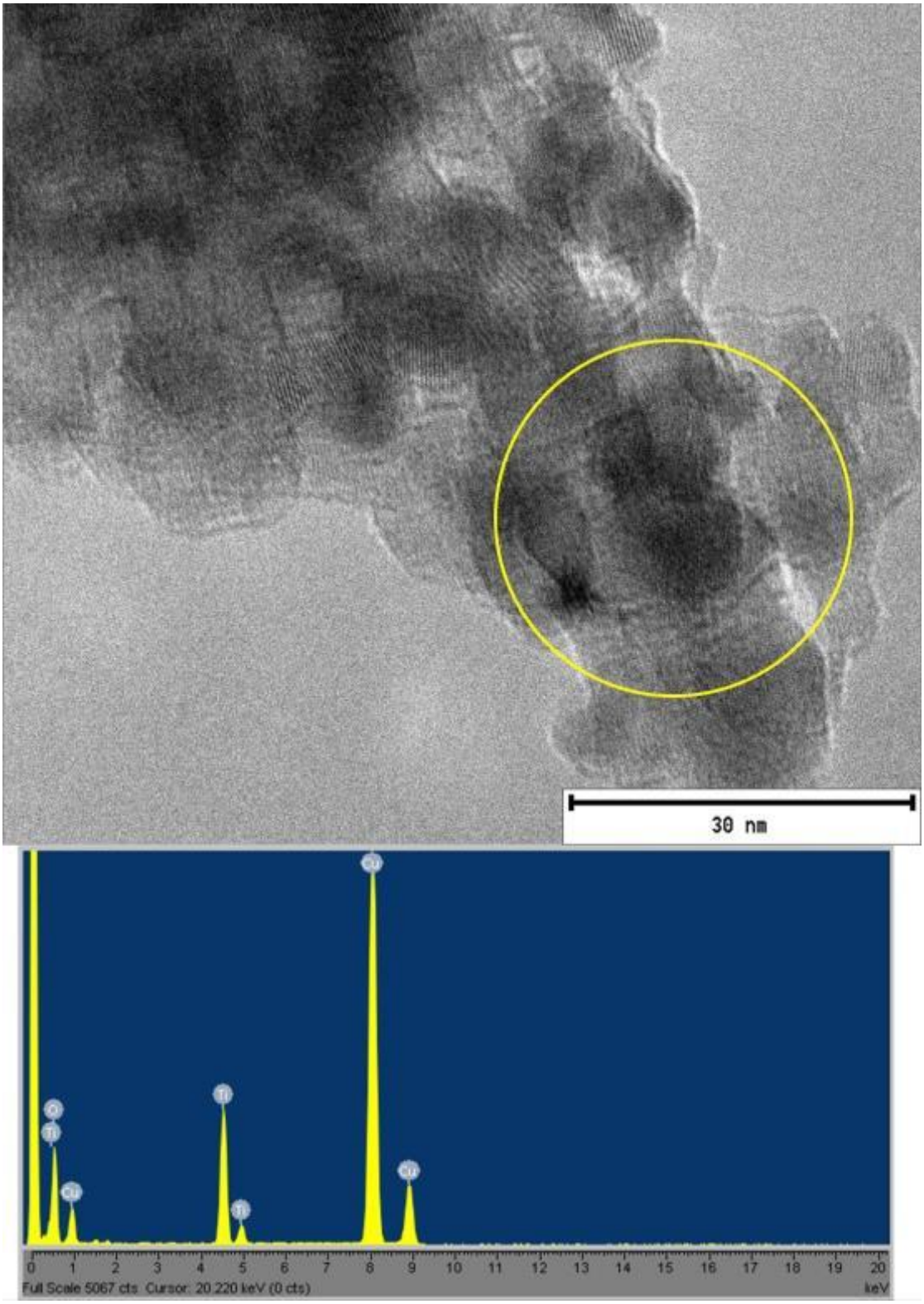

Figure 4.8: Generated from sample 3 before calcination. Nanoparticles composed of TiO_2 were present in this sample.

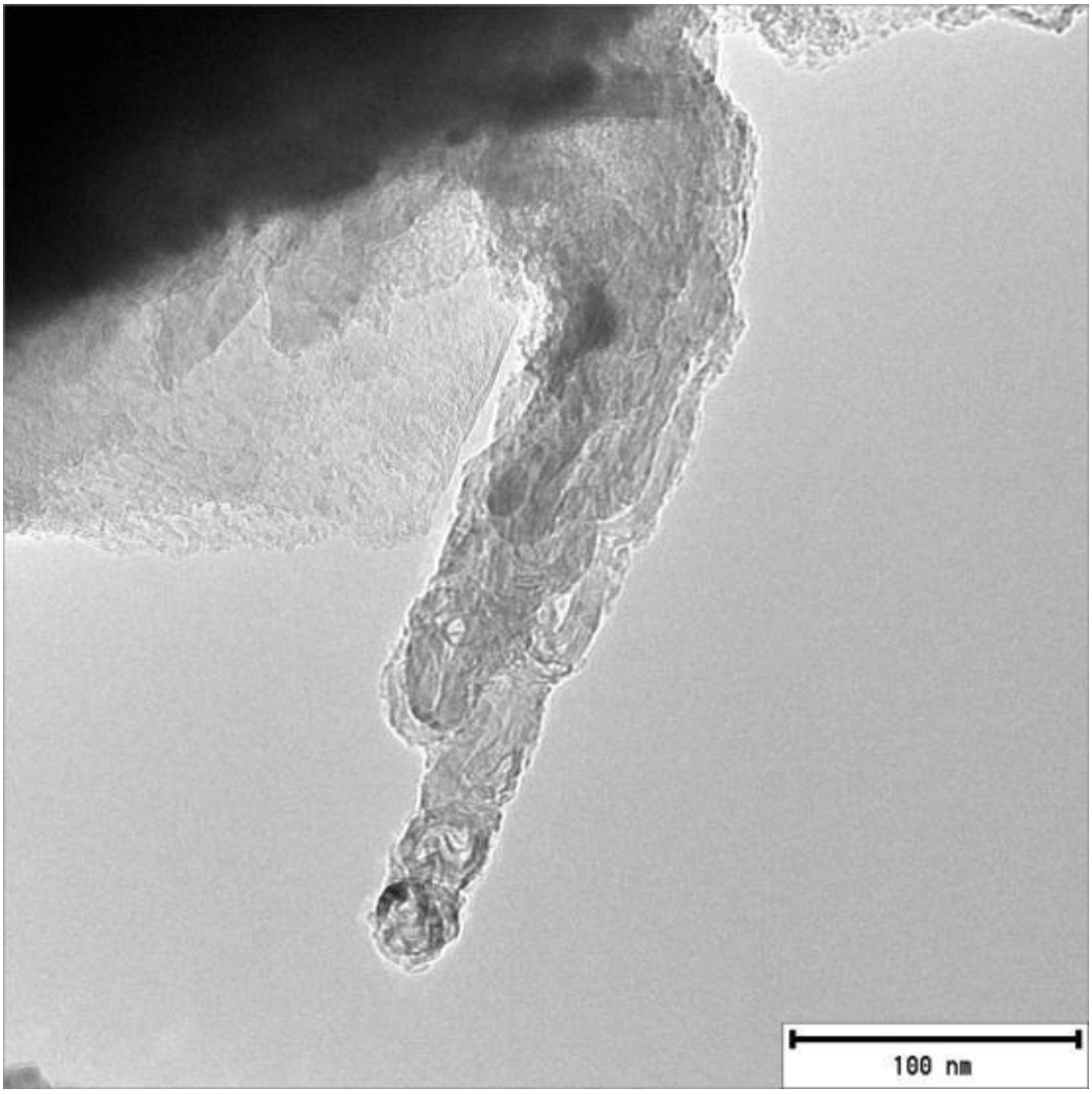

Figure 4.9: Sample 3 also revealed the presence of large structures that were most likely a form of carbon generated from PEI. This structure appears to loop back on itself forming possible cavities for titania nucleation.

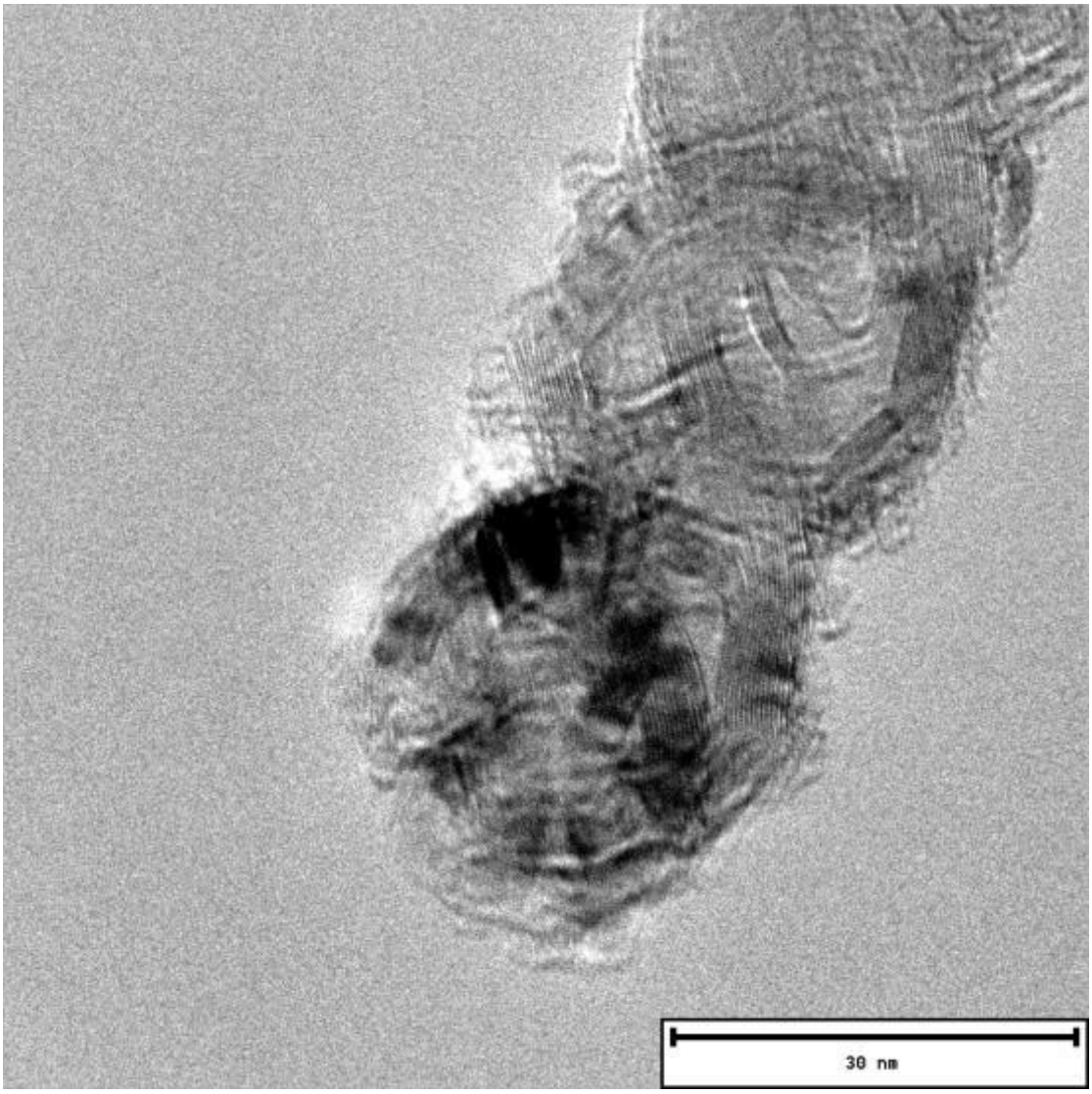

Figure 4.10: Closer inspection of the structure (most likely a form of carbon) in figure 4.9 revealed crystalline features.

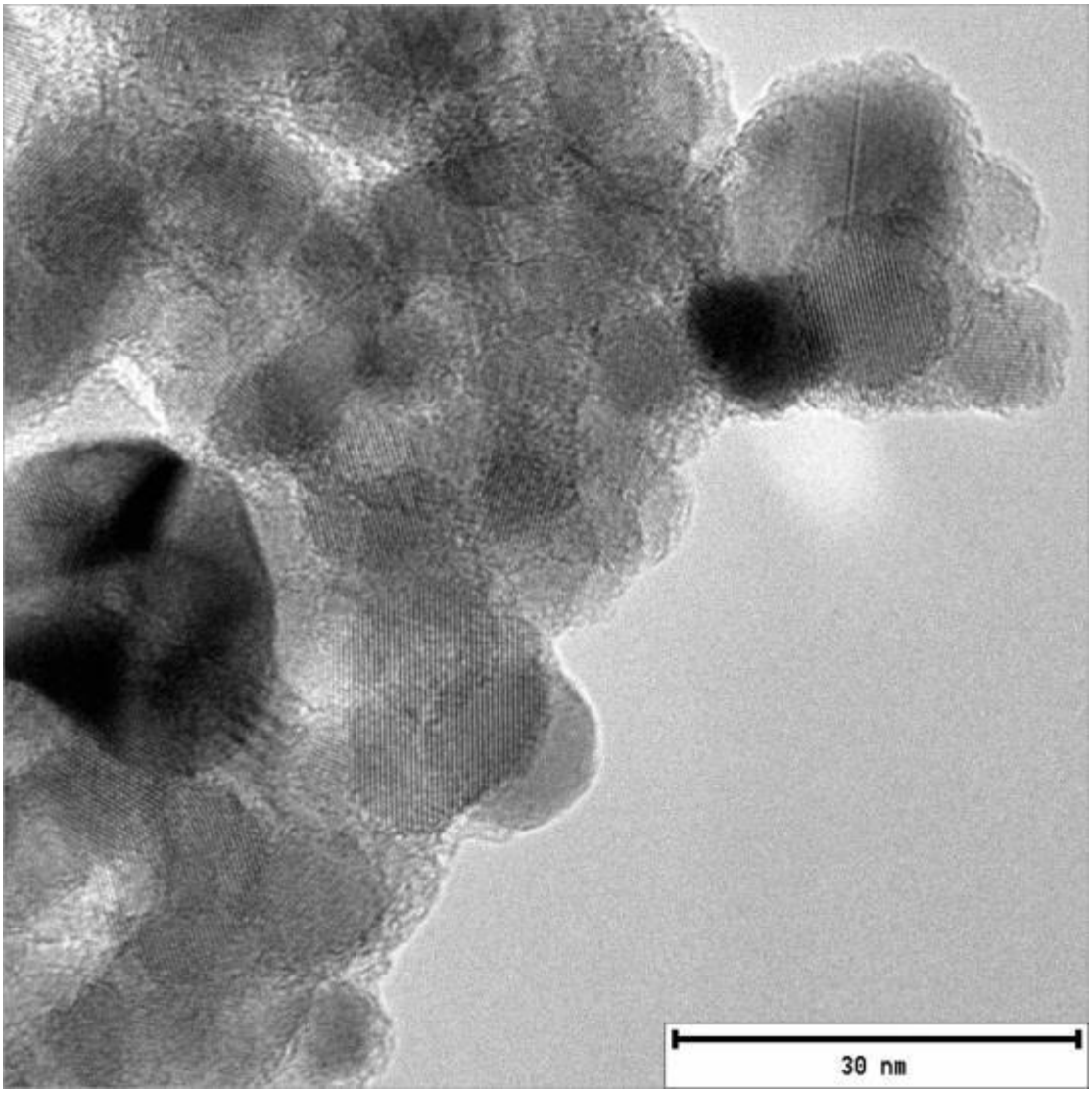

Figure 4.11: Sample 4 produced nearly phase pure anatase as ascertained from XRD.

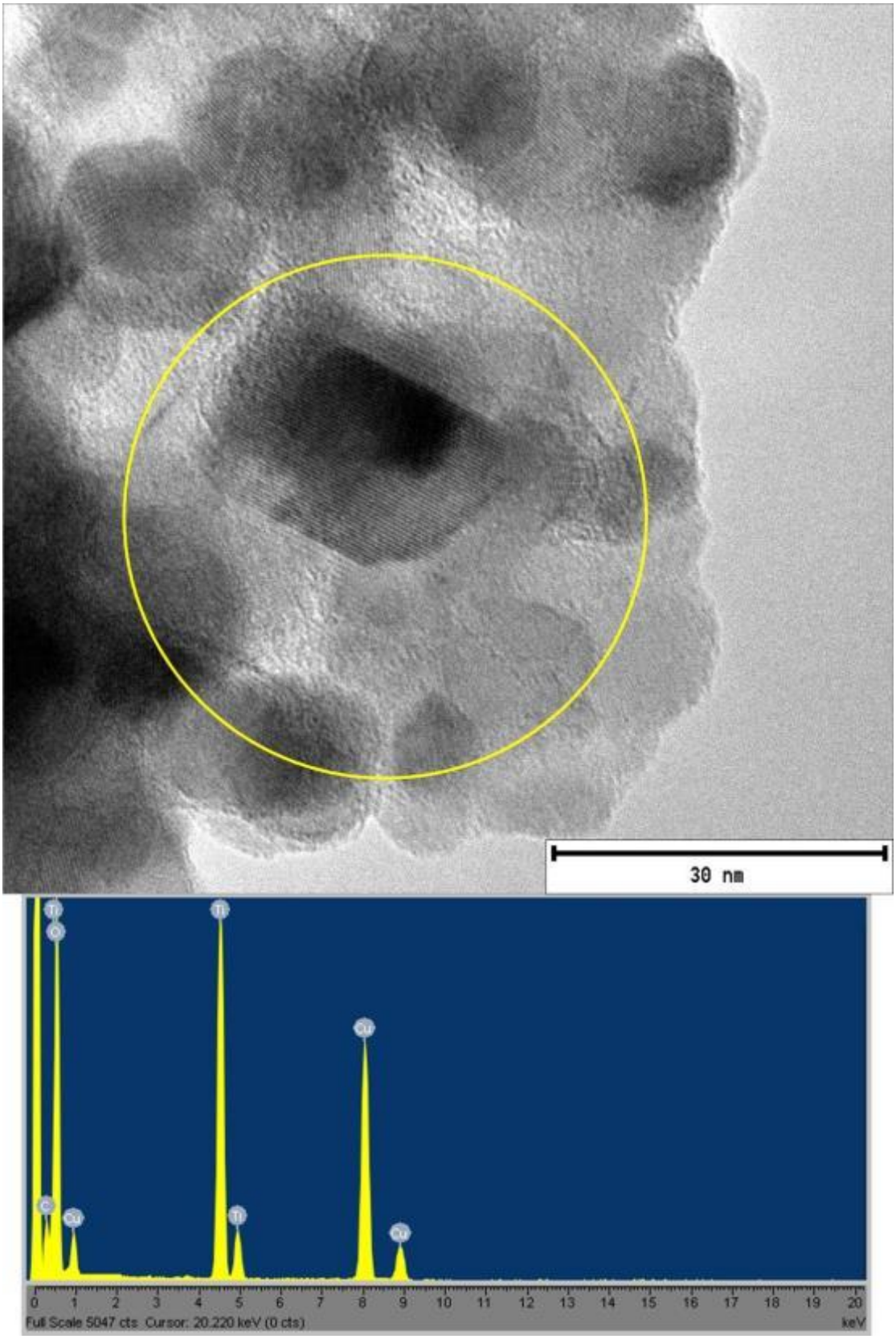

Figure 4.12: Sample 5 produced phase pure anatase crystallites as evidenced from XRD. In this TEM image, the TiO_2 crystallites appear to have well-defined edges.

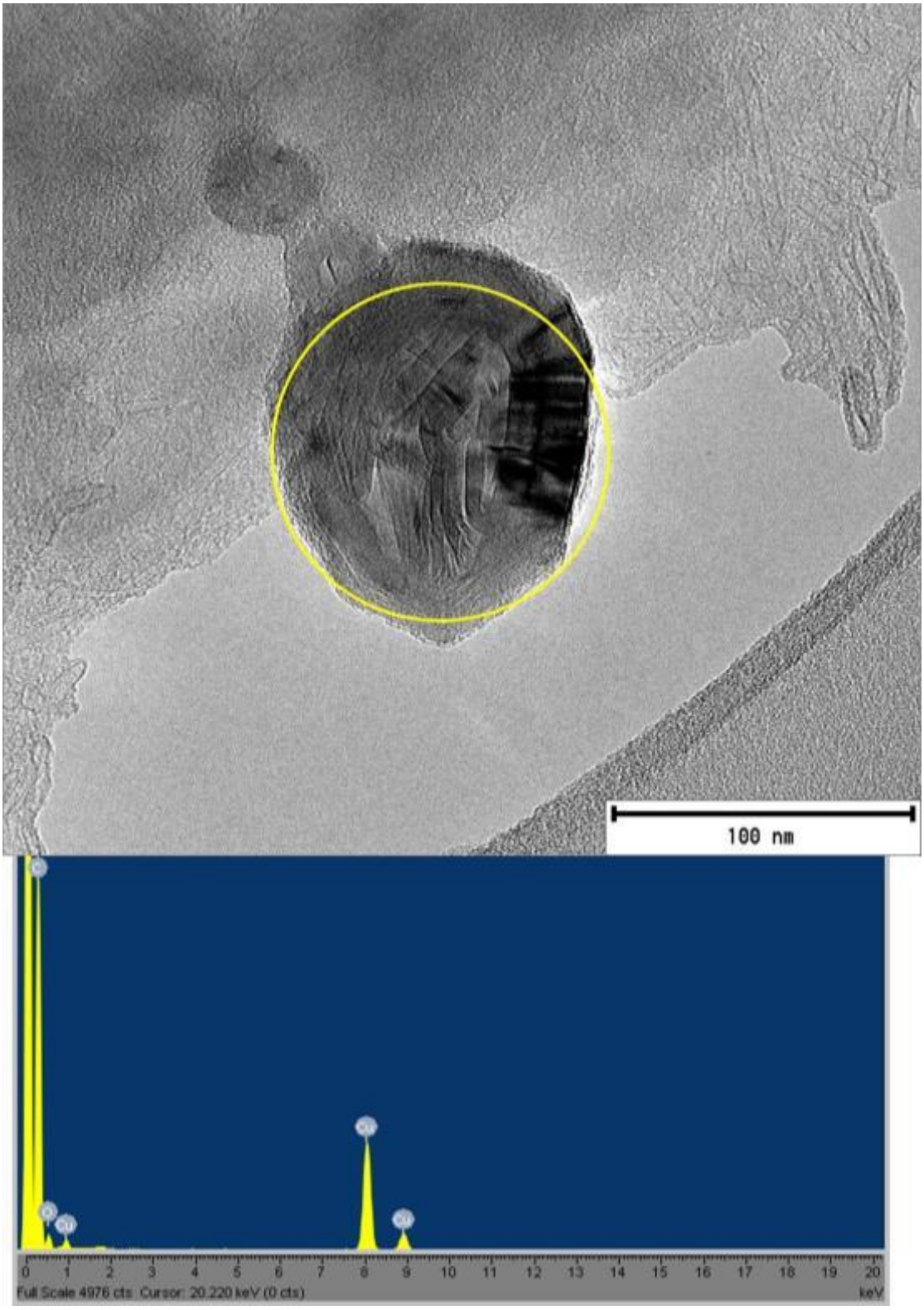

Figure 4.13: Sample 5 produced a structure likely generated from the degradation of PEG. Loops and folds are evident within this structure and are likely areas for TiO_2 nucleation. EDS analysis reveals the structure to be composed of carbon and oxygen – consistent with the decomposition products of PEG. The Cu peaks in the EDS were generated from the TEM grid.

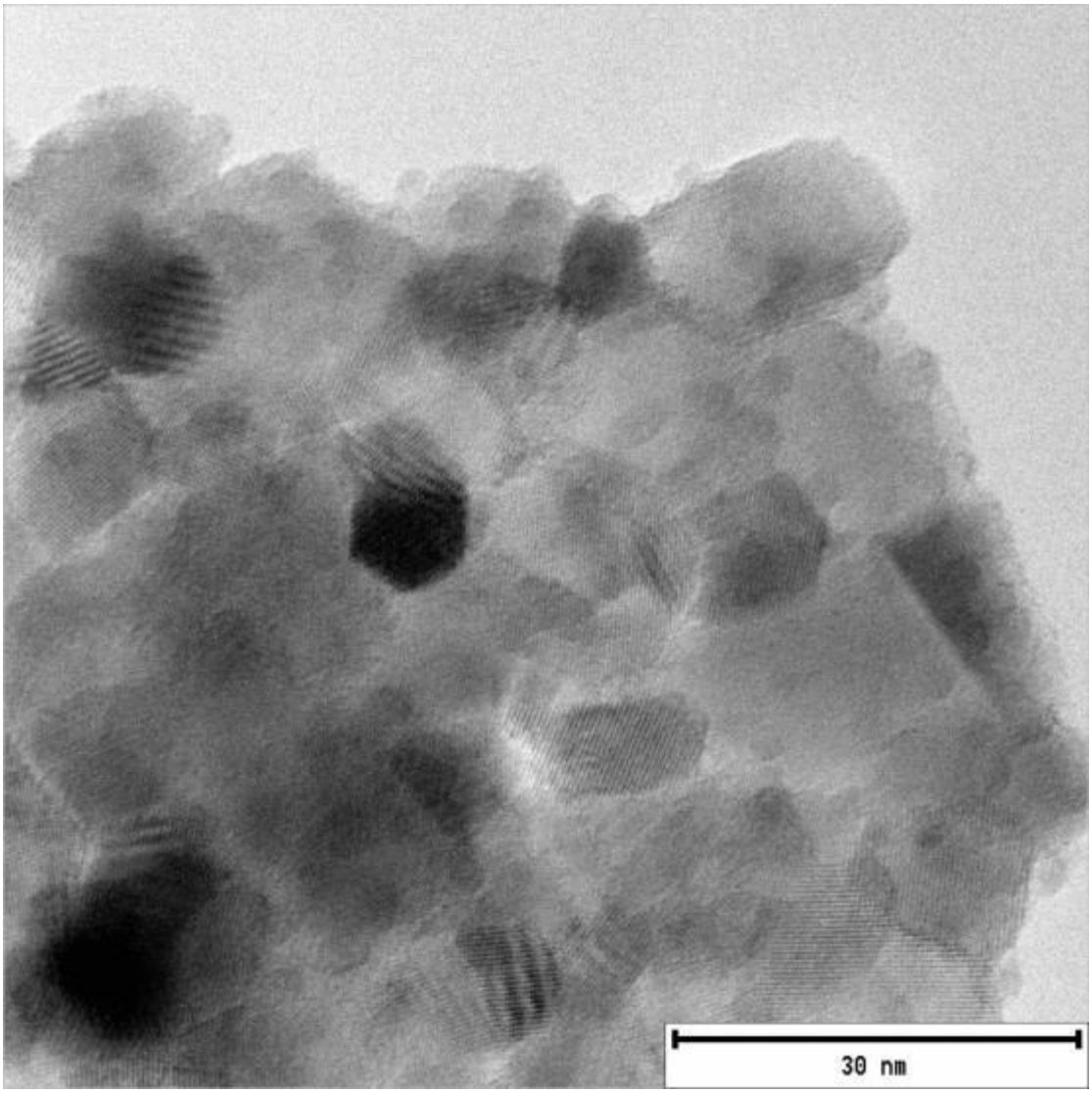

Figure 4.14: Sample 6 shows the presence of numerous well-defined crystallites. From XRD, this sample produced a mixture of anatase and rutile. High aspect ratio rutile nanorods were not evident from this sample.

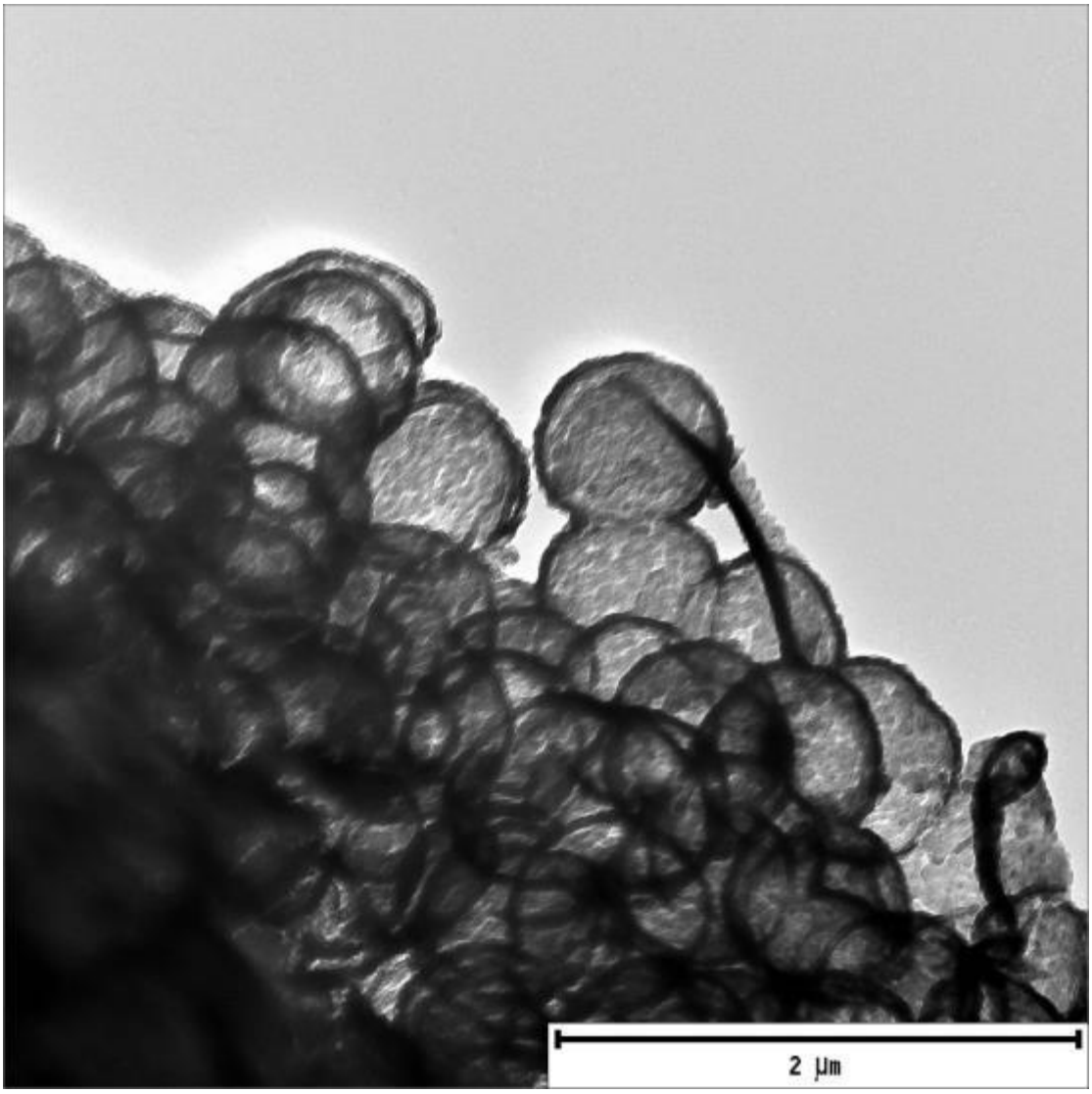

Figure 4.15: Sample 7 (complete O_2 removal) produced these hollow shell superstructures of unknown composition measuring between 650 – 800 nm across their diameters. Expectedly, no TiO_2 nanoparticles were formed.

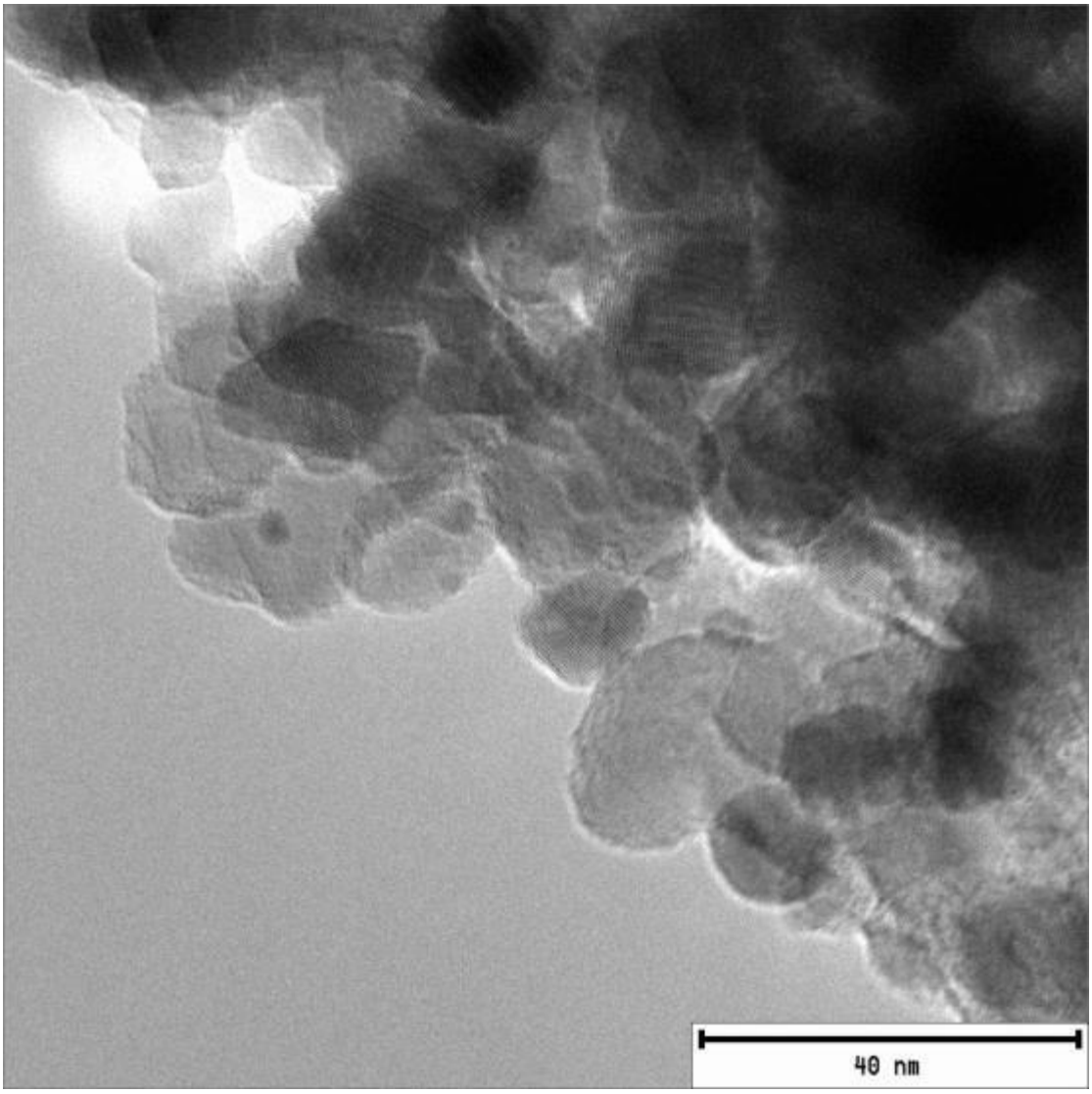

Figure 4.16: Calcination of sample 7 produced titania nanoparticles. This implies that unstable Ti containing species were present in the sample before calcination. These species subsequently reacted with atmospheric O_2 to form TiO_2.

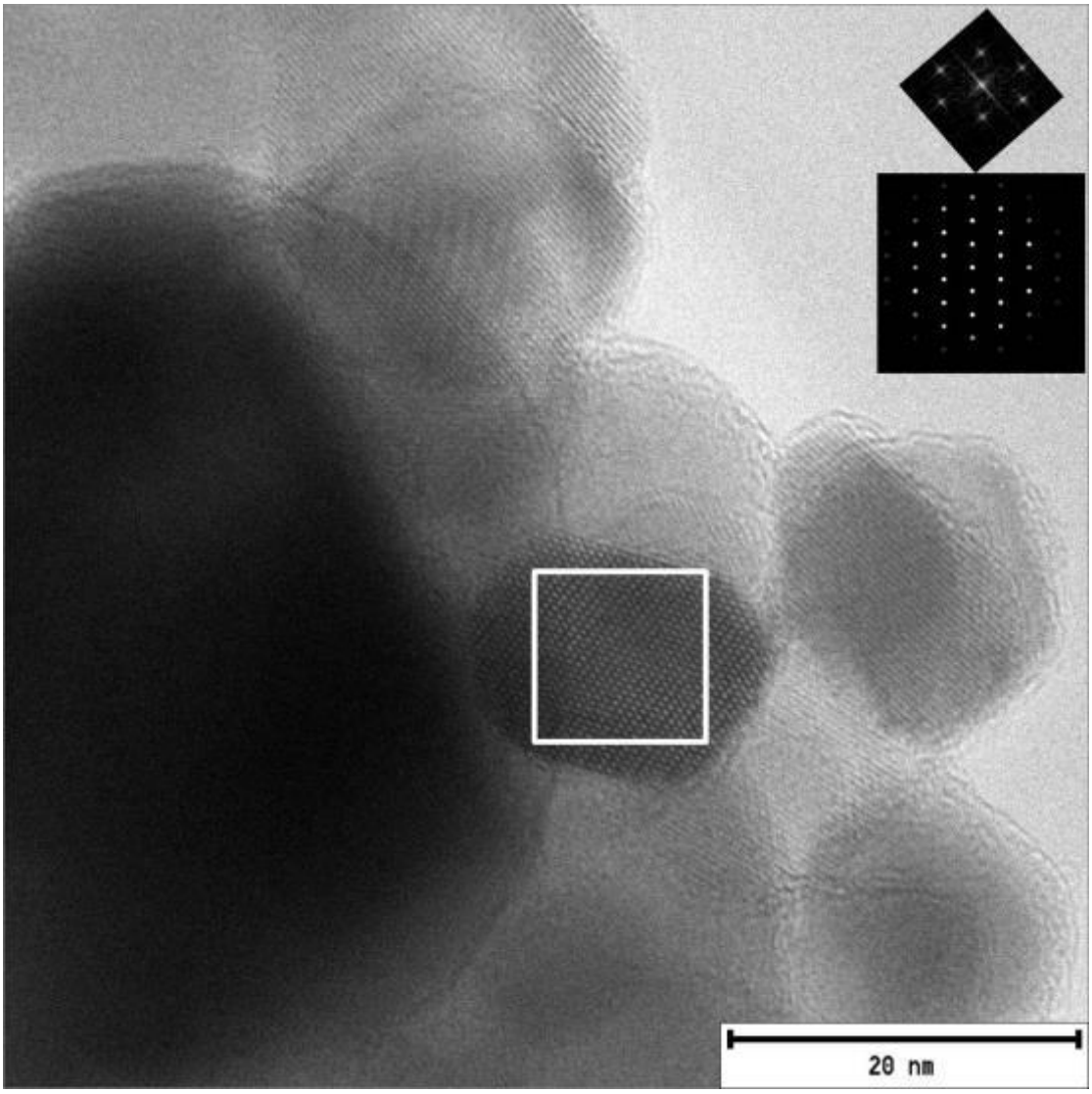

Figure 4.17: Sample 8 produced nearly phase pure rutile according to XRD. This image shows a well-defined rutile crystallite in the [1 1 1] orientation.

The results obtained from this study showed that metal ions bind to oxygen and form titania independent of the source of oxygen in the system. Additionally, the interplay between the source of oxygen in the system can be used a means to control titania polymorph formation. All samples synthesised in N_2 were calcined in air in order to completely remove polymer traces. Since all samples produced TiO_2, the simplicity of synthesis in air compared with N_2 governed that all future syntheses occur under normal atmospheric conditions. An additional benefit of synthesis under oxidising conditions is that there is potential to form phase pure anatase and phase pure rutile.

4.3 References

1. West, A. R. *Basic Solid State Chemistry*. (John Wiley and Sons Ltd, 1999).

2. Vrandečić, N. S., Erceg, M., Jakić, M. & Klarić, I. Kinetic analysis of thermal degradation of poly(ethylene glycol) and poly(ethylene oxide)s of different molecular weight. *Thermochimica Acta* **498,** 71 – 80 (2010).

3. Yang, L., Heatley, F., Blease, T. G. & Thompson, R. I. G. A Study of the Mechanism of the Oxidative Thermal Degradation of Poly(Ethylene Oxide) and Poly(Propylene Oxide) Using ‘H- And 13c-Nmr. *European Polymer Journal* **32,** 535 – 547 (1996).

4. Han, S., Kim, C. & Kwon, D. Thermal/oxidative degradation and stabilization of polyethylene glycol. *Polymer* **38,** 317 – 323 (1997).

Chapter 5: Effects of Solvent and PEG Molecular Weight on Titania Polymorph and Crystallite Size Formation

The aim of this experiment was to investigate the effects of varying the solvent and PEG chain length on the size and type of titania polymorph formed. The two selected solvents were ethanol and water containing HNO_3. A previous study showed that the use of ethanol resulted in the formation of smaller crystallites compared to water[1]. The rationale used by the researchers was that ethanol has a hydrophobic nature and lower dielectric constant compared with water[1]. This is an interesting result as the currently accepted theory of resin-gel synthesis does not describe the solvent as being an important parameter in the formation of nanoparticles. In addition, PEG chain length was varied to observe the effects of polymer molecular weight on titania phase purity and crystallite size.

5.1 Experimental Procedure

The experimental procedure consisted of 4 parts: ethanol mediated synthesis, water containing HNO_3 mediated synthesis, heat treatments, and characterisation.

5.1.1 Ethanol Mediated Synthesis

Excess (330.0 ml) absolute ethanol (99.8%) was introduced into a beaker. 13.5 ml (0.123 mols) $TiCl_4$ (> 99%, Merck) was added to this beaker and stirred using a Teflon coated magnetic stirrer bar. Following complete solution homogenisation (signalled by the formation of an off-white solution), 30 ml of the solution was transferred into 10 separate beakers. A volume equivalent amount of PEG of various molecular weights (400, 1000, 1500, 3000, 4000, 6000, 8000, 10000, 20000, and 35000 g/mol) was added to each of the 10 beakers. This was achieved by adding the respective PEG powders in a freely settled manner (such that no compaction was effected) to a measuring cylinder up to the 34.4 ml mark. Thereafter, each measured PEG powder was transferred to the solution. Each mixture was heated to 50 – 65 °C at ~ 620 mm Hg (lower atmospheric pressure resulted from this experiment being conducted at an altitude of ca. 1750 m above sea level) and concurrently stirred using a glass rod to allow for complete homogenisation and gel formation. Higher

temperatures were required for the homogenisation of mixtures containing PEG of greater molecular weights.

All gels were placed in a fume hood for 12 days to allow for the complete evaporation of excess solvent. Following this period, a solid resin had developed in all samples except for the sample formed from PEG 400.

5.1.2 Water containing HNO_3 Mediated Synthesis

Excess distilled water (330.0 ml) was introduced into a beaker. 13.5 ml (0.123 mols) $TiCl_4$ (> 99%, Merck) was introduced into this beaker. 55% HNO_3 (27 ml) was then added to the mixture to aid solution homogeneity. A Teflon coated magnetic stirrer bar was used to stir the solution to homogeneity. Thereafter, 30 ml of the solution was decanted into 10 different beakers. PEG of different molecular weights was added to each beaker as described in section 5.1.1. Samples were heated and stirred (as described in section 5.1.1) to homogeneity. Thereafter, excess solvent was evaporated from the samples by leaving them in a fume hood for 12 days. All resins had taken on an orange colour after this time. This colour was due to the presence of unreacted nitric acid, as detected by olfactory perception. Owing to the presence of unreacted nitric acid, all resins were placed ~ 50 cm under two 200 W incandescent light bulbs for a further 3 days. Following this time, a hardened resin had formed in samples containing higher molecular weight PEG (> 6000 g/mol). All resins presented an off-white colour.

5.1.3 Heat Treatments

All 20 samples were divided equally so as to introduce a replicate for the heat treatment and analyses that follow.

A sand bath was prepared by introducing acid washed sand into an aluminium cooking pot. The sand bath would afford uniform heating conditions to the resins without melting or sublimating under high temperatures. Resins from each sample were introduced into glazed alumina crucibles and then added into the sand bath (figure 5.1). The underside of the sand bath (containing resins in crucibles) was then heated using the blue flames from a cast iron gas ring burner fuelled by LPG (Afrox Handigas). Once the samples had reached their flash point (the outside of the bottom of the crucibles were 240 – 260 °C at ~ 620 mm Hg), a flaming splint was used to induce ignition in the samples.

Following complete resin ignition, each sample had a black, flaky or granular appearance. The colour was due to the presence of a carbon residue on the samples (figure 5.1). Each sample was then divided further into 2 halves – 1 half to be analysed prior to calcination and the other half to be analysed post-calcination. Calcination was effected by placing samples in alumina boats and heating them to 500 °C at ~ 620 mm Hg in a muffle furnace for 1 hour.

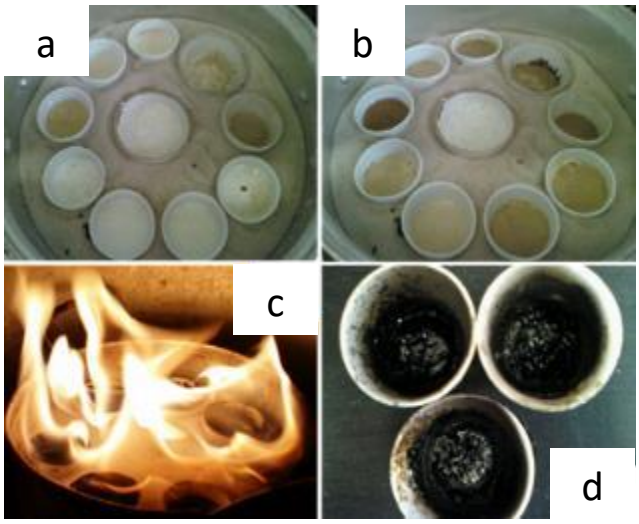

Figure 5.1: Progression of ignition. (a) Appearance of samples a short while after heating had commenced. (b) Sample colour change characteristic of polymer degradation owing to increased temperatures. (c) Pyrolysis after having reached the respective flash temperatures. (d) Black appearance of samples after ignition before calcination.

5.1.4 Characterisation

All samples were ground to a fine, consistent powder using an agate mortar and pestle. Samples were analysed between 10° and 90° 2θ in 0.028 increments counting for 1 second per step using a Bruker D2 Phaser Diffractometer with Cu Kα radiation.

Samples were prepared for TEM analysis using the wet-grind technique: samples were introduced into acetone and ground using an agate mortar and pestle. The suspension was sonicated for 15 minutes. A single drop of the suspension was transferred to a holey carbon coated copper grid suspended by tweezers. Once the acetone had evaporated, the grid was placed in a grid holder prior to analysis. An FEI Tecnai T12 was used for TEM analysis.

5.1.5 Results and Discussion

The data obtained in this study can be compared in a variety of ways. Anatase and rutile were primarily formed in ethanol and water containing HNO_3 respectively. The amount of each phase formed and crystallite size data were obtained pre- and post-calcination across a range of PEG molecular weights. Therefore, 12 plots of data were generated to comprehensively compare formed titania in different ways.

5.1.6 Ethanol Mediated Synthesis

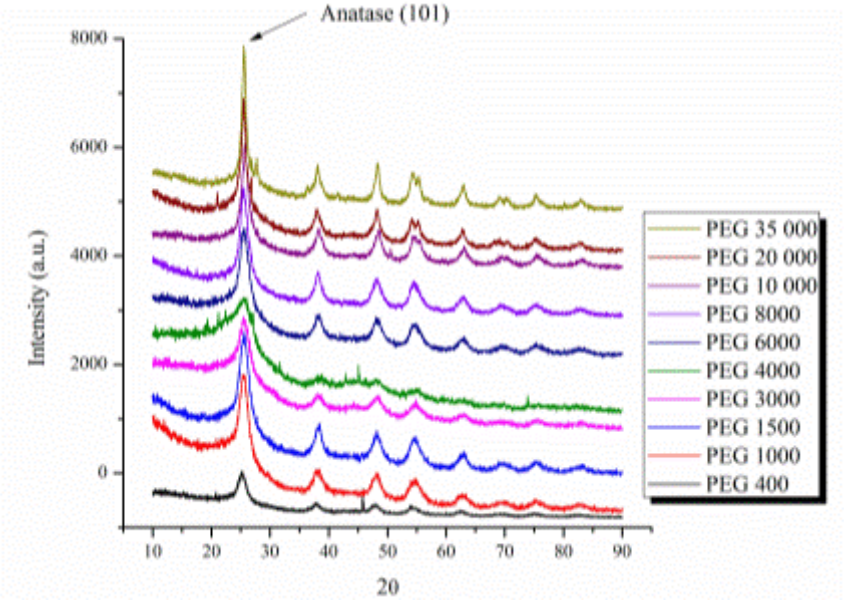

Figure 5.2: PXRD patterns of samples synthesised using ethanol pre-calcination.

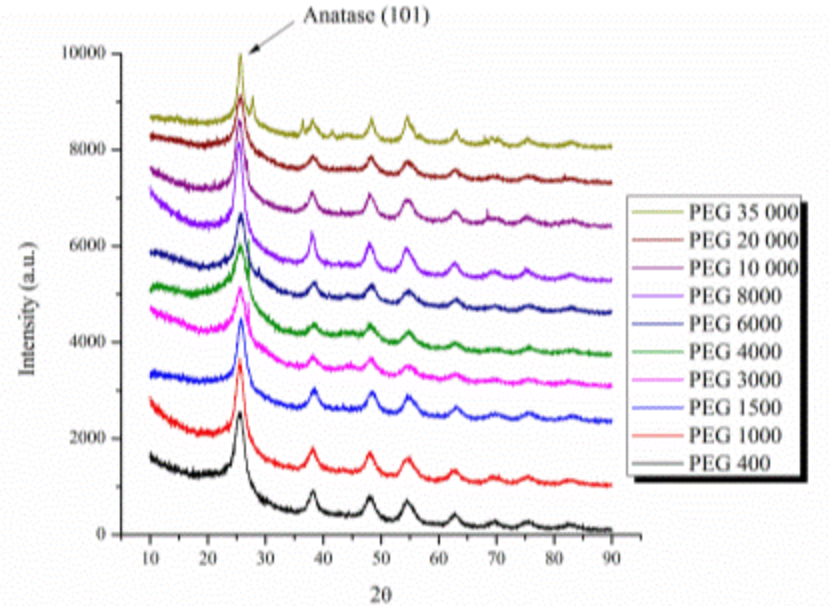

Figure 5.3: PXRD patterns of replicate samples synthesised using ethanol pre-calcination.

Figures 5.2 and 5.3 represents the PXRD patterns of all samples formed using an ethanol solvent and PEG of various molecular weights. The anatase peak of greatest intensity, (1 0 1), is located at 25.325° 2θ; the rutile peak of greatest intensity, (1 1 0), is located at 27.968° 2θ. Immediately obvious from both figures is that anatase is the preferred phase using ethanol. With good reproducibility, a small rutile peak is observed only in the sample synthesised using PEG 35000. This suggests that longer chain polymers influence the formed phase. Most peaks are broad implying the presence of nano-anatase crystallites. The diffraction peaks are shifted.

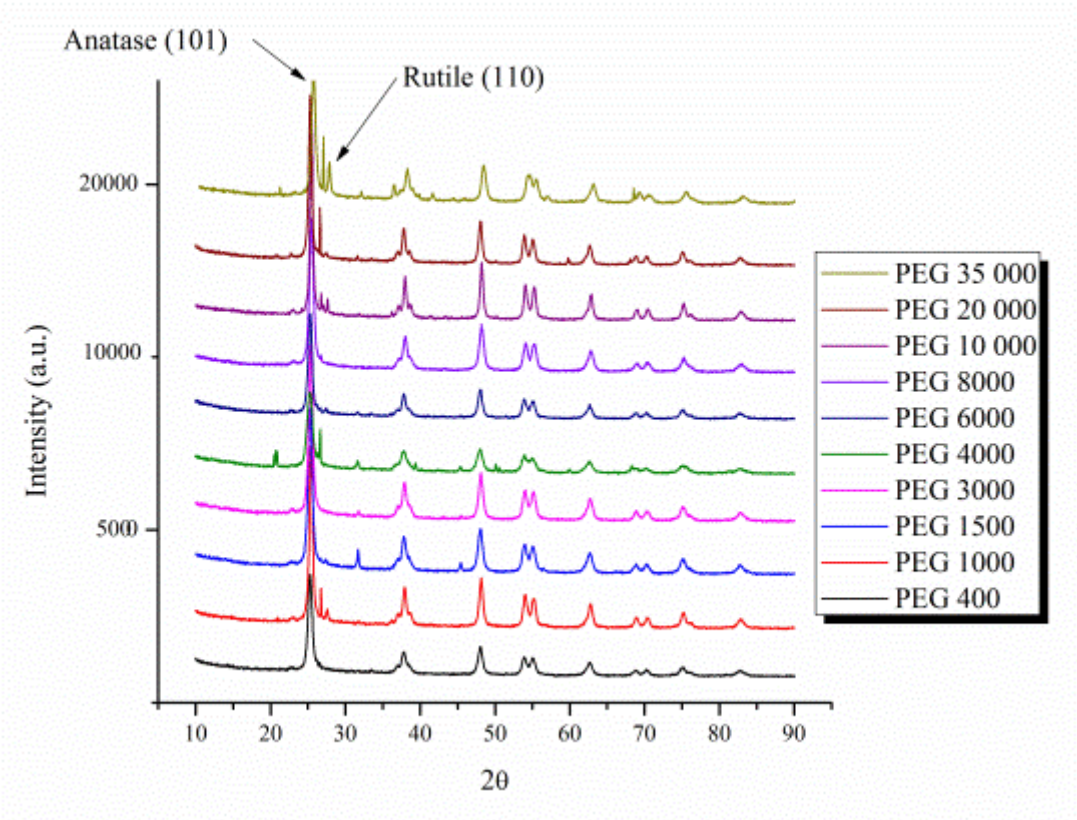

Figure 5.4: PXRD patterns of calcined samples formed from ethanol.

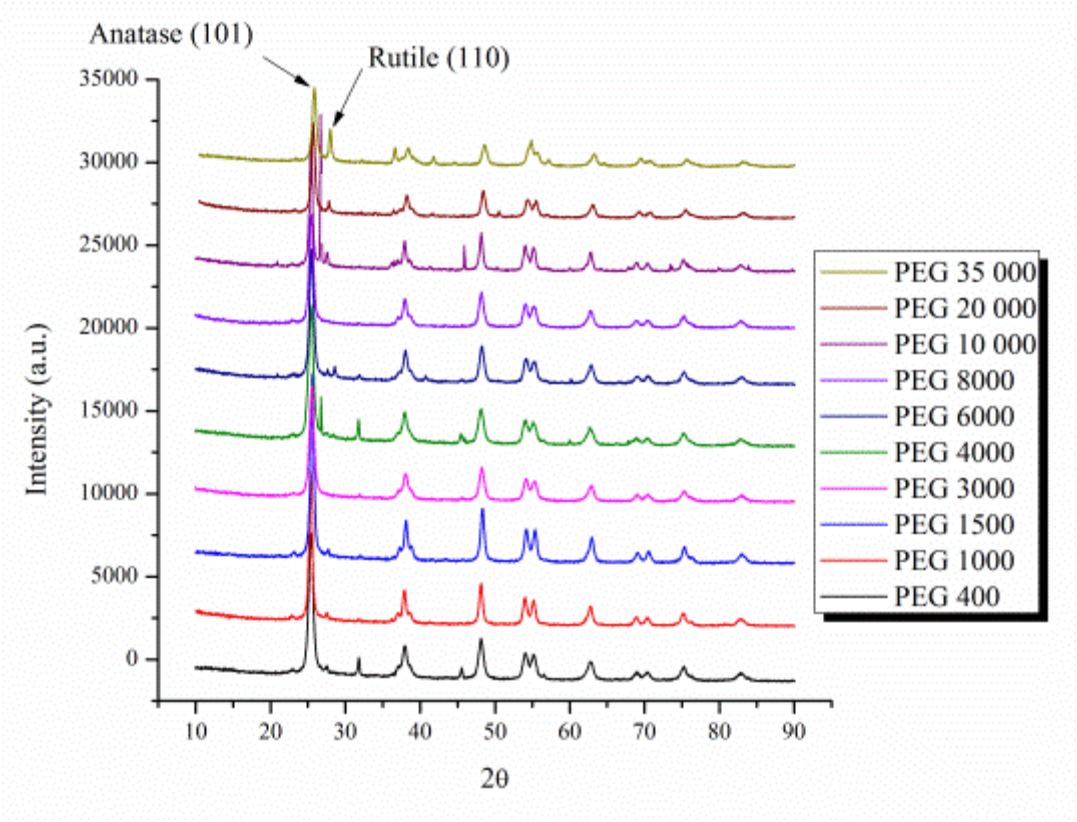

Figure 5.5: PXRD patterns of replicate calcined samples formed from ethanol.

Figure 5.4 shows the PXRD patterns of samples formed from ethanol after they had been calcined. The peaks are narrower indicating that crystallite size had increased as a result of calcination. The rutile peak in the sample synthesised using PEG 35000 is more pronounced, suggesting that the rutile crystallite size had increased after calcination. Peaks at ~ 20.5° 2θ and 26.5° 2θ are due to presence of quartz that entered the crucible post-synthesis, as the samples were being removed from the sand bath. As a result, they should have no effect on the formed product. The anatase (1 0 1) peaks are well aligned in the calcined samples. This suggests that the presence of carbon on the pre-calcined samples caused variable tension on the titania unit cell, and by extension the *d*-spacing. Therefore, the strain imposed by the presence of carbon caused a shift in the position of the anatase peaks. Figure 5.5 suggests excellent reproducibility of the composition and crystallite size of particles formed post-calcination.

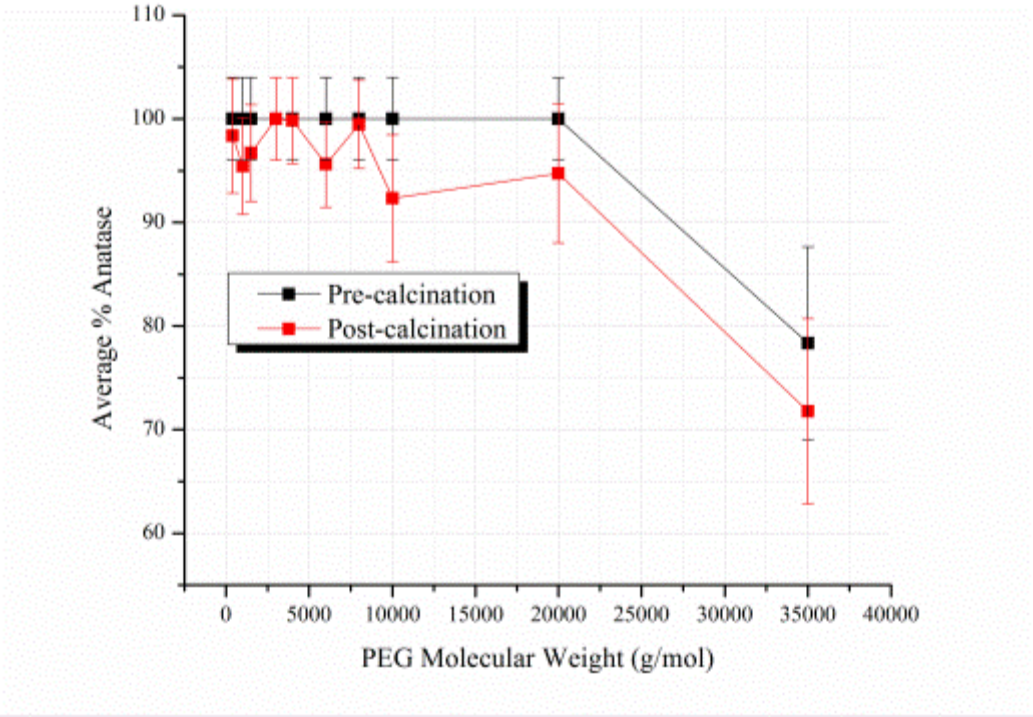

Figure 5.6: Average amount of anatase formed in ethanol pre- and post-calcination.

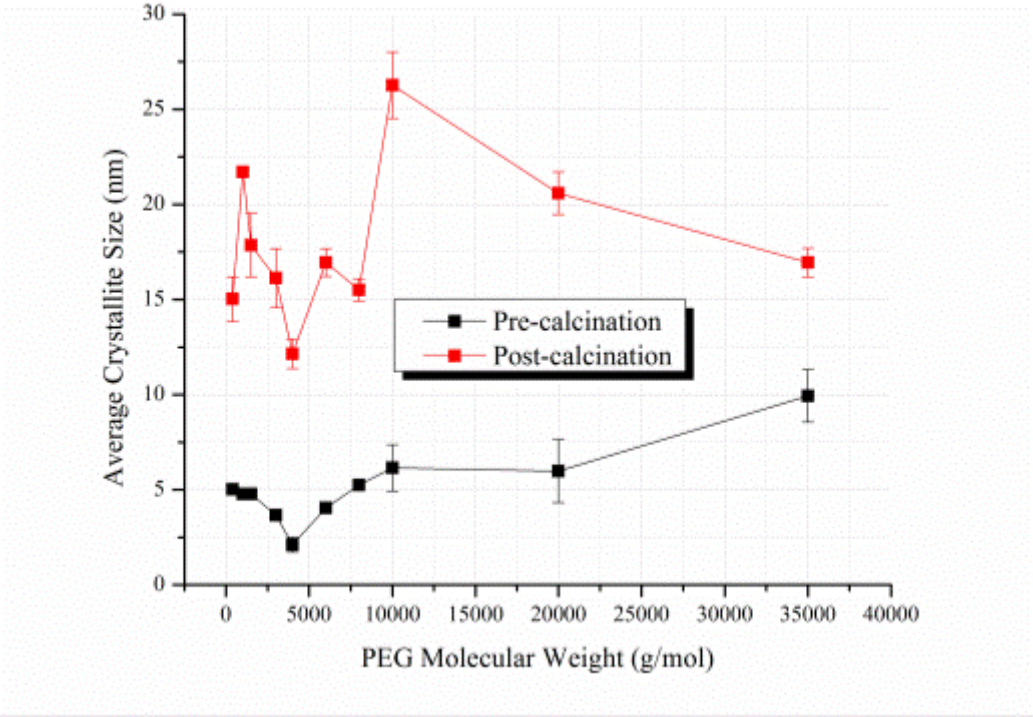

Figure 5.7: Average anatase crystallite size formed in ethanol pre- and post-calcination.

The average percentage of anatase formed using ethanol across a range of PEG molecular weights is given in figure 5.6. Before calcination, anatase was exclusively formed in all PEG molecular weights except PEG 35000. PEG 35000 produced 78.3% anatase (and by extension 21.7% rutile).

Error bars were generated as follows: Spurr and Myers found the standard error in the mass fraction of anatase or rutile to equate to 3 – 4 % of the amount of the respective phase measured[2]. Since all experiments were conducted in duplicate, the standard deviation of the duplicate analyses was added to the inherent 4% error of the Spurr and Myers model to produce a final statistical error. The size of the error bars showed good reproducibility. The largest error in the data was present for the sample synthesised using PEG 35000 (9.3%).

Following calcination of all samples, a small amount of anatase transformed into rutile for most samples. From PEG 400 – 8000, the greatest loss in the amount of anatase was 4.6%. The amount of transformation was not proportional to the PEG molecular weight as PEG 3000, 4000, and 8000 showed the least decrease in the amount of formed anatase. Samples synthesised from larger molecular weight PEG (> 10000 g/mol) displayed the greatest amount of transformation into rutile after calcination. The greatest errors were also present for samples formed using larger PEG molecular weights.

Figure 5.7 shows the average anatase crystallite size obtained for samples formed from ethanol before and after calcination. Prior to calcination, anatase crystallite size decreased and then increased as a function of increasing PEG molecular weight. The smallest crystallites were obtained from samples synthesised using PEG 3000 and PEG 4000 (3.7 and 2.1 nm respectively). Interestingly, samples synthesised from PEG 3000 and PEG 4000 showed the smallest decrease in the amount of anatase after calcination as given in figure 5.6. Crystallite sizes formed as a function of PEG molecular weight displayed a trend for some of the samples: the crystallite sizes for samples formed from PEG 400 and PEG 8000 were 5.0 and 5.3 nm respectively. PEG 8000 has a molecular weight 20 times greater than PEG 400. Crystallite sizes for samples formed from PEG 300 and PEG 6000 were 3.7 and 4.1 nm respectively. PEG 6000 has a molecular weight 2 times greater than that of PEG 3000. The crystallite sizes for samples formed from PEG 10000 and PEG 20000 were 6.2 and 6.0 nm respectively. PEG 20000 has a molecular weight 2 times greater than PEG 10000.

Error bars represent the standard deviation of the replicate analyses. Crystallite size pre-calcination was in excellent agreement given by the small error bars. A curious point of note is that the larger PEG molecular weights resulted in the formation of the largest crystallites with the greatest errors.

After calcination, anatase crystallite size increased in all samples. The increase was not consistent as a function of PEG molecular weight. As a result, there is no trend between the size of anatase crystallites post-calcination and the PEG molecular weights that were used to produce the samples. The greatest error in the data is present for the sample formed from PEG 10000 (1.7 nm). This indicates fairly good reproducibility across the range of samples.

No trends between the amount of anatase and respective crystallite size formed before calcination could be obtained from figure 5.8. However, an interesting point of note is the amount and size of anatase formed from PEG 35000. This PEG molecular weight produced 78.3% anatase with an average size of 9.9 nm. PEG 35000 also resulted in the formation of 21.7% rutile with an average size of 29.9 nm.

There are two possible explanations for this observation 1) Being a longer chain polymer, PEG 35000 has a tendency of producing larger crystallites. This is justified by the larger anatase crystallites formed pre-calcination from PEG 10000 and PEG 20000. 2) Because PEG 35000 allowed for the transformation of anatase into rutile during synthesis, the transformation catalysed coarsening in anatase (it is not possible to comment on whether 29.9 nm is large or small for rutile crystallites at this stage). This is consistent with Gribb and Banfield who found that coarsening of reactant anatase and product rutile occurred concurrently with transformation[3]. Additionally, phase transformation assists with grain growth due to the high mobility of atoms during phase transition[4].

Comparing figures 5.8 and 5.9, it is clear that calcination had a greater effect on crystallite size than on phase transformation (the amount of anatase decreased by 3.5% post-calcination compared with crystallite size that increased by 244% post-calcination). This finding is consistent with the observations made by Banfield *et al.*, of the data by Rao: at 510 °C, 5% transformation of anatase into rutile would occur after more than 41 days[5]. Coarsening was a predicted outcome of calcination.

Tables showing the amount of each phase and crystallite size obtained for each sample with averages and errors are given in appendix C.

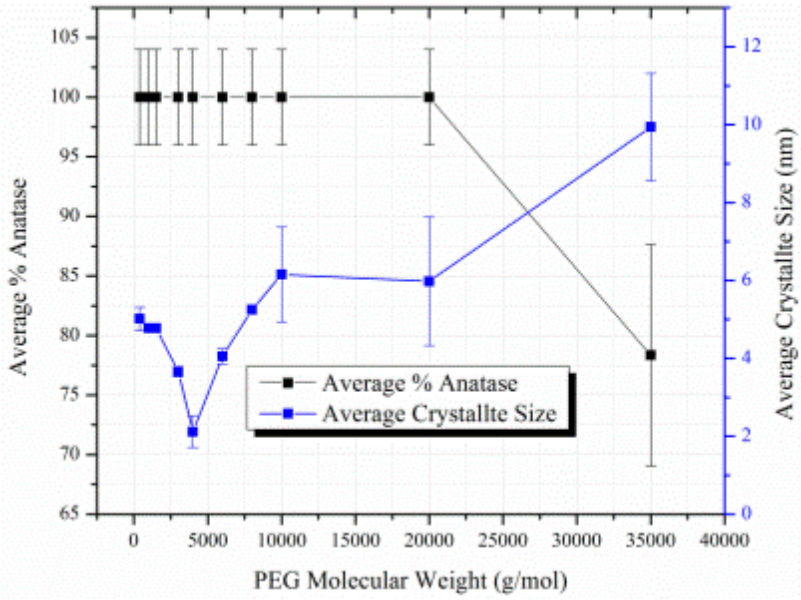

Figure 5.8: Average amount of anatase with associated average crystallite size formed in ethanol pre-calcination.

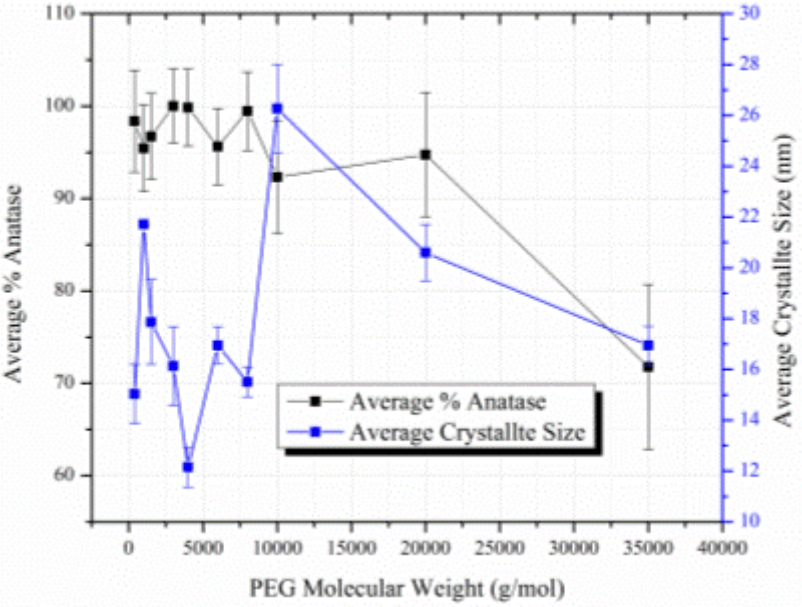

Figure 5.9: Average amount of anatase with associated average crystallite size formed in ethanol post-calcination.

TEM images for the sample synthesised using PEG 4000 in ethanol is given in figure 5.10 and figure 5.11. This molecular weight PEG produced nearly phase pure anatase

with the smallest crystallite size. The images obtained from this sample were compared with those obtained for the calcined version the same sample (figures 5.12 – 5.14) in an attempt to directly view the effects of calcination. Comparing figures 5.12 and 5.13, it is clear that some areas of the sample exhibited particle agglomeration whereas other parts did not. The aggregation depicted in figure 5.14 could be due to fragmented polymer chains forcing particles to aggregate in a specified way during ignition.

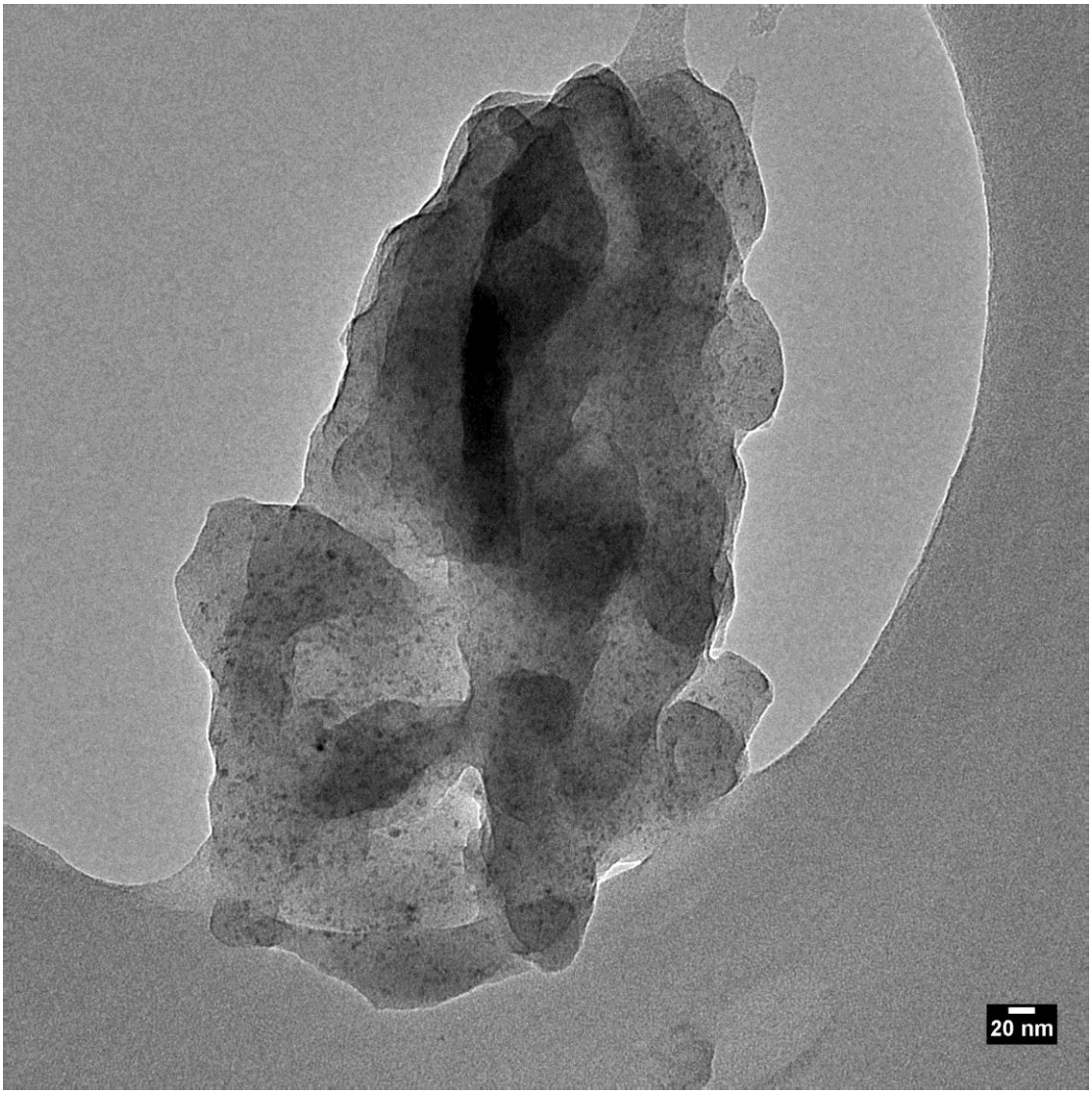

Figure 5.10: (PEG 4000 in ethanol pre-calcination) Distribution of fine anatase particles within the carbon film of the TEM grid.

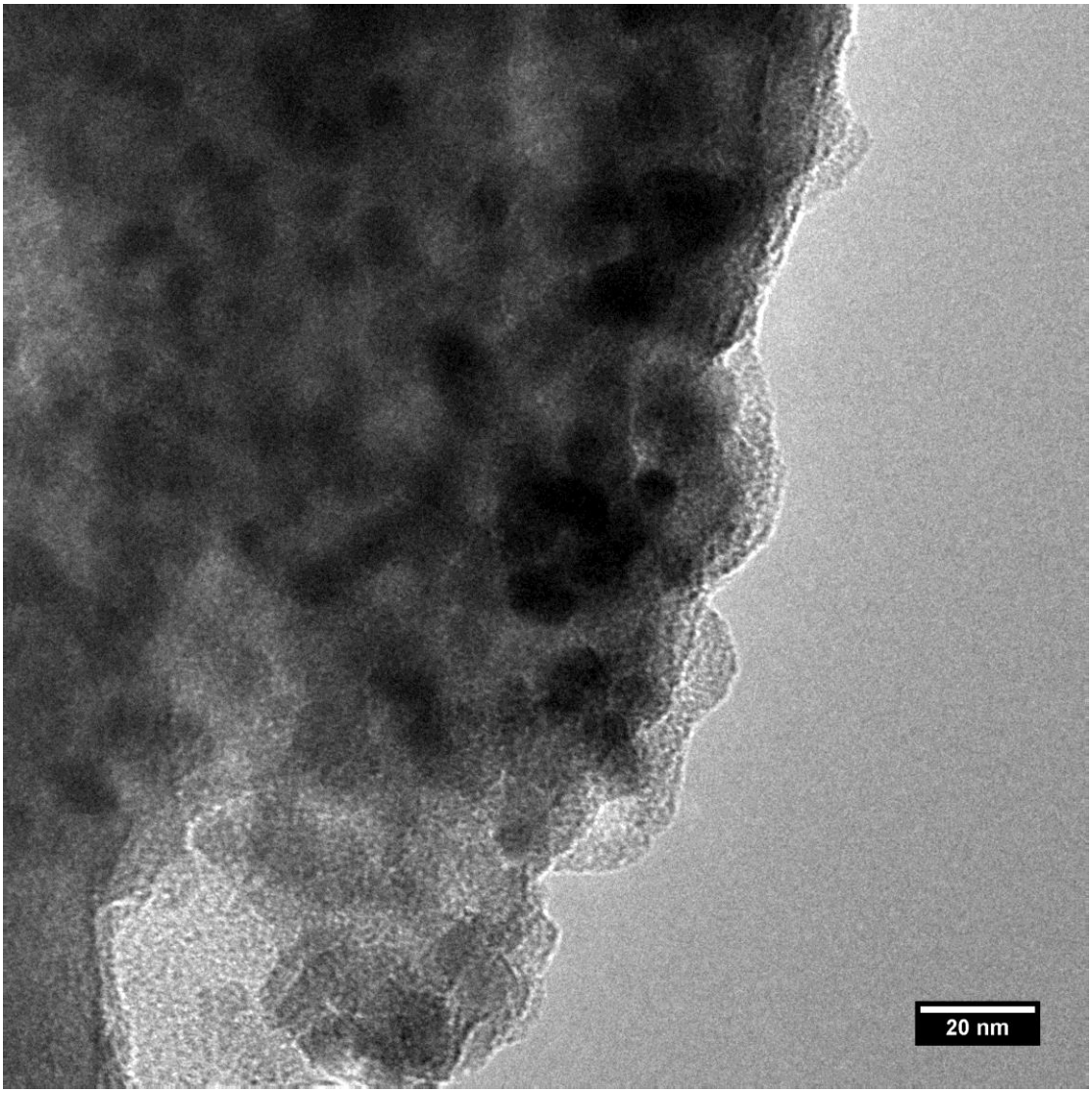

Figure 5.11: (PEG 4000 in ethanol pre-calcination). Agglomeration of anatase particles. The difficulty in distinguishing individual particles is likely due to the presence of carbon on the sample, left over from the ignition of PEG.

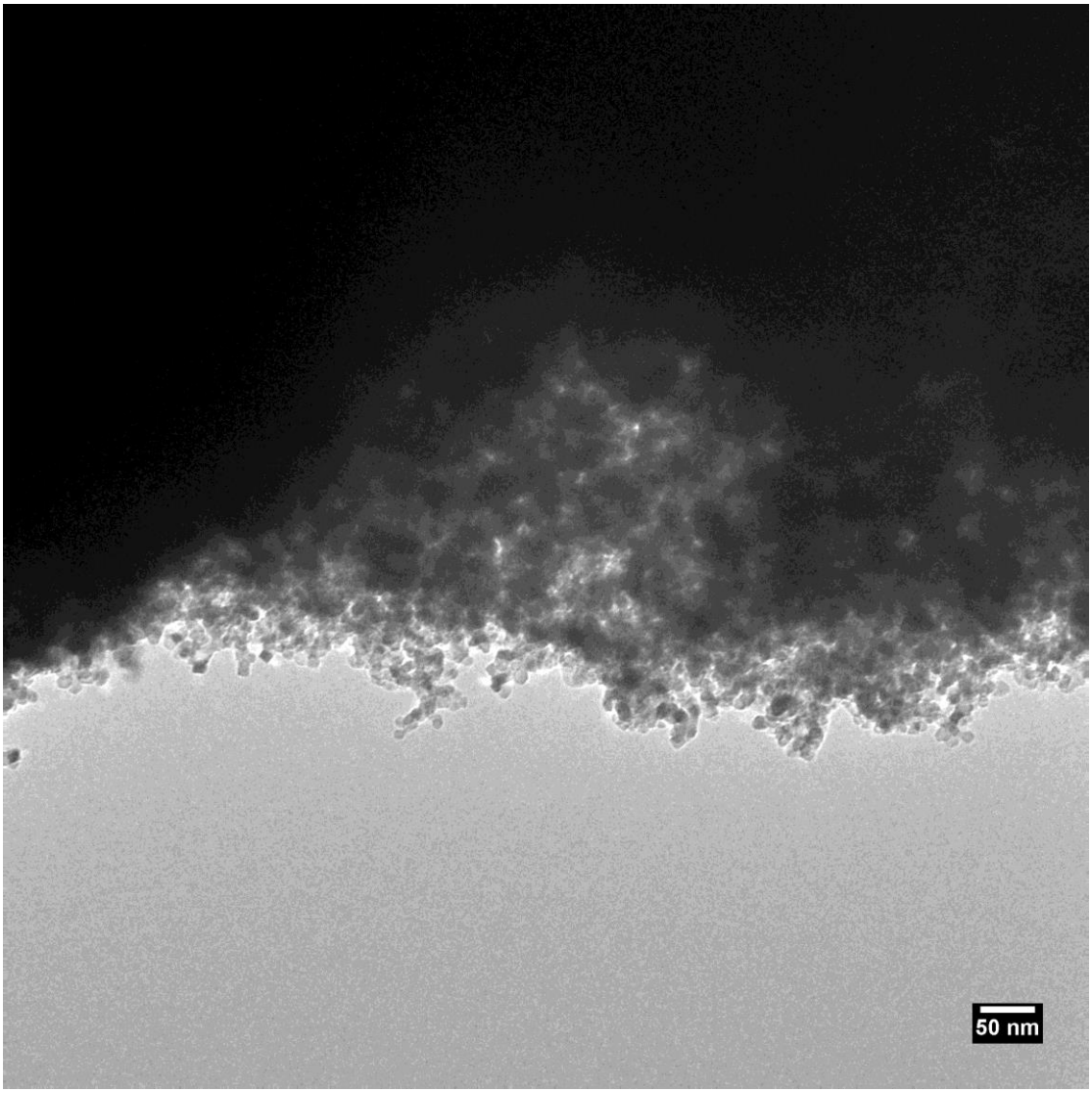

Figure 5.12: (PEG 4000 in ethanol post-calcination). This area shows particles that are nicely separated, in a region of particles that have agglomerated.

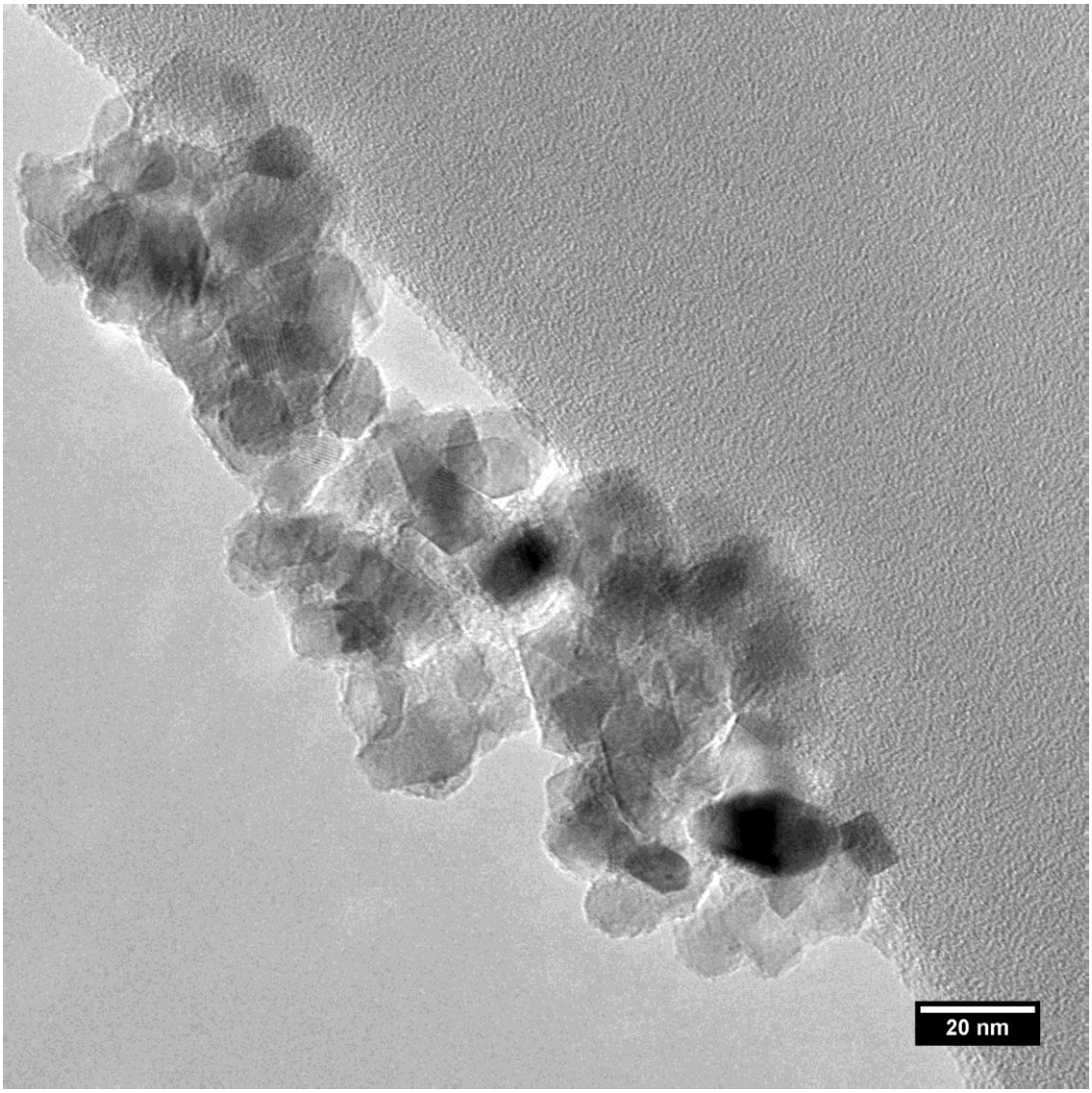

Figure 5.13: (PEG 4000 in ethanol post-calcination). Crystallites appear to have well-defined geometric shapes. Crystallites measure between 10 – 14 nm.

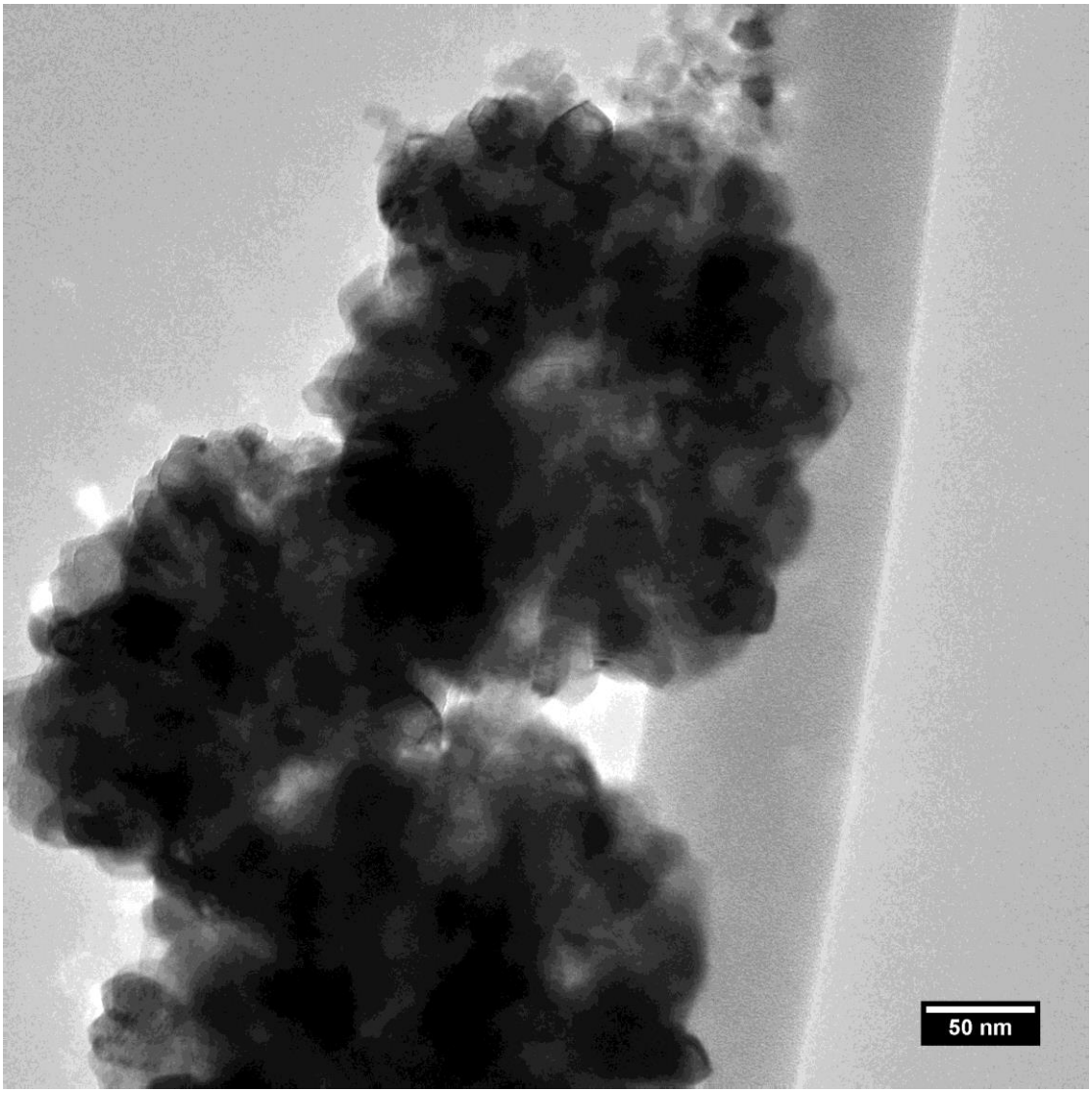

Figure 5.14: (PEG 4000 in ethanol post-calcination). Particles appear to be aggregating around a common point to form a spherical aggregation.

5.1.7 Water containing HNO_3 Mediated Synthesis

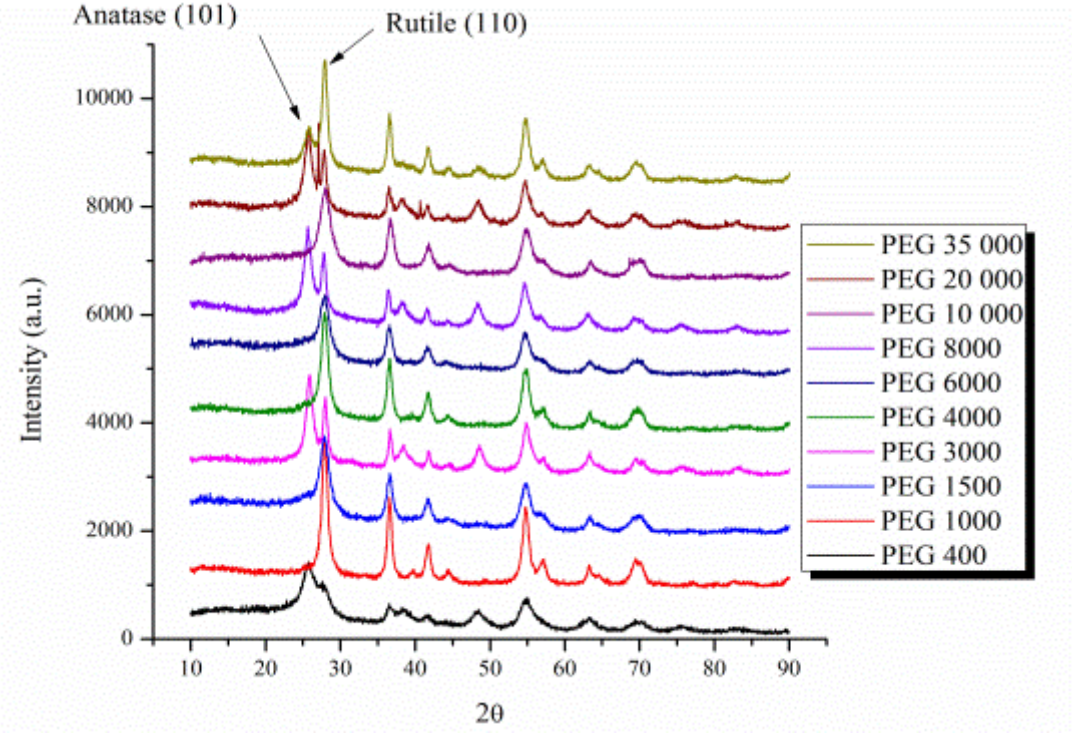

Figure 5.15: PXRD patterns of samples formed from water containing HNO_3 pre-calcination.

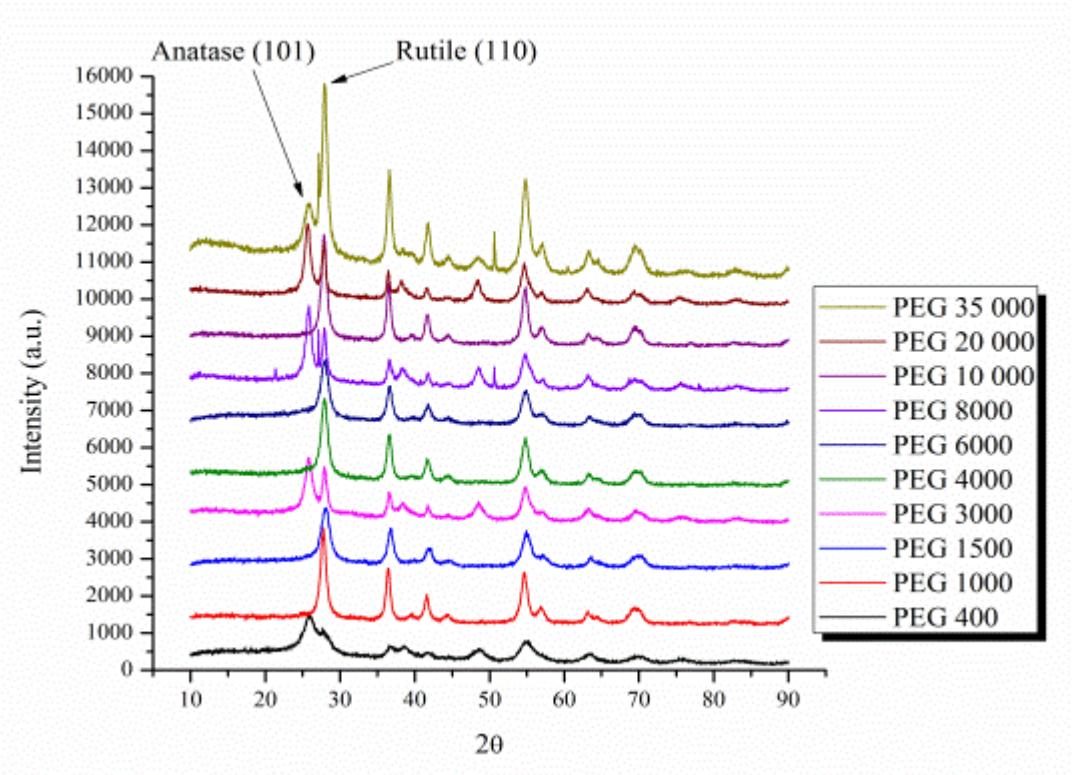

Figure 5.16: PXRD patterns of replicate samples formed from water containing HNO_3 pre-calcination.

Figures 5.15 and 5.16 show the PXRD patterns obtained for samples synthesised using water containing HNO_3 as the solvent across a range of PEG molecular weights. There is good correlation between both figures implying good reproducibility in the experiment. Both figures show that water containing HNO_3 has a tendency to form rutile, although the PEG molecular weight does influence the formed phase. Major anatase peaks can be seen in samples synthesised using PEG with molecular weights of 400, 3000, 8000, and 20000 g/mol. Therefore, there seems to be no direct correlation between PEG molecular weight and the phase purity of the sample. The broadness of the peaks suggests the formation of nano anatase and rutile particles. These patterns also show peak misalignment.

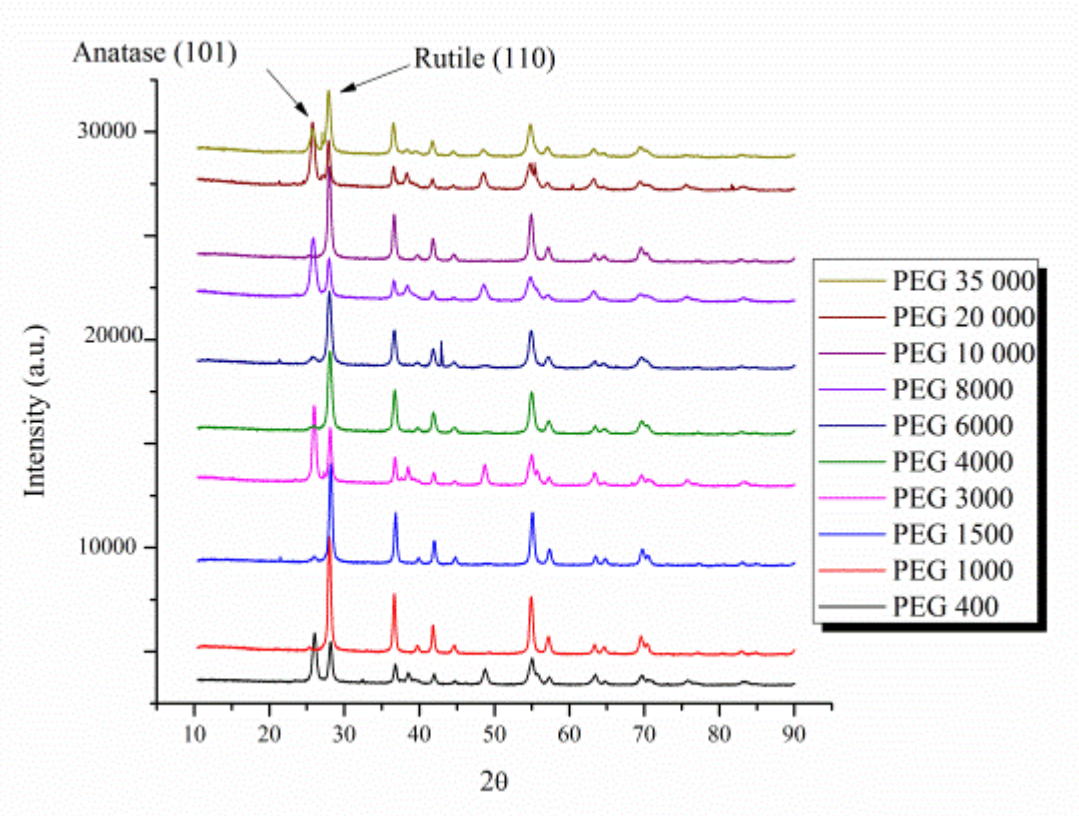

Figure 5.17: PXRD patterns of calcined samples formed from water containing HNO_3.

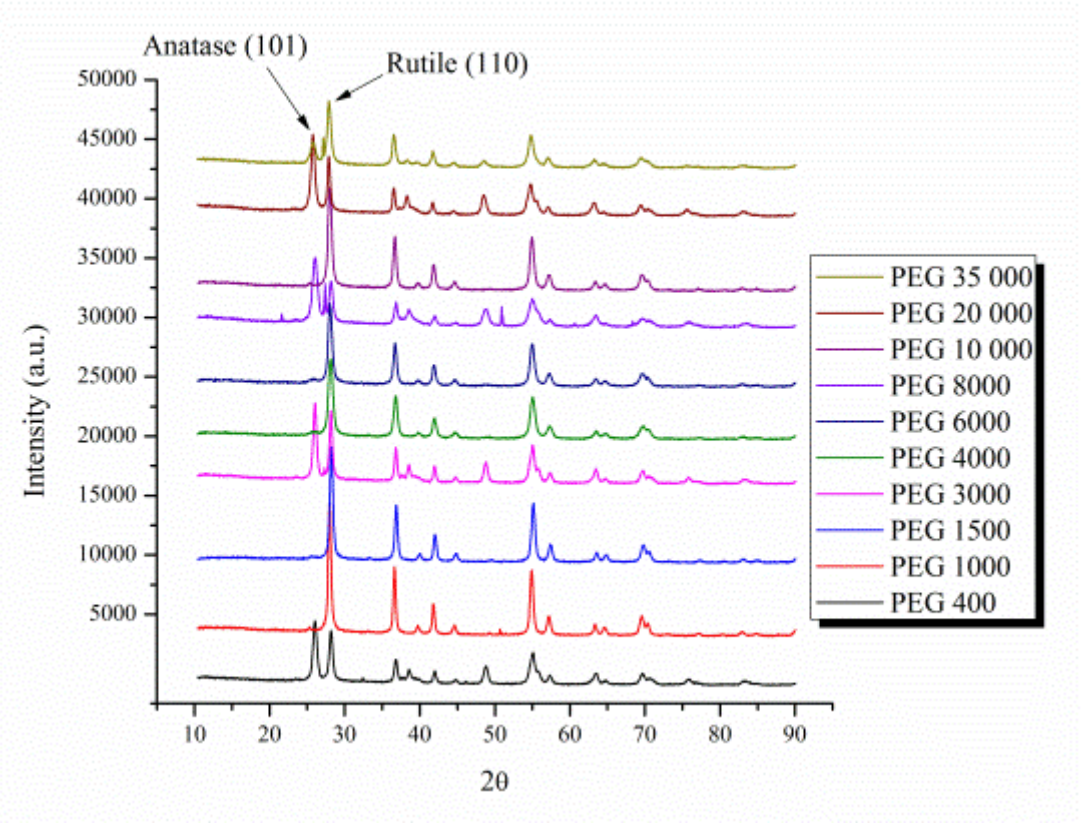

Figure 5.18: PXRD patterns of replicate calcined samples formed from water containing HNO_3.

Figures 5.17 and 5.18 show the change in the PXRD patterns of samples synthesised using a water containing HNO_3 solvent across a range of PEG molecular weights after calcination. The sharpness of the peaks indicates that particle coarsening had occurred during calcination. The rutile peak in the sample synthesised from PEG 400 is better defined suggesting that significant anatase to rutile phase transformation had occurred during calcination. Post-calcination peaks are also better aligned compared with the peaks from pre-calcined samples. This suggests that the presence of carbon on the samples post-synthesis was placing strain on the titania lattice and caused a shift in the peak position – as described for the diffraction patterns obtained for samples synthesised in ethanol. Both sets of diffraction patterns are in good agreement with each other implying good reproducibility.

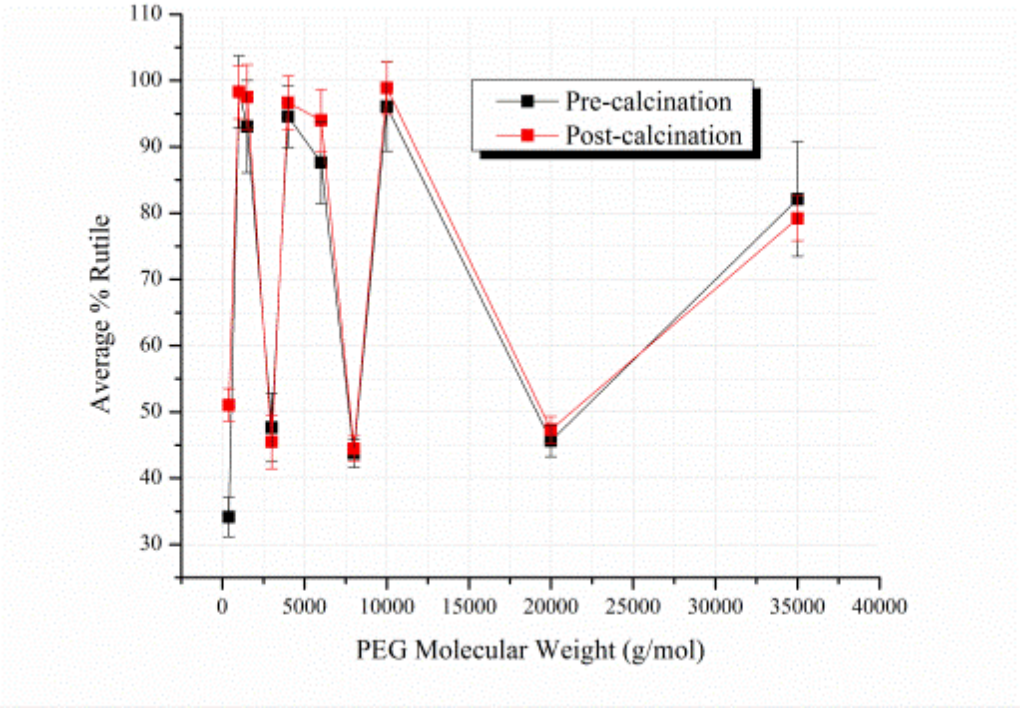

Figure 5.19: Average amount of rutile formed in water containing HNO_3 pre- and post-calcination.

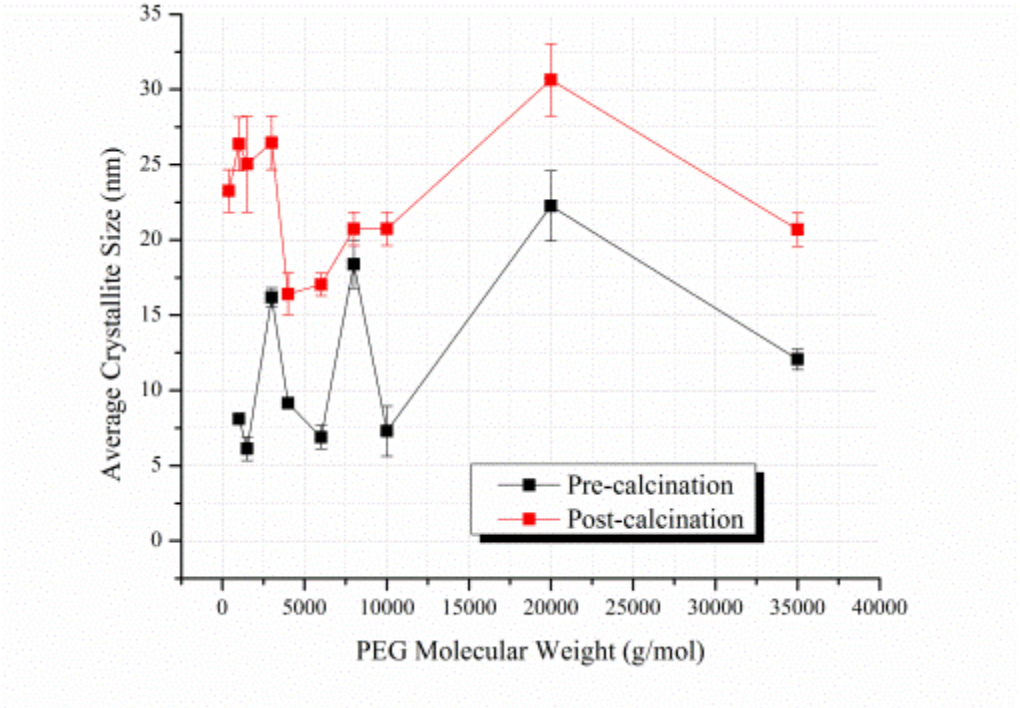

Figure 5.20: Average rutile crystallite size formed in water containing HNO_3 pre- and post-calcination.

Figure 5.19 compares the amount of rutile formed from water containing HNO_3 across a range of PEG molecular weights pre- and post-calcination. From figure 5.19 it can

be seen that water containing HNO_3 favoured the formation of rutile. The PEG molecular weight also affected the amount of formed rutile. The least amount of rutile (34.1%) was formed in the sample synthesised from PEG 400. PEG 3000, 8000, and 20000 resulted in the formation of 47.7%, 43.7%, and 45.7% rutile respectively. This produced an up and down effect of the amount of rutile formed as a function of increasing PEG molecular weight, with good reproducibility. Error bars were obtained by summing the standard deviation of the replicate analyses with 4% of the average amount of rutile formed. The largest error in the data set is present for the sample synthesised using PEG 35000 (8.7%).

With the exception of the samples synthesised from PEG 3000 and PEG 35000, all other samples had shown a slight increase in the amount of formed rutile post-calcination. The samples formed post-calcination from PEG 3000 and PEG 35000 were within error of the pre-calcined samples. Hence the apparent decrease in the amount of formed rutile could be due to poorer reproducibility in these replicate samples. Formed rutile increased by 4% after calcination, across all samples. This is not an unexpected result as it was found that at 510 °C, 5% anatase would transform into rutile over 41 days[5]. The greatest contributor to the 4% overall increase in the amount of rutile post-calcination was the sample synthesised from PEG 400. The amount of rutile in this sample had increased to 51.0% after calcination (this represented an increase of 33.1% compared to the pre-calcined sample). A plausible explanation for this result is that the synthesis was only partially complete after ignition had ended. Therefore, fragments of polymer were present in the sample during the calcination process. The polymer fragments could have catalysed the transformation of anatase to rutile.

According to figure 5.20, rutile crystallites in all samples coarsened during calcination. Before calcination, the average crystallite size displayed up and down behaviour as a function of increasing PEG molecular weight. The data displayed good reproducibility as the largest error was obtained for the samples synthesised using PEG 20000 (2.3 nm). The errors bars in figure 5.20 represent the standard deviation of the replicate analyses. The smallest crystallite sizes (6.1, 6.9, and 7.2 nm) were obtained from samples synthesised using PEG 1500, 6000, and 10000 g/mol respectively. PEG 3000, 8000, and 20000 formed the largest rutile crystallites with average sizes of 16.2, 18.4, and 22.3 nm respectively. With the exception of the

sample formed from PEG 6000 and PEG 8000, all other samples displayed a proportional increase in crystallite size after calcination as a function of increasing PEG molecular weight.

The average crystallite size before calcination across the range of samples was 11.8 nm. After calcination, the average crystallite size across the range of samples had increased to 22.7 nm, representing a 92.4% increase in size.

Figure 5.21 presents an interesting relationship between the amount of rutile with associated crystallite size formed in water containing HNO_3 across a range of PEG molecular weights before calcination. The up and down effect of the amount of rutile formed is nearly identically inverse to the average crystallite size produced as a function of increasing PEG molecular weight. The associated error bars are small enough for the trend to exist at the maximum error of each data point suggesting that this is a real, reproducible trend.

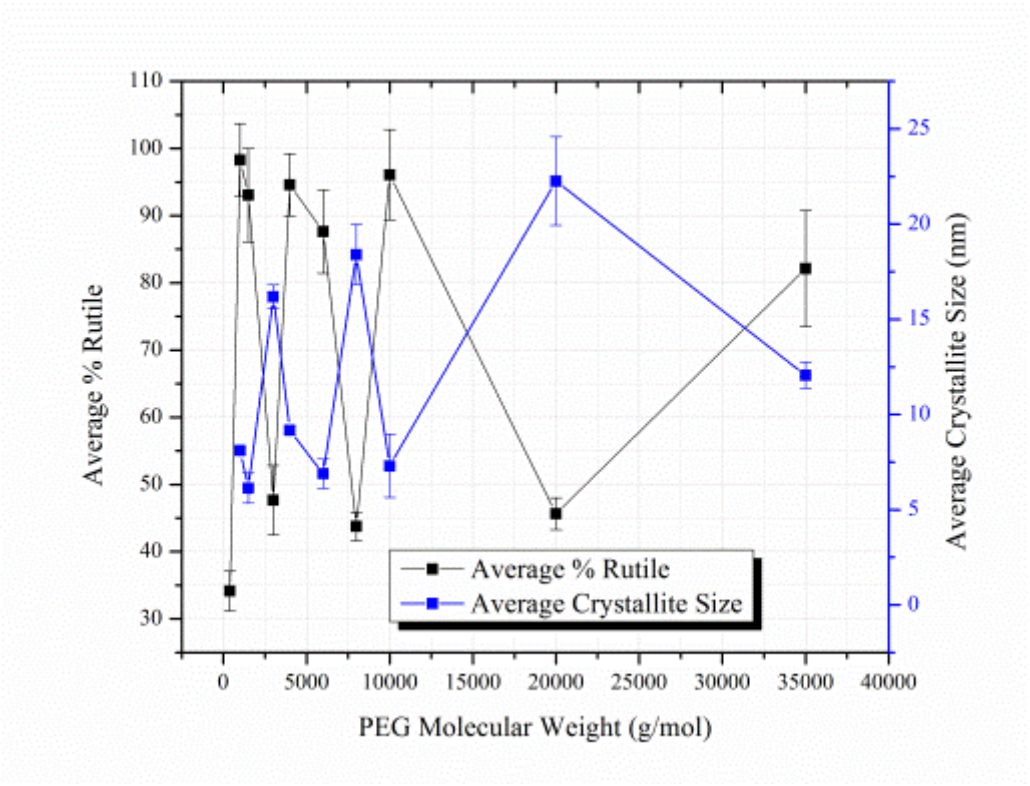

Figure 5.21: Average amount of rutile with associated average crystallite size formed in water containing HNO_3 pre-calcination.

Penn and Banfield discovered a similar inverse relationship between % brookite formed and associated crystallite size as a function of hydrothermal treatment time[6] (discussed in section 1.2.5). Given that the present experimental conditions are different, the inverse relationship is likely a property of titania. Penn and Banfield used oriented attachment to describe the behaviour of brookite. In the present experiment, oriented attachment between anatase and rutile crystallites could have caused rutile to coarsen by addition of material from solution. Additionally, anatase crystals trapped between rutile crystals could have been utilised by transformation into rutile. These two statements then explain how it is possible to have a large amount of rutile existing as small crystallites, and a small amount of rutile existing as large crystallites. Unfortunately, it does not explain why this should occur.

A curious observation is that rutile crystallites were smaller than 11 nm for many of the analysed samples. Titania polymorph stability is dependent on crystallite size and below 11 nm, titania exists as anatase as it is the most stable phase[7]. As was shown in figure 5.21, when a sample contained a large amount of rutile, the rutile existed as small crystallites. A likely mechanism, in addition to oriented attachment, is that during the course of the reaction anatase was nucleated first. Certain PEG molecular weights stabilised the formed, small anatase crystallites during ignition. Since the anatase crystallites were small, transformation into rutile was inhibited. Any transformation that did occur formed rutile crystallites that took up material from the reaction matrix and grew to a larger size. This explains the inverse trend of crystallite size and amount of formed rutile for the reaction completed in water containing HNO_3.

PEG with specific molecular weights were responsible for the formation of a mixture of anatase and rutile when synthesised in water containing HNO_3. These molecular weights were 400, 3000, 8000, and 20000 g/mol. PEG chain length was found to affect coordination to metal ions[8]. It is likely that during heating and ignition, these polymer chains undergo scission at specific points (or multiples of specific points), that allows for the formation of a fragmented polymer which folds upon itself into a reaction chamber.

Chain scission is governed by the bond dissociation energy of C-C and C-O. For diatomic molecules the bond dissociation energy at 298 K of C-C and C-O is 610 ± 2 and 1076.5 ± 0.4 KJ/mol respectively[9]. These values should only be considered

relativistically as other elemental components of PEG will affect the absolute bond dissociation energy.

Within this polymer reaction chamber, titania nucleates. If the chamber is of a size that is favourable to the stabilisation of anatase, then samples generated from these polymer weights are expected to have a large portion of anatase present, with small crystallite sizes, as discussed above.

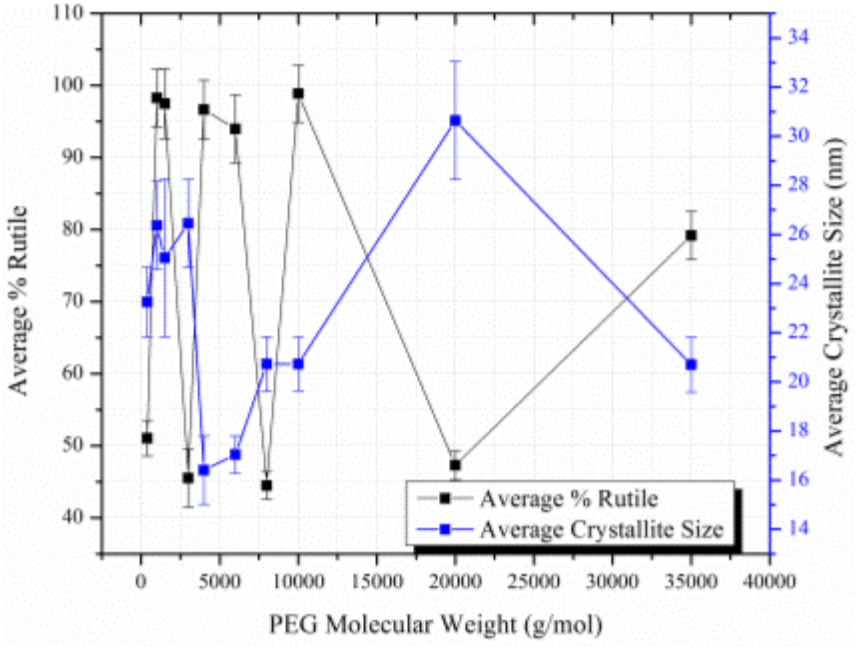

Figure 5.22: Average amount of rutile with associated average crystallite size formed in water containing HNO_3 post-calcination.

Figure 5.22 illustrates that the inverse relationship between the amount of rutile formed and associated crystallite size is maintained post-calcination. Comparing figures 5.21 and 5.22, calcination had a greater effect on crystallite size than phase transformation. Rutile quantity increased by an average of 4% after calcination across all samples. After calcination, crystallite size increased by a total of 92.4%. Calcination at 500 °C would be expected to increase crystallite size more than encourage phase transformation.

Not represented in figures 5.21 and 5.22 is the average anatase crystallite size formed from samples containing PEG that favoured anatase formation in water containing HNO3, pre-calcination. This data is represented in table 5.2.

Tables showing the amount of each phase and crystallite size obtained for each sample with averages and errors are given in appendix C.

Table 5.1: Average anatase crystallite size formed in ethanol and water containing HNO3.

PEG (g/mol)	% Anatase formed in ethanol	Anatase crystallite size in ethanol (nm)	% Anatase formed in water containing HNO_3	Anatase crystallite size in water containing HNO_3 (nm)
400	100 ± 4.0	5.0 ± 0.3	65.8 ± 4.2	5.2 ± 0.4
3000	100 ± 4.0	3.7 ± 0.1	52.3 ± 5.4	9.3 ± 0.4
8000	100 ± 4.0	5.3 ± 0.1	56.3 ± 2.6	10.4 ± 1.5
20000	100 ± 4.0	6.0 ± 1.6	54.3 ± 2.7	11.3 ± 0.0

Table 5.1 clearly shows that for the same molecular weight PEG, anatase crystallites were larger in samples containing a mixture of anatase and rutile. This effect was more pronounced for longer chain PEG (> 3000 g/mol). In the samples synthesised using water containing HNO_3, anatase was the first formed phase. Some anatase crystallites would have transformed into rutile whereas others would have coarsened. Transformation and crystallite growth are competing processes, with transformation encouraging growth. Therefore, it is likely that the high atomic mobility during transformation of anatase to rutile caused an increase in the average crystallite size of anatase[4] formed in water containing HNO_3 compared with ethanol.

Table 5.2 shows that a large presence of anatase in a mixture of anatase and rutile polymorphs caused an increase in the size of rutile crystallites.

Table 5.2: Average rutile crystallite size formed in ethanol and water containing HNO_3.

PEG (g/mol)	% Rutile formed in ethanol	Rutile crystallite size in ethanol (nm)	% Rutile formed in water	Rutile crystallite size in water (nm)
35000	21.7 ± 7	29.9 ± 2.1	82.1 ± 8.7	12.1 ± 0.7

The sample formed from PEG 4000 in water containing HNO_3 was imaged (figures 5.23 and 5.24). This sample exhibited a large amount of small rutile crystallites when analysed via PXRD. Even though the (1 1 0) rutile crystallite size was small relative to the other samples synthesised using water containing HNO_3, the crystallites were still larger than the (1 0 1) anatase crystallites formed in ethanol using PEG 4000. The superstructure depicted in figure 5.24 is unlikely an agglomeration of particles as similar structures were found in other areas of the sample. The formation of rutile superstructures is novel to the resin-gel process

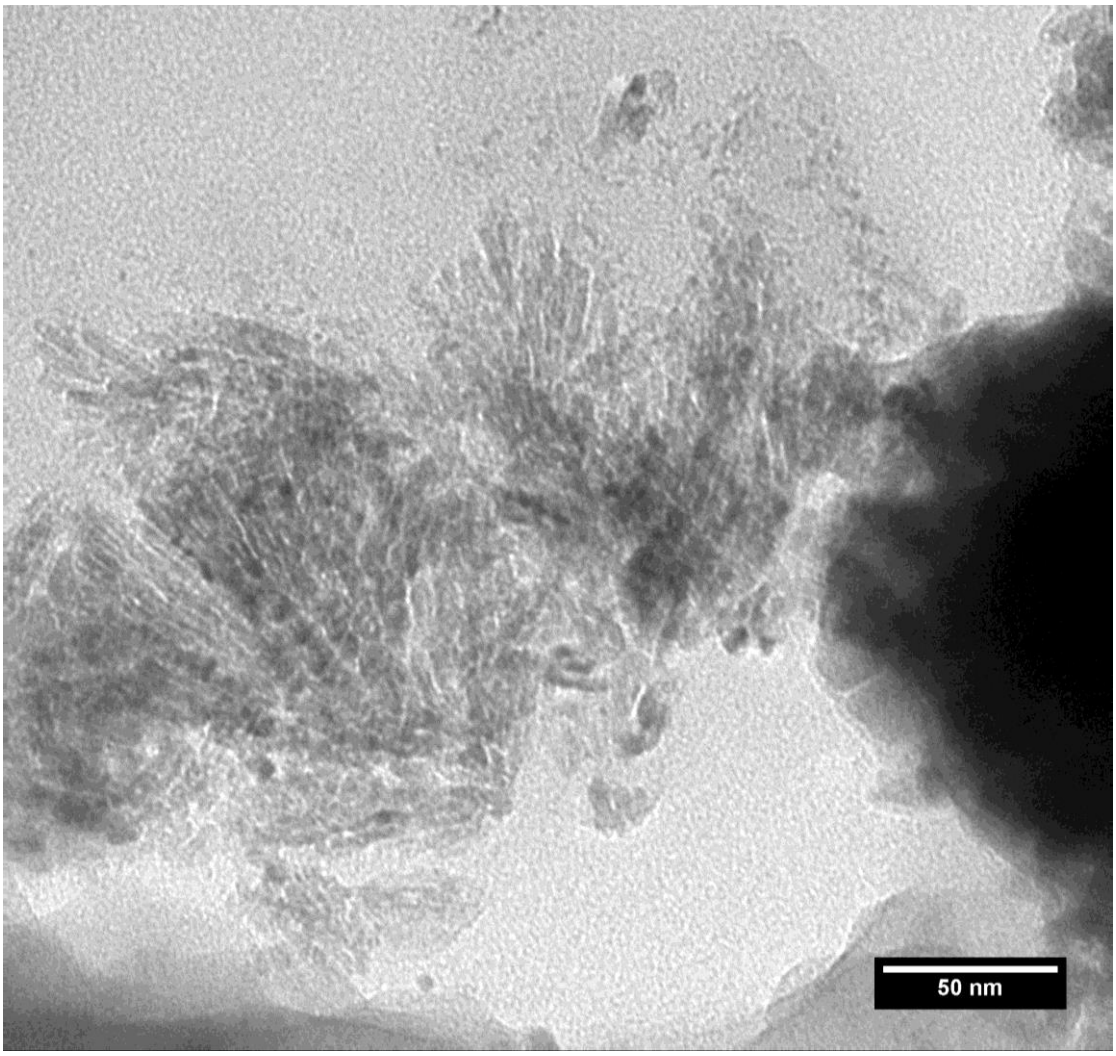

Figure 5.23: (PEG 4000 in water containing HNO_3 pre-calcination). The particles display anisotropic growth, being longer than they are wider and suggesting the formation of rutile nanorods.

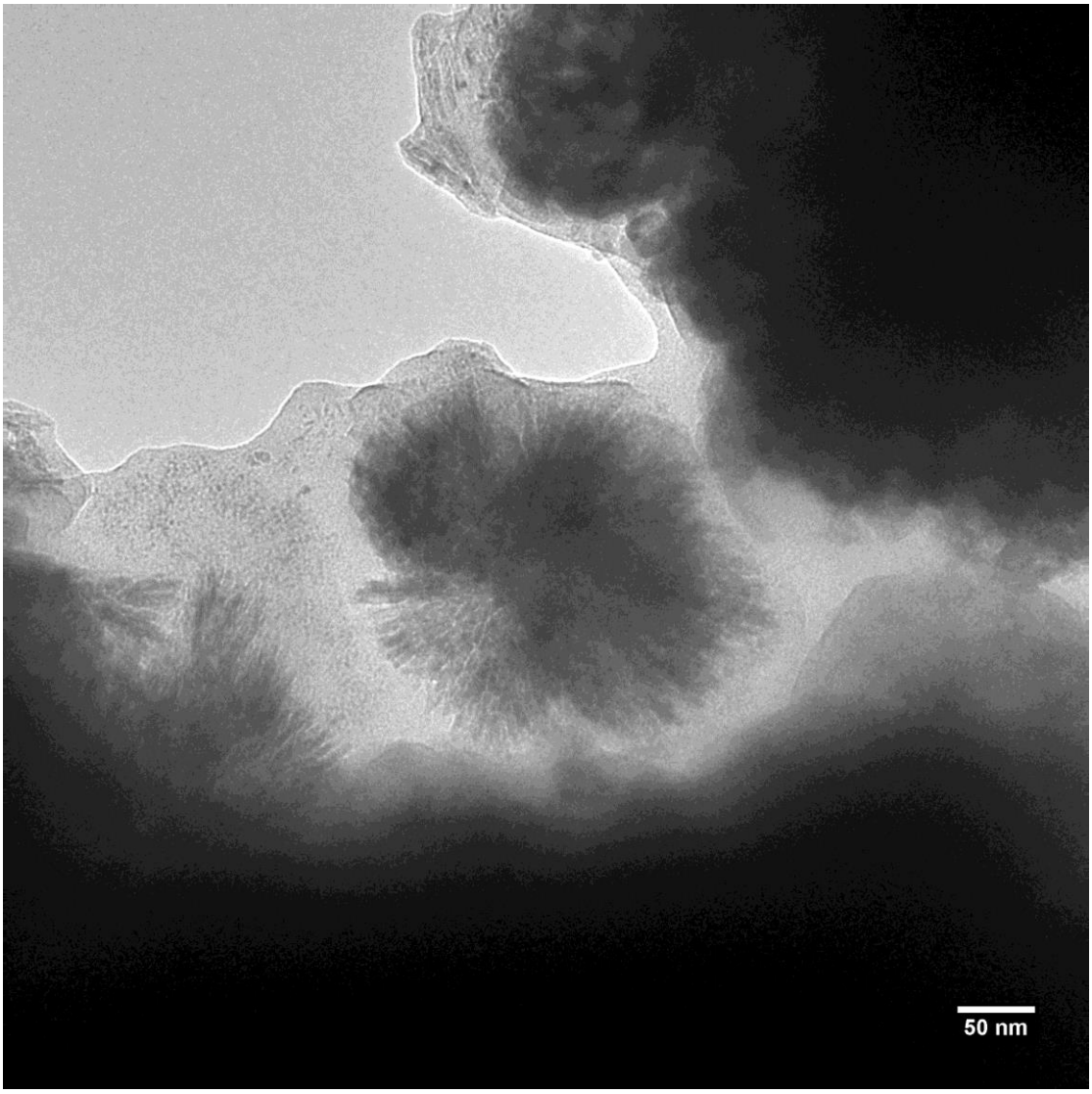

Figure 5.24: (PEG 4000 in water containing HNO_3 pre-calcination). The rutile nanorods appear to aggregate from a common point (or set of common points) forming a superstructure. The length of the rutile nanorods is consistent with crystallite size data obtained via PXRD analysis of the sample. Platelet like particles were also formed.

5.1.8 Comparison of the Effects of Ethanol and Water containing HNO_3

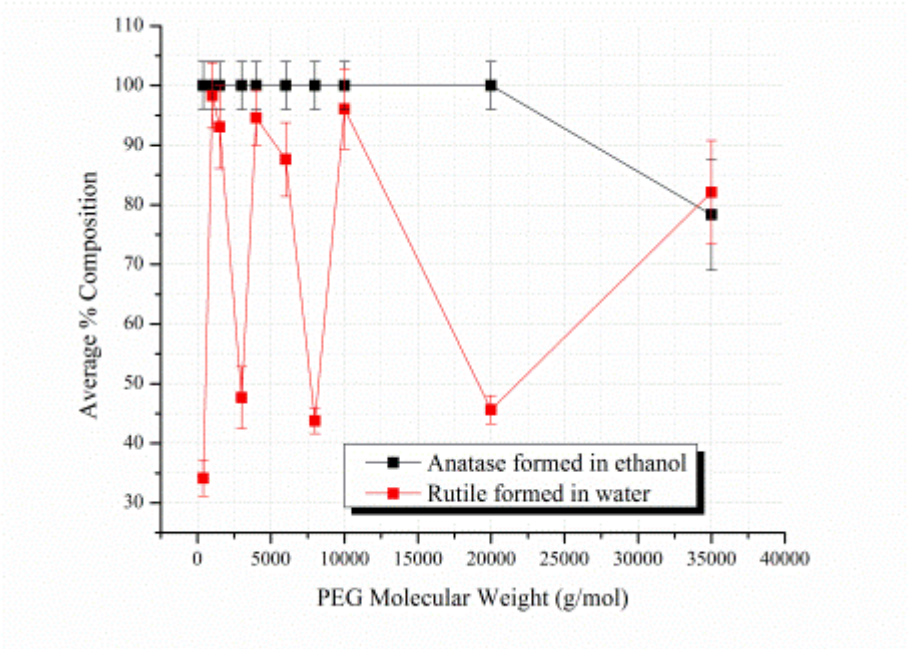

Figure 5.25: Amount of anatase and rutile formed in ethanol and water containing HNO_3 respectively, as a function of increasing PEG molecular weight pre-calcination.

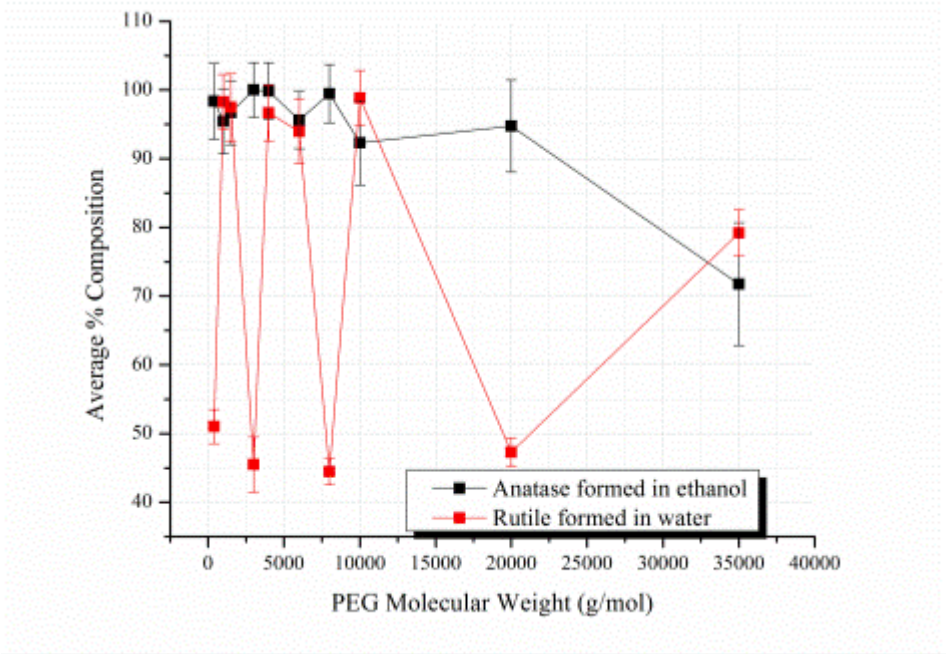

Figure 5.26: Amount of anatase and rutile formed in ethanol and water containing HNO_3 respectively, as a function of increasing PEG molecular weight post-calcination.

Figures 5.25 and 5.26 compares the amounts of anatase formed in ethanol and rutile formed in water containing HNO_3, pre- and post-calcination respectively. The average amount of rutile formed across all PEG molecular weights was 72.2% pre-calcination. This is in contrast to ethanol that resulted in the formation of an average of 97.8% anatase pre-calcination. Given that the largest error in the amount of anatase formed in the ethanol data set also originated from PEG 35000, it may be assumed that longer PEG chains have a tendency of producing more erratic data with poorer reproducibility.

Post-calcination, the amount of rutile increased to 75.3% across all PEG molecular weights. The amount of anatase post-calcination across all PEG molecular weights decreased to 94.4%.

There are two possible explanations for titania phase dependency on solvent under resin-gel synthesis conditions: firstly, hydroxyl groups from the solvent coordinate to the metal ions, forming hydroxyl complexed metal ions. PEG chains helically wrap these metal-hydroxyl complexes. Using water containing HNO_3, the remaining matrix components (H^+ and Cl-) were significantly smaller than the remaining matrix components present in ethanol (CH_3CH_2 and Cl^-). Therefore, the steric impact afforded by the remaining matrix components present in water containing HNO_3 was significantly smaller than that for ethanol. During nanoparticle formation, larger remaining matrix components have the effect of stabilising the nucleated phase. Consequently, anatase crystals are stabilised by the presence of larger remaining matrix components. Stabilising anatase has the effect of inhibiting rutile formation. Due to small anatase crystallites (< 14 nm) possessing lower surface free energy than rutile, anatase is the kinetic product of titania[10]. Therefore, larger remaining matrix components likely impede rutile formation by inhibiting anatase crystallite growth.

Secondly in water containing HNO_3, PEG chains are stabilised by hydrogen bonds formed between the ether oxygen of the polymer and oxygen from water. Polymer stabilisation leads to an increase in its glass transition temperature. In ethanol, similar hydrogen bonding is expected but to a lesser degree. The CH_3CH_2- component of ethanol are significantly larger than the H groups in water. As a result, hydrogen bonding is sterically limited in the case of ethanol. Therefore, the PEG-ethanol structure should be less rigid and more flexible than the PEG-H_2O structure. A more flexible structure is more likely to conform to the changing conditions during

synthesis and contribute toward stabilising newly nucleated anatase particles. A more rigid structure is more likely to struggle to attain any conformations under changing synthesis conditions and will be less effective at protecting and stabilising the high energy surfaces of newly nucleated anatase particles. Therefore, PEG that helically wraps metal ion complexes in water should have a greater tendency to form rutile. PEG that helically wraps metal ion complexes in ethanol should have a greater tendency to form anatase.

These two possibilities are not mutually exclusive. Both effects are expected to occur during different parts of the synthesis. The interplay between both effects controls the titania phase and crystallite size formed.

This model works well to explain the exclusive formation of anatase in ethanol. However, the application of this model suggests that water containing HNO_3 must form rutile exclusively. The results obtained from this chapter show that rutile is the favoured phase but not necessarily the only phase formed in water containing HNO_3.

The formation of polymer reaction chambers of various sizes – induced by heating the resins – can be used to explain the non-exclusive formation of rutile in water containing HNO_3. As described previously, smaller chambers stabilise anatase, inhibiting rutile formation. Larger chambers do not stabilise anatase and therefore rutile transformation is encouraged. It is noteworthy that these chambers are expected to form regardless of the solvent used in the synthesis. The steric effects of the CH_3CH_2- groups in ethanol nullify the effects of larger chambers by sterically stabilising nucleated anatase. Additionally, it is possible that the reduced extent of hydrogen bonding between PEG and ethanol results in the formation of smaller chambers.

It can be argued that since HNO_3 is a good oxidant, the acid increased the reaction temperature in the water containing HNO_3 solvent leading to the formation of predominantly rutile. Therefore, rutile should be formed uniformly, independent of PEG chain length. Clearly, this was not observed. Additionally, no significant differences were observed in the TGA thermogram of loaded and unloaded PEG (figures 4.2 and 4.3) further strengthening the argument that HNO_3 does not cause significant thermal variations.

Figure 5.27 compares the size of anatase and rutile crystallites formed in ethanol and water containing HNO_3 respectively pre-calcination, as a function of increasing PEG molecular weight. The figure shows that rutile crystallites were larger than anatase crystallites synthesised using the same molecular weight PEG. An interesting point of note from figure 5.28 is that anatase crystallite size formed from PEG 8000 in ethanol was larger than rutile crystallites formed in water containing HNO_3 for the same PEG chain length, after calcination. Aside from that sample, rutile crystallites formed from water containing HNO_3 remained larger than anatase crystallites formed from ethanol post-calcination.

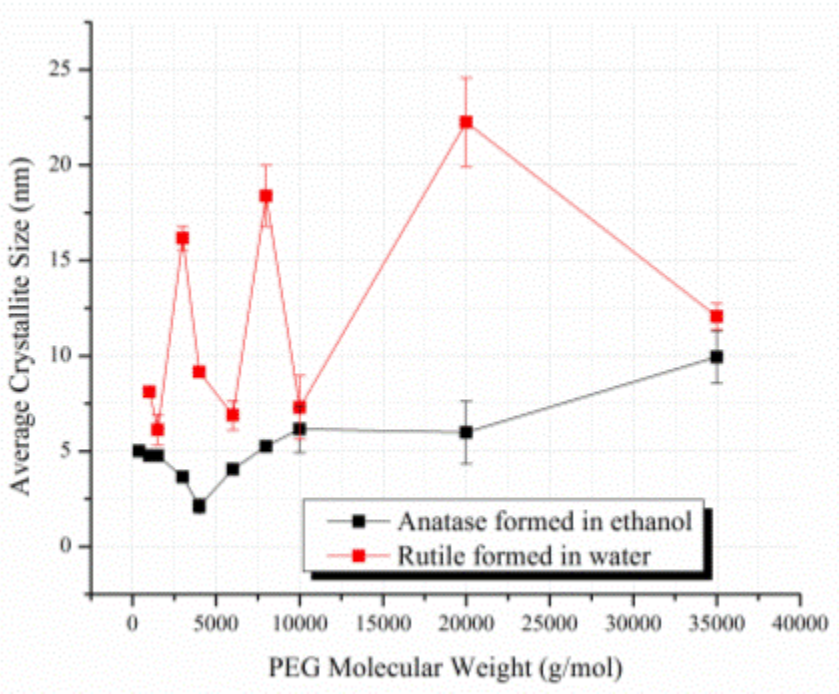

Figure 5.27: Anatase and rutile crystallite size formed in ethanol and water containing HNO_3 respectively, as a function of increasing PEG molecular weight pre-calcination.

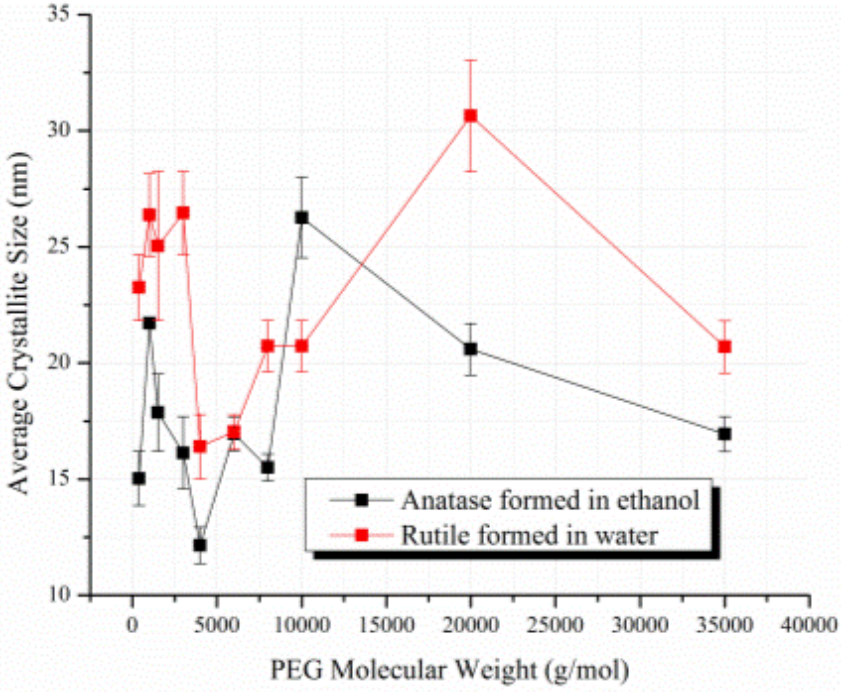

Figure 5.28: Anatase and rutile crystallite size formed in ethanol and water containing HNO_3 respectively, as a function of increasing PEG molecular weight post-calcination.

5.2 Conclusions

The use of ethanol as a solvent in the resin-gel synthesis of titanium dioxide produced anatase exclusively for PEG with molecular weights 200 – 20000 g/mol. Anatase was the major phase formed when PEG 35000 was used. Associated anatase crystallite size decreased and then increased as a function of increasing PEG molecular weight. With good reproducibility, small anatase crystallites were formed in all samples. The largest anatase crystallites measured ~ 10 nm and were obtained from the sample containing the polymer that produced a mixture of polymorphs (i.e.: PEG 35000). TEM analysis of anatase crystallites revealed them to have well-defined geometric shapes.

Rutile was the preferred phase formed from the resin-gel synthesis using water containing HNO_3 as a solvent. Unlike for the samples synthesised using ethanol, PEG molecular weight influenced the amount of rutile formed using water containing HNO_3. The amount of rutile formed displayed an inversely proportional relationship with the respective rutile crystallite size as a function of increasing PEG molecular weight. This trend was rationalised using oriented attachment and the formation of polymer reaction chambers during sample ignition. Rutile crystallites formed from

water containing HNO_3 were larger than anatase crystallites formed from ethanol before calcination. TEM analysis revealed that rutile existed as nanorods aligned radially outward from a common set of points forming rutile superstructures.

Anatase and rutile crystallites were larger in samples containing a mixture of both polymorphs compared with phase pure samples. This effect was explained by considering that phase transformation encouraged crystallite growth.

Calcination of all samples had a greater effect on crystallite size than on the amount of either phase present in the sample. Upon calcination, the amount of anatase decreased slightly corresponding to a slight increase in the amount of rutile per sample. This was due to a calcination temperature of 500 °C that was insufficient to cause major phase change but enough to cause sintering.

All data showed good precision. The largest errors originated from samples synthesised using PEG 35000, indicating that longer chain polymers produced more erratic data.

Titania phase dependency on the solvent used and PEG chain length was rationalised using a model created by considering the interactions between the solvent, polymer and heating of the resin: metal ion hydroxylated complexes form using both water containing HNO_3 and ethanol. The size of the matrix components remaining after the formation of these complexes affords a degree of stabilisation to the nucleated anatase phase. Larger matrix components (generated from ethanol) stabilise anatase better than smaller matrix components (generated from water containing HNO_3). Additionally, steric limitations imposed by ethanol limit the degree of hydrogen bonding between the polymer chains and solvent. Since fewer hydrogen bonds form using ethanol, PEG chains are not as stabilised as they are in water containing HNO_3. A stabilised polymer is less likely to conform to changing conditions during heating and ignition. Therefore, since anatase is less stabilised by the polymer in water, rutile is expected to nucleate. Finally, reaction chambers of various sizes form during heating and ignition. Smaller chambers stabilise anatase, compared with larger chambers that promote rutile formation. Steric effects from ethanol invalidate the effects of larger chambers, and hence favour the formation of anatase. This proposed mechanism is illustrated in figure 5.29.

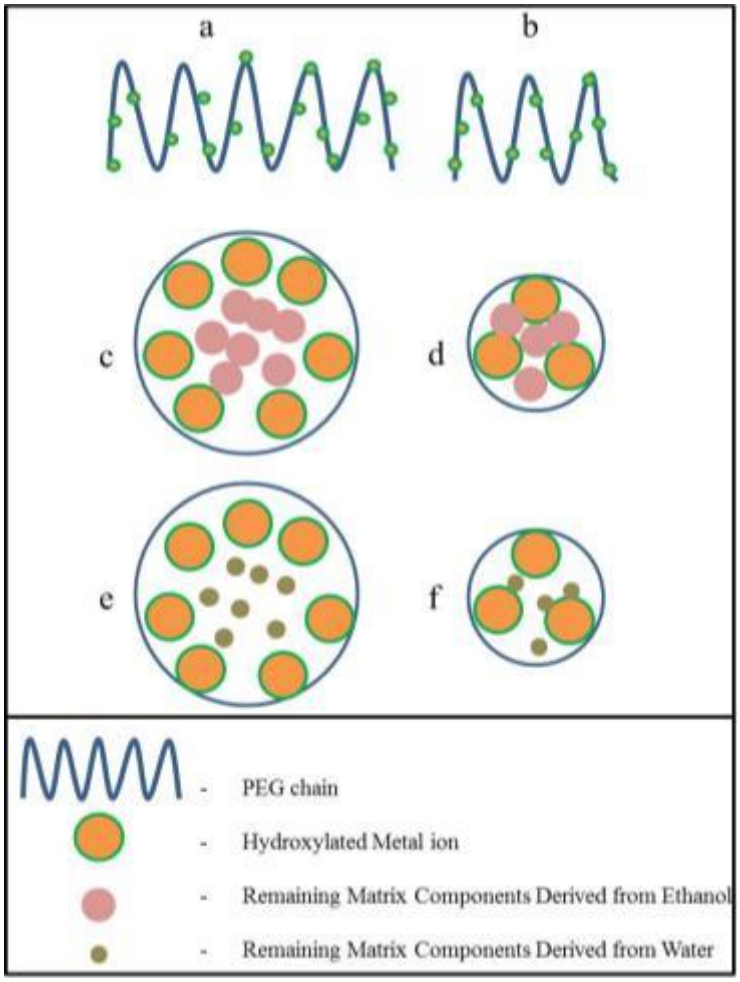

Figure 5.29: Proposed mechanism reflecting effects of polymer chain length and remaining matrix components. (a) Longer and (b) shorter polymer fragments with associated hydroxylated metal ions form larger (c, e) and smaller (d, f) reaction chambers after scission respectively. Smaller chambers better stabilise and cap the nucleating anatase phase. Larger remaining matrix components (c, d) stabilise the nucleated anatase phase better than smaller remaining matrix components (e, f).

5.3 References

1. Dziike Mutambara, F. Resin-gel synthesis and characterisation of copper and titanium mixed metal oxides nanoparticles. (University of the Witwatersrand, 2014).

2. Spurr, R. A. & Myers, H. Quantitative Analysis of Anatase-Rutile Mixtures with an X-Ray Diffractometer. *Analytical Chemistry* **29,** 760 – 762 (1957).

3. Gribb, A. A. & Banfield, J. F. Particle size effects on transformation kinetics and phase stability in nanocrystalline TiO2. *American Mineralogist* **82,** 717 – 728 (1997).

4. Ding, X. & Liu, X. Correlation between anatase-to-rutile transformation and grain growth in nanocrystalline titania powders. *Journal of Materials Research* **13,** 2556 – 2559 (1998).

5. Banfield, J. F., Bischoff, B. L. & Anderson, M. A. TiO2 accessory minerals: coarsening, and transformation kinetics in pure and doped synthetic nanocrystalline materials. *Chemical Geology* **110,** 211 – 231 (1993).

6. Penn, R. L. & Banfield, J. F. Oriented attachment and growth, twinning, polytypism, and formation of metastable phases: Insights from nanocrystalline TiO2. *American Mineralogist* **83,** 1077 – 1082 (1998).

7. Zhang, H. & Banfield, J. F. Understanding Polymorphic Phase Transformation Behavior during Growth of Nanocrystalline Aggregates: Insights from TiO2. *Journal of Physical Chemistry B* **104,** 3481 – 3487 (2000).

8. Rogers, R. D., Zhang, J. & Bauer, C. B. The effects of choice of anion (X=Cl-, SCN-, NO-) and polyethylene glycol (PEG) chain length on the local and supramolecular structures of LnX, /PEG complexes. *Journal of Alloys and Compounds* **249,** 41 – 48 (1997).

9. *CRC Handbook of Chemistry and Physics*. (CRC Press, Boca Raton, FL, 2005).

10. Zhang, H. & Banfield, J. F. Thermodynamic analysis of phase stability of nanocrystalline titania. *Journal of Materials Chemistry* **8,** 2073 – 2076 (1998).

Chapter 6: Effects of an Enhanced Heating Rate on Titania Polymorph and Crystallite Size Formation

Following on from chapter 5, the primary aim of this experiment was to investigate the effects of an enhanced heating rate on the phase purity and associated crystallite size of anatase and rutile. The synthesis was performed in ethanol and water containing HNO_3 solvents and a range of different PEG molecular weights, as described previously. In addition to heating samples from below, in this experiment, samples were subjected to a heat source from above. This was done to observe the effects of faster polymer degradation on titania nanoparticles formed in solvents that favoured the formation of different phases. The effects of faster polymer degradation would aid in developing the mechanism of nanoparticle formation using resin-gel synthesis.

6.1 Experimental Procedure

This experiment consisted of 4 parts: ethanol mediated synthesis, water containing HNO_3 mediated synthesis, heat treatments, and characterisation.

6.1.1 Ethanol Mediated Synthesis

Excess (360.0 ml) absolute ethanol was introduced into a beaker. 15.0 ml (0.136 mols) $TiCl_4$ (> 99%, Merck) was added to this beaker. The solution was stirred using a Teflon coated magnetic stirrer bar. Complete solution homogenisation was indicated by the solution taking on an off-white colour. 30 ml of the solution was decanted into 11 separate beakers. A volume equivalent amount of PEG of various molecular weights (200, 400, 1000, 1500, 3000, 6000, 8000, 10000, 12000, 20000, and 35000 g/mol) was added to each of the 11 beakers. Each mixture was heated as appropriate and concurrently stirred using a glass rod to ensure complete homogenisation. Samples containing shorter PEG chains were heated to ~ 45 °C at ~ 620 mm Hg. Longer PEG chain containing samples required higher temperatures to attain homogeneity (~ 60 °C at ~ 620 mm Hg).

6.1.2 Water containing HNO_3 Mediated Synthesis

Excess (360.0 ml) distilled water was introduced into a beaker. 15.0 ml (0.136 mols) $TiCl_4$ (> 99%, Merck) was added to this beaker. 55% HNO_3 (30 ml) was added to the solution to ensure complete dissolution of $TiCl_4$ in water. The solution was stirred using a Teflon coated magnetic stirrer bar until it was homogeneous, indicated by the consistent off-white colour. 30 ml of this solution was introduced into 11 separate beakers. Various molecular weight PEG was added to each beaker as described in section 5.1.1. Samples were heated and stirred to homogeneity as described above.

6.1.3 Heat Treatments

All 22 gels were placed in a fume hood ~ 30 cm under two 200 W incandescent light bulbs for a period of 14 days. This was to ensure complete solvent evaporation from each sample. Following this period, hard, solid resins had formed in samples containing higher PEG molecular weights. Softer, solid resins had formed in samples containing PEG with lower molecular weights. Following solvent evaporation, all samples were divided equally to introduce a replicate for the impending heat treatments.

Resins were introduced into a sand bath as described in chapter 5. The sand bath was heated from below using blue flames fuelled by LPG (Afrox Handigas). Additionally, samples were subjected to the blue flame from a Bunsen burner directed into the crucible until ignition occurred. This heating method caused resins to reach their flash point in approximately 1.5 hours. This is compared with the conventional heating method (chapter 5) that caused the samples to ignite in approximately 4 hours.

Samples presented a black, flaky or granular appearance following the end of pyrolysis. This colour was due to the presence of carbon residue on the samples. Each sample was then divided in half. The first half was to be analysed directly; the second half was to be calcined in a muffle furnace at 500 °C for 1 hour and then analysed. Performing the analysis in this manner would allow for the observation of the effects of calcination on the formed crystallites.

6.1.4 Characterisation

PXRD analysis was performed using a Siemens D5000 diffractometer and Cu Kα radiation. Samples were analysed between 20° and 50° 2θ in increments of 0.04 counting for 5 seconds per step. Longer count times were necessary to produce data of similar quality as that obtained using the D2 in chapter 5. Scan times were 36 minutes

per sample compared with 10 minutes per sample using the D2 in chapter 5. This diffractometer possessed a forty-position sample changer containing flat-plate, shallow-well sample holders. Due to the lack of compatible zero-background sample holders, the present sample holders had to be completely filled with sample and then adjusted to a uniform sample height. TEM analysis was achieved using the FEI Tecnai T12.

6.2 Results and Discussion

Samples have been designated throughout this chapter using the following notation: PEG *n* + Solvent (where '*n*' represents the molecular weight of the polymer and 'solvent' represents either water containing HNO_3 (H_2O) or ethanol (EtOH) that was used to generate the sample). A (2) at the end of the notation indicates the replicate sample and an 'O' preceding PEG indicates a calcined sample. Not all comparative graphs will be shown. This section shall focus on the data reflecting the effects of an enhanced heating rate.

6.2.1 Ethanol Mediated Synthesis

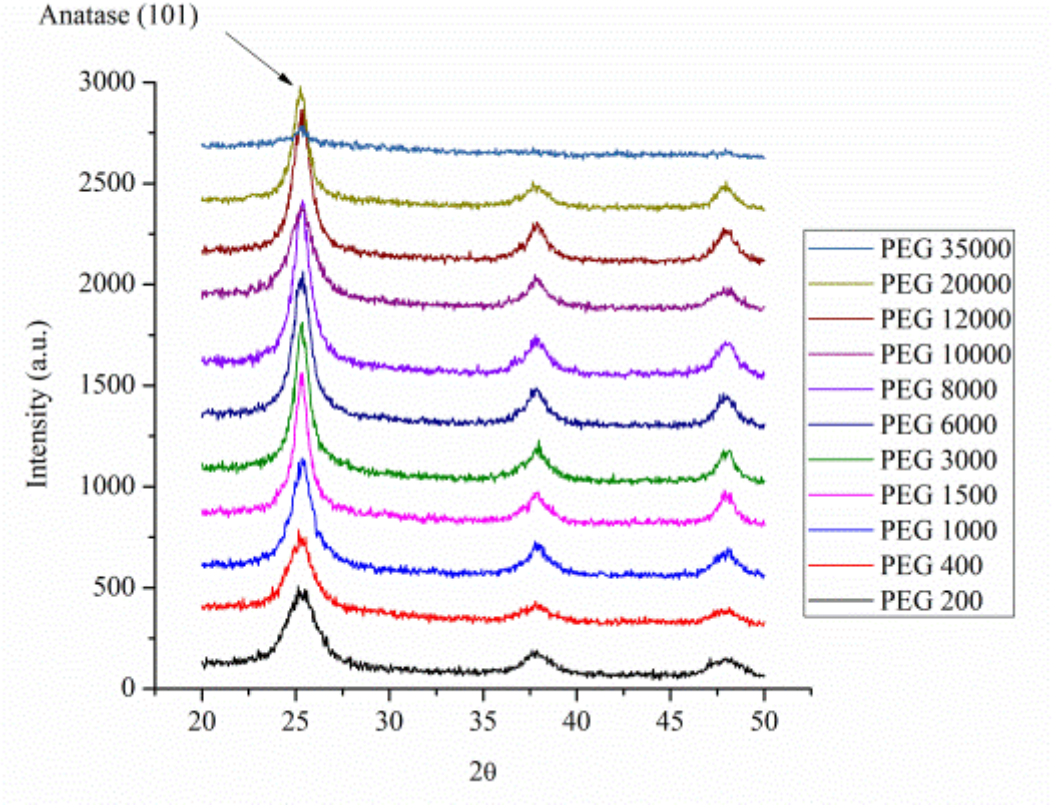

Figure 6.1: PXRD patterns of samples synthesised using ethanol pre-calcination.

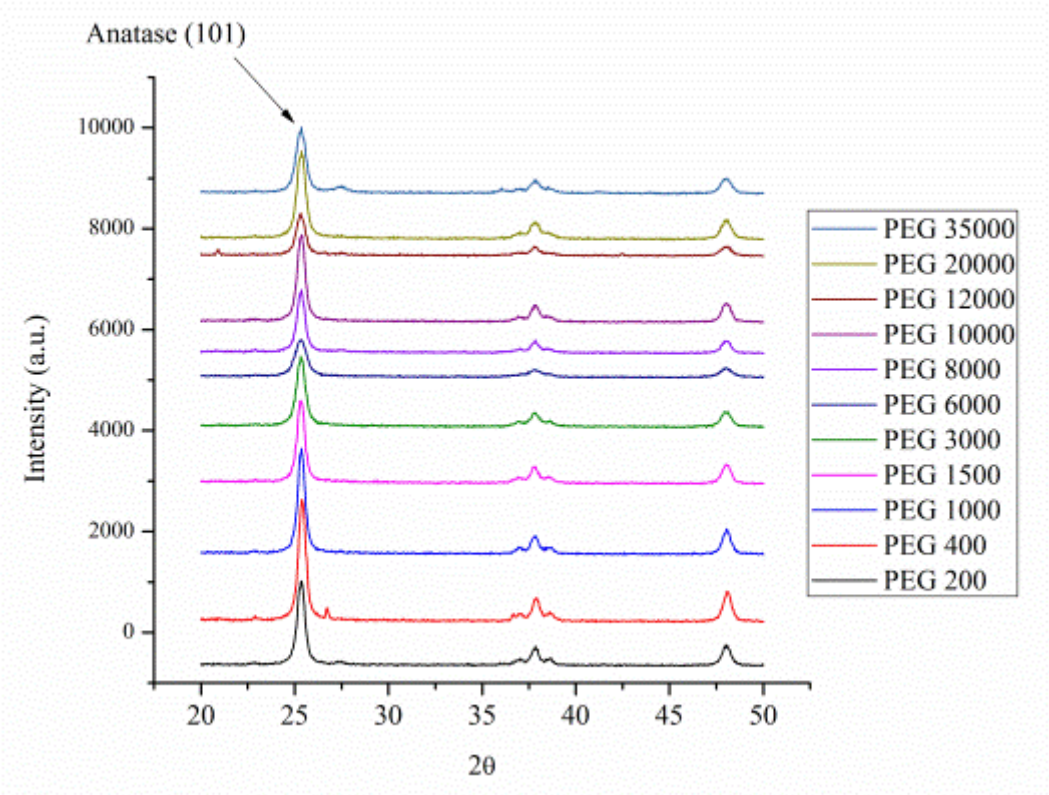

Figure 6.2: PXRD patterns of samples synthesised using ethanol post-calcination.

Figures 6.1 and 6.2 give the PXRD patterns of samples synthesised using ethanol at an enhanced heating rate, before and after calcination. Both figures show the exclusive formation of anatase indicating that calcination did not result in phase transformation. The anatase (1 0 1) peaks in figure 6.1 are broad suggesting the formation of anatase nanoparticles from ethanol. The PXRD pattern corresponding to PEG 35000 reflects a poor signal to noise ratio, as seen in figure 6.1. During synthesis, this sample (and replicate sample) did not go through a viscous, waxy intermediate before ignition. Rather, these samples ignited as a solid resin. The difference in ignition pattern may account for the poor signal to noise ratio. Peaks appear to be slightly misaligned in figure 6.1. This suggests that the carbon residue on the samples impacted non-uniform strain on the lattice as described for samples synthesised using the conventional heating method in chapter 5.

In figure 6.2, the anatase (1 0 1) peak had become narrower indicating crystallite growth as a result of sintering. Peak alignment after removal of residual carbon is proof of the effect of non-uniform strain on the titania lattice imparted by carbon. The sample OPEG 35000 + EtOH has a better signal to noise ratio post-calcination. Given

the different ignition pathway undertaken by this sample, the better signal to noise ratio post-calcination implies that incomplete synthesis had occurred post-ignition. Fragments of unignited PEG were likely present in the sample before calcination. Calcination had the effect of completing the sample synthesis by removing all PEG traces. A small rutile (1 1 0) peak is observed in the sample OPEG 35000 + EtOH. This is consistent with the findings obtained using a conventional heating method as described in chapter 5.

No samples were synthesised from PEG 4000 in this data set. Given the similarities in the data obtained for samples synthesised in ethanol using either conventional or enhanced heating rates, the effects of PEG 4000 on the formed crystallites are likely the same under both heating conditions.

The replicate PXRD patterns obtained before and after calcination are not included for brevity. Figures 6.3 and 6.4 illustrate the precision in the data from samples and their respective replicates.

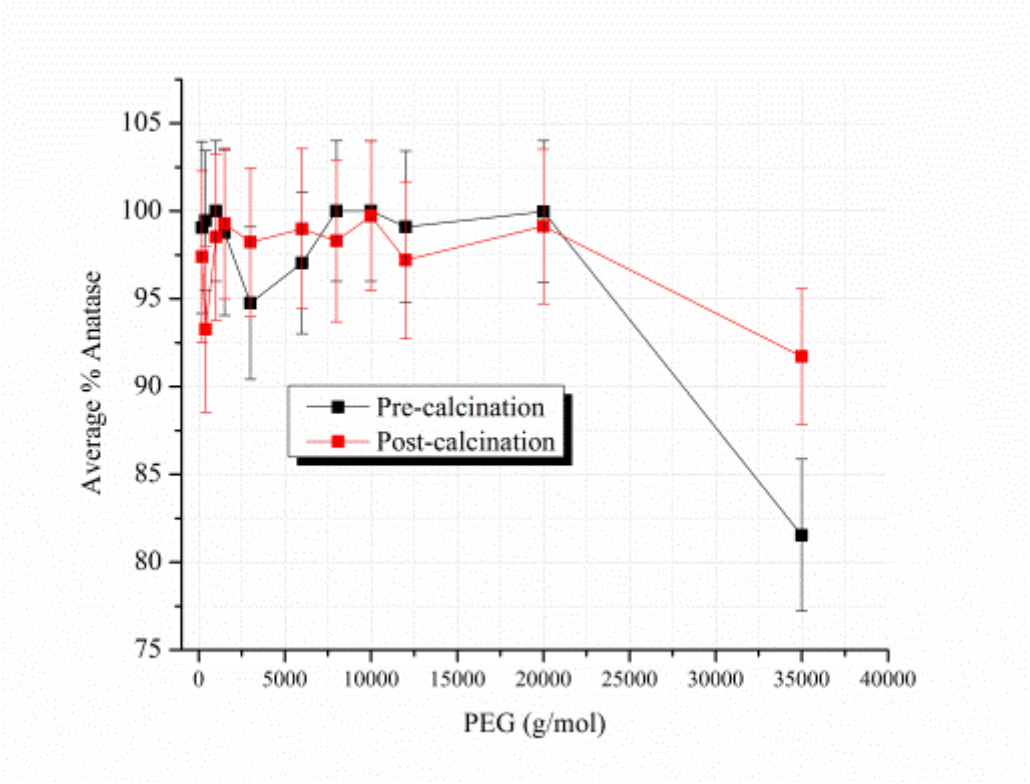

Figure 6.3: Average amount of anatase formed in ethanol pre- and post-calcination.

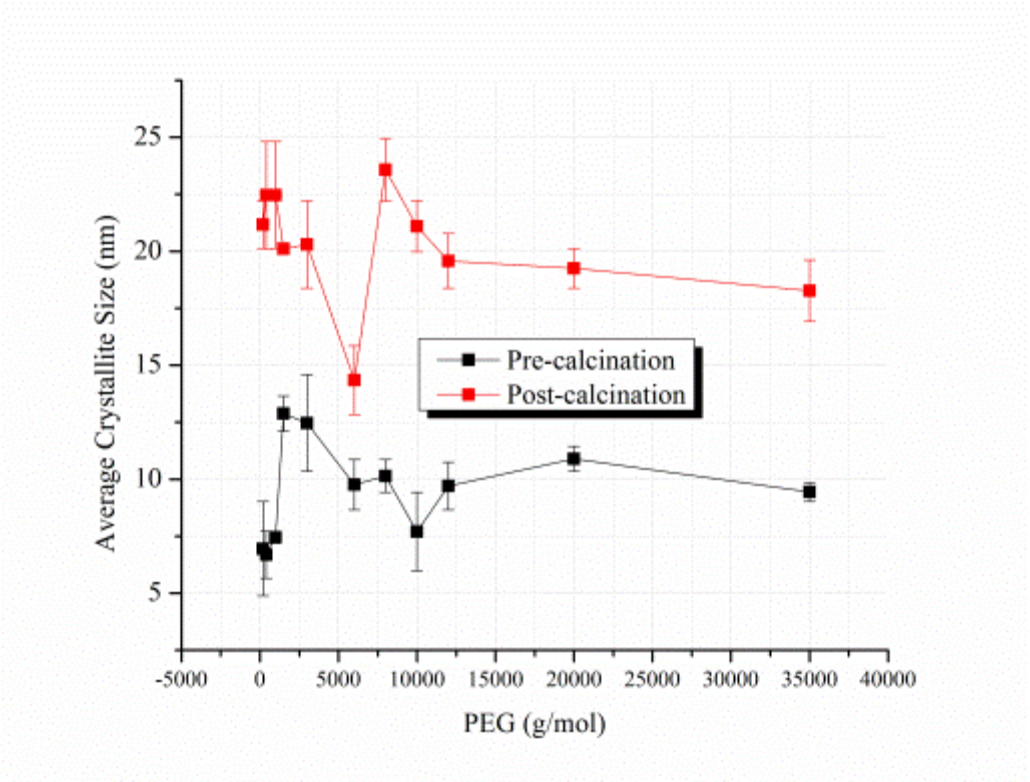

Figure 6.4: Average anatase crystallite size formed in ethanol pre- and post-calcination.

Figure 6.3 shows the average amount of anatase formed in ethanol pre- and post-calcination using an enhanced heating rate. Before calcination, anatase was the preferred phase formed in ethanol across most PEG molecular weights. PEG 3000, 6000, and 35000 produced the least amount of anatase at 94.8%, 97.1% and 81.5% respectively. The results obtained from PEG 3000 are surprising given the trend observed from the other PEG molecular weights. The data reflects good precision as the largest error was 4.9%. Error bars were obtained by adding the standard deviation of the amount of anatase formed in the replicate analyses to 4% of the average amount of anatase formed.

The effects of calcination were interesting. A small decrease in the amount of anatase formed was observed for samples that contained ~ 100% anatase before calcination. Samples synthesised from PEG 3000, 6000, and 35000 displayed an increase in the amount of anatase formed after calcination. This observation suggests that calcination converted amorphous titania that was present in the sample, into anatase. A likely cause for this behaviour was the presence of PEG fragments that were not fully removed during pyrolysis. Enhanced heating rapidly heated the polymer that was

directly exposed to the flame, shielded the polymer in the middle of the sample and caused a temperature gradient within the sample. These fragments likely entangled with the nucleating anatase crystals, inhibited the nucleation process and forced the formation of amorphous titania. Calcination at 500 °C completely removed all polymer fragments and transformed amorphous titania into anatase. This explanation is more plausible for PEG 35000 + EtOH as it contained a long chain polymer and the PXRD pattern displayed a poor signal to noise ratio. It is unknown why this behaviour was exhibited in shorter chain PEG 3000 and 6000, and not in PEG 8000, 10000, 120000, and 20000.

Figure 6.4 shows the average anatase crystallite size of samples synthesised in ethanol pre- and post-calcination. Before calcination, similar PEG molecular weights produced similar anatase crystallite sizes. PEG 1500 and 3000 resulted in the formation of the largest anatase crystallites: 12.9 and 12.5 nm respectively. This is in contrast to PEG 200 and 400 that produced the smallest anatase crystallites: 6.9 and 6.7 nm respectively. Error bars were generated from the standard deviation of the replicate analyses. After calcination, average anatase crystallite size increased for all samples. Crystallite size increase was not consistent across the range of samples.

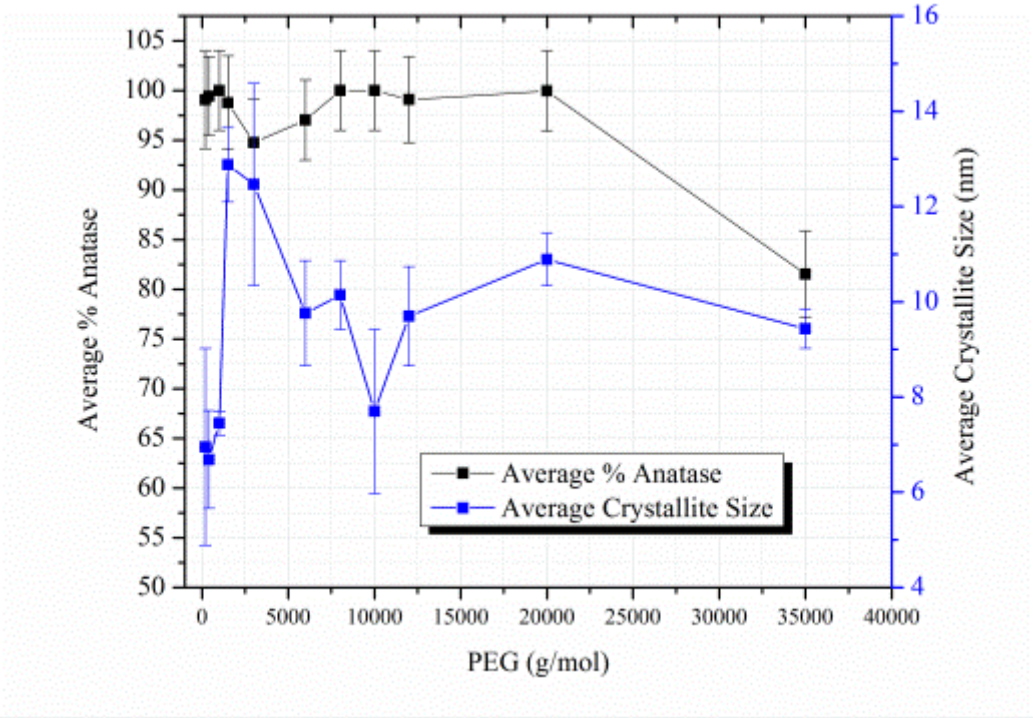

Figure 6.5: Average amount of anatase with associated crystallite size formed from ethanol pre-calcination.

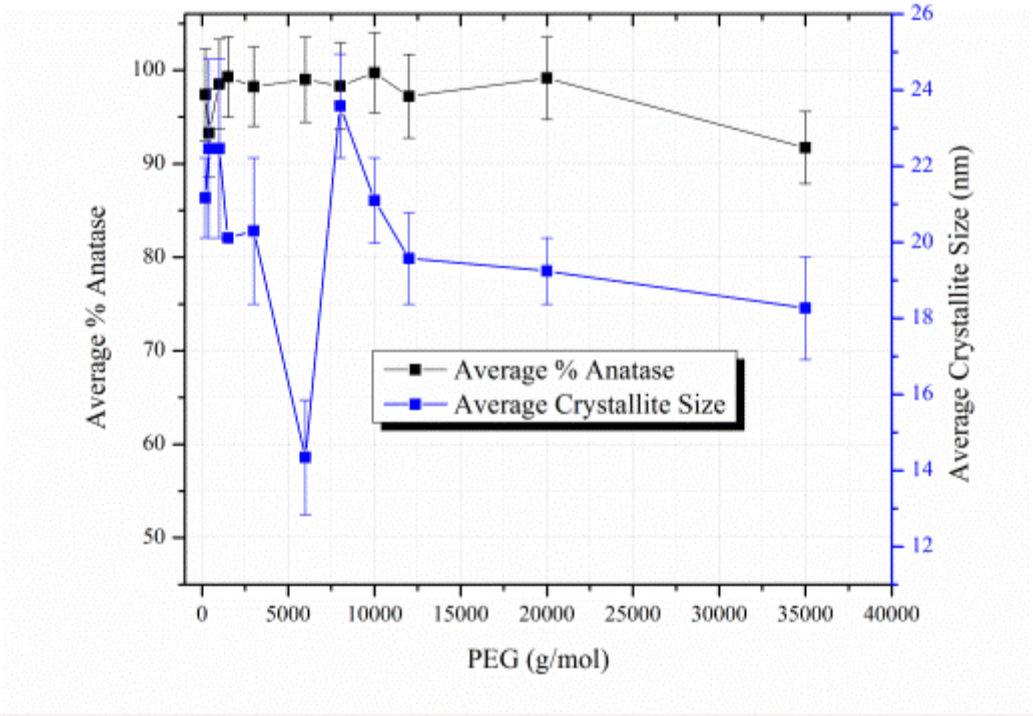

Figure 6.6: Average amount of anatase with associated crystallite size formed from ethanol post-calcination.

Figure 6.5 shows no obvious trends relating the amount and associated crystallite size of anatase formed. Given that PEG 35000 produced the least amount of anatase (and by extension the most amount of rutile) of all the PEG molecular weights, it is surprising that this polymer was not responsible for the formation of the largest anatase crystallites. As explained in chapter 5, the anatase to rutile phase transformation encourages crystallite growth.

Comparing the data obtained in figure 6.6, calcination had a greater effect on anatase crystallite size than on phase transformation. The decrease in the amount of anatase formed post-calcination is negligible across the range of samples. This is in contrast to anatase crystallite size that increased by 112.6% across the range of samples. The explanation for this behaviour is that 500 °C is not sufficiently hot enough to encourage a significant amount of anatase to rutile transformation. It is enough however, to cause sintering between crystallites[1].

Tables showing the amount of each phase and crystallite size obtained for each sample with averages and errors are given in appendix D.

A TEM image for the sample PEG 8000 + EtOH under enhanced heating conditions is given in figure 6.7. This sample formed phase pure anatase (1 0 1) with crystallites

measuring in the range of 9 – 11 nm. One-dimensional lattice fringes are visible on some crystallites. TEM analysis was also performed on the calcined version of the same sample and is represented by figure 6.8.

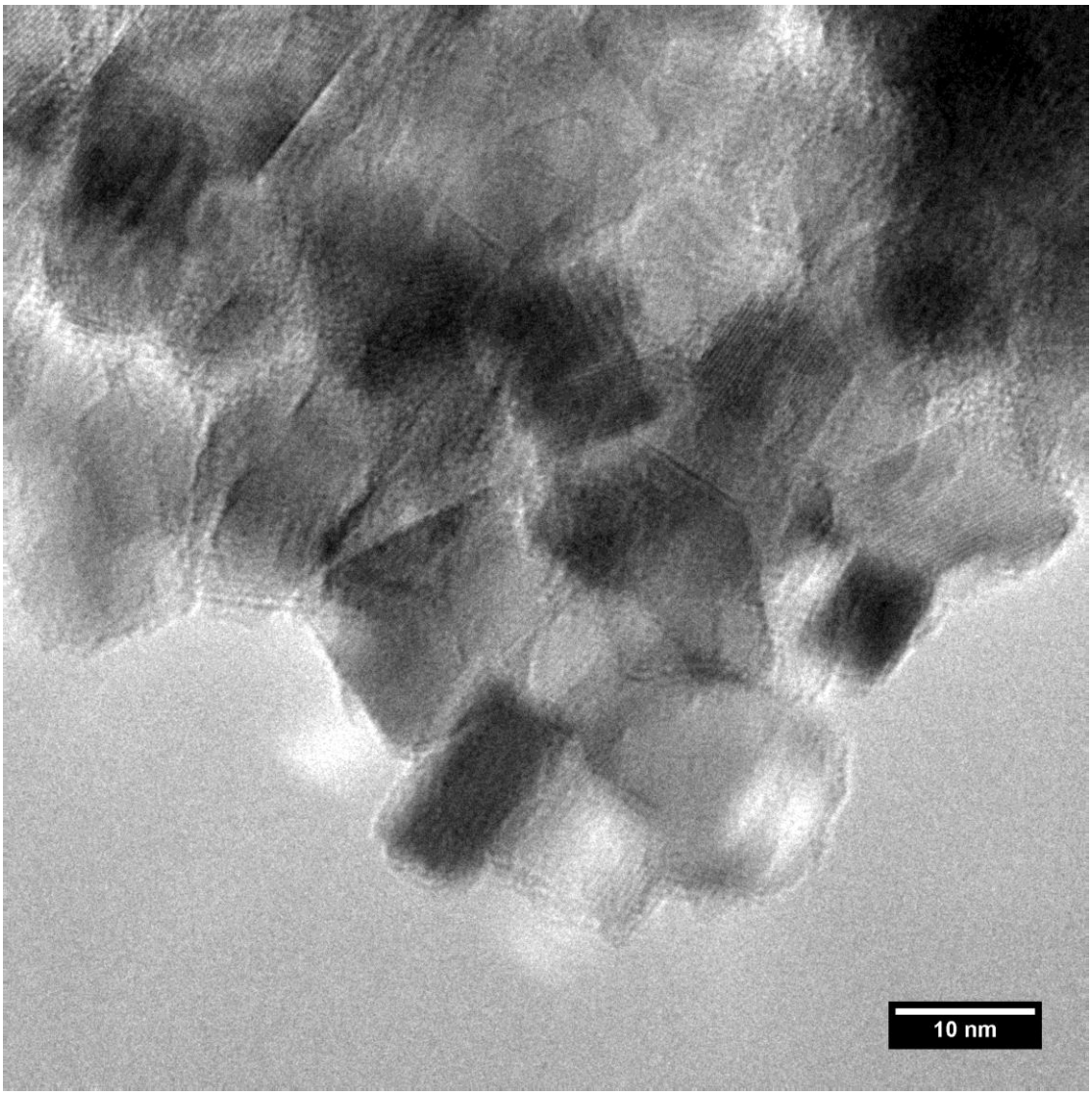

Figure 6.7: Well defined, seemingly elongated cubic anatase crystallites exhibited by PEG 8000 + EtOH under enhanced heating conditions.

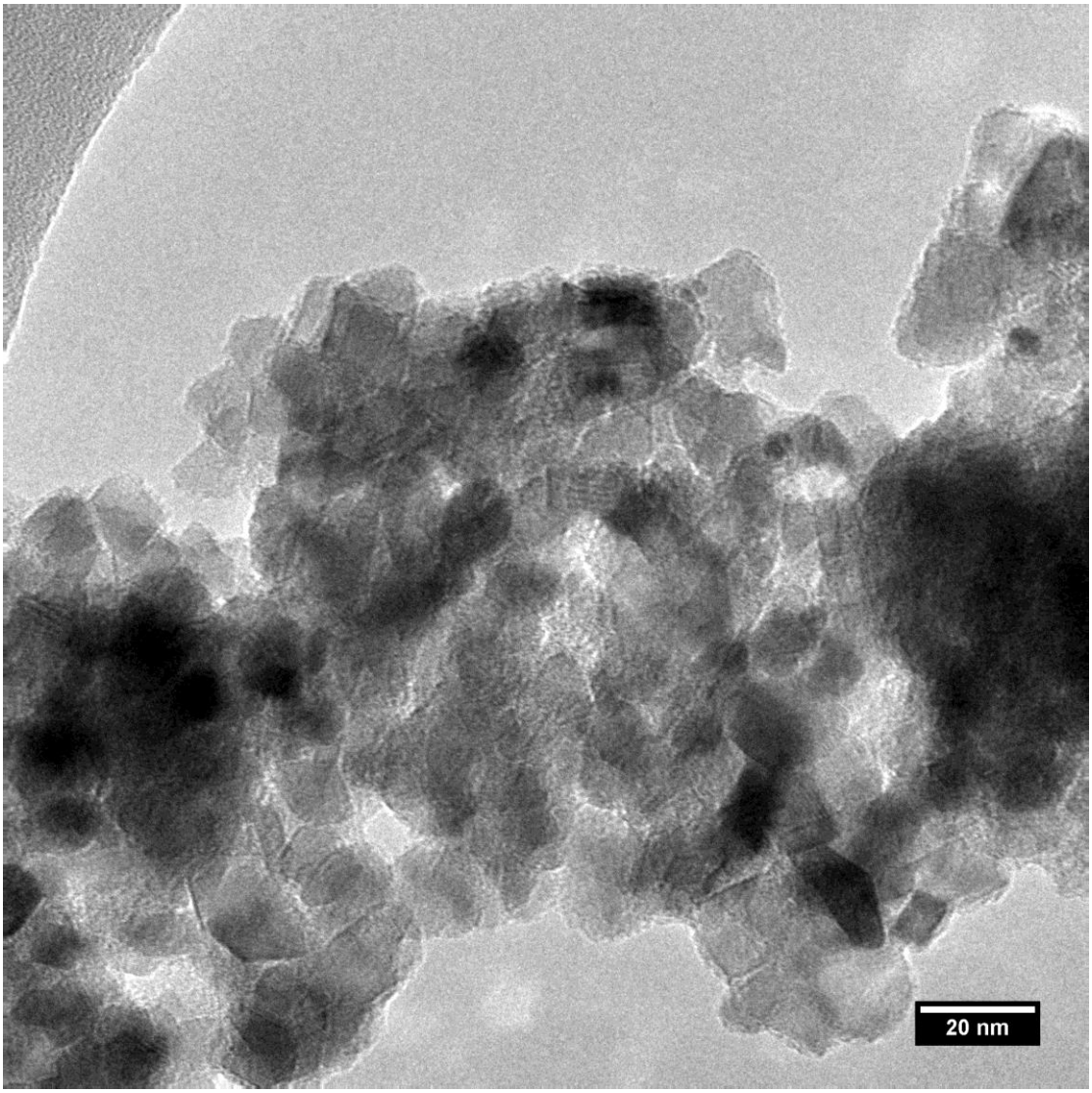

Figure 6.8: (PEG 8000 + EtOH post-calcination). Anatase is visible with a degree of agglomeration in some parts of the sample. Calcination caused particle sintering.

6.2.2 Conventional and Forced Heating using an Ethanol Solvent

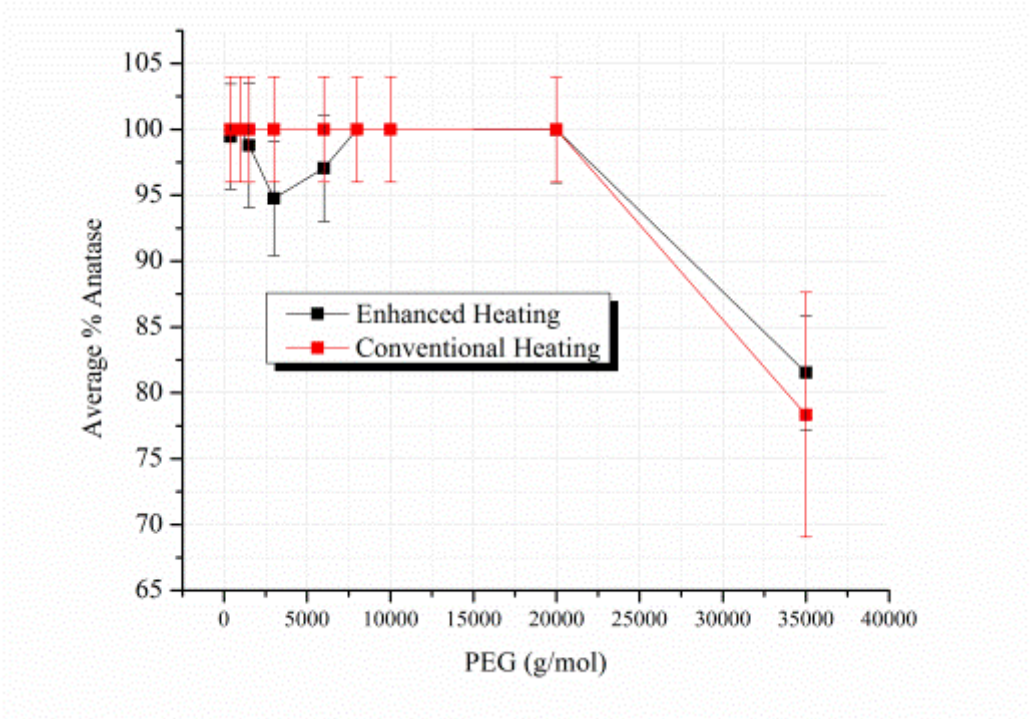

Figure 6.9: Comparison of average amount of anatase formed in ethanol under conventional and enhanced heating methods.

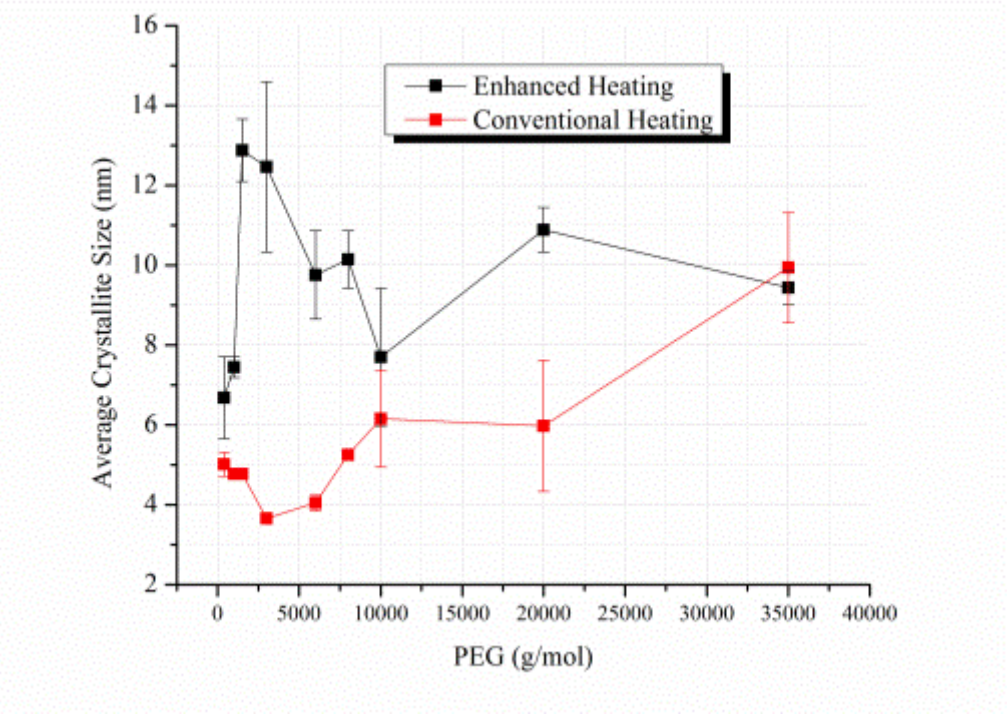

Figure 6.10: Comparison of average anatase crystallite size formed in ethanol under conventional and enhanced heating methods.

Figure 6.9 compares the amount of anatase formed from ethanol using two different heating methods. Conventional heating data was obtained from the synthesis using ethanol pre-calcination in chapter 5. The data suggests that anatase is the preferred phase formed in ethanol regardless of the heating method employed in the synthesis. Samples synthesised from PEG 3000 and 6000 using the enhanced heating method deviates from the samples synthesised using the same PEG molecular weight under conventional heating conditions. This deviation is slight and the error bars suggest that the amount of anatase formed from these PEG molecular weights could be closer to 100%. Similar amounts of anatase were formed in samples synthesised from PEG 35000 using both heating methods (81.5% anatase formed using enhanced heating and 78.3% anatase formed using conventional heating). This result suggests that the transformation of anatase to rutile in samples synthesised using ethanol is not affected by the heating method. Ethanol had a greater impact than heating rates on phase purity when low molecular weight PEG was employed in the reaction. Phase purity was dependent on PEG molecular weight when long chain PEG was employed in the synthesis.

Figure 6.10 compares the average anatase crystallite size obtained for samples synthesised in ethanol using the conventional and enhanced heating rate methods, pre-calcination. The data for conventional heating was obtained from samples synthesised using ethanol in chapter 5. Excluding the samples synthesised using PEG 35000, average anatase crystallite size was larger using the enhanced heating method. This is an expected result. Higher synthesis temperatures provide the reaction system with sufficient energy to favour the formation of larger crystallites. This is due to larger crystallites being more thermodynamically favoured – since they possess a lower volume potential – than smaller crystallites[2].

The largest anatase crystallites formed using an enhanced heating rate were smaller than 14 nm. Zhang and Banfield[3] proved through experimental and theoretical analysis that anatase is more stable than rutile for crystallites smaller than 14 nm. Comparing the data obtained using an enhanced heating rate in figures 6.10 and 6.11, PEG 1500 and 3000 formed less than 100% anatase and the largest crystallites. This result can be explained in the following way: during enhanced heating, anatase crystallites are encouraged to grow. Once they reach a threshold value (< 14 nm), anatase crystallites undergo oriented attachment and nucleate rutile. The combination

of enhanced heating and PEG 1500 and 3000 probably caused the formation of a polymer reaction chamber that was sufficiently large to encourage the nucleation of rutile.

Figure 6.10 shows a near inverse relationship between the anatase crystallite sizes formed using the two different heating methods as a function of increasing PEG molecular weight. Data representing enhanced heating is not as precise as that obtained for conventional heating. The near inverse trend is still valid despite the discrepancy in precision.

Similar sized anatase crystallites were obtained from samples synthesised using PEG 35000 under both heating conditions. This is an interesting result as PEG 35000 was also responsible for producing the most amount of rutile using either heating method. As explained in chapter 5, phase transformation catalyses crystallite growth[4]. Given the similarity in data, the mechanism governing the result should be the same for samples synthesised using either heating condition. In keeping with the presiding mechanism of the formation of polymer reaction chambers, it is possible that PEG 35000 undergoes polymer entanglement. Scission at different points along the chain cause the formation of reaction chambers, the size of which is not sufficiently small to stabilise the anatase phase. Therefore, phase transformation occurs. Enhanced heating does not seem to have an effect on this process when the synthesis is performed in ethanol.

6.2.3 Water containing HNO_3 Mediated Synthesis

PXRD patterns collected from titania samples synthesised in water containing HNO_3 using an enhanced heating rate before calcination are given in figure 6.11. The patterns show that anatase was the favoured phase when low molecular weight PEG (200 – 1500 g/mol) was employed in the synthesis. Medium molecular weight PEG (3000 – 8000 g/mol) was responsible for the formation of a mixture of anatase and rutile. High molecular weight PEG (10000 – 35000 g/mol) favoured the formation of rutile. Broad peaks are an indication of the formation of nanoparticles. The patterns are slightly misaligned.

Figure 6.12 shows that PXRD patterns of the titania samples synthesised in water containing HNO_3 at an enhanced heating rate after calcination. There appears to be no change in the preference of formed phase by various PEG molecular weights. Narrower peaks indicate that the calcination process caused coarsening of anatase and

rutile crystallites. Peak alignment implies that carbon present on the samples pre-calcination placed non-uniform strain on the lattice and was subsequently removed during calcination.

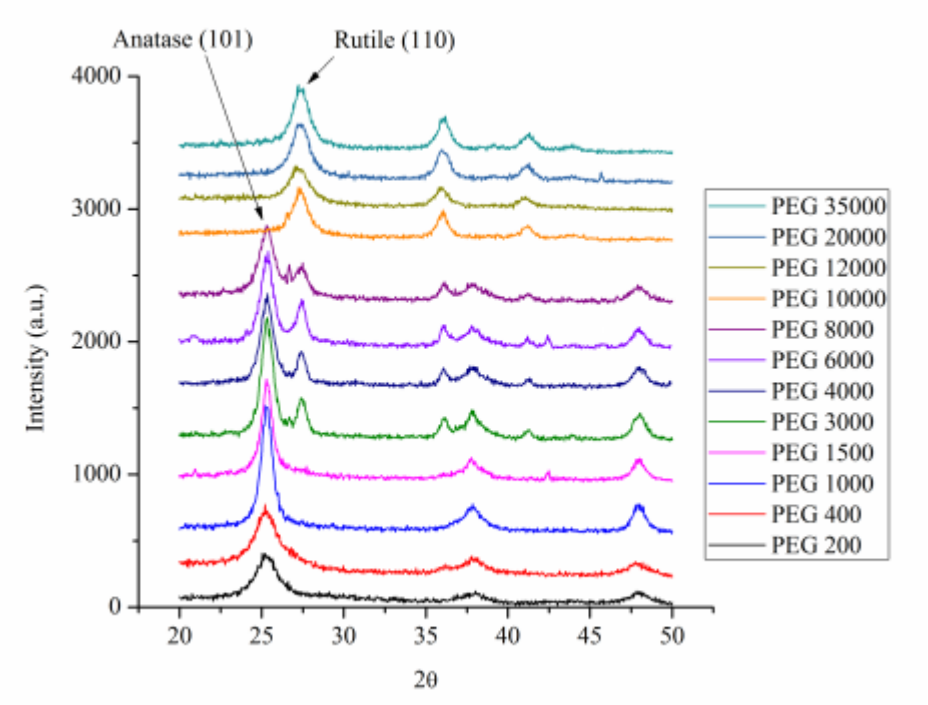

Figure 6.11: PXRD patterns of samples synthesised using water containing HNO_3 pre-calcination.

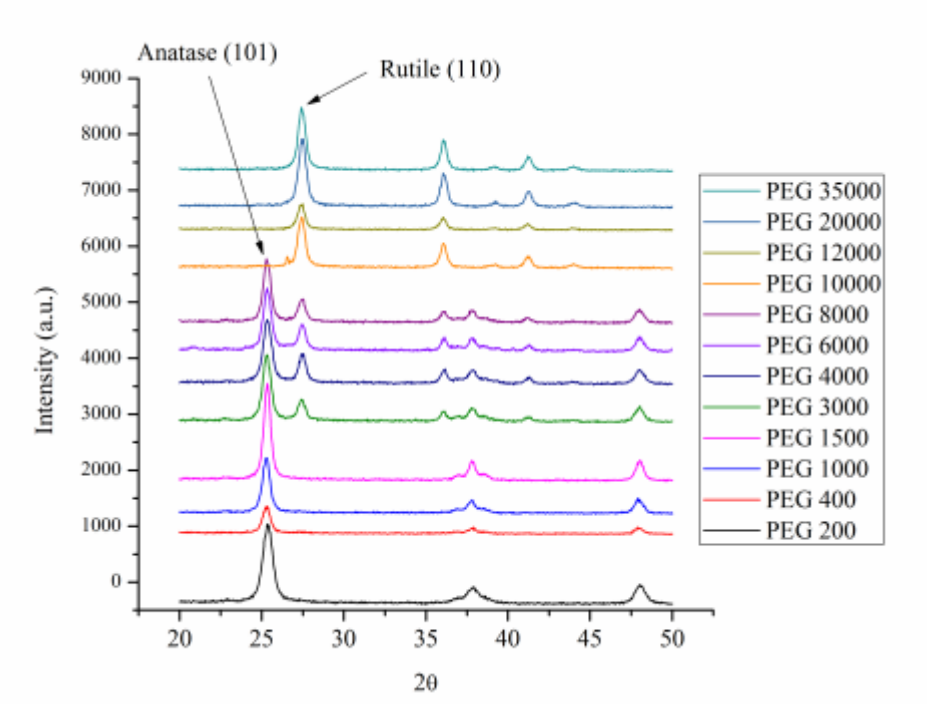

Figure 6.12: PXRD patterns of samples synthesised using ethanol post-calcination.

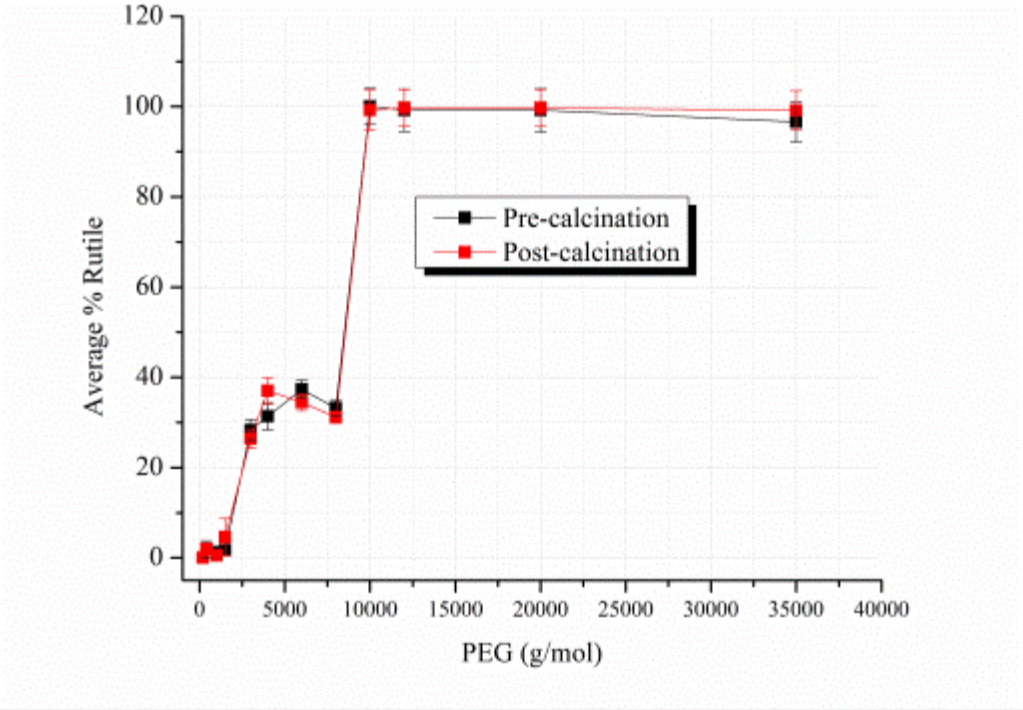

Figure 6.13: Average amount of rutile formed in water containing HNO_3 pre- and post-calcination.

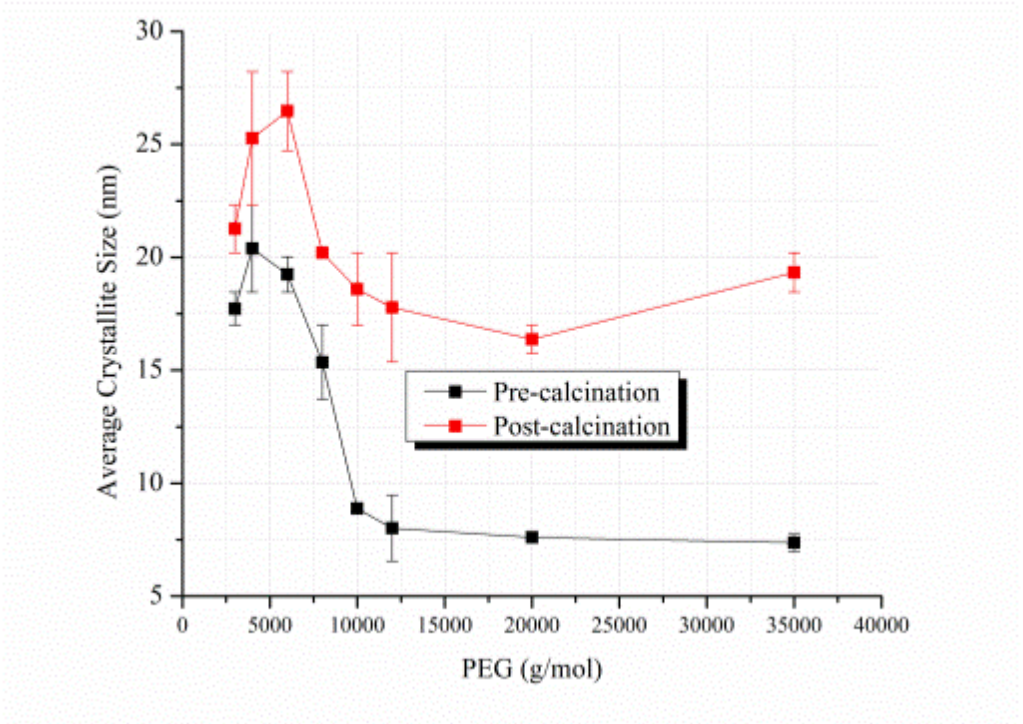

Figure 6.14: Average rutile crystallite size formed in water containing HNO_3 pre- and post-calcination.

The average amount of rutile formed in water containing HNO_3 pre- and post-calcination is given in figure 6.13. The amount of rutile formed in water containing HNO_3 using the enhanced heating method is clearly dependent on the PEG molecular weight used in the synthesis. Low molecular weight PEG (200 – 1500 g/mol) produced an average of 1.2% rutile. Medium molecular weight PEG (3000 – 8000 g/mol) produced an average of 32.6% rutile. High molecular weight PEG (10000 – 35000 g/mol) produced an average of 99.5% rutile. The data reflects good precision. Error bars were obtained by summing the standard deviation of the replicate analyses with 4% of the average amount of rutile formed. As expected, the amount of rutile did not change appreciably post-calcination. The average amount of rutile formed post-calcination increased by 0.7%.

Figure 6.14 contains the average rutile crystallite size formed in water containing HNO_3 using the enhanced heating method. The figure reflects crystallite size data from PEG molecular weights that produced a significant amount of rutile (i.e.: > PEG 3000). Before calcination, the size of rutile crystallites increased, decreased and then stabilised as a function of increasing PEG molecular weight. Lower PEG molecular weights were responsible for the formation of the largest rutile crystallites. Calcination had a dramatic effect on the size of rutile crystallites. Before calcination the average rutile crystallite size across the range of PEG molecular weights was 13.1 nm. Calcination caused a 53.4% increase in the average size of rutile crystallites across the range of PEG molecular weights. This was an expected result. Rutile crystallite size data was more erratic post-calcination. Aside from the sample synthesised using PEG 35000, average crystallite size increased proportionally after calcination. The errors bars in figure 6.14 represent the standard deviation of the replicate analyses.

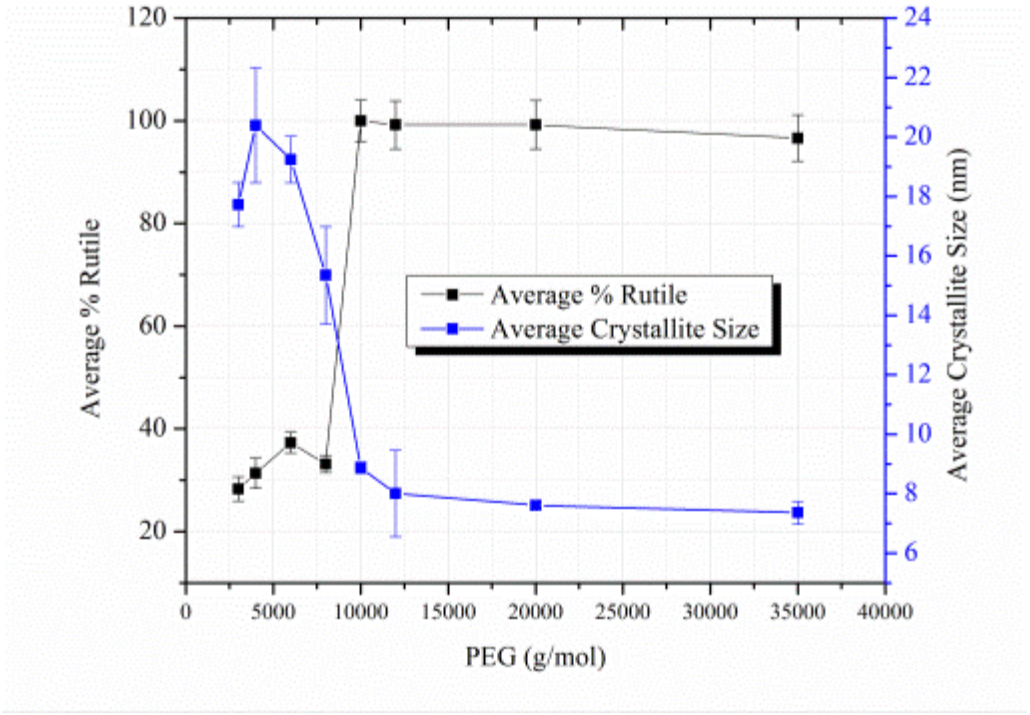

Figure 6.15: Average amount of rutile with associated average crystallite size formed in water containing HNO_3 pre-calcination.

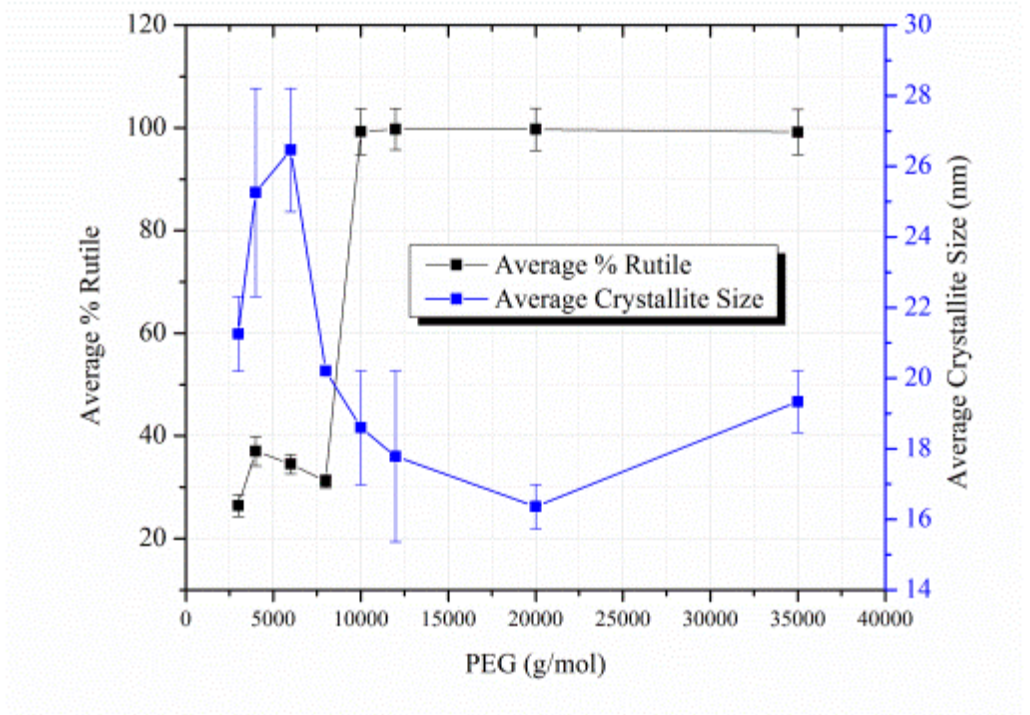

Figure 6.16: Average amount of rutile with associated average crystallite size formed in water containing HNO_3 post-calcination.

An interesting relationship between the amount of rutile and associated crystallite size formed in water containing HNO_3 using an enhanced heating rate, before calcination, is represented in figure 6.16. The amount of rutile formed is inversely proportional to the size of rutile crystallites per sample as a function of increasing PEG molecular weight. The precision in the data is sufficient to suggest that this is a real, reproducible relationship. This relationship was also observed for samples synthesised in water containing HNO_3 using a conventional heating rate. A similar relationship was observed for the amount and size of brookite crystallites formed as a function of reaction time[5]. This relationship was rationalised in terms of the polymer stabilising nucleated anatase crystallites, inhibiting transformation into rutile. Any nucleated rutile coarsened by consuming material from the reaction matrix. This rationalisation is warranted by the size of rutile crystallites being directly proportional to the amount of anatase present in the sample.

Figure 6.16 shows that the relationship between the amount and size of rutile crystallites formed in water containing HNO_3 using enhanced heating is maintained post-calcination. This is mainly due to a near proportional increase in rutile crystallite size post-calcination. Crystallites from the sample synthesised using PEG 35000 + H_2O increased disproportionately in size after calcination.

Comparing figures 6.15 and 6.16, it is clear that calcination had a greater effect on crystallite size than on the amount of rutile transformed. This is an expected result as discussed previously.

Not represented in figures 6.15 and 6.16 is the average anatase crystallite size formed from samples containing PEG that favoured anatase formation in water containing HNO_3, pre-calcination. This data is represented in table 6.1

Excluding PEG 200, for the same PEG molecular weight, ethanol produced more anatase than water containing HNO_3. Additionally, anatase crystallites were larger in samples synthesised using water containing HNO_3, excluding PEG 200. As previously explained phase transformation assists coarsening and is a likely explanation for this observation. The caveat to this observation is: the size difference between anatase crystallites synthesised using ethanol and water containing HNO_3 is not as pronounced under enhanced heating conditions as it was for conventional heating.

Table 6.1: Average anatase crystallite size formed in ethanol and water containing HNO_3.

PEG (g/mol)	% Anatase formed in ethanol	Anatase crystallite size in ethanol (nm)	% Anatase formed in water containing HNO_3	Anatase crystallite size in water containing HNO_3 (nm)
200	99.1 ± 4.9	6.9 ± 2.1	100.0 ± 4.0	5.4 ± 0.6
400	99.5 ± 4.0	6.7 ± 1.0	98.2 ± 5.7	8.6 ± 2.8
1000	100 ± 4.0	7.5 ± 0.3	98.7 ± 5.2	12.5 ± 0.4
1500	98.8 ± 4.7	12.9 ± 0.8	98.3 ± 4.5	13.7 ± 0.1
3000	94.8 ± 4.3	12.5 ± 2.1	71.7 ± 4.1	12.5 ± 0.4
6000	97.1 ± 4.0	9.8 ± 1.1	62.7 ± 3.0	13.7 ± 0.1
8000	100 ± 4.0	10.1 ± 0.7	66.8 ± 3.0	10.6 ± 0.3

Another point of note is that there was no relationship between the amount of rutile and anatase crystallite size in samples containing a mixture of polymorphs. Using conventional heating methods, samples containing about a 50/50 mix of anatase and rutile contained larger anatase crystallites than mixtures containing excess anatase. This could be due to the mechanism of crystallite formation under enhanced heating conditions. Due to higher temperatures, enhanced heating favoured the formation of larger crystallites. Anatase is the first formed phase as it is more stable than rutile. However, above 14 nm, anatase converts into rutile via oriented attachment[3]. From table 6.1, the largest anatase crystallites formed from enhanced heating were 13.7 nm.

No significant amounts of rutile were formed in ethanol using enhanced heating. Therefore a comparison of rutile crystallite size between the two solvents cannot be made.

The growth of anatase crystallites after calcination in samples synthesised using water containing HNO_3 and enhanced heating is documented in table 6.2. Intriguingly, calcination caused anatase crystallites present in phase pure samples to exhibit greater

growth than crystallites in samples containing a mixture of phases. A possible explanation for this observation is that after synthesis, smaller anatase crystallites have greater growth potential than larger crystallites. Therefore, smaller crystallites grow faster and to a larger size (up to a limit of between ~ 16 – 20 nm). Larger crystallites would grow at a slower rate. Anatase is not expected to transform into rutile despite crystallite size exceeding 14 nm. This is because the calcination temperature was insufficient to promote transformation. Additionally, oriented attachment occurs in solution or during co-nucleation of both phases on a substrate. Calcination conforms to neither of those requirements.

Table 6.2: Increase in anatase crystallite size from samples synthesised using water containing HNO_3 and enhanced heating.

PEG (g/mol)	% Anatase (Pre-calcination)	Crystallite size (nm) (Pre-calcination	% Anatase (Post-calcination)	Crystallite size (nm) (Post-calcination
200	100.0 ± 4.0	5.4 ± 0.6	100.0 ± 4.0	17.9 ± 4.3
400	98.2 ± 5.7	8.6 ± 2.8	98.0 ± 4.4	21.2 ± 1.1
1000	98.7 ± 5.2	12.5 ± 0.4	99.5 ± 4.5	17.6 ± 0.7
1500	98.3 ± 4.5	13.7 ± 0.1	95.4 ± 7.7	20.3 ± 1.9
3000	71.7 ± 4.1	12.5 ± 0.4	73.6 ± 4.0	16.9 ± 0.0
4000	68.6 ± 4.4	11.4 ± 0.1	63.0 ± 3.9	15.8 ± 1.2
6000	62.7 ± 3.0	13.7 ± 0.1	65.5 ± 3.1	18.5 ± 1.6
8000	66.8 ± 3.0	10.6 ± 0.3	68.8 ± 2.8	17.9 ± 2.2

TEM imaging was performed on samples synthesised from PEG 200 (figure 6.17), PEG 1000 (figure 6.18), PEG 4000 (figure 6.19), and PEG 6000 (figure 6.20) in water containing HNO_3 using enhanced heating post-calcination. Samples synthesised from PEG 200 and 1000 exhibited phase pure (100%) and near phase pure (98%) anatase formation respectively. Samples synthesised from PEG 4000 and 6000 produced a

mixture of anatase and rutile (63% and 66% anatase respectively). Interestingly, figure 6.20 provided evidence of the existence of superstructures, and was likely composed of rutile crystallites. These superstructures were evidenced in multiple parts of the sample. Crystallites surrounding the superstructure could be either anatase or rutile.

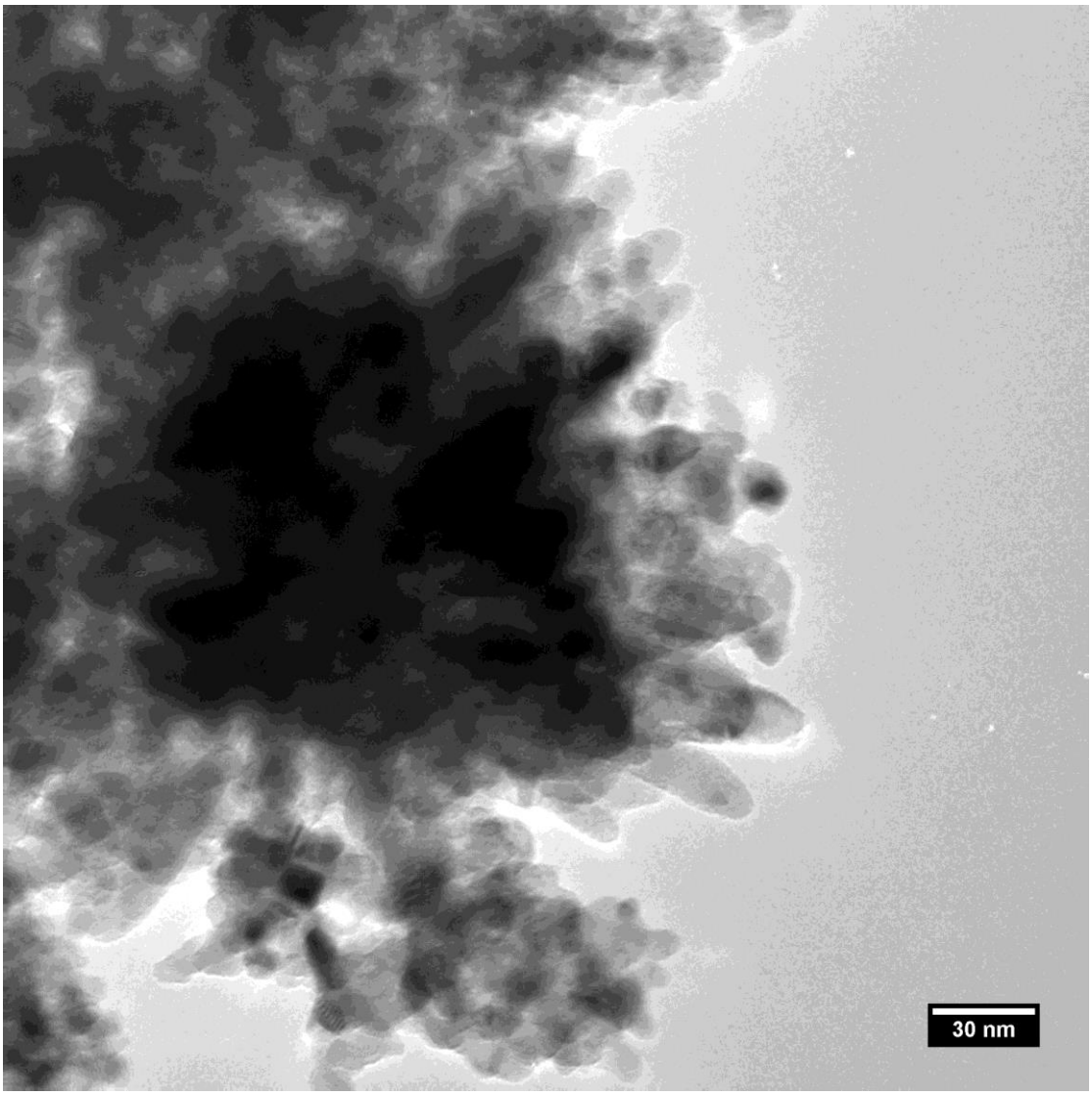

Figure 6.17: Agglomerated anatase crystallites observed from sample OPEG 200 + H_2O. This image shows a variety of crystallites of different sizes. Some crystallites exhibit anisotropic growth.

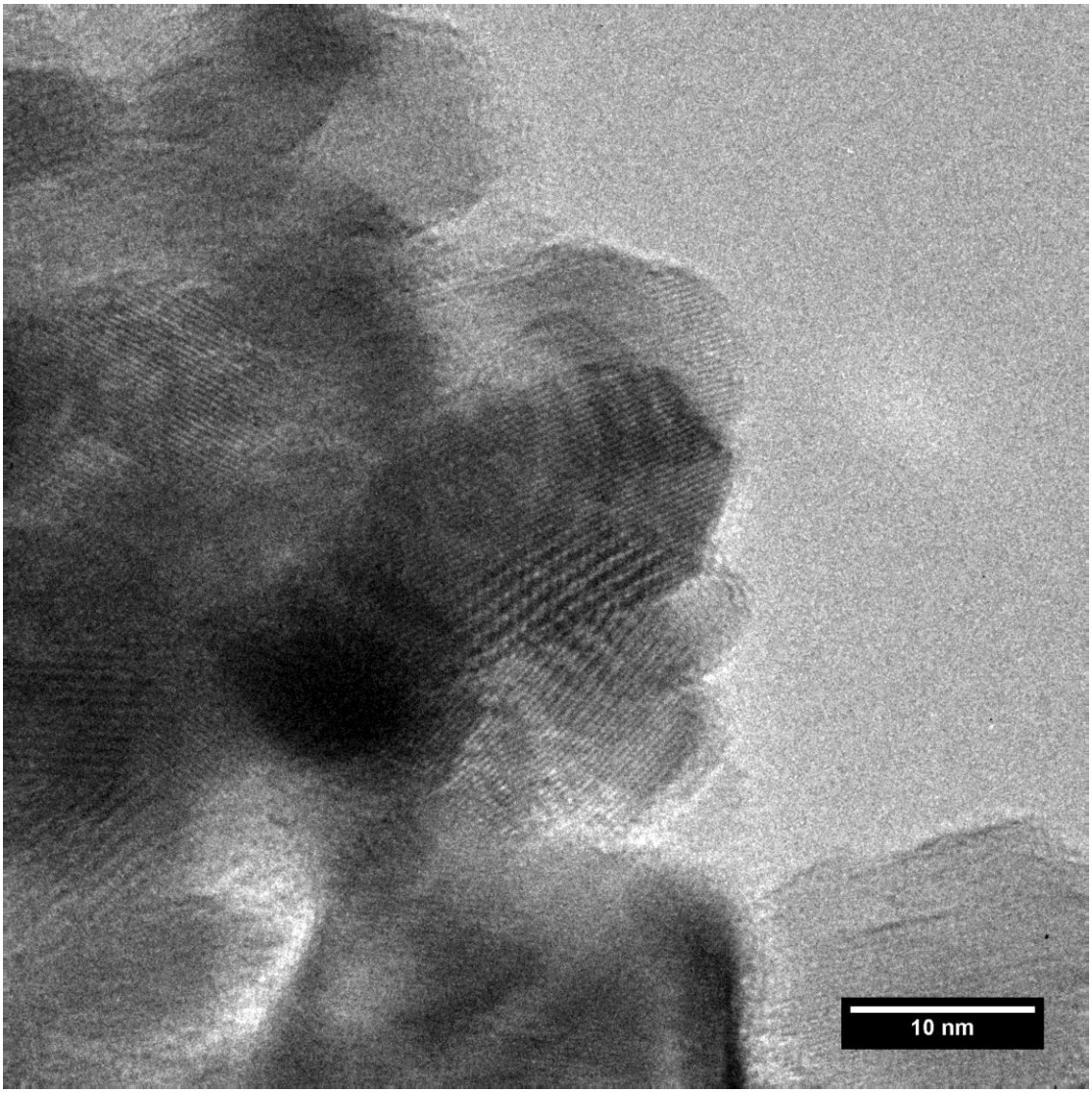

Figure 6.18: Well-defined anatase crystallites formed from sample OPEG 1000 + H_2O. One-dimensional lattice fringes are visible for most crystals. Moiré fringe artefacts are evident.

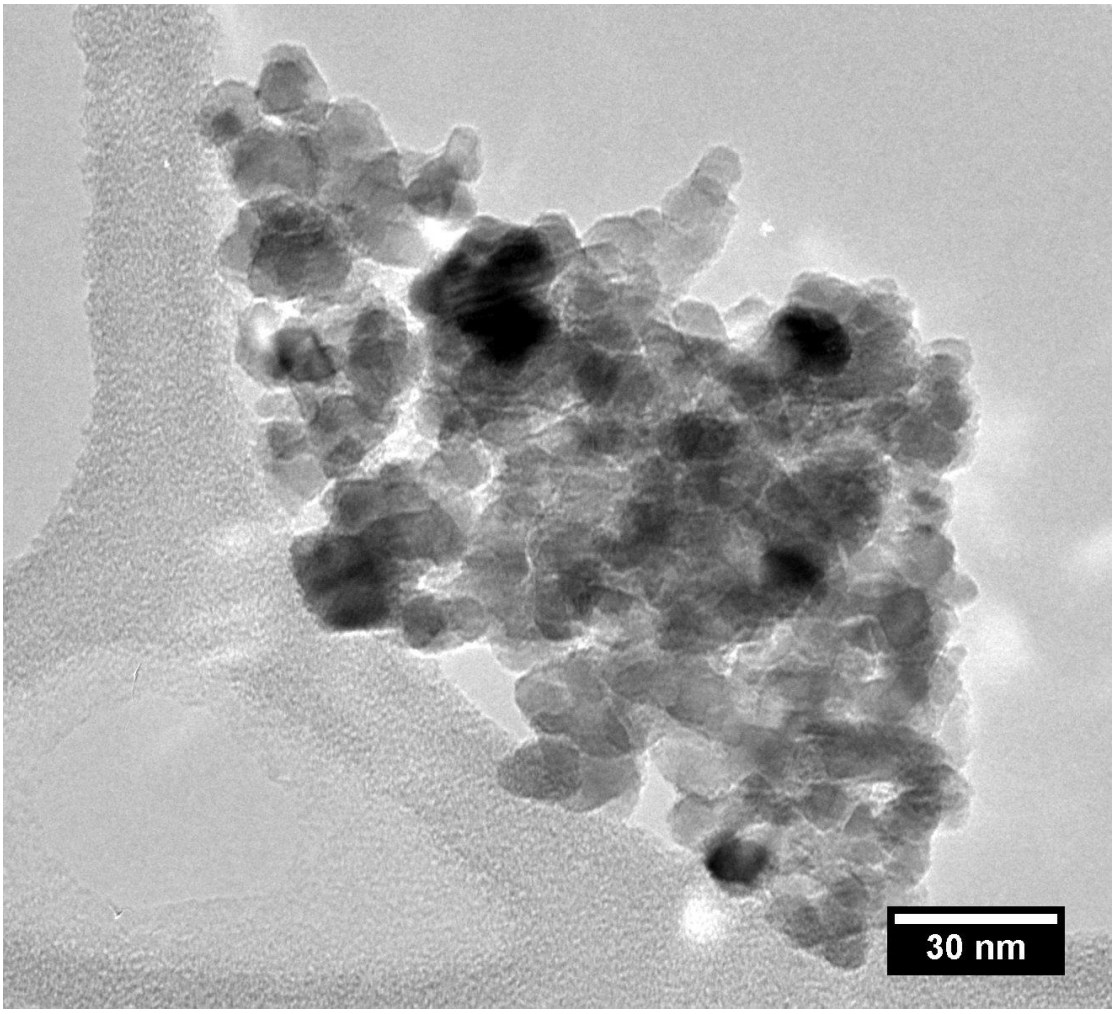

Figure 6.19: Anatase crystallites of various sizes and shapes from OPEG 4000 + H_2O.

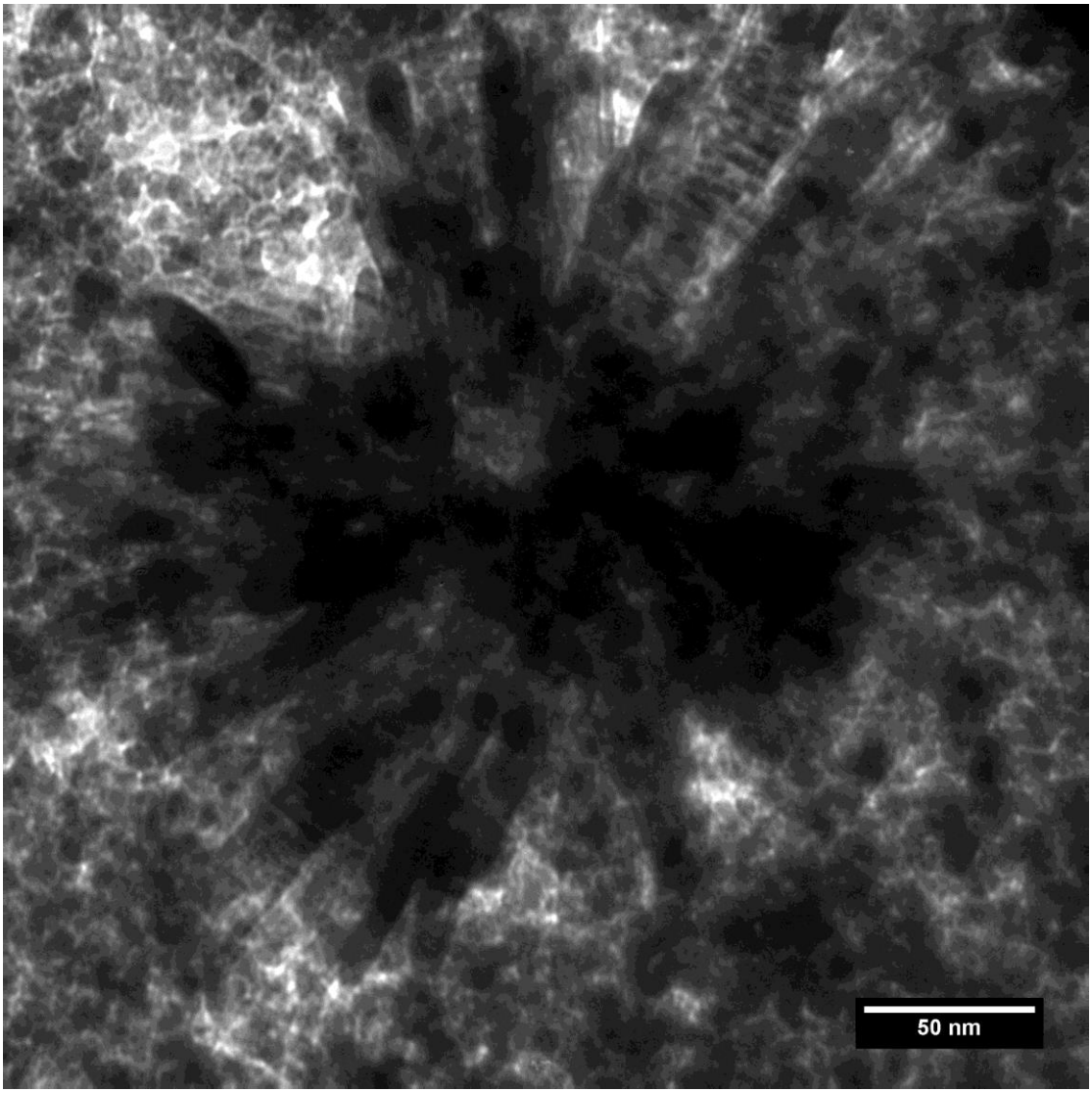

Figure 6.20: An area of sample OPEG 6000 + H_2O containing a mixture of rutile and anatase crystallites.

6.2.4 Conventional and Forced Heating using a Water containing HNO_3 Solvent

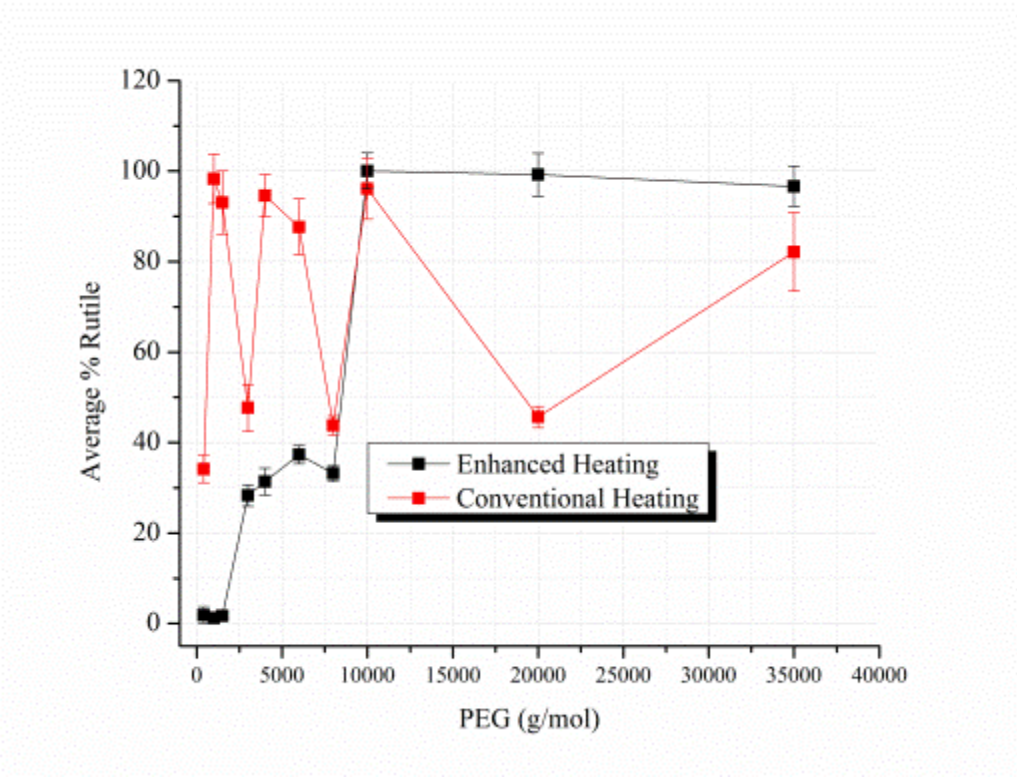

Figure 6.21: Comparison of average amount of rutile formed in water containing HNO_3 under conventional and enhanced heating methods.

Figure 6.21 compares the amount of rutile formed in water containing HNO_3 using conventional and enhanced heating. Data for conventional heating was obtained from the amount of rutile formed in water containing HNO_3 pre-calcination in chapter 5. Using conventional heating methods, rutile was formed in the presence of water containing HNO_3, regardless of the PEG molecular weight used in the synthesis. PEG molecular weight caused the amount of rutile formed to fluctuate between ~ 45% – 100% using conventional heating. Enhanced heating did not result in the formation of rutile in all samples. The amount of rutile formed increased as a function of increasing PEG molecular weight, with low molecular weight PEG producing nearly phase pure anatase. Medium molecular weight PEG produced nearly the same amount of rutile, compared with high molecular weight PEG that produced phase pure rutile. PEG 8000, 10000, and 35000 g/mol produced similar amounts of rutile using both heating methods. The up and down behaviour of the amount of rutile formed as a function of increasing PEG molecular weight was not present under enhanced heating conditions.

Rutile formation using enhanced heating is a surprising result. Gopal *et al.*, showed that fast heating a sol containing titanium metal ions produced anatase exclusively[6]. Although the system presented in this study is resin-gel synthesis and not sol-gel synthesis, the mechanism proposed by Gopal *et al.*, is valid. They proposed that two crystallised octahedra would share a corner with a third octahedra, in a simple nucleation model. The second corner of the third octahedra can bind to the growing chain in one of three ways. Two of those ways result in the formation of anatase; one way results in the formation of rutile. Therefore, the kinetic product (i.e.: the product of rapid heating) should be anatase as it is statistically favoured. In keeping with the developing hypothesis, it is likely that water stabilises PEG chains in solution and makes them more rigid. This has the effect of reducing the propensity of PEG to stabilise the anatase phase. Consequently anatase converts to rutile when water containing HNO_3 is employed as the solvent in resin-gel synthesis.

This hypothesis does not explain why long chain PEG forms rutile exclusively, and forms decreasing amounts of rutile as the chain is shortened. The following is proposed to explain the effects of enhanced heating on the amount of rutile formed across a range of PEG molecular weights: rapid heating the resin causes the polymer chains to undergo scission at a faster rate. It is possible that the faster rate of PEG degradation causes scission at specific points along the chain, forming reaction chambers of a specific size. Under the action of enhanced heating, small chain PEG rapidly forms small reaction chambers (as a result of quicker degradation). Smaller chambers inhibit the transformation of anatase to rutile by stabilising the growing anatase phase. By contrast, the longer the PEG chain, the more likely chain entanglement is to occur. Rapid heating would still cause scission at a faster rate, but it is likely that the reaction chambers will be larger (owing to the presence of longer chains and entanglement that serves to increase the size of the chambers). As a result, anatase is not stabilised efficiently, and the growing crystallites transform into rutile.

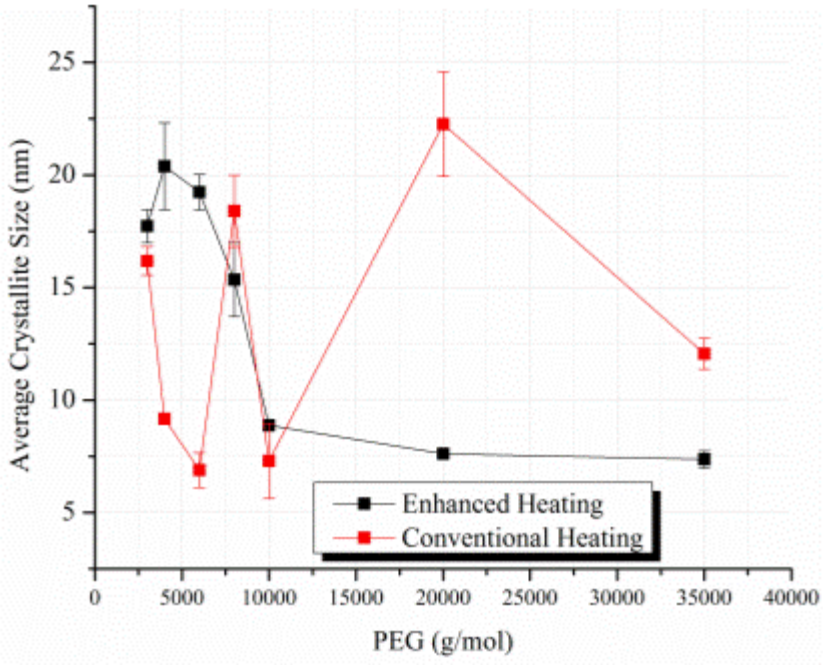

Figure 6.22: Comparison of average rutile crystallite size formed in water containing HNO_3 under conventional and enhanced heating methods.

Figure 6.22 compares the rutile crystallite size formed in water containing HNO_3 using conventional and enhanced heating, as a function of increasing PEG molecular weight. Data for conventional heating was obtained from rutile crystallite size formed in water containing HNO_3 pre-calcination, in chapter 5. Rutile crystallite size exhibited up and down behaviour when synthesised using conventional heating. This is in contrast to enhanced heating that produced similar sized rutile crystallites for similar PEG molecular weights. Using enhanced heating, the smallest rutile crystallites were formed in samples containing long chain PEG. PEG 3000, 8000, and 10000 g/mol resulted in the formation of similarly sized rutile crystallites using both heating methods. Greater data precision was obtained for samples synthesised using enhanced heating.

Tables showing the amount of each phase and crystallite size obtained for each sample with averages and errors are given in appendix D.

6.3 Conclusions

Using enhanced heating, samples synthesised using ethanol produced nearly phase pure material for PEG molecular weights 200 – 20000 g/mol. Anatase was the major phase formed when PEG 35000 g/mol was used. Associated anatase crystallites were small, with the largest crystallites measuring ~ 13 nm. Small increases in the amount of anatase formed post-calcination were attributed to incomplete synthesis during ignition. This was due to the polymer directly exposed to the flame shielding the polymer in the middle of the sample. Calcination at 500 °C caused any amorphous titania present in the sample to convert into anatase. Despite this, calcination had a greater effect on crystallite size than on phase transformation. TEM analysis of samples synthesised in ethanol revealed the presence of small crystallites with well-defined geometric shapes.

When ethanol was employed as the solvent, almost phase pure anatase was produced regardless of the type of heating method (conventional or forced) used. Therefore, ethanol inclusion was a greater determinant of phase formation than heating method. This was evidenced by the fact that ethanol produced nearly phase pure anatase using both conventional and enhanced heating methods. Average anatase crystallite size was larger for crystallites synthesised using enhanced heating. This is expected as higher temperatures caused enhanced sintering and crystallite growth. Crystallite size data obtained using conventional heating displayed an inverse relationship to that of enhanced heating. PEG 35000 resulted in the formation of similarly sized anatase crystallites and similar amounts of anatase using both heating methods. This is likely due to polymer entanglement and the formation of larger polymer chambers that encouraged the transformation of anatase to rutile.

When water containing HNO_3 was used as the solvent, calcination caused anatase crystallites present in phase pure samples to exhibit greater growth than crystallites in samples containing a mixture of phases.

TEM imaging of samples synthesised in water containing HNO_3 revealed similar looking anatase crystallites as those formed in ethanol. Titania superstructures were also observed in a sample containing a mixture of phases.

The amount of rutile formed using water containing HNO_3 and enhanced heating was dependent on the PEG molecular weight. Low molecular weight PEG produced

almost zero rutile, medium weight PEG produced ~ 33% rutile. High molecular weight PEG produced nearly phase pure rutile. Calcination had little effect on phase transformation. Average rutile crystallite size coarsened significantly post-calcination. The amount of rutile formed was inversely proportional to its respective crystallite size. Rutile crystallite size was proportional to the amount of anatase contained within the sample.

The steric stabilisation effects of the remaining matrix components from the solution on nucleated anatase were documented in chapter 5. Additionally, PEG structural integrity differentiation afforded by the solution on account of hydrogen bonding was described. Heating was hypothesised as forming polymer reaction chambers. Given that PEG of different chain lengths was added to metal ions in a volumetric manner, the total volume of polymer added to each solution was the same. Therefore, it is possible that enhanced heating caused polymer chains to cleave at better defined points, forming chambers with a smaller size distribution. Accordingly, small chain PEG formed smaller chambers in contrast to longer chain PEG that formed larger chambers. The stabilisation effects of polymer chambers of various sizes were described in chapter 5.

6.4 References

1. Banfield, J. F., Bischoff, B. L. & Anderson, M. A. TiO2 accessory minerals: coarsening, and transformation kinetics in pure and doped synthetic nanocrystalline materials. *Chemical Geology* **110,** 211 – 231 (1993).

2. Lorenz, R. & Voorhees, P. W. *Growth and Coarsening: Ostwald Ripening in Material Processing*. (Springer-Verlag, 2002).

3. Zhang, H. & Banfield, J. F. Thermodynamic analysis of phase stability of nanocrystalline titania. *Journal of Materials Chemistry* **8,** 2073 – 2076 (1998).

4. Ding, X. & Liu, X. Correlation between anatase-to-rutile transformation and grain growth in nanocrystalline titania powders. *Journal of Materials Research* **13,** 2556 – 2559 (1998).

5. Penn, R. L. & Banfield, J. F. Oriented attachment and growth, twinning, polytypism, and formation of metastable phases: Insights from nanocrystalline TiO2. *American Mineralogist* **83,** 1077 – 1082 (1998).

6. Gopal, M., Chan, W. J. M. & De Jonghe, L. C. Room temperature synthesis of crystalline metal oxides. *Journal of Materials Science* **32,** 6001 – 6008 (1997).

Chapter 7: Effects of Citric Acid on Titania Polymorph and Crystallite Size Formation

Chapters 5 and 6 focussed on the role of the solvent in titania phase discrimination and crystallite size variation. The data obtained from these chapters suggested that the solvent was an active reaction component. Polymer chains coordinated to hydroxylated metal ion species formed between metal ions and solvent components. To strengthen these conjectures, citric acid (figure 7.1) was employed in this synthesis.

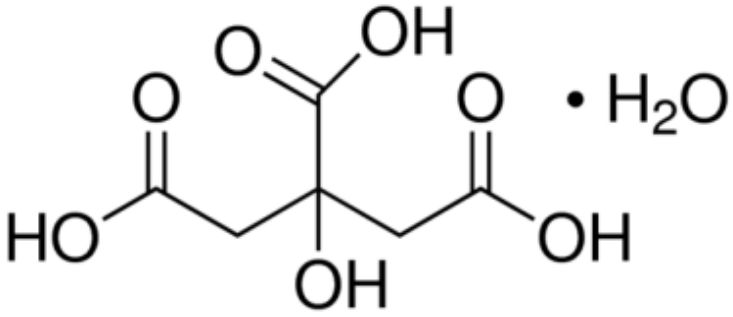

Figure 7.1: Structural formula of citric acid monohydrate.

Yin *et al.* found that in the hydrothermal synthesis of TiO_2 from a $TiCl_4$ precursor, citric acid played a pivotal role in forming phase pure anatase nanoparticles[1]. The researchers concluded that interactions between citric acid and $TiCl_4$ prevented rapid hydrolysis[1]. Since the crystal field splitting of the citrate anion is stronger than Cl^- and OH^-, citrate should form part of the coordination complex of partially hydrolysed Ti. The resulting effect is that formed complexes are stabilised relative to those without citrate. These stabilised complexes favoured the formation of the less stable anatase phase[1]. Additionally, citrate anion coordination inhibited crystal growth[1].

The effects of citrate in a sol-hydrothermal process was reported[2]. Citrate was found to favour anatase formation, dependent on the mol ratio of citrate to $TiCl_4$. The ratio of citrate to $TiCl_4$ also affected the size and morphology of nano-TiO_2 particles[2]. A high ratio of citrate produced a small size distribution of particles[2].

Franklyn *et al.* found that the inclusion of citric acid in the hydrothermal synthesis of titanium dioxide produced anatase exclusively[3]. When citric acid was omitted from

the system, rutile was the favoured product. The researchers concluded that the presence of organic acids stabilised the surface of small anatase crystals by binding hydroxyl and proton species. Consequently, the interaction of surface capped anatase with solution components and other nucleated anatase crystals was limited. In this manner, anatase transformation into rutile was inhibited[3].

Although the abovementioned study applied to the hydrothermal and sol-hydrothermal syntheses, citrate modified Ti^{+} coordination complexes should still form under resin-gel synthesis conditions. Additionally, anatase surface capping, protection, and stabilisation by citric acid should apply for the present resin-gel system – at least during the solution and gelation stages. Therefore, the aim of this experiment was to observe the effects of citric acid on the amount of each titania phase formed and its respective crystallite size. If similar results were obtained (to previous studies), the solvent component stabilisation hypothesis developed in chapter 5 will be strengthened.

7.1 Experimental Procedure

For this experiment, Ti^{+} ions were added stoichiometrically to PEG of various molecular weights in a (1 : 1) ratio. The implications for stoichiometric addition are discussed in chapter 8. Two batch solutions of metal ions were created – that were further divided. Two batch solutions were synthesised as a practical consideration toward the mass of PEG required when high molecular weight PEG was used. Since the ratio of Ti^{+} : PEG remained constant at (1 : 1) for all samples, the absolute amount of $TiCl_4$ added is irrelevant. The experiment consisted of 3 parts: addition of Ti^{+} ions to PEG in a (1 : 1) ratio, heat treatments, and characterisation. Water containing citric acid was used as the solitary solvent for all experiments. Concentrated nitric acid was not used in this synthesis.

7.1.1 Addition of Ti^{+} ions to PEG in a (1 : 1) Ratio

For the first batch solution 4.0 ml (0.036 mols) $TiCl_4$ (> 99%, Merck) was added into excess distilled water (96.0 ml) containing 5.2 g citric acid monohydrate. The solution was stirred to homogeneity using a Teflon coated magnetic stirrer bar. Thereafter, the solution was decanted equally into four separate beakers, such that each beaker contained 1.0 ml (0.0091 mols) $TiCl_4$. Stoichiometric amounts of PEG 1000, 1500, 3000, and 4000 g/mol (as given in table 7.1) were added to each beaker respectively.

The second batch solution was synthesised by adding 0.75 ml (0.0068 mols) $TiCl_4$ (> 99%, Merck) into excess distilled water (18.0 ml) containing 0.975 g of citric acid. After homogeneity was achieved, the solution was divided equally into three beakers such that each beaker contained 0.25 ml (0.0023 mols) $TiCl_4$. Stoichiometric amounts of PEG 10000, 12000, and 20000 g/mol (as given in table 7.1) were added into each beaker respectively.

Table 7.1: Quantities of Ti ions and PEG added to achieve a (1 : 1) stoichiometry.

Batch number	Quantity of $TiCl_4$ added (mols)	PEG molecular weight used (g/mol)	Quantity of PEG (mols) required	Quantity of PEG added (g)
1	0.0091	1000	0.0091	9.0989
	0.0091	1500	0.0091	13.6484
	0.0091	3000	0.0091	27.2968
	0.0091	4000	0.0091	36.3958
2	0.0023	10000	0.0023	22.7474
	0.0023	12000	0.0023	27.2968
	0.0023	20000	0.0023	45.4948

7.1.2 Heat Treatments

All mixtures were heated (PEG 1000 – 50 °C, PEG 1500 – 52°C, PEG 3000 – 55 °C, PEG 4000 – 57 °C, PEG 10000 – 60 °C, PEG 12000 – 62 °C, PEG 20000 - 65 °C) and simultaneously stirred using a glass rod by hand to attain complete homogenisation. Afterwards, all 7 gels were placed ~ 30 cm under two 200 W infrared lamps for 14 days to allow for solvent evaporation. The dehydrated resins were divided equally to introduce a replicate for the heat treatment.

Resins were placed in alumina glazed crucibles and then placed into a sand bath. Conventional heating to ignition was achieved as described in chapter 5. Due to the samples presenting with a black appearance, all samples were divided into 2 halves – one half to be analysed before calcination and the other half to be analysed after calcination. Calcination was effected in a muffle furnace at 500 °C (at ~ 620 mm Hg) for 1 hour.

7.1.3 Characterisation

PXRD data was obtained using a Bruker D2 Phaser diffractometer. The setup of the D2 Phaser has been described in chapter 5. Samples were analysed between 20° and 50° 2θ in 0.04 increments counting for 1 second per step. HRTEM analysis was achieved using a JEOL 3011.

7.2 Results and Discussion

7.2.1 Effects of Citric Acid

Figure 7.2 contains the PXRD patterns recorded from samples synthesised using citric acid, pre-calcination. The patterns confirm that all samples contain anatase. Interestingly, the signal to noise ratio of the anatase (1 0 1) peak decreased as the PEG chain length increased. This, combined with slight peak misalignment, suggests that carbon residue or polymer fragments reduced X-ray penetration into the samples. Another possibility is that the large quantity of polymer present favoured the formation of amorphous titanium dioxide. Peak width increased as PEG molecular weight increased. This phenomenon could be due to polymer fragments contained in samples containing long chain polymers protecting crystallites and inhibiting coarsening.

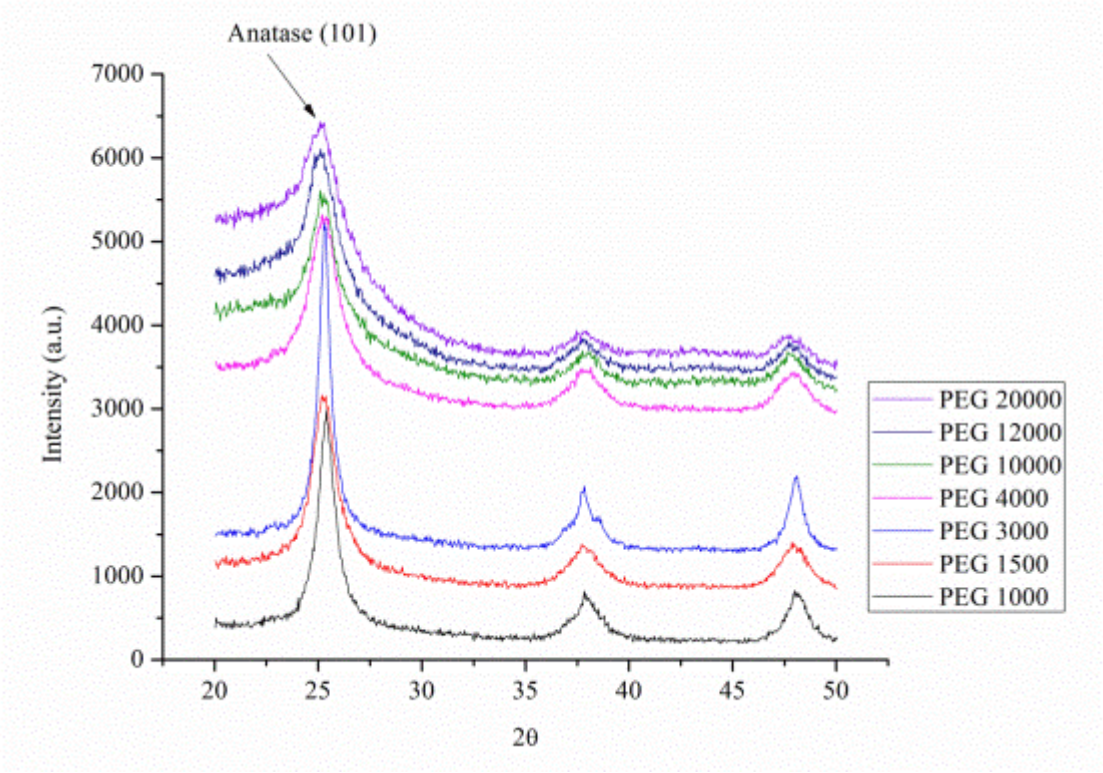

Figure 7.2: PXRD patterns of samples pre-calcination.

Figure 7.3 contains the PXRD patterns corresponding to the replicate samples synthesised using citric acid. Comparisons between figures 7.1 and 7.2 suggest that the synthesis produced samples displaying good reproducibility.

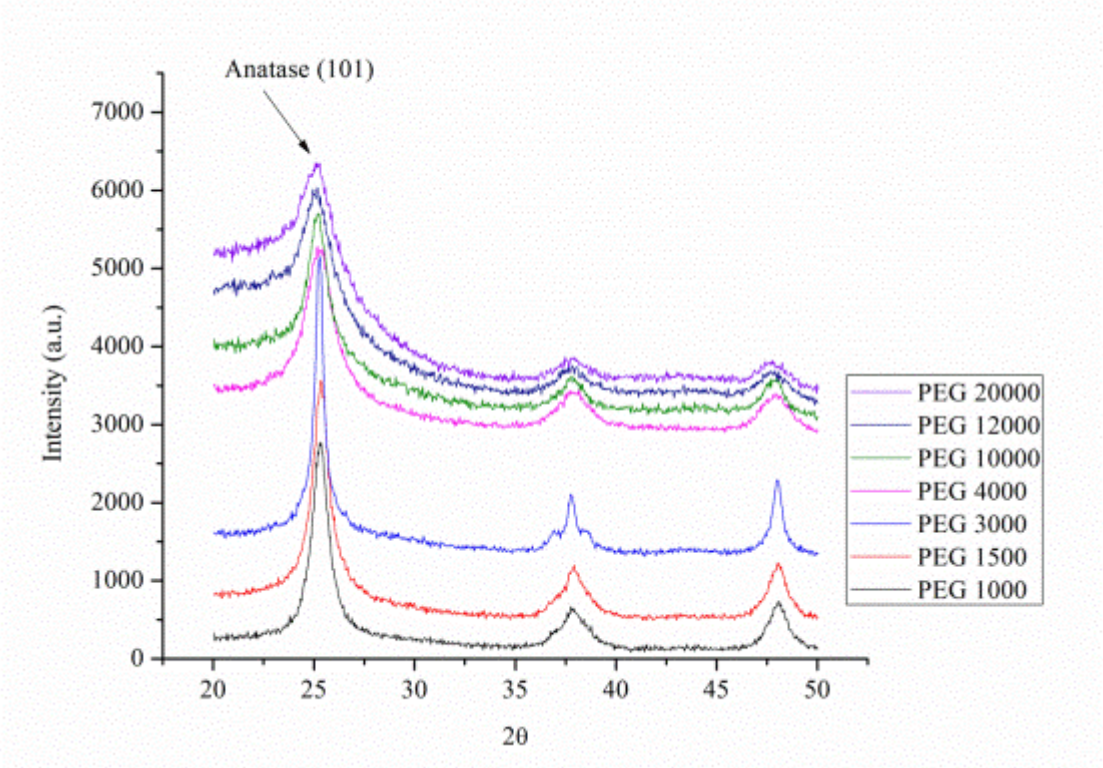

Figure 7.3: PXRD patterns of replicate samples pre-calcination.

From figure 7.4 it can be seen that calcination did not nucleate rutile. This was an expected result. The improved signal to noise ratio observed for patterns contained in figure 7.4 can be attributed to calcination successfully removing residual carbon and polymer fragments from samples. However, the improved signal to noise ratio for the samples synthesised using PEG 20000 g/mol is not as pronounced as for the other samples. This may be due to the calcination temperature and time being insufficient to remove all traces of residual polymer fragments. In the interest of consistency, and not to impact crystallite size, calcination times and temperatures were kept constant for all samples. Better peak alignment is further confirmation of the success of calcination. Narrower anatase peaks are indicative of crystallite coarsening. The data generated from all samples shows good reproducibility with their respective replicates.

Figure 7.5 illustrates good reproducibility between the original and replicate data sets after calcination. A statistical account of the correlation between data generated from the original and replicate data sets will be provided later.

Tables showing the amount of each phase and crystallite size obtained for each sample with averages and errors are given in appendix E.

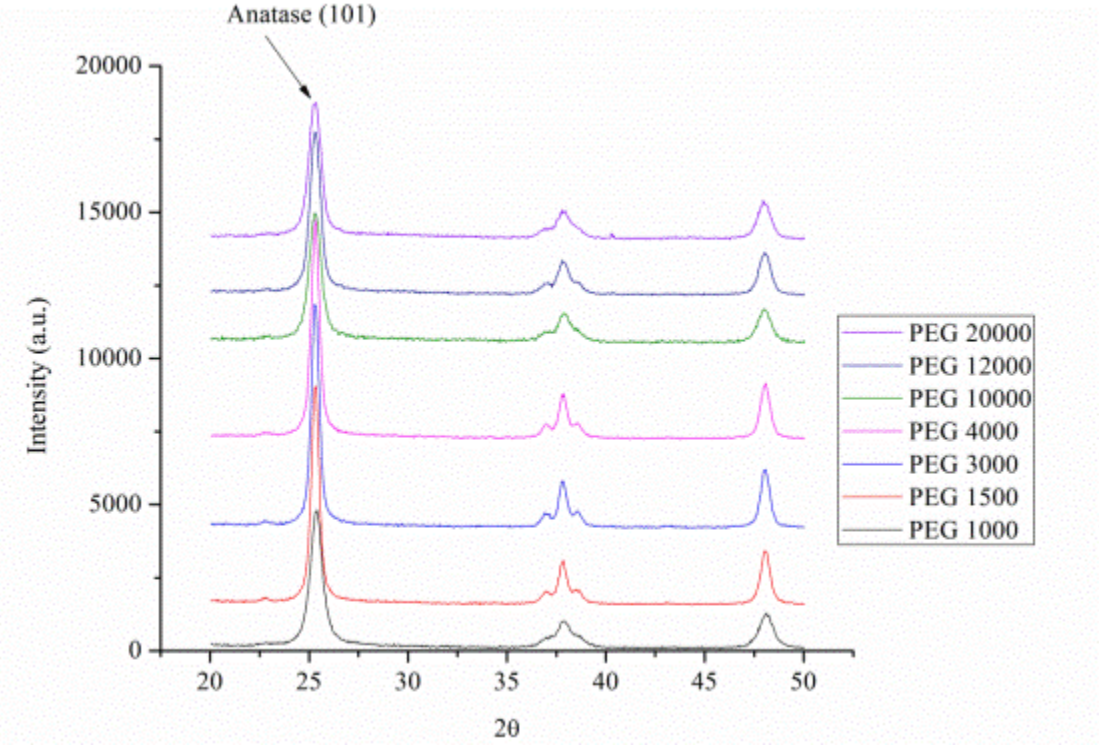

Figure 7.4: PXRD patterns of calcined samples.

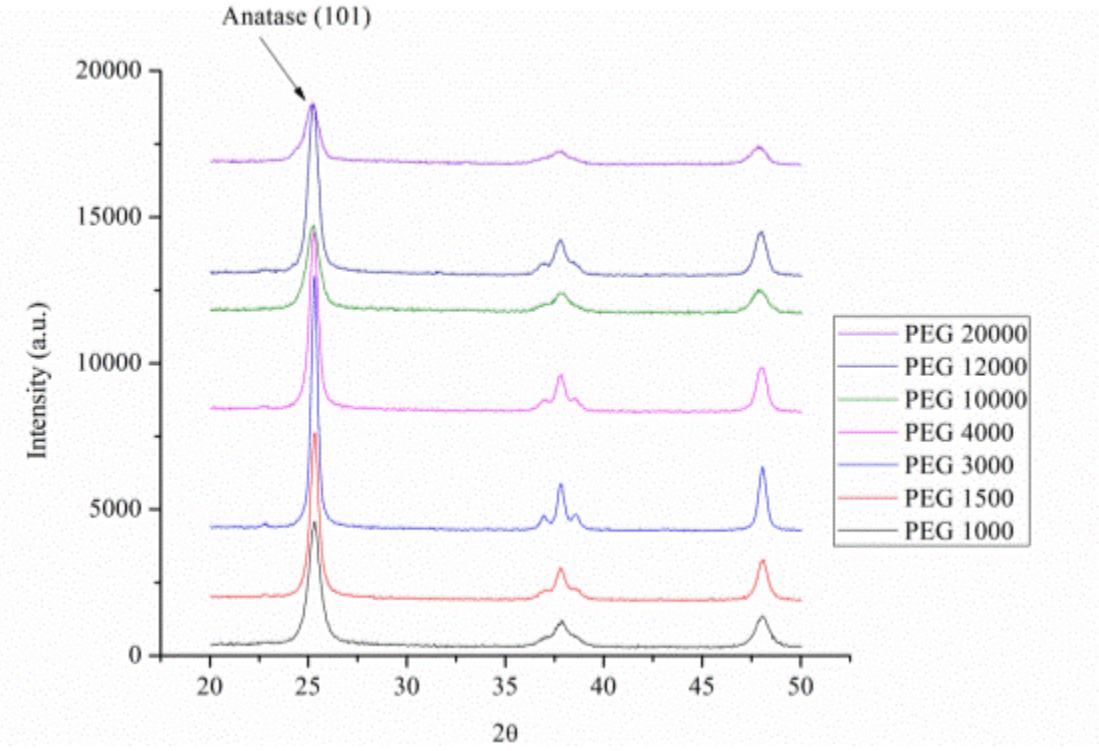

Figure 7.5: PXRD patterns of replicate calcined samples.

Figure 7.6 shows the change in mass percentage of anatase formed as a function of increasing PEG molecular weight. Evidently, intermediate and long chain PEG (3000 – 20000 g/mol) produce phase pure anatase. Shorter chain PEG (1000 – 1500 g/mol) are biased toward almost exclusive anatase formation (98.5% and 99.2 % anatase formed from PEG 1000 g/mol and 1500 g/mol respectively). The average amount of anatase formed across all samples was 99.6%. The near phase pure production of anatase across all samples concludes that rutile transformation was inhibited when citric acid was employed in the reaction.

The largest error in the data was obtained for the sample synthesised using PEG 1500 g/mol (4.8%). Given that errors were generated by summing 4% of the average amount of anatase formed to the standard deviation of the replicate analyses, the data reflects excellent precision. Additionally, it suggests that PEG 1000 and 1500 g/mol could have produced phase pure anatase. It is unlikely that the amount of anatase decreased to ~ 94% – 96% as suggested by the error bars, as no rutile peaks were evident in the PXRD patterns. Moreover, it is not possible for a sample to contain more than 100% anatase – as suggested by the error bars. Positive and negative error bars were introduced into the data set by the analysis software.

The amount of anatase formed post-calcination did not change proportionally with the respective pre-calcination data. Aside from the samples synthesised using PEG 1500 and 20000 g/mol, all other samples showed a slight decrease in the amount of anatase formed as a result of calcination. Based on previously obtained results in this study, this was an expected finding. The overall decrease in the amount of anatase formed across all samples post-calcination was 0.4%.

Samples synthesised using PEG 1500 g/mol exhibited a small increase in the amount of anatase formed after calcination (0.3%). The increase in anatase formed post-calcination was likely due to the statistical error inherent in the data. Based on previously obtained data, long chain PEG such as PEG 20000 g/mol was expected to form more anatase post-calcination than pre-calcination. Given that the PXRD patterns corresponding to the pre-calcined PEG 20000 g/mol samples revealed a poorer signal to noise ratio, it was inferred that amorphous material may be present in the sample. As the amount of anatase remained the same pre- and post-calcination, the long chain polymer did not form amorphous titania. Instead, the weak signal to noise

ratio can be attributed to PEG 20000 g/mol polymer impeding X-ray penetration into the titania crystals.

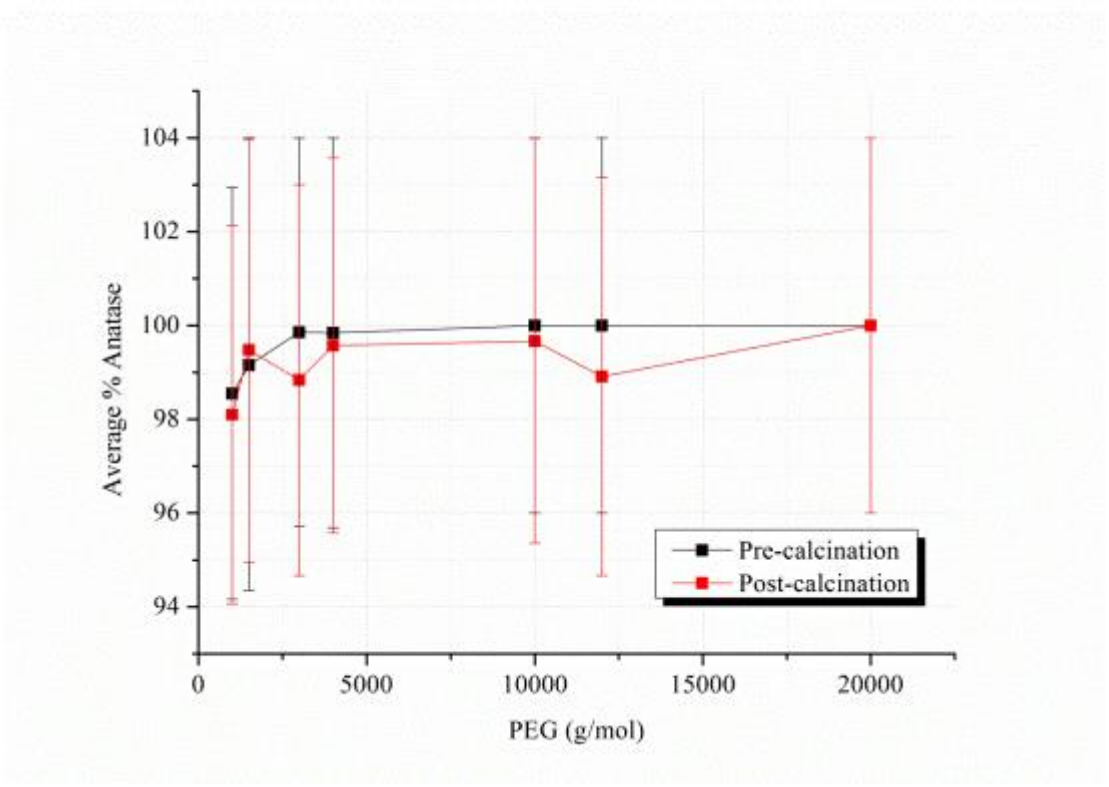

Figure 7.6: Average amount of anatase formed pre- and post-calcination.

Figure 7.7 shows the change in anatase crystallite size obtained as a function of increasing PEG molecular weight for samples synthesised using citric acid. Excluding the data obtained from the samples synthesised using PEG 3000 g/mol, all other samples produced anatase crystallites that measured $\leq$ 10 nm. Accordingly, the average anatase crystallite size formed across all samples measured 8.7 nm. Samples synthesised using PEG 4000 – 20000 g/mol produced anatase crystallites that differed by 3 nm in size. PEG 3000 g/mol resulted in the formation of anatase crystallites that measured 16.7 nm compared with PEG 20000 g/mol that produced the smallest anatase crystallites (4.6 nm). Crystallite size data obtained from PEG 3000 g/mol is interesting as anatase crystallites measuring < 14 nm are more stable than rutile[4]. It is possible that the polymer and citric acid stabilised and protected anatase crystallites inhibiting rutile transformation.

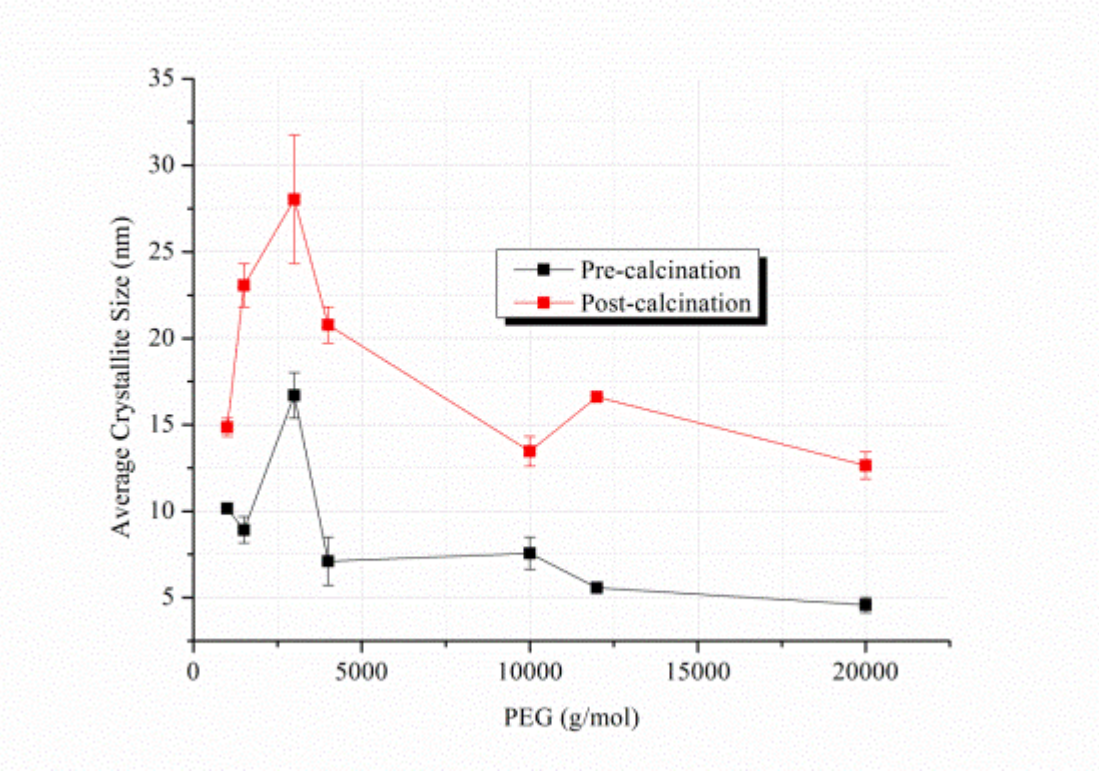

Figure 7.7: Average anatase crystallite size formed pre- and post-calcination.

Expectedly, anatase crystallite size increased after calcination. Although this increase was not proportional, the average crystallite size across all samples post-calcination measured 18.5 nm. This represented an increase of 112%. Post-calcination crystallite size data appeared to be more erratic than data obtained pre-calcination. However, the data was sufficiently precise for the trends to occur at the maximum of each error. Error bars were generated from the standard deviation of the replicate synthesis.

Figure 7.8 shows no definitive relationship between the amount of anatase formed and its respective crystallite size. Despite near phase pure anatase forming in all samples, crystallite size fluctuated. Excluding the sample synthesised using PEG 3000 g/mol, anatase crystallite size appeared to decrease disproportionally as the PEG chain length increased. This behaviour may be explained by considering that long chain polymers undergo chain entanglement. Given that the ratio of Ti^{+} to PEG was (1 : 1), the volume of polymer present in samples synthesised using long chain polymers could have served to stabilise the anatase phase and inhibit its transformation into rutile. This stabilisation effect was likely intensified by the presence of citric acid. Rutile transformation is inhibited by favouring the formation of the more energetically stable, small crystal anatase[4].

Because calcination caused an increase in crystallite size and almost no change in the amount of anatase formed, the relationship between the amount of anatase formed and its respective crystallite size was maintained post-calcination (figure 7.9).

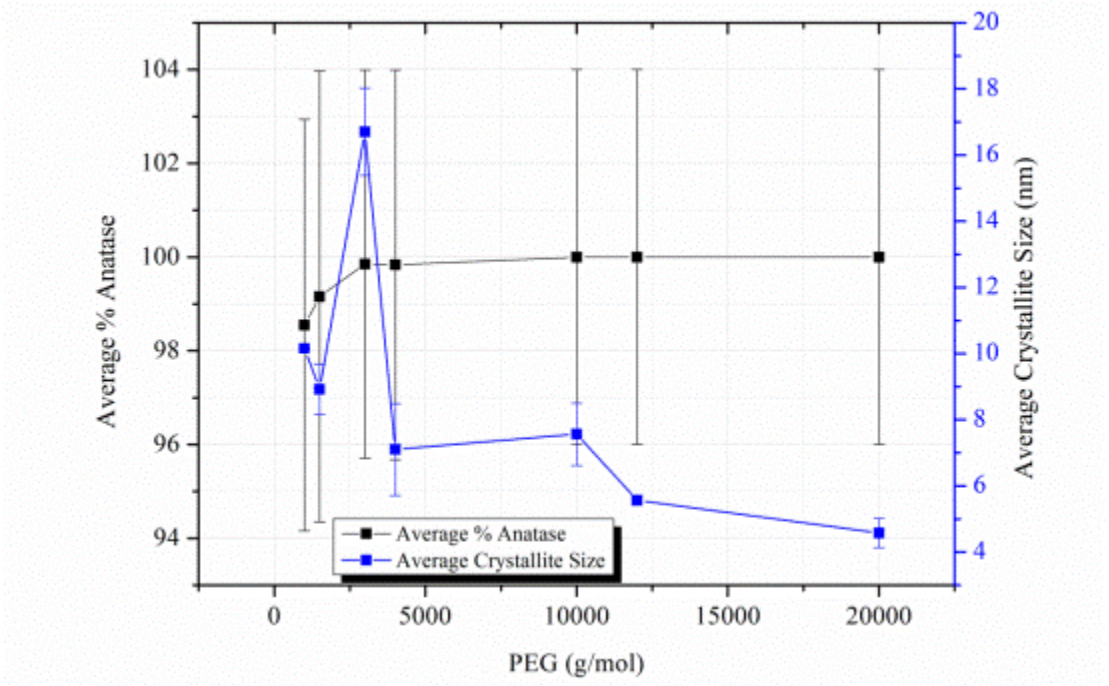

Figure 7.8: Average amount of anatase with associated crystallite size formed pre-calcination.

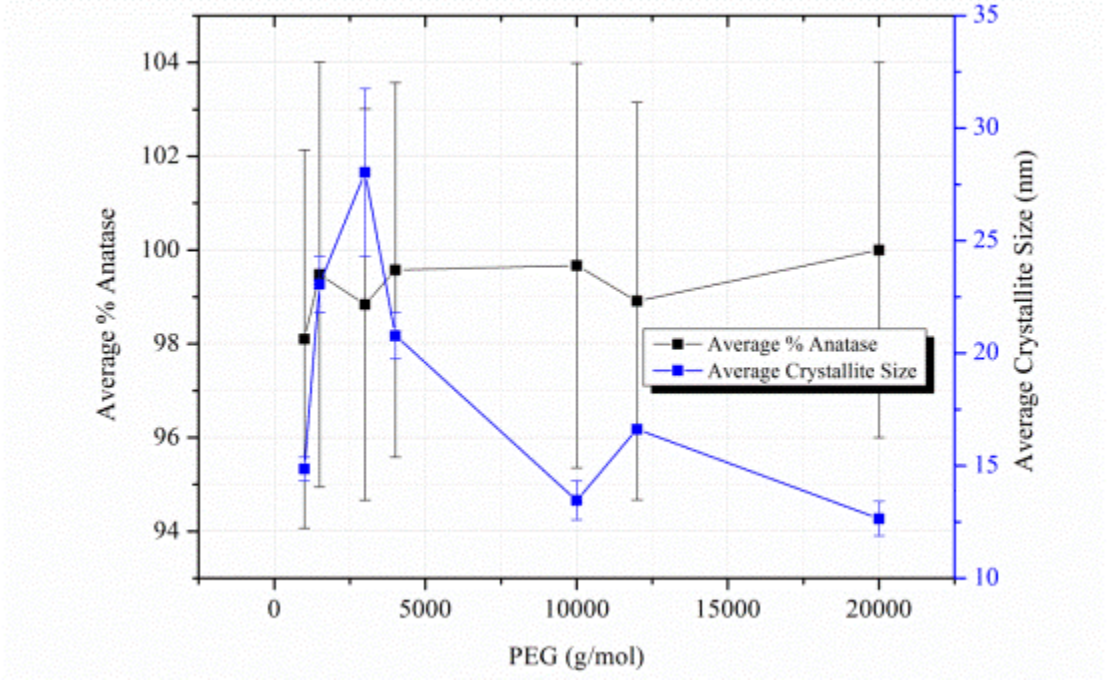

Figure 7.9: Average amount of anatase with associated crystallite size formed post-calcination.

An HRTEM image corresponding to the sample synthesised from PEG 1000 g/mol follows (figure 7.10). All crystals imaged in this study had a similar appearance.

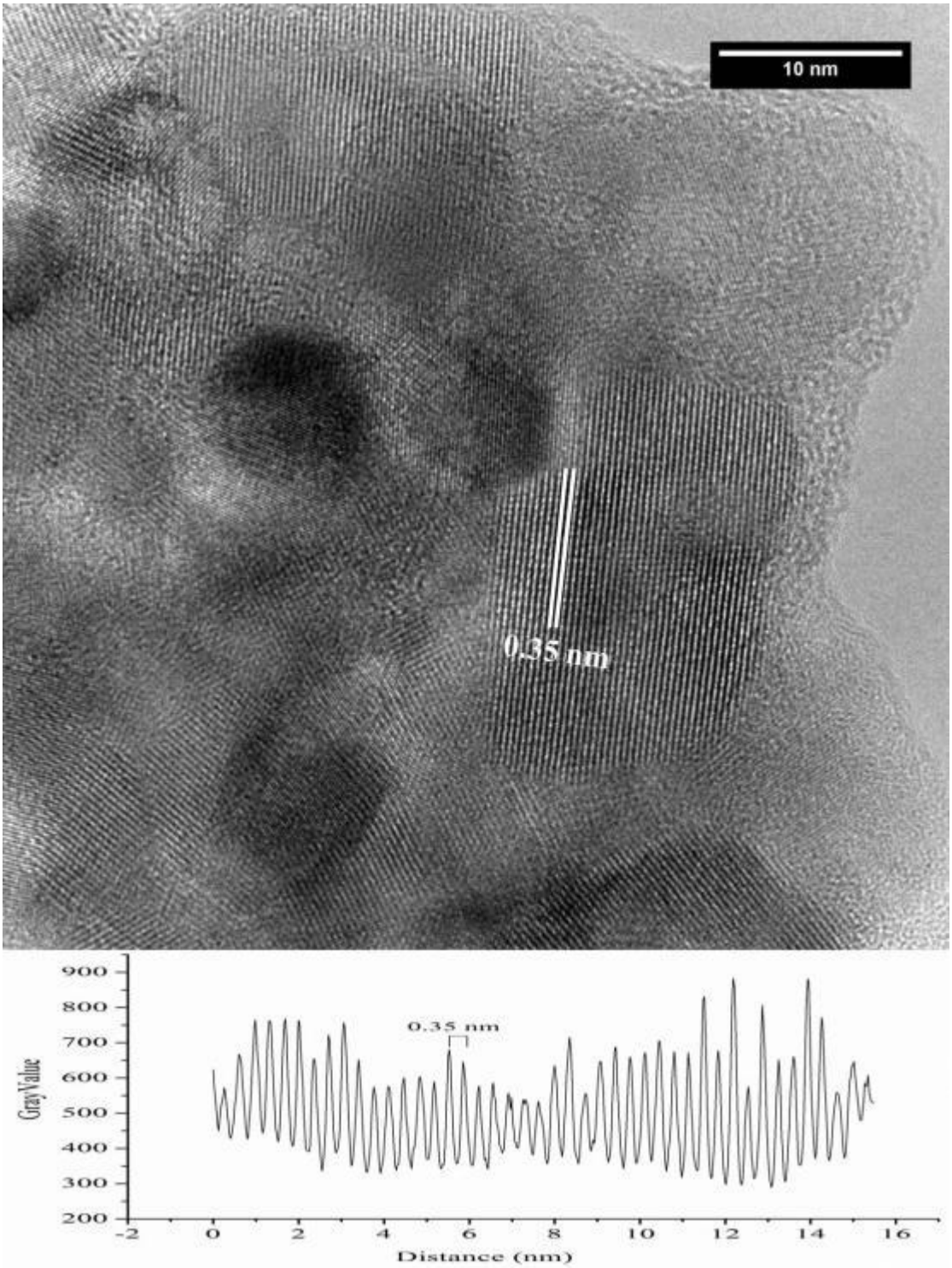

Figure 7.10: (PEG 1000 g/mol). Anatase crystallites measuring between 9 – 12 nm. The line profile of the large crystal on the right of the image confirms the presence of anatase as the lattice spacing measures 0.35 nm. This is consistent for anatase in the (1 0 1) orientation[5].

7.2.2 Comparison of the Effects of Citric Acid

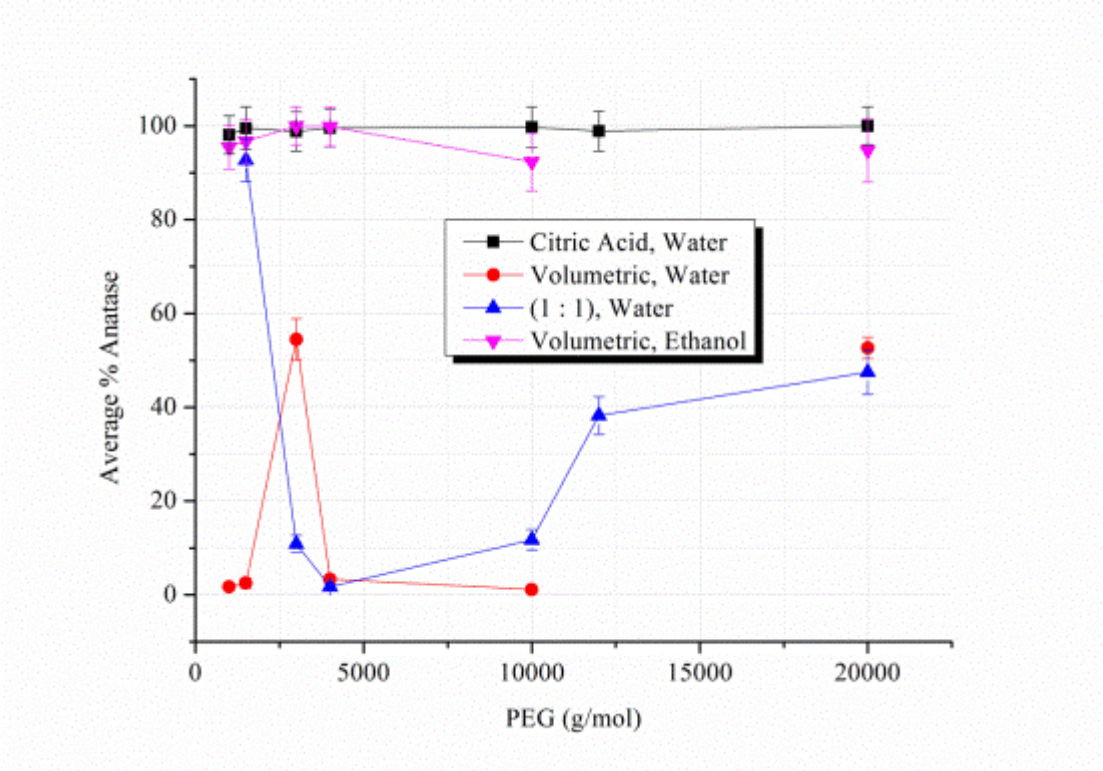

Figure 7.11: Variation in the amount of anatase formed in different experiments.

The results from this study suggest that citric acid favoured anatase formation. However, since this study was conducted using an equivalent stoichiometric amount of polymer, the effects of this type of polymer addition on the formed phase must be taken into account. To this end, figure 7.11 is presented. Figure 7.11 compares the amount of anatase formed as a function of increasing PEG molecular weight using different types of polymer addition. Data for (Volumetric, Water) and (Volumetric, Ethanol) PEG addition was obtained from chapter 5. Data for ((1 : 1), Water) PEG addition was obtained from chapter 8. Though it is unusual to present data that is only to be discussed in the next chapter, it is necessary to included it here so that the effects of stoichiometric PEG addition can be identified and the effects of citric acid isolated. A detailed discussion on stoichiometric PEG addition will follow in chapter 8. Only samples that were synthesised using the same PEG molecular weights across different experiments were included in figure 7.11.

Clearly, in the absence of citric acid, stoichiometric and volumetric addition of PEG in water containing HNO_3 caused the amount of anatase formed to fluctuate as a function of increasing PEG molecular weight. The largest mass percentage of anatase

formed using volumetric addition in water containing HNO_3 equalled 54.5% and was generated from the sample synthesised using PEG 3000 g/mol. PEG 1500 g/mol generated the largest mass percentage of anatase using stoichiometric addition in water containing HNO_3 (92.6%). The average amount of anatase formed using the volumetric and stoichiometric addition of PEG in water containing HNO_3 across all samples represented in figure 7.11 equalled 19.3% and 33.8% respectively. This was in contrast to the average amount of anatase formed across all samples using citric acid (99.2%). Evidently, volumetric and stoichiometric PEG additions in water containing HNO_3 were biased toward rutile formation.

The bias toward rutile formation using volumetric addition of PEG in water containing HNO_3 was attributed to three factors:

1) Maintenance of PEG structural integrity through non-sterically inhibited hydrogen bonds between water and PEG chains – this reduced PEG conformation during heating.

2) Poor stabilisation of the nucleated anatase phase by small matrix components remaining after the formation of hydroxylated species – encouraging rutile nucleation.

3) Conventional heating induced chain cleavage at a range of different points along the PEG chains forming reaction chambers of various sizes.

The bias toward rutile formation using (1 : 1) stoichiometric addition of PEG in water containing HNO_3 was explained by considering the modification to the abovementioned third factor by the amount of polymer added. Since the amount of polymer added increased with increasing PEG chain length, reaction chamber stability varied with chain length. Smaller, more stable chambers stabilised anatase. Slightly larger, yet stable chambers allowed rutile to nucleate. As the reaction chambers increased in size with increasing PEG chain length, they became unstable and formed many smaller chambers. The volume of long chain PEG provided sufficient steric stabilisation for the nucleated anatase phase.

The results obtained using citric acid best approximate those obtained using volumetric addition of PEG in ethanol. Near phase pure anatase was formed independent of the PEG chain length used in the synthesis involving ethanol. The result was rationalised by considering the steric protection effect of anatase

crystallites afforded by larger remaining reaction components in ethanol than in water. Additionally, the structural integrity of PEG chains were reduced on account of greater steric hindrance impeding hydrogen bonding.

In this study, reaction chambers dependent on chain length likely formed as described above for the (1 : 1) stoichiometric synthesis. However, the system produced nearly phase pure anatase regardless of the PEG chain length used. Therefore, it can be concluded that the amount of polymer added in this study had little bearing on the amount of anatase formed. Anatase production was mainly dependent on the presence of citric acid. Since $TiCl_4$ was added to water containing citric acid, metal-hydroxyl complexes likely formed between Ti^+ ions and the OH^- groups from citric acid. The large remaining matrix components sterically stabilised the nucleated anatase phase and inhibited its transformation into rutile. The citric acid structure suggests that it can better support the structural integrity of PEG chains via hydrogen bonding. This serves to render the PEG chains less likely to conform to the changing conditions during heating and hence favour rutile formation. However, since anatase was the major phase formed, crystallite capping and protection is a greater determinant of phase formation than PEG structure stabilisation.

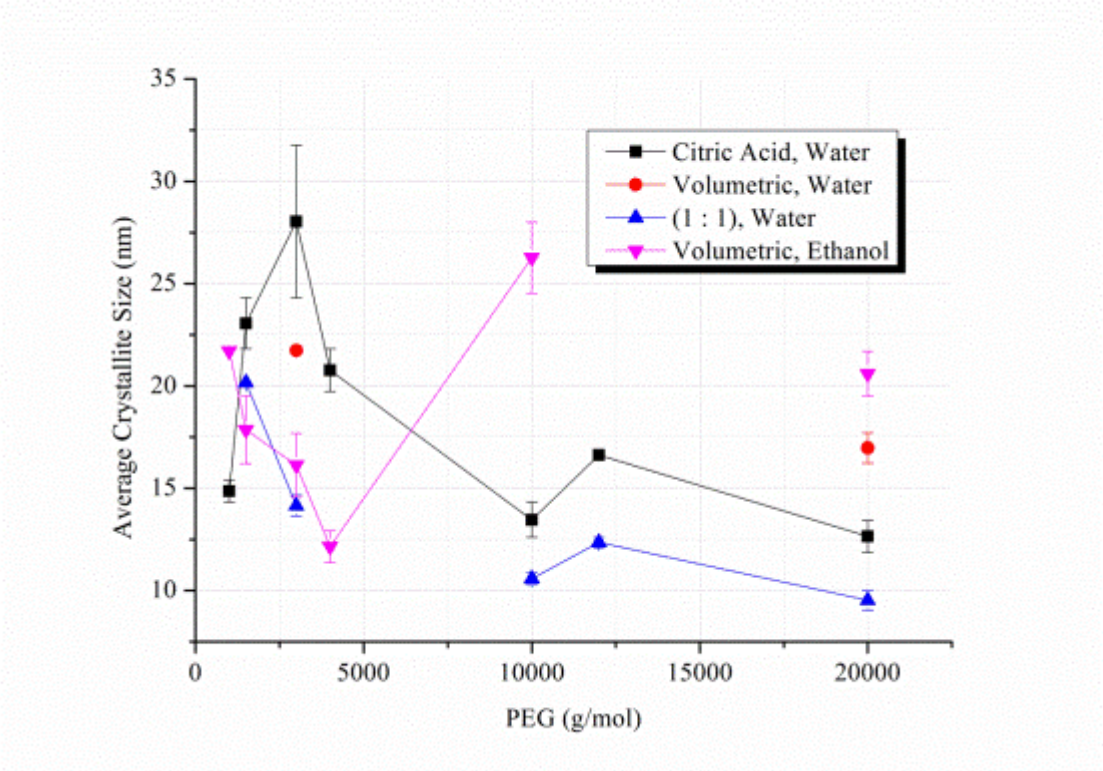

Figure 7.12: Variation anatase crystallite size formed in different experiments.

Figure 7.12 contains anatase crystallite size data produced from different experiments, and was constructed as described for figure 7.11. Data reflects samples post-calcination. The variation between the various systems suggests that the quantity of polymer in the reaction matrix has a significant bearing on crystallite size. For the citric acid and ((1 : 1), water) synthesis, crystallite size data appeared to be correlated for long chain polymers. This can be rationalised considering that the citric acid synthesis also employed the use of PEG in a (1 : 1) ratio. Absolute crystallite size was determined by the reaction components and conditions.

7.3 Conclusions

All samples synthesised using citric acid in water produced either phase pure or near phase pure anatase, independent of the polymer chain length used in the reaction.

PXRD patterns revealed a decrease in signal to noise ratio of pre-calcined samples synthesised using long chain PEG. This phenomenon was explained by considering that ignition was inadequate at removing all polymer fragments when long chain polymers were used. Calcination served to remove all polymer traces and hence increased the signal to noise ratio of all peaks.

The quantity of PEG used in this experiment had little or no bearing on the amount of anatase produced. Anatase formation was dependent on the presence of citric acid. The quantity and chain length of the polymer used in the reaction determined the anatase crystallite size formed.

As previously concluded by Franklyn *et al.*, citric acid protects and stabilises the anatase surface, inhibiting its transformation into rutile[3]. Additionally, anatase crystallites smaller than 14 nm are more thermodynamically stable than rutile crystallites[4]. Most anatase crystallites formed pre-calcination in this study were smaller than 10 nm. Therefore, rutile transformation is likely inhibited by the protecting action of citric acid reducing the propensity of anatase crystallites to coarsen.

This experiment has strengthened the hypothesis that polymer chains coordinate to metal-hydroxyl complexes formed between the metal ion precursor and solvent components. Additionally, the mechanism of rein-gel nanoparticle formation is modified to place greater emphasis on the protection of crystallites than on the stabilisation of the PEG structure via hydrogen bonding.

7.4 References

1. Yin, H. *et al.* Novel synthesis of phase-pure nano-particulate anatase and rutile TiO2 using TiCl4 aqueous solutions. *Journal of Materials Chemistry* **12,** 378 – 383 (2002).

2. Guo, Z., Li, C., Lu, S., Pan, Y. & Gu, H. Citrate/F- assisted phase control synthesis of TiO2 nanostructures and their photocatalytic properties. *RSC Advances* **5,** 74230 – 74237 (2015).

3. Franklyn, P. J., Levendis, D. C., Coville, N. J. & Maaza, M. Phase Transformation of Hydrothermally Synthesized Nanoparticle TiO2: from Anatase to Rutile Nanorods. *South African Journal of Chemistry* **60,** 71 – 75 (2007).

4. Zhang, H. & Banfield, J. F. Thermodynamic analysis of phase stability of nanocrystalline titania. *Journal of Materials Chemistry* **8,** 2073 – 2076 (1998).

5. Mao, Y., Kanungo, M., Hemraj-Benny, T. & Wong, S. S. Synthesis and Growth Mechanism of Titanate and Titania One-Dimensional Nanostructures Self-Assembled into Hollow Micrometer-Scale Spherical Aggregates. *Journal of Physical Chemistry B* **110,** 702 – 710 (2006).

Chapter 8: Effects of Polyethylene Glycol Molecular Weight and Stoichiometry on Titania Polymorph and Crystallite Size Formation

The effects of polyethylene glycol (PEG) molecular weight and stoichiometry on the formed phase and crystallite size of titanium dioxide were investigated in this study. Stoichiometric effects were established by varying the ratio of polymer chains to $TiCl_4$. Two ratios were selected, Ti^+ : PEG = (1 : 1) and (1 : 0.5), and monitored across a range of polymer molecular weights ranging from 200 – 20000 g/mol. PEG 4000, 6000, and 12000 g/mol were selected for synthesis in a Ti^+ : PEG ratio of (1 : 0.1).

The polymer molecular weight was used to determine the stoichiometric equivalent amount of PEG to be added. Therefore, the mass of PEG added to satisfy stoichiometry increased with increasing molecular weight. Thus, the ratio of metal ions to the number of PEG chains of different molecular weights remained the same. This is in contrast to the volumetric addition of PEG method (chapters 5 and 6). Equivalent volumetric addition of PEG required a decrease in the number of PEG chains added in an inversely proportional way, to the PEG molecular weight.

8.1 Experimental Procedure

Due to the variation in PEG chain length, (from 200 – 20000 g/mol), three batch solutions of metal ions were created – that would be further divided. This was in an attempt to optimise the amount of PEG used for a replicate synthesis and minimise wastage while concurrently maintaining the chosen Ti^+ : PEG ratio. The experiment consisted of 5 parts with water containing HNO_3 used as the solitary solvent for all experiments:

- addition of Ti ions to PEG in a (1 : 1) ratio
- addition of Ti ions to PEG in a (1 : 0.5) ratio
- addition of Ti ions to PEG in a (1 : 0.1) ratio

- heat treatments
- characterisation

8.1.1 Addition of Ti ions to PEG in a (1 : 1) Ratio

Three batch solutions were synthesised. For the first batch solution 7.0 ml (0.064 mols) $TiCl_4$ (> 99%, Merck) was added into excess distilled water (168.0 ml) containing 14.0 ml of 55% HNO_3. Homogeneity was achieved by stirring using a Teflon coated magnetic stirrer bar. The solution was decanted equally into two separate beakers, such that each beaker contained 3.5 ml (0.032 mols) $TiCl_4$ Stoichiometric amounts of PEG 200 and 400 g/mol (as given in table 8.1) were added to each beaker respectively.

The second batch solution was synthesised by adding 2.0 ml (0.018 mols) $TiCl_4$ (> 99%, Merck) into excess distilled water (48.0 ml) containing 4.0 ml of 55% HNO_3. The solution was stirred to homogeneity using a Teflon coated magnetic stirrer bar. Thereafter, the solution was divided equally into 4 beakers such that each beaker contained 0.5 ml (0.0045 mols) $TiCl_4$. Stoichiometric amounts of PEG 1500, 3000, 4000, and 6000 g/mol (as given in table 8.1) were added into each beaker respectively.

The final batch solution was synthesised as follows: 0.75 ml (0.0068 mols) $TiCl_4$ (> 99%, Merck) was introduced into 18.0 ml distilled H_2O containing 1.5 ml of 55% HNO_3. After attaining homogeneity, the solution was divided equally into 3 separate beakers such that each beaker contained 0.25 ml (0.0023 mols) $TiCl_4$. Stoichiometric amount of PEG 10000, 12000, and 20000 g/mol (as given in table 8.1) were added to each beaker respectively.

Table 8.1: Quantities of Ti ions and PEG added to achieve a (1 : 1) stoichiometry.

Batch number	Quantity of $TiCl_4$ added (mols)	PEG molecular weight used (g/mol)	Quantity of PEG (mols) required	Mass of PEG added (g)
1	0.032	200	0.032	6.3692
	0.032	400	0.032	12.7389
2	0.0045	1500	0.0045	6.8242
	0.0045	3000	0.0045	13.6484
	0.0045	4000	0.0045	18.1979
	0.0045	6000	0.0045	27.2969
3	0.0023	10000	0.0023	22.7474
	0.0023	12000	0.0023	27.2968
	0.0023	20000	0.0023	45.4948

8.1.2 Addition of Ti ions to PEG in a (1 : 0.5) Ratio

For the first batch solution, 7.0 ml (0.064 mols) $TiCl_4$ (> 99%, Merck) was introduced into excess distilled water (168.0 ml) containing 14.0 ml of 55% HNO_3. After stirring induced homogeneity was achieved, the solution was decanted equally into 2 beakers such that each beaker contained 3.5 ml of (0.032 mols) $TiCl_4$. Stoichiometric amounts of PEG 200 and 400 g/mol (as given in table 8.2) were added into each beaker respectively.

The second batch solution was synthesised as follows: 4.0 ml (0.036 mols) $TiCl_4$ (> 99%, Merck) was added to excess distilled water (96.0 ml) containing 8.0 ml of 55% HNO_3. The solution was made homogeneous as described above. Thereafter, the solution was decanted equally into 4 separate beakers, such that each beaker contained 1.0 ml (0.0091 mols) $TiCl_4$. Stoichiometric amounts of PEG 1500, 3000, 4000, and 6000 g/mol (as given in table 8.2) were added into each beaker respectively.

The last batch solution was synthesised as follows: 1.5 ml (0.014 mols) $TiCl_4$ was introduced into excess distilled water (36.0 ml) containing 3.0 ml of 55% HNO_3. The solution was homogenised as described above, and then divided equally into 3 beakers

such that each beaker contained 0.5 ml (0.0045 mols) $TiCl_4$. Stoichiometric amounts of PEG 10000, 12000, and 20000 g/mol (as given in table 8.2) were added into each beaker respectively.

Table 8.2: Quantities of Ti ions and PEG added to achieve a (1 : 0.5) stoichiometry.

Batch number	Quantity of $TiCl_4$ added (mols)	PEG molecular weight used (g/mol)	Quantity of PEG (mols) required	Mass of PEG added (g)
1	0.032	200	0.016	3.1846
	0.032	400	0.016	6.3692
2	0.0091	1500	0.0046	6.8242
	0.0091	3000	0.0046	13.6484
	0.0091	4000	0.0046	18.1979
	0.0091	6000	0.0046	27.2969
3	0.0045	10000	0.0023	22.7474
	0.0045	12000	0.0023	27.2969
	0.0045	20000	0.0023	45.4948

8.1.3 Addition of Ti ions to PEG in a (1 : 0.1) Ratio

A single batch solution was synthesised by adding 15.0 ml (0.136 mols) $TiCl_4$ (> 99%, Merck) to excess distilled H_2O (120.0 ml) containing 10.0 ml of 55% HNO_3. The resulting solution was stirred until homogenous. Thereafter, the solution was divided equally into 3 separate beakers such that each beaker contained 5.0 ml (0.045 mols) $TiCl_4$. Stoichiometric amounts of PEG 4000, 6000, and 12000 g/mol (as given in table 8.3) were added to each beaker respectively.

Table 8.3: Quantities of Ti ions and PEG added to achieve a (1 : 0.1) stoichiometry.

Batch number	Quantity of $TiCl_4$ added (mols)	PEG molecular weight used (g/mol)	Quantity of PEG (mols) required	Mass of PEG added (g)
1	0.045	4000	0.0045	18.1979
	0.045	6000	0.0045	27.2969
	0.045	12000	0.0045	54.5938

8.1.4 Heat Treatments

All mixtures were heated as necessary and stirred using a glass rod until homogenous. Mixtures synthesised using a Ti^+ : PEG = (1 : 1) ratio required higher temperatures to enable complete homogenisation to occur. Thereafter, all 21 gels were placed in a fume hood ~ 30 cm under two 200 W infrared light bulbs for a fortnight. Following complete solvent evaporation from all gels, the hardened resins were divided equally. This division allowed for the introduction of replicate samples for the imminent heat treatment.

A sand bath was chosen to effect uniform heat transfer. The sand bath was created as described previously (chapters 5). Resins were placed into alumina glazed crucibles that were then placed into the sand bath. The conventional heating method (described in chapter 5) was employed to heat the samples, with the exception that a Bunsen burner was used to ignite the samples after they had reached their flash point.

Following complete pyrolysis, samples presented a black, flaky or granular appearance, due to the presence of carbon residue. All samples were divided into 2 halves – one half to be analysed before calcination and the other half to be analysed after calcination. Calcination was effected in a muffle furnace at 500 °C (at ~ 620 mm Hg) for 1 hour.

8.1.5 Characterisation

PXRD data was obtained using either the Bruker D2 Phaser or the Siemens D5000 diffractometer. The setup of the D2 Phaser has been described in chapter 5, with the exception that Co Kα radiation (λ = 1.7903 Å) was used. Samples were analysed

between 20° and 60° 2θ in 0.023 increments counting for 1 second per step. The setup of the Siemens D5000 has been described in chapter 6. Two HRTEMs were employed in this study: a field emission FEI Tecnai F20 and a JEOL 3011.

8.2 Results and Discussion

8.2.1 Addition of Ti ions to PEG in a (1 : 1) Ratio

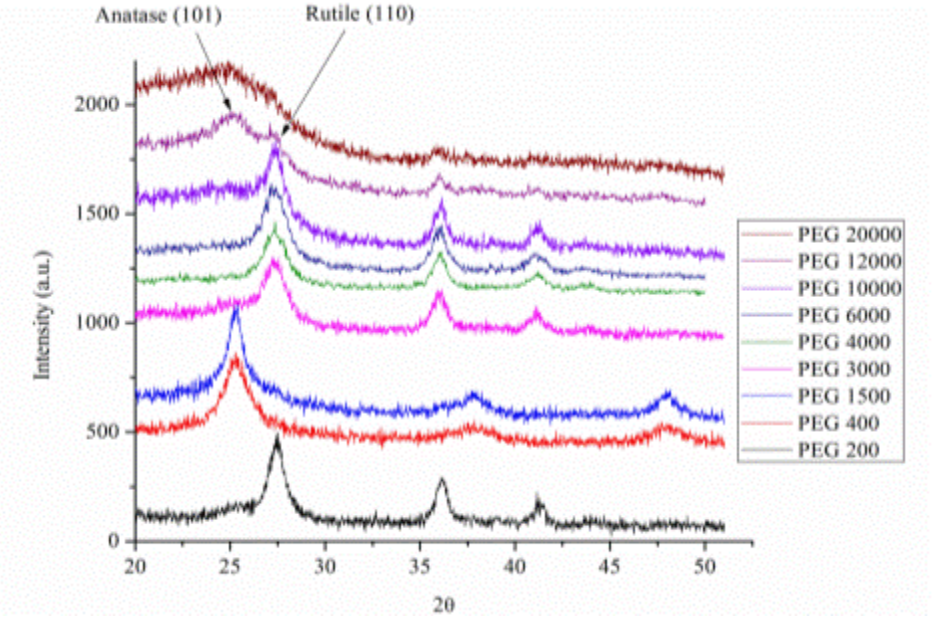

Figure 8.1: PXRD patterns of samples synthesised in a (1 : 1) ratio pre-calcination.

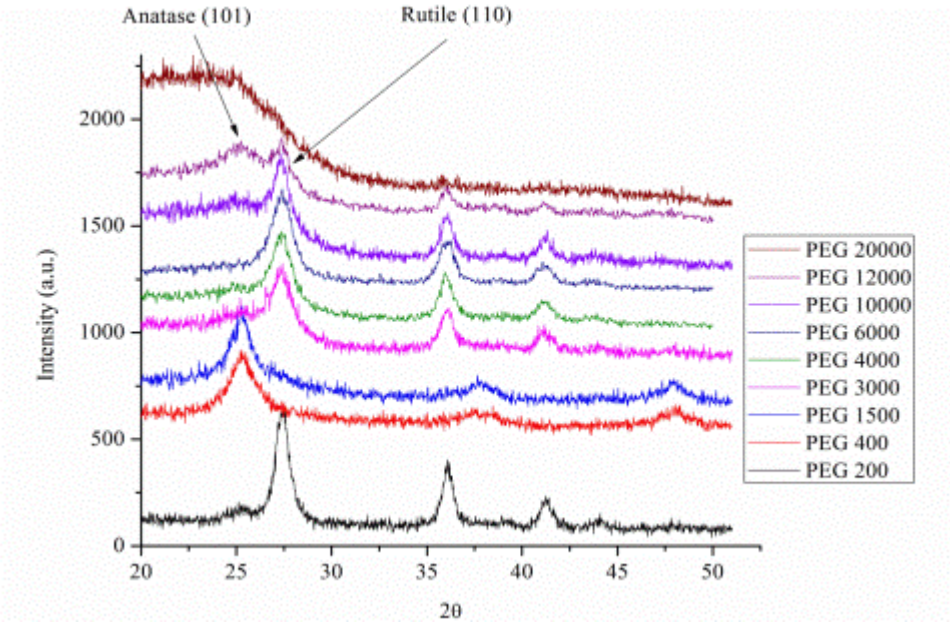

Figure 8.2: PXRD patterns of replicate samples synthesised in a (1 : 1) ratio pre-calcination.

Figures 8.1 and 8.2 show the diffraction patterns collected for all samples synthesised in a (1 : 1) ratio. An interesting observation from the patterns is that nearly all samples contain mostly anatase or rutile. Samples synthesised from PEG 12000 g/mol appear to be the only samples to contain a significant mixture of both phases.

Peak intensity decreased as PEG molecular weight increased to the point that no distinct peaks are discernible from samples synthesised using PEG 20000 g/mol. A plausible reason for this observation is that the large quantities of longer chain polymers were not fully removed during the pyrolysis process. It is also possible that longer chain polymers left behind large amounts of carbon residue on the surface of TiO_2 crystallites. This could have inhibited X-ray penetration and hence no peaks were observed in the pattern.

Misalignment of peaks suggests that carbon may be straining the titania lattice by imparting non-uniform strain. Peak broadness is an indication of the formation of nano anatase and rutile. Initial observations of the original data set with its replicate suggest good data reproducibility.

Calcination served to improve the signal to noise ratio of all peaks, as evidenced in figures 8.3 and 8.4. This effect could be caused by the presence of polymer fragments in the sample after ignition. Calcination had the effect of removing residual carbon and hence improving the signal to noise ratio. Sharper peaks in these figures indicated crystallite growth. After calcination, samples synthesised from PEG 200, 3000, 10000, 12000, and 20000 g/mol appear to contain a more significant mixture of anatase and rutile. This observation suggests that large amounts of PEG in the sample prior to ignition resulted in the formation of amorphous TiO_2. Calcination caused the amorphous particles to crystallise into anatase. It is unknown why this effect was not observed in samples synthesised from PEG 4000 and 6000 g/mol.

Post-calcination peak intensity was low for samples synthesised from longer chain PEG. This is likely due to the calcination time being insufficient to completely remove all traces of carbon prior to analysis. For the sake of consistency and to not impact the post-calcination crystallite size, all calcination times and temperatures were kept consistent for all samples. The data generated from all samples shows good reproducibility with their respective replicates.

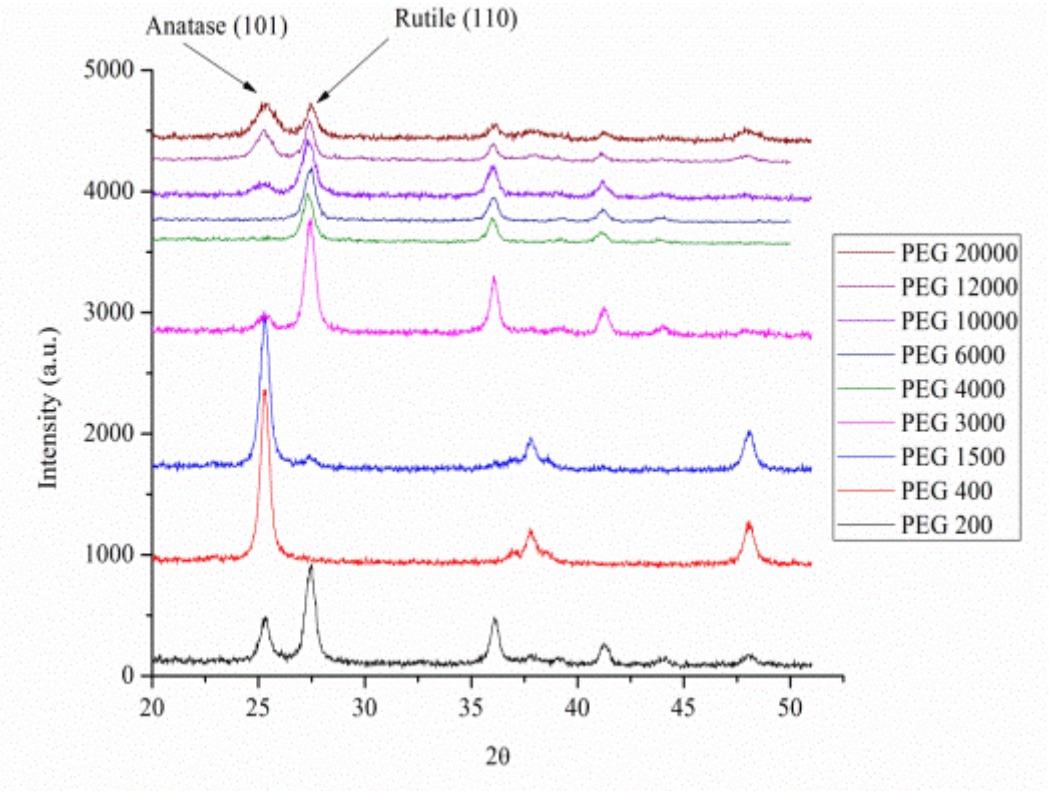

Figure 8.3: PXRD patterns of calcined samples synthesised in a (1 : 1) ratio.

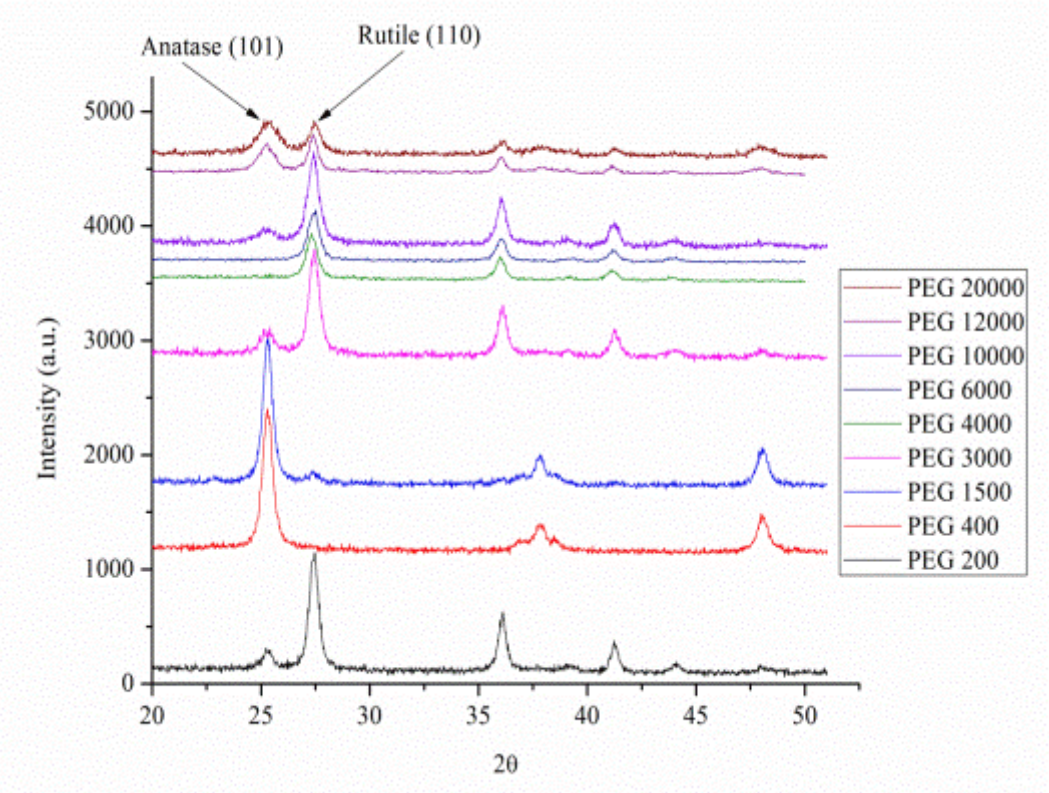

Figure 8.4: PXRD patterns of replicate calcined samples synthesised in a (1 : 1) ratio.

Figure 8.5 depicts the change in the amount of rutile formed as a function of increasing PEG molecular weight, synthesised in a (1 : 1) ratio, before and after calcination. No comparison for samples synthesised from PEG 20000 g/mol could be made as no peak was discernible from the pattern corresponding to these samples pre-calcination.

Before calcination, PEG 400 and 1500 g/mol resulted in the formation of the least amount of rutile (5.3% and 9.9% respectively). PEG 12000 g/mol produced 40.6% rutile by mass. The average amount of rutile produced across all samples before calcination was 61.1%, suggesting that rutile was the favoured phase. This was not an unexpected result as chapters 5 and 6 showed that water containing HNO_3 favoured the formation of rutile. The effects of stoichiometric addition of PEG with volumetric addition of PEG will be discussed later. As PEG molecular weight increased, the amount of rutile decreased, then increased, and finally decreased.

After calcination, the amount of rutile changed as a function of increasing PEG molecular weight in a similar manner to that witnessed pre-calcination. The content of rutile in samples synthesised from short chain PEG (200, 400, and 1500 g/mol) appears to have decreased after calcination. The data generated from these samples are sufficiently erratic to suggest that the amount of rutile synthesised after calcination could be greater than that synthesised before calcination.

The precision in the data obtained from samples generated from longer chain PEG shows an expected increase in the amount of rutile formed after calcination. After calcination, the average amount of rutile formed across all samples equalled 64.3%. This represents a 5.2% overall increase in the amount of rutile formed after calcination. PEG 20000 g/mol resulted in the formation of 52.5% $\pm$ 4.9% rutile after calcination. The overall increase in the amount of rutile formed post-calcination can be used to extrapolate a plausible value for the amount of rutile formed from PEG 20000 g/mol pre-calcination. Due to the nature of longer chain PEG, the data generated from these polymers are often erratic (as seen in chapters 5 and 6), therefore, the extrapolated value should be considered carefully, before being accepted as a true representation. Using this extrapolation technique, 49.9% of rutile was formed from PEG 20000 g/mol pre-calcination. Error bars were generated by adding 4% of the average amount of anatase formed to the standard deviation of the replicate analyses.

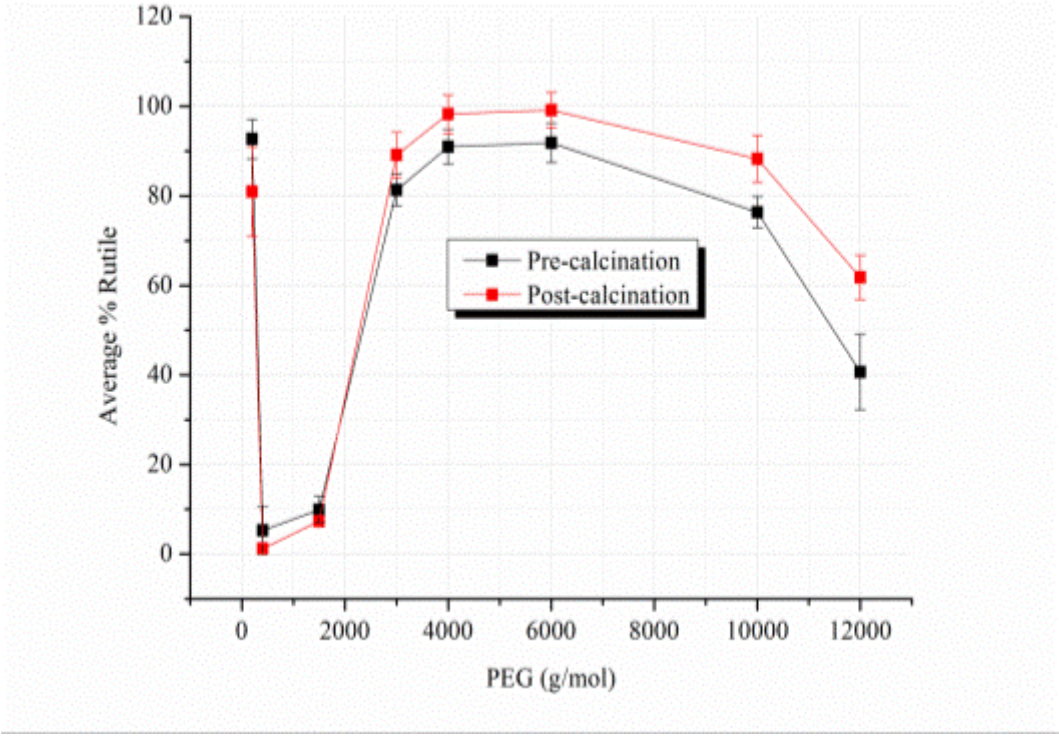

Figure 8.5: Average amount of rutile formed from a (1 : 1) ratio pre- and post-calcination.

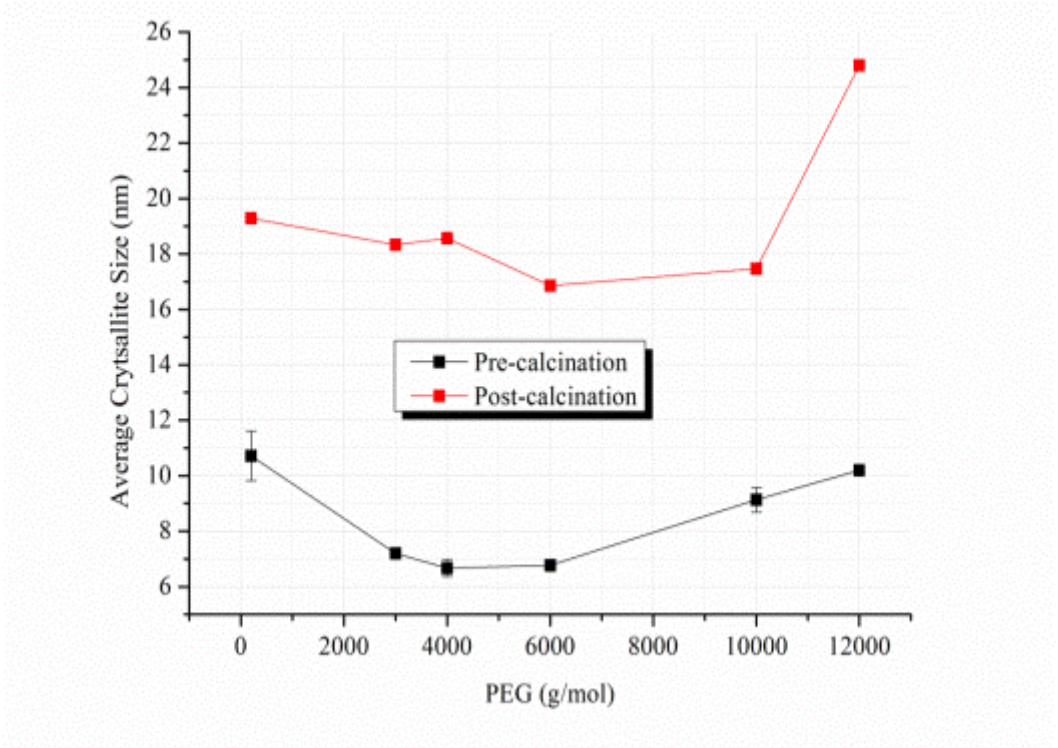

Figure 8.6: Average rutile crystallite size formed from a (1 : 1) ratio pre- and post-calcination.

Figure 8.6 shows the change in average rutile crystallite size as a function of increasing PEG molecular weight, pre- and post-calcination, synthesised in a (1 : 1) ratio. This figure does not contain any data pertaining to the size of rutile crystallites synthesised from PEG 400, 1500 or 20000 g/mol. Due to the small amount of rutile formed in PEG 400 and 1500 g/mol, accurate dimensional analyses of rutile crystallites could not be made. As described above, no data is available for samples generated from PEG 20000 g/mol.

Before calcination, PEG 3000, 4000, and 6000 g/mol resulted in the formation of the smallest rutile crystallites: 7.2 nm, 6.7 nm, and 6.8 nm respectively. PEG 200, 10000 and 20000 g/mol produced the largest rutile crystallites: 10.7 nm, 9.1 nm, and 10.2 nm respectively. The average rutile crystallite size produced across all samples measured 6.3 nm. The greatest error in the data was present for samples synthesised using PEG 200 g/mol: 0.9 nm. Error bars represent the standard deviation of the replicate synthesis.

After calcination, rutile crystallite size had increased in all samples. The average crystallite size across all samples measured 17.1 nm. This represented a crystallite size increase of 171% after calcination. It was previously shown (chapters 5 and 6) that calcination had a greater effect on crystallite size than phase transformation and hence this is an expected result. This is due to the calcination temperature (500 °C) being insufficient to encourage significant transformation[1]. Interestingly, crystallites formed from PEG 12000 g/mol post-calcination showed the most significant increase in size. PEG 20000 g/mol generated rutile crystallites that measured 18.4 nm after calcination. By extrapolation (as explained above), the average rutile crystallites obtained from PEG 20000 g/mol pre-calcination should measure 6.8 nm. This value should be considered carefully due to the erratic nature of long chain polymers.

The greatest error in the data was present for the samples synthesised from PEG 4000, 6000, and 12000 g/mol: 0.1 nm. Error bars were generated from the standard deviation of the replicate synthesis.

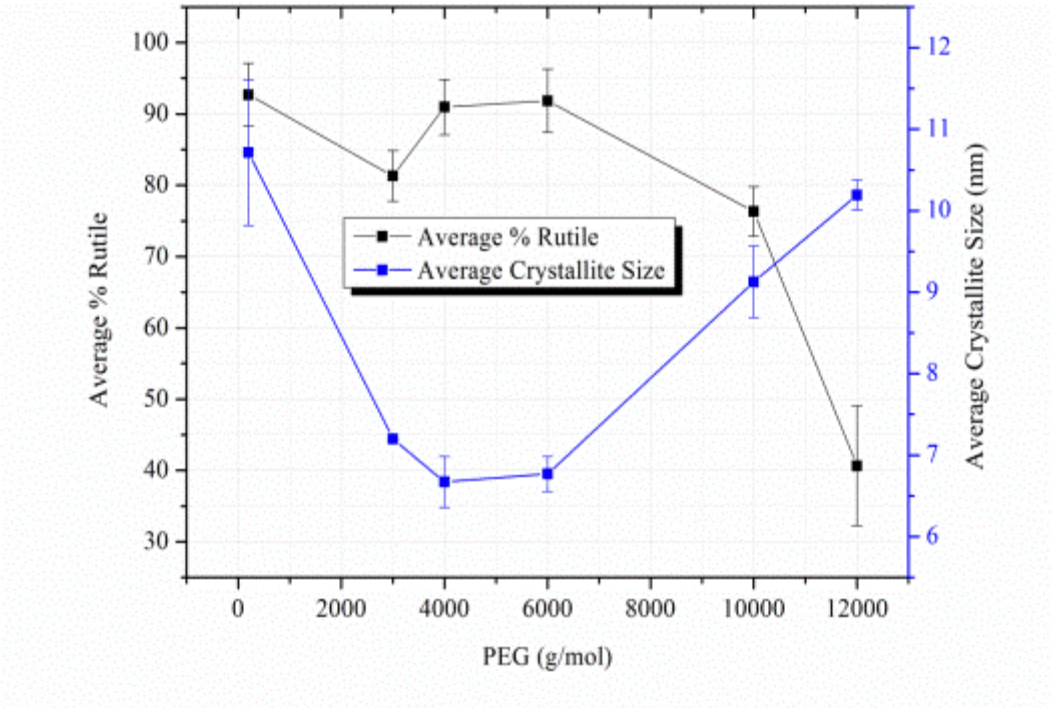

Figure 8.7: Average amount of rutile with associated crystallite size formed in a (1 : 1) synthesis pre-calcination.

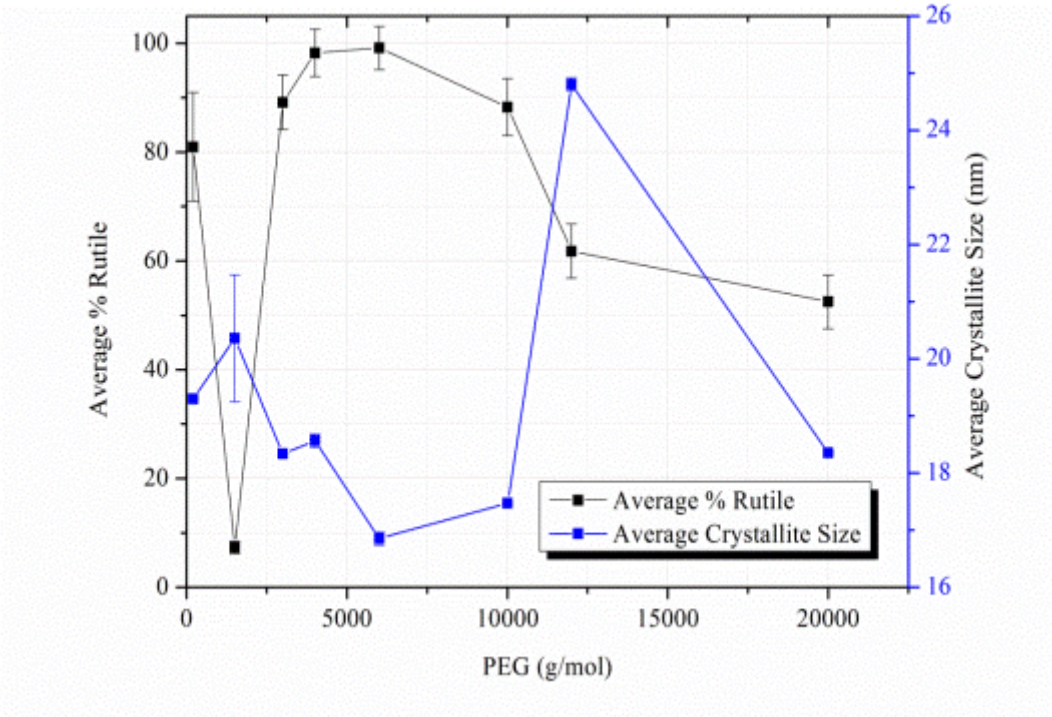

Figure 8.8: Average amount of rutile with associated crystallite size formed in a (1 : 1) synthesis post-calcination.

Figure 8.7 illustrates the inverse relationship between the amount of rutile formed and its respective crystallite size. As discussed previously, oriented attachment[2] and polymer reaction chambers may be responsible for this inverse relationship. This explanation is further strengthened by the fact that most rutile crystallites were smaller than 11 nm. Unlike for volumetric addition of PEG to Ti^{+} ions, stoichiometric addition does not produce a nearly identical inverse relationship for all PEG molecular weights. This is evidenced for samples synthesised from PEG 200 and 3000 g/mol.

Figure 8.8 shows that the imperfect inverse relationship between the amount of rutile produced and its respective crystallite size is maintained after calcination. This is mainly due to the near proportional increase in crystallite size post-calcination. All error bars are small enough for the inverse trend to exist at the maximum of each error. Therefore, the inverse relationship is a real, reproducible trend that is maintained under the conditions of stoichiometric addition of PEG.

Not currently shown is the amount of anatase and its respective crystallite size formed under the present synthesis conditions. Samples that contained sufficient anatase and rutile for a direct comparison to be made have been included in table 8.4. Table 8.4 contains post-calcination data.

Table 8.4: Average amount of anatase and respective crystallite size formed in a (1 : 1) synthesis, post-calcination.

PEG (g/mol)	Average %Anatase	Average anatase crystallite size (nm)	Average %Rutile	Average rutile crystallite size (nm)
200	19.1 ± 7.5	22.0 ± 0.7	80.9 ± 10.0	19.3 ± 0.1
1500	92.7 ± 4.6	20.2 ± 0.1	7.3 ± 1.1	20.4 ± 1.1
3000	10.9 ± 1.9	14.1 ± 0.5	89.1 ± 5.0	18.3 ± 0.1
10000	11.7 ± 2.2	10.6 ± 0.3	88.3 ± 5.3	17.5 ± 0.1
12000	38.2 ± 4.0	12.4 ± 0.3	61.8 ± 5.0	24.8 ± 0.1
20000	47.5 ± 4.7	9.5 ± 0.5	52.5 ± 4.9	18.4 ± 0.1

As given in table 8.5, for the same PEG molecular weight, rutile crystallites are generally larger than anatase crystallites. This effect is augmented at higher PEG molecular weights. An exception to this observation occurs for the sample synthesised from PEG 200 g/mol. The data suggests that low molecular weight PEG (200 and 400 g/mol) has a tendency of producing larger anatase crystallites, after calcination. This was rationalised (in chapter 6) in terms of smaller crystallites having a greater growth potential than larger crystallites, pre-calcination. It is likely that PEG 200 and 400 g/mol resulted in the formation of smaller anatase crystallites after pyrolysis.

Not shown in table 8.5 is the comparison of the amount of anatase and rutile crystallite size obtained pre-calcination. PEG 12000 g/mol was the only sample that allowed for accurate generation of crystallite size data pertaining to both phases. This sample produced anatase (1 0 1) crystallites measuring 5.1 nm and rutile (1 1 0) crystallites measuring 10.2 nm. Clearly rutile crystallites were twice as large as anatase. Interestingly, following calcination, both anatase and rutile crystallites increased in size by 143% (as evidenced in table 8.5).

Tables showing the amount of each phase and crystallite size obtained for each sample with averages and errors are given in appendix F.

HRTEM images corresponding to samples synthesised from PEG 6000 g/mol (figures 8.9 – 8.12) in a Ti^{+} : PEG ratio of (1 : 1) follow. PEG 6000 g/mol produced an average of 91.8% of rutile with an average (1 1 0) crystallite size of 6.8 nm.

The imperfection observed in the lattice in figure 8.10 is likely due to imperfect oriented attachment forming a twin boundary. Twin boundaries can serve as a nucleation site for other polymorphs[2] – as described in section 1.2.5.

Figure 8.11 illustrates a superstructure with distinct sections. The darker areas within the superstructure combined with the appearance of multiple sections imply that several seed sites exist within the assembly. These seeds nucleate several rutile nanorods. When the seed particles bond together, a dandelion is formed. It is not possible, at this stage, to comment on the order of the reactions responsible for the proposed mechanism of mesocrystal formation.

From the nanorods observed in figure 8.12, it is not possible to state whether the rods grow outward from a single seed particle, or whether multiple crystals undergo oriented attachment from a few seed anisotropic rutile crystals.

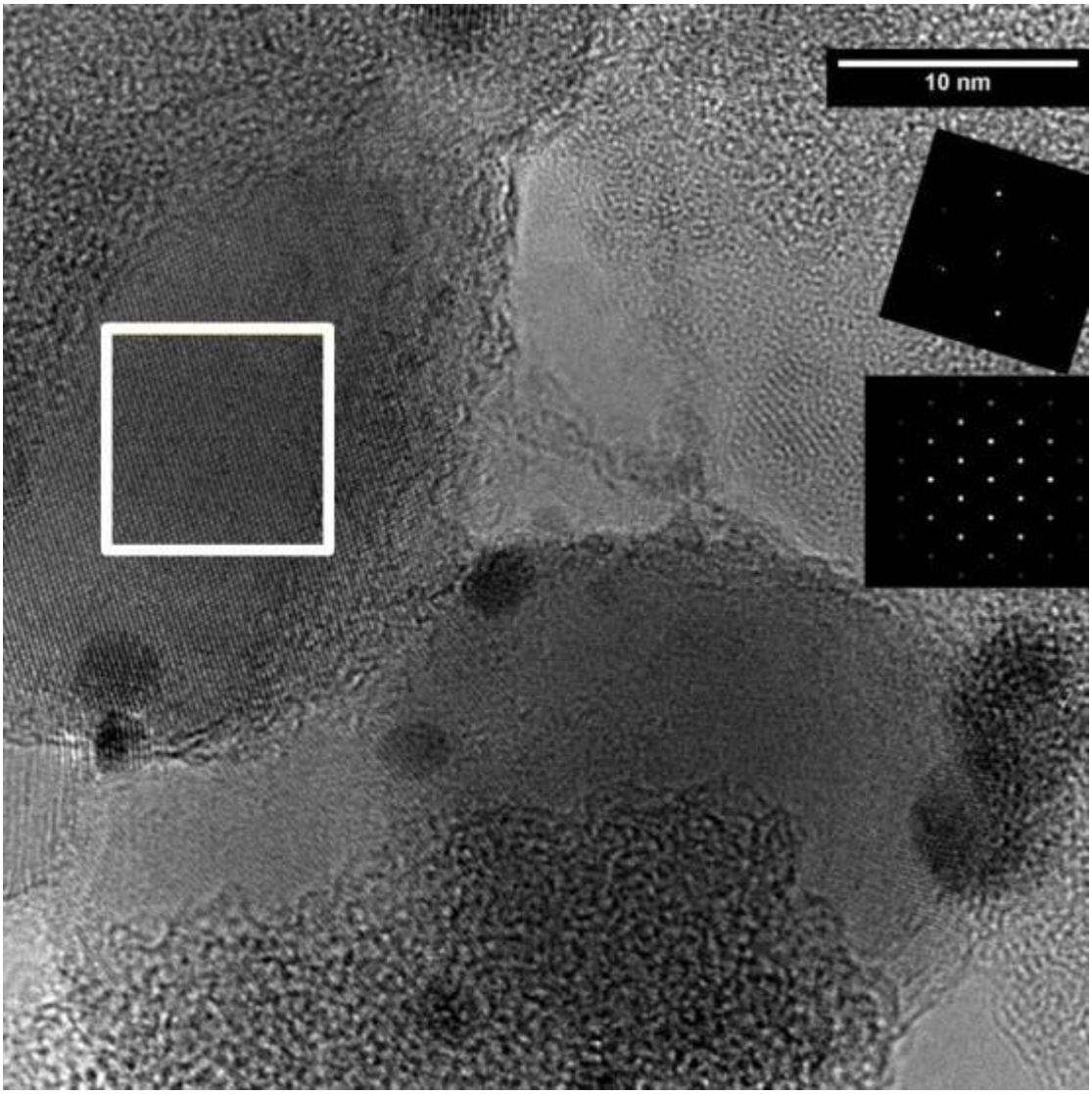

Figure 8.9: (PEG 6000 g/mol in a Ti^{+} : PEG ratio of (1 : 1)). This region of the sample showed a mixture of crystals of different sizes. Larger crystals measure ~ 25 – 30 nm. Smaller crystals measure ~ 2 – 7 nm. Also visible are large amounts of amorphous material that is most likely carbon. The insert compares the experimental and simulated FFT's (experimental FFT obtained from area delineated within the square). The selected crystal is rutile in the (0 1 0) or (1 0 0) orientation.

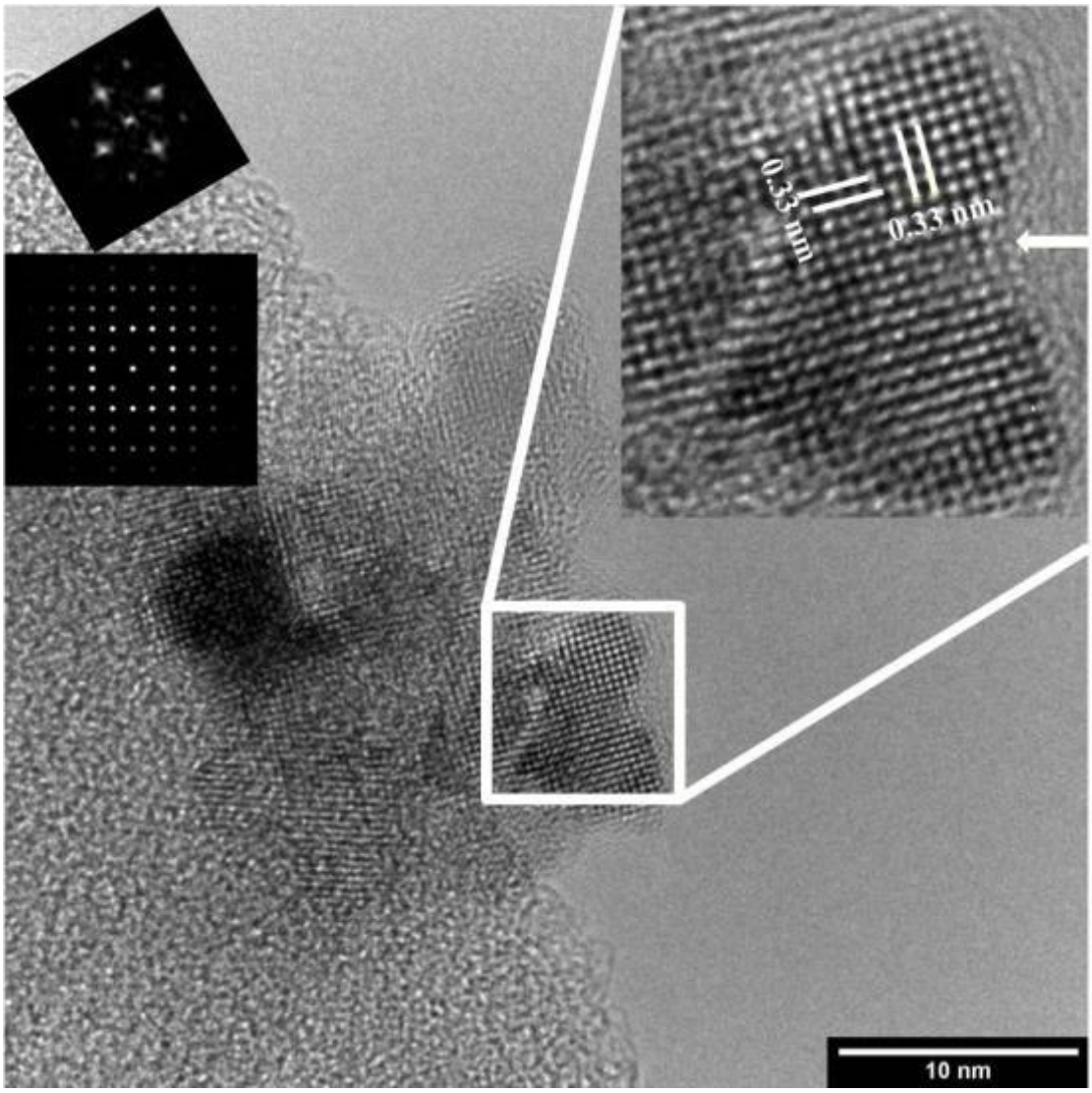

Figure 8.10: (PEG 6000 g/mol in a Ti^{+} : PEG ratio of (1 : 1)). Appearance of a twinned rutile crystal in the (0 0 1) orientation. This crystal measures approximately 10 nm across. The insert is a magnified version of the crystal showing a lattice spacing of 0.33 nm. The arrow indicates an imperfection in the lattice.

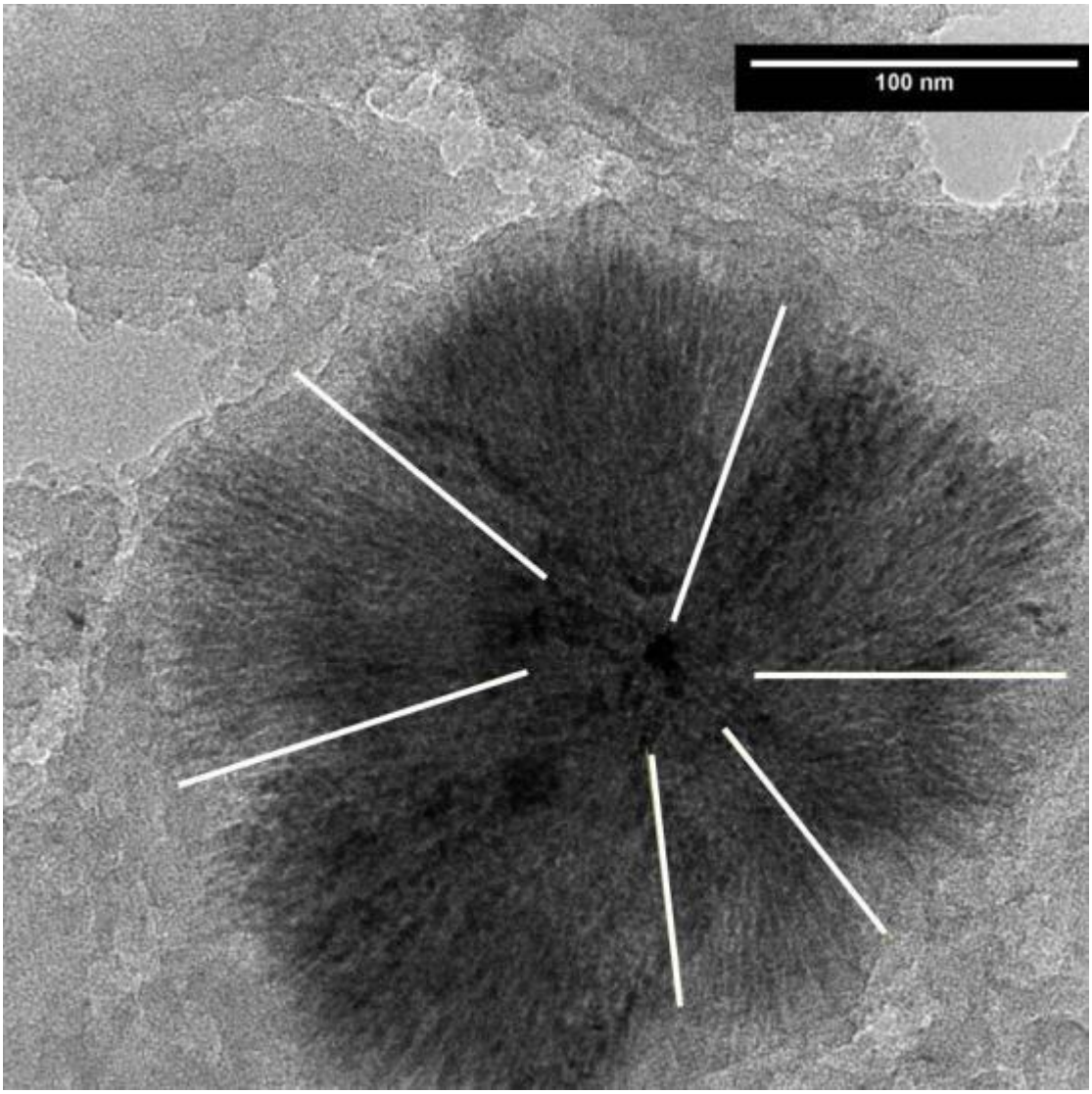

Figure 8.11: (PEG 6000 g/mol in a Ti^{+} : PEG ratio of (1 : 1)). In addition to forming small crystals, the sample synthesised from PEG 6000 also exhibited rutile mesocrystals. This mesocrystal measured approximately 270 nm end to end. It also appeared to consist of 6 distinct sections (separated by lines).

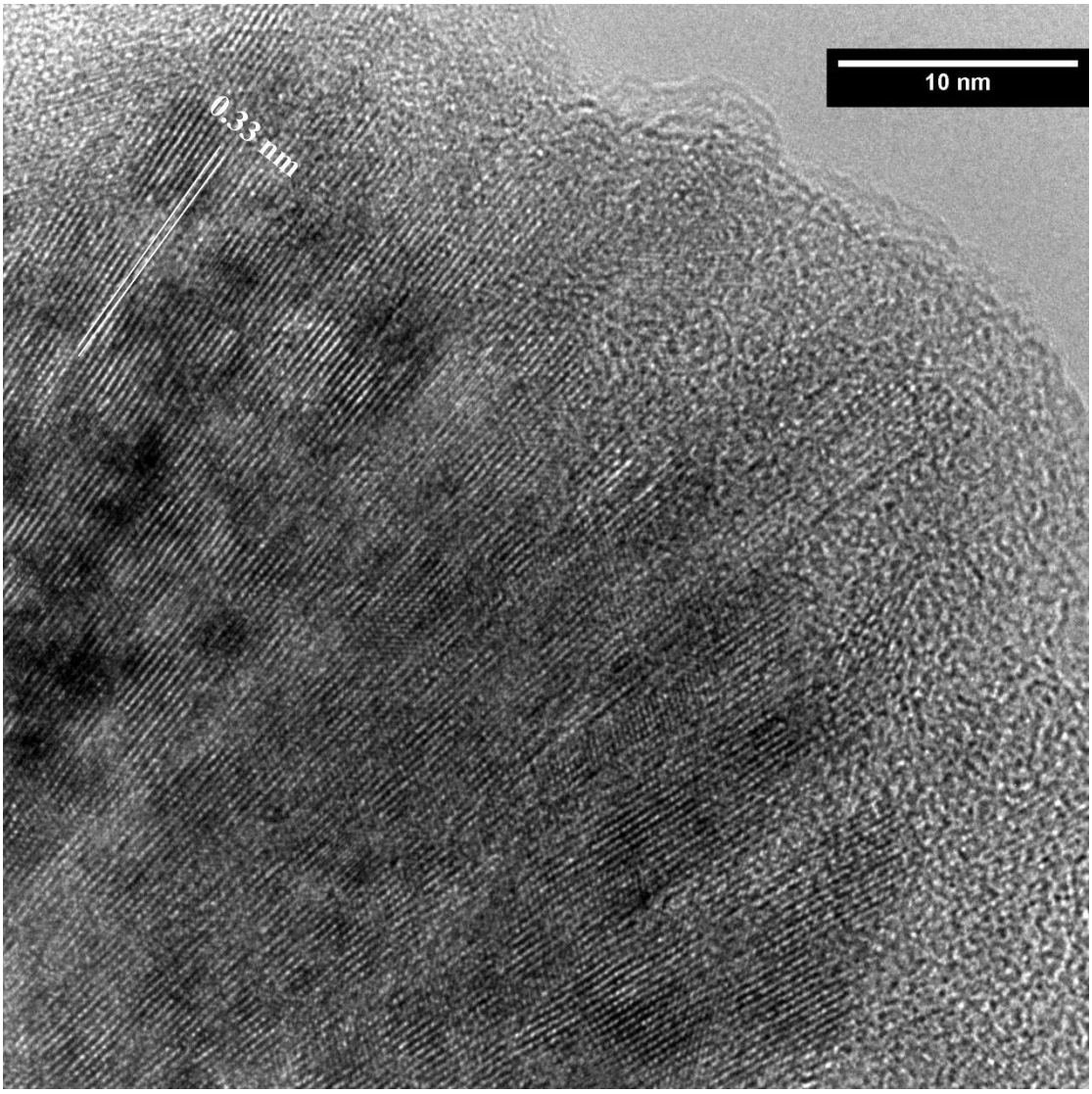

Figure 8.12: (PEG 6000 g/mol in a Ti^{+} : PEG ratio of (1 : 1)). A magnified portion of the rutile dandelion in figure 8.11. Rutile crystallites exhibit anisotropic growth to form nanorods. If the nanorods are assumed to be continuous particles, they measure approximately 50 nm from the bottom left corner of the image to the tips of the rods. The lattice spacing measures 0.33 nm. The amorphous content is part of the holey carbon film.

Samples synthesised using PEG 12000 g/mol in a Ti^{+} : PEG ratio of (1 : 1) (figures 8.13 – 8.16) resulted in the formation of an average of 40.6% rutile with an average (1 1 0) crystallite size of 10.2 nm. Anatase (1 0 1) crystallites measured an average of 5.1 nm. The high energy surface observed in figure 8.13 could nucleate anatase growth or rutile transformation – depending on post-synthesis conditions.

The information contained within figure 8.14 was insufficient to deduce the polymorph comprising the fragmented structure. Incomplete synthesis is likely responsible for the formation of the incomplete titania fragment. Ultra-sonication was shown to be unable to break superstructures[3].

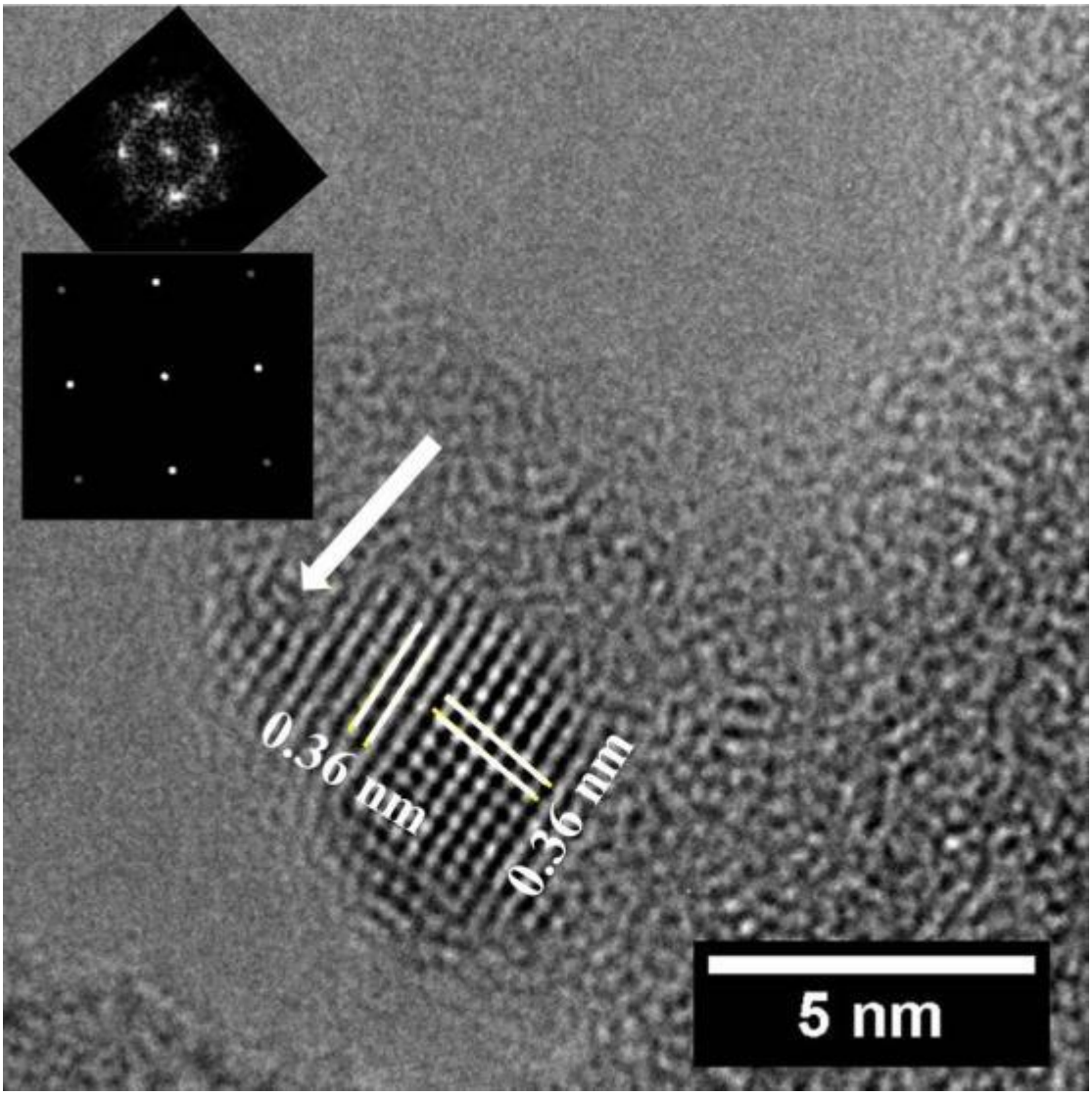

Figure 8.13: (PEG 12000 g/mol in a Ti^{+} : PEG ratio of (1 : 1)). Single crystal anatase in the (0 0 1) orientation. This crystal measures approximately 6.4 nm across with a lattice spacing of 0.36 nm. The arrow indicates a potential high energy surface.

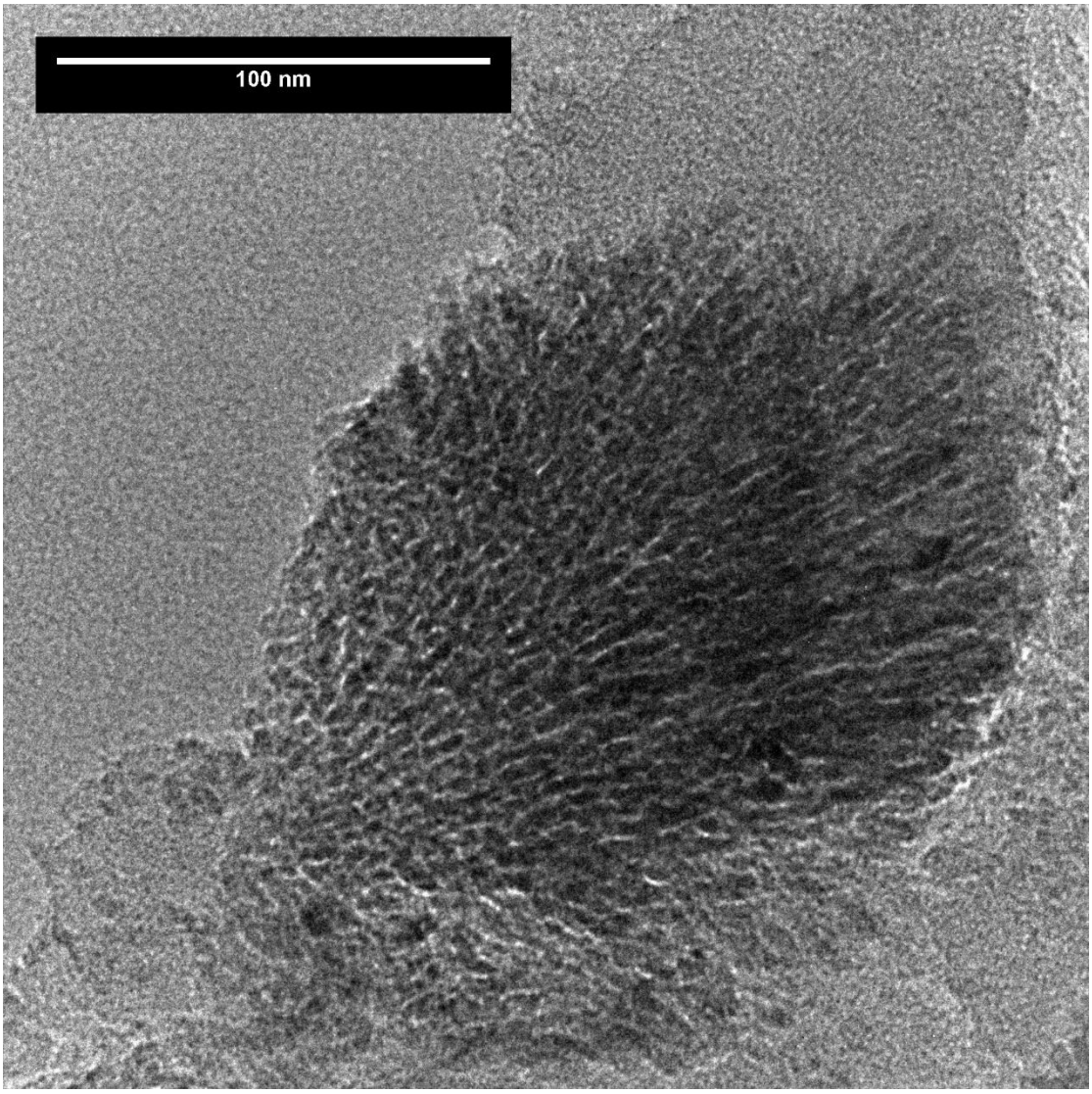

Figure 8.14: (PEG 12000 g/mol in a Ti^{+} : PEG ratio of (1 : 1)). Appearance of a fragment of assembled titania measuring 218 nm and 175 nm across the length and width respectively. This assembly resembles a fragment of the superstructure present in figure 8.11.

Figure 8.15 is a high magnification image of figure 8.14. From this image it is clear that the fragmented structure in figure 8.14 is composed of high aspect ratio rutile crystals. Interestingly, despite this sample producing 59.4% anatase, there was no evidence of anatase mesocrystals.

The structure depicted in figure 8.16 disintegrated under semi-condensed beam conditions. The presence of undecomposed polymer in this figure confirms the weak PXRD signal to noise ratio of samples synthesised using high molecular weight PEG.

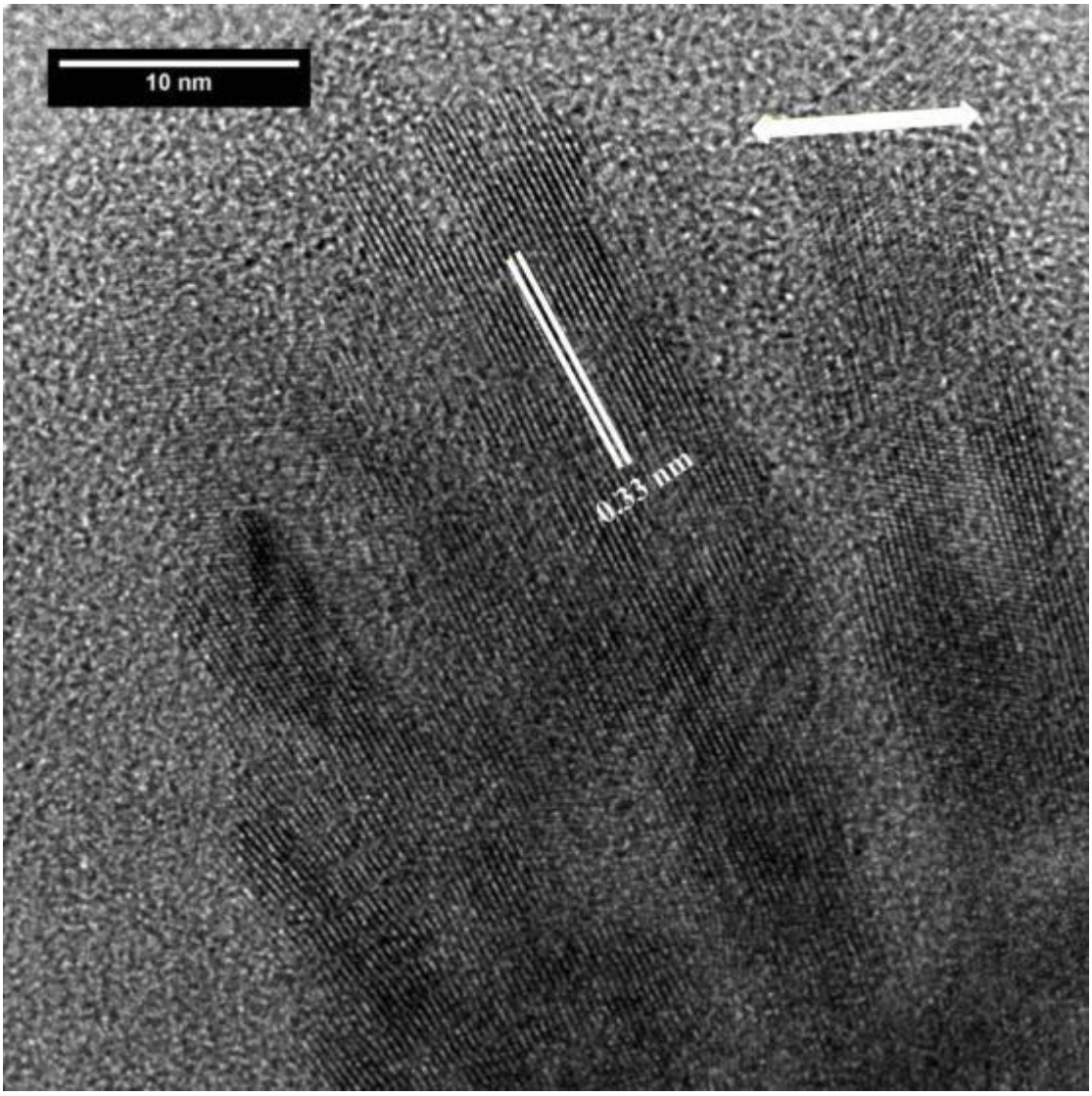

Figure 8.15: (PEG 12000 g/mol in a Ti^{+} : PEG ratio of (1 : 1)). Based on the lattice spacing of 0.33 nm, the fragment presented in figure 8.14 is likely composed of high aspect ratio rutile crystals. The width of the discernible rutile nanorod (highlighted with a double headed arrow) measured approximately 10 nm.

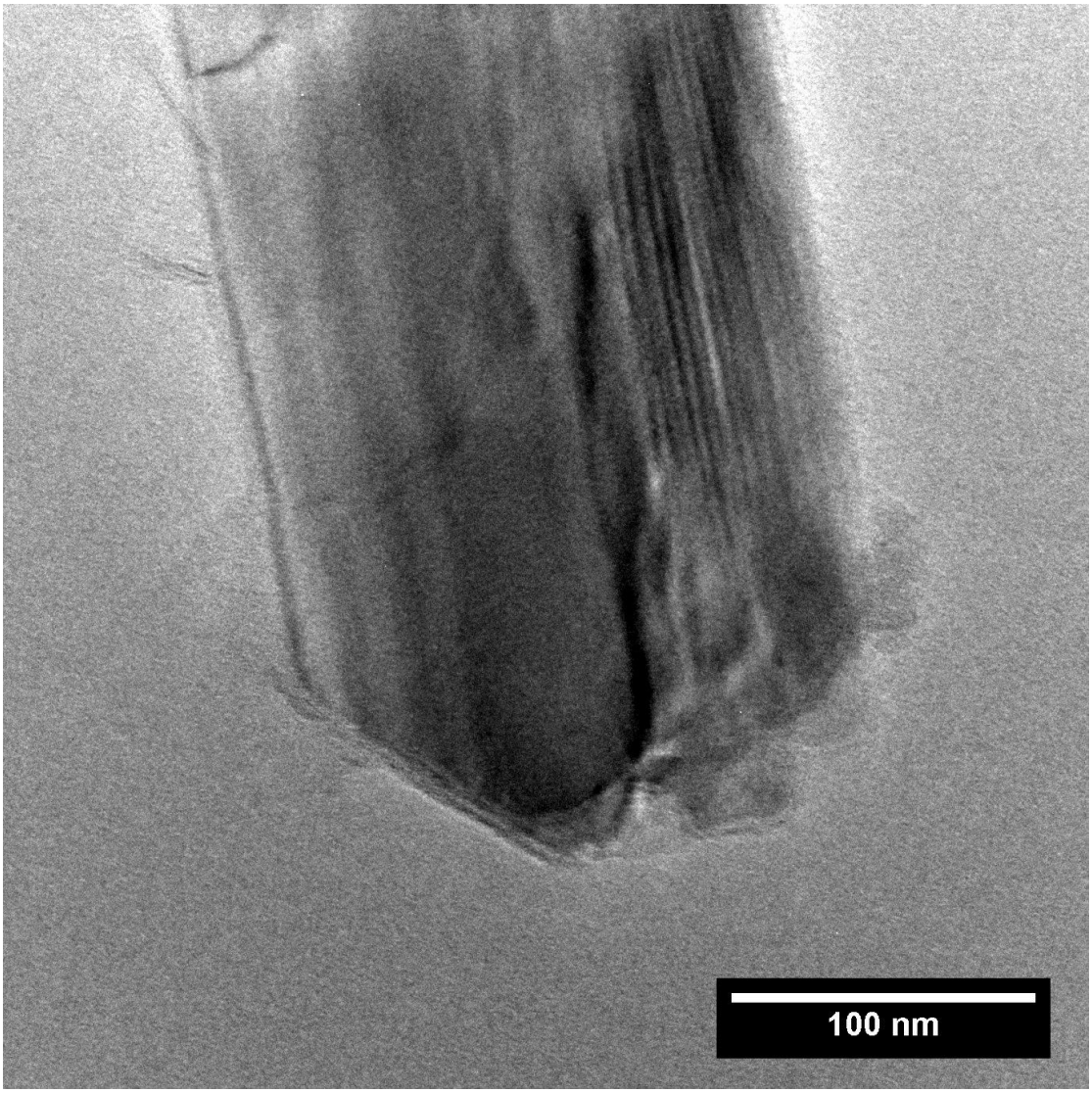

Figure 8.16: (PEG 12000 g/mol in a Ti^{+} : PEG ratio of (1 : 1)). The size of this structure suggests that it is undecomposed polymer remaining in the sample after pyrolysis. This conjecture is further supported by the observation that no lattice fringes were obtained from this structure.

8.2.2 Addition of Ti ions to PEG in a (1 : 0.5) Ratio

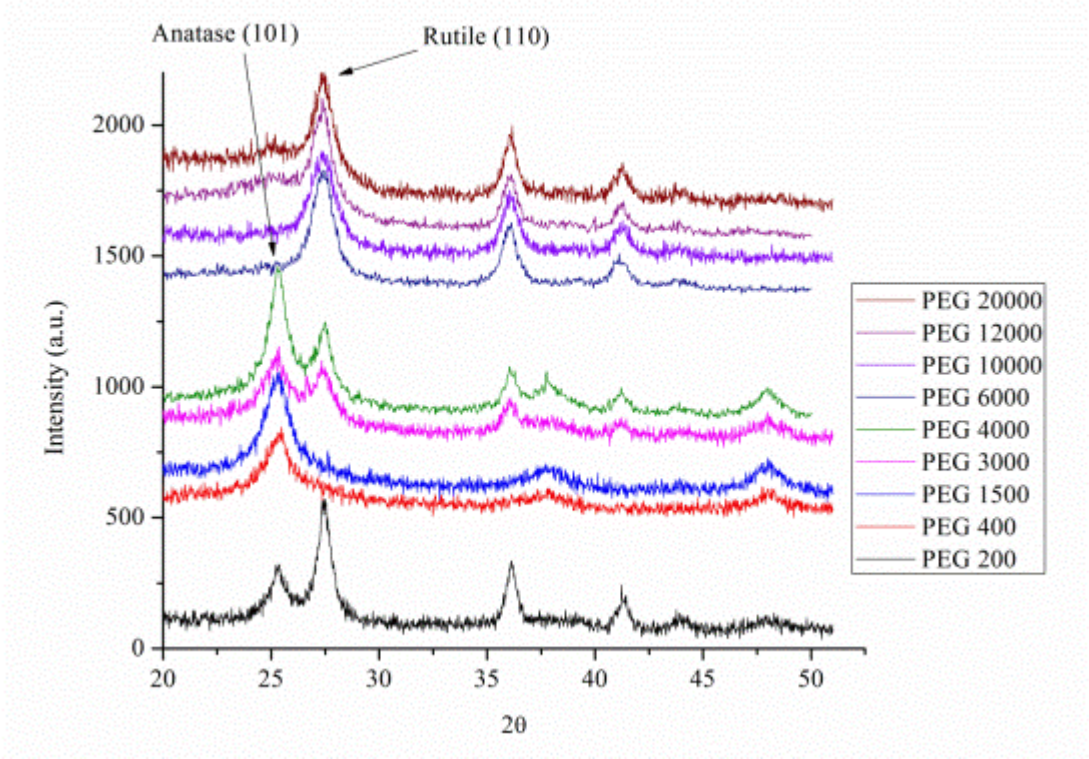

Figure 8.17: PXRD patterns of samples synthesised in a (1 : 0.5) ratio pre-calcination.

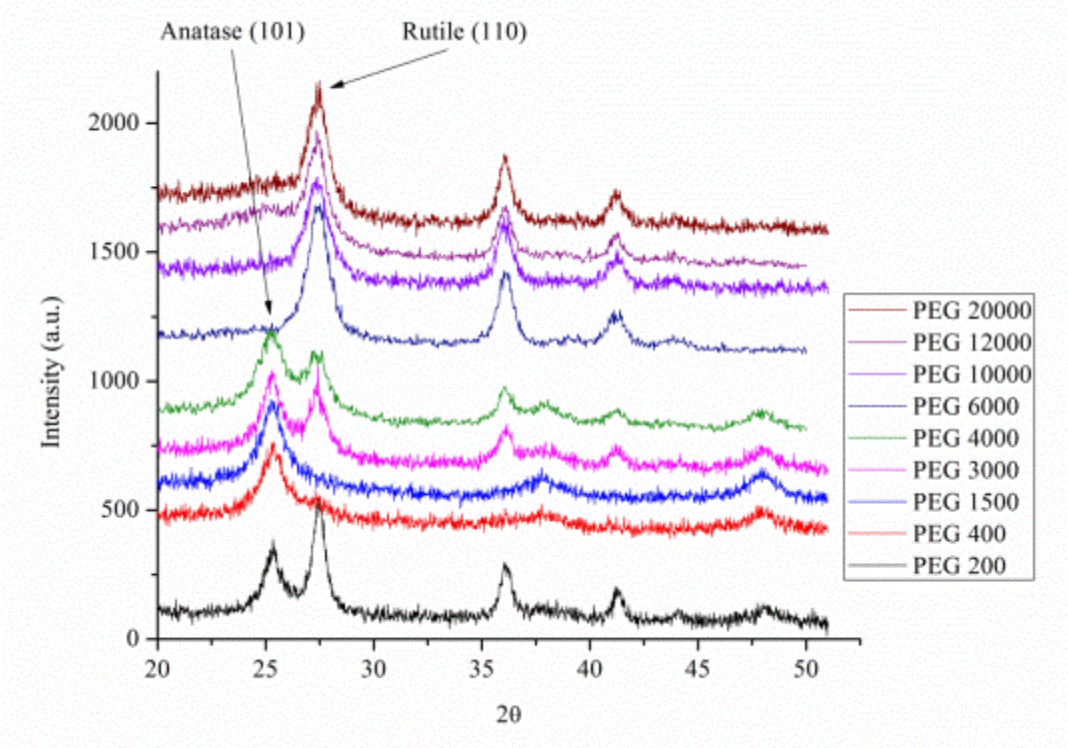

Figure 8.18: PXRD patterns of replicate samples synthesised in a (1 : 0.5) ratio pre-calcination.

Figures 8.17 and 8.18 show the PXRD patterns for all samples synthesised in a Ti^{+} : PEG ratio of (1 : 0.5). PEG 200 g/mol resulted in the formation of a mixture of phases. This is in contrast to the other low molecular weight PEG (400 and 1500 g/mol) that favoured anatase formation. PEG with intermediate molecular weights (3000 and 4000 g/mol) resulted in the formation of both phases, compared with slightly larger PEG (6000 and 10000 g/mol) that favoured rutile formation. Interestingly, large PEG molecular weights (12000 and 20000 g/mol) produced rutile and anatase as a major and minor phase respectively.

It should be noted that the signal to noise ratio appears to be better than for samples synthesised in a (1 : 1) ratio. In a (1 : 0.5) ratio, a rutile (1 1 0) peak is discernible from the sample synthesised from PEG 20000 g/mol – in contrast to the data obtained for the same sample using (1 : 1) synthesis conditions. Peak width and misalignment is indicative of nanomaterial formation with carbon present on the particle surfaces respectively. Initial observations of the original data set with its replicate suggest good experimental reproducibility. This inference will be confirmed statistically later.

Following calcination, the signal to noise ratio of all peaks increased, as evidenced in figures 8.19 and 8.20. This observation suggests that the presence of un-ignited polymer post-pyrolysis impeded X-ray penetration into the titania crystallites. Any left-over polymer was subsequently removed during calcination.

From the narrower peak shape, it can be concluded that calcination served to increase crystallite size. Better peak alignment and the white appearance of samples post-calcination is an indication of the success of calcination in removing carbon from the samples. The anatase peak originating from samples synthesised using PEG 12000 and 20000 g/mol, is better defined post-calcination. This is a likely consequence of a better signal to noise ratio.

Good experimental reproducibility is observed from a comparison of the original data set with its replicate. Statistical confirmation of reproducibility will be given later.

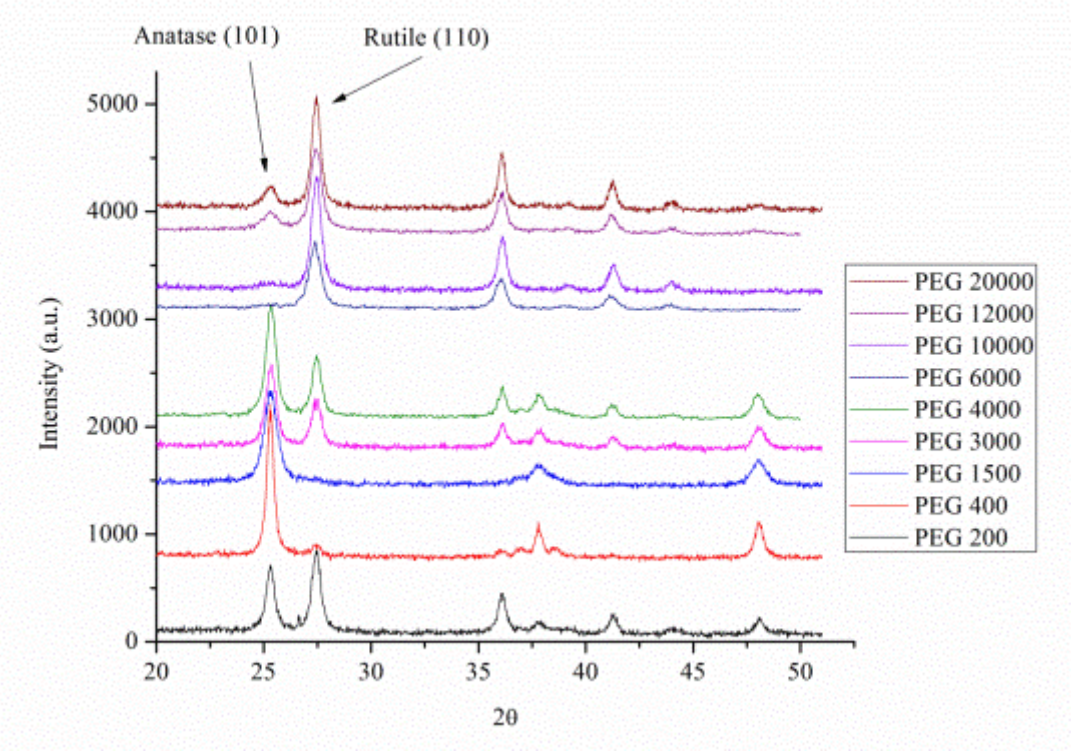

Figure 8.19 PXRD patterns of samples synthesised in a (1 : 0.5) ratio post-calcination.

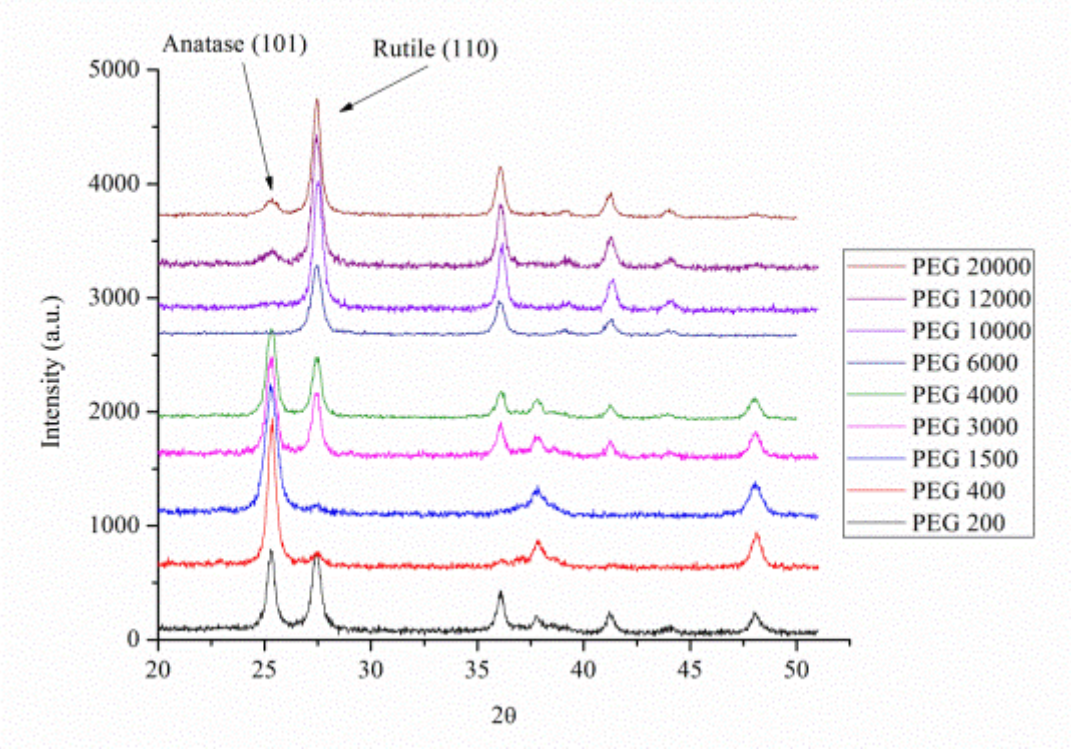

Figure 8.20: PXRD patterns of replicate samples synthesised in a (1 : 0.5) ratio post-calcination.

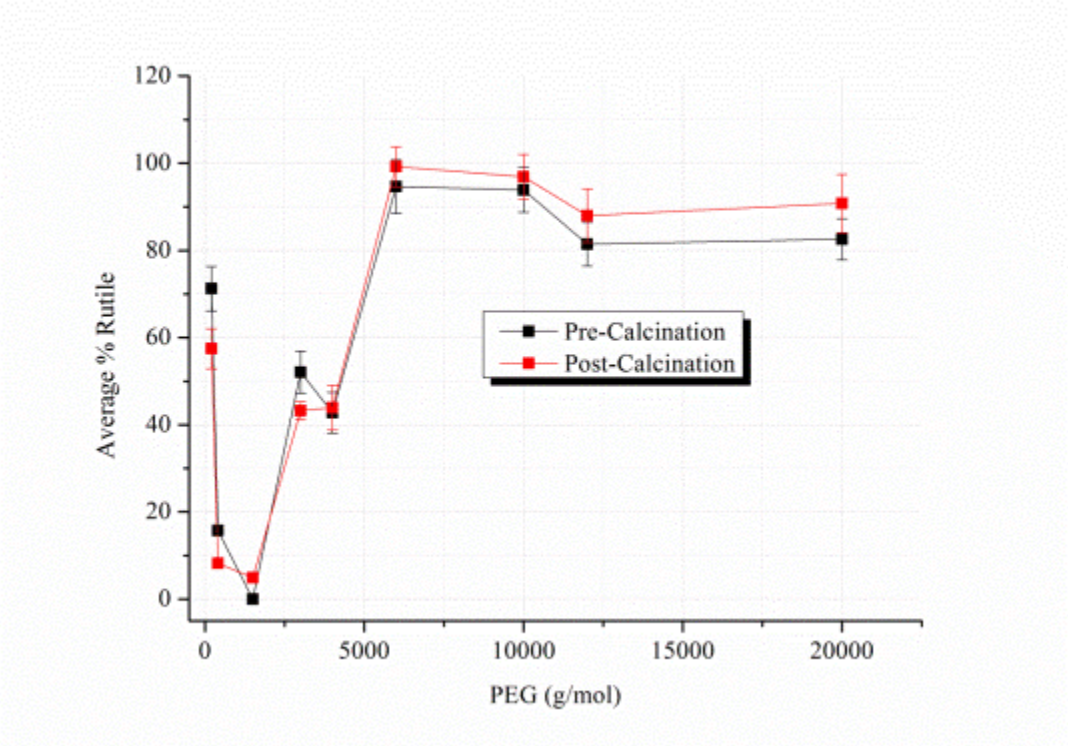

Figure 8.21: Average amount of rutile formed from a (1 : 0.5) ratio pre- and post-calcination.

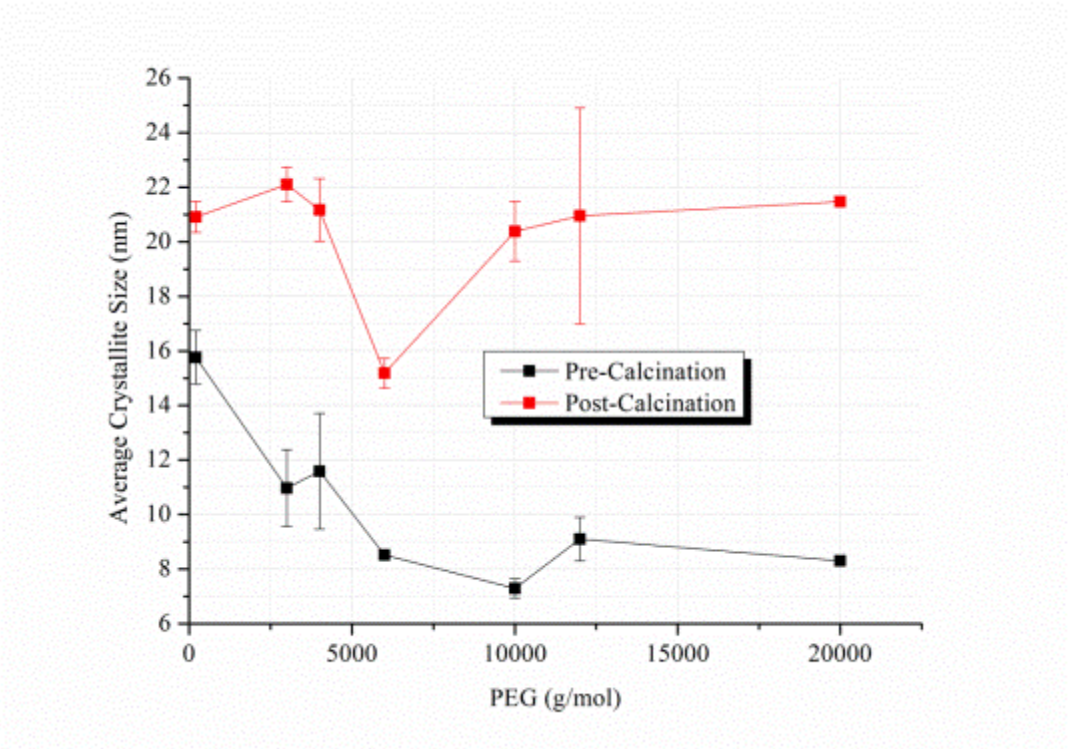

Figure 8.22: Average rutile crystallite size formed from a (1 : 0.5) ratio pre- and post-calcination.

Figure 8.21 compares the effects of calcination on the amount of rutile formed using a Ti^{+} : PEG ratio of (1 : 0.5) as a function of increasing PEG molecular weight. Aside from the amount of rutile formed from PEG 200 g/mol, the overall data resembles that obtained in figure 6.13 (chapter 6): low molecular weight PEG (400 and 1500 g/mol) produced little rutile, intermediate molecular weight PEG (3000 and 4000 g/mol) produced about 47% of rutile, high molecular weight PEG (6000 – 20000 g/mol) was biased toward rutile formation.

The average amount of rutile formed pre-calcination across all samples was 59%. This is similar to the average amount of rutile formed across all samples using (1 : 1) synthesis conditions. Based on previously obtained results, it was expected that water containing HNO3 favoured the formation of rutile.

Post-calcination data revealed a similar trend of the amount of rutile formed as a function of increasing PEG molecular weight. Curiously, the amount of rutile decreased post-calcination in samples synthesised from low molecular weight PEG. Error bars (generated as described previously) pertaining to these samples are sufficiently small to suggest that this is a reproducible result. This is a similar finding to that described in chapter 6. The following is presented as an explanation for this observation: after pyrolysis, amorphous titania is formed in samples prepared using low molecular weight PEG. Calcination causes anatase to nucleate from the amorphous content. The calcination temperature is insufficient to cause significant phase change to rutile. The construction of the Spurr and Myers equation allows for an increase in anatase content with a simultaneous decrease in rutile content. Hypothesising amorphous titania as the cause of lower rutile content post-calcination is predicated on the poor signal to noise ratio observed in the PXRD patterns (figures 8.17 and 8.18). An expected small increase in the amount of rutile formed post-synthesis was observed in samples synthesised using large molecular weight PEG.

Figure 8.22 shows the effects of calcination on the average rutile crystallite size obtained as a function of increasing PEG molecular weight synthesised in a Ti^{+} : PEG ratio of (1 : 0.5). Because anatase was the preferred phase in samples synthesised from PEG 400 and 1500, it was not possible to generate rutile crystallite size data from these samples. Before calcination, rutile crystallites decreased in size as PEG molecular weight increased. Samples synthesised from PEG 200 g/mol exhibited the largest rutile crystallites (~ 15 nm), compared with the smallest rutile crystallites that

measured ~ 8 nm, generated from PEG 10000 g/mol. Average rutile crystallite size across all samples before calcination measured ~ 10 nm. The data appears to be more erratic for samples synthesised from lower molecular weight PEG.

Calcination had a predictable effect of increasing crystallite size in all samples. This increase was disproportional. The average crystallite size obtained across all samples post-calcination was 18 nm.

An interesting point of note is that post-calcination, samples synthesised from PEG 6000 g/mol resulted in the formation of the smallest crystallites (~15 nm). These crystallites were approximately the same size as those produced from PEG 200 g/mol pre-calcination. Under the present calcination conditions, rutile (1 1 0) crystallites appear to coarsen to a maximum of ~ 22 nm. Crystallite size data generated from PEG 12000 g/mol produced the greatest error (4 nm). All other data points reveal good reproducibility (errors generated as previously described for crystallite size data).

Figure 8.23 shows the inverse relationship between the amount of rutile formed and respective crystallite size as a function of increasing PEG molecular weight synthesised in a (1 : 0.5) ratio pre-calcination. The caveat to the inverse relationship is the amount of rutile formed from PEG 200 g/mol. Only data from samples that allowed for a direct comparison of amount of rutile formed and associated crystallite size has been included (data from samples synthesised using PEG 400 and 1500 g/mol are not included). Error bars are sufficiently small for the data to represent a real, reproducible trend. This trend was previously observed for all previous experiments synthesised using water containing HNO_3 and was rationalised using oriented attachment and the formation of polymer reaction chambers.

An imperfect inverse relationship between the amount of rutile formed and its respective crystallite size presented post-calcination, as evidenced in figure 8.24. The imperfect inverse relationship occurred as a result of calcination having a negligible effect on the amount of rutile formed while concurrently causing a disproportional increase in rutile crystallite size. This effect is most prominent for the data obtained from PEG 10000 g/mol. In order to make a direct comparison of rutile crystallite size and amount of formed phase, data from PEG 1500 g/mol was excluded. This is because no crystallite size data could be extracted from that sample owing to the small amount of rutile formed.

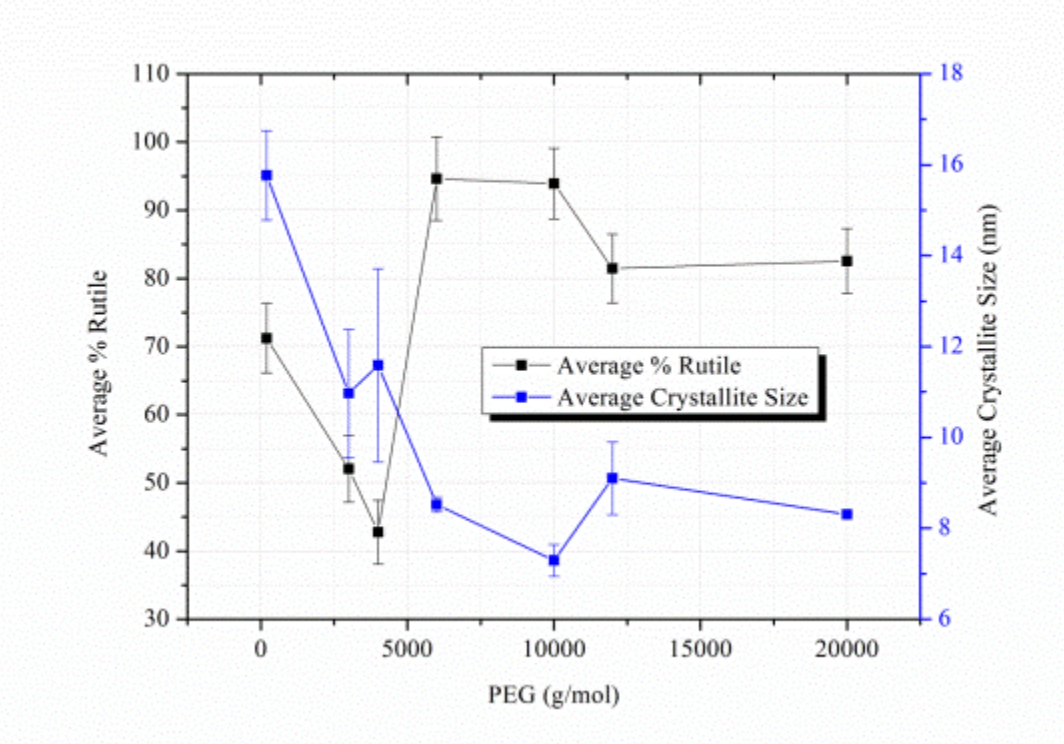

Figure 8.23: Average amount of rutile with associated crystallite size formed in a (1 : 0.5) synthesis pre-calcination.

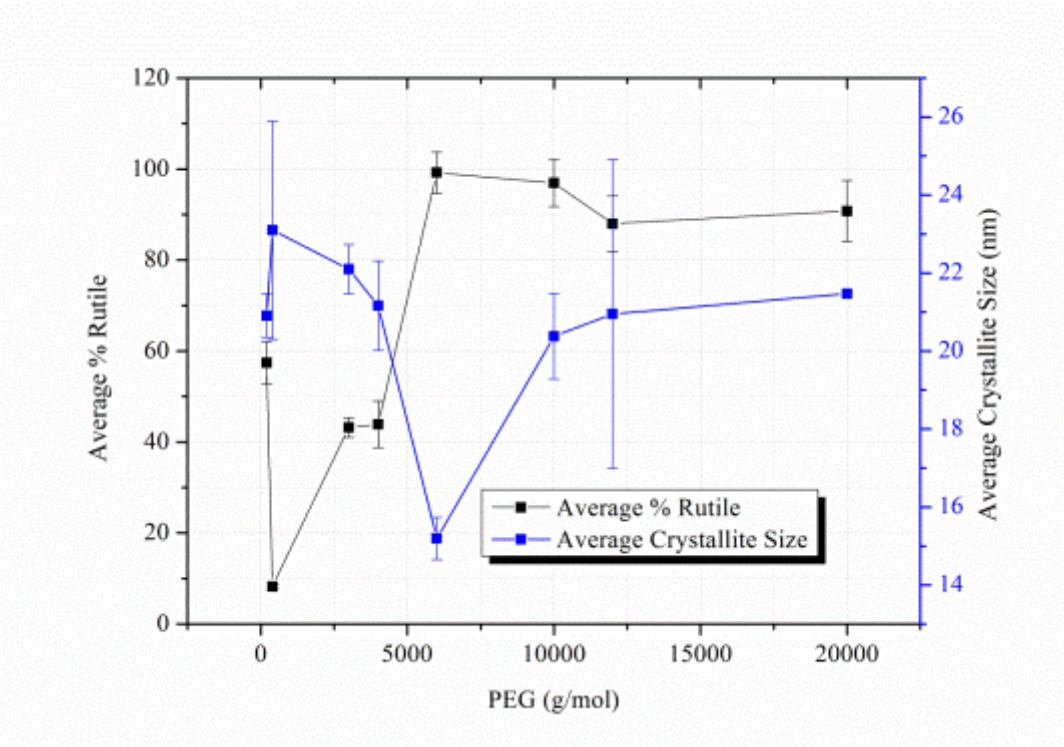

Figure 8.24: Average amount of rutile with associated crystallite size formed in a (1 : 0.5) synthesis post-calcination.

Table 8.6 compares the average amount of anatase (1 0 1) formed with respective crystallite size from selected samples pre-calcination. As previously observed, PEG 200 g/mol resulted in the formation of the largest anatase crystallites. PEG 3000 and 4000 g/mol produced similarly sized anatase crystallites. Expectedly, for the same PEG molecular weight, rutile crystallites were larger than anatase crystallites.

Table 8.5: Average amount of anatase and respective crystallite size formed in a (1 : 0.5) synthesis, pre-calcination.

PEG (g/mol)	Average %Anatase	Average anatase crystallite size (nm)	Average %Rutile	Average rutile crystallite size (nm)
200	28.8 ± 3.4	13.8 ± 1.5	71.2 ± 5.1	15.8 ± 1.0
3000	47.9 ± 4.7	9.5 ± 1.4	52.1 ± 4.9	11.0 ± 1.4
4000	57.2 ± 5.3	9.9 ± 1.6	42.8 ± 4.7	11.6 ± 2.1

Table 8.6: Average amount of anatase and respective crystallite size formed in a (1 : 0.5) synthesis, post-calcination.

PEG (g/mol)	Average %Anatase	Average anatase crystallite size (nm)	Average %Rutile	Average rutile crystallite size (nm)
200	42.5 ± 4.0	25.8 ± 1.8	57.5 ± 4.6	20.9 ± 0.6
400	91.8 ± 3.9	27.7 ± 2.0	8.2 ± 0.5	23.1 ± 2.8
3000	56.8 ± 2.6	18.7 ± 0.5	43.2 ± 2.1	22.1 ± 0.6
4000	56.1 ± 5.6	19.2 ± 0.9	43.9 ± 5.1	21.2 ± 1.1
12000	12.0 ± 3.1	15.1 ± 0.5	88.0 ± 6.1	21.0 ± 4.0
20000	9.2 ± 3.5	15.4 ± 1.2	90.8 ± 6.7	21.5 ± 0.1

Post-calcination anatase crystallite size data is given in table 8.7. Crystallite size increased dramatically post-calcination. Anatase crystallites from samples synthesised using PEG 200, 3000 and 4000 exhibited growth of 87%, 97% and 94% respectively. This is in contrast to rutile crystallites (synthesised from the same samples) that exhibited growth of 32%, 100% and 82% respectively. For this reason, post-calcination, anatase crystallites synthesised using low molecular weight PEG (200 g/mol) are larger than rutile crystallites. A plausible explanation for this observation is that smaller rutile crystallites formed pre-calcination have greater growth potential that is manipulated during calcination. Rutile crystallites formed from longer PEG chains ($\geq$ 3000 g/mol) are larger than corresponding anatase crystallites.

Table 8.7: Comparison of anatase formation using (1 : 1) and (1 : 0.5) synthesis conditions, pre-calcination.

	(1 : 1)		(1 : 0.5)	
PEG (g/mol)	**Average %Anatase**	**Average anatase crystallite size (nm)**	**Average %Anatase**	**Average anatase crystallite size (nm)**
400	94.7 $\pm$ 8.9	5.9 $\pm$ 0.1	84.3 $\pm$ 3.6	8.4 $\pm$ 1.1
1500	90.1 $\pm$ 6.2	8.4 $\pm$ 0.8	100 $\pm$ 4.0	7.2 $\pm$ 0.3

Table 8.8 compares the amount of anatase formed using different Ti^{+} : PEG ratios as a function of different PEG molecular weights. The data suggests that low molecular weight PEG tends to form an abundance of anatase regardless of the synthesis ratio used. Additionally, lesser anatase content in a sample correlates with larger anatase crystallites. This could be due to rutile transformation encouraging anatase growth but is more likely a consequence of the amorphous TiO_2 content within the samples.

Table 8.9 compares the amount and size of anatase formed in a (1 : 1) and (0.5 : 1) synthesis after calcination, as a function of different PEG molecular weights. The amount of anatase formed in a (1 : 0.5) ratio increases and then decreases as a function of increasing PEG molecular weight. A similar trend was not observed for anatase formed in a (1 : 1) ratio.

Table 8.8: Comparison of anatase formation using (1 : 1) and (1 : 0.5) synthesis conditions, post-calcination.

PEG (g/mol)	(1 : 1)		(1 : 0.5)	
	Average %Anatase	Average anatase crystallite size (nm)	Average %Anatase	Average anatase crystallite size (nm)
200	19.1 ± 7.5	22.0 ± 0.7	42.5 ± 4.0	25.8 ± 1.8
400	98.8 ± 5.0	20.2 ± 1.1	91.8 ± 3.9	27.7 ± 2.0
1500	92.7 ± 4.6	20.2 ± 0.1	95.0 ± 4.3	14.4 ± 0.3
3000	10.9 ± 1.9	14.1 ± 0.5	56.8 ± 2.6	18.7 ± 0.5
12000	38.2 ± 4.0	12.4 ± 0.3	12.0 ± 3.1	15.1 ± 0.5
20000	47.5 ± 4.7	9.5 ± 0.5	9.2 ± 3.5	15.4 ± 1.2

For the same PEG molecular weight, excluding PEG 1500, anatase crystallites synthesised using a (1 : 0.5) ratio were larger than crystallites synthesised using a (1 : 1) ratio. Intriguingly, this trend is valid despite similarities and differences between the amounts of anatase formed for a specific PEG molecular weight. This result was unexpected due to the following: a synthesis ratio of (1 : 1) has twice the amount of polymer than a (1 : 0.5) ratio. In keeping with the developing hypothesis regarding the formation of polymer chambers, it is likely that twice the amount of chambers were formed using a (1 : 1) synthesis than in a (1 : 0.5) synthesis. Since the number of metal ions were the same in both experiments, the ratio of metal ions to polymer chambers was two times greater under (1 : 0.5) synthesis conditions than (1 : 1) synthesis conditions. Since the (1 : 1) polymer chambers contained fewer ions per

chamber, they would have resulted in the formation of smaller anatase crystallites. As noted in chapter 6, smaller anatase crystallites formed after sample ignition, resulted in larger anatase crystallites observed after calcination.

Since the data does not agree with the above prediction of crystallite size, there must be another factor influencing the system. It is hypothesised that the presence of large amounts of undecomposed polymer post-ignition formed in a (1 : 1) synthesis absorbed some of the energy supplied to the system during calcination. This heat would otherwise be used to increase anatase crystallite size. Hence, a system that contains less polymer [i.e.: (1 : 0.5)] is more susceptible to anatase crystallite size increases than a system that contains more polymer [i.e.: (1 : 1)]. Undecomposed PEG was evidenced in PXRD patterns and TEM images of samples synthesised in a (1 : 1) ratio.

Tables showing the amount of each phase and crystallite size obtained for each sample with averages and errors are given in appendix F.

HRTEM images obtained from samples synthesised using PEG 6000 in a (1 : 0.5) ratio post-calcination follow (figures 8.25 and 8.26). This sample contained 99.2% rutile with average rutile (1 1 0) crystallites measuring 15.2 nm.

The {1 1 1} orientation observed in figure 8.25 was previously described as the pyramidal plane capping rutile nanorods[4]. Steps indicated in this image are indicative of a high energy surface and is likely the position along the crystal that promotes growth (dependent on reaction conditions). The shape variation of the crystals presented in figures 8.25 and 8.26 is noteworthy.

Figures 8.27 and 8.28 represent the pre-calcined samples obtained from PEG 6000 g/mol using a (1 : 0.5) ratio.

Figure 8.27 shows the presence of a superstructure surrounded by carbon. Given that this image was captured from the sample before it was calcined, it is likely that the carbon originated from undecomposed polymer. The dark spots within the carbon are possibly crystallite titania that would have become part of the superstructure if the reaction had proceeded further.

The (0 0 1) axis described in figure 8.28 is the axis along which rutile exhibits anisotropic growth[5]. This evidence of single crystal nanorods found in figure 8.28 lends credence to the work by Zhang *et al*., suggesting that rutile nanorods comprising

mesocrystals are single crystal in nature[6]. Additionally, as highlighted, the nanorod appears to be pyramidically capped as suggested by Kakiuchi *et al*[4].

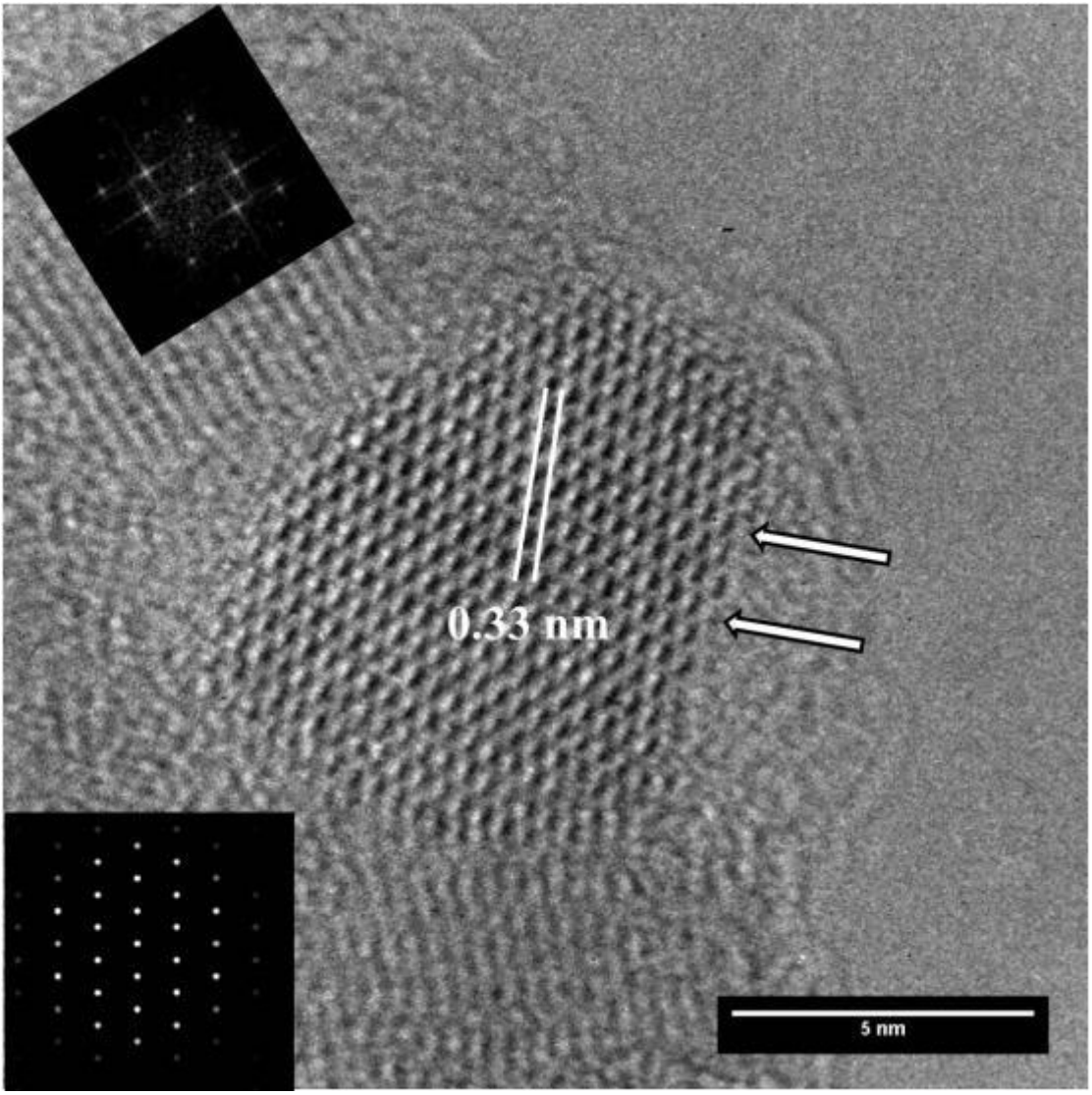

Figure 8.25: (PEG 6000 in a (1 : 0.5) ratio post-calcination). Single rutile crystal in the (1 1 1) orientation. This crystal measured ~ 9 nm top to bottom and ~ 7 nm across. Morphologically, it appeared to occur as a pentagon. Arrows indicate steps along the crystal.

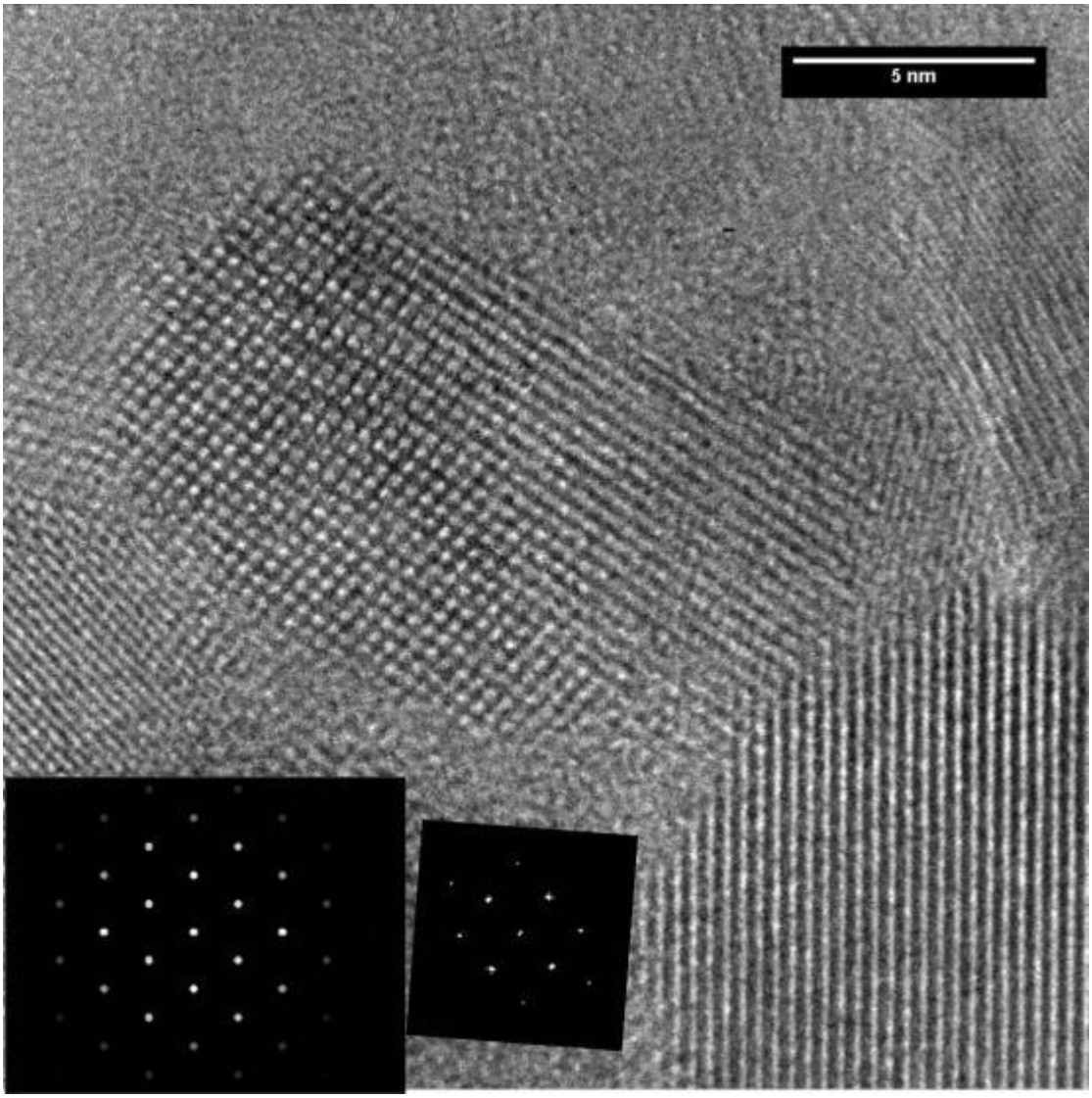

Figure 8.26: (PEG 6000 in a (1 : 0.5) ratio post-calcination). Anisotropic rutile crystal in the (0 1 0) or (1 0 0) orientation. This crystal measures approximately 15.5 nm across its length and 8.5 nm across its width.

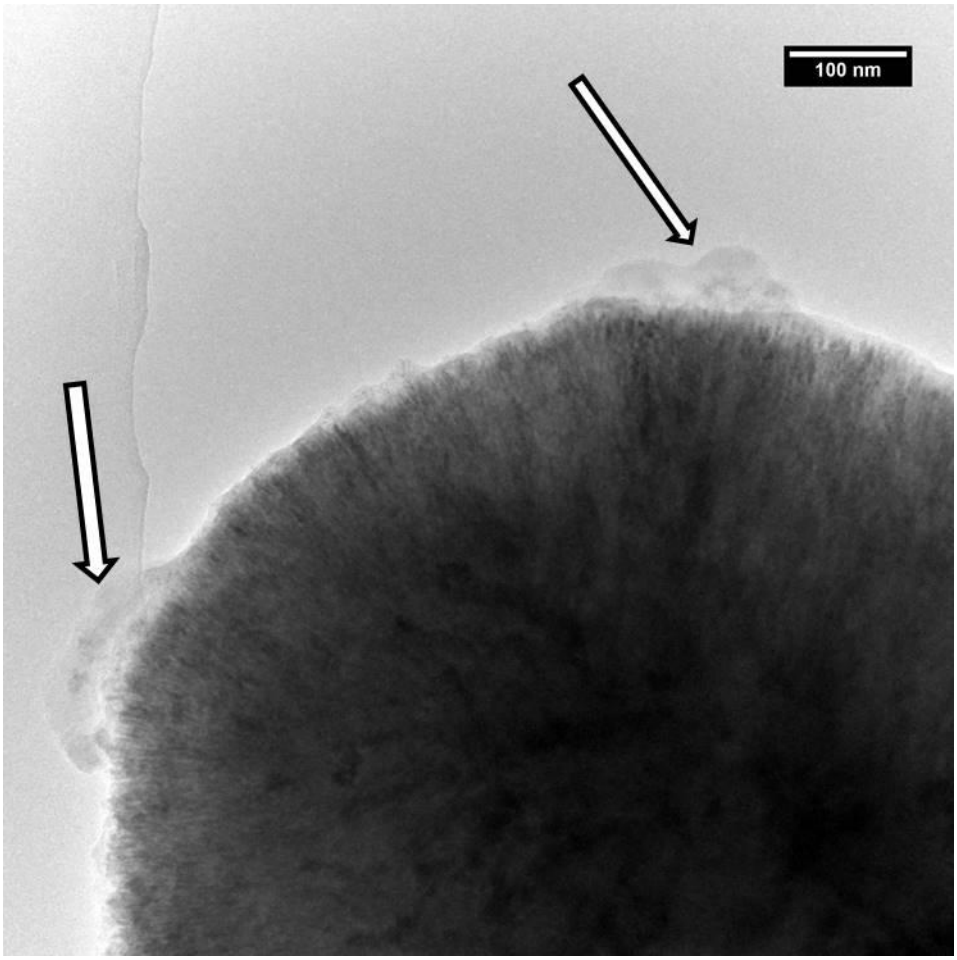

Figure 8.27: (PEG 6000 in a (1 : 0.5) ratio pre-calcination). This sample produced rutile superstructures. Arrows in the image indicate carbon deposited on the surface of the superstructure. This radius of this superstructure measured approximately 500 nm.

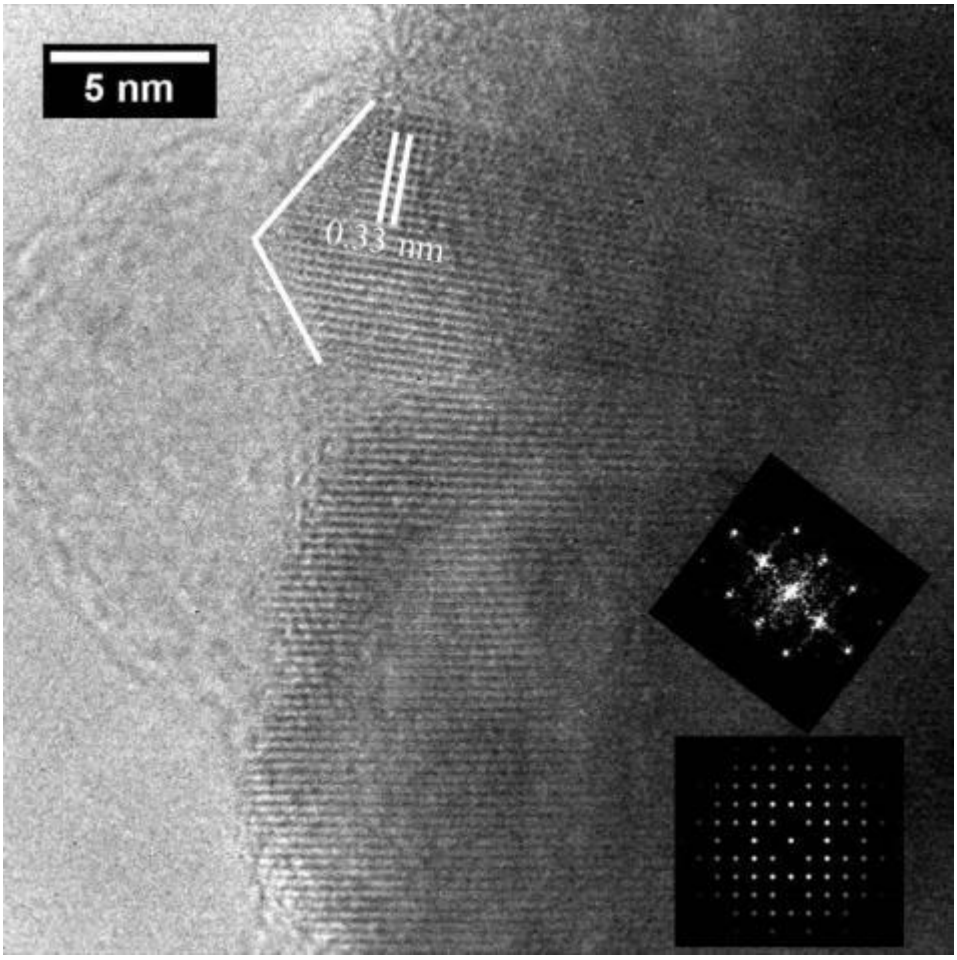

Figure 8.28: (PEG 6000 in a (1 : 0.5) ratio pre-calcination). Appearance of the ends of the superstructure imaged in figure 8.27. The rutile nanorod in the upper part of the image is pyramidically capped, occurs along (0 0 1) and measures approximately 8 nm across its width. From this image it appears that the nanorod is a continuous single crystal that extends far into the superstructure.

8.2.3 Addition of Ti ions to PEG in a (1 : 0.1) Ratio

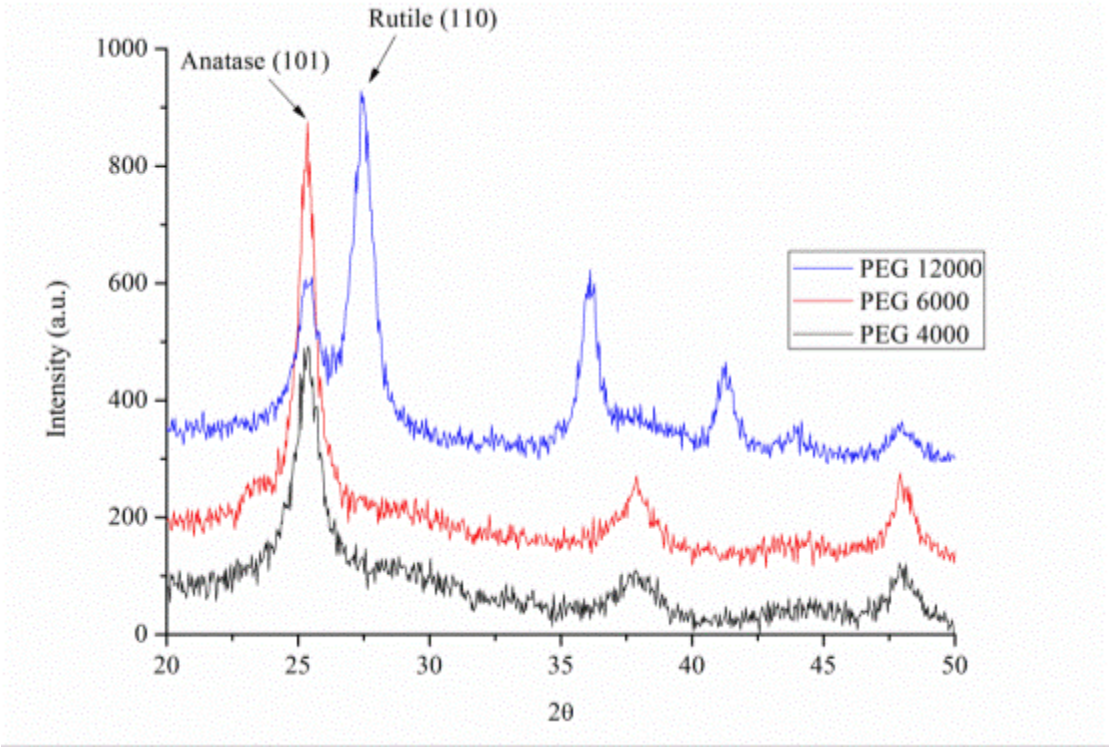

Figure 8.29: PXRD patterns of samples synthesised in a (1 : 0.1) ratio pre-calcination.

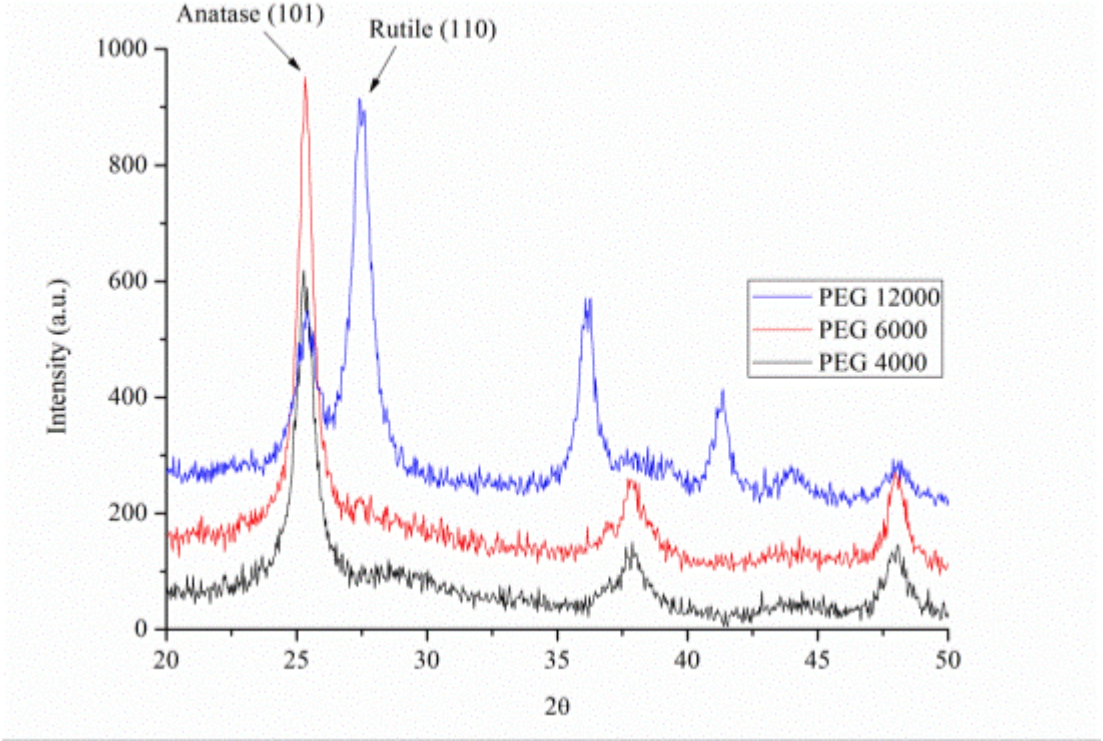

Figure 8.30: PXRD patterns of replicate samples synthesised in a (1 : 0.1) ratio pre-calcination.

Figures 8.29 represents the PXRD patterns of samples synthesised in a (1 : 0.1) ratio pre-calcination. Only three polymers were selected for this synthesis: PEG 4000, 6000, and 12000 g/mol. The patterns reflect that PEG 4000 and 6000 g/mol favoured the formation of anatase. PEG 12000 g/mol resulted in the formation of both anatase and rutile with the latter being the major phase. Peaks are generally sharper and better aligned than previously witnessed for (1 : 1) and (1 : 0.5) syntheses. The patterns also reflect a better signal to noise ratio than previously observed. Since these samples contain 10 times and 5 times less polymer than those synthesised in a (1 : 1) and (1 : 0.5) ratio respectively, the improved signal to noise ratio is likely due to sample ignition adequately removing most of the polymer from the samples.

Figure 8.30 represents the PXRD patterns collected for the replicate synthesis. There appears to be good correlation between the data collected from the samples and their replicates.

Figure 8.31 contains the PXRD patterns corresponding to samples synthesised in a (1 : 0.1) ratio after calcination. As expected, there is an improvement in peak alignment and in the signal to noise ratio.

As observed from figure 8.32, data collected from samples containing PEG 4000 and 12000 g/mol reflect good reproducibility. The PXRD pattern of the replicate sample synthesised using PEG 6000 g/mol shows a small rutile peak that is not as pronounced in the original sample. Since the calcination temperature of 500 °C is insufficient to cause significant conversion of anatase to rutile, it is plausible that this sample contained an impurity that served to catalyse the transformation. The extent of deviation between the original data and its respective replicate will be confirmed later.

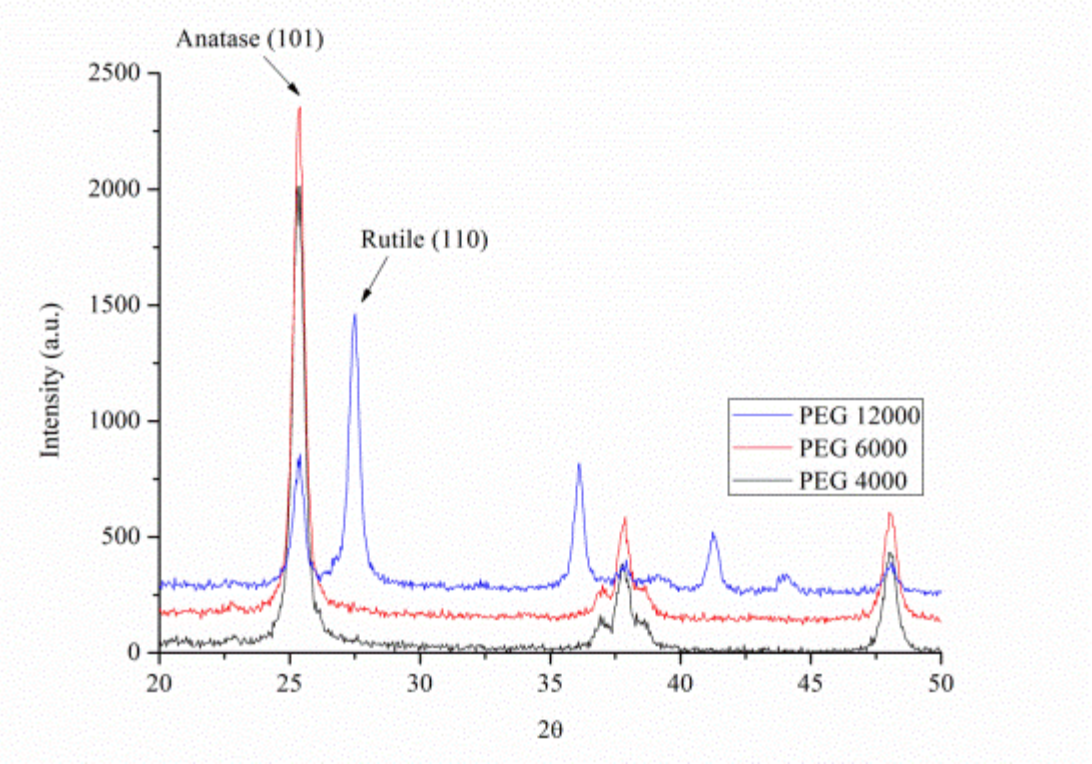

Figure 8.31: PXRD patterns of samples synthesised in a (1 : 0.1) ratio post-calcination.

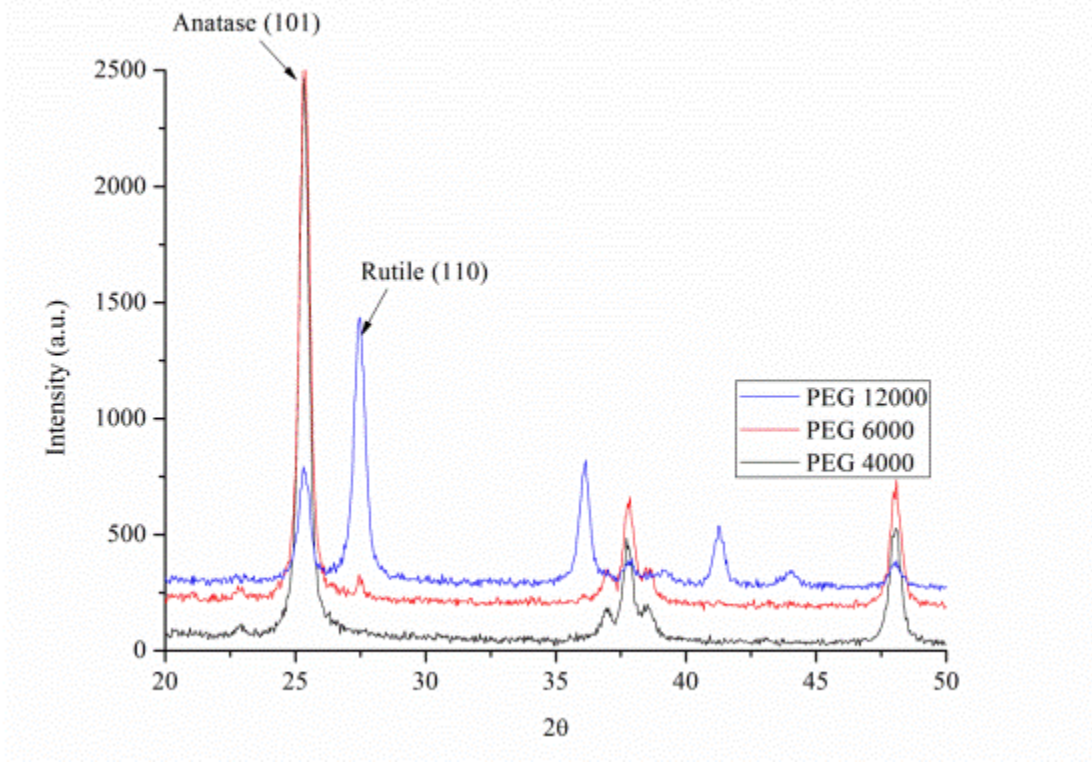

Figure 8.32: PXRD patterns of replicate samples synthesised in a (1 : 0.1) ratio post-calcination.

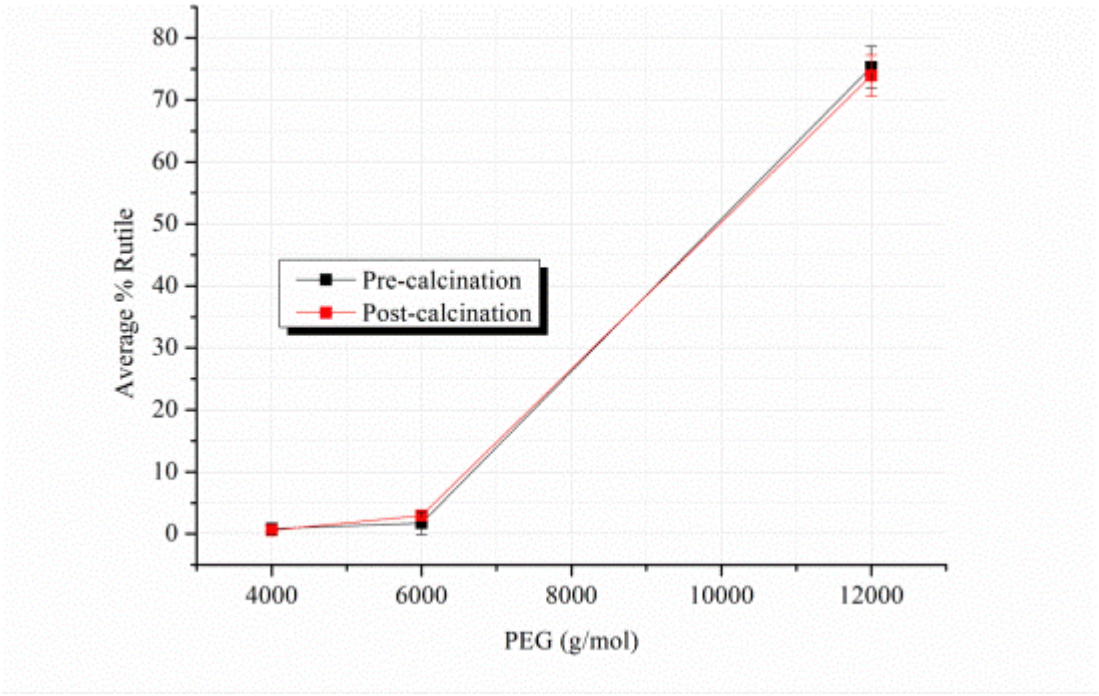

Figure 8.33: Average amount of rutile formed from a (1 : 0.1) ratio pre- and post-calcination.

Figure 8.33 shows the effects of calcination on the amount of rutile formed in samples synthesised using a (1 : 0.1) synthesis. Before calcination, PEG 4000 g/mol resulted in the formation of the least amount of rutile (0.8%). In comparison, PEG 6000 g/mol that produced 1.7% rutile and PEG 12000 g/mol formed the most amount of rutile (75.3%). The data suggests that long chain PEG favours the formation of rutile. However, this inference should be carefully considered given that this experiment employed the use of only three 3 polymers, and that the amount of rutile was shown to oscillate as a function of PEG molecular weight (chapter 5). In addition, the average amount of rutile formed across all three polymers was 26% suggesting that a synthesis ratio of (1 : 0.1) favours the formation of anatase. Calcination had a negligible effect on the amount of rutile formed from all samples. Error bars are sufficiently small suggesting excellent experimental reproducibility.

Because of the small amount of rutile formed in samples containing PEG 4000 and 6000 g/mol, no accurate crystallite size data could be obtained. Rutile (1 1 0) crystallites formed in the sample synthesised using PEG 12000 g/mol measured 12.2 $\pm$ 0.7 nm before calcination. After calcination, the crystallites coarsened to 23.6 nm $\pm$ 1.3 nm.

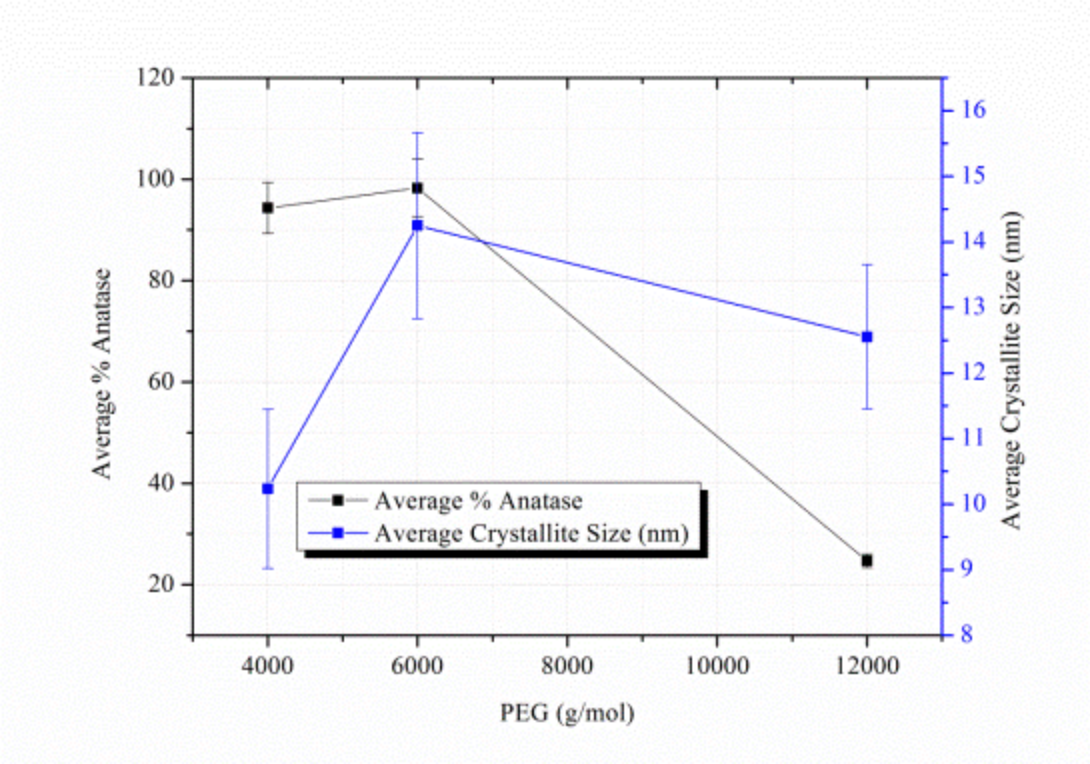

Figure 8.34: Average amount of anatase with associated crystallite size formed in a (1 : 0.1) synthesis pre-calcination.

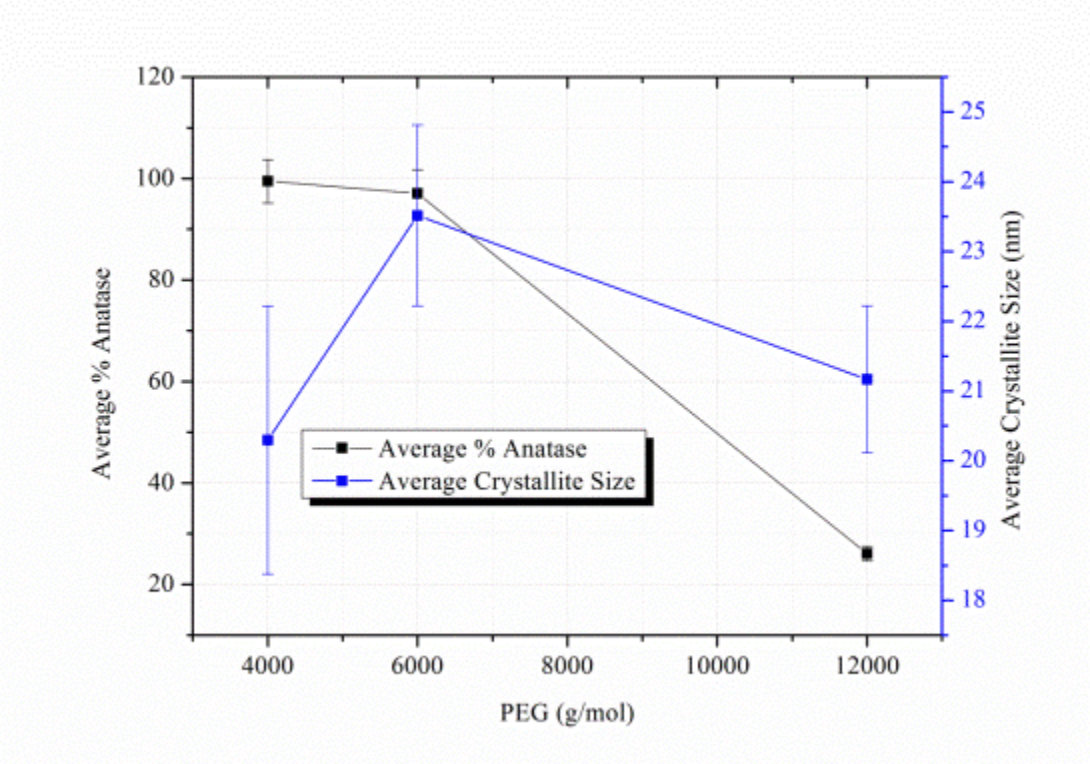

Figure 8.35: Average amount of anatase with associated crystallite size formed in a (1 : 0.1) synthesis post-calcination.

Figure 8.34 shows the relationship between the amount of anatase formed and its respective crystallite size formed in a (1 : 0.1) synthesis pre-calcination. In contrast to the comparative graphs obtained for rutile, anatase does not exhibit the same inverse relationship between the amount of formed phase and respective crystallite size. Samples synthesised using PEG 6000 and 12000 g/mol resulted in the formation of the largest anatase (1 0 1) crystallites (14.2 nm and 12.6 nm respectively). PEG 4000 g/mol resulted in the formation of the smallest crystallites measuring 10.2 nm. This data suggests that anatase crystallite size distribution did not extend over a large range using (1 : 0.1) synthesis conditions.

Curiously, anatase crystallites formed in the sample synthesised using PEG 12000 g/mol were similar in size to rutile crystallites formed in the same sample. From previous experimentation, rutile crystallites were expected to be larger than anatase crystallites. This effect was understood to occur as a result of transformation encouraging growth. The similarity between the size of rutile crystallites synthesised using PEG 12000 g/mol under (1 : 1), (1 : 0.5) and (1 : 0.1) syntheses conditions suggests that anatase crystallites synthesised in this experiment are large.

Comparing figures 8.34 and 8.35, calcination caused anatase to coarsen more than it caused phase transformation. Anatase crystallite size increase was nearly proportional across the range of different PEG molecular weights. This was an expected result.

Table 8.9: Variation in anatase formation using different PEG stoichiometries.

	(1 : 1)		**(1 : 0.5)**		**(1 : 0.1)**	
PEG (g/mol)	**Average %Anatase**	**Average anatase crystallite size (nm)**	**Average %Anatase**	**Average anatase crystallite size (nm)**	**Average %Anatase**	**Average anatase crystallite size (nm)**
4000	9.0 ± 0.6		57.2 ± 5.3	9.9 ± 1.6	99.2 ± 4.8	10.2 ± 1.2
6000	8.2 ± 1.1		5.4 ± 2.6		98.3 ± 5.7	14.2 ± 1.4
12000	59.4 ± 9.2	5.1 ± 0.1	18.6 ± 2.6		24.7 ± 1.3	12.6 ± 1.1

Table 8.10 compares the amount and size of anatase formed using PEG 4000, 6000 and 12000 g/mol across all three PEG stoichiometries. The data suggests that medium length PEG (4000 and 6000 g/mol) tends to form rutile as the number of PEG chains in the system is increased. In contrast, longer chain PEG (12000 g/mol) tends to favour the formation of anatase and rutile as the number of PEG chains in the system is increased. This is a strange occurrence and is likely caused by a combination of long polymer chain entanglement, system thermodynamics, entropy, and different multiple scission points along different PEG chains.

Tables showing the amount of each phase and crystallite size obtained for each sample with averages and errors are given in appendix F.

Figure 8.36 represents an HRTEM image corresponding to the sample synthesised using PEG 4000 g/mol in a (1 : 0.1) ratio post-calcination.

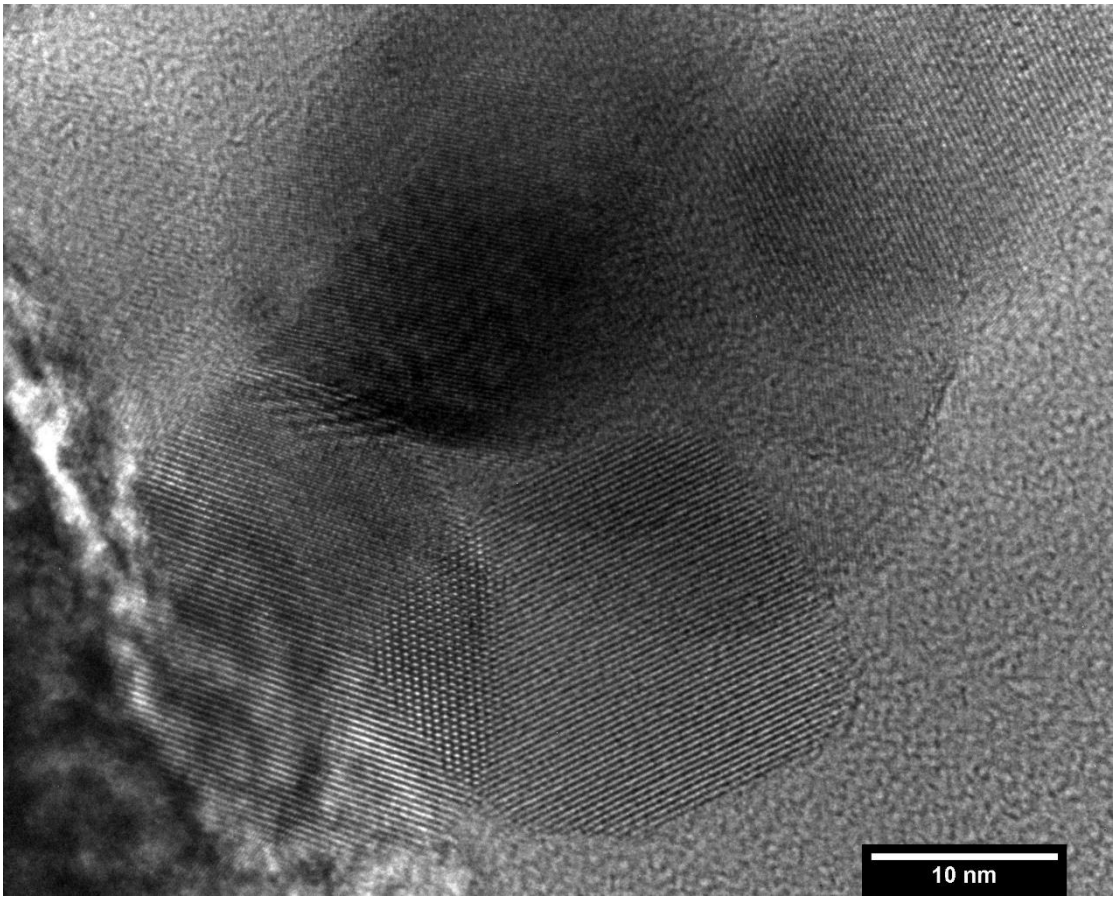

Figure 8.36: (PEG 4000 g/mol in a (1 : 0.1) ratio post-calcination) showing well-defined anatase crystallites. The crystal appearing in the lower right part of the image measures ~ 20 nm top to bottom and ~ 22 nm left to right. This is consistent with PXRD findings.

8.2.4 Comparison of the Effects of PEG Stoichiometry

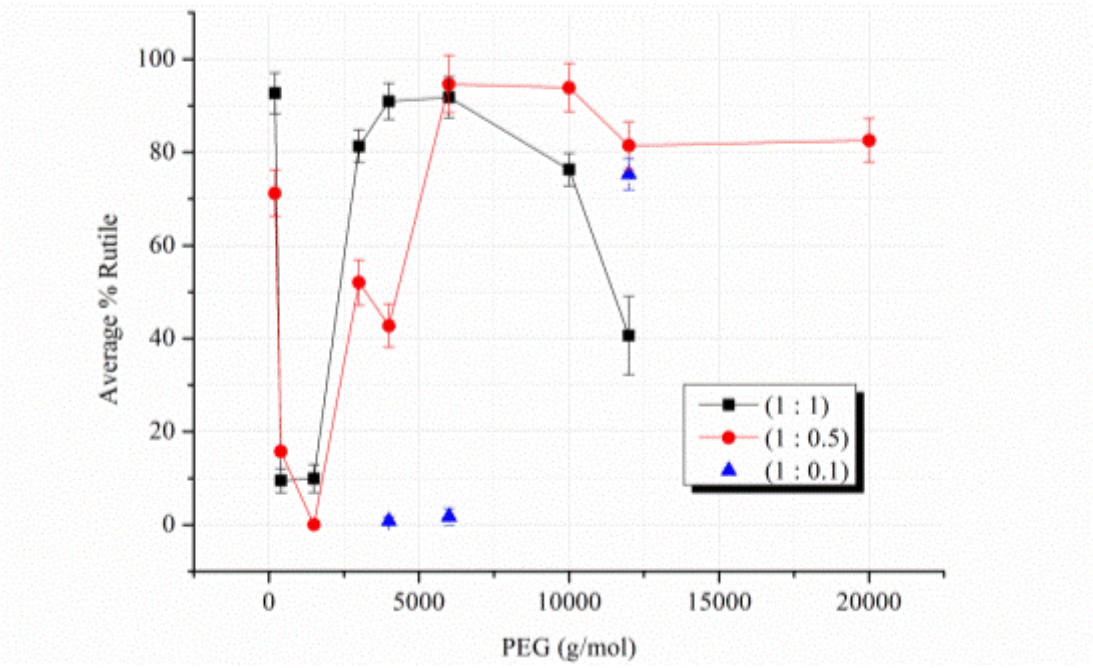

Figure 8.37: Effects of different PEG stoichiometries on the amount of rutile formed pre-calcination.

Figure 8.37 compares the effects of various PEG stoichiometries on the amount of rutile formed, as a function of increasing PEG chain length, pre-calcination. Interestingly, when the ratio of metal ions to PEG was (1 : 1) and (1 : 0.5), the amount of rutile formed displayed a similar trend as PEG chain length increased. The amount of rutile formed decreased, then increased and then decreased again. This effect was more pronounced for samples synthesised using a (1 : 1) ratio than for samples synthesised using a (1 : 0.5) ratio. In addition, the amount of rutile formed in a (1 : 1) synthesis was greater than for a (1 : 0.5) synthesis for all samples synthesised using PEG $<$ 6000 g/mol. Above PEG 6000 g/mol, samples synthesised in (1 : 0.5) conditions produced more rutile. For (1 : 1) and (1 : 0.5) syntheses, similar amounts of rutile were formed in samples containing PEG 400 and 6000 g/mol. The subset of data collected from the samples synthesised in a (1 : 0.1) ratio suggest that rutile is the preferred phase when PEG chain length is increased. For (1 : 0.5) and (1 : 0.1) syntheses, similar amounts of rutile were formed in samples containing PEG 12000 g/mol.

Based on the current hypothesis concerning the formation of polymer reaction chambers, the following is presented in an attempt to rationalise the data contained in

figure 8.37: during heating and prior to ignition, PEG of all molecular weights undergo varying degrees of decomposition. For a given heating rate and metal ion concentration, the level of decomposition is likely due to the quantity and length of the polymer chains present in the mixture.

For small chain polymers (such as PEG 200 g/mol), chain entanglement is unlikely to occur. PEG 200 g/mol chains likely form reaction chambers that are large enough to produce anatase and rutile, and small enough that they do not undergo further decomposition to form smaller chambers. Smaller chambers would impede rutile formation, as discussed previously. For this reason, samples synthesised from PEG 200 g/mol in a (1 : 0.5) synthesis exhibit a mixture of anatase and rutile. The increased quantity of PEG 200 g/mol in a (1 : 1) synthesis provides more fuel during ignition. From a thermodynamics perspective, since the energy of the system has increased, the system would move to a more energetically stable state. Thus rutile formation is encouraged. From a chemistry perspective, increased fuel in the reaction mixture would result in longer and hotter ignitions favouring the formation of rutile.

Longer chain PEG (such as PEG 400 and 1500 g/mol) plausibly forms larger reaction chambers. During decomposition, longer chains are less stable than shorter chains and therefore, break apart. The high energy dangling bonds of the large chain fragments will move to decrease energy by bonding in such a manner to create smaller chambers. Given that PEG 400 and 1500 g/mol are not long chain polymers, cleavage along the chain can produce smaller chambers than those formed by PEG 200 g/mol. As discussed previously, small polymer chambers favour the formation of anatase.

PEG chains of intermediate length (PEG 3000 – 6000 g/mol) will form reaction chambers of intermediate size. The PEG chains will decompose under the action of heating causing the high energy dangling bonds of the polymer fragments to stabilise through bonding. Because the PEG fragments are larger than for those created by smaller PEG chains, the resulting reaction chambers should be larger. Larger chambers have the ability to nucleate anatase and rutile. This is evidenced for samples synthesised using (1 : 0.5) synthesis conditions. It does not explain the large amount of rutile formed using (1 : 1) synthesis conditions. It is possible that the increased number of polymer chains used in a (1 : 1) synthesis cause polymer entanglement. This is plausible given that the PEG chains are of intermediate length and in a (1 : 1) synthesis, there are twice as many chains compared with a (1 : 0.5) ratio. Polymer

entanglement will have the effect of increasing the size of formed reaction chambers. Therefore, rutile will be the preferred phase.

Further increasing the polymer chain length (PEG 10000 – 20000 g/mol) is expected to cause an increase in the number of large polymer chambers obtained. Therefore rutile is expected to be present as the major phase. This is evidenced for samples synthesised using (1 : 0.5) synthesis conditions. Samples containing long chain polymers synthesised using (1 : 1) synthesis conditions exhibit decreasing amounts of rutile as PEG chain length is increased. This is contradictory to the trend observed for (1 : 0.5) synthesis conditions. However, since the number of polymer chains are doubled in a (1 : 1) synthesis, it is possible that the sheer volume of polymer present in the sample causes steric stabilisation of the nucleated anatase phase. Stabilisation has the effect of inhibiting the transformation of anatase to rutile, as previously discussed.

The data obtained from the (1 : 0.1) synthesis suggests that for smaller PEG chains, at a (1 : 0.1) ratio, there is insufficient polymer present in the mixture to form large reaction chambers. Small chambers stabilise the nucleated anatase phase and impede rutile formation. Increasing the length of the polymer causes the formation of larger reaction chambers and allows for rutile nucleation.

Lee and Lee found that increasing the ratio of ethylene glycol to metal ions tended to produce rutile[7]. The researchers suggested that insufficient ethylene glycol caused an inhomogeneous distribution of cations, leading to anatase formation[7]. In this experiment, increasing the quantity of PEG (i.e.: increasing the chain length) at (1 : 0.1) and (1 : 0.5) ratios had a similar effect of producing more rutile. As explained, the quantity of added polymer impacts steric stabilisation and therefore impacts the formed phase. However, since this system considers polyethylene glycol and not ethylene glycol, other factors must be considered – as discussed. The consideration of other factors is warranted by the (1 : 1) system deviating from rutile phase formation at long PEG chain lengths.

Volumetric addition of PEG to metal ions saw the amount of rutile formed as a function of increasing PEG chain length oscillate between 40% and 100%. Volumetric addition implied decreasing the number of PEG chains as the PEG chain length was increased, such that the volume of PEG added to all solutions was

equivalent. Thus, the system had no driving force, aside from the supplied heat, to encourage chain cleavage at specific points. For that reason, formed reaction chambers could be of various sizes, despite the chain length used in the reaction – causing the amount of rutile formed to fluctuate.

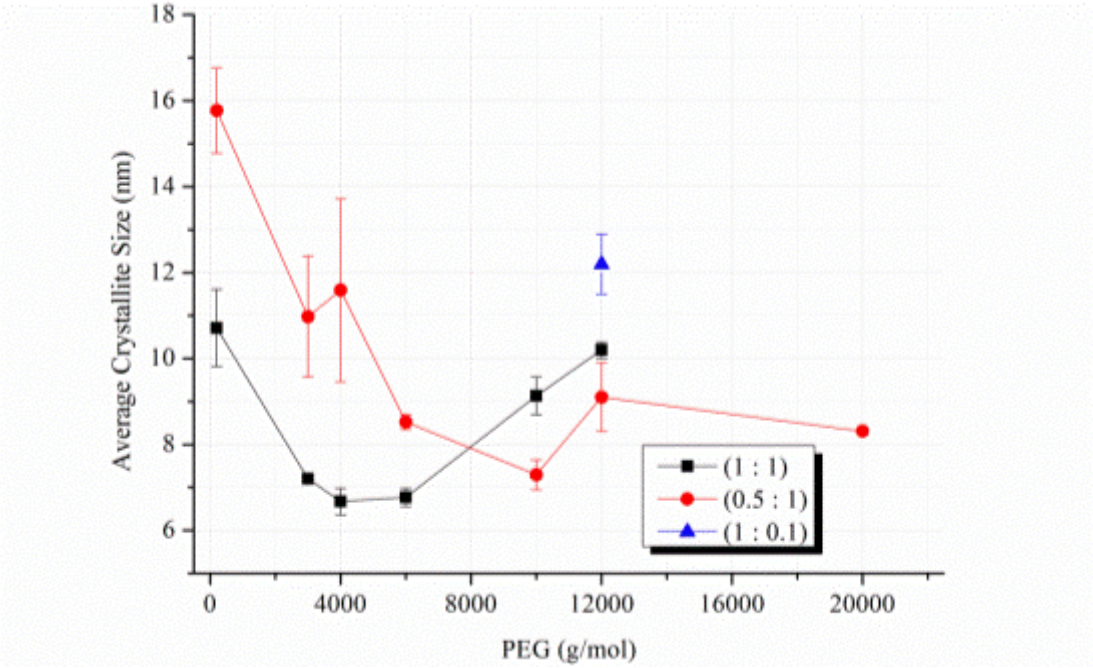

Figure 8.38: Effects of different PEG stoichiometries on rutile crystallite size formed pre-calcination.

Figure 8.38 shows the variation in rutile crystallite size formed using (1 : 1), (1 : 0.5) and (1 : 0.1) syntheses, as a function of increasing PEG molecular weight. For PEG $<$ 6000 g/mol, rutile crystallites synthesised in a (1 : 1) synthesis were smaller than crystallites synthesised in a (1 : 0.5) synthesis. Above PEG 10000 g/mol, rutile crystallites synthesised in a (1 : 1) synthesis were larger than in a (1 : 0.5) synthesis. The largest rutile crystallites were formed using a (1 : 0.5) synthesis and PEG 200 g/mol; and a (1 : 0.1) synthesis, using PEG 12000 g/mol. The smallest rutile crystallites are formed using a (1 : 0.5) synthesis and PEG 4000 g/mol. Figure 8.38 can be understood in terms of the inverse relationship between the amount of rutile formed and its respective crystallite size for the (1 : 1) and (1 : 0.5) syntheses. The inverse relationship was rationalised using oriented attachment and anatase crystal stabilisation (or lack thereof) by small polymer chambers.

8.3 Conclusions

Both (1 : 1) and (1 : 0.5) syntheses produced an average amount of rutile across all samples of ~ 60%. This was an expected result given that water containing HNO_3 was employed as the solvent for these syntheses. Rutile (1 1 0) crystallites formed in (1 : 1) and (1 : 0.5) syntheses pre-calcination coarsened between ~ 7 – 11 nm and ~ 8 – 16 nm respectively. In samples containing a mixture of both phases, rutile crystallites were typically larger, as expected. An imperfect inverse relationship between the amount and size of rutile crystallites was observed for both the (1 : 1) and (1 : 0.5) systems.

For the (1 : 1) system, before calcination, no peaks were observed in the PXRD patterns generated from samples containing PEG 20000 g/mol. This was due to excess undecomposed polymer inhibiting X-ray penetration after ignition – confirmed by HRTEM. For all three experiments, calcination removed all polymer traces but did not significantly contribute to phase transformation as it did to crystallite coarsening. Post-calcination, rutile crystallites did not coarsen beyond ~ 25 nm.

HRTEM revealed the presence of anatase and rutile single crystals, and rutile mesocrystals. Additionally, rutile nanorods forming mesocrystals were found to be pyramidically capped and most likely single crystal in nature.

Addition of Ti^{4+} ions to PEG chains in a (1 : 1) and (1 : 0.5) ratio produced either anatase or rutile dependent on the PEG chain length. As PEG molecular weight increased, the amount of rutile formed in a (1 : 1) synthesis, decreased, then increased and finally decreased. This trend was similar to the reaction performed in a (1 : 0.5) synthesis for low and medium PEG chain length. Long chain PEG favoured rutile formation using a (1 : 0.5) synthesis. For a (1 : 0.1) synthesis, intermediate PEG length was found almost exclusively to favour anatase formation. Long chain PEG produced both phases, with rutile as the major phase.

These results were explained by considering the variation in PEG decomposition, chain entanglement, and steric entrapment afforded by high polymer concentrations. These factors were predicated on the formation of polymer reaction chambers within the mixture. Hence, the developing hypothesis has been modified and strengthened based on the results of varying PEG stoichiometry and chain length.

8.4 References

1. Banfield, J. F., Bischoff, B. L. & Anderson, M. A. TiO2 accessory minerals: coarsening, and transformation kinetics in pure and doped synthetic nanocrystalline materials. *Chemical Geology* **110,** 211 – 231 (1993).

2. Penn, R. L. & Banfield, J. F. Oriented attachment and growth, twinning, polytypism, and formation of metastable phases: Insights from nanocrystalline TiO2. *American Mineralogist* **83,** 1077 – 1082 (1998).

3. Li, Y., Liu, J. & Jia, Z. Morphological control and photodegradation behavior of rutile TiO2 prepared by a low-temperature process. *Materials Letters* **60,** 1753 – 1757 (2006).

4. Kakiuchi, K., Hosono, E., Imai, H., Kimura, T. & Fujihara, S. {1 1 1}-faceting of low-temperature processed rutile TiO2 rods. *Journal of Crystal Growth* **293,** 541 – 545 (2006).

5. Hosono, E., Fujihara, S., Kakiuchi, K. & Imai, H. Growth of Submicrometer-Scale Rectangular Parallelepiped Rutile TiO2 Films in Aqueous TiCl3 Solutions under Hydrothermal Conditions. *Journal of the American Chemical Society* **126,** 7790 – 7791 (2004).

6. Zhang, D., Li, G., Wang, F. & Yu, J. C. Green synthesis of a self-assembled rutile mesocrystalline photocatalyst. *CrystEngComm* **12,** 1759 – 1763 (2010).

7. Lee, S. J. & Lee, C. H. Fabrication of nano-sized TiO2 powder via an ethylene glycol entrapment route. *Materials Letters* **56,** 705 – 708 (2002).

Chapter 9: Effects of Rapid Heating on Titania Polymorph and Crystallite Size Formation

Chapter 9 focuses on the interplay between rapid heating and PEG stoichiometry. Thus, the primary aim of this experiment was to explore the effects of rapid heating on the formed phase and crystallite size of titanium dioxide. PEG-metal ion mixtures were prepared according to two Ti^{+} to PEG stoichiometric ratios: (1 : 1) and (1 : 0.5) – as described in chapter 8. PEG of various molecular weights (200 – 20000 g/mol) was selected for use in the stoichiometric syntheses. This allowed for the effects of rapid heating to be monitored as a function of PEG stoichiometry and chain length. The results obtained will aid in better understanding the mechanism of resin-gel synthesis particle formation under rapid polymer degradation conditions.

Rapid heating was effected by adding homogeneous polymer mixtures to a pre-heated vessel at 915 °C. Powdered samples were synthesised and calcined in less than 40 seconds. A short reaction time was expected, however, it does decrease the contact time between the resins and the source of polymer degradation. Therefore, the effects of the interplay between a high synthesis temperature and short reaction time are noteworthy.

9.1 Experimental Procedure

The experimental procedure followed for this experiment consisted of 4 parts: Addition of Ti ions to PEG in a (1 : 1) ratio, addition of Ti ions to PEG in a (1 : 0.5) ratio, heat treatments, and characterisation. Resin synthesis (i.e.: parts 1 and 2) in this experiment was conducted in exactly the same manner for PEG 1500, 3000, 6000, 10000, 12000 and 20000 g/mol as described in chapter 8. For this reason, resin synthesis from these specified PEG molecular weights will not be described.

9.1.1 Heat Treatments

All mixtures were heated and stirred as necessary to allow for complete homogenisation. Samples synthesised in a (1 : 1) ratio had to be heated at a higher temperature for a longer period of time to attain homogeneity. All 12 gels were placed

in a fume hood ~ 30 cm under two 200 W infrared light bulbs for two weeks. This was to ensure complete solvent evaporation and resin formation. Replicate samples were introduced by dividing each resin prior to ignition. Resins were heated sufficiently to encourage flow prior to pyrolysis. Heating was successful in forming molten resin-gel synthesised samples for all polymer chain lengths excluding PEG 200 and 400 g/mol. Mixtures containing PEG 200 and 400 g/mol have a tendency of forming near solid resins that do not go through a molten intermediate when heated. They typically ignite as a solid. For this reason, this experiment did not consider samples synthesised from PEG 200 and 400 g/mol.

A commercially available cast iron jaffle maker (figure 9.1) was employed as the heating vessel for this experiment. The vessel was allowed to attain thermal equilibrium inside a muffle furnace set to 915 °C. Once the desired temperature was acquired, the vessel was removed from the furnace and placed atop a clay brick. The temperature at which synthesis was initiated was 900 °C $\leq$ x < 915 °C on account of the vessel cooling once removed from the furnace. Molten resin-gels were introduced into the vessel swiftly after it was removed from the furnace. Both compartments of the jaffle maker were used in the ignition. One compartment contained the sample, while the other contained the respective replicate sample. The sample synthesised using PEG 12000 g/mol in a (1 : 0.5) ratio was ignited first.

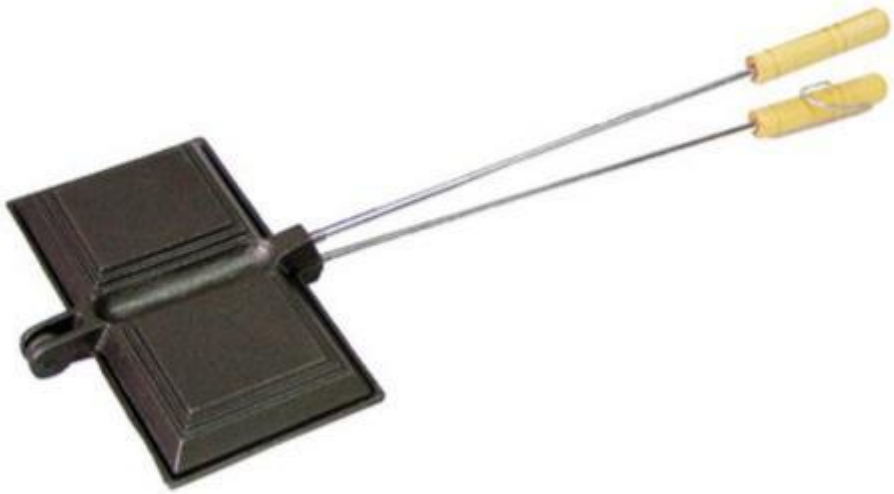

Figure 9.1: Cast iron jaffle maker employed as the heating vessel for the rapid heat synthesis experiments. The inside surfaces of the vessel were used to heat the resin-gels.

Upon contact with the heated vessel, the molten resin-gel burst into flames. Seemingly instant ignition occurred because the vessel was heated to beyond the auto-ignition point of the mixture. Upon closer inspection, it was found that 'droplets' of the resin-gel had separated from the mass and were skittering across the surface of the vessel following initial contact. This observation was consistent with the Leidenfrost effect[1]. The resin-gel sample moved to fill the area of the vessel and bubbled during the course of its ignition. Prior to the end of ignition, there was visual evidence of vapour escape from the sample, combined with an audible hissing sound. Ignition occurred for < 30 seconds following which, the sample presented with a black, appearance. Approximately 10 seconds thereafter, the sample had calcined and presented with a distinct yellow appearance. White powders were collected once the vessel had cooled to room temperature. These powders were either flaky or granular in texture. This process was repeated for all resin-gels. Figure 9.2 illustrates the ignition process from sample addition until calcination.

9.1.2 Characterisation

PXRD data was obtained using a Bruker D2 Phaser diffractometer. The setup of the D2 Phaser was described in chapter 5, with the exception that Co Kα radiation (λ = 1.7903 Å) was used. Samples were analysed between 20° and 60° 2θ in 0.023 increments counting for 1 second per step. A JEOL 3011 HRTEM was employed for this investigation.

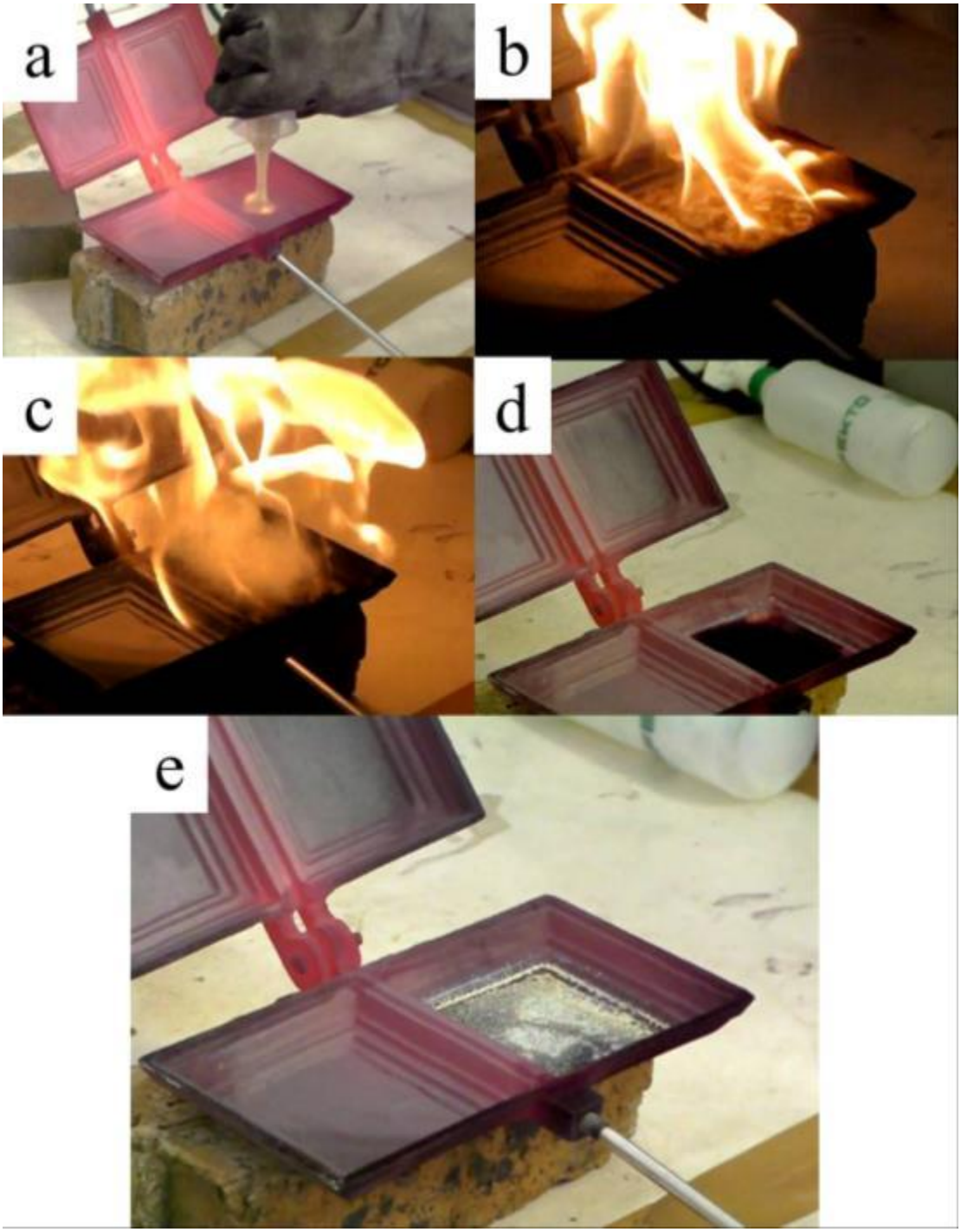

Figure 9.2: Progression of rapid heat synthesis. (a) Initial addition of molten resin-gel to the vessel. (b) After a few seconds, the mixture moved to fill the area of the vessel accompanied by bubbling and sputtering. (c) Toward the end of the ignition, vapour was emitted with an audible hissing sound. (d) A thin film of black powder was formed post-ignition that was (e) calcined after a few seconds. The yellow appearance of the sample gave way to white after the powder was cooled to room temperature.

9.2 Results and Discussion

9.2.1 Rapid heating samples prepared in a (1 : 1) ratio

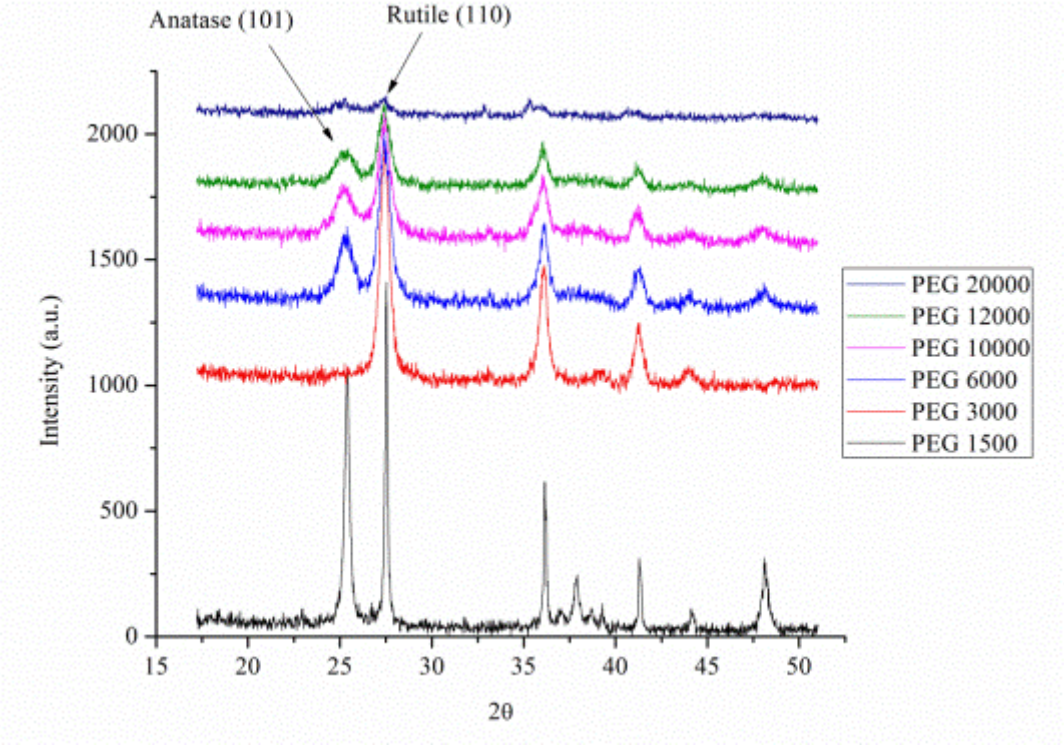

Figure 9.3: PXRD patterns of calcined samples synthesised in a (1 : 1) ratio.

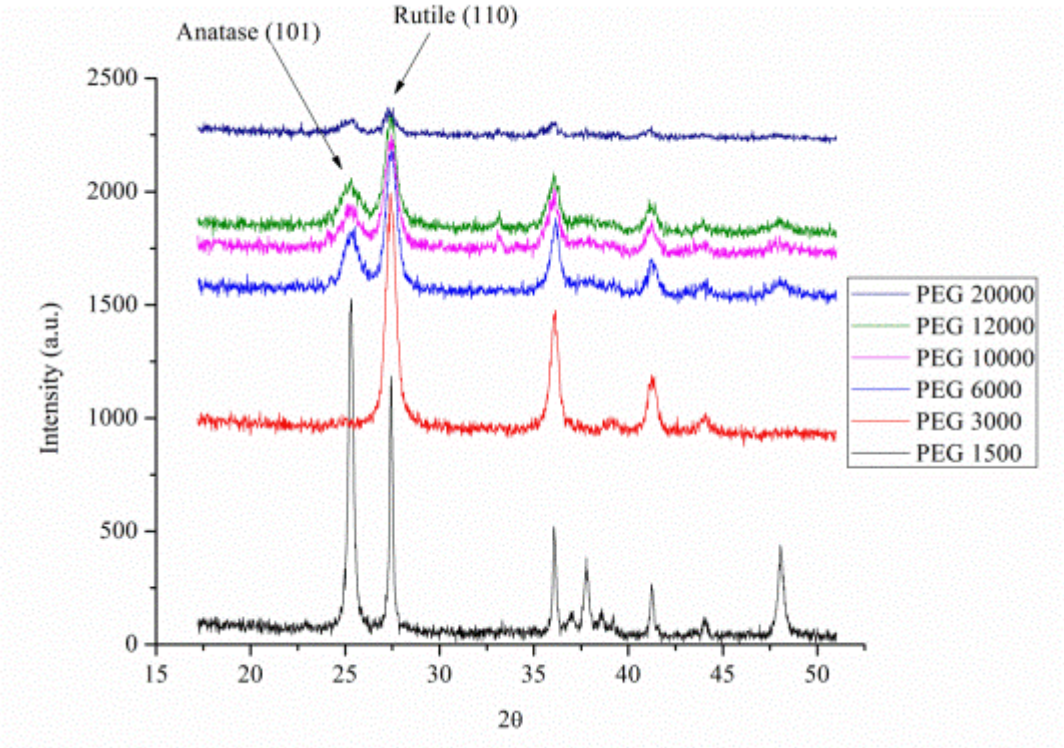

Figure 9.4: PXRD patterns of replicate calcined samples synthesised in a (1 : 1) ratio.

Figure 9.3 contains the diffraction patterns for samples synthesised in a (1 : 1) ratio after rapid heat ignition. Initial comparisons of the patterns suggest that peak signal to noise ratio decreased as PEG molecular weight increased. Weak signal to noise ratio was observed in chapter 8 for samples synthesised in a (1 : 1) ratio using long chain PEG. The phenomenon was rationalised by considering that pyrolysis did not successfully remove all polymer fragments. These fragments inhibited X-ray penetration into the crystal and therefore, reduced the peak signal to noise ratio obtained. Calcination improved the signal to noise ratio by successfully removing all polymer fragments and carbon from the samples. This result indicates that calcination at 500 °C for 1 hour is more effective at removing PEG fragments and carbon deposits from titania samples than rapid calcination on a swiftly cooling reaction vessel.

Decreasing peak intensity does not render the experiment moot since the ratio of the anatase (1 0 1) and rutile (1 1 0) peaks are considered per sample. Since the intensity of both peaks decreased per sample, the ratio remained consistent.

The poor signal to noise ratio can be explained by considering that polymers typically have lower thermal conductivity compared with metals[2]. Thus, although the reaction vessel was much hotter than the crucibles used in previous experiments, it is likely that the resin-gels did not conduct all of the supplied heat. Longer chain polymers were especially resilient to rapid heat conduction. Additionally, water present in the mixture served as an anti-plasticizer, increasing the glass transition temperature of the polymer chains to which it was bound[3]. This served to increase the endurance of the polymer chains in a rapid, high temperature synthesis, and contributed to PEG fragments remaining undecomposed in the collected sample. The action of water protecting PEG is further strengthened by the observation of vapour from the mixture prior to the end of ignition. This vapour could have originated from water.

Calculating the rate of heat transfer between the reaction vessel and resin is complicated by the amount of metal ions bound to the PEG molecular chains. This coupled with the multiple PEG chain lengths employed in this study, the various PEG stoichiometries, solution additives (such as citric acid and nitric acid) and solvents used, make correctly ascertaining and comparing rates of heat transfer a complex study, beyond the scope of this research.

Curiously, in this experiment analysed samples were white, suggesting that samples did not contain carbon remnants from PEG. Accordingly, initially formed black samples were calcined in the reaction vessel immediately following synthesis (figure 9.2e). A plausible interpretation of the physical appearance of the samples is that rapid heat completely removed most polymer chains, while leaving others undecomposed. PEG has a white appearance prior to decomposition.

The presence of undecomposed polymer is further supported by peak misalignment generated from samples containing higher molecular weight PEG. In the preceding chapters, peaks were misaligned in pre-calcined samples. Calcination served to remove all carbon deposits causing better peak alignment. The white appearance of the present samples coupled with peak misalignment is indicative of an entity imparting non-uniform strain on the titania lattice. The absence of PXRD peaks corresponding to other metals suggests that the strain is not due to metal leaching from the jaffle maker. This will be further confirmed using HRTEM.

Except for the sample synthesised using PEG 3000 g/mol, all other samples appear to produce both anatase and rutile, with the latter being the major phase. This is a surprising result given that 900 °C is sufficiently hot to encourage anatase to rutile transformations in most samples (including sol-gel synthesised powders)[4]. The formation of anatase is indicative of the role of undecomposed polymer in rapid heat synthesis.

Anatase and rutile peaks obtained from the sample synthesised using PEG 1500 g/mol are sharp, signalling the presence of large crystallites. Peak width increases as PEG molecular weight increases. This is indicative of the formation of smaller crystallites. Based on the postulation of undecomposed polymer remaining in the sample, it is possible that these coordinated polymer fragments inhibited crystallite growth. The mechanism of inhibition could be due to polymer-metal ion complex coordination and consequently fewer ions available to grow the developing crystallites. It could also be due to polymer fragments protecting nucleated crystallites and shielding them from growth.

Both of the abovementioned plausible mechanisms can be responsible for the formation of amorphous titania. It is possible that titania nuclei develop quickly once exposed to the reaction vessel. The poor thermal conductivity of the polymer and

rapidly cooling vessel provide unfavourable conditions for crystallisation of anatase and by extension rutile. In this manner, the poor signal to noise ratio may also be due to amorphous titania present in the sample – its formation directly proportional to the PEG chain length.

Figure 9.4 contains PXRD data from replicate samples synthesised in a (1 : 1) ratio. Comparing figures 9.3 and 9.4, there is good agreement between the original data set and its replicate for all samples except PEG 1500 g/mol. Samples synthesised using PEG 1500 g/mol appear to produce varying amounts of anatase and rutile. The variation in quantity and crystallite size will be statistically confirmed later.

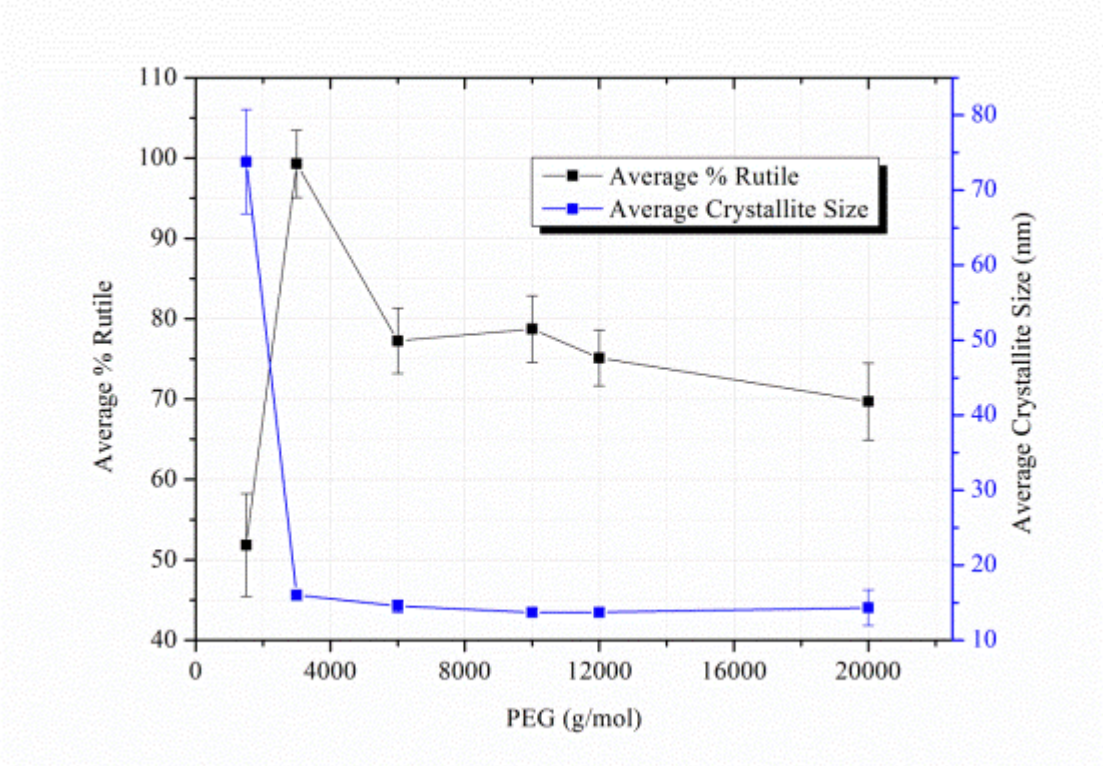

Figure 9.5: Average amount of rutile with associated crystallite size formed in a (1 : 1) synthesis.

Figure 9.5 shows the relationship between the amount and crystallite size of rutile formed as a function of increasing PEG chain length synthesised in a (1 : 1) ratio. Interestingly, samples synthesised from PEG 1500 g/mol produced the least amount of rutile (51.8%). This is in contrast to PEG 3000 g/mol that produced nearly phase pure rutile (99.3%). Decreasing amounts of rutile were formed as PEG chain length increased from 6000 – 20000 g/mol. Despite decreasing, rutile formation was always ≥ 70% for samples synthesised in this PEG chain length range. The average amount

of rutile formed across all samples (75.3%) suggested that rutile was the preferred phase. This was expected given that water containing HNO_3 was used as the solvent for this study.

This trend can be explained by considering that PEG 1500 g/mol is a small chain polymer and likely forms polymer reaction chambers small enough to stabilise anatase. PEG 3000 g/mol likely forms larger chambers favouring the transformation of anatase to rutile. Longer chain polymers likely form the largest chambers favouring rutile formation, however, due to the volume of polymer present in the sample at a (1 : 1) ratio, chain entanglement stabilises anatase.

The largest error in the data (6.4%) was present for the sample synthesised using PEG 1500 g/mol. This is due to both samples displaying a near 50/50 mix of anatase and rutile (as evidenced in figures 9.3 and 9.4). Error bars were generated by adding 4% of the average amount of anatase formed to the standard deviation of the replicate analyses.

PEG 1500 g/mol was responsible for the formation of the largest crystallites (73.8 nm). This is in contrast to the other PEG chain lengths that resulted in the formation of crystallites between ~ 13 – 16 nm. Average rutile crystallite size obtained from samples synthesised using PEG 3000 – 20000 g/mol was ~ 14.5 nm. The average rutile crystallite size produced across the range of PEG chain lengths was 24.4 nm. Large rutile crystallites formed from PEG 1500 g/mol is surprising. The high temperature synthesis likely caused nucleated rutile to coarsen due to a lack of protection by the short chain PEG 1500 g/mol.

The greatest error in the data was present for the sample synthesised using PEG 1500 g/mol (7.0 nm). Error bars were generated from the standard deviation of the replicate synthesis.

PEG 1500 g/mol produced both the smallest amount of and the largest rutile crystallites. The remaining PEG molecular weights produced rutile as the major phase and smaller crystallites. This is indicative of an inverse relationship between the size and amount of rutile formed as a function of increasing PEG chain length. As previously discussed the formation of polymer reaction chambers within the mixture and oriented attachment between titania crystallites can lead to the observation of this inverse trend.

Anatase crystallite size data was obtained from samples containing PEG 1500 g/mol, and 6000 – 20000 g/mol PEG. This data is represented in figure 9.6. From figure 9.6, it appears that anatase crystallite size is directly proportional to the amount of anatase formed per sample, as a function of increasing PEG molecular weight. The largest crystallites (43.4 nm) were obtained from PEG 1500 g/mol. This sample also produced the most amount of anatase (48.2%). PEG 6000, 10000, and 12000 g/mol produced similar sized anatase crystallites (14.5 nm, 13.7 nm, and 13.7 nm respectively). These samples also produced similar amounts of anatase (22.7%, 21.3% and 24.9% respectively). Anatase crystallites did not increase in size corresponding with an increase in the amount of anatase formed in the sample containing PEG 20000 g/mol. This suggests that the directly proportional relationship between amount and size of anatase crystallites deviated for samples containing high molecular weight PEG.

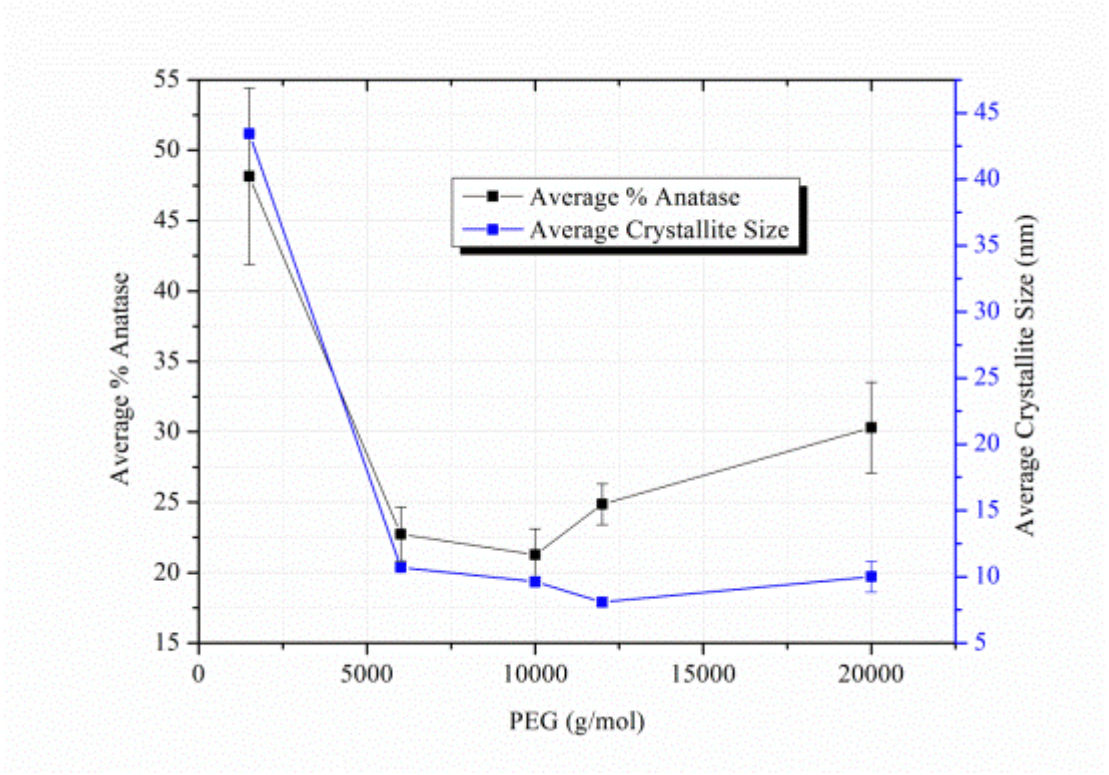

Figure 9.6: Average amount of anatase with associated crystallite size formed in a (1 : 1) synthesis.

A similar relationship between the amount and size of anatase crystallites was observed in chapter 8, for samples synthesised in a (1 : 1) ratio. The result was explained by considering that PEG of different molecular weights produced chambers

of different sizes. It was postulated that chains of PEG 1500 g/mol will undergo scission to form small reaction chambers stabilising the anatase phase therefore reducing rutile transformation. Anatase crystal growth is then expected. Longer chain PEG's produce larger chambers that do not stabilise the anatase phase sufficiently. Therefore, rutile is nucleated. Rutile nucleation occurs at the expense of anatase growth. High molecular weight PEG forms more anatase than intermediate chain PEG owing to the volume of PEG added in a (1 : 1) ratio. A large volume of PEG is likely to undergo entanglement and stabilise anatase to an extent. Therefore, evidence of a directly proportional relationship between the amount and size of anatase formed is favourable to the current narrative involving the creation of polymer reaction chambers.

Peculiarly, the largest anatase crystallites coarsened to 43.4 nm. Because PEG 1500 g/mol is a small chain polymer, it is likely that the reaction chambers formed from it, decomposed rapidly and completely during ignition. Therefore, only a portion of the sample was constrained into forming anatase before complete polymer degradation. Gopal *et al* showed that rapid heating statistically favoured the formation of anatase[5]. Given that this study employed the use of rapid heating, nucleated anatase continued to coarsen by taking up material from the mixture.

It is interesting to note that the behaviour of anatase was similar for a (1 : 1) system regardless of the heating method used. Therefore, polymer stoichiometry is a greater determinant of phase and crystallite size than heating rate. This is an expected result given the poor thermal conductivity of PEG, protection against rapid thermal degradation of PEG afforded by water, and the rapid completion of the reaction in this study. The caveat to the similarity between the two systems is rapid heating PEG 1500 g/mol produced approximately 50% by mass of anatase. This was in contrast to the near phase pure anatase formed using conventional heating of a (1 : 1) system containing PEG 1500 g/mol. This difference was justified considering that rapid heating likely degraded small polymer chambers swiftly, inhibiting complete anatase formation, and encouraging crystallite coarsening. The directly proportional relationship between mass percentage and crystallite size of anatase was not observed for any heating method in a volumetric addition of PEG to Ti^{+} ions.

Figure 9.7 compares the average rutile (1 1 0) and anatase (1 0 1) crystallite size synthesised in a (1 : 1) ratio as a function of increasing PEG molecular weight. The

figure does not contain any data generated from PEG 3000 g/mol as this polymer chain length resulted in the formation of nearly phase pure rutile. As expected, for any given PEG chain length, rutile crystallites were larger than anatase crystallites. For PEG molecular weight between 6000 – 20000 g/mol, rutile crystallites appear to be proportionally larger than anatase. This is not the case for the sample synthesised using PEG 1500 g/mol as it contains significantly larger rutile than anatase crystallites.

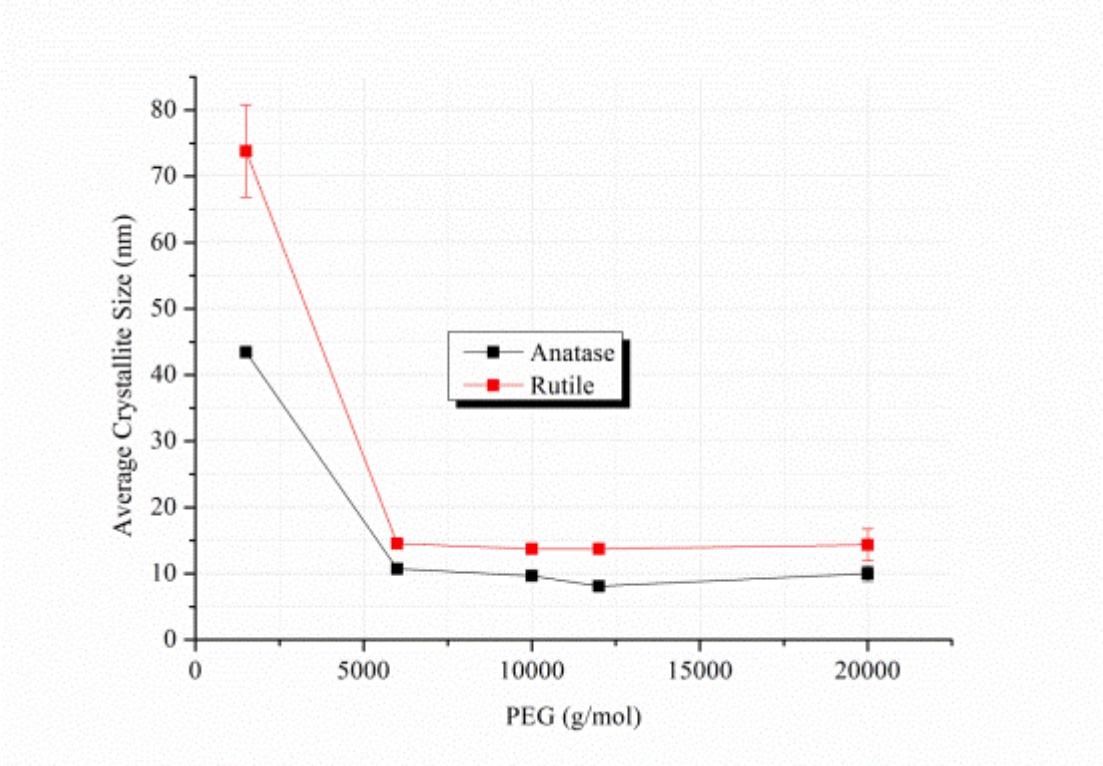

Figure 9.7: Comparison between the size of anatase and rutile crystallites formed in a (1 : 1) synthesis.

Tables showing the amount of each phase and crystallite size obtained for each sample with averages and errors are given in appendix G.

HRTEM images corresponding to the sample synthesised using PEG 3000 g/mol in a Ti^{+} : PEG ratio of (1 : 1) follow (figures 9.8 – 9.12).

From figure 9.8, it can be argued that since (0 0 1) is the documented anisotropic growth axis of rutile[6], steps on this axis are the likely source of crystal growth. The longer arrows toward the top of the image show the positions of oriented attachment.

In this experiment, oriented attachment could have occurred between 2 anatase crystals that nucleated rutile. Oriented attachment could have also occurred between 2 rutile crystals in an attempt to reduce total energy by stabilising dangling bonds.

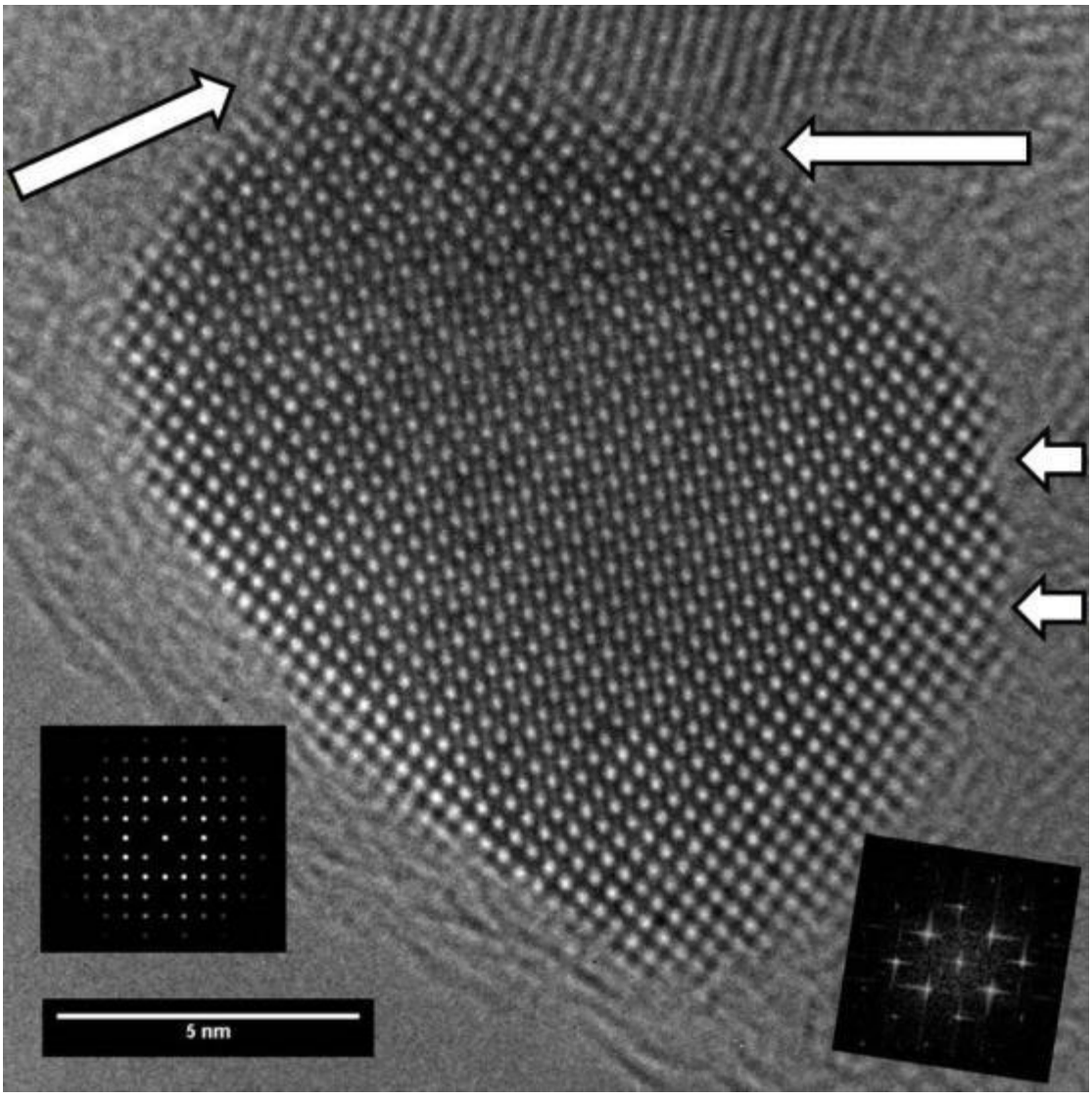

Figure 9.8: (PEG 3000 g/mol in a Ti^{+} : PEG ratio of (1 : 1)). Single rutile crystallite in the (0 0 1) orientation. The short arrows on the right indicates the position of steps on the right side of the crystal. This crystal measures 15.69 nm down its length and 11.87 nm across its width. Long arrows toward the top of the image point to the position of oriented attachment. This is especially visible on the left side of the image where the 2D lattice fringes appear to merge with the 1D fringes from another crystal.

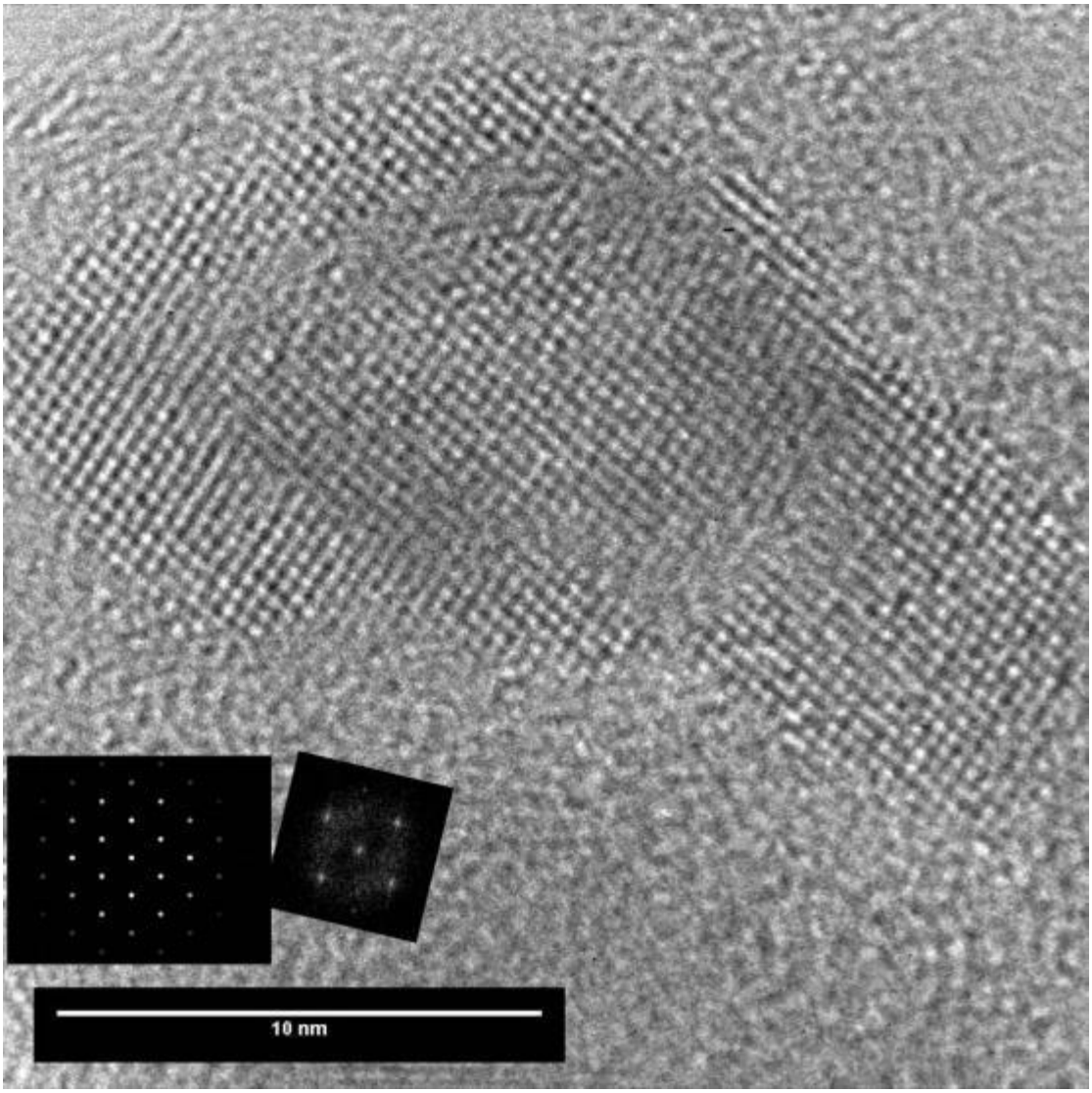

Figure 9.9: (PEG 3000 g/mol in a Ti^{+} : PEG ratio of (1 : 1)). Single rutile crystal in the (0 1 0) or (1 0 0) orientation. Notice the inconsistent shape of this anisotropic shaped crystal. It measures ~ 23 nm top to bottom and ~ 15 nm along its width. The semi-amorphous ring may be attributed to residual carbon or polymer components.

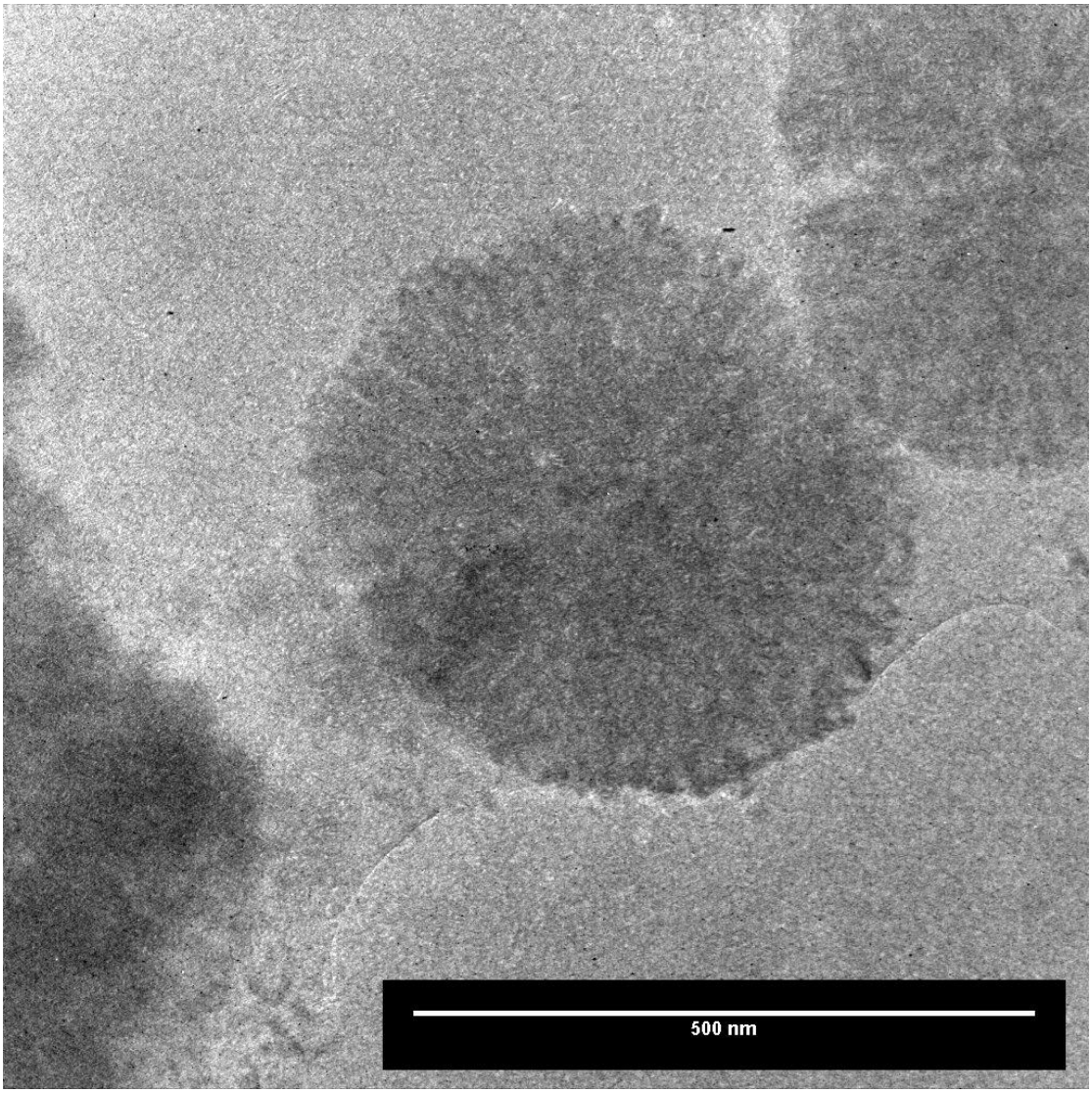

Figure 9.10: (PEG 3000 g/mol in a Ti^{+} : PEG ratio of (1 : 1)). Rutile mesocrystals were evident in this sample. This superstructure appears to be slightly fragmented along its centre. It has a diameter of ~ 500 nm.

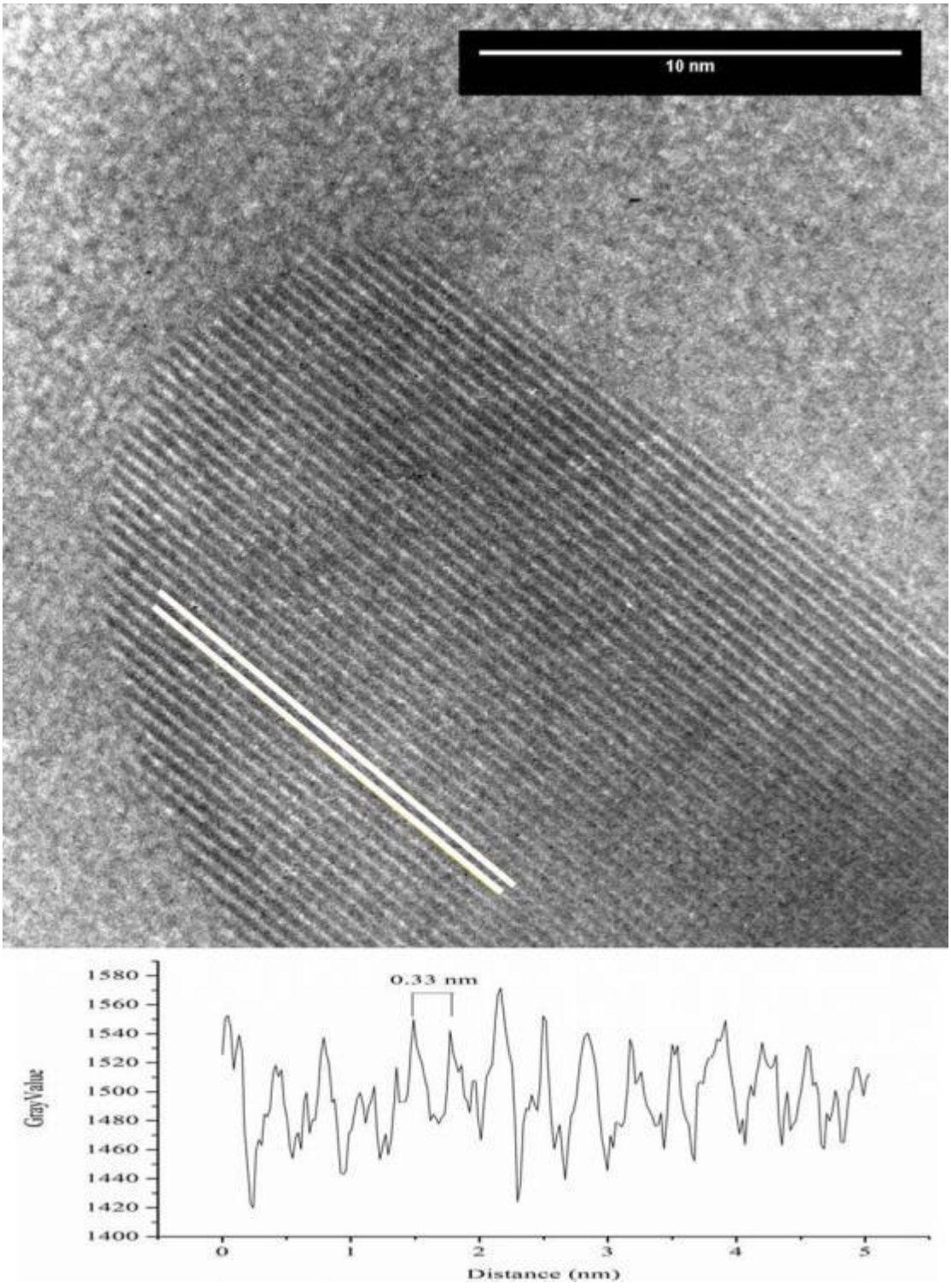

Figure 9.11: (PEG 3000 g/mol in a Ti^{+} : PEG ratio of (1 : 1)). The tip of a rutile mesocrystal measuring ~ 16 nm across its width and more than 23 nm across its length. Rutile was confirmed by measuring the distance between peaks (0.33 nm) generated in the line profile. The tip of this crystal is inconsistent and shows a degree of tapering.

The large rutile nanorod size obtained in figure 9.12 was unusual as previously imaged rutile nanorods comprising mesocrystals measured < 10 nm across. Rutile coarsening in this study is likely due to rapid heating. The curved nanorod tip observed in this figure was explained by considering that rapid heating caused the crystal to coarsen uniformly along its tip. The mechanism of rutile mesocrystal formation suggests that anatase transforms into rutile within the reaction chamber (as previously described). Multiple rutile crystals serve as mesocrystal seed particles and coarsen anisotropically along (0 0 1).

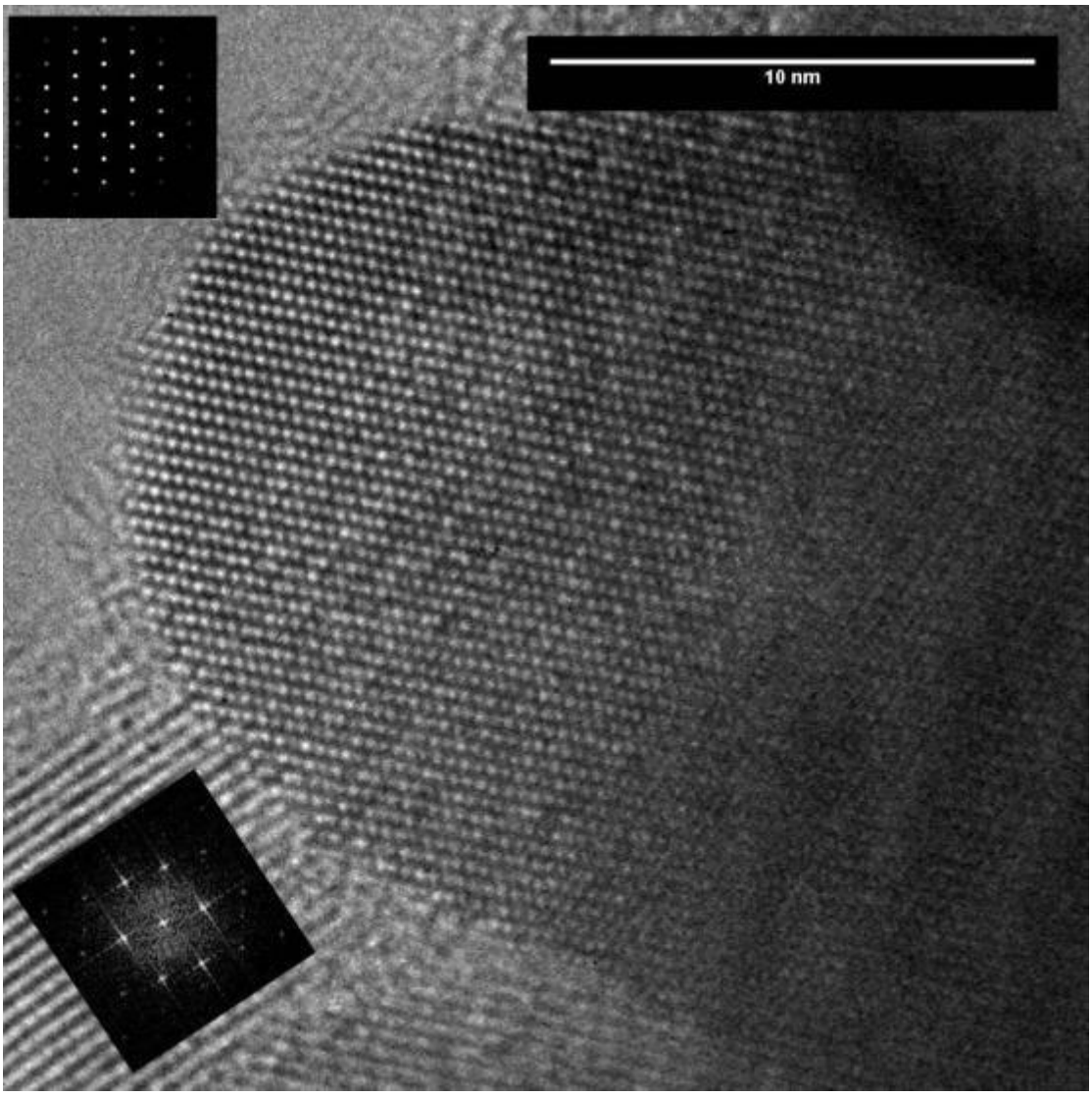

Figure 9.12: (PEG 3000 g/mol in a Ti^{+} : PEG ratio of (1 : 1)). Well-defined rutile nanorod imaged at the tip of a mesocrystal. This crystal was aligned along (1 1 1) and measured ~ 18 nm across its width and over 22 nm down its length. The tip is also curved rather than flat as previously described[7]. From this image, it appears that the nanorod is made up of a single anisotropic crystal.

9.2.2 Addition of Ti ions to PEG in a (1 : 0.5) Ratio

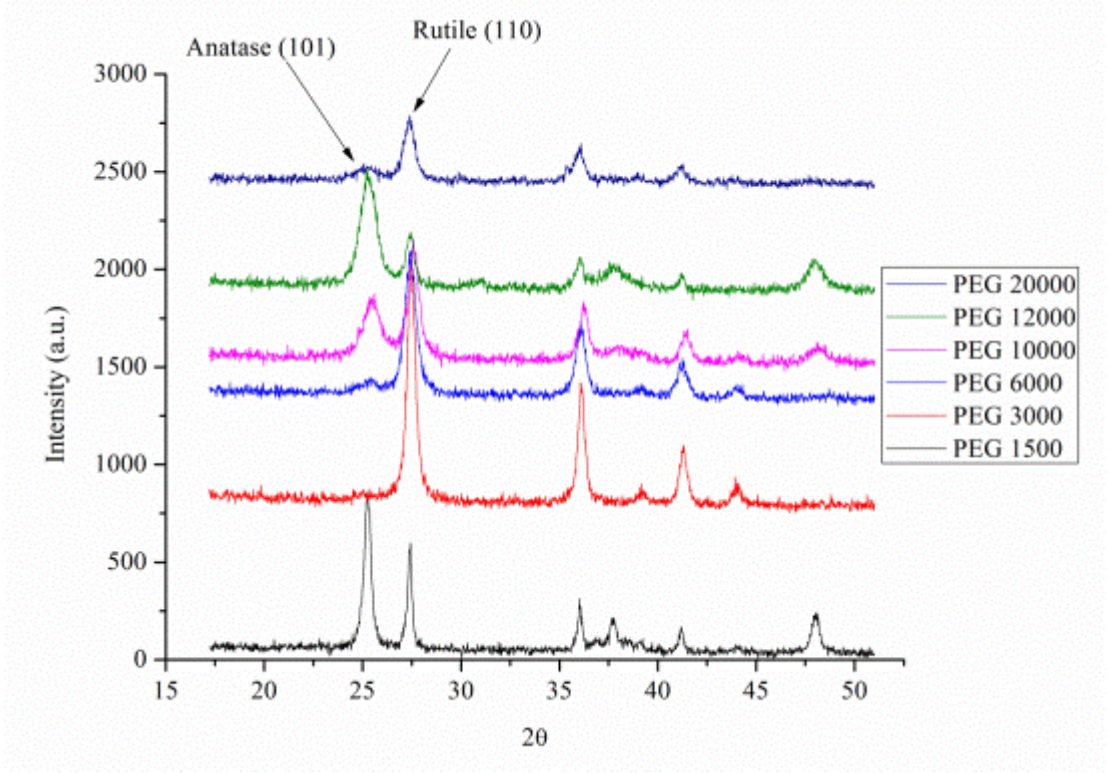

Figure 9.13: PXRD patterns of calcined samples synthesised in a (1 : 0.5).

Figure 9.13 shows the PXRD patterns collected form samples synthesised in a (1 : 0.5) ratio. The decrease in signal to noise ratio proportional to PEG molecular weight is not as pronounced at this ratio as it was for a (1 : 1) synthesis. For the (1 : 1) synthesis, poor PEG thermal conduction and water induced protection of PEG chains was considered to explain the poor signal to noise ratio. A better signal to noise ratio for samples synthesised using longer chain PEG in a (1 : 0.5) ratio is expected as there are fewer polymer chains present in all samples. Therefore, there should be a reduced presence of undecomposed polymer in all samples relative to those synthesised in a (1 : 1) ratio.

Peak misalignment is characteristic of non-uniform lattice strain. As discussed above, this strain is most likely due to the presence of undecomposed polymer in the sample.

Samples synthesised from PEG 6000, 10000 and 20000 g/mol produce both anatase and rutile as the minor and major phases respectively. This is in contrast to samples produced from PEG 3000 g/mol that appear to contain mainly rutile. Samples synthesised from PEG 1500 g/mol and 12000 g/mol produce both anatase and rutile as the major and minor phases respectively.

There appears to be good correlation between the original samples and their replicates as given in figure 9.14. Unlike for the (1 : 1) system, PEG 1500 g/mol produced anatase as the major phase for both the original and replicate sample. Peak misalignment is evident in the replicate data set.

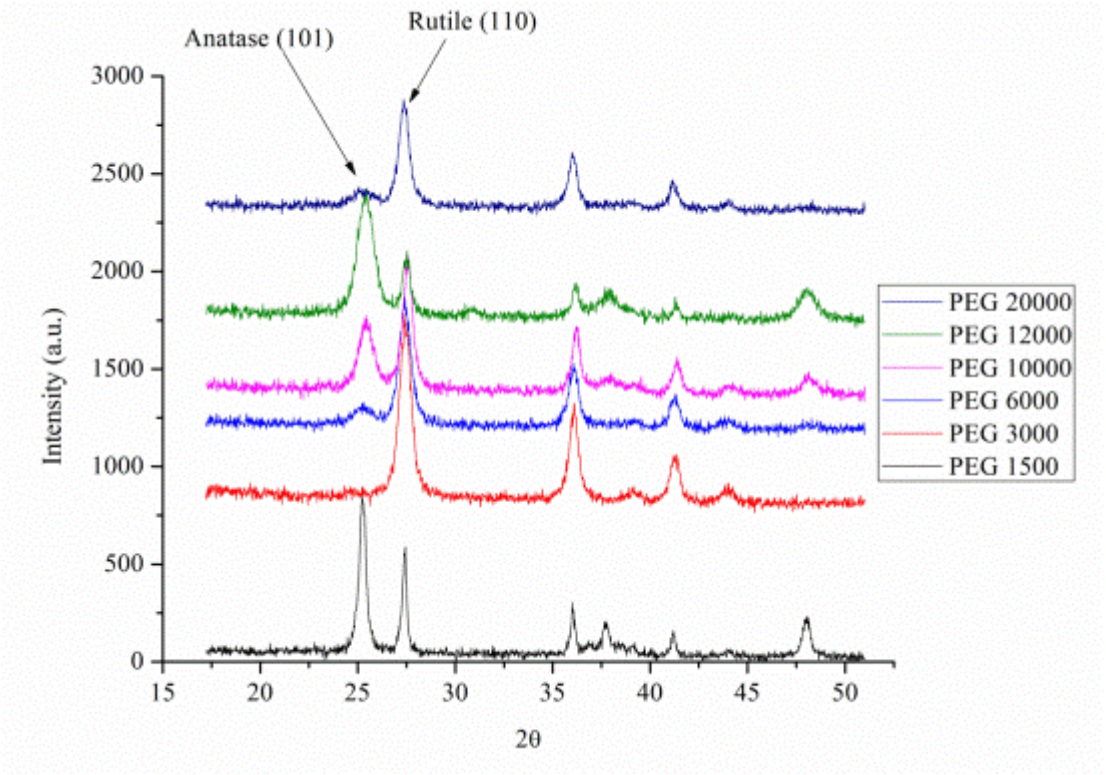

Figure 9.14: PXRD patterns of replicate calcined samples synthesised in a (1 : 0.5) ratio.

Figure 9.15 depicts the relationship between the amount and size of rutile crystallites formed in a (1 : 0.5) ratio, as a function of increasing PEG molecular weight. Samples synthesised from PEG 1500 g/mol and 12000 g/mol produced the least amount of rutile (41.1% and 35.7% respectively). This is in contrast to PEG 3000 g/mol that produced phase pure material. The remaining samples (PEG 6000, 10000 and 20000 g/mol) favoured rutile formation. The average amount of rutile formed across all samples (71.7%) indicated that this system was biased toward rutile formation. This was an expected finding. Error bars were generated as previously described, and indicate good reproducibility.

Data obtained from the samples synthesised using PEG 1500 – 10000 g/mol and PEG 20000 g/mol can be rationalised by considering that short chain polymers produce small reaction chambers that stabilise anatase. Increasing chain length forms larger

chambers that allow for rutile nucleation. Larger chambers are unstable and break apart into smaller chambers. Additionally, the large volume of polymer present at high stoichiometric ratios should stabilise anatase. Therefore, long chain polymers produce a mixture of phases.

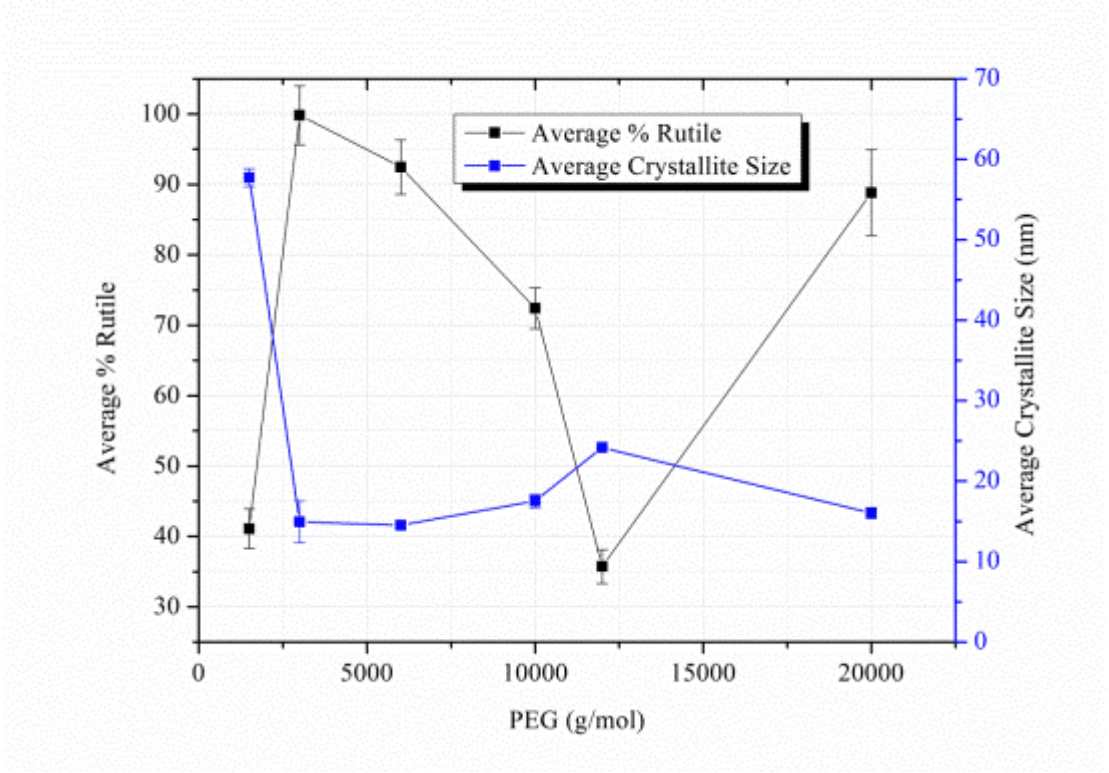

Figure 9.15: Average amount of rutile with associated crystallite size formed in a (1 : 0.5) synthesis.

The data obtained from PEG 12000 g/mol is peculiar. According to the current model, PEG 12000 g/mol should produce a mixture of anatase and rutile with the latter as the major phase. Evidently, this does not occur – with excellent reproducibility.

The generation of this erratic data point could be due to this present sample being the first to be ignited in the newly acquired jaffle maker. The manufacturers' specifications pertaining to this specific jaffle maker could not be obtained. However, cast iron cooking equipment is typically treated by the manufacturer. This treatment is usually a bio-adhesive, water soluble, polymer such as shellac[8]. Shellac is a linear, coordinating, straight chain polyester[9]. During heat curing, esterification occurs between shellac chains forming an infusible 3D structure. It is therefore possible that this structure was present during the initial use of the jaffle maker and interacted with the resin-gel during ignition. Other treatments include the use of polymerised

vegetable fat[10]. As previously described in chapter 7, additional solvent components can stabilise the anatase phase, inhibiting rutile formation.

Interestingly, the largest rutile crystallites (57.7 nm) were obtained from the sample synthesised using PEG 1500 g/mol. PEG 3000, 10000, and 20000 g/mol produced rutile crystallites in the size range of 14.5 – 17.5 nm). The average rutile crystallite size across the range of all samples equalled 24.2 nm. Error bars (generated as described previously) imply excellent reproducibility.

There is an imperfect inverse relationship between the amount of rutile formed and its respective crystallite size. Crystallite size is greater in samples that contain less rutile by mass. Although this relationship is valid for PEG 12000 g/mol, according to the current model of polymer based reaction chamber formation, crystallites formed in this sample were expected to be larger, given the small mass percentage of rutile formed. However, considering that other reaction components may be stabilising formed anatase, smaller anatase, and by extension smaller rutile crystallites are expected. This relationship was also observed for the (1 : 1) system and rationalised using oriented attachment and the formation of reaction chambers.

Figure 9.16 shows the relationship between the amount and size of anatase crystallites formed as a function of increasing PEG molecular weight synthesised in a (1 : 0.5) ratio. Note that this data set does not include PEG 3000 g/mol as this sample produced insufficient anatase for an accurate measurement of crystallite size to be made. As was evident for the (1 : 1) system, anatase crystal size appears to be correlated with the mass percentage of anatase contained within a sample. This is mainly true for samples synthesised from PEG 1500 – 6000 g/mol, and PEG 20000 g/mol. Interestingly, anatase (1 0 1) crystallites generated from the sample containing PEG 1500 g/mol measured 30.4 nm. This is expected considering that PEG 1500 g/mol is a short chain polymer that likely decomposed swiftly leaving nucleated anatase crystallites unprotected against coarsening.

For the sample synthesised using PEG 12000 g/mol, anatase crystallites were small (9.7 nm) when the mass percentage of anatase was high (64.3%). The mass percentage of anatase formed represents an irregular result and is likely due to the presence of a polymeric coating on the reaction vessel. As observed in chapter 7,

coordinating solvent additives stabilise the anatase phase while simultaneously hindering growth of anatase crystallites.

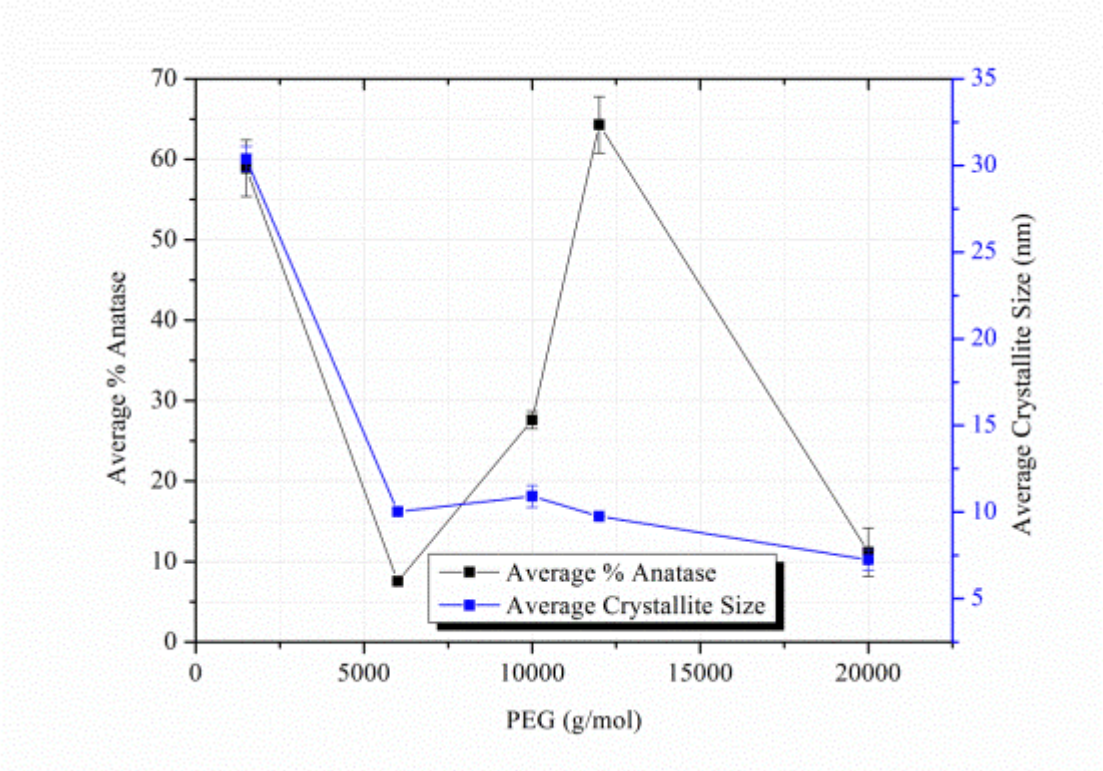

Figure 9.16: Average amount of anatase with associated crystallite size formed in a (1 : 0.5) synthesis.

Figure 9.17 compares the size of anatase (1 0 1) and rutile (1 1 0) crystallites obtained from samples synthesised in a (1 : 0.5) ratio. No crystallite size data from PEG 3000 g/mol is presented as this sample produced insufficient anatase to make a direct comparison. As expected, rutile crystallites were larger than anatase crystallites for any given PEG molecular weight. Unlike for samples synthesised in a (1 : 1) ratio, rutile crystallites did not coarsen in proportion to anatase crystallites. This was evidenced by larger rutile crystallites formed in samples containing PEG 1500 and 12000 g/mol.

Tables showing the amount of each phase and crystallite size obtained for each sample with averages and errors are given in appendix G.

HRTEM images corresponding to the sample synthesised using PEG 1500 g/mol in a Ti^{+} : PEG ratio of (1 : 0.5) follow (figures 9.18 – 9.19). Figures 9.20 and 9.21 were generated from the sample synthesised using PEG 6000 g/mol in a (1 : 0.5) ratio.

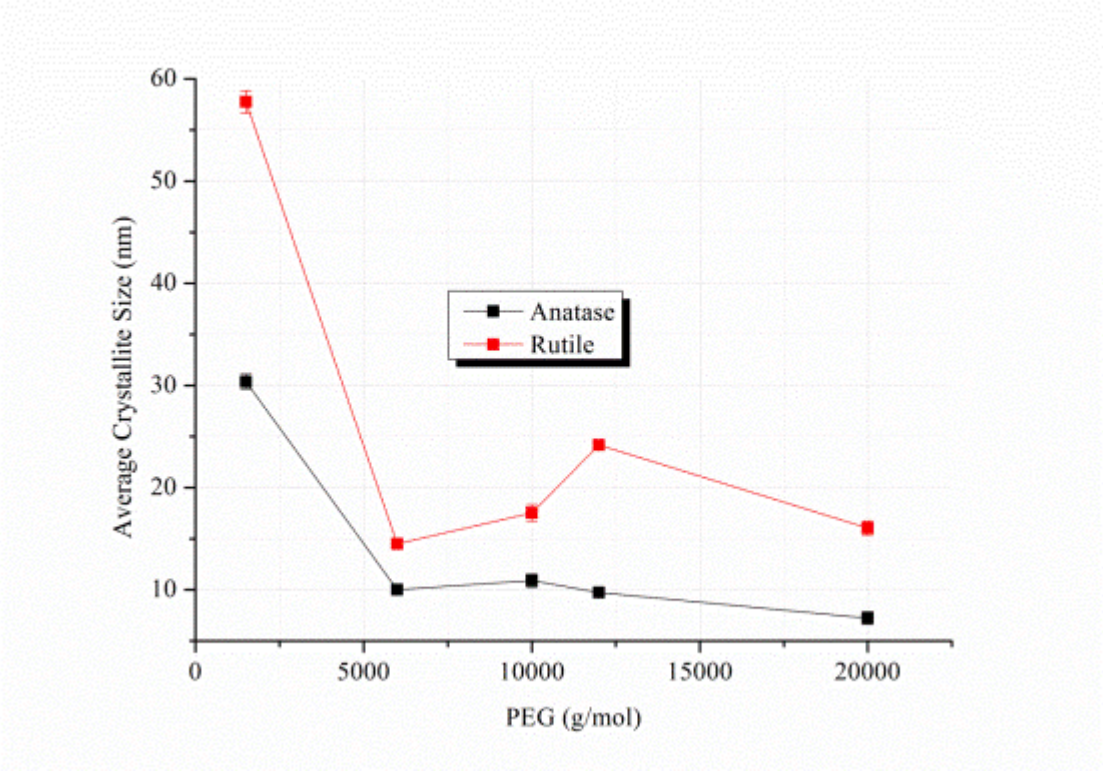

Figure 9.17: Comparison between the size of anatase and rutile crystallites formed in a (1 : 0.5) synthesis.

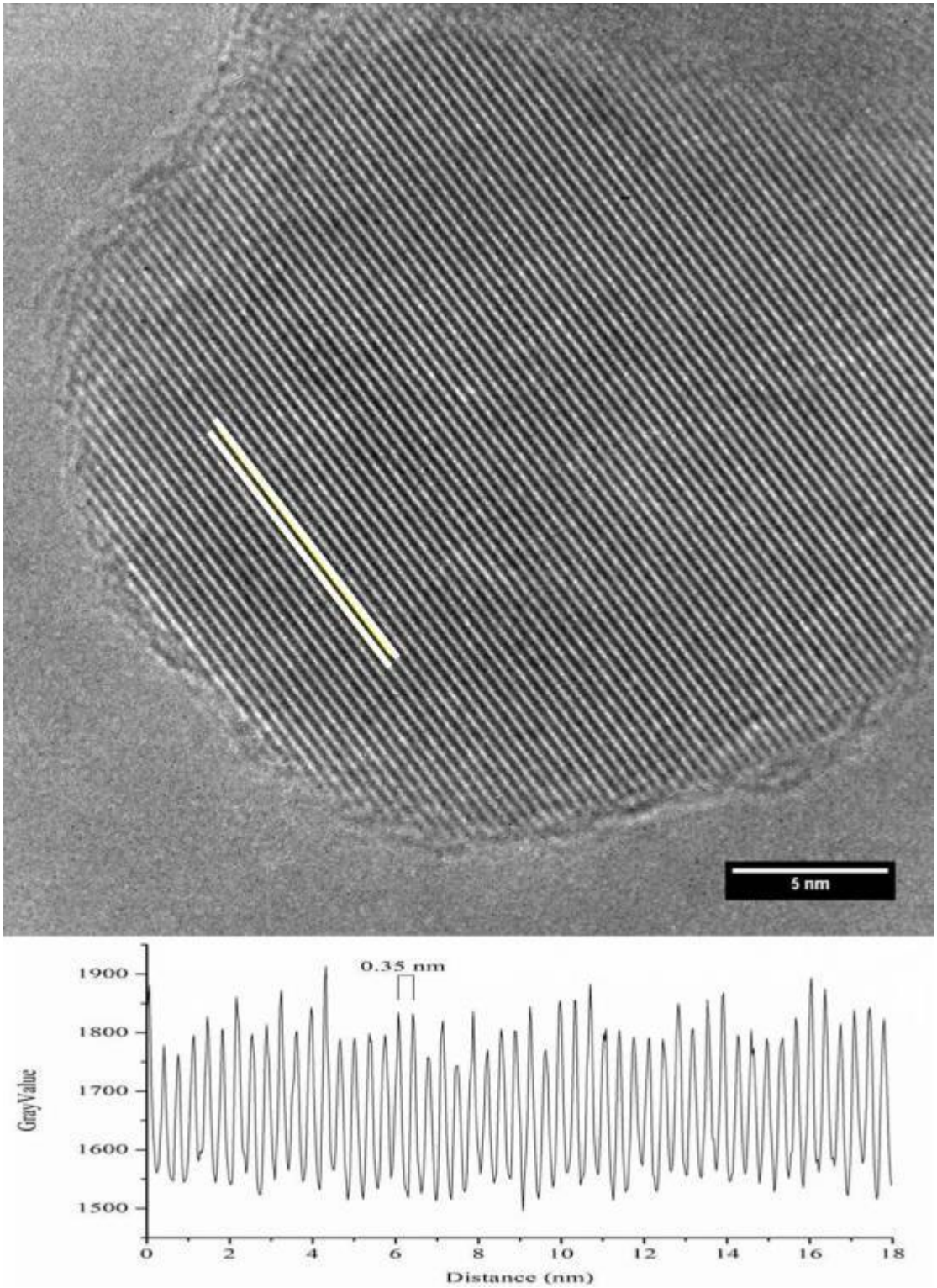

Figure 9.18: (PEG 1500 g/mol in a Ti+ : PEG ratio of (1 : 0.5)). Well-defined single crystal. This crystal measured ~ 30 nm across its width and ~ 27 nm top to bottom. 2D lattice fringes were not obtained from this crystal, however, a line profile revealed the lattice spacing to be 0.35 nm and is consistent with anatase in the (1 0 1) orientation[7].

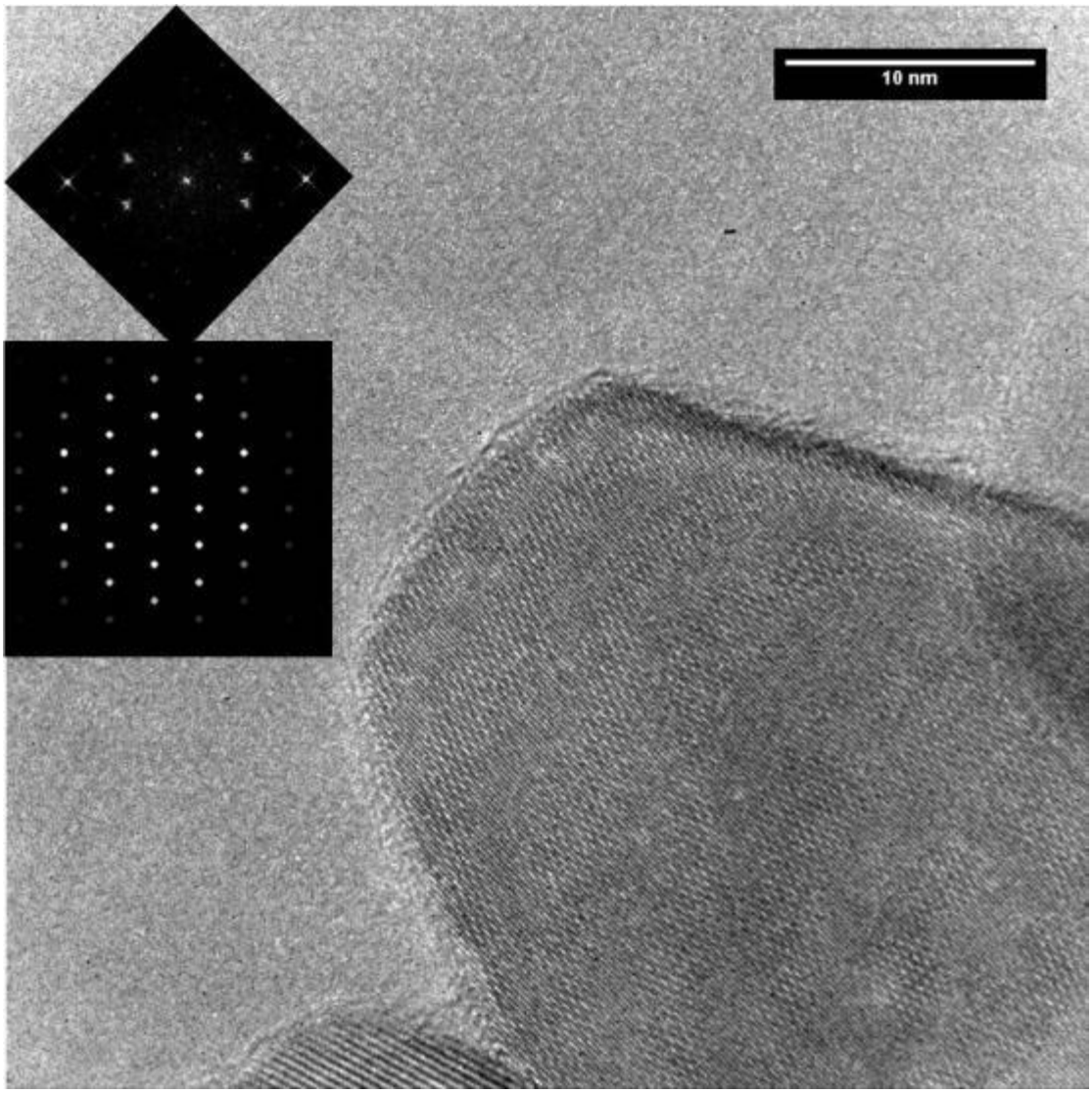

Figure 9.19: (PEG 1500 g/mol in a Ti+ : PEG ratio of (1 : 0.5)). Rutile crystallite in the (1 1 1) orientation. This crystallite measured ~ 34 nm top to bottom and ~ 30 nm across its width. The crystal appears to be tapered toward the tip and is characteristic of rutile nanorods comprising mesocrystals.

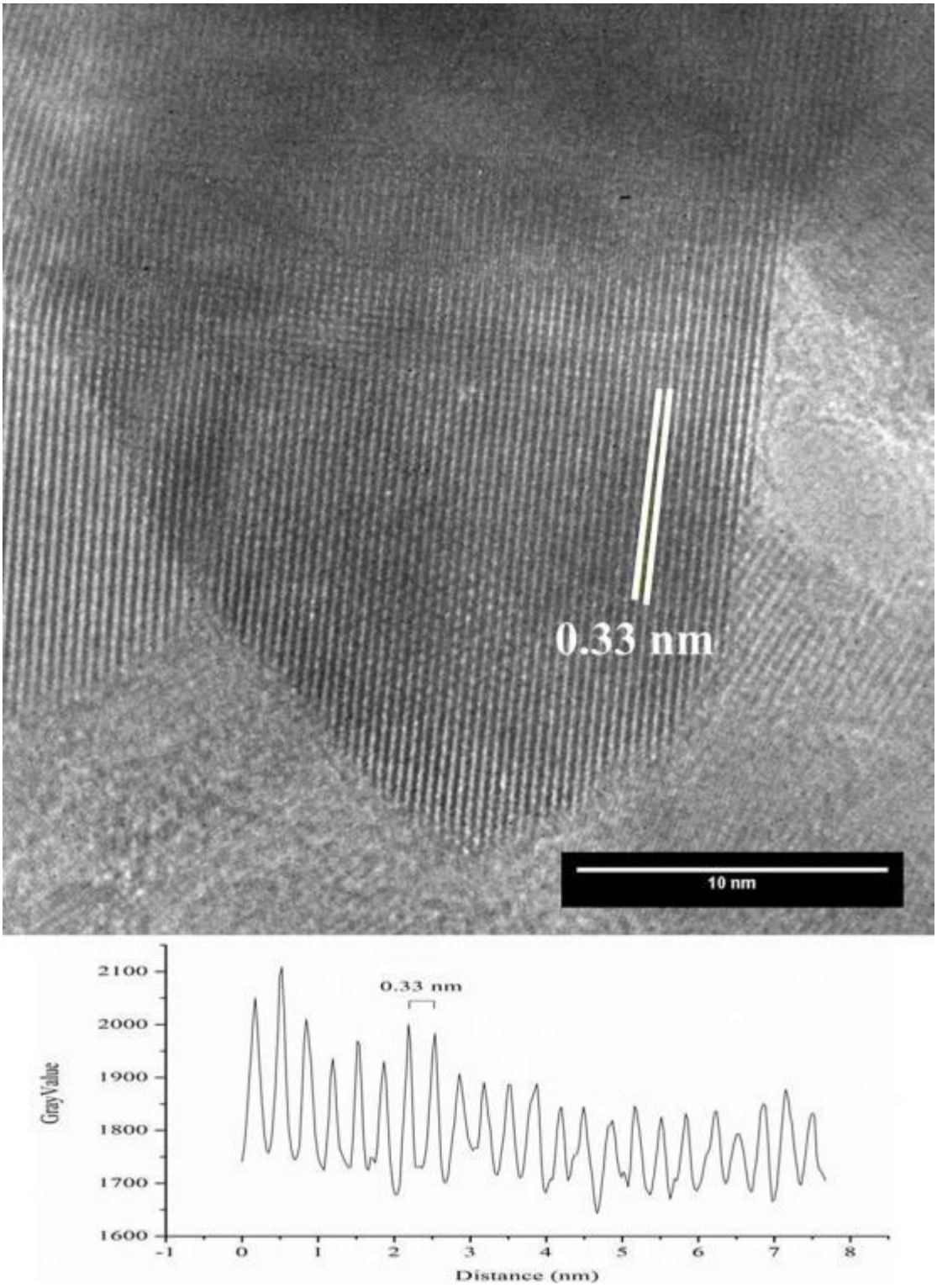

Figure 9.20: (PEG 6000 g/mol in a Ti+ : PEG ratio of (1 : 0.5)). Rutile crystal presenting with a tapered tip. Interestingly, this particular crystal did not form part of a mesocrystal. This crystal measured ~ 23 nm across its width and over 27 nm down its length. Rutile was confirmed by measuring the distance between peaks in the line profile.

The amorphous content surrounding the crystal in figure 9.21 was unlikely amorphous titania as amorphous content readily crystallises in the presence of titania crystals[11]. Additionally, amorphous titania readily converts to anatase at relatively low temperatures[11]. Therefore, the amorphous content surrounding the crystal was most probably a form of carbon. Carbon had originated from PEG chains. This is confirmation of the poor signal to noise ratio witnessed in the PXRD patterns of samples synthesised from long chain PEG.

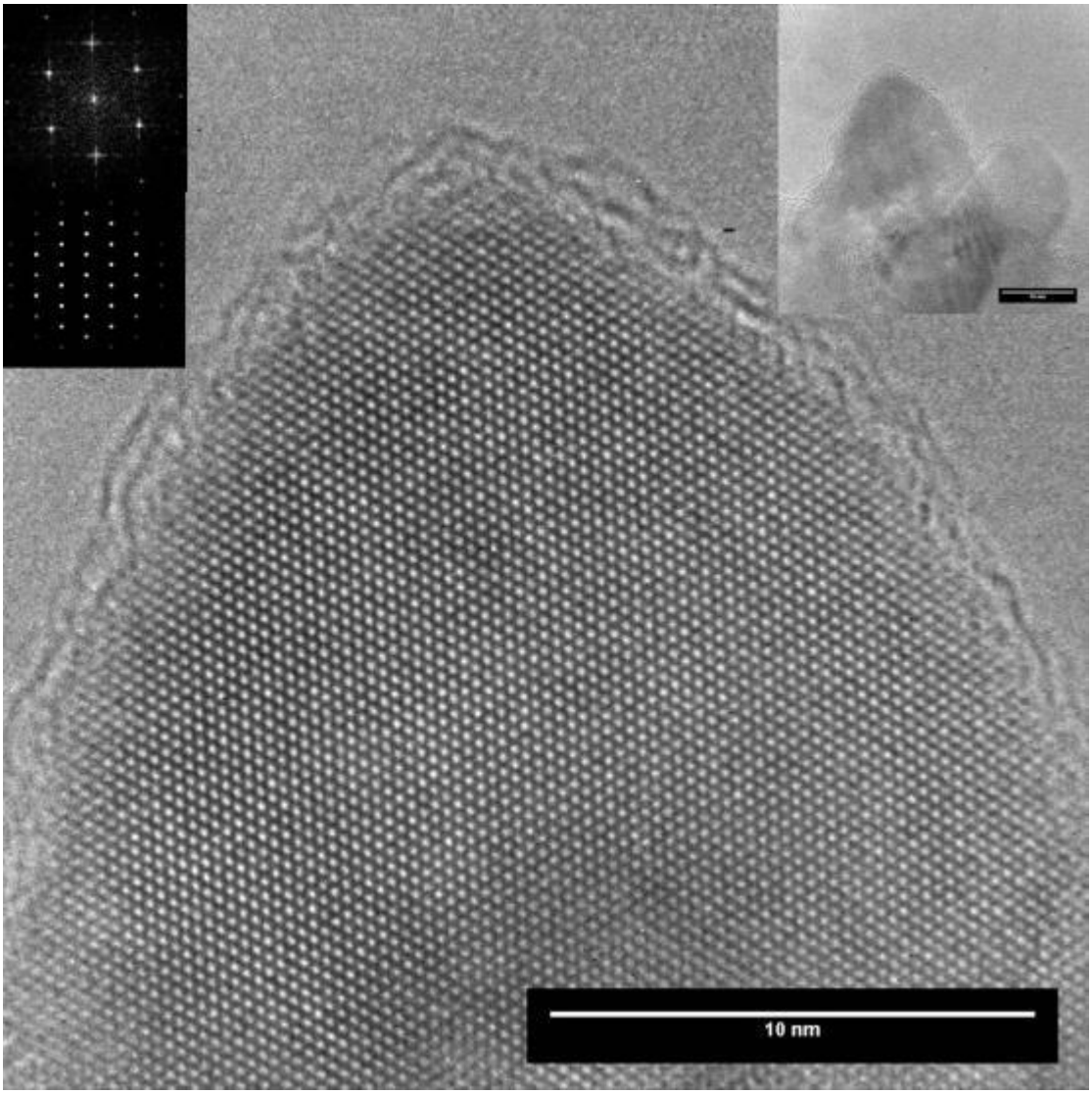

Figure 9.21: (PEG 6000 g/mol in a Ti+ : PEG ratio of (1 : 0.5)). Tapered tip of a rutile crystal along (1 1 1). The insert shows the crystal at lower magnification in relation to other crystals. This crystal did not form part of a mesocrystal despite possessing the characteristics of a rutile nanorod in a mesocrystal. The crystal measured ~ 20 nm across its width and at least 18 nm from top to bottom. Amorphous material surrounded the crystal.

9.2.3 Comparison of the Effects of Rapid Heating

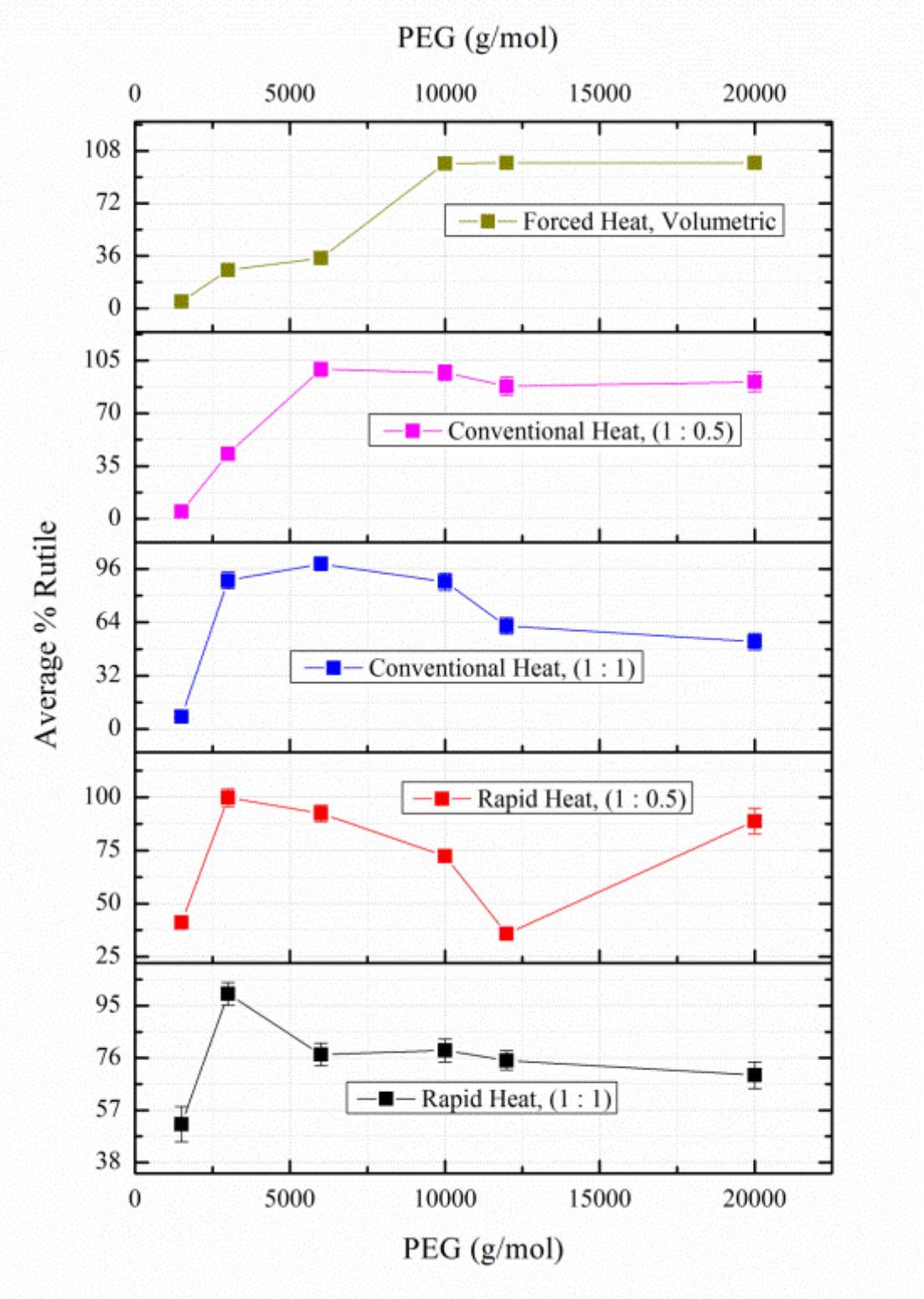

Figure 9.22: Effects of different heating rates on the mass percentage of rutile formed in different experiments.

Figure 9.22 compares the effects of different heating methods on the amount of rutile formed in samples containing various amounts of polymer, as a function of increasing PEG chain length. Only samples that allowed for a direct comparison of the mass percentage of rutile formed were included, for all non-rapid heat synthesised samples. Conventional heating data at different stoichiometric ratios was obtained from chapter 8. Forced heating data was obtained from volumetrically prepared samples (chapter 6). All data presented in figure 9.22 was generated from samples prepared using water containing HNO_3 as the solvent.

For samples synthesised using rapid heating, a (1 : 1) ratio resulted in an average amount of 75.3% rutile formed across all samples. This was 3.6% more than the average amount of rutile formed across all samples synthesised in a (1 : 0.5) ratio. The similarity in the amount of rutile formed is largely due to PEG 1500, 3000, and 10000 g/mol producing similar amounts of rutile using both synthesis ratios. PEG 6000 g/mol formed slightly more rutile when present in a (1 : 0.5) ratio. Higher PEG molecular weight produced more rutile when present in a (1 : 0.5) ratio than in a (1 : 1) ratio. The biggest deviation in the amount of formed rutile between the (1 : 1) and (1 : 0.5) systems existed for samples synthesised using PEG 12000 g/mol. As previously explained, during ignition of the (1 : 0.5) synthesised sample, polymer coatings on the surface of the jaffle maker likely promoted anatase formation.

Excluding the sample formed using PEG 12000 g/mol in a (1 : 0.5) system, all other results can be explained using the current hypothesis of the formation of reaction chambers – as previously explained. Significant variation between the (1 : 1) and (1 : 0.5) system accrue for samples synthesised using long chain polymers. This is due to the volume of PEG in a (1 : 1) system causing significantly more chain entanglement and consequently resulting in the protection and stabilisation of formed anatase.

The similarities in the amounts of rutile formed as a function of increasing PEG molecular weight between rapid and conventional heating of both the (1 : 1) and (1 : 0.5) systems, indicates that the polymer chain length significantly contributed to the phase formed. The amount of rutile formed using both heating systems was initially low for low molecular weight PEG, increased with increasing PEG molecular weight and then decreased as PEG chain length was further increased. This behaviour was explained using the formation of polymer reaction chambers. The systems deviate in terms of the absolute amount of rutile formed per PEG chain length. For example, for

PEG 1500 and 3000 g/mol, more rutile was formed using rapid rather than conventional heating. Both systems formed similar amounts of rutile using PEG 6000 g/mol. For PEG 10000 g/mol, more rutile was formed using conventional rather than rapid heating.

These differences are likely due to rapid heating decreasing the probability of the system acquiring thermal equilibrium – especially given that PEG is a poor thermal conductor further stabilised against decomposition by water.

Samples synthesised using long chain polymers appeared to be more manipulated by the volume of polymer in the system than heating rate. This was confirmed by PEG 20000 g/mol producing more rutile for the (1 : 0.5) system than for the (1 : 1) system, regardless of the heating method used.

Data obtained from forced heating samples prepared in a volumetric manner do not correlate with conventional or rapid heating samples prepared in a stoichiometric manner. Polymer reaction chambers form using both stoichiometric and volumetric preparation methods. However, since in volumetric addition, the total volume of polymer added to metal ions is equivalent for all polymer chain lengths, there is no driving force for the formation of sterically constrained polymer reaction chambers. Forced heating simply enhances the probability of chain cleavage at specific points along the chain. Using volumetric addition, shorter chains are encouraged to form smaller chambers and longer chains are encouraged to form larger chambers. These allow for the formation of anatase and rutile respectively.

Figure 9.23 shows the variation in rutile crystallite size formed using different heating methods, as a function of increasing PEG molecular weight. The figure was prepared in the same manner as figure 9.22. Additionally, crystallite size data was obtained from calcined samples.

For PEG 1500 and 3000 g/mol, rutile crystallites prepared using rapid heating were larger in the (1 : 1) system than in the (1 : 0.5) system. All others polymer chain lengths (excluding PEG 12000 g/mol) produced similar sized rutile crystallites in both the (1 : 1) and (1 : 0.5) systems. The average rutile crystallite size across all samples was 24.2 nm for both systems synthesised using rapid heating. These results are unsurprising given that the mass percentage of rutile formed in both systems was similar.

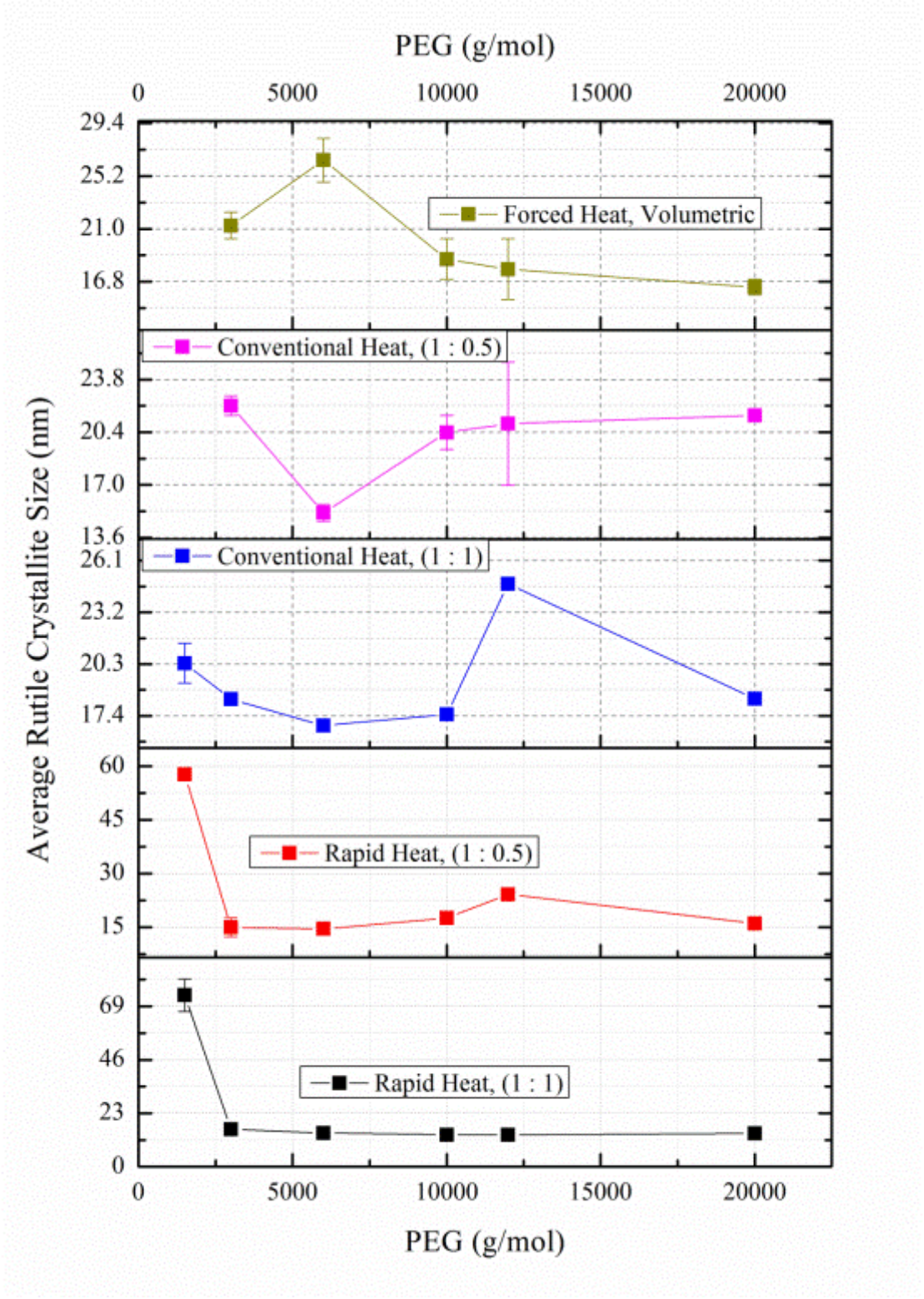

Figure 9.23: Effects of different heating rates on rutile crystallite size formed in different experiments.

Rutile crystallites generated using rapid heating and PEG 1500 g/mol were large compared with conventional synthesis of stoichiometrically prepared samples. This

was expected considering that the short chain likely degraded during rapid heating, causing formed rutile to coarsen significantly. Long chain polymers formed larger rutile crystallites when samples were ignited using conventional heating, regardless of the stoichiometry of the system. This was an unexpected result and suggested that longer chain undecomposed polymers shield the growing rutile nanocrystals during the swift rapid heat reaction.

Using forced heating, long chain polymers produce rutile crystallites of a size between those formed using rapid and conventional heating. All systems displayed an inverse relationship between the mass percentage and rutile crystallite size formed as a function of PEG molecular weight. The variation in rutile crystallite size indicates that the degree of inverse correlation changes depending on the system.

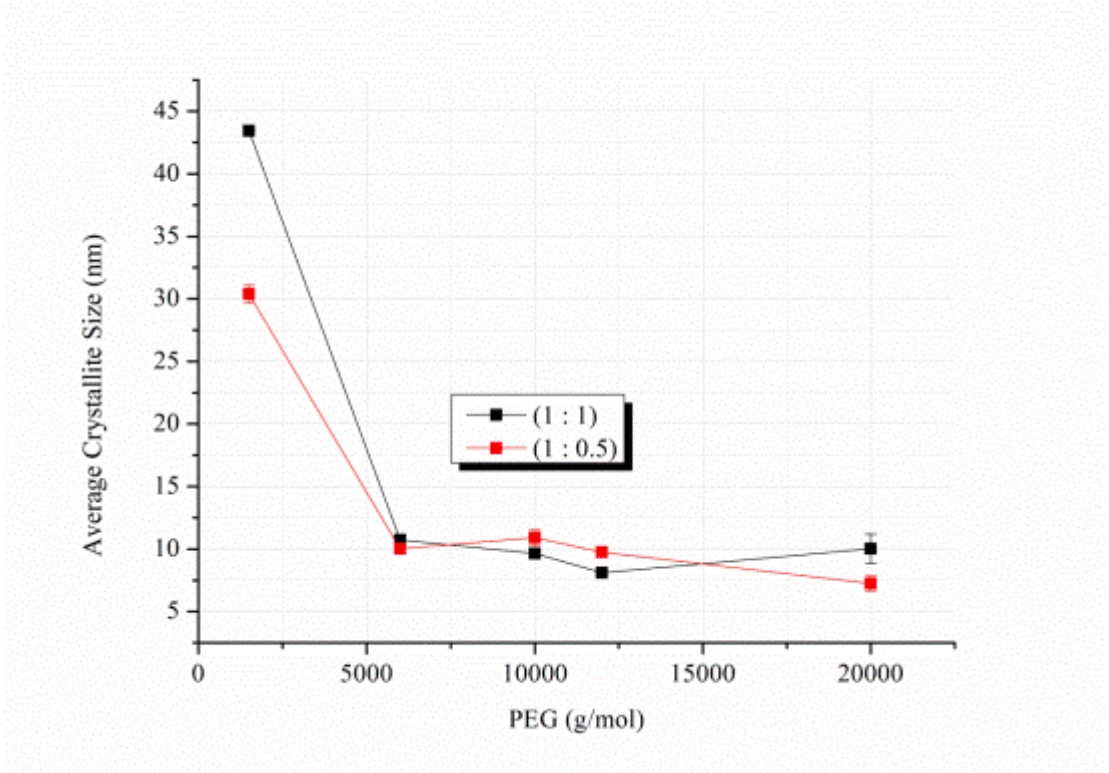

Figure 9.24: Effects of rapid heating on anatase crystallite size formed in a (1 : 1) and (1 : 0.5) synthesis.

Figure 9.24 shows similar sized anatase crystallites formed for samples containing PEG 6000 – 20000 g/mol using rapid heating and both (1 : 1) and (1 : 0.5) synthesis. Larger anatase crystallites were formed using PEG 1500 g/mol in a (1 : 1) synthesis compared with a (1 : 0.5) synthesis.

9.3 Conclusions

For samples synthesised in a (1 : 1) ratio, PXRD peak intensity decreased drastically as the polymer chain length was increased. While this did not impact the results obtained from the experiment, it did suggest that an entity was inhibiting X-ray penetration into the sample. Based on the white colour of the sample and peak misalignment, it was concluded that undecomposed polymer is the likely cause of decreasing peak intensity. Peak intensity did not decrease as much for the (1 : 0.5) system.

Further, it was concluded that the rapidly cooling vessel, low thermal conductivity of the polymer combined with the added thermal protection afforded by hydrogen bonded water molecules caused some polymer chains to remain undecomposed in the final samples. This was not the case for short chain PEG 1500 g/mol that likely decomposed rapidly forming large crystallites of anatase and rutile.

The average amount of rutile formed across all samples synthesised in both a (1 : 1) and (1 : 0.5) manner was > 71%. This was expected as synthesis was conducted in water containing HNO_3. PEG 3000 g/mol produced phase pure rutile irrespective of the stoichiometry used. PEG 1500 g/mol resulted in the formation of the largest anatase crystallites in both systems: 73.8 nm for the (1 : 1) system and 57.7 nm for the (1 : 0.5) system. For the remaining PEG chain lengths, rutile (1 1 0) crystallites formed in (1 : 1) and (1 : 0.5) syntheses coarsened between 13.7 – 16.0 nm and 14.5 – 24.2 nm respectively. Rutile crystallites were larger than anatase crystallites in all samples containing a significant mixture of both polymorphs. Both systems displayed an imperfect inverse relationship between the amount of rutile formed and its respective crystallite size. Additionally, there was a direct correlation between the amount and size of anatase crystallites formed. Both relationships fit into the developing model of the formation of polymer reaction chambers.

HRTEM revealed the presence of well-defined rutile and anatase crystals, as well as rutile mesocrystals. Moreover, most anisotropic rutile crystals displayed tapered tips and were single crystal in nature. This suggested that the mechanism of rutile mesocrystal formation was anatase transforming into rutile crystals within a large polymer reaction chamber. Depending on the size of the polymer chamber, transformed rutile could serve as seed particles and grow anisotropically along (0 0 1)

to form superstructures. Each nanorod was likely to consist of a single anisotropic rutile crystal. The tip of some nanorods comprising mesocrystals took on a non-tapered, non-pyramidal, non-flat, curved appearance. This is the first observation of such nanorods. HRTEM also revealed the presence of amorphous material surrounding the rutile crystal. This material was most likely carbon based and originated from undecomposed PEG chains.

For rutile formed using long chain polymers, rapid heating was a greater determinant of crystallite size, compared with PEG stoichiometry that was a greater determinant of the mass percentage of rutile formed. Differences between crystallite sizes formed using both heating methods were small.

The current model involving the formation of PEG reaction chambers of various sizes was successfully applied to the data generated in this chapter. Additionally, the model was refined to consider the effects on undecomposed polymer on the formation of anatase and rutile.

9.4 References

1. Gottfried, B. S., Lee, C. J. & Bell, K. J. The leidenfrost phenomenon: film boiling of liquid droplets on a flat plate. *International Journal of Heat and Mass Transfer* **9,** 1167 – 1188 (1966).

2. Vlachopoulos, J. & Strutt, D. Basic Heat Transfer and Some Applications in Polymer Processing. in *Plastics Technician's Toolbox* **2,** 21 – 33 (Society of Plastics Engineers, 2002).

3. Graham, N. B., Zulfiqar, M., Nwachuku, N. E. & Rashid, A. Interaction of poly(ethylene oxide) with solvents: 2. Water-poly(ethylene glycol). *Polymer* **30,** 528 – 533 (1989).

4. Hanaor, D. A. & Sorrell, C. C. Review of the anatase to rutile phase transformation. *Journal of Materials Science* **46,** 855 – 874 (2011).

5. Gopal, M., Chan, W. J. M. & De Jonghe, L. C. Room temperature synthesis of crystalline metal oxides. *Journal of Materials Science* **32,** 6001 – 6008 (1997).

6. Kakiuchi, K., Hosono, E., Imai, H., Kimura, T. & Fujihara, S. {1 1 1}-faceting of low-temperature processed rutile TiO2 rods. *Journal of Crystal Growth* **293,** 541 – 545 (2006).

7. Mao, Y., Kanungo, M., Hemraj-Benny, T. & Wong, S. S. Synthesis and Growth Mechanism of Titanate and Titania One-Dimensional Nanostructures Self-Assembled into Hollow Micrometer-Scale Spherical Aggregates. *Journal of Physical Chemistry B* **110,** 702 – 710 (2006).

8. Baboo, B. & Goswami, D. N. *Processing, Chemistry and Applications of Lac*. (Indian Council of Agricultural Research, 2010).

9. Barnes, C. E. Chemical Nature of Shellac. *Industrial and Engineering Chemistry* **30,** 449 – 451 (1938).

10. Canter, S. Sheryl's Blog. *Chemistry of Cast Iron Seasoning: A Science-Based How-To*

11. Zhang, H. & Banfield, J. F. Kinetics of Crystallization and Crystal Growth of Nanocrystalline Anatase in Nanometer-Sized Amorphous Titania. *Chemistry of Materials* **14,** 4145 – 4154 (2002).

Chapter 10: Effects of Precursor Variation on Titania Polymorph and Crystallite Size Formation

Building on the developing hypothesis for the mechanism of particle formation using resin-gel synthesis, this chapter focuses on the role of the titanium ion precursor in titania phase selectivity and crystallite size formation. To this end, six different Ti ion containing precursors were used: titanium (IV) oxysulfate, titanium (IV) isopropoxide, titanium (IV) 2-ethylhexyloxide, titanium diisopropoxide bis (acetylacetonate), titanium (IV) bis (ammonium lactato) dihydroxide, and titanium (IV) (triethanolaminato) isopropoxide. All precursors employed in this study have Ti ions bonded directly to oxygen (in contrast to $TiCl_4$).

Previous chapters showed that metal ion hydroxyl complexes formed between precursor $TiCl_4$ and solvent generated OH^-. PEG chains then coordinated to these complexes forming reaction chambers of various sizes dependent on the amount of polymer used and the heating rate. Solution additives such as citric acid favoured the exclusive formation of anatase. Based on the results obtained using ethanol (chapter 5) and citric acid (chapter 7), increasing the size of the ligands attached to the titanium ion precursor is likely to have a similar effect of encouraging anatase formation. If anatase is formed exclusively, it is likely due to protecting effects afforded by the precursor ligands. If anatase is not formed exclusively, the results obtained from this chapter will allow for comments to be made concerning the formation of metal hydroxyl species and polymer coordination.

10.1 Experimental Procedure

The synthesis procedure involved addition of the respective metal ion precursor to excess distilled water containing 55% HNO_3, if required. The volume of distilled water added to each solution equalled 12 times the volume of precursor used. If required, the volume of 55% HNO_3 added to each solution equalled 2 times the volume of precursor used (the inclusion or omission of HNO_3 is specified in sections 10.1.1 – 10.1.6 as they relate to individual metal ion containing precursors). After stirring induced homogeneity was achieved, stoichiometric quantities of PEG chains

with molecular weights between 200 – 20000 g/mol were added to each beaker containing the metal ion solution (Ti^+ : PEG = 1 : 0.5).

10.1.1 Titanium (IV) oxysulfate synthesis

The abbreviation 'TiOxS' is designated to titanium (IV) oxysulfate – $TiOSO_4$ – (15% in H_2SO_4, Aldrich, figure 10.1) and used throughout this chapter. Quantities of the precursor and PEG of various molecular weights used are included in table 10.1. HNO_3 was not employed in this synthesis.

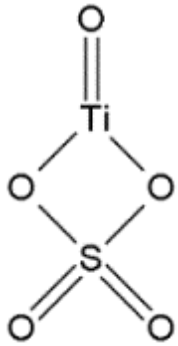

Figure 10.1: Structural representation of titanium (IV) oxysulfate.

Table 10.1: TiOxS and PEG added to achieve a (1 : 0.5) stoichiometry.

Batch number	TiOxS		PEG Mn	PEG	
	ml	mols	g/mol	mols	g
1	66.66	0.08508	200	0.04254	8.5083
	66.66	0.08508	400	0.04254	17.0167
2	6.66	0.00851	1500	0.00425	6.3812
	6.66	0.00851	3000	0.00425	12.7625
	6.66	0.00851	4000	0.00425	17.0167
	6.66	0.00851	6000	0.00425	25.5251
	6.66	0.00851	8000	0.00425	34.0335
3	0.66	0.00085	10000	0.00043	4.2541
	0.66	0.00085	12000	0.00043	5.1050
	0.66	0.00085	20000	0.00043	8.5083

10.1.2 Titanium (IV) isopropoxide synthesis

The abbreviation 'Ti-isopro' is designated to titanium (IV) isopropoxide – $Ti[OCH(CH_3)_2]_4$ – (≥ 97%, Aldrich, figure 10.2) and used throughout this chapter. Quantities of the precursor and PEG of various molecular weights used are included in table 10.2. HNO_3 was employed in this synthesis.

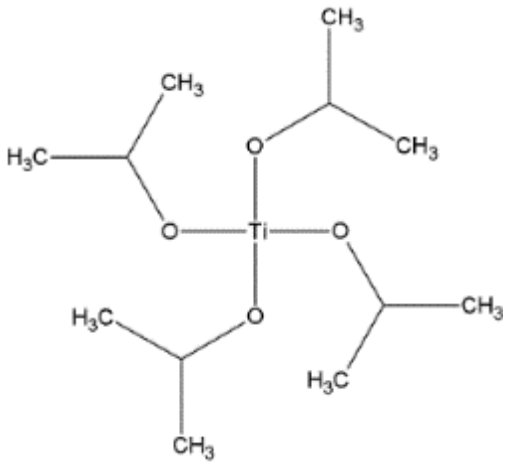

Figure 10.2: Structural representation of titanium (IV) isopropoxide.

Table 10.2: Ti-isopro and PEG added to achieve a (1 : 0.5) stoichiometry.

Batch number	Ti-isopro		PEG Mn	PEG	
	ml	mols	g/mol	mols	g
1	5.0	0.017	200	0.0084	1.6710
	5.0	0.017	400	0.0084	3.3420
2	2.0	0.0067	1500	0.0033	5.0130
	2.0	0.0067	3000	0.0033	10.0260
	2.0	0.0067	4000	0.0033	13.3680
	2.0	0.0067	6000	0.0033	20.0520
	2.0	0.0067	8000	0.0033	26.7360
3	0.2	0.00067	10000	0.00033	3.3420
	0.2	0.00067	12000	0.00033	4.0104
	0.2	0.00067	20000	0.00033	6.6840

10.1.3 Titanium (IV) 2-ethylhexyloxide synthesis

The abbreviation 'Ti-EHOx' is designated to titanium (IV) 2-ethylhexyloxide – $Ti[OCH_2CH(C_2H_5)(CH_2)_3CH_3]_4$ – (95%, Aldrich, figure 10.3) and used throughout this chapter. Quantities of the precursor and PEG of various molecular weights used are included in table 10.3. HNO_3 was used in this synthesis.

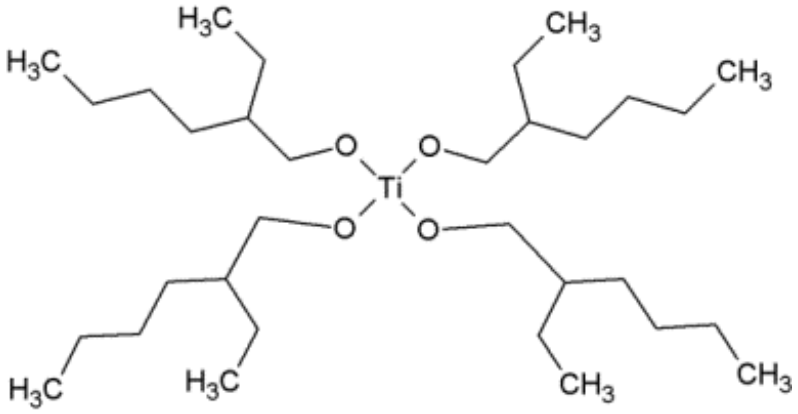

Figure 10.3: Structural representation of titanium (IV) 2-ethylhexyloxide.

Table 10.3: Ti-EHOx and PEG added to achieve a (1 : 0.5) stoichiometry.

Batch number	Ti-EHOx		PEG Mn	PEG	
	ml	mols	g/mol	mols	g
1	30.0	0.0492	200	0.0246	4.9243
	30.0	0.0492	400	0.0246	9.8486
2	5.0	0.0082	1500	0.0041	6.1553
	5.0	0.0082	3000	0.0041	12.3107
	5.0	0.0082	4000	0.0041	16.4143
	5.0	0.0082	6000	0.0041	24.6215
	5.0	0.0082	8000	0.0041	32.8286
3	1.0	0.0016	10000	0.00082	8.2071
	1.0	0.0016	12000	0.00082	9.8486
	1.0	0.0016	20000	0.00082	16.4143

10.1.4 Titanium diisopropoxide bis(acetylacetonate) synthesis

The abbreviation 'Ti-AcAc' is designated to titanium (IV) diisopropoxide bis(acetylacetonate) – $[(CH_3)_2CHO]_2Ti(C_5H_7O_2)_2$ – (75% in isopropanol, Aldrich, figure 10.4) and used throughout this chapter. Quantities of the precursor and PEG of various molecular weights used are included in table 10.4. HNO_3 was used in this synthesis.

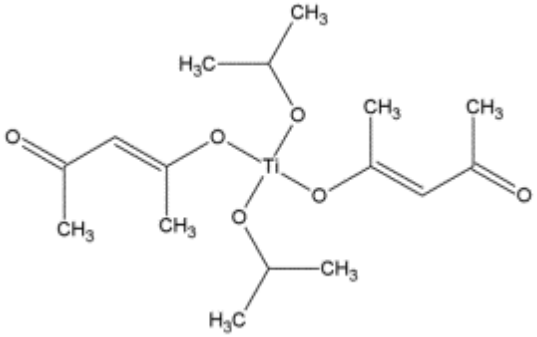

Figure 10.4: Structural representation of titanium diisopropoxide bis(acetylacetonate).

Table 10.4: Ti-AcAc and PEG added to achieve a (1 : 0.5) stoichiometry.

Batch number	Ti-AcAc		PEG Mn	PEG	
	ml	mols	g/mol	mols	g
1	22.20	0.04548	200	0.02274	4.5480
	22.20	0.04548	400	0.02274	9.0961
2	4.44	0.00910	1500	0.00455	6.8220
	4.44	0.00910	3000	0.00455	13.6114
	4.44	0.00910	4000	0.00455	18.1922
	4.44	0.00910	6000	0.00455	27.2883
	4.44	0.00910	8000	0.00455	36.3844
3	0.88	0.0018	10000	0.00091	9.0961
	0.88	0.0018	12000	0.00091	10.9153
	0.88	0.0018	20000	0.00091	18.1922

10.1.5 Titanium (IV) bis (ammonium lactato) dihydroxide solution synthesis

The abbreviation 'Ti-AmOH' is designated to titanium (IV) bis (ammonium lactato) dihydroxide – $[CH_3CH(O-)CO_2NH_4]_2Ti(OH)_2$ – (50% in water, Aldrich, figure 10.6) and used throughout this chapter. Quantities of the precursor and PEG of various molecular weights used are included in table 10.6. HNO_3 was not employed in this synthesis.

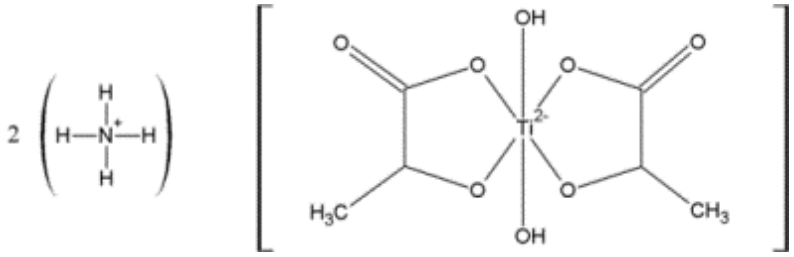

Figure 10.5: Structural representation of titanium (IV) bis (ammonium lactato) dihydroxide solution.

Table 10.5: Ti-AmOH and PEG added to achieve a (1 : 0.5) stoichiometry.

Batch number	Ti-AmOH		PEG Mn	PEG	
	ml	mols	g/mol	mols	g
1	21.89	0.04548	200	0.02274	4.5480
	21.89	0.04548	400	0.02274	9.0960
2	4.38	0.00910	1500	0.00455	6.8251
	4.38	0.00910	3000	0.00455	13.6502
	4.38	0.00910	4000	0.00455	18.2003
	4.38	0.00910	6000	0.00455	27.3005
	4.38	0.00910	8000	0.00455	36.4007
3	0.88	0.0018	10000	0.00091	9.1417
	0.88	0.0018	12000	0.00091	10.9700
	0.88	0.0018	20000	0.00091	18.2834

10.1.6 Titanium (IV) (triethanolaminato) isopropoxide synthesis

The abbreviation 'Ti-EApro' is designated to titanium (IV) (triethanolaminato) isopropoxide – $C_9H_{19}NO_4Ti$ – (80% in isopropanol, Aldrich, figure 10.5) and used throughout this chapter. Quantities of the precursor and PEG of various molecular weights used are included in table 10.5. HNO_3 was not used in this synthesis.

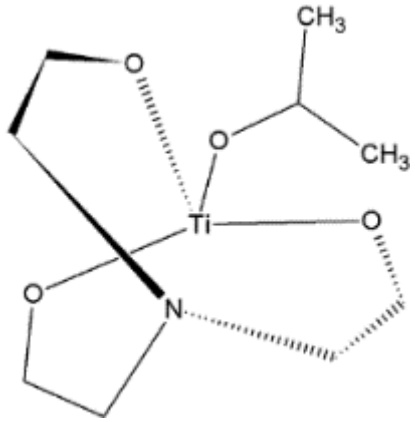

Figure 10.6: Structural representation of titanium (IV) (triethanolaminato) isopropoxide.

Table 10.6: Ti-EApro and PEG added to achieve a (1 : 0.5) stoichiometry.

Batch number	Ti-EApro		PEG Mn	PEG	
	ml	mols	g/mol	mols	g
1	13.24	0.004548	200	0.02274	4.5486
	13.24	0.004548	400	0.02274	9.0972
2	2.65	0.00910	1500	0.00455	6.8281
	2.65	0.00910	3000	0.00455	13.6562
	2.65	0.00910	4000	0.00455	18.2082
	2.65	0.00910	6000	0.00455	27.3124
	2.65	0.00910	8000	0.00455	36.4165
3	0.53	0.0018	10000	0.00091	9.1041
	0.53	0.0018	12000	0.00091	10.9249
	0.53	0.0018	20000	0.00091	18.2082

10.1.7 Heat Treatments

All mixtures were stirred and heated as appropriate to induce homogeneous gelation. Thereafter, all 60 gels were placed approximately 30 cm under 2 commercially available 250 W infrared spot lights. Following solvent evaporation, all resins were divided equally to introduce a replicate. The conventional heating method (described in chapter 5) was used to effect ignition. All powders were then calcined at 500 °C at ~ 620 mm Hg for 1 hour.

10.1.8 Characterisation

PXRD data was obtained using a Bruker D2 Phaser diffractometer. The setup of the D2 Phaser was described in chapter 5, with the exception that Co Kα radiation (λ = 1.7903 Å) was used. Samples were analysed between 20° and 60° 2θ in 0.023 increments counting for 1 second per step. TEM analysis was achieved using the FEI Tecnai T12. Selected samples synthesised using TiOxS were analysed using a JEOL JEM 2100.

10.2 Results and Discussion

Calcination had a minimal impact on the decrease and increase in the amount of anatase and rutile formed respectively – as witnessed in the preceding chapters. Furthermore, calcination caused slight disproportional coarsening in all samples, as a function of increasing PEG molecular weight. Considering that this chapter describes resin-gel synthesis based on 6 precursors, PXRD analysis was conducted post-calcination only.

Therefore, each system will exhibit PXRD patterns generated from calcined samples. PXRD patterns generated from replicate calcined samples will not be shown. The relationship between the amount of a particular phase and its respective crystallite size will be investigated per system, post-calcination. These graphs will consider data from the original and replicate data sets.

10.2.1 Titanium (IV) oxysulfate

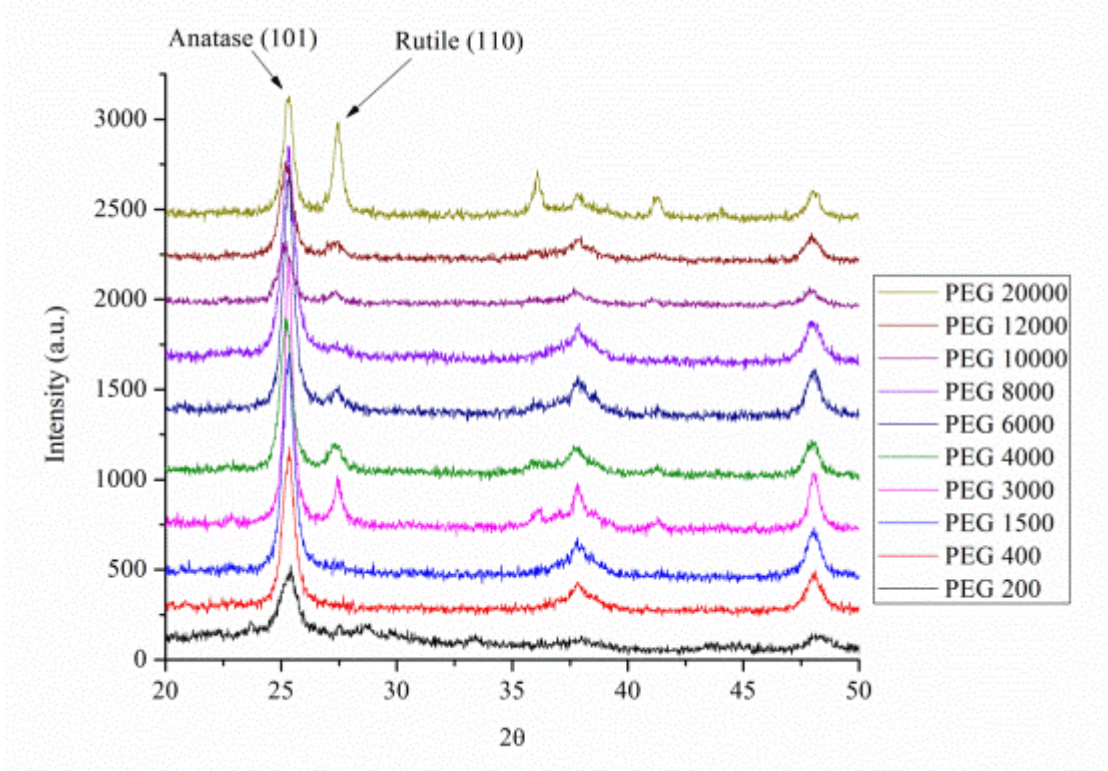

Figure 10.7: PXRD patterns of TiOxS generated samples.

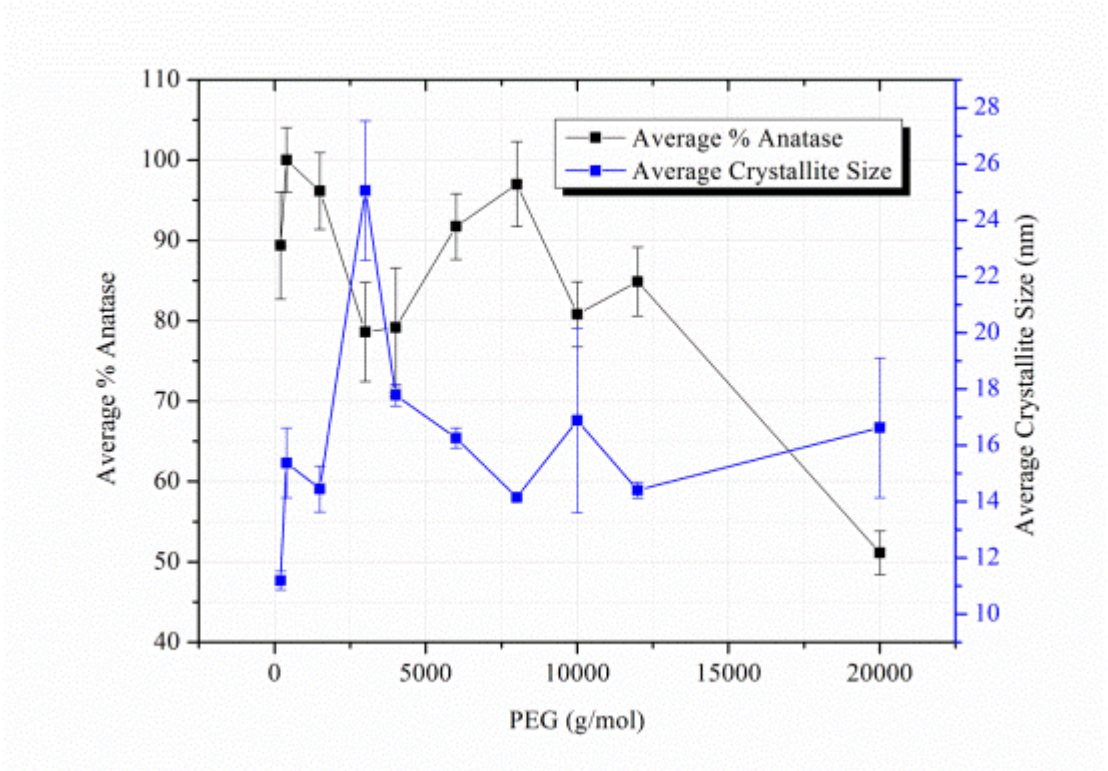

Figure 10.8: Average amount of anatase with associated crystallite size formed using TiOxS.

Figure 10.7 contains PXRD patterns obtained from calcined samples synthesised using TiOxS. Patterns collected from all samples synthesised using PEG ≥ 400 g/mol exhibited good signal to noise ratio. This is characteristic of calcined samples – as observed in previous chapters. It is currently unknown why PEG 200 g/mol produced an anatase (1 0 1) peak with poor intensity. Interestingly, slight peak misalignment is evident. This implies that either the calcination time or temperature was insufficient at removing all carbon residues. Narrow anatase peaks are indicative of crystallite coarsening under the action of calcination.

Lower molecular weight PEG (200 – 1500 g/mol) appeared to produce nearly phase pure anatase. The rutile (1 1 0) peak is clearly evidenced for samples synthesised using longer chain PEG (≥ 3000 g/mol). PEG 20000 g/mol resulted in the formation of the greatest mixture of anatase and rutile. For samples containing a mixture of polymorphs, the rutile (1 1 0) peak width suggests that rutile crystallites were larger than anatase crystallites. Rutile transformation assisted coarsening is therefore expected[1]. Calcination would have caused a nearly proportional increase in crystallite size. Therefore, as previously witnessed, rutile crystallites were expected to be larger than anatase crystallites.

Figure 10.8 shows the relationship between the amount and size of anatase crystallites formed as a function of increasing PEG molecular weight synthesised in a (1 : 0.5) ratio. Samples synthesised using PEG 400, 1500, and 8000 g/mol produced nearly phase pure anatase. All other samples excluding PEG 20000 g/mol resulted in the formation of ≥ 80% anatase. The least amount of anatase was produced from the samples synthesised using PEG 20000 g/mol (51.1%). For short and intermediate PEG chain lengths (200 – 8000 g/mol), the data suggests that similar polymer molecular weights produced similar amounts of anatase. Long chain PEG (10000 – 20000 g/mol) tended to produce decreasing quantities of anatase as the chain length increased. Based on the average amount of anatase formed across all samples (84.9%), TiOxS evidently favoured anatase formation.

The largest error in the data set was obtained from the samples synthesized using PEG 4000 g/mol (7.9%). Error bars were generated by summing 4% of the average amount of anatase formed to the standard deviation of the replicate analyses. Therefore, the data reflects good precision.

Initial observations of figure 10.8 reveal no obvious trend for anatase crystallite size formed as a function of increasing PEG molecular weight. Additionally, there appears to be no relationship between the amount of anatase formed and its respective crystallite size. Anatase crystallite size is dependent on PEG molecular weight.

Samples synthesised using PEG 200 and 3000 g/mol resulted in the formation of the smallest and largest anatase crystallites respectively (11.2 nm and 25.1 nm respectively). All other samples produced anatase crystallites that measured between ~ 14 18 nm, such that the average crystallite size obtained across all samples measured 16.2 nm. The sizes of these crystallites were a consequence of calcination induced coarsening. Therefore, anatase crystallites larger than 14 nm were expected[2]. Samples synthesised using PEG 10000 g/mol exhibited the greatest variation (3.3 nm in crystallite size). Given that error bars represent the standard deviation of the replicate analysis, the data reflects good precision.

Given that this experiment employed the use of conventional heating and a (1 : 0.5) stoichiometric synthesis, the experimental conditions best approximate those used with $TiCl_4$ in chapter 8. Despite the present synthesis employing a hydrocarbon-free metal ion precursor – TiOxS (similar to $TiCl_4$ in chapter 8), the currently obtained results do not approximate those obtained in chapter 8. The results obtained using citric acid (chapter 7) and an ethanol solvent (chapter 5) provide better but imperfect approximations to the results obtained in this chapter. This is a peculiar finding given that citric acid and ethanol were found to complex to the $TiCl_4$ precursor forming hydroxylated species with remaining hydrocarbon and oxygen based matrix components. Polymer chains then coordinated to these metal ion complexes. The hydrocarbon based remaining matrix components protected and stabilised the nucleated anatase phase inhibiting rutile transformation. In the present study, a hydrocarbon-free precursor (TiOxS) was responsible for preferentially but not exclusively forming anatase.

Therefore, the results obtained in this study must be a consequence of the titanium ion precursor employed in the synthesis. Based on the use of $TiCl_4$, the developing model implicitly assumes the formation of metal-hydroxyl complexes in solution. This assumption is warranted based on the probability of solvation, leading to the formation of HCl and $Ti(OH)_x$ species in solution. Based on the differences in

electronegativity between the sulphur species in TiOxS and the chloride species in $TiCl_4$, it is unlikely that the former readily dissociates in solution. Moreover, the presence of H_2SO_4 likely discouraged the dissociation of the SO_2 species to form more H_2SO_4. It is possible that hydrogen bonds formed between oxygen groups from TiOxS and H generated from the solvent. This likely resulted in the formation of $Ti(OH)_x(SOH)_y(H_2SO_4)_z$ species in solution.

Accordingly, Dambournet *et al*. found that in water, $TiOSO_4$ formed an oxysulfate-sulphuric acid complex hydrate ($TiOSO_4 \bullet H_2O \bullet H_2SO_4$). The researchers also found that this complex resulted in the formation of anatase after subjection to mild thermolysis[3]. This led to the conclusion that the sulphate species served as a directing agent favouring anatase formation[3]. Sulphate species served as directing agents by favouring condensation of opposed coplanar edges and hence favouring anatase[3]. The researchers were able to improve anatase crystallinity by introducing additional SO_4^{2-} anions[3]. In contrast, anatase crystallinity was worsened when Cl^- ions were added to the solution[3].

The work conducted by Dambournet *et al.* supports the assumption that PEG coordinated to $Ti(OH)_x(SOH)_y(H_2SO_4)_z$ in the present experiment. Therefore, it is likely that a form of $(SOH)_y$ and $(H_2SO_4)_z$ species were present in the polymer reaction chambers. Additionally, based on the work by Dambournet *et al*., these species served as directing agents favouring the formation of anatase. Because the present system did not result in the exclusive formation of anatase across all samples, the model developed by Dambournet *et al.* is not valid in its entirety. The effects of polymer reaction chamber coordination to sulphur containing species must be explored.

The presence of $(SOH)_y$ and $(H_2SO_4)_z$ species likely imposed a form of protection and stabilisation on the developing anatase crystals within the reaction chambers. Compared with citric acid, the protection afforded by the sulphur containing species in this solution was likely not as influential in rutile transformation inhibition. This assumption is supported by the fact that anatase crystallinity was improved with the addition of additional SO_4^{2-}, as concluded by Dambournet *et al*[3]. Moreover, the larger size of citric acid assisted in sterically controlling anatase crystal growth and impeding anatase to rutile transformation.

Based on lanthanide containing PEG complexes, Rogers *et al*. concluded that the primary coordination spheres were governed by steric effects within the complexes[4]. The mode of polymer wrapping was affected by the anion present in the system[4]. By extension, these effects likely occurred in the present system under investigation. This lends credibility to the abovementioned argument regarding the protection and stabilisation of anatase crystallites in the polymer reaction chambers by $(SOH)_y$ and $(H_2SO_4)_z$ species.

The covalent radius of a sulphur atom[5] (1.02 Å) is 39.73% greater than the covalent radius of an oxygen atom[5] (0.73 Å). Therefore, it is unlikely that significantly large quantities of sulphur displaced oxygen in the TiO_2 lattice. Accordingly, PXRD did not reveal the presence of explicit Ti_xS_y complexes. It is important to note that it is possible for sulphur to be present in the TiO_2 lattice as an impurity causing non-uniform strain on the lattice. This has the effect of causing peak misalignment as evidenced in figure 10.7. Moreover, S impurities in the TiO_2 lattice likely provided a barrier to rutile transformation – although there is no evidence of such a phenomenon in the literature.

The presence of titanium double bonded to oxygen possibly favoured the formation of anatase in the following way: more energy is required to break a double bond. Additionally, the formation of TiO_2 from TiOxS required greater structural changes to occur. It is likely that the energy transferred to the high molecular mobility system under the action of heating was sufficient to break the double bond and cause sufficient structural changes to favour the formation of anatase TiO_2.

The variation in the amount of anatase formed as a function of increasing PEG molecular weight is consistent with the formation of polymer reaction chambers of various sizes. The limited anatase crystal protection potential of the solvent species allowed the size of the formed chambers to become somewhat influential in phase formation. The following description of the behaviour of polymer reaction chambers is adapted from chapter 8 to account for the limited protection afforded by solvent species: it is likely that short chain PEG (200 – 1500 g/mol) produced chambers that were small enough to stabilise anatase crystallites. As the size of the PEG chains increased (3000 and 4000 g/mol), decomposition produced larger chambers that encouraged rutile transformation. Longer PEG chains (6000 and 8000 g/mol) were

likely unstable as large chambers and moved to improve stability by decomposing into smaller chambers favouring the formation of anatase. As the chain length continued to increase (10000 – 20000 g/mol), the polymers likely continued to decompose into smaller chambers, but the size of these smaller chambers likely increased. It is also possible that the size distribution of the decomposed polymer increased for long chain PEG. This had the effect of favouring rutile formation.

To test the abovementioned hypothesis of the protection effects afforded by sulphur species on anatase phase discrimination, $BaCl_2$ was added to the TiOxS precursor. This was done in an attempt to form an $OTiCl_x$ species and $BaSO_4$ in accordance with equation 10.1. Since $BaSO_4$ is insoluble in water, it was easily isolated from the target $OTiCl_x$ species by precipitation. The $OTiCl_x$ product, when used in a typical resin-gel synthesis, should then yield similar results as that obtained using $TiCl_4$.

$$\mathbf{TiOSO_4 + BaCl_2 \longrightarrow OTiCl_2 + BaSO_4} \qquad \mathbf{(10.1)}$$

An investigation scanning across the range of polymer molecular weights was deemed redundant. PEG 400 g/mol was selected for use in this resin-gel synthesis as it resulted in the formation of sufficiently different amounts of anatase in two different systems. When used with $TiCl_4$ in a volumetric addition, PEG 400 g/mol resulted in the formation of 48.9% of anatase after calcination. Respective anatase crystallites measured 17.7 nm after calcination. These results were obtained from chapter 5. When used with TiOxS, PEG 400 g/mol resulted in the formation of 100.0% anatase with respective crystallites measuring 15.4 nm.

Accordingly, 20.0 ml (0.0255 mol) TiOxS (15% in H_2SO_4, Aldrich) was added to 240 ml distilled H_2O. 10.6304 g (0.0511 mol) $BaCl_2$ was added to this solution. The number of moles of $BaCl_2$ added to the solution equalled 2 times the number of moles of TiOxS used. This was done in an attempt to saturate the system with Cl^- ions and form $OTiCl_x$ species that better represented $TiCl_4$. After separating the insoluble precipitate from the supernatant containing the $OTiCl_x$ species, PEG 400 g/mol was added to the solution in a volumetric equivalent manner. The mixture was stirred and heated as appropriate to induce homogeneity, following which, the gel was dried and heated to ignition using conventional heating as described earlier. The experiment was completed in duplicate. PXRD and TEM analysis were performed as described earlier. Peaks were analysed for phase composition and crystallite size as described earlier.

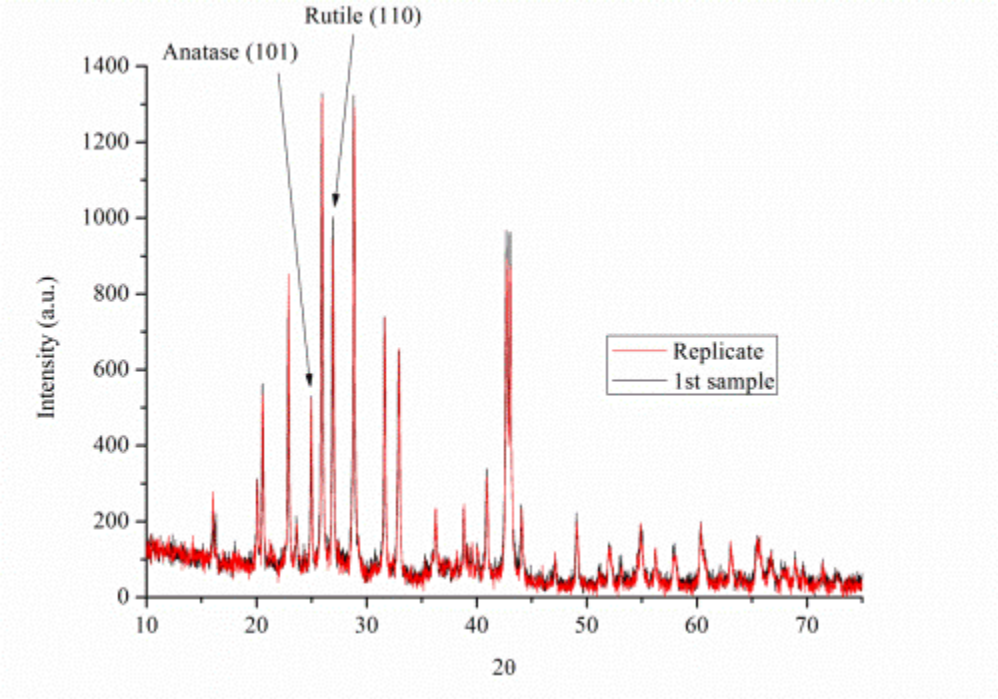

Figure 10.9: PXRD patterns of $OTiCl_x$ generated samples.

Figure 10.9 contains the PXRD patterns corresponding to samples synthesised using $OTiCl_x$ and PEG 400 g/mol, post-calcination. The patterns contained in figure 10.9 contain many peaks, all of which cannot be indexed to TiO_2. Since the system contained excess $BaCl_2$, it is likely that Ba^{2+} and Cl^- containing species were present in the collected powder samples. The presence of these species will be confirmed using TEM and EDS later. Figure 10.9 contains peaks corresponding to both anatase and rutile. The data reveals excellent precision. Sharp peaks are characteristic of large crystallites. Calcination was expected to cause an increase in crystallite size, however the effect of calcination on crystallite coarsening is not as pronounced as that observed in figure 10.9. Therefore, it can be inferred that the presence of Ba^{2+} and Cl^- species caused coarsening of both anatase and rutile crystallites.

Table 10.7 compares the amount of anatase and respective crystallite size formed using $OTiCl_x$ with samples synthesised using $TiCl_4$ (chapter 5) and TiOxS (chapter 10). All samples were synthesised using PEG 400 g/mol and calcined. Errors corresponding to data generated from $OTiCl_x$ samples were generated as described previously.

Table 10.7: Variation in the amount and size of anatase formed using different Ti^{+} precursors.

PEG (g/mol)	$TiCl_4$		$OTiCl_x$		TiOxS	
	Average %Anatase	Average anatase crystallite size (nm)	Average %Anatase	Average anatase crystallite size (nm)	Average %Anatase	Average anatase crystallite size (nm)
400	48.9 ± 2.4	17.7 ± 0.1	42.8 ± 6.4	102.3 ± 0.6	100.0 ± 4.0	15.4 ± 1.2

From table 10.7, the standard deviation of the average amount of anatase formed between $OTiCl_x$ and $TiCl_4$ equals 3.05%. The standard deviation of the average amount of anatase formed between $OTiCl_x$ and TiOxS equals 28.6%. Therefore, the use of $OTiCl_x$ better approximates the amount of anatase formed using $TiCl_4$ than TiOxS. The $OTiCl_x$ precursor is void of any sulphur groups. Hence, this experiment successfully proved that the presence of sulphur containing species within polymer reaction chambers hindered rutile transformation by stabilising and protecting anatase crystallites.

The differences in the amounts of anatase obtained using $TiCl_4$ and $OTiCl_x$ can be attributed to the differences in the precursors used, and the presence of Ba^{2+} and Cl^{-} complexes in the solution when the latter was employed. The presence of these ions was also responsible for the significantly larger anatase crystallites obtained using $OTiCl_x$. It is possible that Ba^{2+} ions sequestrated excess coordinating ligands. In this manner, no counter ions / ligands were available to hinder crystallite growth.

Tables showing the amount of each phase and crystallite size obtained for each sample with averages and errors using both TiOxS and $OTiCl_x$ precursors are given in appendix H.

HRTEM images corresponding to samples synthesised using PEG 1500 g/mol follow (figures 10.10 and 10.11. Although previously reported in literature[6], figure 10.10 shows the first observation of an anatase mesocrystal formed using resin-gel synthesis.

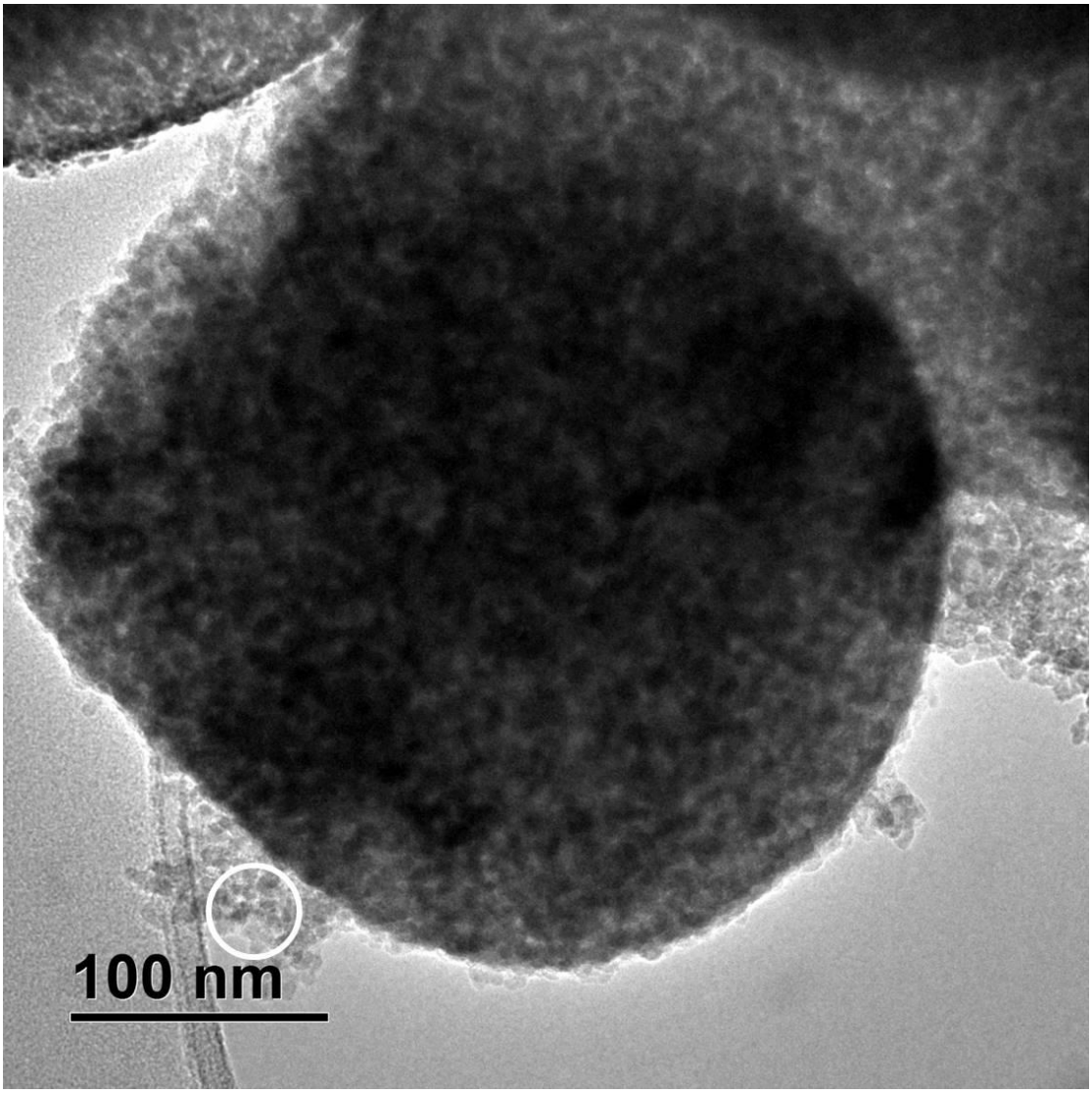

Figure 10.10: (PEG 1500 g/mol). An imperfect spherical aggregation of anatase crystallites distended toward the left side of the image. The vertical and horizontal diameters measured ~ 320 nm and 360 nm respectively. Crystallites contained within the circle were imaged further, and represented in the following image.

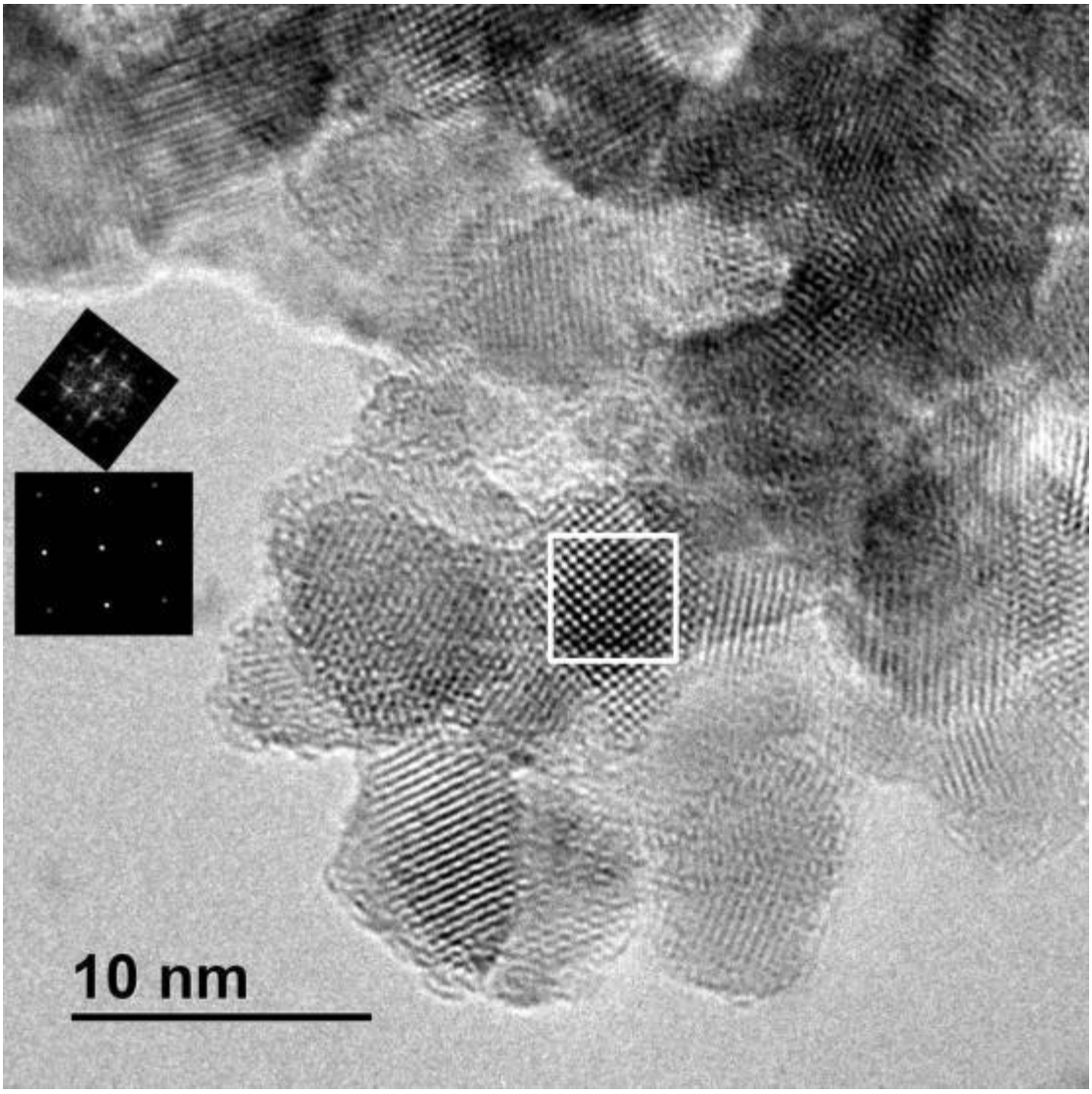

Figure 10.11: (PEG 1500 g/mol). A magnified portion of crystals occurring at the edge of the anatase mesocrystal. Anatase crystallites measured between ~ 5.5 – 8.5 nm. The highlighted crystal presented along (0 0 1).

Figures 10.12 – 10.15 represents HRTEM images generated from the sample synthesised using PEG 3000 g/mol.

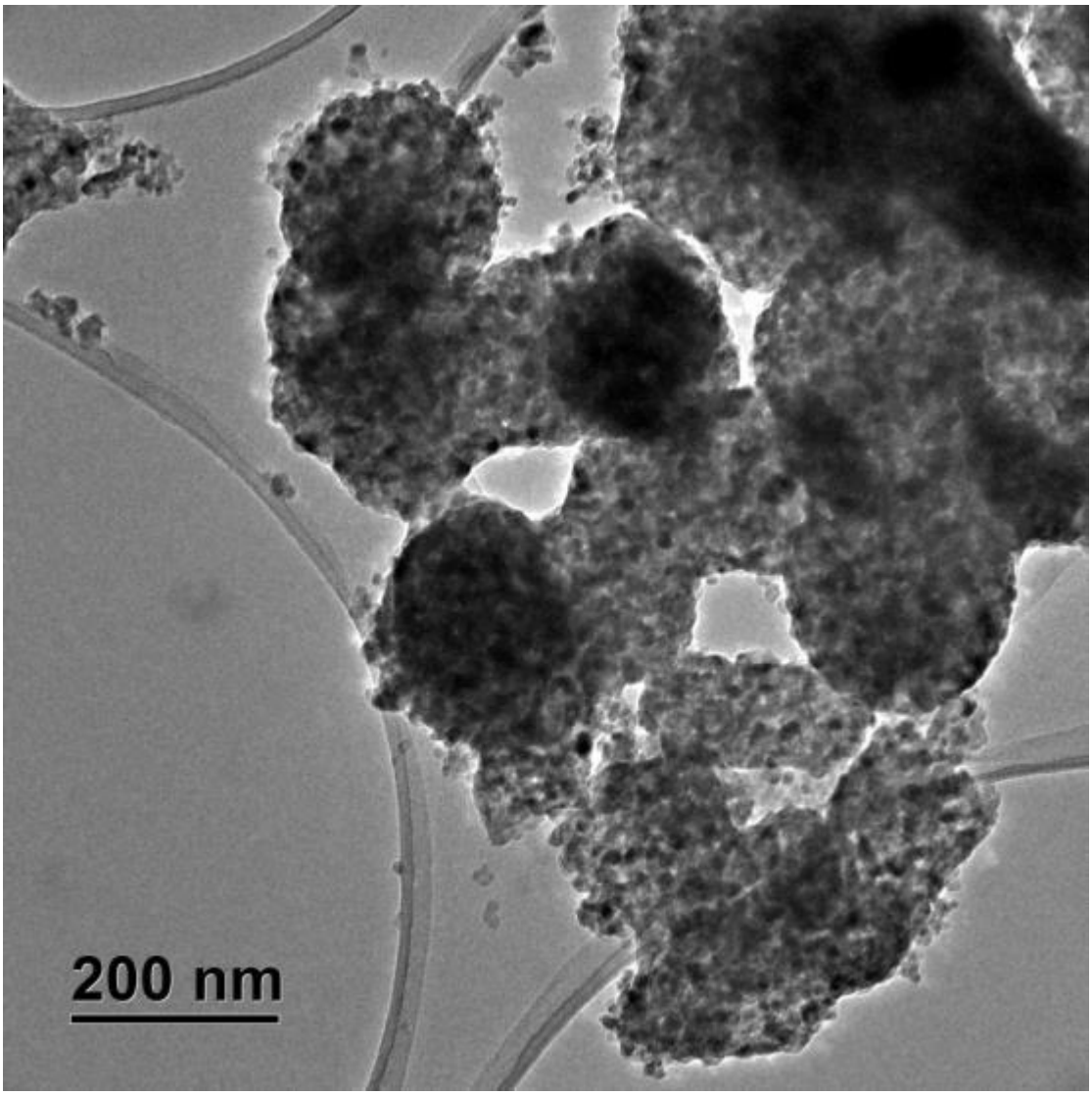

Figure 10.12: (PEG 3000 g/mol). Anatase mesocrystals appeared to fuse together via irregularly aggregated anatase crystallites. Additionally, the anatase mesocrystals displayed an imperfect spherical shape.

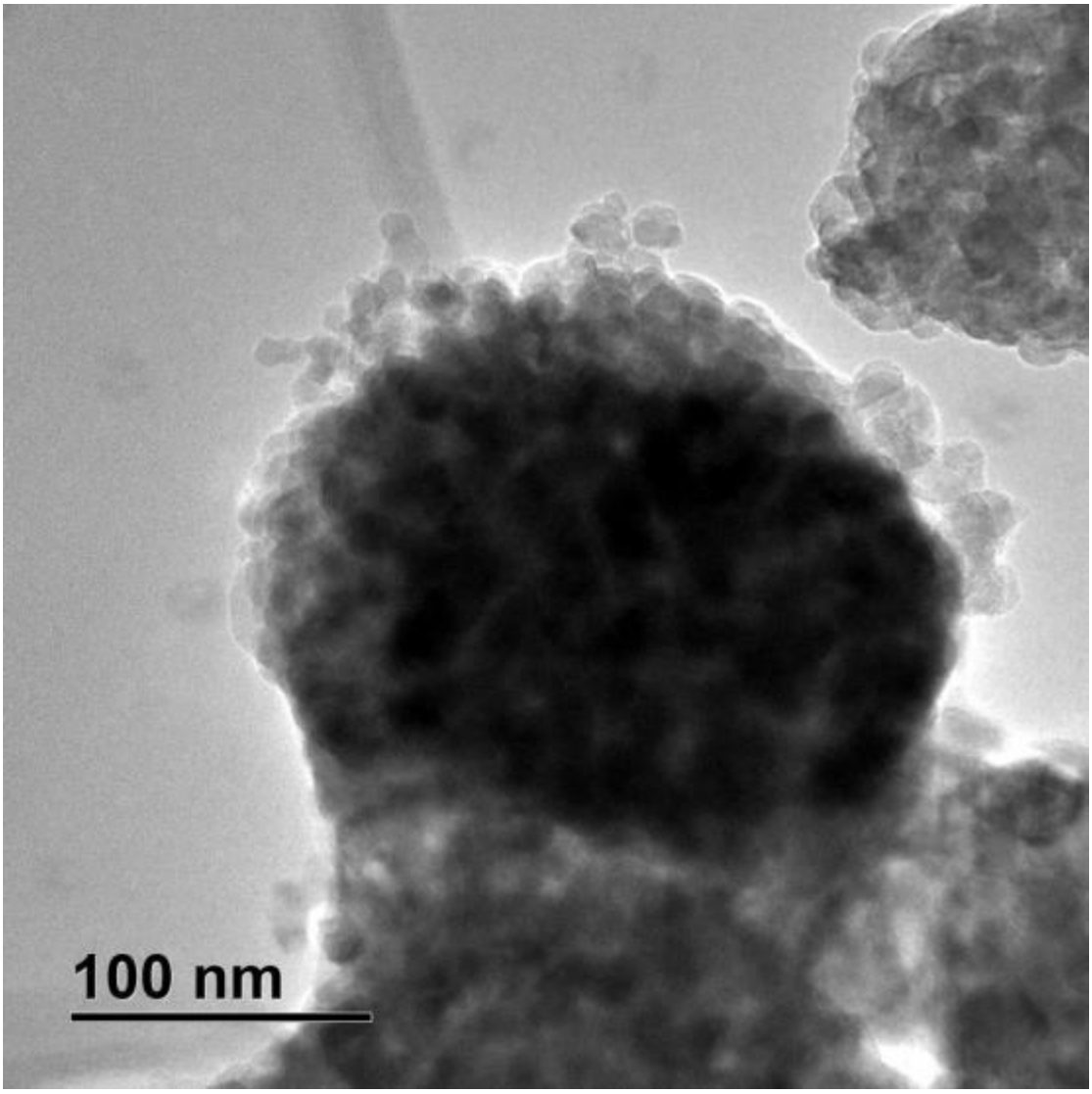

Figure 10.13: (PEG 3000 g/mol). This anatase mesocrystal appeared to be flattened on one side and had a more rounded appearance on the opposite side. The flattened shape was validated by it measuring ~ 240 nm across its width and ~ 190 nm across its length. Due to the differences in amplitude contrast, it appeared that the anatase crystallites comprising the 'bridge' between two mesocrystals were not as concentrated as the mesocrystals themselves.

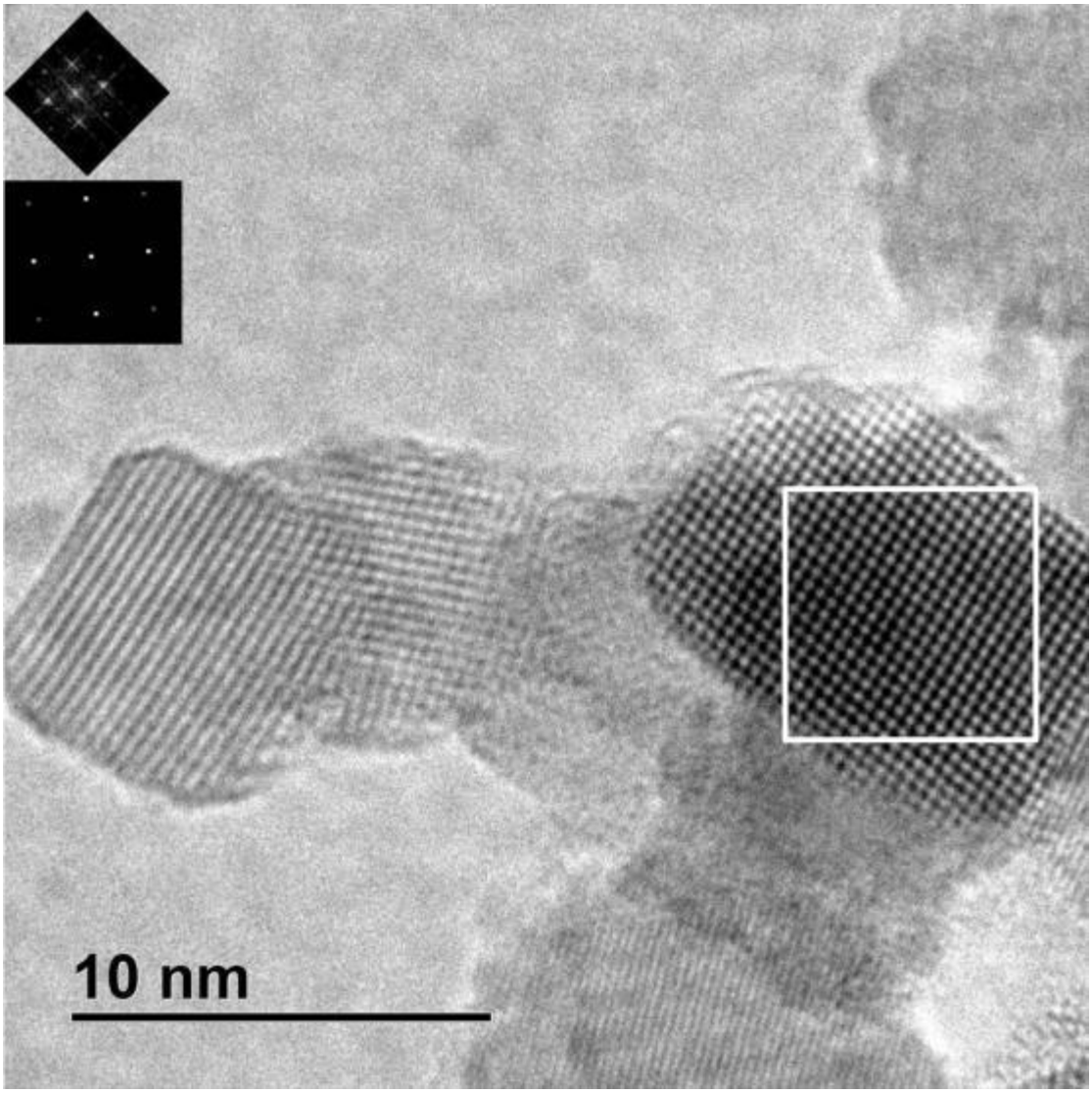

Figure 10.14: (PEG 3000 g/mol). Anatase crystals with well-defined edges. The highlighted anatase crystal measured 8.1 nm across its width and 11.2 nm across its length and was in the (0 0 1) orientation.

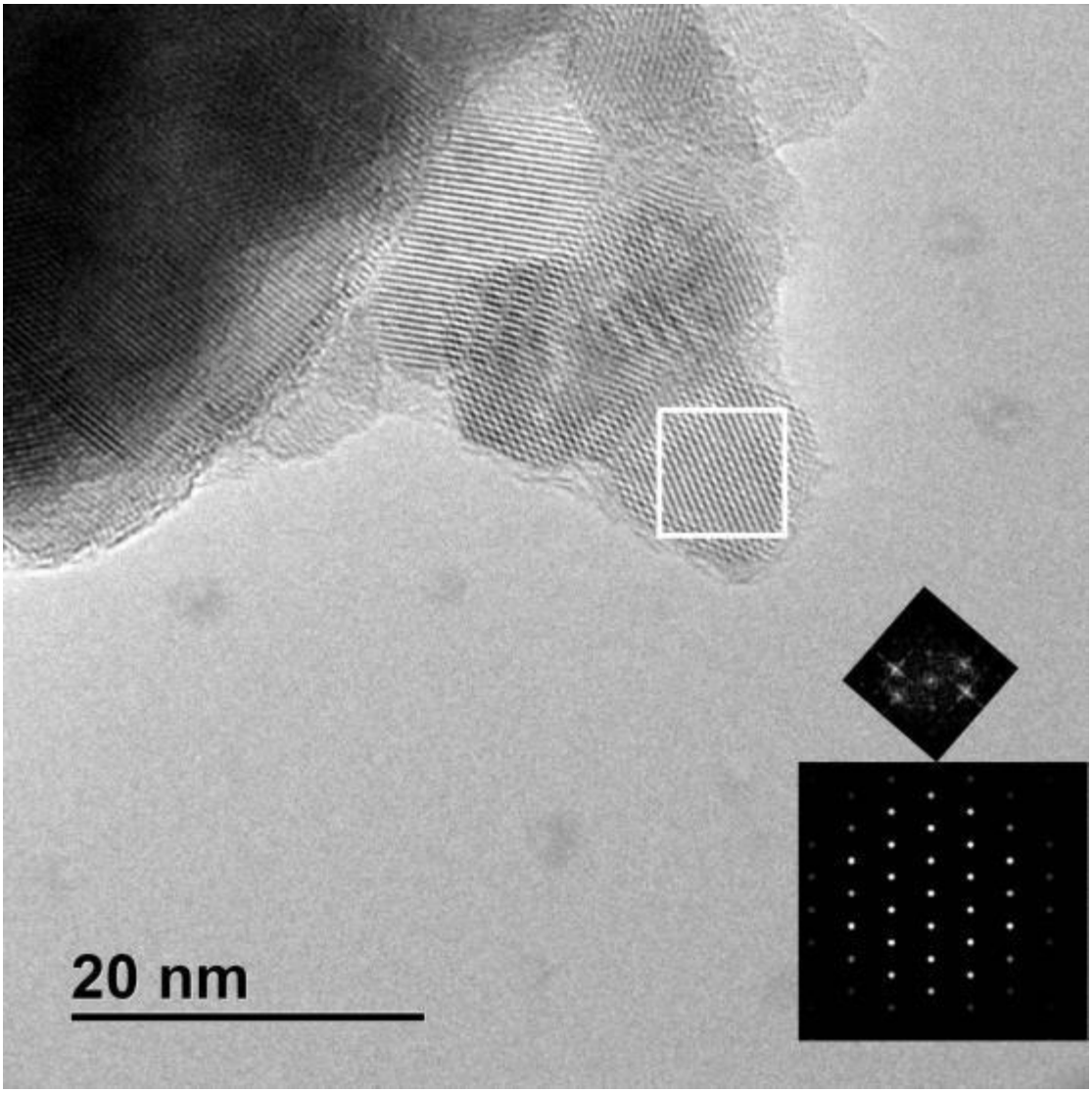

Figure 10.15: (PEG 3000 g/mol). The highlighted rutile crystal was oriented along (1 1 1). This crystal did not have well-defined edges as observed for anatase single crystals formed in this sample.

Figure 10.16 was obtained from the sample synthesised using PEG 4000 g/mol. Comparisons of this image with figure 10.12 suggest that the polymer molecular weight employed in the synthesis governed the amount of anatase mesocrystals formed.

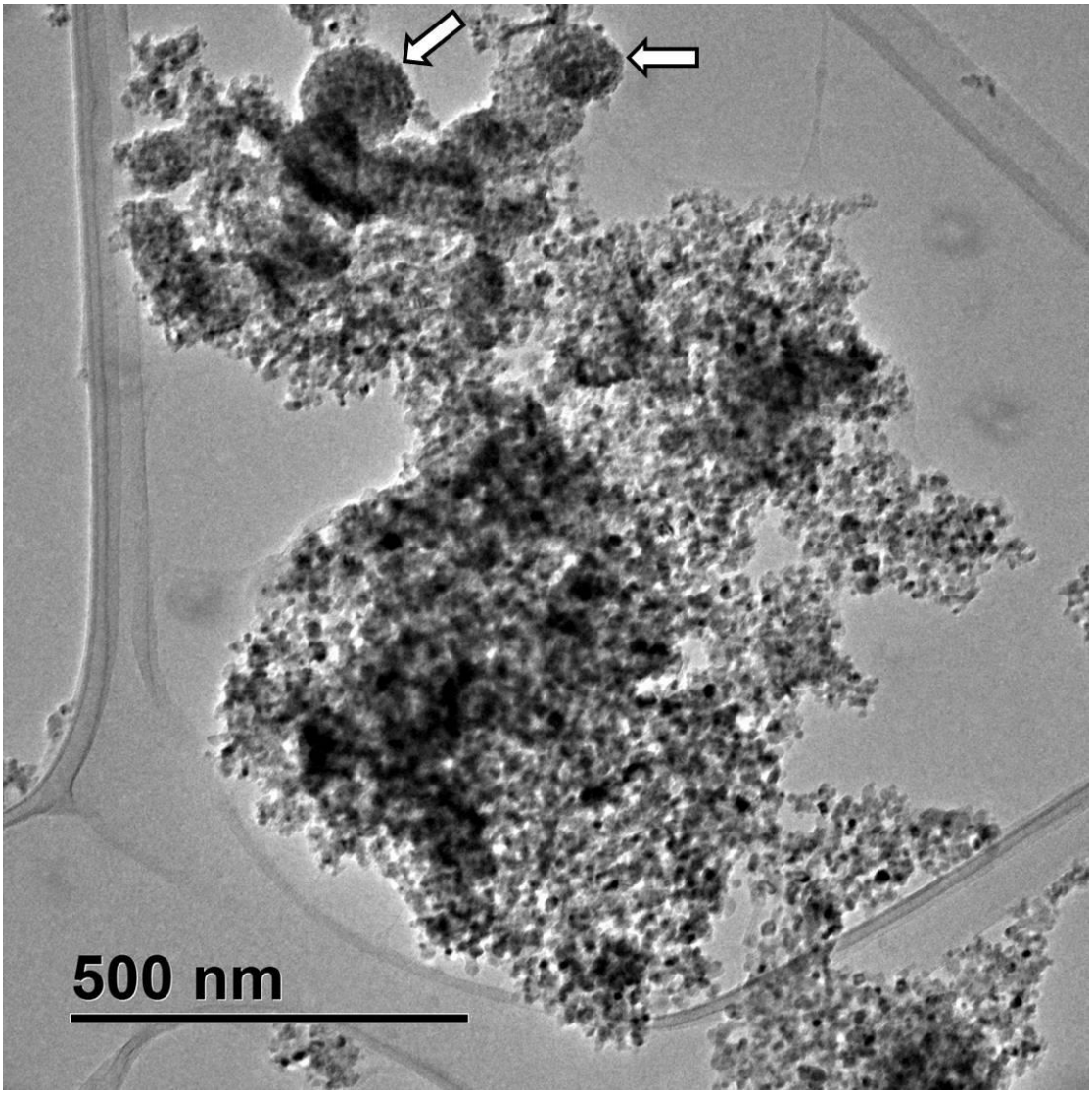

Figure 10.16: (PEG 4000 g/mol). Formation of two anatase mesocrystals (arrows) in a region of sample dominated by agglomerated anatase crystallites.

TEM images and EDS spectra corresponding to samples synthesised using $OTiCl_x$ are given (figures 10.17 – 10.20). EDS analysis was conducted using an Oxford INCA EDS system on an FEI Tecnai T12 TEM at 120 kV employing a LaB_6 source.

The mesocrystal observed in figure 10.17 was most likely comprised of rutile nanorods aligned radially outward from several rutile seed crystals. No rutile superstructures were obtained when TiOxS was used exclusively. Therefore, sulphur

containing ligands served as directing agents, altering PEG coordination to the formed precursor clusters.

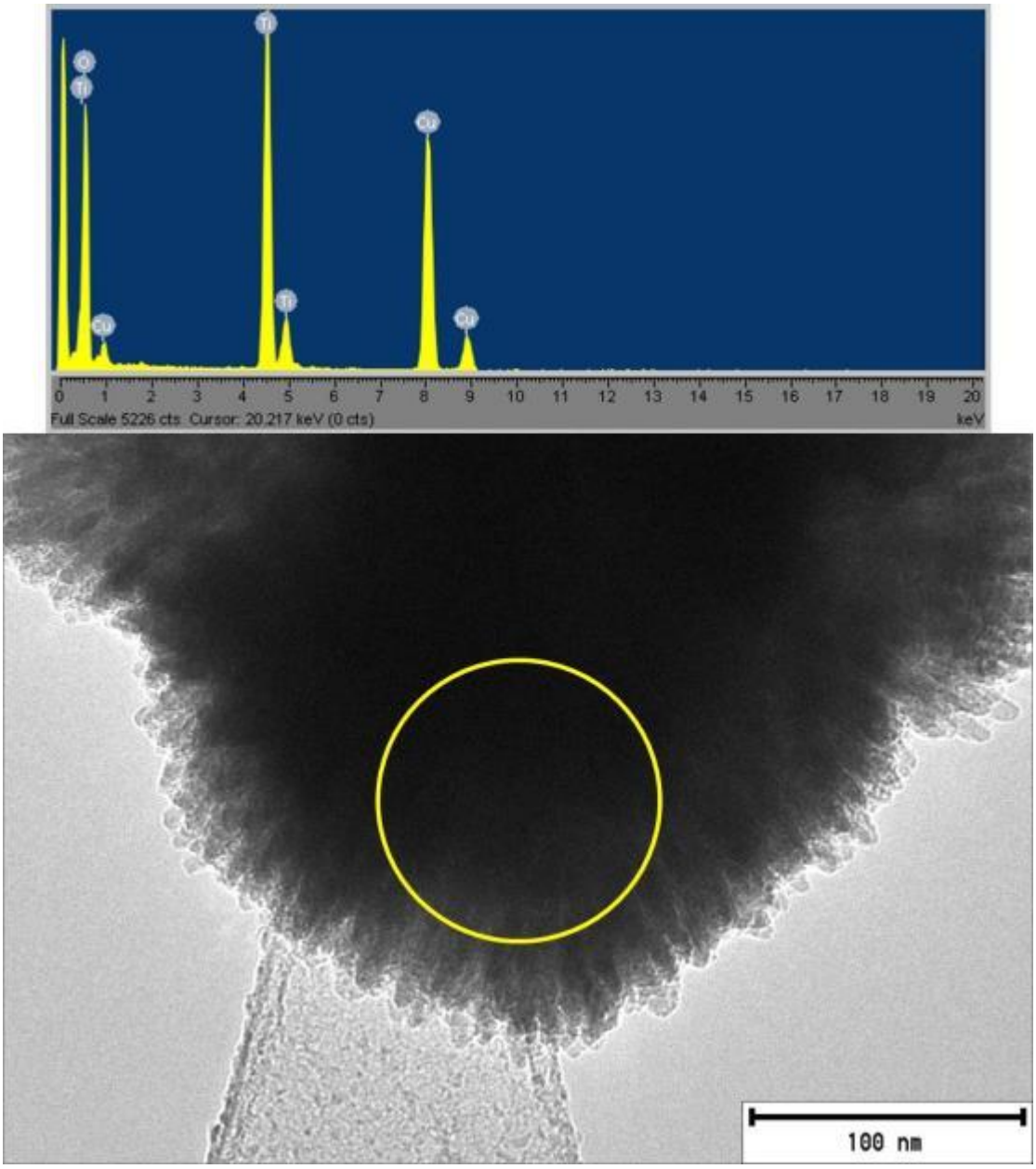

Figure 10.17: ($OTiCl_x$, PEG 400 g/mol). Evidence of superstructures was obtained when $BaCl_2$ was employed in the synthesis. According to the EDS spectrum, the highlighted area of the superstructure (yellow circle) consisted of Ti^+ and O^- exclusively. Cu signals observed in the EDS spectrum as likely generated from the TEM grid. This mesocrystal measured ~ 280 nm across its width.

The cluster observed in figure 10.18 was not probed further for more crystalline information as this was deemed beyond the aims of this chapter. The composition of these particles correlate with the PXRD pattern obtained for this sample.

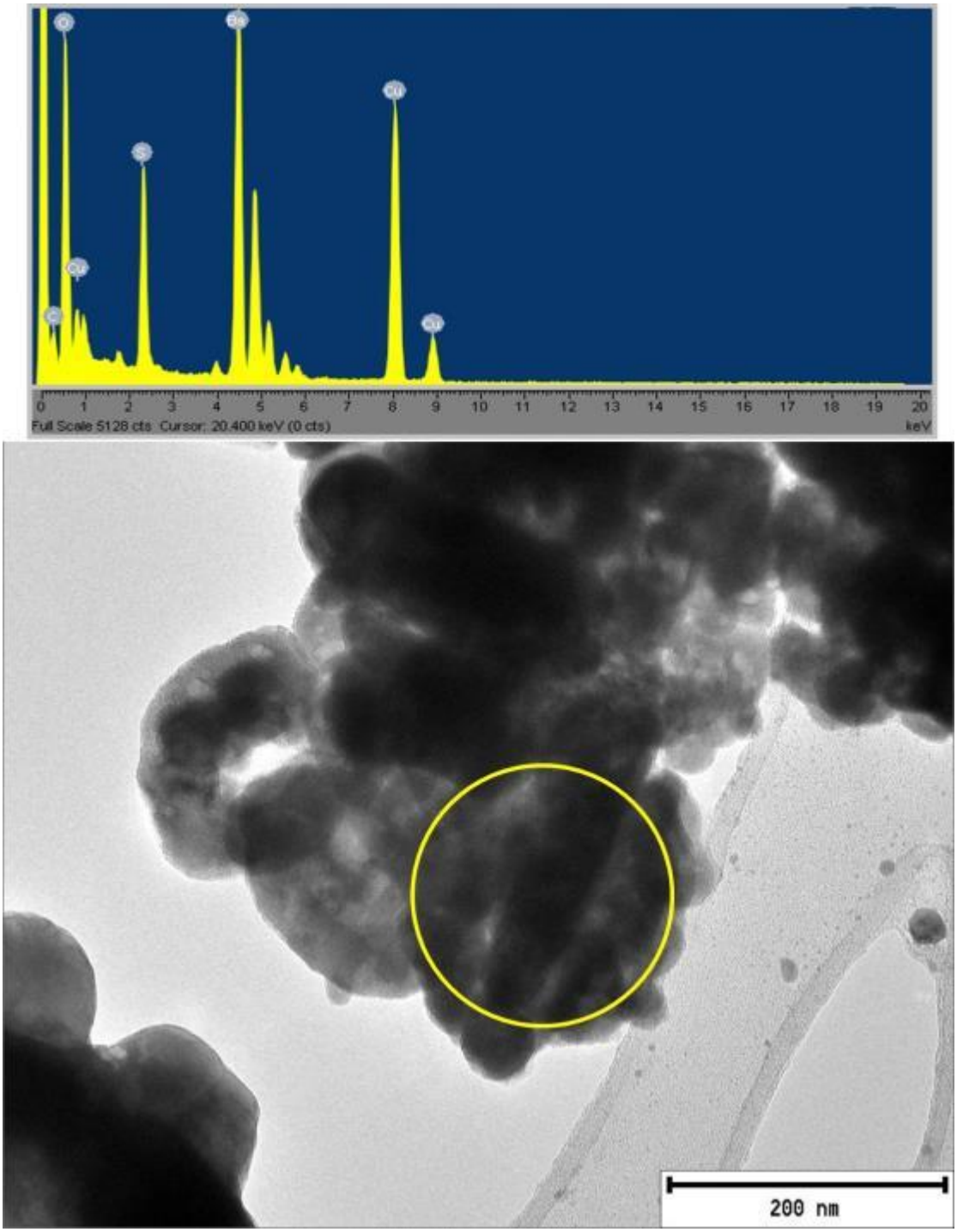

Figure 10.18: ($OTiCl_x$, PEG 400 g/mol). This area of the sample revealed an aggregation of particles with an elemental composition of Ba, S, C, and O.

The change in the relative intensities of the Ba and S peaks observed in the EDS of figure 10.19 suggest that the clusters represent a different Ba containing polymorph than those represented in figure 10.18. The particles comprising this structure are likely responsible for some of the peaks observed in the PXRD pattern generated for this sample.

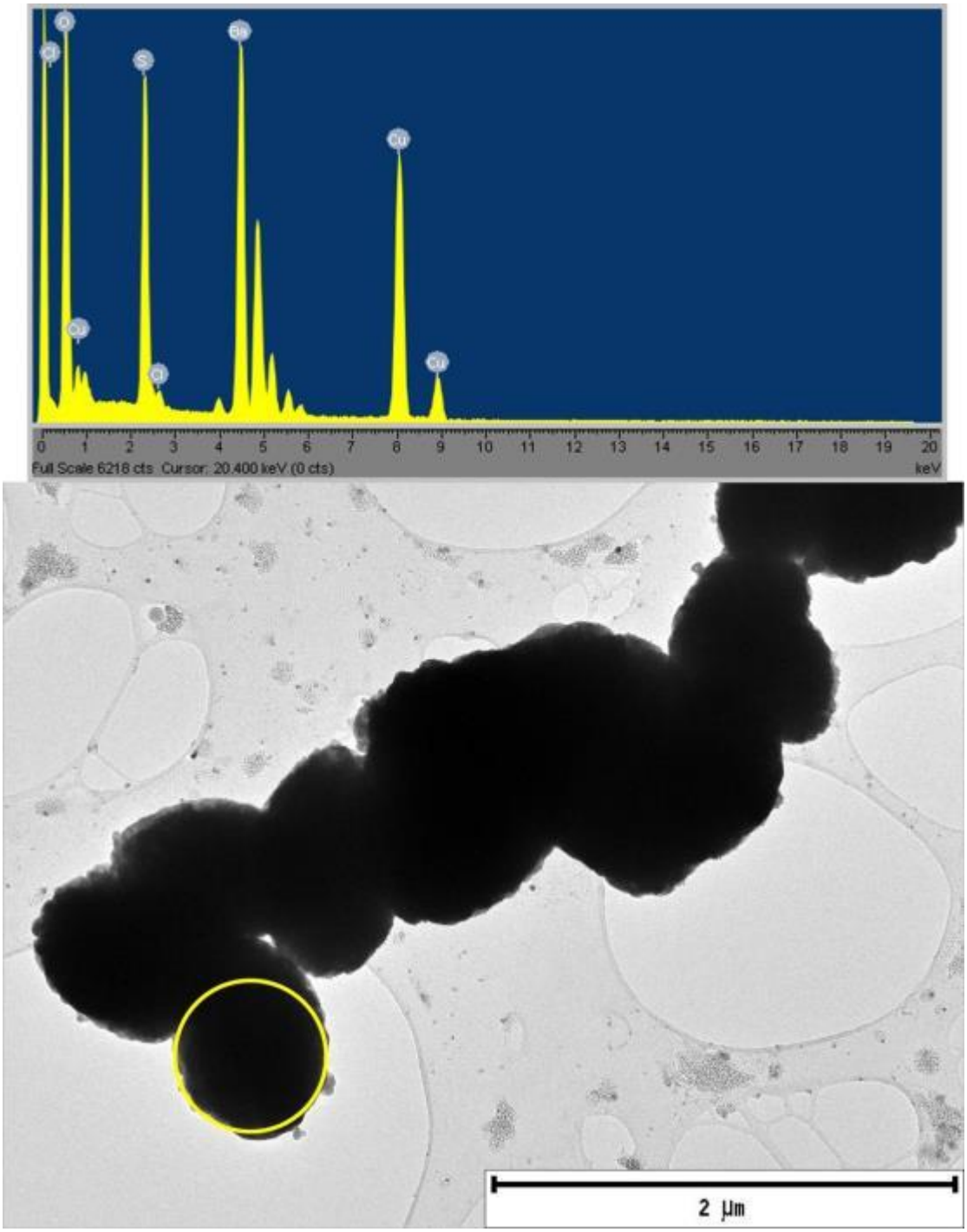

Figure 10.19: ($OTiCl_x$, PEG 400 g/mol). The highlighted structure measured ~ 700 nm across its width and had an elemental composition of Ba, S, O, and Cl.

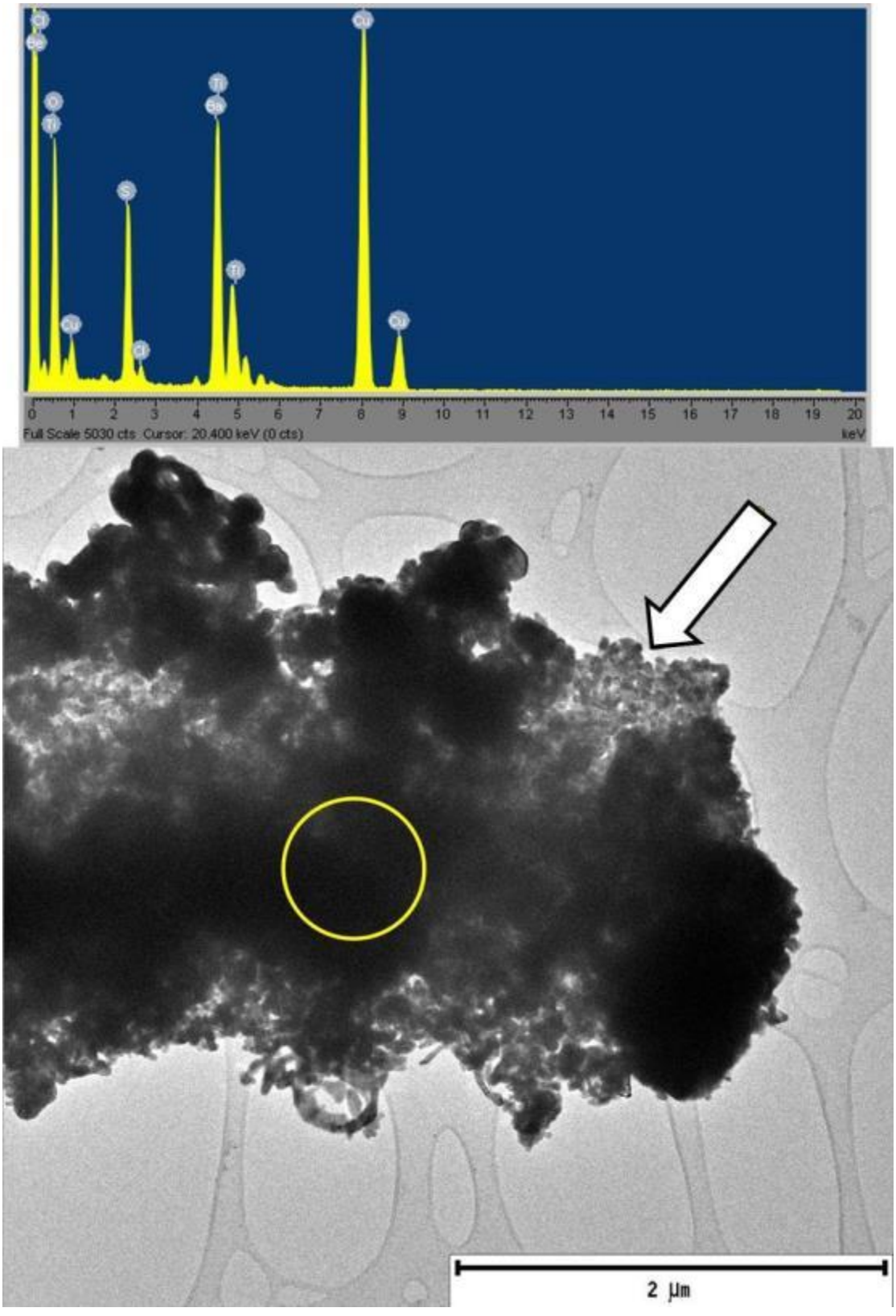

Figure 10.20: ($OTiCl_x$, PEG 400 g/mol). These particles were composed of Ti, O, Ba, S, and Cl. It is unclear whether these elements formed a unique crystal structure or existed separately as TiO_2 and Ba containing crystals, in the same part of the sample. The arrow indicates crystals that appear to be TiO_2.

10.2.2 Titanium (IV) isopropoxide

Figure 10.21 contains the PXRD patterns generated from the samples synthesised using Ti-isopro, post-calcination. Immediately obvious is that the use of Ti-isopro is biased toward the formation of anatase. All samples excluding PEG 4000 g/mol produced a major anatase (1 0 1) and minor rutile (1 1 0) peak. PEG 4000 g/mol resulted in the formation of anatase exclusively. An interesting point of note is that the rutile (1 1 0) peak profile did not correlate with the PEG molecular weight used in the synthesis. The samples synthesised using PEG 200, 10000, and 12000 g/mol resulted in the formation of rutile (1 1 0) peaks with the greatest intensity.

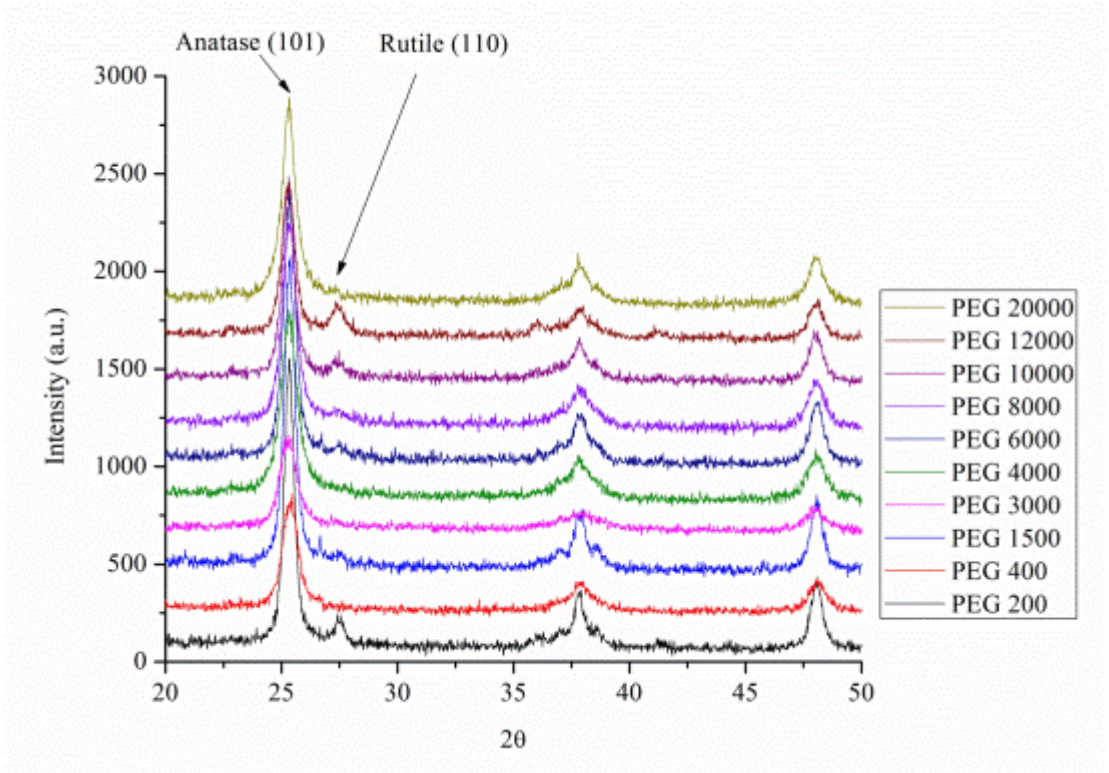

Figure 10.21: PXRD patterns of Ti-isopro generated samples.

The data reflects good peak alignment and signal to noise ratio for all samples. This is indicative of an effective calcination procedure – removing all carbon residues. Moreover, since this system employed the use of a precursor containing Ti^{4+}, hydrocarbons, and oxygen, no other species were present to impart non-uniform strain on the titania lattice. Peak width appeared to fluctuate with increasing PEG molecular weight. The overall narrow anatase (1 0 1) peak width is an indication of crystallite coarsening. This was an expected consequence of calcination.

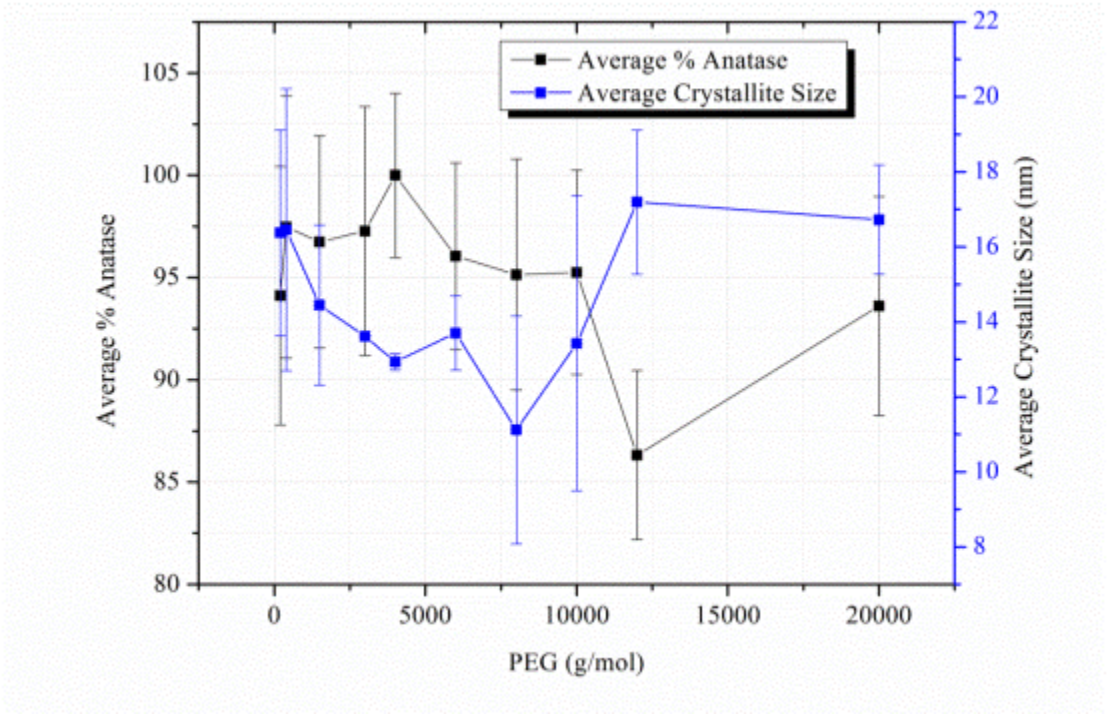

Figure 10.22: Average amount of anatase with associated crystallite size formed using Ti-isopro.

Figure 10.22 shows the relationship between the amount of anatase formed and its respective crystallite size as a function of increasing PEG molecular weight. Samples synthesised using PEG 4000 g/mol resulted in the formation of phase pure anatase. This was in contrast to samples synthesised using PEG 12000 and 20000 g/mol that produced the least amount of anatase (86.3% and 93.6% respectively). PEG 400 – 3000 g/mol and 6000 – 10000 g/mol produced similar amounts of anatase. Among these samples, the greatest difference between the most anatase (PEG 3000 g/mol) and the least anatase (PEG 8000 g/mol) was 2.1%. The average amount of anatase produced across all samples was 95.2%. This result confirmed the observations from PXRD suggesting that this system is biased toward anatase formation.

The largest error was obtained from the sample synthesised using PEG 400 g/mol (6.4%). This is indicative of excellent reproducibility achieved from all samples. Error bars were generated as previously described.

Interestingly, anatase crystallites appeared to decrease and then increase in size as a function of increasing PEG molecular weight. Crystallite sizes varied between ~ 11 – 17 nm, with the average crystallite size across all samples measuring 14.6 nm. Many samples generated crystallites that measured more than 14 nm. This was expected

given that the data represented in figure 10.22 was obtained post-calcination. The greatest error in the data was obtained for the sample synthesised using PEG 10000 g/mol (3.9 nm). Error bars were generated as described previously. A curious observation is the imperfect pseudo inverse relationship between the amount of anatase formed and its respective crystallite size. Shorter chain PEG (< 10000 g/mol) produced a large mass percentage of anatase crystallites that were smaller in size. Longer chain PEG produced a smaller mass percentage of anatase crystallites that were larger in size. A pseudo inverse relationship between the amount of anatase formed and its respective crystallite size was observed in chapter 5, for the synthesis employing ethanol.

From chapter 5 it was inferred that addition of $TiCl_4$ to ethanol produced Ti-ethylhydroxyl species with coordinating CH_3CH_2 groups. These groups were present in the polymer reaction chambers and served to stabilise and protect nucleated anatase. In a similar manner Ti-isopro likely formed hydroxylated species in H_2O via the action of hydrogen bonding between solvent generated hydrogen and oxygen generated from the precursor. Therefore, given that in solution, the Ti-isopro hydroxyl species and Ti-ethylhydroxyl species have similar structures, the results obtained using both precursors should also be similar. A comparison of the amount of anatase obtained using Ti-isopro in water containing HNO_3, and $TiCl_4$ in ethanol (volumetric PEG addition – chapter 5) is given in figure 10.23. Only samples that allowed for a direct comparison to be made were included in figure 10.23.

Based on the data represented in figure 10.23, the average amount of anatase formed using Ti-isopro equalled 96.4%. This value was marginally lower than the average amount of anatase formed using $TiCl_4$ in ethanol (97.1%). Therefore, the data in figure 10.23 suggests that a similar mechanism drove the formation of anatase using both systems. That mechanism is likely anatase protection afforded by similarly structured coordinating groups.

The amount of anatase formed per PEG chain length between the two systems was similar. This indicated that the quantity of polymer added played a less important role in phase determination than similarly structured protecting species present within the reaction chambers. Variation in the amount of anatase formed as a function of different PEG molecular weights was likely due to the formation of polymer reaction chambers of various sizes.

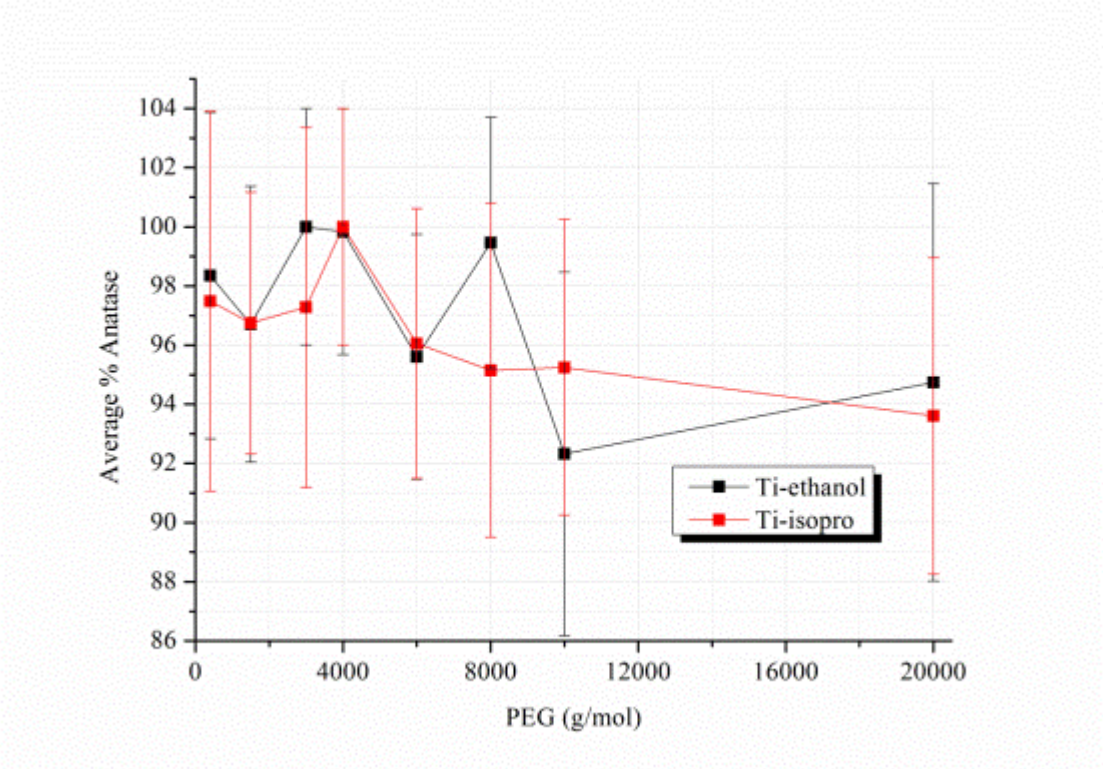

Figure 10.23: Post-calcination comparison of the average amount of anatase formed using $TiCl_4$ in ethanol with Ti-isopro in water containing HNO_3.

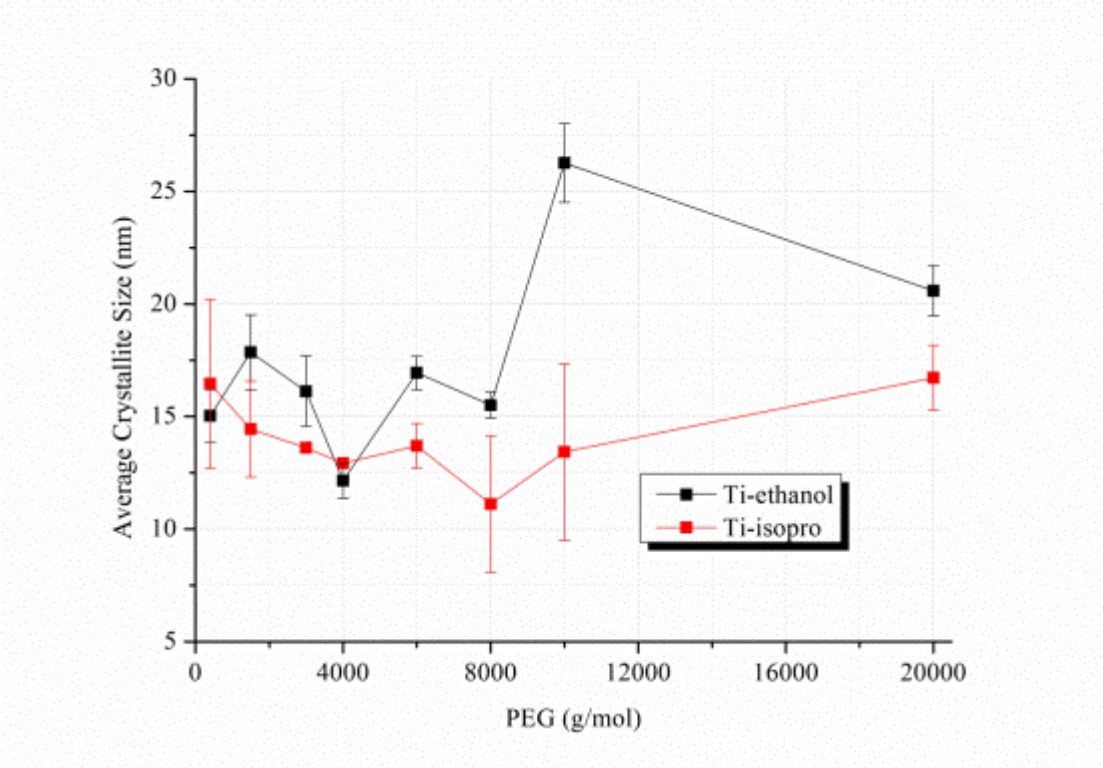

Figure 10.24: Post-calcination comparison of the average anatase crystallite size obtained using $TiCl_4$ in ethanol with Ti-isopro in water containing HNO_3.

Figure 10.24 compares $TiCl_4$ in ethanol (volumetric PEG addition – chapter 5) with Ti-isopro in water containing HNO_3 for anatase crystallite size data. Based on the data contained within figure 10.24, the average anatase crystallite size obtained across all samples using $TiCl_4$ in ethanol measured 17.5 nm. This was 24.9% larger than the average anatase crystallite size obtained using Ti-isopro (14.1 nm). The variation between the two systems as a function of PEG molecular weight suggests that the quantity of polymer in the system influenced anatase crystallite size more than the quantity of anatase formed.

Tables showing the amount of each phase and crystallite size data obtained for each sample with averages and errors using Ti-isopro are given in appendix H.

TEM images corresponding to samples synthesised using PEG 400 g/mol (figures 10.25 and 10.26) and 4000 g/mol follow (figure 10.27).

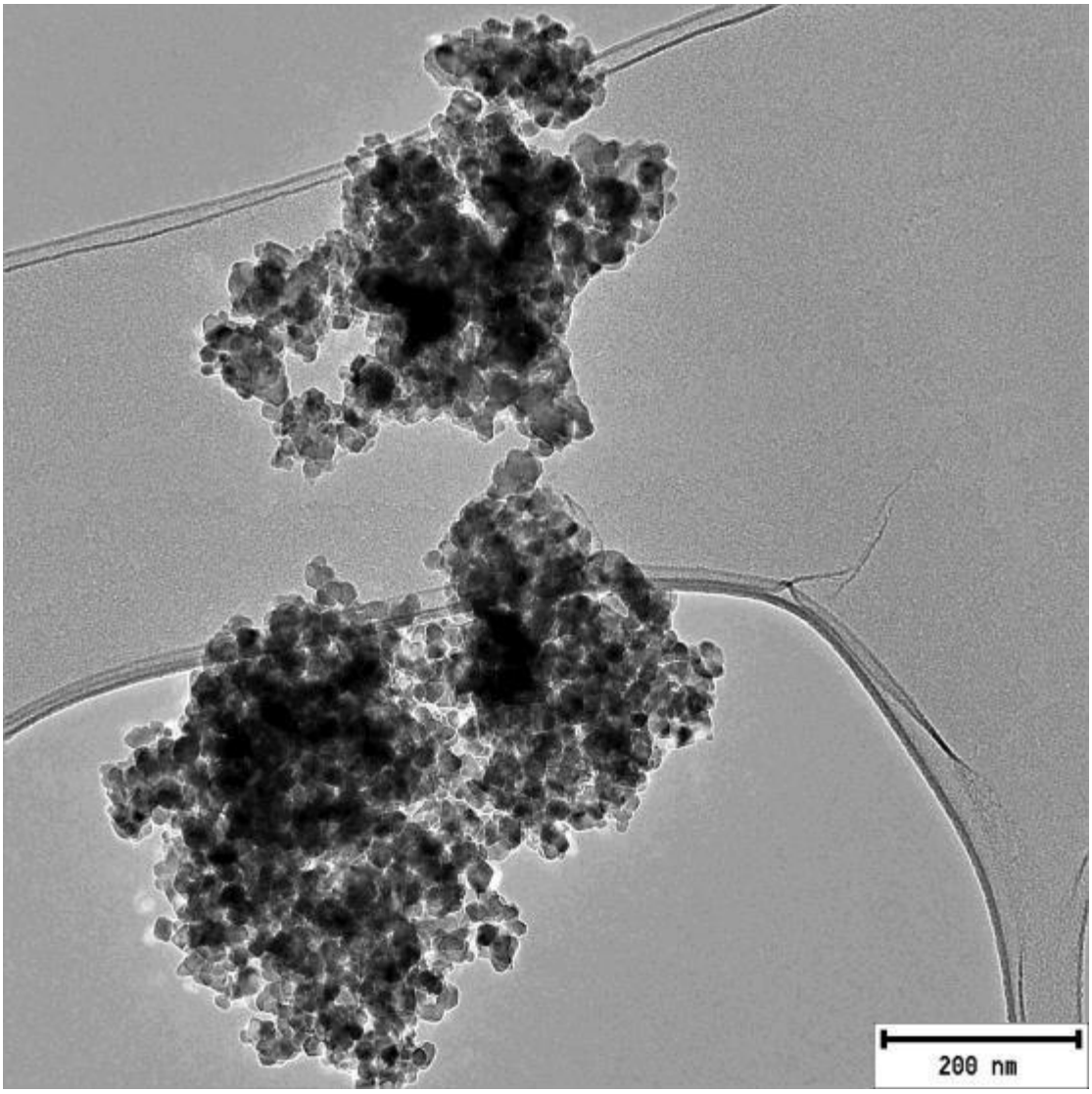

Figure 10.25: (PEG 400 g/mol). Anatase crystallites consistent in shape and size when Ti-isopro was employed as the precursor.

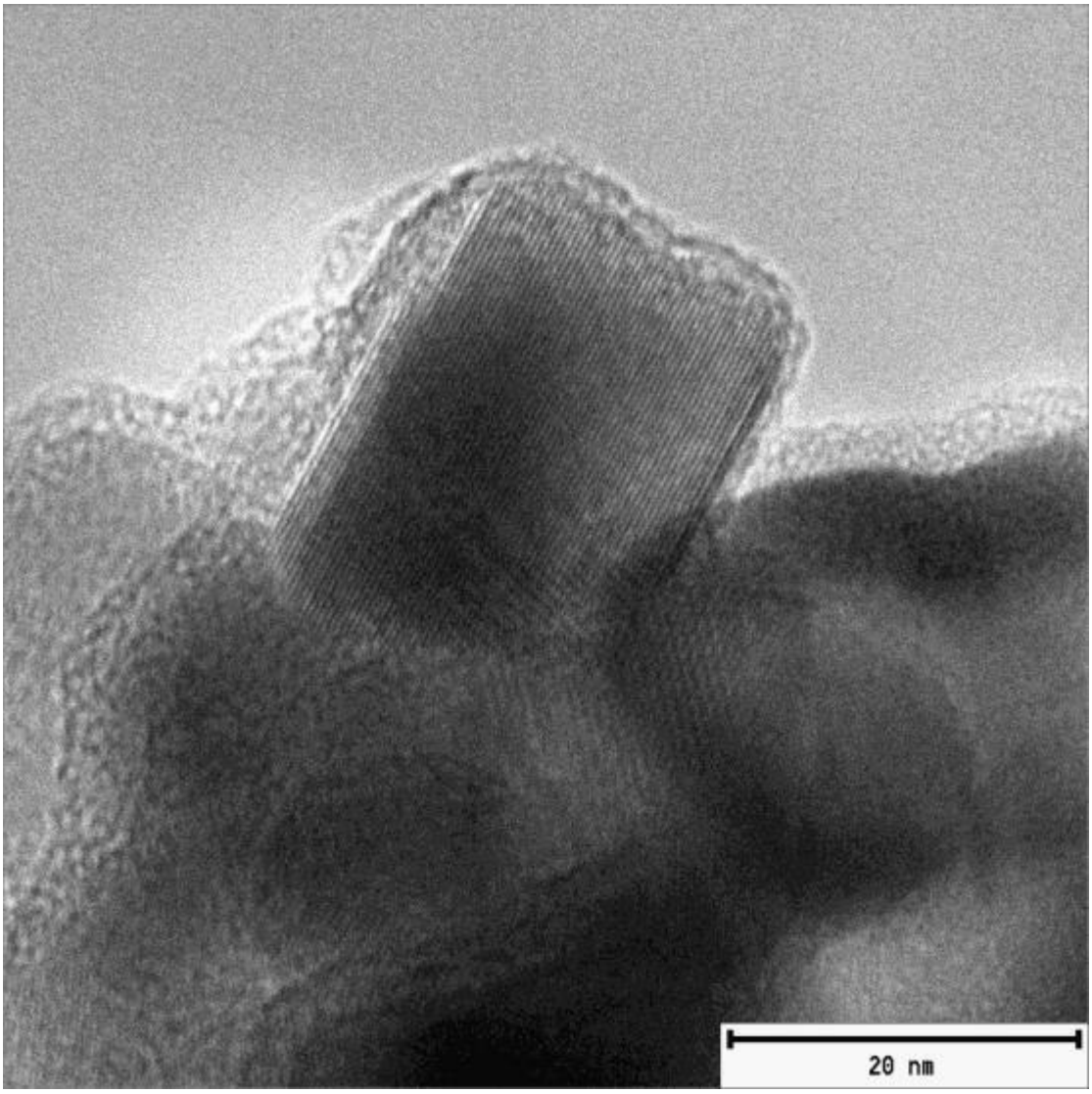

Figure 10.26: (PEG 400 g/mol). Well defined cubic shape of an anatase crystal. This crystal measured ~ 22 nm and ~ 28 nm across its width and length respectively.

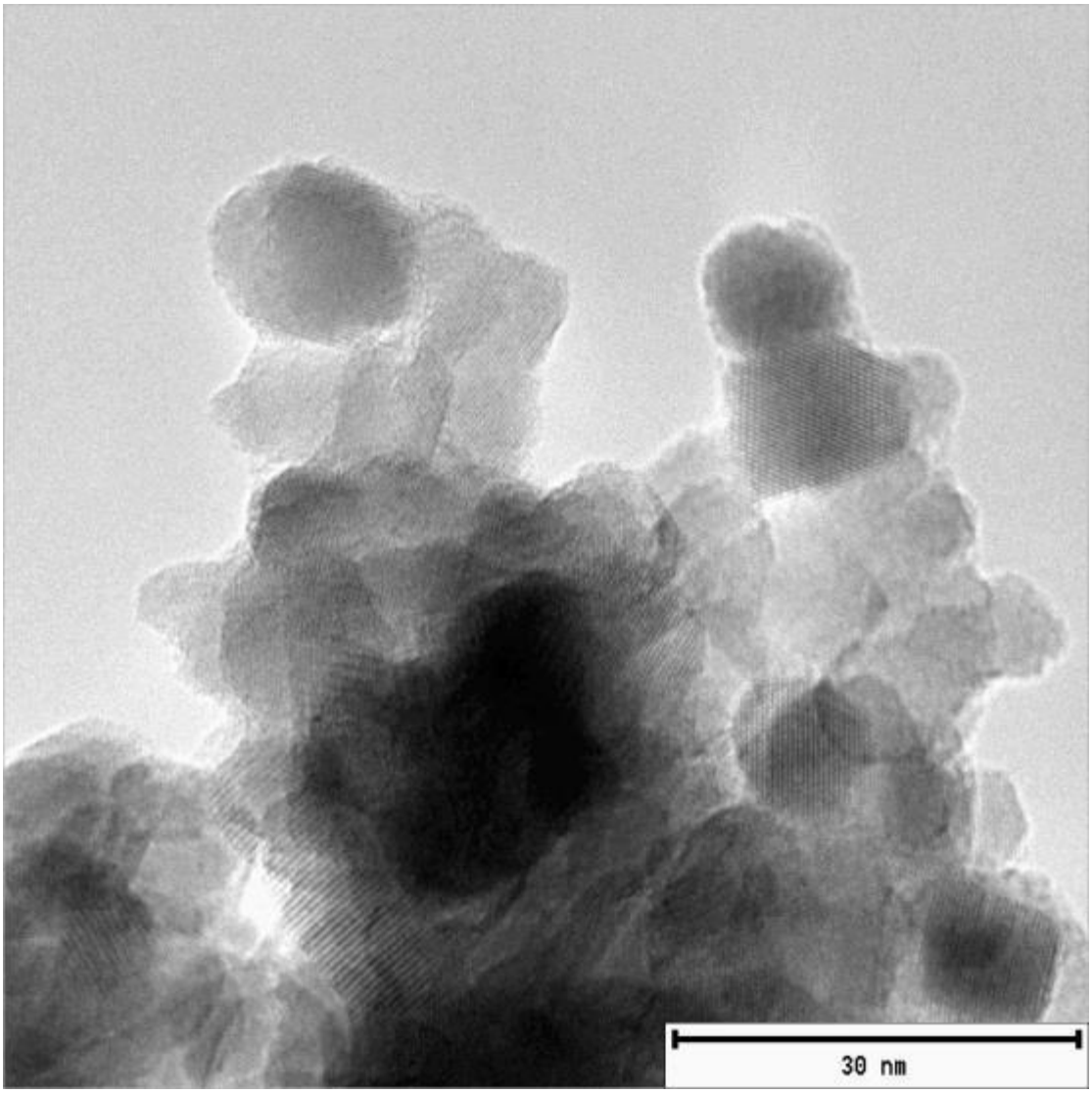

Figure 10.27: (PEG 4000 g/mol). Anatase crystallites exhibiting various shapes, as documented previously.

10.2.3 Titanium (IV) 2-ethylhexyloxide

Figure 10.28 shows the PXRD patterns collected from the experiment conducted using Ti-EHOx, post-calcination. Samples synthesised using PEG 1500 g/mol, 12000 g/mol and 20000 g/mol produced rutile as the major phase. PEG 20000 g/mol appeared to produce almost phase pure rutile. This is the first observation of samples synthesised using a hydrocarbon and oxygen based precursor producing rutile as the major phase. PEG 3000 g/mol produced phase pure anatase. All other samples produced a mixture of phases with anatase as the major phase.

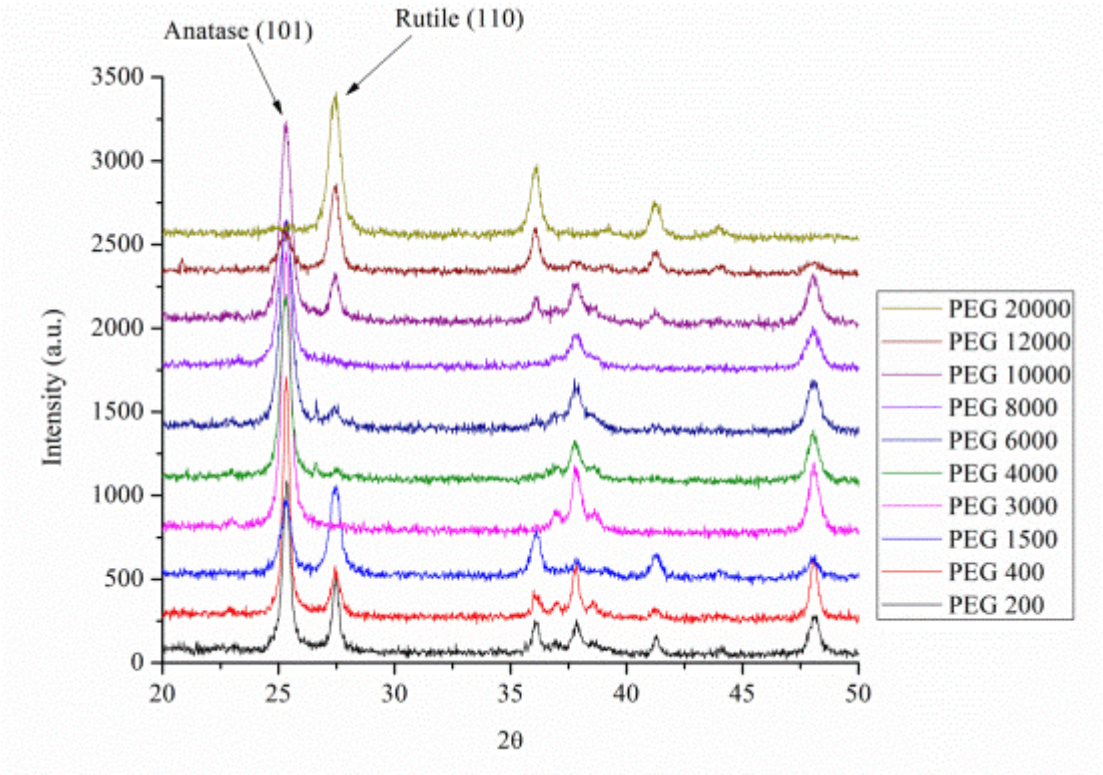

Figure 10.28: PXRD patterns of Ti-EHOx generated samples.

Good peak alignment and signal to noise ratio is indicative of the effectiveness of calcination at removing carbon from the samples. Observed sharp peaks were expected as a consequence of calcination.

Figure 10.29 shows the relationship between the amount and size of anatase crystallites formed using Ti-EHOx. Low molecular weight PEG (200 – 1500 g/mol) favoured the formation of both anatase and rutile. Intermediate molecular weight PEG (3000 – 8000 g/mol) resulted in the formation of nearly phase pure anatase. High molecular weight PEG (12000 – 20000 g/mol) produced rutile as the major phase. The average amount of anatase formed across all samples equalled 68.3%. From this

value it may be inferred that Ti-EHOx marginally favoured the formation of anatase. This value also represents the lowest average amount of anatase formed using any hydrocarbon and oxygen based precursor (including TiOxS and $TiCl_4$ in ethanol). Small error bars were generated as previously described and are indicative of good reproducibility.

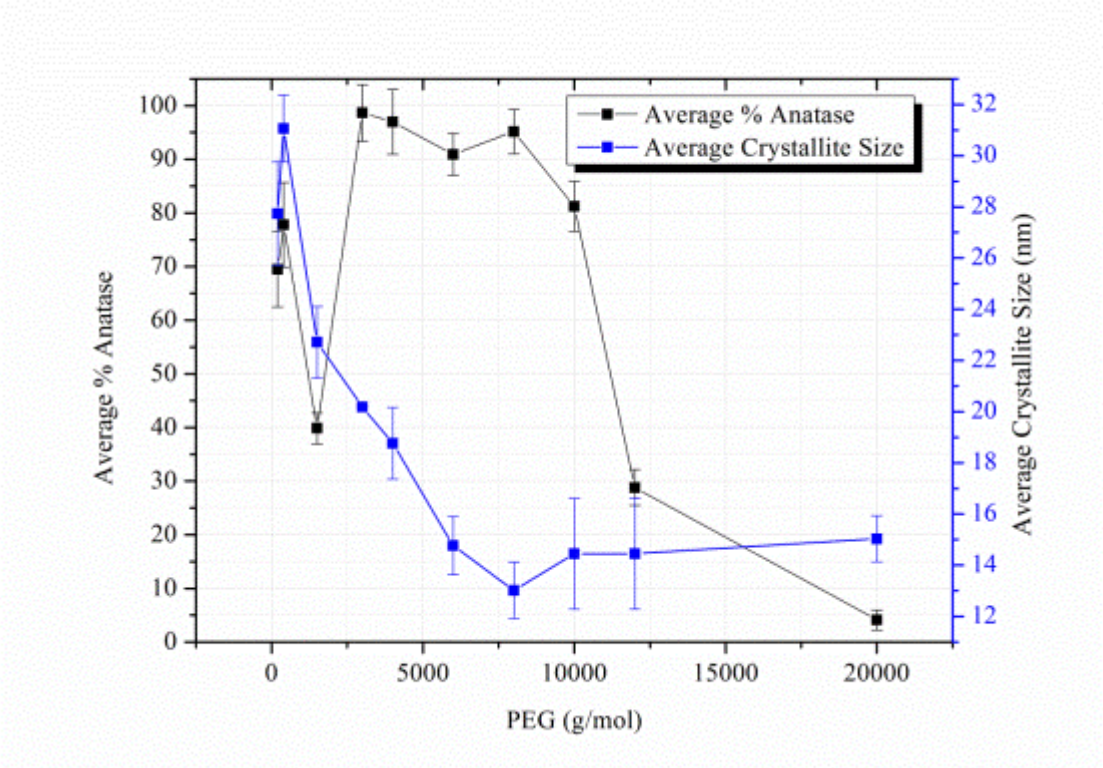

Figure 10.29: Average amount of anatase with associated crystallite size formed using Ti-EHOx.

The largest anatase crystallites were formed from the sample synthesised using PEG 400 g/mol (31.1 nm). This was in contrast to PEG 8000 g/mol that resulted in the formation of the smallest anatase crystallites (13.0 nm). Thus anatase crystallite size appeared to decrease significantly and then slightly increase as a function of increasing PEG molecular weight. The average anatase crystallite size across all samples measured 19.2 nm. This average is currently the largest of all precursors employed in this study thus far. Error bars were generated as previously described. There appeared to be no apparent relationship between the amount of anatase formed and its respective crystallite size.

Given the structural similarities between Ti-EHOx and Ti-isopro (single bonded hydrocarbon and oxygen based precursors), the variation in the amount of anatase

produced was unexpected. Since all other experimental parameters were kept constant, the variation in the data between the two abovementioned precursors must be due to the length of the ligands attached to Ti^{4+} in Ti-EHOx. When Ti-EHOx was introduced into solution, a hydroxyl species likely formed. This species was likely further coordinated to 4 ligands, each comprising 6 carbon atoms along the chain and a single branch of 2 carbon atoms. This is in contrast to the 2 carbon atom (with a solitary branch) coordinating hydroxyl chain formed when Ti-isopro was introduced into solution. Furthermore, the ethyl-hydoxyl species formed when $TiCl_4$ was introduced into ethanol (chapter 5) consisted of a coordinating chain comprising 2 carbon atoms. As witnessed previously, $TiCl_4$ in ethanol and Ti-isopro produced similar amounts of anatase. Therefore, the size of the Ti-hydroxyl species in solution governs the propensity of the precursor to form anatase.

This inference can be disputed considering that when citric acid was employed in the synthesis, the coordinated citrate anion based ligand consisted of a 5 carbon chain (and a single branched carbon). However, this ligand also consisted of 6 terminating oxygen atoms (excluding the oxygen atoms directly bonded to Ti) that could coordinate to the PEG chain.

The size of hydrocarbon and oxygen based coordinating precursors plays a pivotal role in anatase formation in the following way: small precursors coordinate to and are easily engulfed by polymer chains during the formation of reaction chambers. Within these chambers, ligands serve to protect and stabilise the nucleated anatase phase. This phenomenon also occurs for larger precursors that have multiple points for coordination to the polymer. Large precursors that do not have multiple points for coordination to the polymer are not easily enveloped by the polymer chains. Anatase nucleates, and is still likely protected by precursor ligands. This protection is limited by poorly formed polymer reaction chambers. Reduced anatase protection encourages rutile transformation.

Since the amount of anatase formed varied with PEG chain length, the effects of PEG molecular weight must considered. As described previously, small chain PEG (200 – 400 g/mol) likely provided sufficient protection, in addition to the C based ligands from Ti-EHOx, to favour the formation of anatase. Longer PEG chains (3000 g/mol) were probably unstable and decomposed to form smaller chambers that could not envelop the precursor components. Therefore, rutile formation was encouraged.

Increasing the PEG molecular weight further (3000 – 10000 g/mol) increased the size of the decomposed chambers sufficiently to wrap around the precursor inhibiting rutile transformation. Due to the large volume of high molecular weight PEG used, it was expected that long chain polymers (12000 – 20000 g/mol) would encourage anatase formation due to steric effects (described in chapter 8). This is clearly not the case as these polymer chain lengths produced rutile as the major phase. A possible explanation for this observation is that the precursor employed in the current study was not terminated with coordinating O groups. As a result, despite possessing the ability to fully engulf the precursor, long chain PEG's formed large reaction chambers that did not stabilise nucleated anatase. As a result, nucleated anatase crystallites were encouraged to transform into rutile.

Tables showing the amount of each phase and crystallite size data obtained for each sample with averages and errors using Ti-EHOx are given in appendix H.

Figures 10.30 and 10.31 represent the TEM images generated from the samples synthesised using PEG 3000 g/mol. TEM images obtained from the sample synthesised using PEG 20000 g/mol are given in figures 10.32 and 10.33.

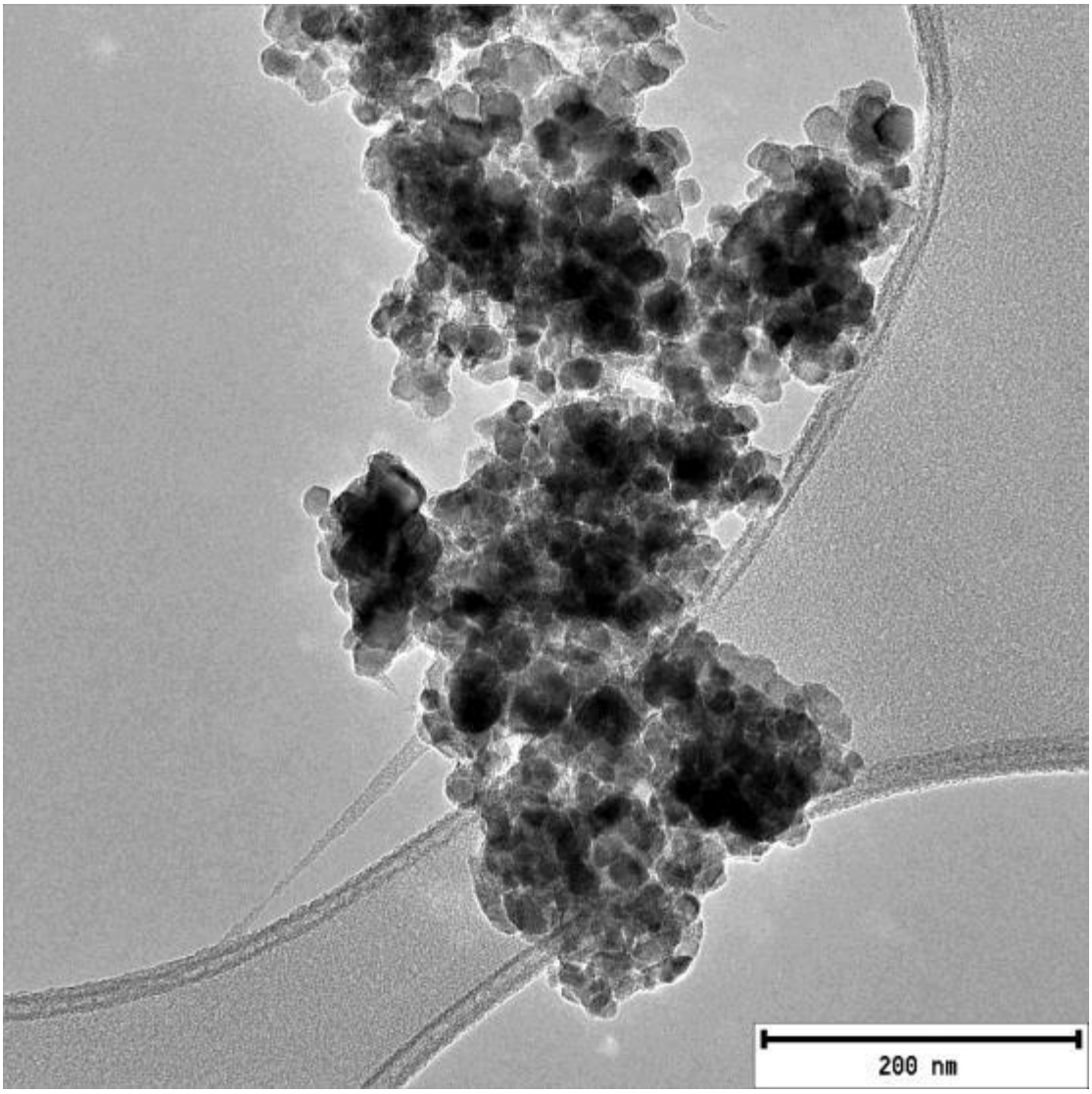

Figure 10.30: (PEG 3000 g/mol). Anatase crystallites consistent in appearance to that previously observed in this study.

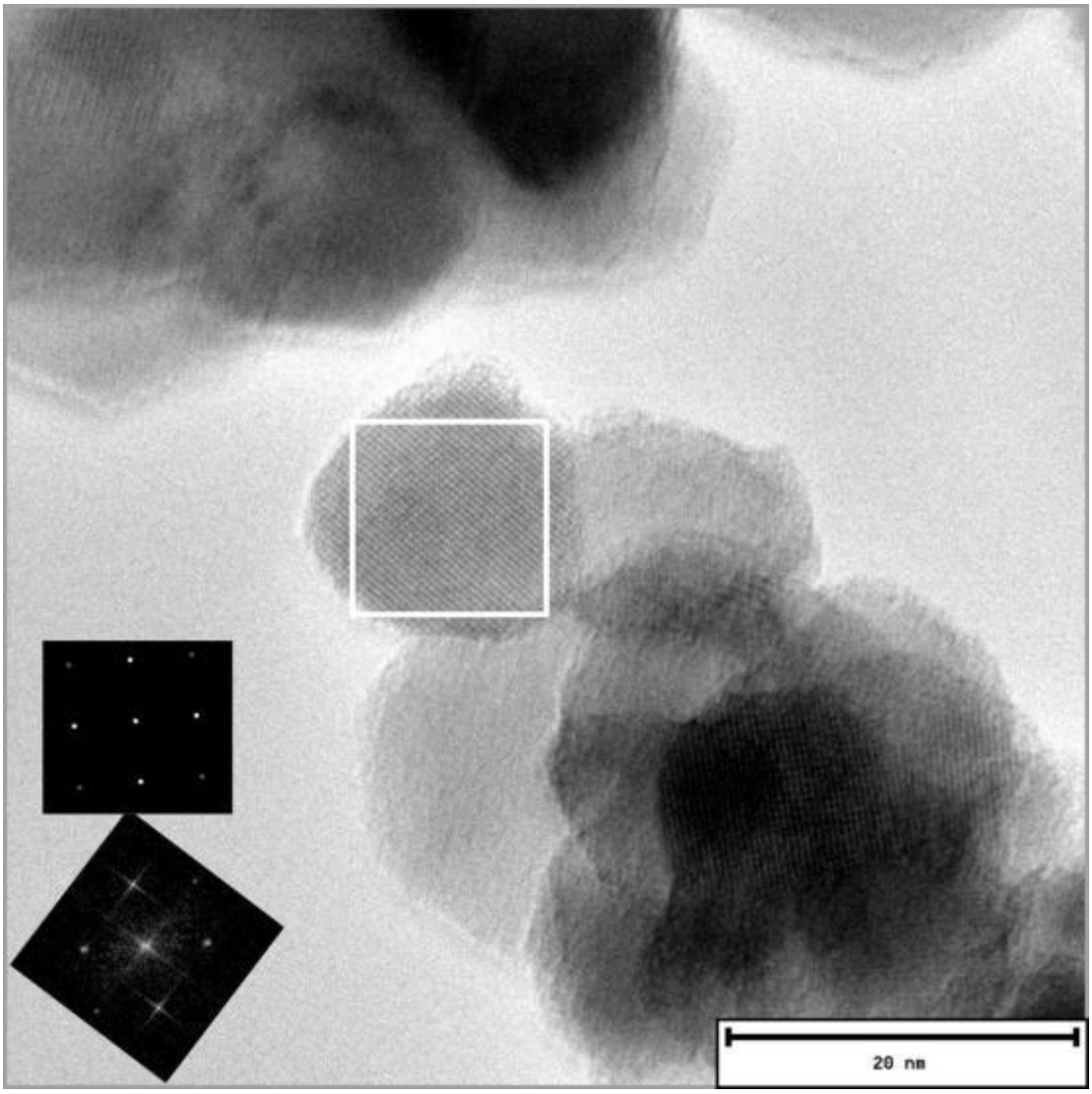

Figure 10.31: (PEG 3000 g/mol). The highlighted anatase crystal measured approximately 15 nm across its length and width. This crystal was aligned along (0 0 1) as evidenced by a comparison of the generated and simulated FFT's. Note that this crystal does not have well defined edges.

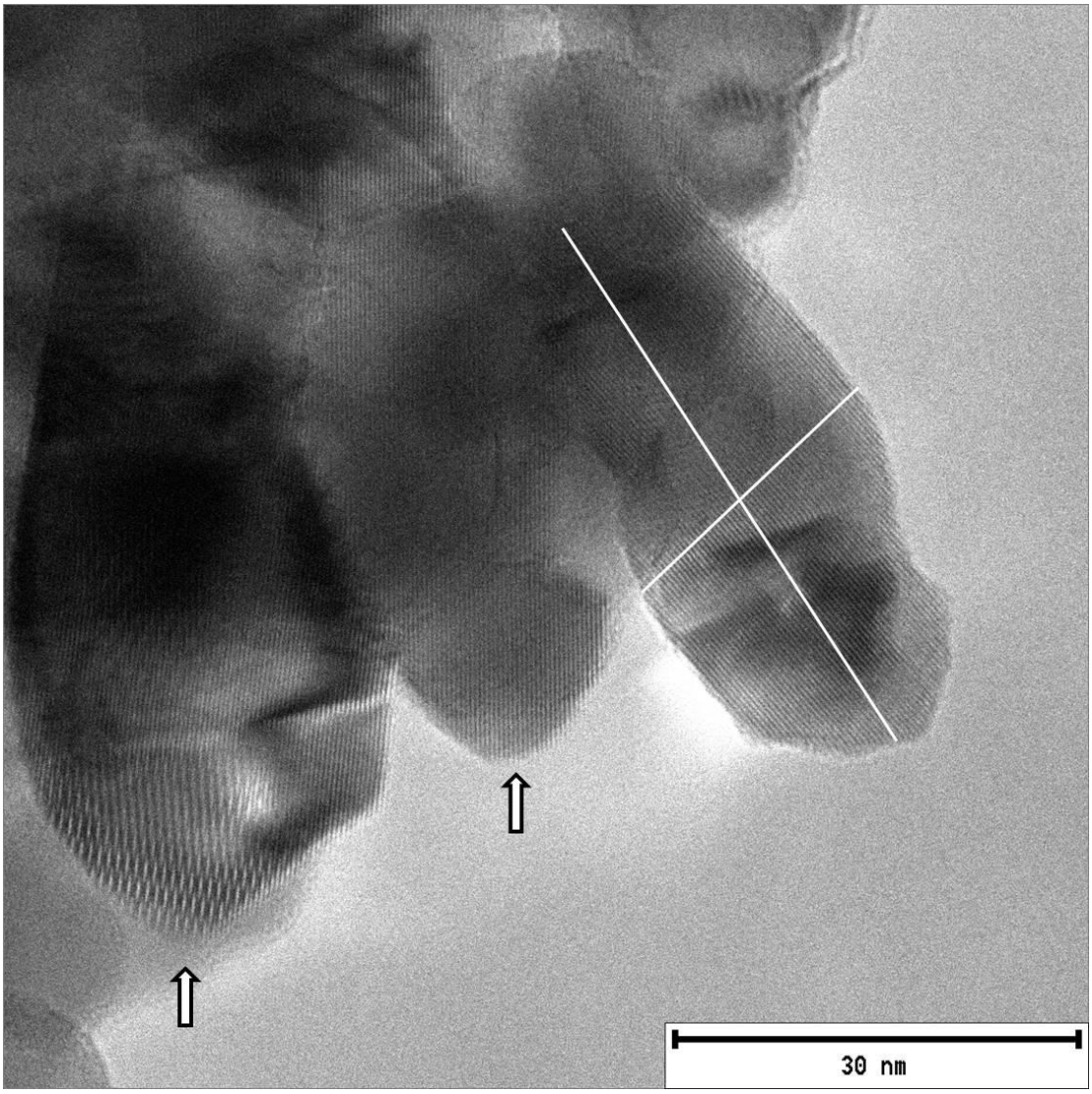

Figure 10.32: (PEG 20000 g/mol). The arrows indicate tapered, pyramidically capped ends of rutile crystallites. This is characteristic of rutile crystals[7]. The white lines denote an anisotropic rutile crystal measuring > 48 nm in length and approximately 22 nm across its width.

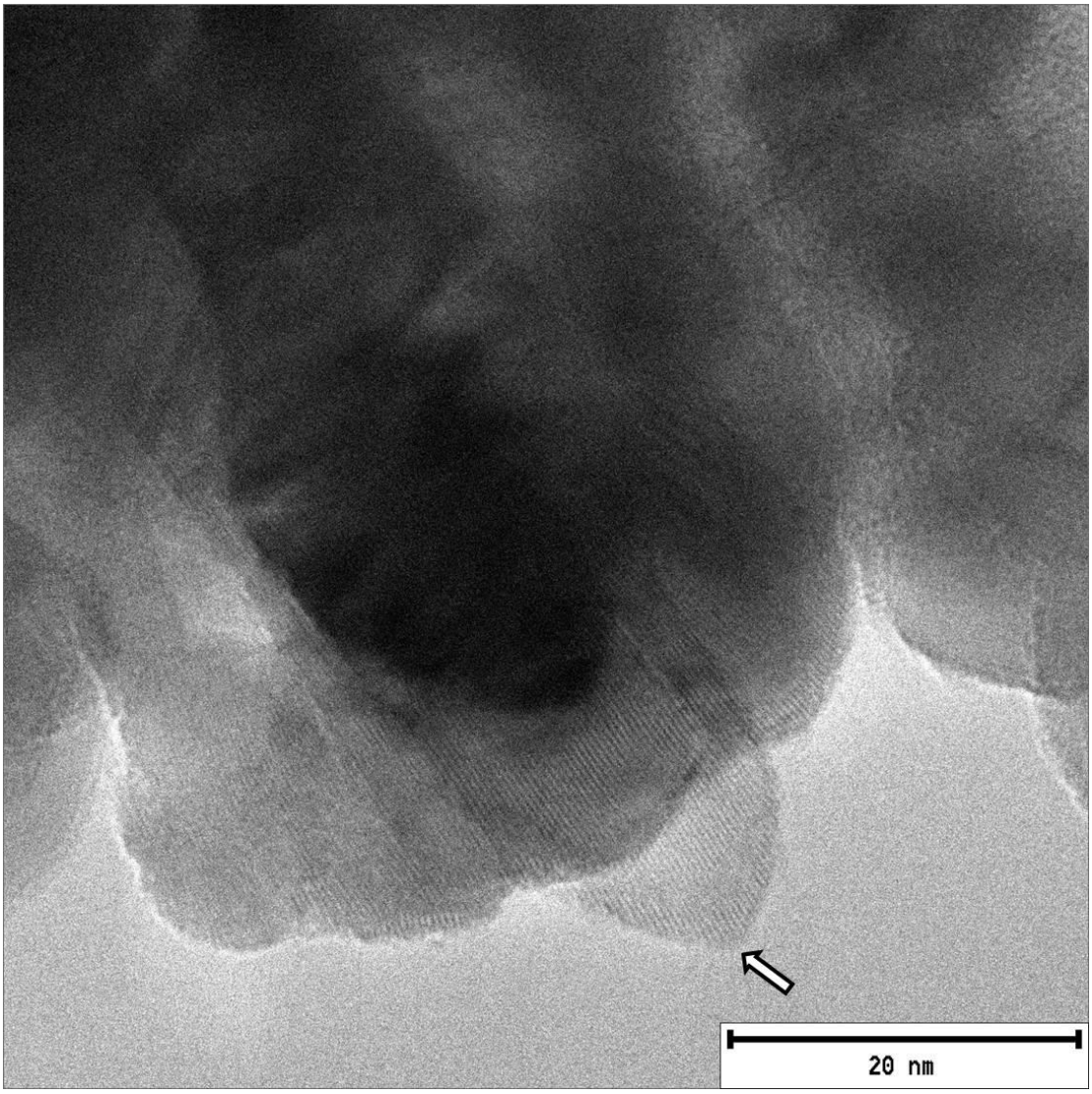

Figure 10.33: (PEG 20000 g/mol). Further confirmation of anisotropic rutile crystals. The arrow indicates the tapered end of a rutile crystal. An interesting note is that rutile mesocrystal formation was not observed, despite the formation of anisotropic rutile crystals.

10.2.4 Titanium diisopropoxide bis(acetylacetonate)

Figure 10.34 contains the PXRD patterns generated from samples synthesised using Ti-AcAc, post-calcination. All samples produced either phase pure anatase, or anatase as the major phase. Distinct rutile (1 1 0) peaks were observed for samples synthesised using PEG 200, 12000 and 20000 g/mol. As previously observed, good peak alignment and signal to noise ratio is an indication of an effective calcination procedure. Narrow peaks were expected due to crystallite coarsening induced by calcination.

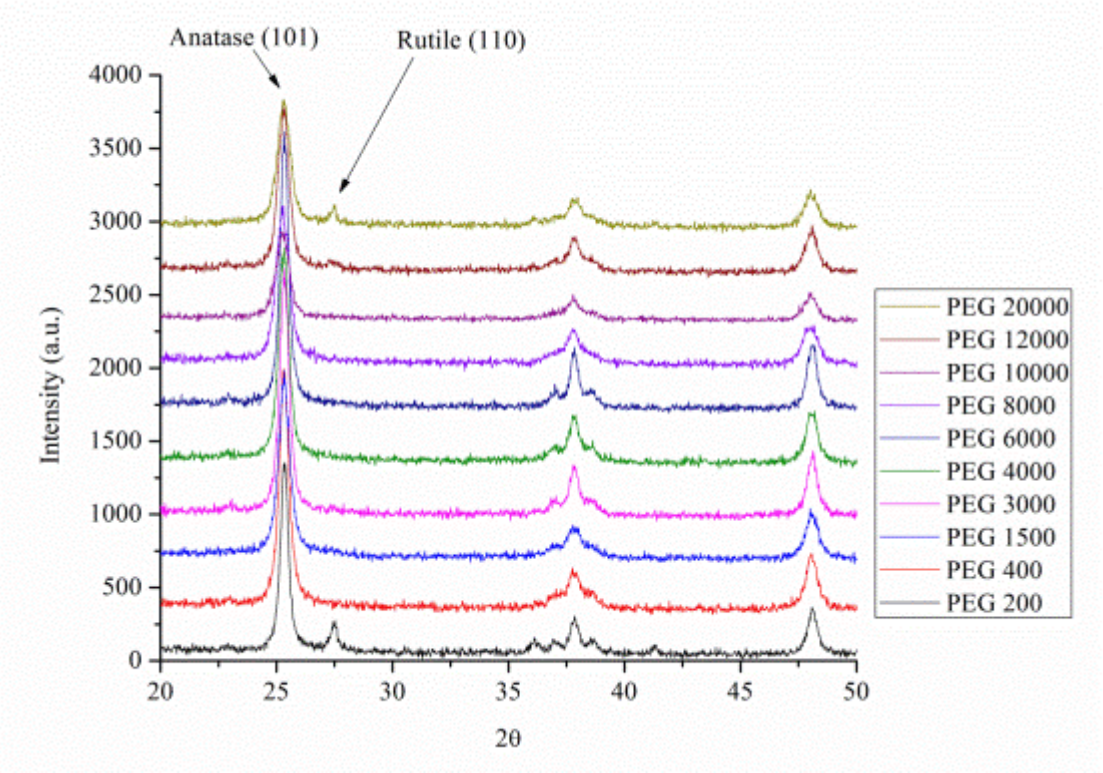

Figure 10.34: PXRD patterns of Ti-AcAc generated samples.

Figure 10.35 shows the relationship between the amount of anatase formed and its respective crystallite size as a function of increasing PEG molecular weight, using a Ti-AcAc precursor, post-calcination. The sample synthesised using PEG 200 g/mol produced the least amount of anatase (85.5%). PEG 400 – 8000 g/mol produced nearly phase pure anatase. Long chain PEG (10000 – 20000 g/mol) produced decreasing amount of anatase corresponding to increasing PEG molecular weight. The average amount of anatase formed across all samples equalled 96.9%. This value shows that this system was biased toward anatase formation. Error bars were generated as previously described.

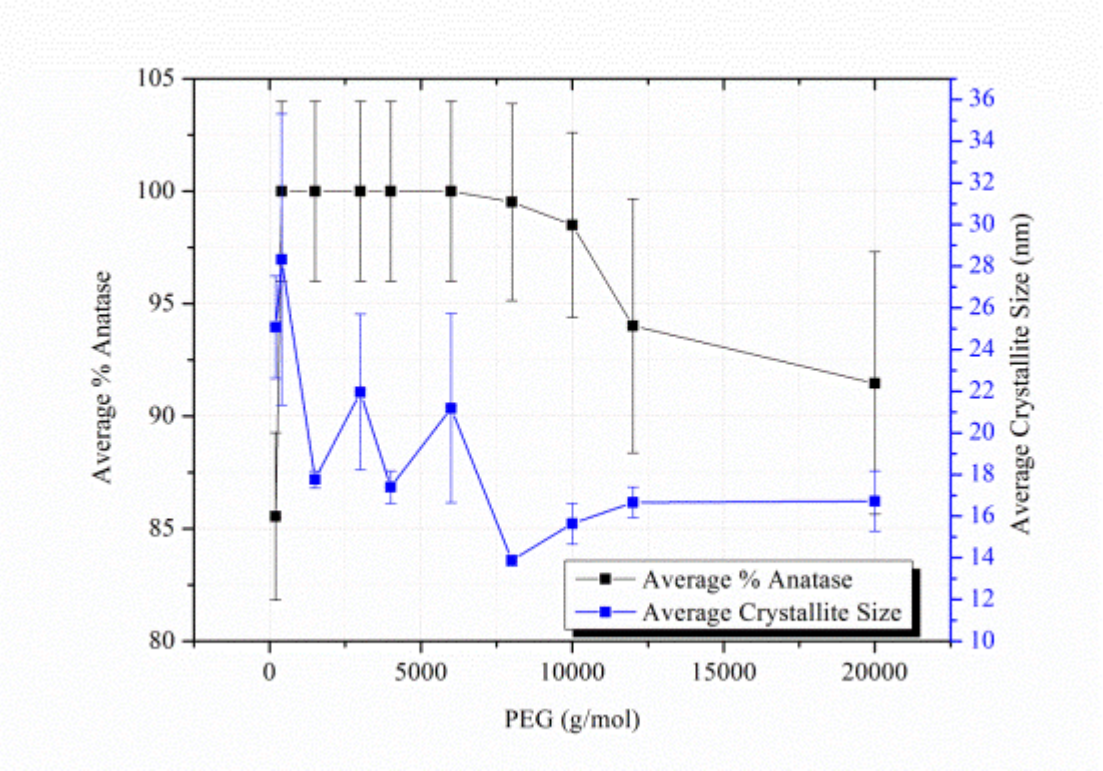

Figure 10.35: Average amount of anatase with associated crystallite size formed using Ti-AcAc.

Anatase crystallite size data did not appear to correlate with PEG molecular weight. Samples synthesised using PEG 200 – 8000 g/mol produced anatase crystallites between ~ 14 – 28 nm in size. Long chain PEG (10000 – 20000 g/mol) produced anatase crystallites of a similar size. As a result there appeared to be no obvious trend between the amount of anatase formed and its respective crystallite size as a function of increasing PEG molecular weight. The average anatase crystallite size across all samples measured 19.5 nm. This value is comparable with that obtained using Ti-EHOx. Crystallite size data was more erratic when obtained from low to intermediate molecular weight PEG (200 – 6000 g/mol). Longer chain PEG (8000 – 20000 g/mol) produced precise anatase crystallite size data.

Since Ti-AcAc contains only hydrocarbons and oxygen, the model developed using $TiCl_4$ in ethanol (chapter 5), $TiCl_4$-citric acid (chapter 7), Ti-isopro, and Ti-EHOx can be applied to explain the anatase bias obtained in this study. According to the model, a two-fold protection effect occurs within the polymer reaction chambers. The extent of anatase protection is governed by 1) the size of precursor ligands within polymer reaction chambers and 2) the number of oxygen coordination sites on precursor-

solvent complexes available for PEG coordination. The latter is essential to anatase formation as it controls the protection effects afforded by the polymer reaction chambers. If the polymer does not coordinate well to precursor complexes, the driving force for polymer chains to wrap around the precursor complexes is limited. Any polymer reaction chambers that do form (on account of the supplied energy to the system) will be poorly coordinated to the precursor complexes. As a result, the polymer reaction chambers impart poor protection effects and encourage rutile nucleation to an extent.

Ti-AcAc has 4 ligands in total. Two (smaller) ligands are each comprised of a 2 carbon chain with a single carbon containing branch. These ligands are identical to those found in Ti-isopro. The remaining two (larger) ligands are each comprised of a 3 carbon chain with 2 single carbon containing branches. Additionally, each of these ligands are terminated by oxygen groups. Thus, for Ti-AcAc, it is expected that the presence of the 2 smaller ligands served to protect the nucleated anatase phase within the polymer reaction chambers. It is expected that the larger ligands provided 1) protection effects to the nucleated anatase and 2) coordination sites for PEG chains.

Since the amount of anatase formed was affected by PEG chain length, these effects are described: low molecular weight PEG (200 g/mol) was likely too short to wrap around the polymer and form effective reaction chambers therefore rutile transformation was encouraged. Increasing PEG chain length (400 – 6000 g/mol) served to increase the size of coordinating reaction chambers that contributed to anatase stabilisation. Long polymer chains were expected to form larger chambers and due to the amount of polymer present in the system, sterically stabilise anatase. This did not occur as PEG 8000 – 20000 g/mol produced both phases – with an increase in rutile production corresponding to an increase in chain length. This phenomenon was observed in chapter 5 when PEG 35000 g/mol was found to produce a significant amount of rutile using an ethanol solvent. It is possible that larger reaction chambers formed, but did not effectively coordinate with the precursor complexes. This may be due to limited available oxygen coordination sites (relative to the citrate precursor complexes – chapter 7).

Tables showing the amount of each phase and crystallite size data obtained for each sample with averages and errors using Ti-AcAc are given in appendix H.

TEM images obtained from samples synthesised using PEG 10000 g/mol (figure 10.36) and 20000 g/mol (figure 10.37) follow. Figure 10.37 suggests that crystals were composed entirely of either anatase or rutile.

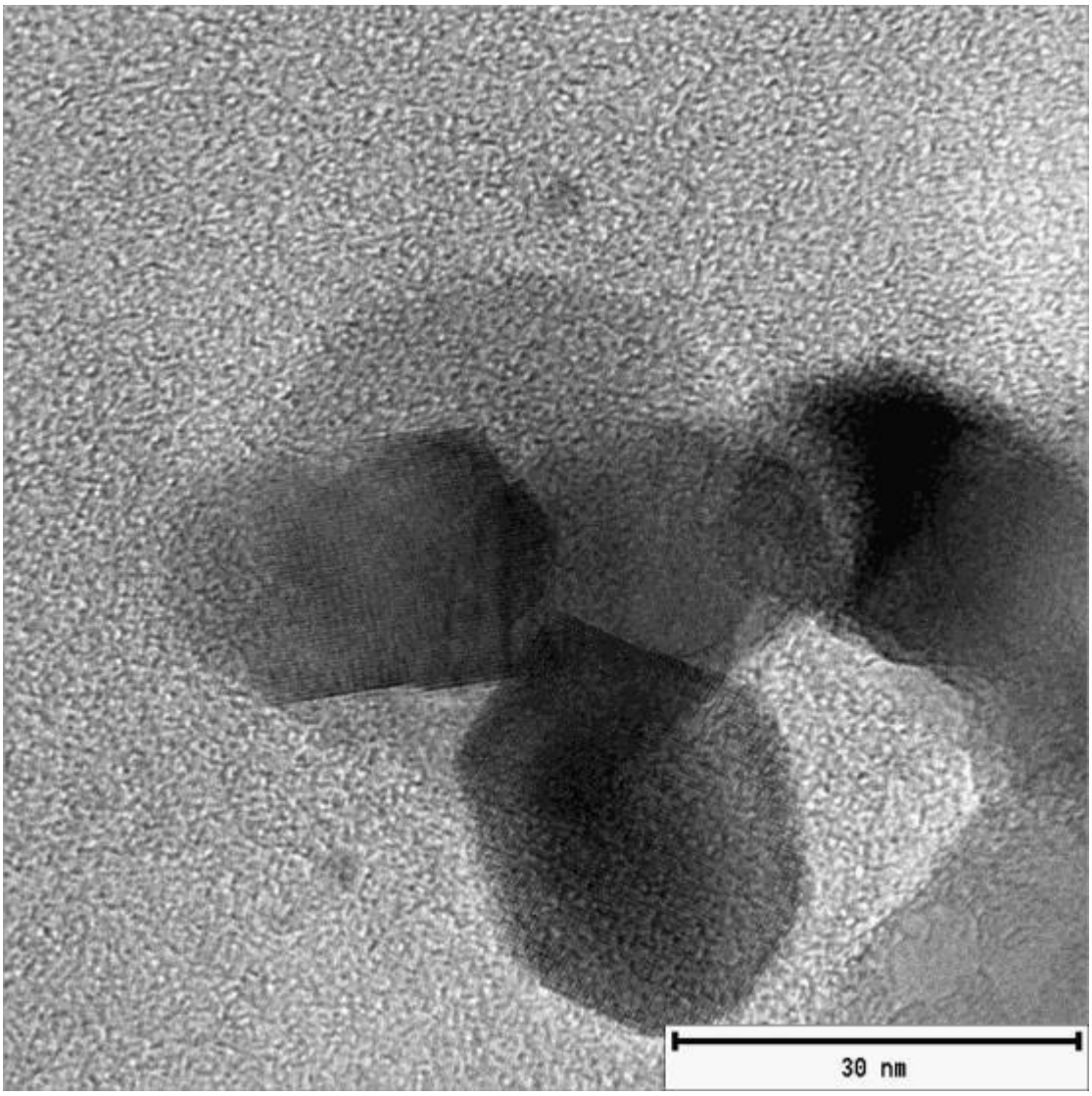

Figure 10.36: (PEG 10000 g/mol). Anatase crystals seemingly hexagonal in shape.

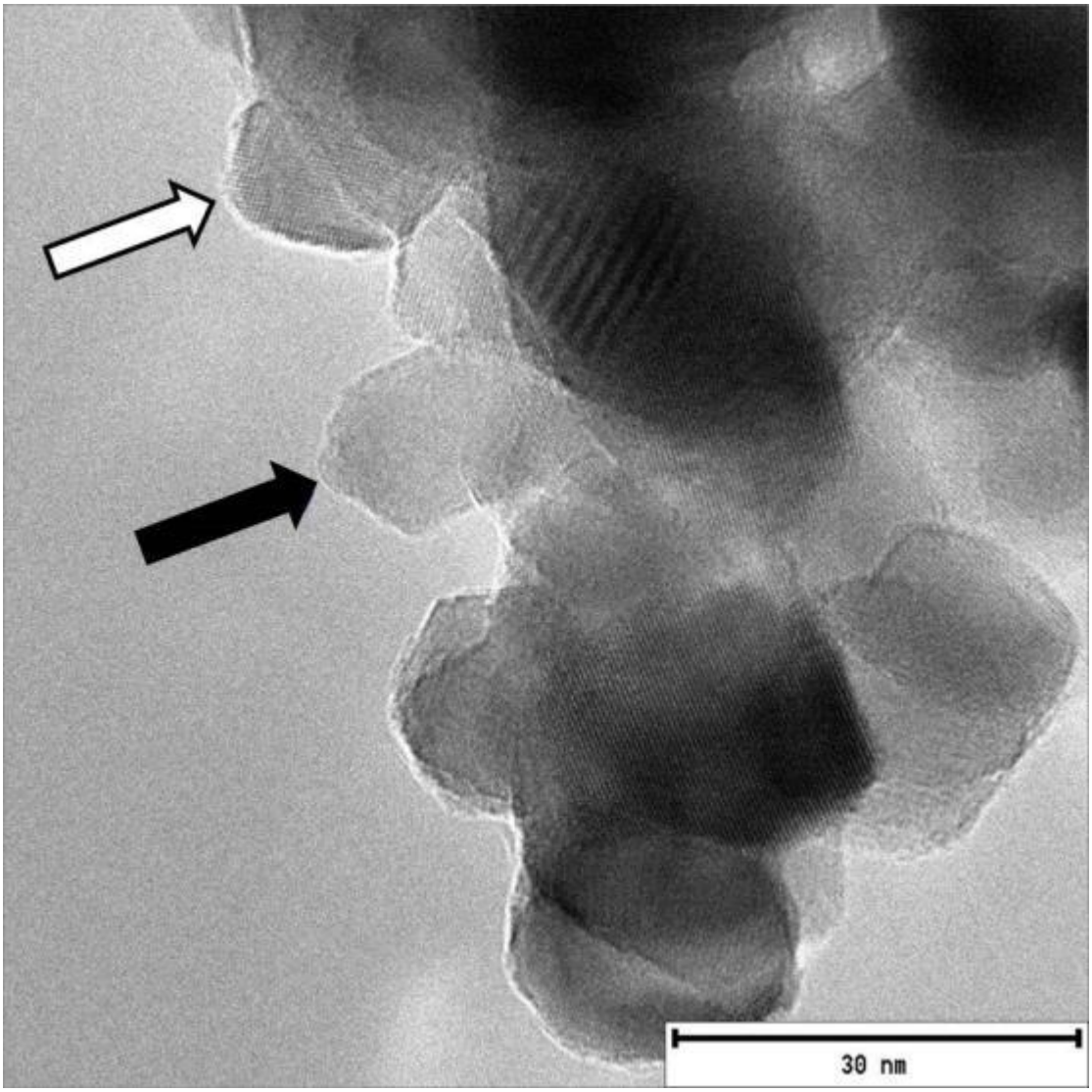

Figure 10.37: (PEG 20000 g/mol). The image reveals variation in crystal shape. The black arrow points to an anisotropic crystal with a tapered tip that is characteristic of rutile. This is in contrast to the square crystal with rounded edges pointed to by the white arrow. The shape of that crystal is characteristic of anatase.

10.2.5 Titanium (IV) bis (ammonium lactato) dihydroxide solution

Figure 10.38 contains the PXRD patterns generated for the samples synthesised using Ti-AmOH, post-calcination. The excellent signal to noise ratio implied the exclusive formation of highly crystalline anatase in all samples. Narrow peak widths denoted the presence of coarsened crystallites. This was an expected outcome of calcination. Given that all samples were calcined, peak misalignment is an interesting observation. Peak misalignment is indicative of an entity imparting non-uniform strain on the titania lattice[8]. That entity could be carbon (suggesting an inadequate calcination procedure) or it could be due to the presence of NH_4 species – with N atoms in the titania lattice.

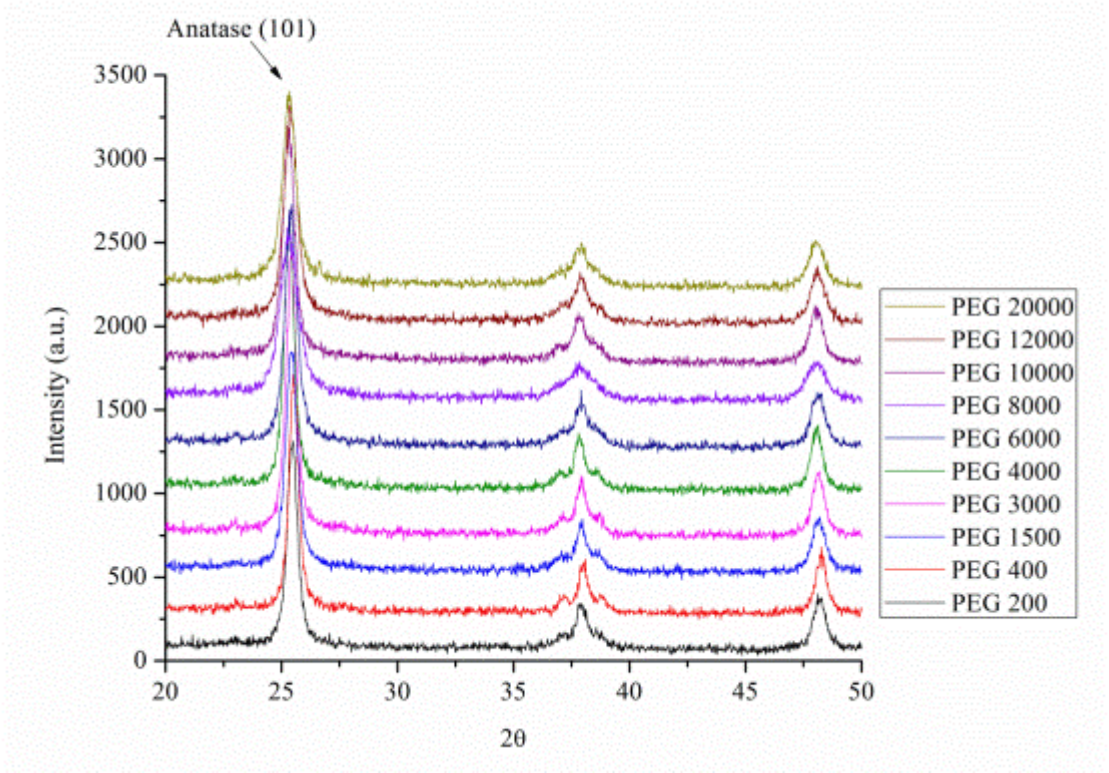

Figure 10.38: PXRD patterns of Ti-AmOH generated samples.

Figure 10.39 compares the amount of anatase formed with its respective crystallite size as a function of increasing PEG molecular weight, post-calcination. Since all samples produced 100.0% anatase, PEG molecular weight did not affect phase formation. Given that the greatest error in the data equalled 4.0%, the data reflects excellent precision. Error bars were generated as previously described.

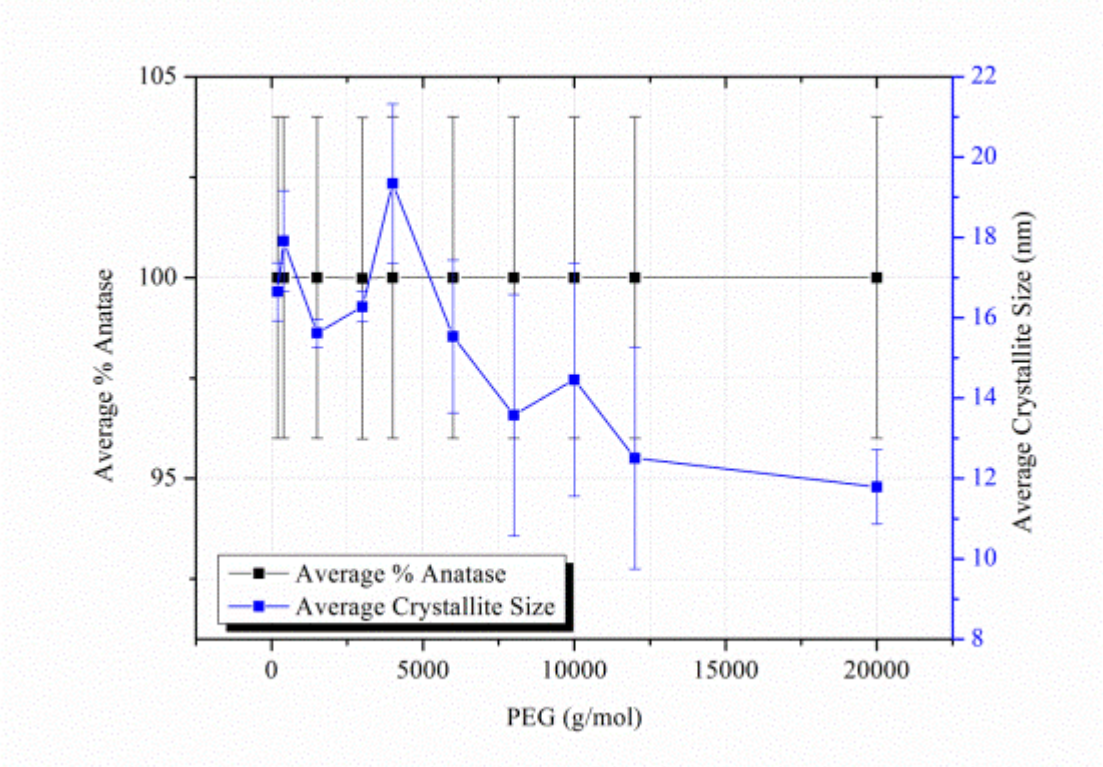

Figure 10.39: Average amount of anatase with associated crystallite size formed using Ti-AmOH.

The sample synthesised using PEG 4000 g/mol resulted in the formation of the largest anatase crystallites (19.3 nm). Smaller anatase crystallites were formed from samples synthesised using high molecular weight PEG (8000 – 20000 g/mol). The average anatase crystallite size formed across all samples measured 15.4 nm. This was 4.9% smaller than anatase crystallites formed using TiOxS, and 5.5% larger than anatase crystallites formed using Ti-isopro across all PEG molecular weights respectively. No other trends could be ascertained relating anatase crystallite size to PEG molecular weight. As such, there was no trend between the amount of anatase formed and its respective crystallite size. Error bars were generated as previously described.

Based on the developed precursor protection and PEG coordination mechanism in this study, the bias toward anatase formation using Ti-AmOH was expected. Ti-AmOH consists of Ti^{2-} coordinated to 2 hydroxyl species and 2 bidentate ligands. These ligands are each comprised of a 3 carbon chain and 3 oxygen sites for potential coordination to PEG chains. This combination allowed the nucleated anatase phase to be stabilised within the polymer reaction chambers. Polymer reaction chambers would have developed tightly around the nanocrystals on account of the many available

coordination sites on the precursor. This would have provided further protection and stabilisation of the anatase phase. This point is elaborated further.

Based on the results obtained from syntheses using Ti-isopro, Ti-EHOx, and Ti-AcAc, PEG chain length was expected to play a minor role in phase determination. As previously described, it is likely that short chain polymers were unable to completely wrap around the precursor. Additionally, long chain polymers likely formed larger chambers as described previously in this study. However, the results obtained in this study closely resemble those obtained when $TiCl_4$ was added to water containing citric acid (chapter 7). The formation of anatase independent of PEG chain length was likely due to the number of oxygen sites on the precursor that were able to coordinate to the PEG chains. Thus, by tightly coordinating to the precursor, the polymer chains were able to protect the nucleated phase, regardless of the formation of polymer reaction chambers of different sizes. The size of formed reaction chambers, governed by the PEG chain length employed in the synthesis, affected anatase crystallite size.

While expected, the results obtained using Ti-AmOH are interesting given that this is the first use of a hydrocarbon, oxygen and nitrogen containing precursor in this study. Other studies showed the exclusive formation of anatase using Ti-AmOH[9, 10, 11, 12]. No Ti_xN_y products were detected using PXRD or TEM in this study. EDS analysis performed by Lee *et al*., on TiO_2 synthesised by the hydrolysis and condensation of Ti-AmOH in the presence of PEI showed the exclusive formation of anatase[9]. The authors found no Ti_xN_y products, consistent with the findings in this study. Chemical mechanisms for exclusive anatase formation were not provided.

Möckel *et al*., synthesised phase pure anatase by thermohydrolysis of Ti-AmOH[11]. The researchers found the precursor to be stable in water at ambient temperatures[11]. Additionally, the authors proposed a mechanism of anatase formation based on OH^- substitution of the ligands attached to Ti^{2-}, the formation of oxo bridges, and surface blocking by solvent components. The formation of $Ti(OH)_x$ species in solution is implicit in this work for all precursors used. Since this study focused on the role of the polymer reaction chambers and steric protection effects related to the presence of precursor components, the mechanism developed by Möckel *et al*. will not be discussed further.

Tables showing the amount of each phase and crystallite size data obtained for each sample with averages and errors using Ti-AmOH are given in appendix H.

TEM images corresponding to the sample synthesised using PEG 12000 g/mol is provided in figures 10.40 – 10.42.

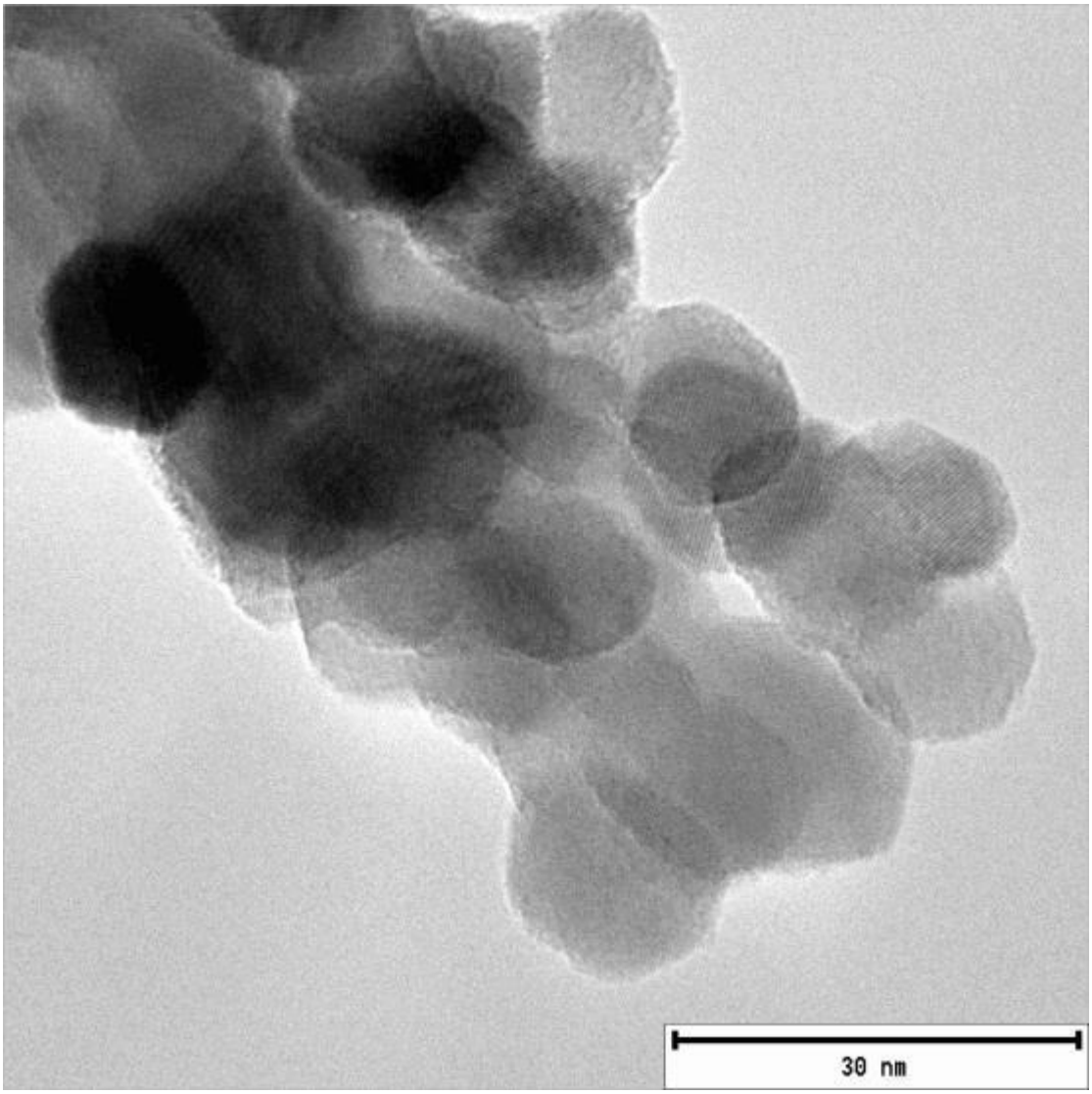

Figure 10.40: (PEG 12000 g/mol). Appearance of anatase crystals composed of various shapes including characteristic oblate habitus.

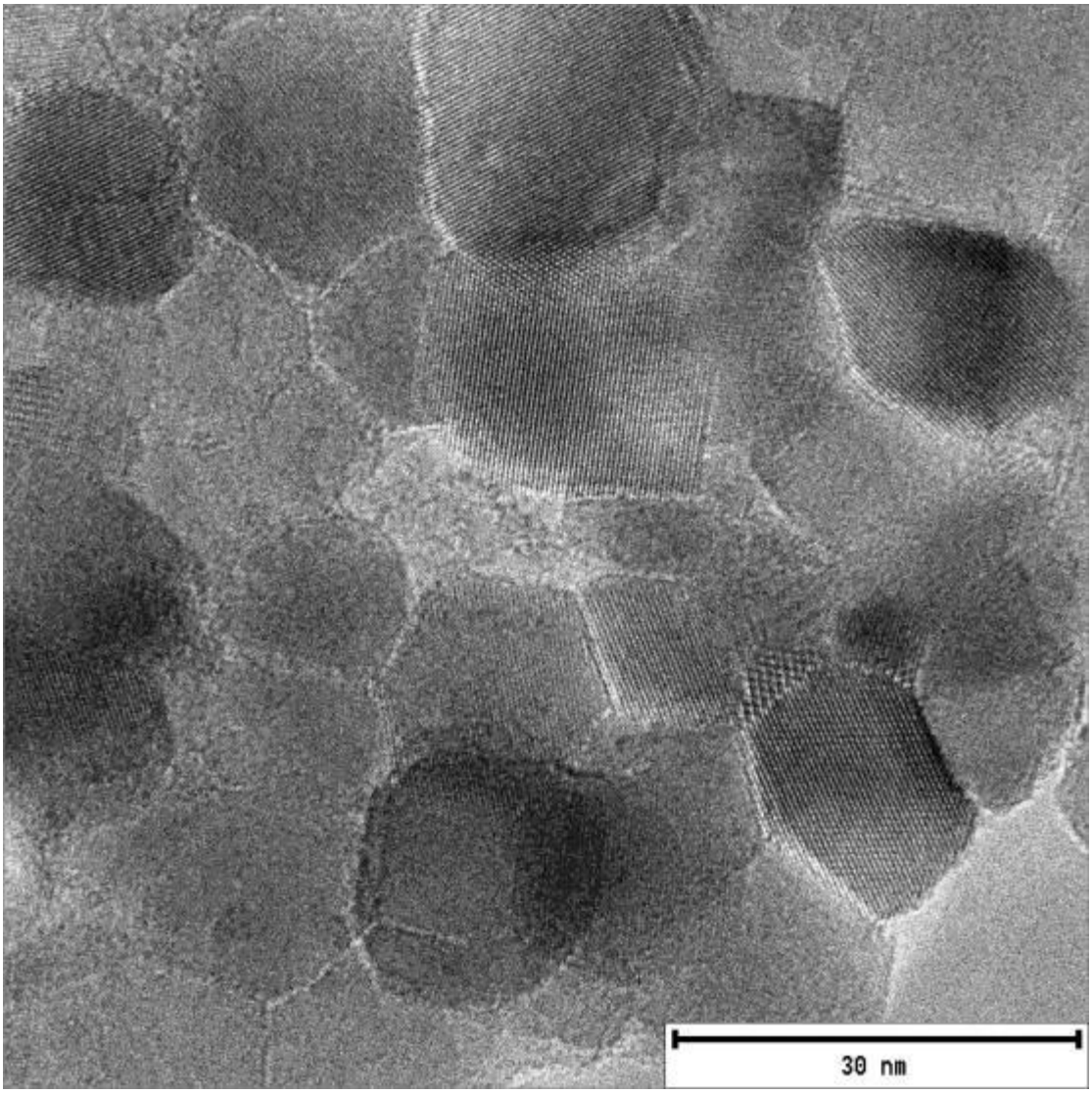

Figure 10.41: (PEG 12000 g/mol). Anatase crystals depicting various shapes were synthesised as evidenced in this TEM image. These crystals have well-defined edges and appear to pack together in a distinct manner. Unequal hexagonally shaped anatase crystals have been previously documented in this study.

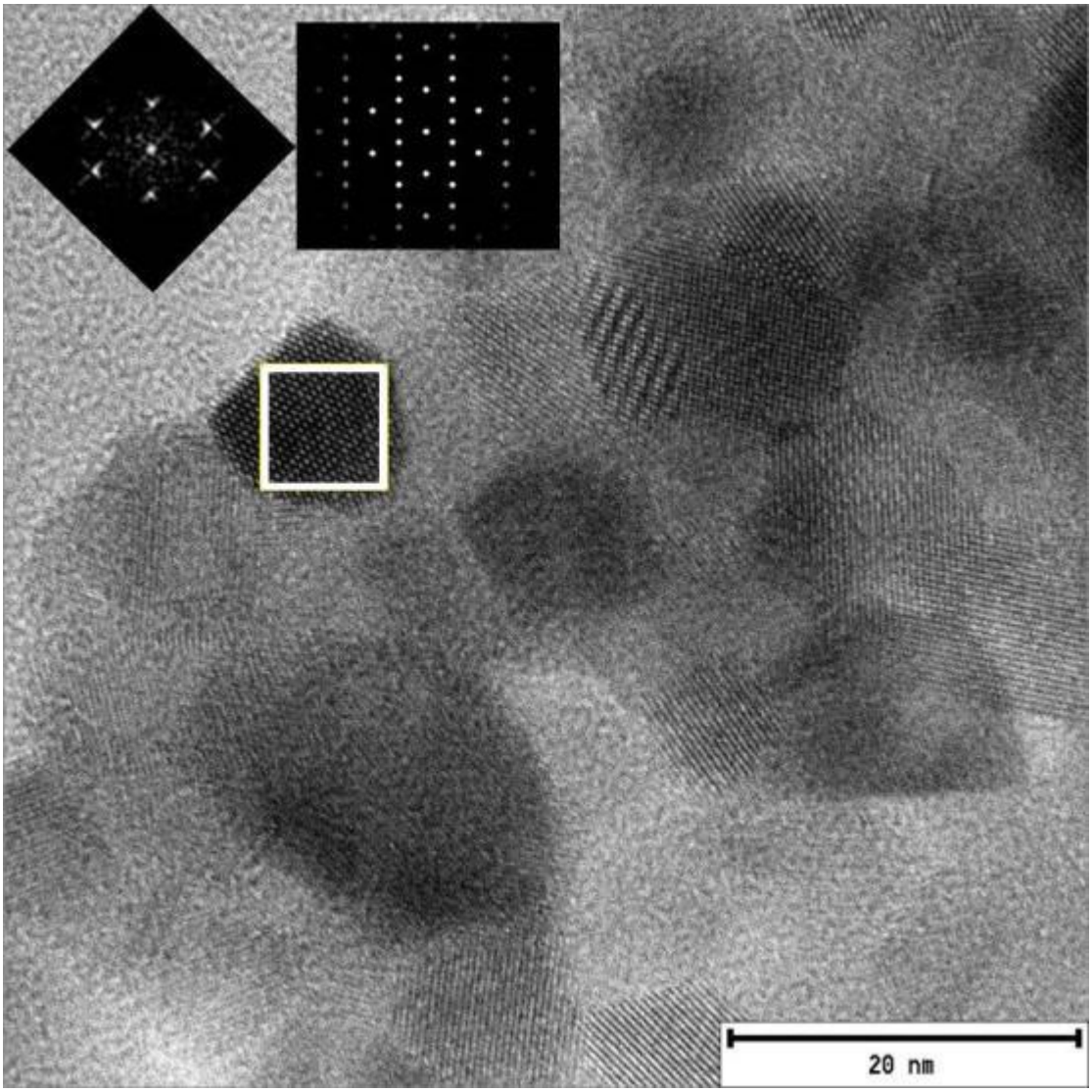

Figure 10.42: (PEG 12000 g/mol). This TEM image reveals the presence of anatase crystals comprising distinct and indistinct edges. The highlighted anatase crystal occurs along (0 1 0) and has distinct edges. The generated FFT was magnified for clarity. This was to compensate for the limited resolving power of the low resolution TEM.

10.2.6 Titanium (IV) (triethanolaminato) isopropoxide

Figure 10.43 contains the PXRD patterns for samples synthesised using Ti-EApro, post-calcination. All samples produced anatase as the major phase with rutile as the minor phase. Samples synthesised using PEG 400 g/mol and 6000 g/mol produced rutile (1 1 0) peaks with the greatest intensity. This suggests that the quantity of rutile formed did not directly correlate with the polymer molecular weight employed in the synthesis.

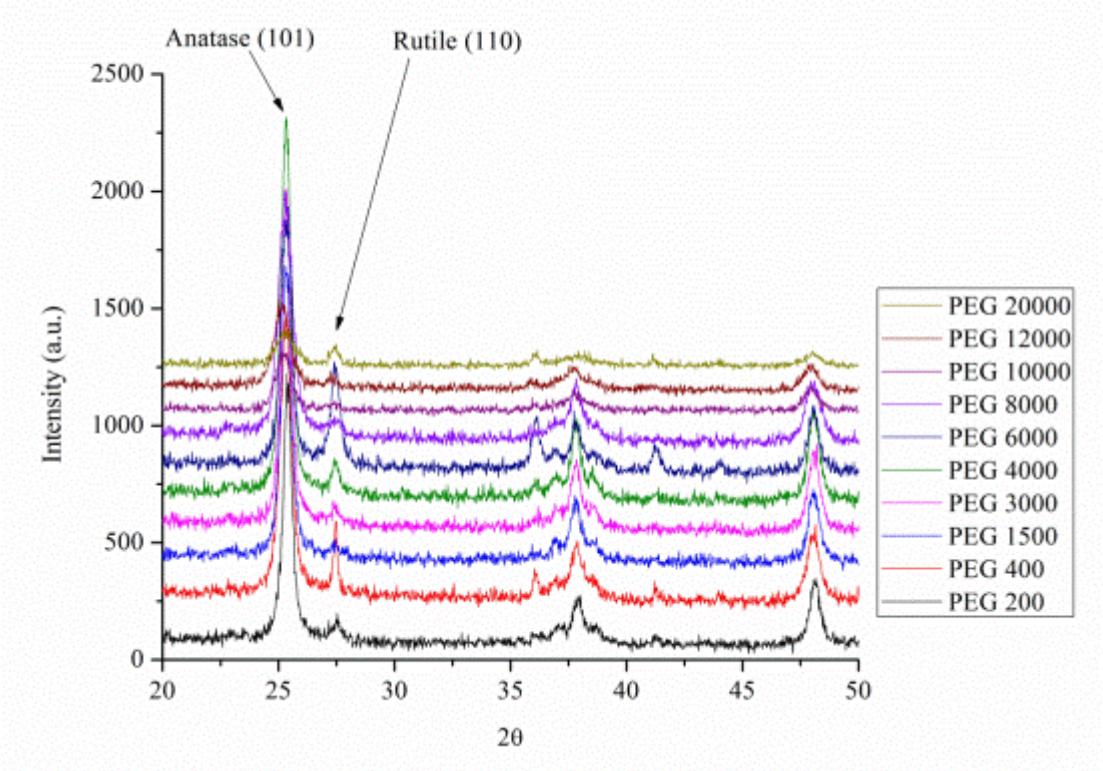

Figure 10.43: PXRD patterns of Ti-EApro generated samples.

Interestingly, the signal to noise ratio decreased as PEG molecular weight increased. Decreased signal to noise ratio is indicative of poor crystallinity. Poor crystallinity is induced by the presence of entities that reduce the probability of nucleation and growth. Good peak alignment was observed for all samples synthesised using PEG < 20000 g/mol suggesting the absence of entities that could have imparted non-uniform strain on the lattice. Given that all samples were calcined at 500 °C for 1 hour, and good peak alignment was observed in the PXRD patterns, a significant portion of decomposed polymer (in the form of carbon) was removed from the product. Therefore, the poor signal to noise ratio was not caused by the presence of carbon.

Ti-EApro is the only precursor employed in this study that contained a nitrogen atom within the primary precursor environment, albeit not directly bonded to Ti^{4+}. The covalent radius of a nitrogen atom (0.75 Å) is comparable to that of the covalent radius of an oxygen atom (0.73 Å). No Ti_xN_y products were evidenced in PXRD patterns and TEM images. Therefore, the presence of nitrogen atoms in close proximity to the PEG coordinated hydroxyl-Ti-EApro precursor likely served as an impurity that impeded anatase nucleation and growth. These effects were augmented as the PEG chain length increased.

As postulated throughout this study, longer chain polymers produced larger reaction chambers. Thus, the effects of nitrogen impeding anatase nucleation and growth were amplified within larger chambers. This can be explained by considering that larger chambers coordinated to a larger number of hydroxylated precursors, which increased the number of nitrogen atoms within the chambers accordingly. A larger quantity of nitrogen atoms present as the reaction progresses afforded a greater barrier to anatase nucleation, and hence reduced crystallinity. Smaller chambers coordinated to fewer hydroxylated precursors and hence the quantity of nitrogen atoms within the chambers was minimised. Since anatase nucleation was not as severely impeded, better crystallinity was obtained.

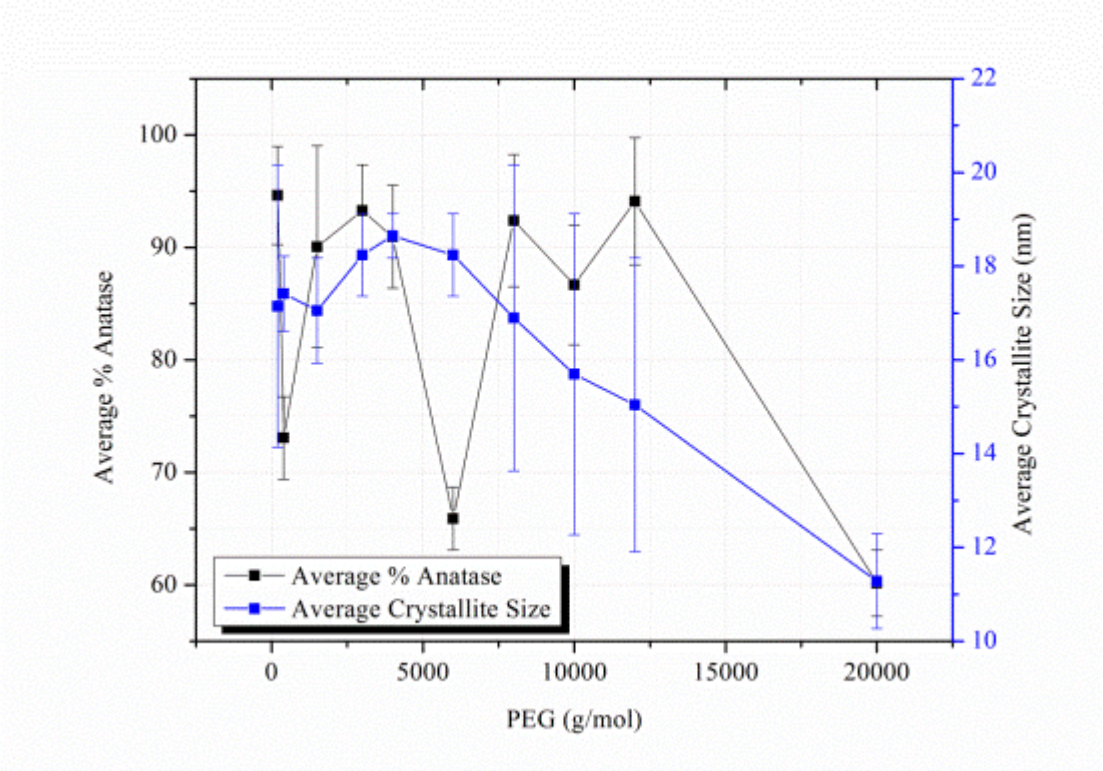

Figure 10.44: Average amount of anatase with associated crystallite size formed using Ti-EApro.

Figure 10.44 compares the amount of anatase formed with its respective crystallite size as a function of increasing PEG molecular weight, post-calcination. PEG 400, 6000, and 20000 g/mol produced the least amount of anatase. PEG 20000 g/mol in particular resulted in the formation of 60.2% anatase. Samples synthesised using all other PEG molecular weights produced > 85% anatase. The average amount of anatase formed across all samples equalled 84.1% suggesting that this system favoured anatase formation. Error bars were generated as previously described.

Anatase crystallite size displayed an interesting trend as a function of increasing PEG molecular weight. Low molecular weight PEG (200 – 1500 g/mol) produced anatase crystallites measuring ~ 17 nm. Intermediate PEG molecular weight (3000 – 6000 g/mol) produced anatase crystallites measuring ~ 18 nm. When high molecular weight PEG was employed in the synthesis (8000 – 20000 g/mol), anatase crystallite size decreased with increasing PEG molecular weight. The average anatase crystallite size obtained across all samples equalled 16.6 nm. No trend could be obtained relating the amount of anatase formed with its respective crystallite size. Error bars were generated as previously described.

The average amount of anatase formed across all PEG molecular weights using TiOxS (84.9%) is comparable to that obtained using Ti-EApro. Excluding the samples synthesised using PEG 400 and 6000 g/mol, figure 10.45 shows fairly good correlation between the amounts of anatase formed as a function of increasing PEG molecular weight between TiOxS and Ti-EApro. This correlation is stronger for samples synthesised using long chain PEG.

The average anatase crystallite size obtained across all samples using TiOxS (16.2 nm) is comparable to that obtained using Ti-EApro. Excluding samples synthesised using PEG 200, 3000, and 20000 g/mol, from figure 10.46 it can be seen that fairly good correlation exists between the sizes of anatase crystallites obtained using TiOxS and Ti-EApro.

The correlation in figures 10.45 and 10.46 suggests that the polymer had a significant influence in phase and crystallite size determination when precursors containing components other than hydrocarbons and oxygen were employed in the synthesis. It is likely that the amount and size of anatase formed per PEG chain length was governed by the size of polymer reaction chambers formed, as previously discussed.

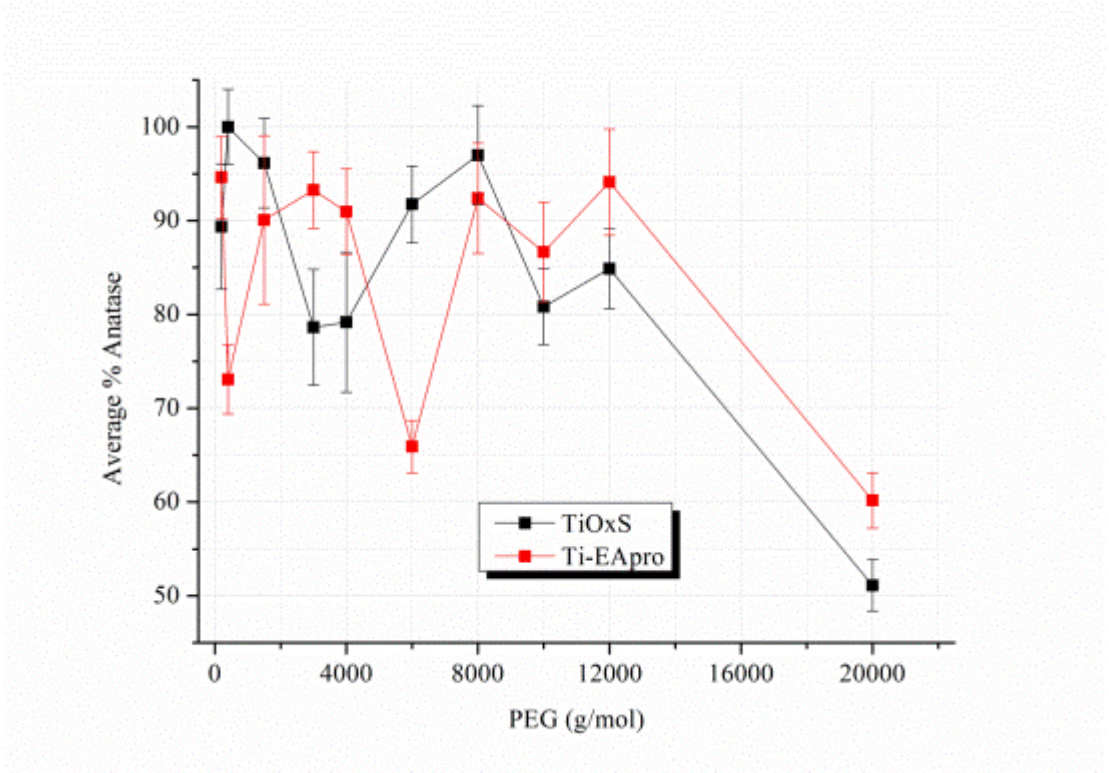

Figure 10.45: Post-calcination comparison of the average amount of anatase formed using TiOxS and Ti-EApro.

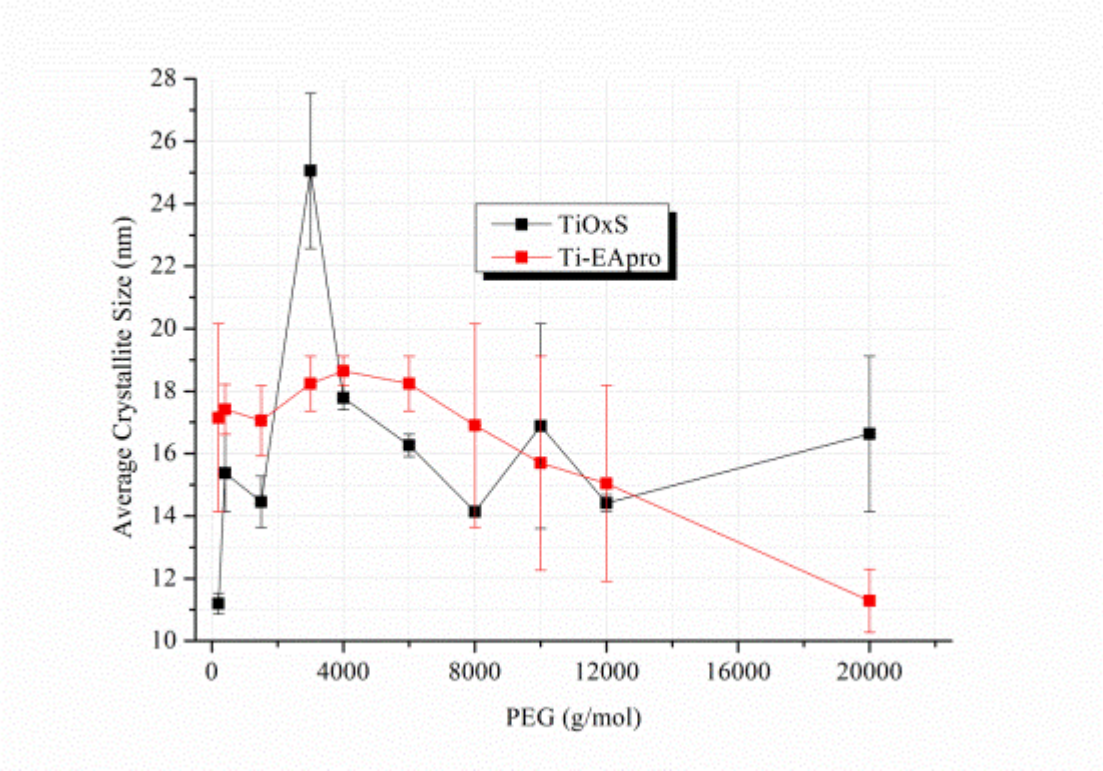

Figure 10.46: Post-calcination comparison of the average anatase crystallite size obtained using TiOxS and Ti-EApro.

It was shown that the tendency of a hydroxylated precursor to form anatase was governed by the size of protecting groups occurring within the reaction chambers and the number of sites available for coordination to PEG chains. Hydroxyl-Ti-EApro contained 4 carbon chains of 2 atoms each (including 1 branched chain containing 1 carbon atom) that likely imparted a degree of anatase protection within the reaction chambers. However, hydroxyl-Ti-EApro contained only 4 oxygen atoms that could potentially coordinate to PEG chains. Therefore, it is likely that polymer chains did not tightly coordinate to the hydroxylated precursor. Hence, protection effects afforded by PEG chains were limited. This had the effect of encouraging rutile transformation.

An additional consideration is the presence of a solitary nitrogen atom per hydroxyl-Ti-EApro precursor. As discussed above, the presence of this atom likely caused a hindrance to anatase nucleation. Any anatase that did nucleate was protected against coarsening by the presence of nitrogen. It is expected that the anatase growth hindrance effect afforded by nitrogen atoms were not as pronounced as those afforded by carbon chains. This is due to the ability of carbon chains to provide better steric

stabilisation to the growing crystals. PEG chains could potentially form hydrogen bonds with nitrogen atoms thereby enhancing their effects within the reaction chambers. A study of lanthanide containing PEG complexes by Rogers *et al*., revealed that the presence of various anions changed the mode of polymer wrapping[4]. This suggests that the presence of nitrogen atoms in system could have changed the manner by which reaction chambers formed around the hydroxylated precursor.

In conclusion, the results obtained using Ti-EApro can be explained by considering that anatase formed from the hydroxylated precursor benefited from a degree of protection afforded by the carbon chains and to a lesser degree, nitrogen atoms. Nitrogen atoms served to impede anatase nucleation and then growth of nucleated anatase crystallites. This contributed to the formation of anatase. The limited number of oxygen atoms contained in Ti-EApro reduced the propensity of PEG coordination to the hydroxylated precursor. Reduced coordination reduced the protection effects afforded by reaction chambers. This had the effect of encouraging rutile transformation. Thus, this system produced anatase as the major phase, with rutile as the minor phase. The formation of reaction chambers of various sizes caused the amount of anatase to vary per PEG chain length.

Tables showing the amount of each phase and crystallite size data obtained for each sample with averages and errors using Ti-EApro are given in appendix H.

TEM images corresponding to the samples synthesised using PEG 200 g/mol and 20000 g/mol are provided in figures 10.47 and 10.48 respectively.

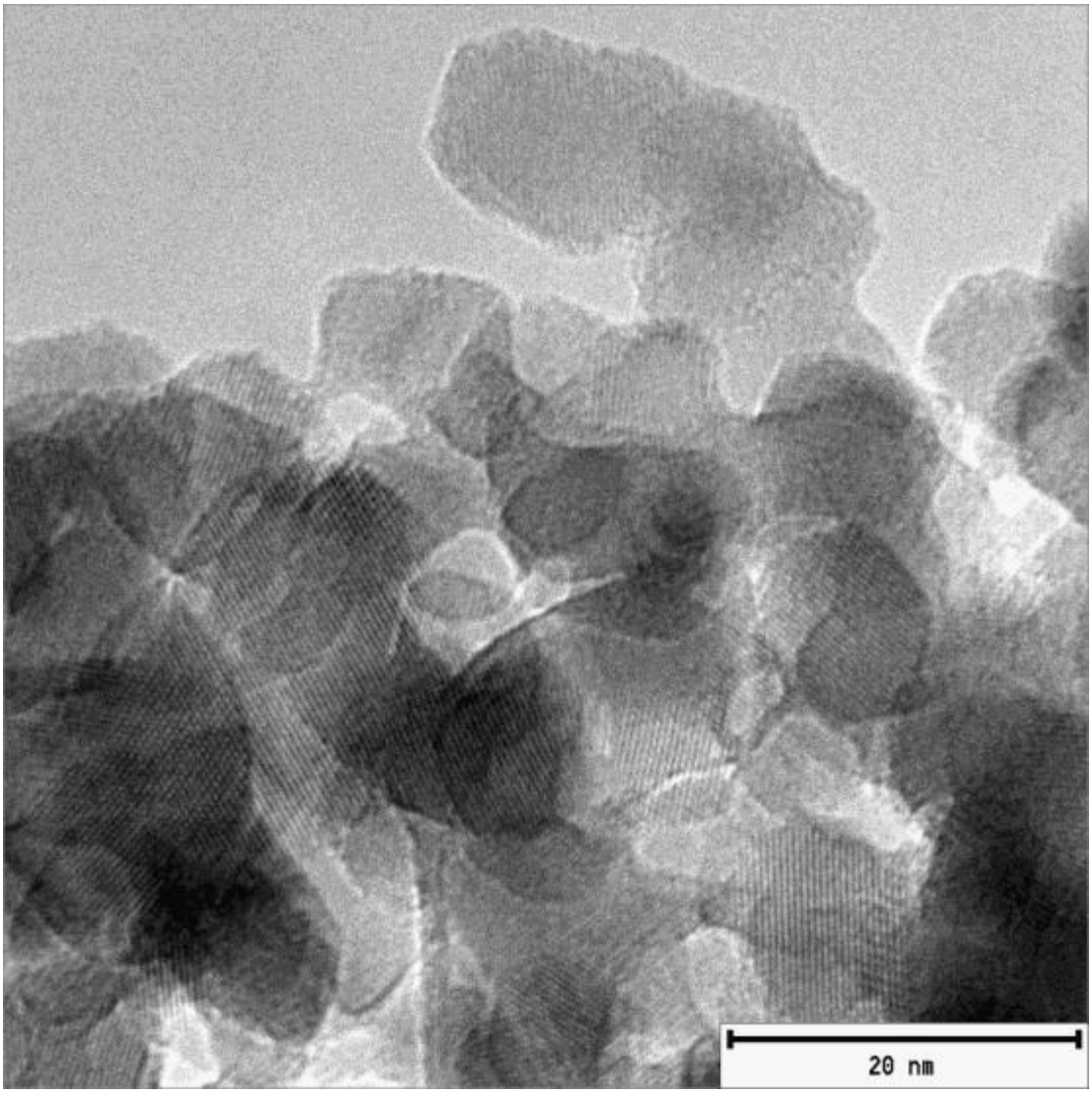

Figure 10.47: (PEG 200 g/mol). Anatase crystals with various sizes. This is consistent with previously observed anatase crystals.

Figure 10.48 is interesting as it likely contains a region of the sample that consisted of small anatase crystals and anisotropic rutile crystals (highlighted in white). The identity of the crystallites could not be confirmed through crystallographic techniques (SAED or FFT comparisons) as the sample was imaged using a low resolution TEM. The crystallites were identified by comparisons with previously obtained TEM images of anatase and rutile. No rutile mesocrystals were evidenced.

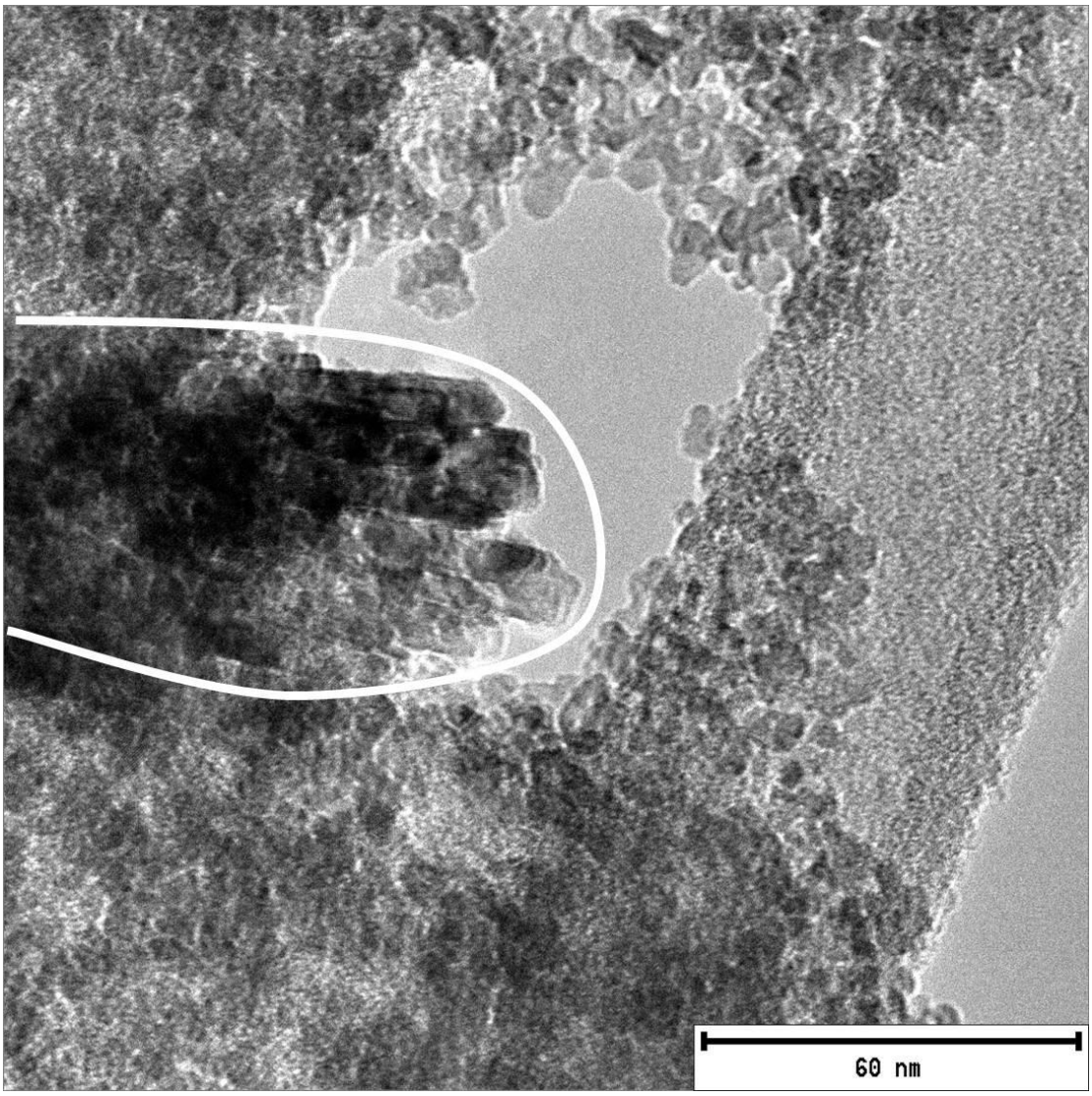

Figure 10.48: (PEG 20000 g/mol). A mixture of anatase and rutile crystallites (highlighted in white).

10.3 Conclusions

All precursors favoured the formation of anatase as the major or exclusive phase. The size and constituents of the precursors determined if PEG chain length would be a factor in controlling the amount of anatase formed. PEG chain length was a greater determinant of crystallite size than of the amount of anatase formed.

TiOxS was found to favour anatase formation but was dependent on PEG chain length. The results were rationalised by considering that sulphur species served as directing agents, favouring the anatase phase. However, they were not as adept as citrate ions at stabilising the anatase phase, leading to PEG chain length dependency. The introduction of $BaSO_4$ yielded results similar to that obtained using $TiCl_4$ in water containing HNO_3. This result confirmed that precursor ligands influence the formed phase.

Ti-EApro favoured anatase formation but with a dependence on PEG chain length. The generated products produced PXRD patterns that had poor signal to noise ratio as the polymer chain used in the synthesis increased. This was attributed to the presence of a large quantity of nitrogen atoms within large polymer reaction chambers that impeded anatase nucleation. Dependence on PEG chain length closely resembled that obtained using Ti-EHOx. Therefore, it was concluded that the small number of available oxygen sites for coordination to the polymer for a hydroxylated precursor of this size was responsible for encouraging rutile transformation dependent on PEG chain length. Additionally, the protection effects afforded by the presence of nitrogen atoms were not as robust as that achieved by carbon chains.

Ti-isopro produced nearly phase pure anatase for all PEG chain lengths. A comparison of the amount of anatase formed using Ti-isopro and $TiCl_4$ in water revealed striking similarities. The similarity in the data implied a similar mechanism of particle formation given the similarities in the hydroxylated structures. By this argument, it was concluded that the presence of small carbon chains within the polymer reaction chambers served to stabilise the anatase phase. The interplay between the number of oxygen coordinating sites available to PEG and the small size of the protecting carbon chains nullified the effects of polymer chambers of various sizes.

Ti-AcAc and Ti-AmOH produced near phase pure and phase pure anatase respectively for all PEG molecular weights despite these precursors consisting of ligands that were different to Ti-isopro. This result was rationalised by considering the number of oxygen sites available for coordination to PEG reaction chambers. A multiple coordinated hydroxylated-precursor increased the protection and stabilisation effects afforded by PEG reaction chambers. This combined with the presence of stabilising ligands served to promote the formation of anatase.

Ti-EHOx had the same number of oxygen sites available for coordination to PEG, however, the protecting carbon chains were longer than for Ti-isopro. Thus, this precursor favoured the formation of anatase but the dependence on PEG chain length was more significant than for T-isopro (PEG 20000 g/mol produced rutile as the major phase). It was concluded that short chain PEG chains do not fully wrap around the large hydroxylated precursor. Large reaction chambers struggled to coordinate to the hydroxylated precursor due to the size of the attached ligands. Therefore, reaction chamber protection and stabilisation was inhibited.

Based on the findings in this study, an added layer of complexity was added to the developing mechanism of particle formation using resin-gel synthesis: the tendency of a precursor to form anatase was dependent on the interplay between the number of sites available for coordination to PEG chains, and on the ability of precursor ligands to protect and stabilise the nucleated anatase phase. Hydroxylated precursors coordinate to PEG chains. The degree of coordination is dependent on the number of oxygen atoms contained in the precursor. If the hydroxylated precursor has sufficient sites for coordination to the polymer, then the formed polymer reaction chambers will stabilise the nucleated anatase phase. The second source of stabilisation occurs from the size of protecting ligands attached to the metal ion. If the ligands are small, they will not be able to effect significant steric stabilisation of the nucleated anatase phase. If they are too large, the hydroxylated precursor may not be sufficiently engulfed by the reaction chambers, reducing the polymer protection effects. If the protecting ligands are of a fair size and with sufficient oxygen sites available for coordination to the polymer, the nucleated anatase phase will benefit from protection afforded by the ligands and the polymer.

Direct comparisons between the various precursors employed in this study on the amount and size of anatase crystallites formed is concluded graphically in figures 10.49 and 10.50 respectively.

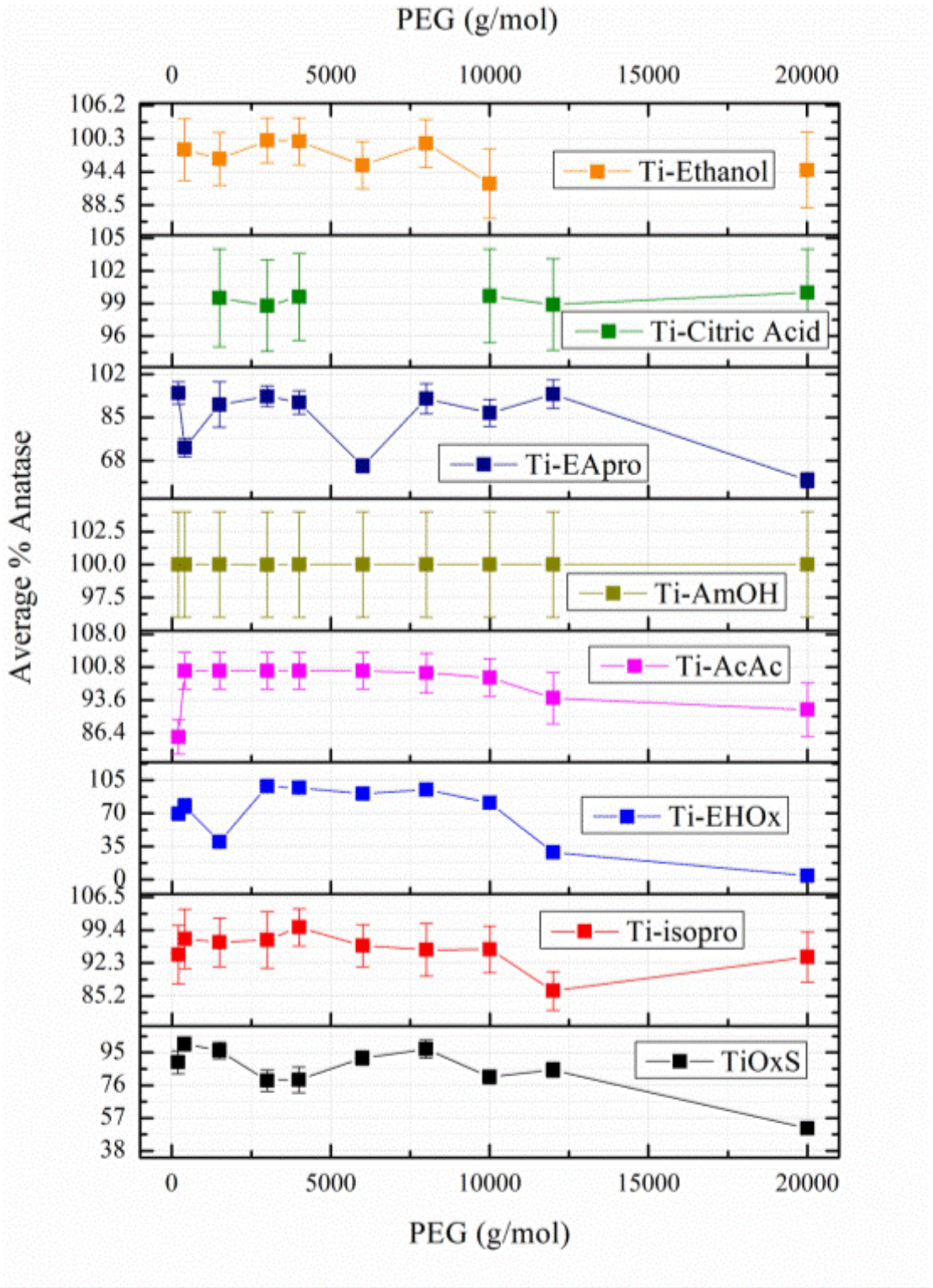

Figure 10.49: Effects of different Ti precursors on the mass percentage of anatase formed.

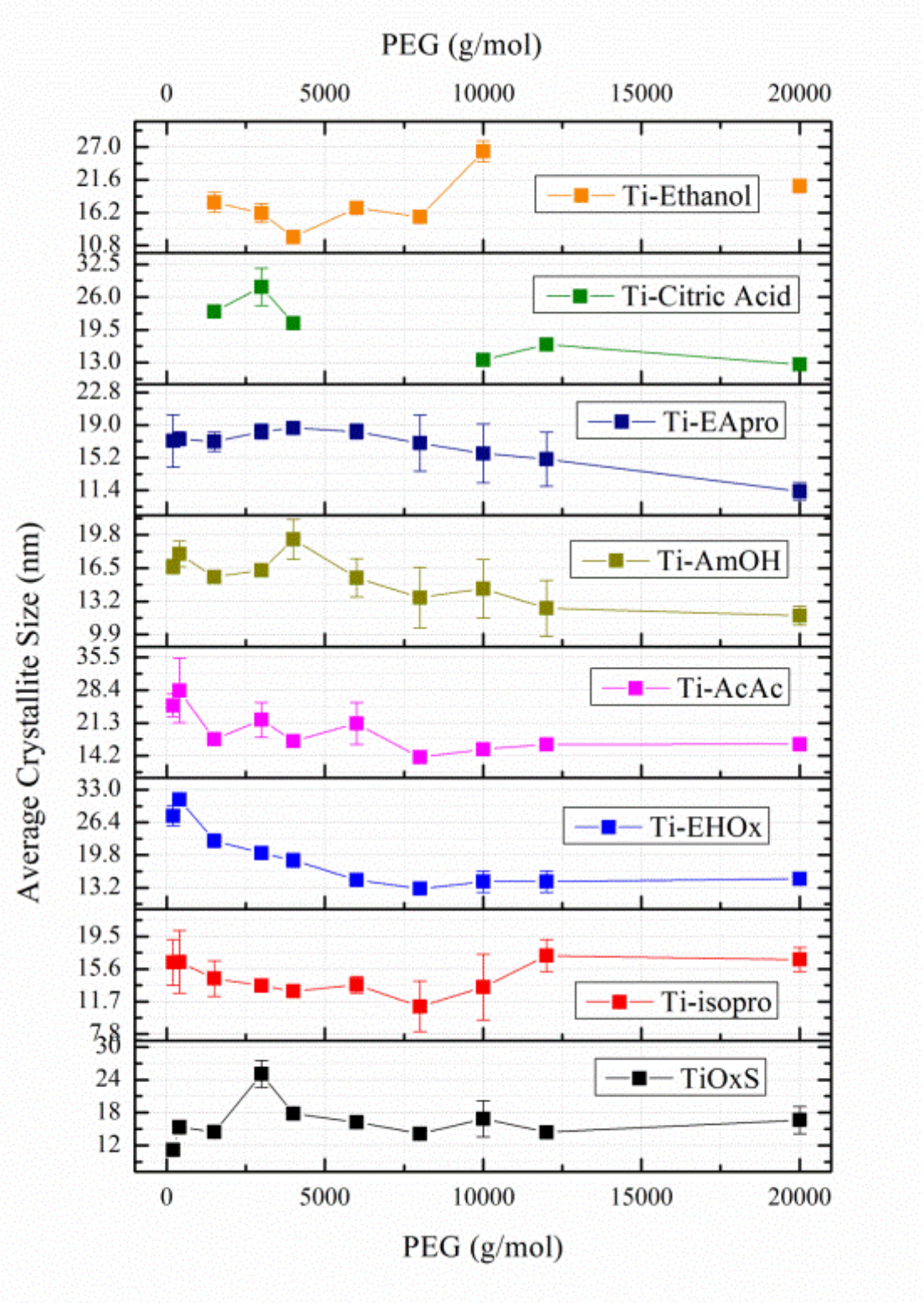

Figure 10.50: Effects of different Ti precursors on anatase crystallite size.

10.4 References

1. Ding, X. & Liu, X. Correlation between anatase-to-rutile transformation and grain growth in nanocrystalline titania powders. *Journal of Materials Research* **13,** 2556 – 2559 (1998).

2. Zhang, H. & Banfield, J. F. Thermodynamic analysis of phase stability of nanocrystalline titania. *Journal of Materials Chemistry* **8,** 2073 – 2076 (1998).

3. Dambournet, D., Belharouak, I. & Amine, K. Tailored Preparation Methods of TiO2 Anatase, Rutile, Brookite: Mechanism of Formation and Electrochemical Properties. *Chemistry of Materials* **22,** 1173 – 1179 (2010).

4. Rogers, R. D., Zhang, J. & Bauer, C. B. The effects of choice of anion (X=Cl-, SCN-, NO-) and polyethylene glycol (PEG) chain length on the local and supramolecular structures of LnX, /PEG complexes. *Journal of Alloys and Compounds* **249,** 41 – 48 (1997).

5. Table of Periodic Properties of the Elements. (1993).

6. Tartaj, P. Sub-100 nm TiO2 mesocrystalline assemblies with mesopores: preparation, characterization, enzyme immobilization and photocatalytic propertieswz. *Chemical Communications* **47,** 256 – 258 (2011).

7. Kakiuchi, K., Hosono, E., Imai, H., Kimura, T. & Fujihara, S. {1 1 1}-faceting of low-temperature processed rutile TiO2 rods. *Journal of Crystal Growth* **293,** 541 – 545 (2006).

8. Dinnebier, R. E. & Billinge, S. J. L. Principles of Powder Diffraction. in *Powder Diffraction: Theory and Practice* (eds. Dinnebier, R. E. & Billinge, S. J. L.) 1 – 19 (The Royal Society of Chemistry, 2008).

9. Lee, S., Drwiega, J., Wu, C.-Y., Mazyck, D. & Sigmund, W. M. Anatase TiO2 Nanoparticle Coating on Barium Ferrite Using Titanium Bis-Ammonium Lactato Dihydroxide and Its Use as a Magnetic Photocatalyst. *Chemistry of Materials* **16,** 1160 – 1164 (2004).

10. Hao, Y., Rui, Y., Li, Y., Zhang, Q. & Wang, H. Size-tunable TiO2 nanocrystals from titanium (IV) bis (ammonium lactato) dihydroxide and towards enhance the performance of dye-sensitized solar cells. *Electrochimica Acta* **117,** 268 – 275 (2014).

11. Möckel, H., Giersig, M. & Willig, F. Formation of uniform size anatase nanocrystals from bis(ammonium lactato)titanium dihydroxide by thermohydrolysis. *Journal of Materials Chemistry* **9,** 3051 – 3056 (1999).

12. Lee, S. & Sigmund, W. M. Formation of anatase TiO2 nanoparticles on carbon nanotubes. *Chemical Communications* **6,** 780 – 781 (2003).

Chapter 11: Attempts at Directly Observing Titanium Dioxide Formation Using Controlled Temporal Intermittent Resin-gel Synthesis

The final attempts at probing the mechanism of resin-gel synthesis involved endeavours at directly observing nanoparticle formation. Ideally, direct observation would be achieved via a combination of techniques such as VT-XRD, and *in situ* HRTEM equipped with a hot stage. The methods used and results obtained in this study were crude and qualitative in nature, but provided key insights into confirming the method of nano-titania formation using resin-gel synthesis.

11.1 Experimental Procedure

11.1.1 Liquid N_2 induced quenching

6.0 ml $TiCl_4$ was introduced into excess distilled water (144 ml) containing 55% HNO_3 (12.0 ml). After stirring until homogeneous, a stoichiometric amount of PEG 200 g/mol (5.4593 g) was added to the beaker containing the metal ion solution such that the ratio of Ti^{4+} : PEG = 1 : 0.5. After solvent removal via evaporation, the hardened resins were divided into 3 portions. Two of these portions were introduced into separate crucibles. Samples were heated using the conventional heating method (described in chapter 5). Once visible colour changes were observed (off-white to dark brown and dark brown to black) the contents of the crucible was decanted into vessels containing sufficient liquid N_2 to quench the reaction. No heat treatments were applied to the third portion. The experiment was completed in duplicate.

XRD data was generated using a Bruker D2 Phaser diffractometer. The setup of this instrument was described in chapter 5. Samples were analysed using between 20° and 50° 2θ in 0.04 increments counting for 1 second per step. TEM imaging was achieved using a JEOL 3011.

11.1.2 Aluminium rod generated molten drops

All samples were prepared by adding an amount of $TiCl_4$ to distilled water containing 55% HNO_3 and homogenised. For each sample, the volumes of distilled water and HNO_3 used were 24 times and 2 times the volume of $TiCl_4$ used respectively. PEG of various molecular weights was added to each solution in a (Ti^{4+} : PEG = 1 : 1)

stoichiometric manner and homogenised. The amount of $TiCl_4$ and PEG used for each sample is given in table 11.1. Following solvent removal via evaporation, the hardened resins were divided equally to introduce a replicate. Each of these portions were introduced into separate crucibles and heated in accordance with the conventional heating method (chapter 5). A flat aluminium rod was dipped into the resin-gels, at various points during heating (after 1 hour, 3.5 hours, and when the resin-gels were ignited). The molten drop remaining on the aluminium rod was carefully transferred onto holey carbon TEM grids. Paper towel was used to clear excess sample remaining on the TEM grids.

Table 11.1: $TiCl_4$ and PEG added to achieve a (1 : 1) stoichiometry.

$TiCl_4$		PEG Mn	PEG	
ml	**mols**	**g/mol**	**mols**	**g**
1.0	0.0091	3000	0.0091	27.2968
1.0	0.0091	4000	0.0091	36.3958
0.5	0.0045	6000	0.0045	27.2968
0.25	0.0023	10000	0.0023	22.7474
0.25	0.0023	12000	0.0023	27.2968

By visual observation, the viscosity of the drops obtained later in the reaction was lower than the viscosity of the drops obtained earlier in the reaction. Given that a new aluminium rod was used for each sampling point, it was unlikely that the metal caused any contamination. Additionally, since the metal rod was at room temperature before being inserted into the resin-gel, it was expected that the realisation of a lower thermal equilibrium would result in the slowing down of the reaction progression. Figure 11.1 shows the appearance of collected samples. In this experiment, samples were collected after a specific time period. This differed to sampling in the liquid N_2 induced quenching experiment that occurred as a result of sample colour changes.

Due to the small quantity of samples obtained using this method, XRD analysis was not possible. TEM analysis was conducted using an FEI Tecnai T12.

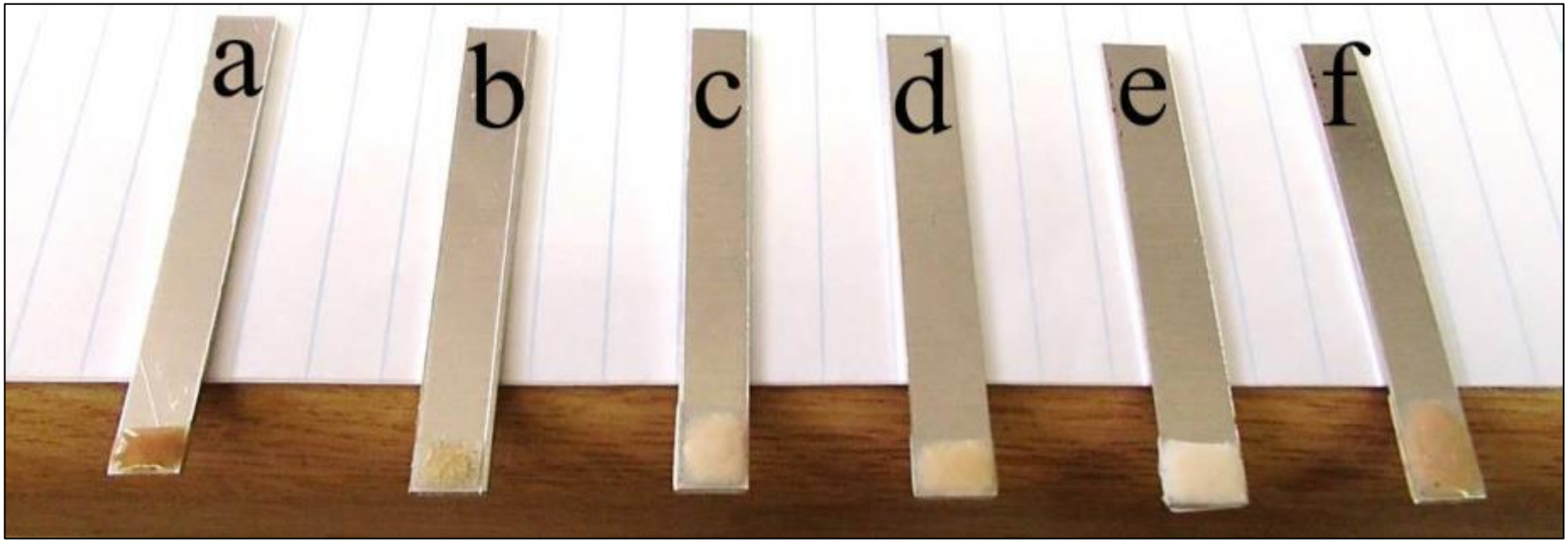

Figure 11.1: Appearance of specimens collected on aluminium sheets prior to being transferred to holey carbon TEM grids. Samples were synthesised using PEG (a) 3000 g/mol, (b) 4000 g/mol, (c) 6000 g/mol, (d) 8000 g/mol, (e) 10000 g/mol, and (f) 12000 g/mol.

11.2 Results and Discussion

11.2.1 Liquid N_2 induced quenching

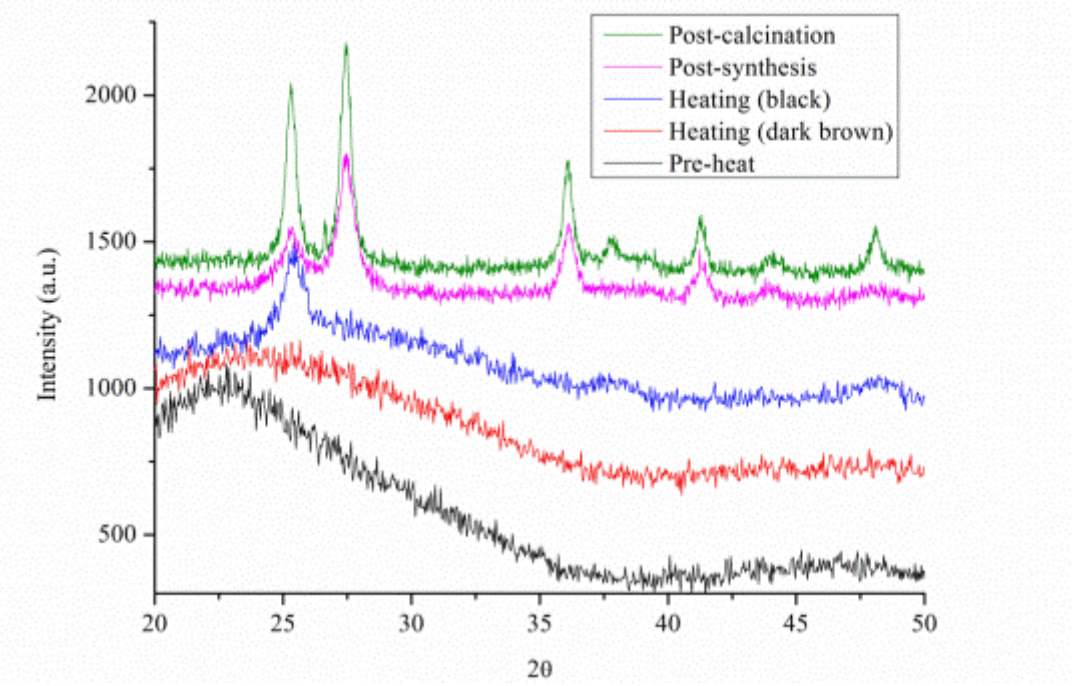

Figure 11.2: PXRD patterns showing the evolution of an anatase peak as the reaction proceeded.

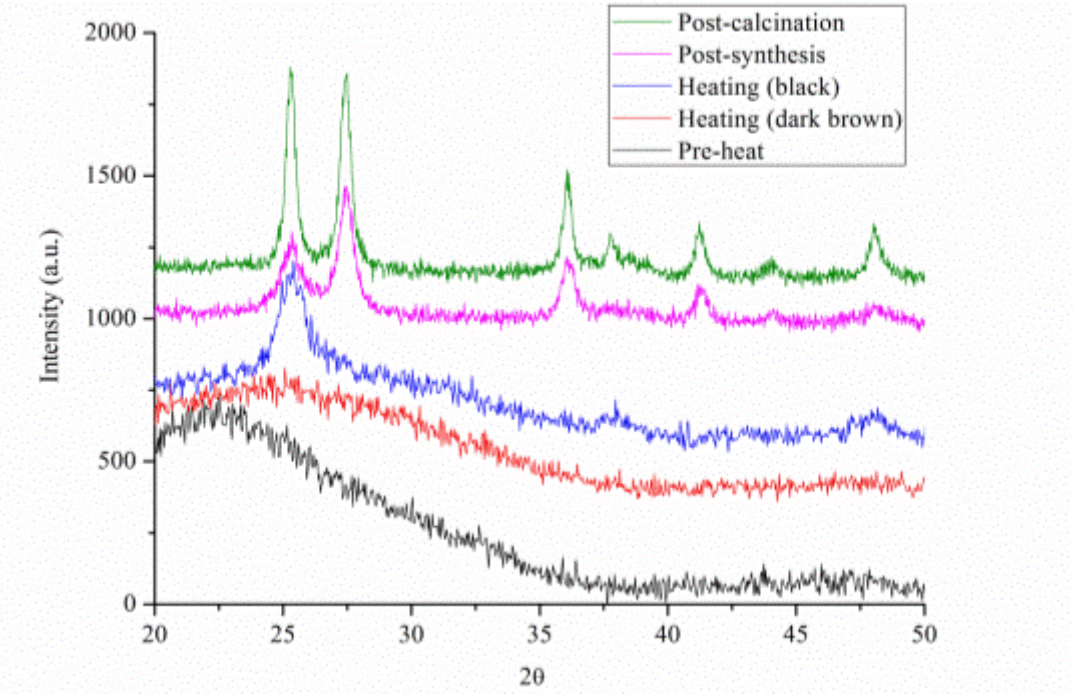

Figure 11.3: PXRD patterns of replicate samples showing the evolution of an anatase peak as the reaction proceeded.

Figure 11.2 shows the evolution of an anatase (1 0 1) peak as the reaction progressed toward completion. Following solvent evaporation, samples synthesised using PEG 200 g/mol appeared to be crystalline in nature. Single crystal XRD revealed these apparent crystals to be amorphous. This result was confirmed using PXRD given that the sample analysed pre-heat treatment did not exhibit any peaks. The pattern generated from the sample when it turned dark brown is different to that obtained from the sample before heating. Despite this change, no discernible peaks are observed. The pattern generated from the sample when it turned black shows the presence of an anatase (1 0 1) peak with poor signal to noise ratio. Strong peaks were not expected given that the reaction had not run to completion. Additionally, the sample was not calcined.

Incomplete syntheses likely produced samples containing a significant portion of amorphous material. Since amorphous material is not accounted for by the Spurr and Myers equation, caution should be taken when attempting to quantify the presence of anatase in the sample[1]. For this reason, the quantity of anatase in the sample was not ascertained.

For the incompletely synthesised sample (heating (black)), given no observable rutile peak, it may be assumed that the system produced amorphous material and some of that material transformed into anatase. This inference is strengthened by considering the change in the quantity of anatase formed from samples post-synthesis and post-calcination (data obtained from chapter 8). Rutile appears to be the favoured phase post-synthesis, with the amount of anatase increasing post-calcination. Since all transformations to rutile are irreversible[2], the result can be explained as follows: during heating and ignition, amorphous material was transformed into anatase. This nucleated anatase transformed into rutile simultaneously as more amorphous material was transformed into anatase. The data suggests that during synthesis, the transformation of amorphous material into anatase was dominated by the transformation of anatase to rutile. Therefore, by the end of the synthesis, the sample consisted of rutile as the major phase. It is possible that calcination caused some anatase to transform into rutile; calcination favoured the transformation of amorphous material into anatase.

The variation in transformation between synthesis and calcination may be explained using oriented attachment. Oriented attachment occurred during synthesis as the

system exhibited greater molecular mobility[3]. This had the effect of encouraging anatase to rutile transformation. However, the lack of mobility and low temperature during calcination was insufficient to cause significant anatase to rutile transformation. Calcination was sufficient to cause amorphous material to transform into anatase as this transformation required less energy and did not necessarily call for high system mobility[4].

Comparing the original data set to its replicate (figure 11.3) suggests that the experiment exhibited good reproducibility. This is a remarkable finding given the chaotic nature of the burning process and is an important consideration for the use of this technique in any synthesis system.

TEM images corresponding to samples collected before and during heating follow. Associated figures are given below:

- before heating: figures 11.4 and 11.5
- during heating (dark brown): figures 11.6 – 11.10
- during heating (black): figures 11.11 – 11.13

It was not possible to obtain 2D lattice fringe data from the darker regions of the image given in figure 11.4. Hence the crystallographic identity of these regions remains unknown.

The formation of nanoparticles before heating and ignition is not impossible, given that $TiCl_4$ forms $Ti(OH)_4$. These hydroxylated species can then form TiO_2 through the action of condensation. The efficacy of heating and ignition of the polymer mixture in resin-gel synthesis is exemplified in figure 11.5 by the lack of marked lattice fringe data.

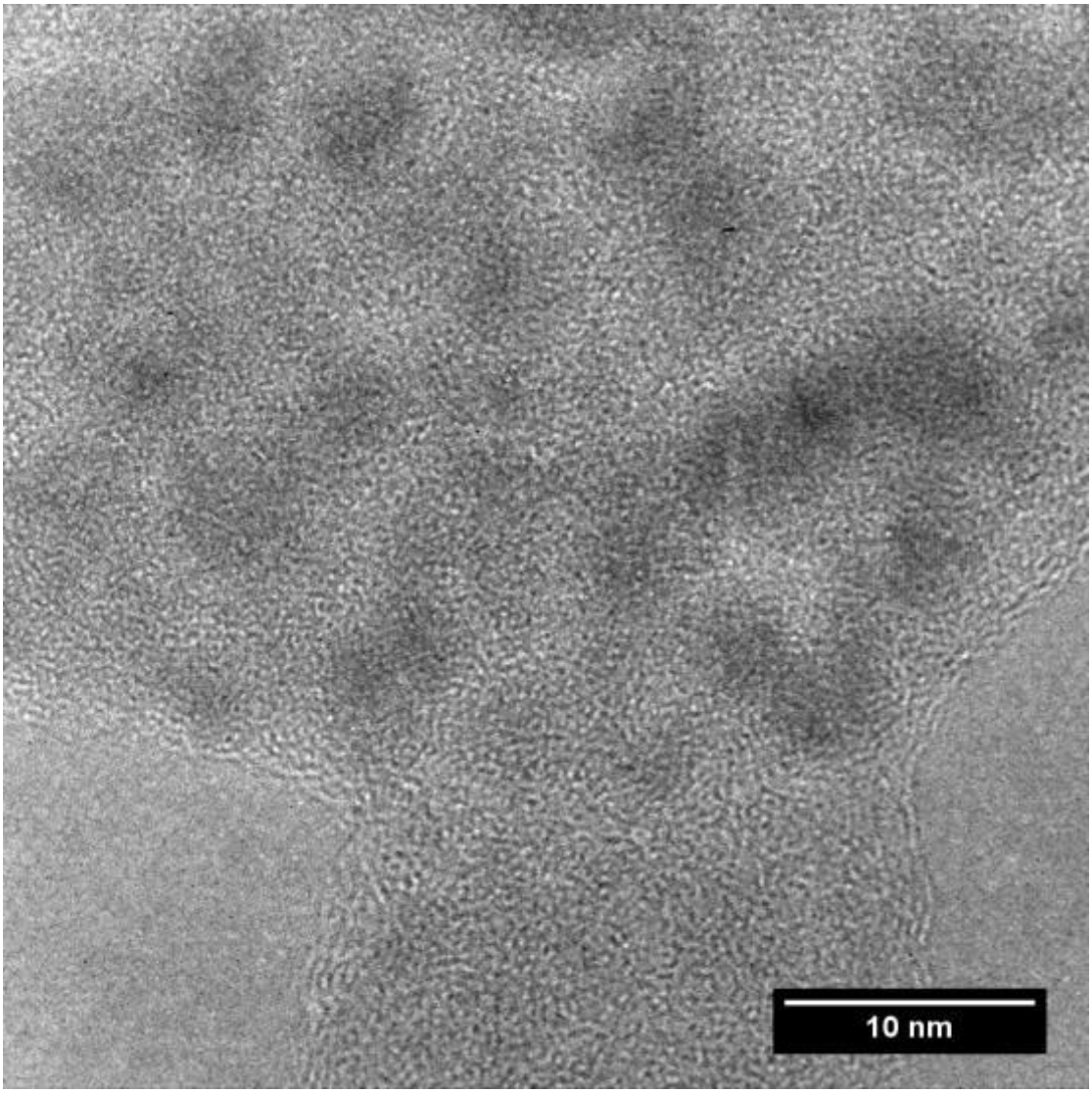

Figure 11.4: (before heating). This image was generated from the sample after solvent evaporation and before heating. The darker regions within this image represent crystallite ordering.

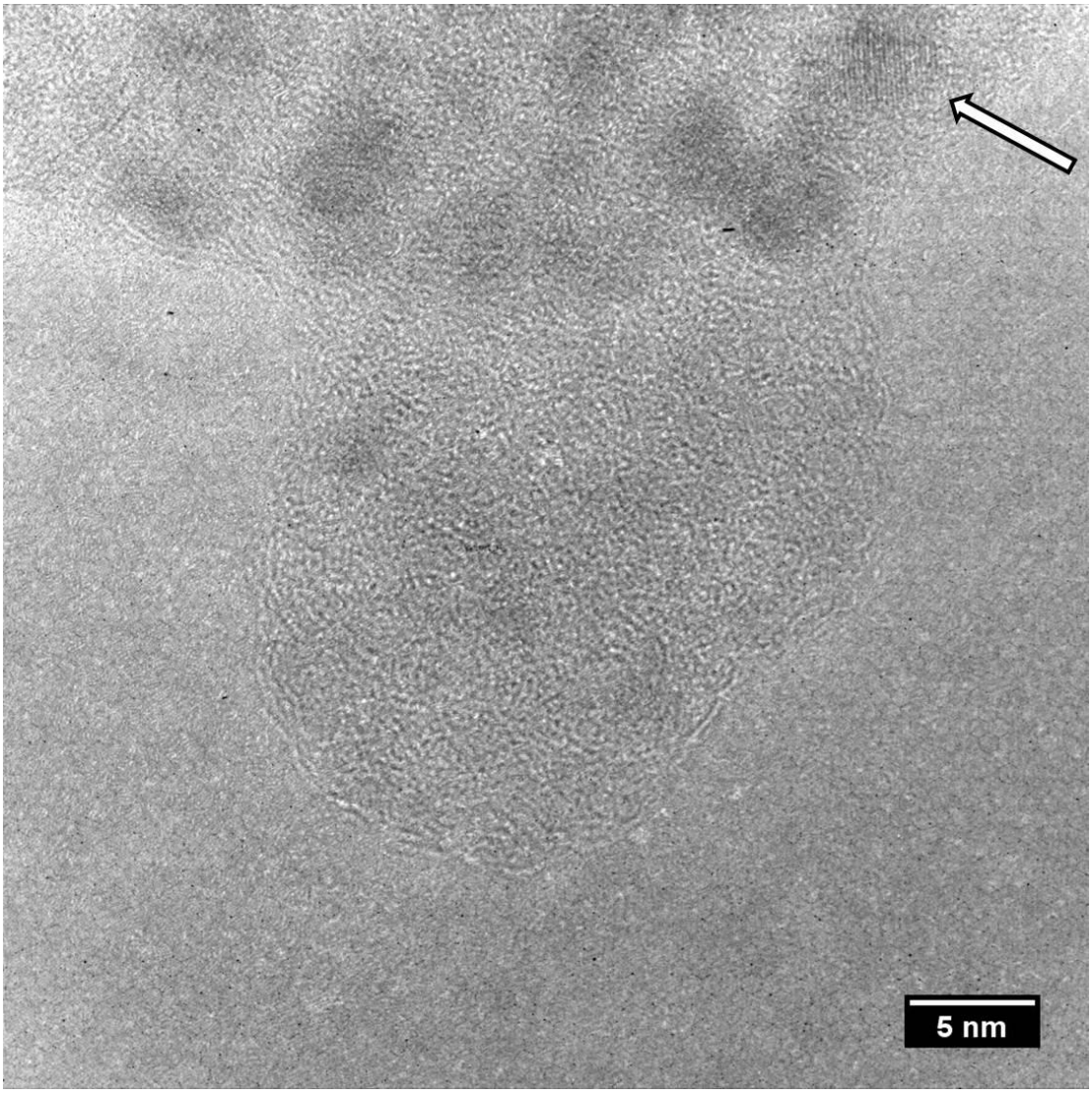

Figure 11.5: (before heating). By adjusting focus to minimum contrast focus, the above region of the sample revealed the presence of faint 1D lattice fringes (highlighted by the arrow).

From figure 11.6, the formation of PEG sheets is not unexpected[5]. These sheets typically have a thickness of 10 nm. From this image no precursor complexes associated with the polymer were observed. It should be noted that the low magnification performance of this instrument was sub-optimum given that it was optimised for high magnification work. Thus, the apparent absence of nanoparticles should not be concluded as a definite absence.

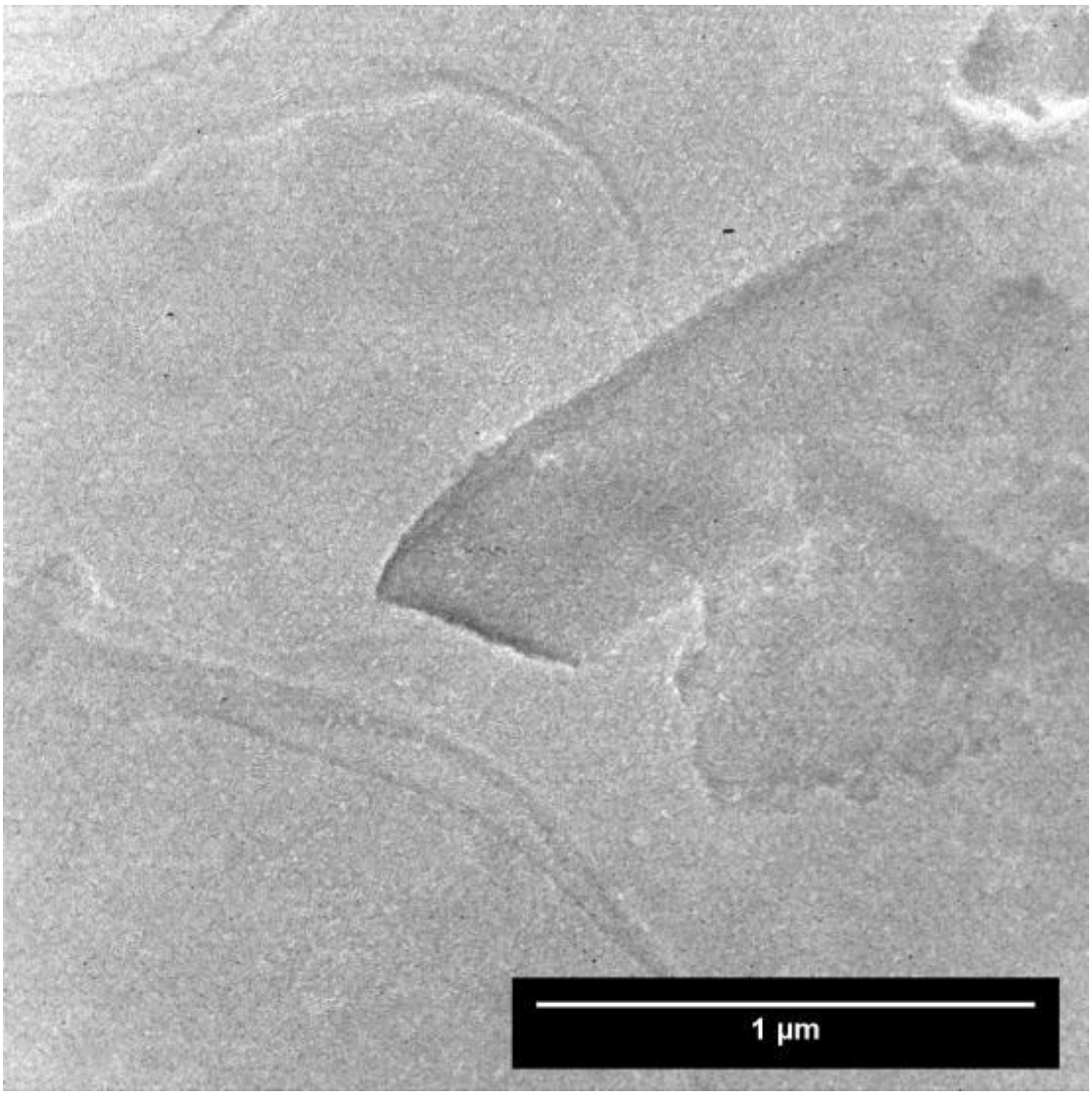

Figure 11.6: (during heating (dark brown)). A region of the sample containing a sheet of PEG. This structure measured > 0.45 µm in width and > 1.1 µm in length.

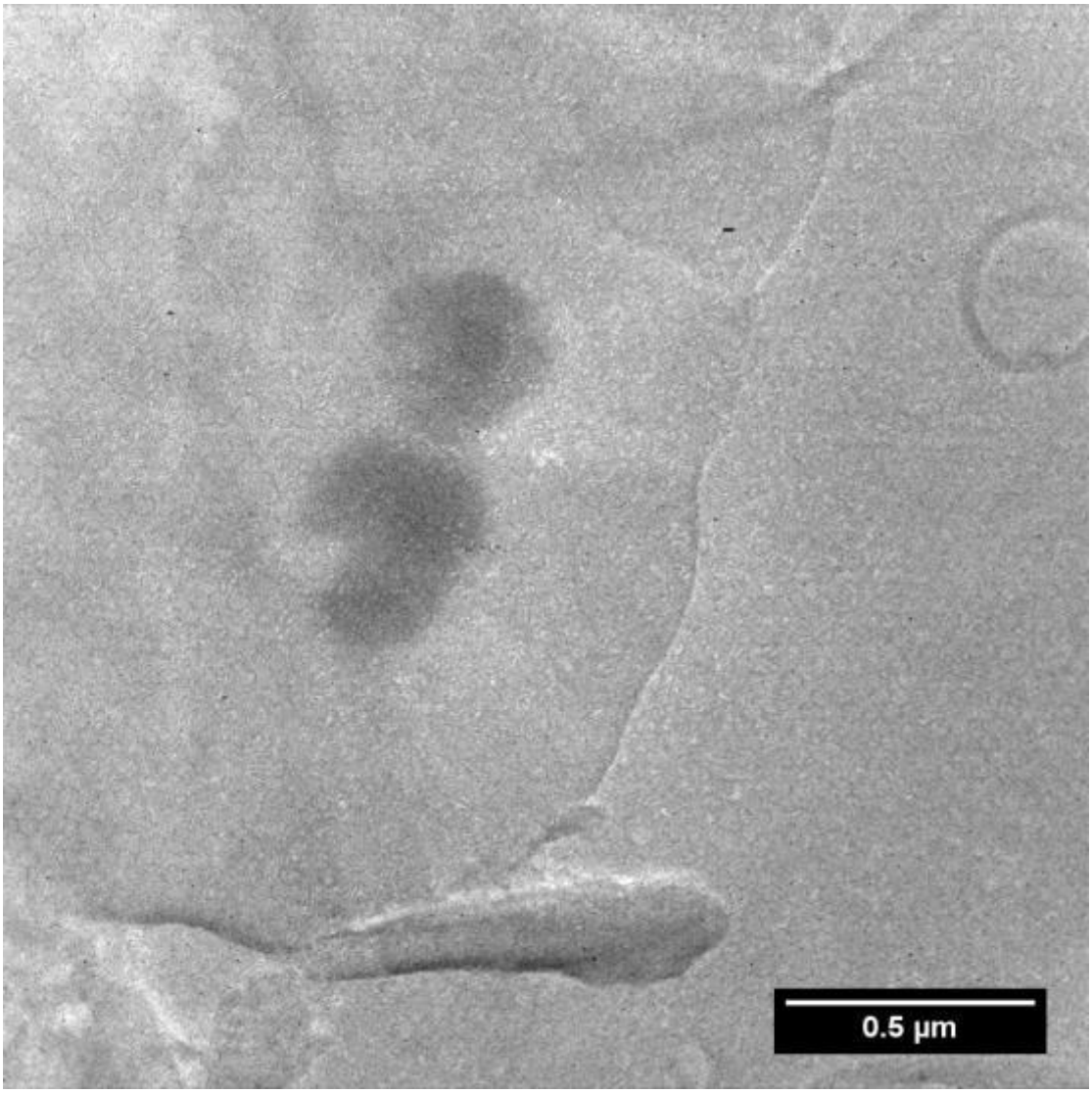

Figure 11.7: (during heating (dark brown)). Adjusting focus to near minimum contrast focus revealed the presence of large PEG sheets. These sheets contained material represented by the darker areas within the sheet in this image. The size of these darker regions implied that it was unlikely TiO_2 nanoparticles. The upper darker region within this PEG sheet was imaged and is represented in the next image.

With reference to figure 11.8, it is likely that the large PEG structures decomposed as the reaction progressed to ignition, resulting in the formation of smaller reaction chambers. A possible reason for the formation of polymer sheets and structures with varied shapes within the same reaction is likely due to a thermal gradient being setup during synthesis. Since the crucibles were only heated from the bottom, with the top exposed to the atmosphere, it is possible that reaction components at the bottom of the crucible experienced greater temperatures. This had the effect of producing different PEG structures. Similar structures decomposed under the beam. Therefore, low dose conditions were necessary to image these structures. Low dose imaging inherently produces grainy images.

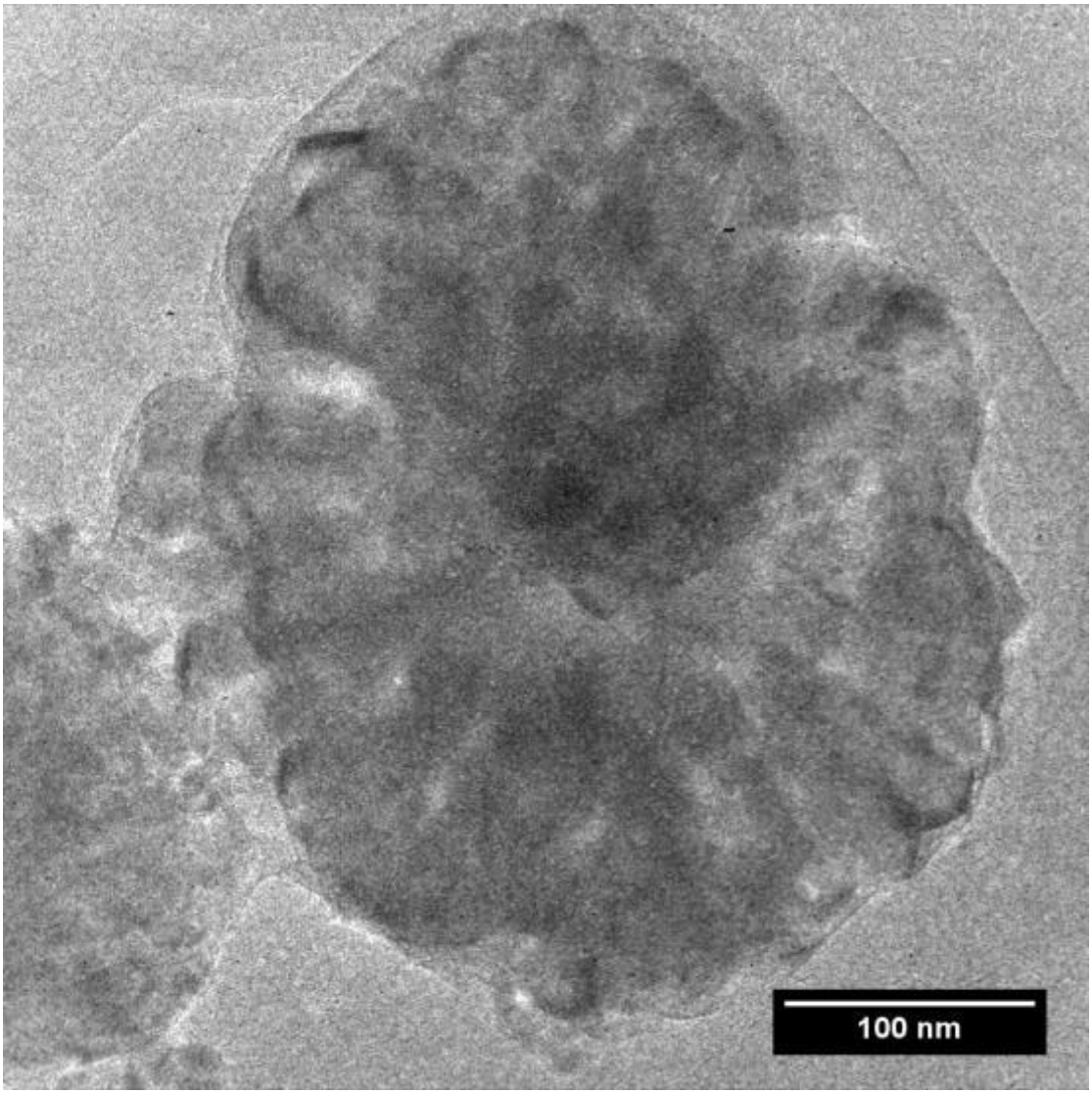

Figure 11.8: (during heating (dark brown)). This large structure corresponded to PEG and measured ~ 350 nm in width and ~ 400 nm in length.

From figure 11.9, the presence of crystalline TiO_2 in some parts of the sample lends credibility to the suggestion of a thermal gradient being setup within the crucible.

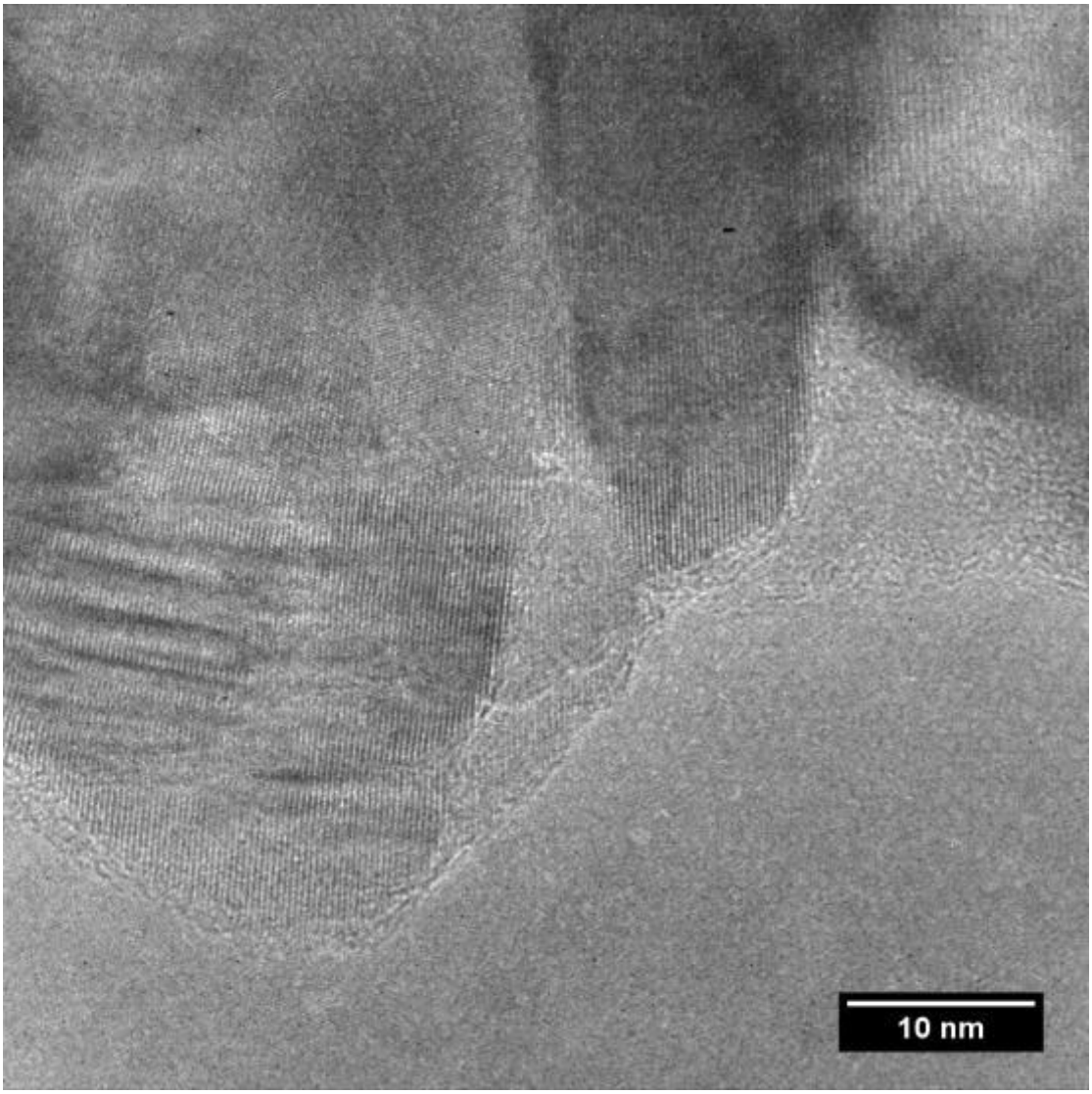

Figure 11.9: (during heating (dark brown)). Interestingly, some regions of the sample revealed the presence of crystalline material associated with PEG superstructures. Based on the anisotropic characteristics of these crystallites, they were most likely rutile aligned along [0 0 1].

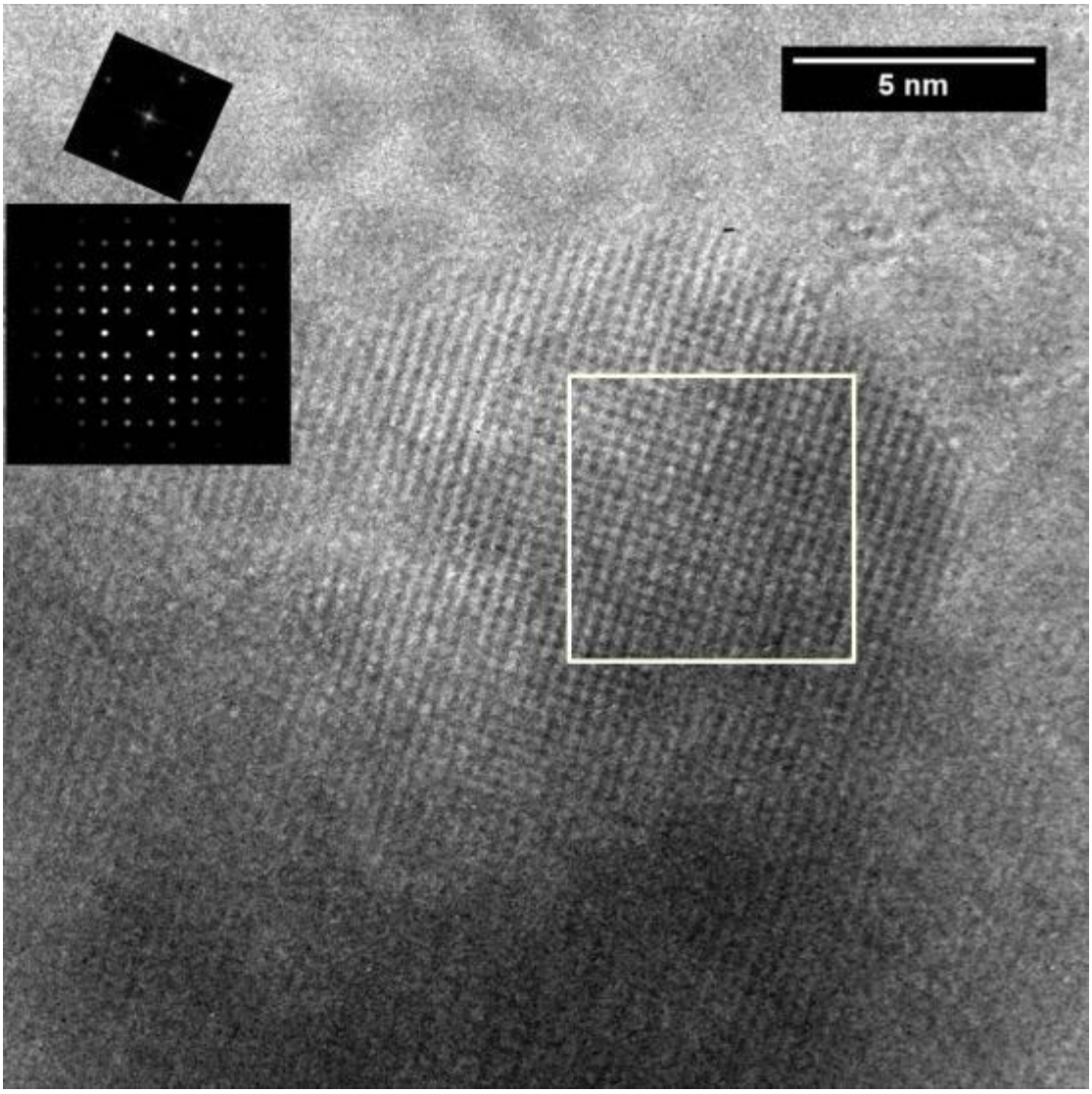

Figure 11.10: (during heating (dark brown)). Confirmation of the presence of anisotropic rutile in the sample. As confirmed by FFT, this crystal was aligned along [0 0 1]. It measured 14 nm across its width and > 20 nm across its length. The tip of the nanorod was tapered as previously documented[6]. No rutile mesocrystals were observed in this sample.

As given in figure 11.11, PEG sheet width variation as a function of fragmentation supports the thermal gradient conjecture to an extent. However, because this image was recorded from the sample later on during heating, the presence of large polymer sheets cannot be solely due to a thermal gradient. An additional possibility is that due to the low quantity of polymer added to the reaction, there was insufficient fuel to support an extensive ignition. This would leave the reaction cooler than required for complete polymer decomposition. This second possibility combined with oriented attachment and calcination at 500 °C then explains why the amounts of anatase and rutile fluctuate post-synthesis and post-calcination.

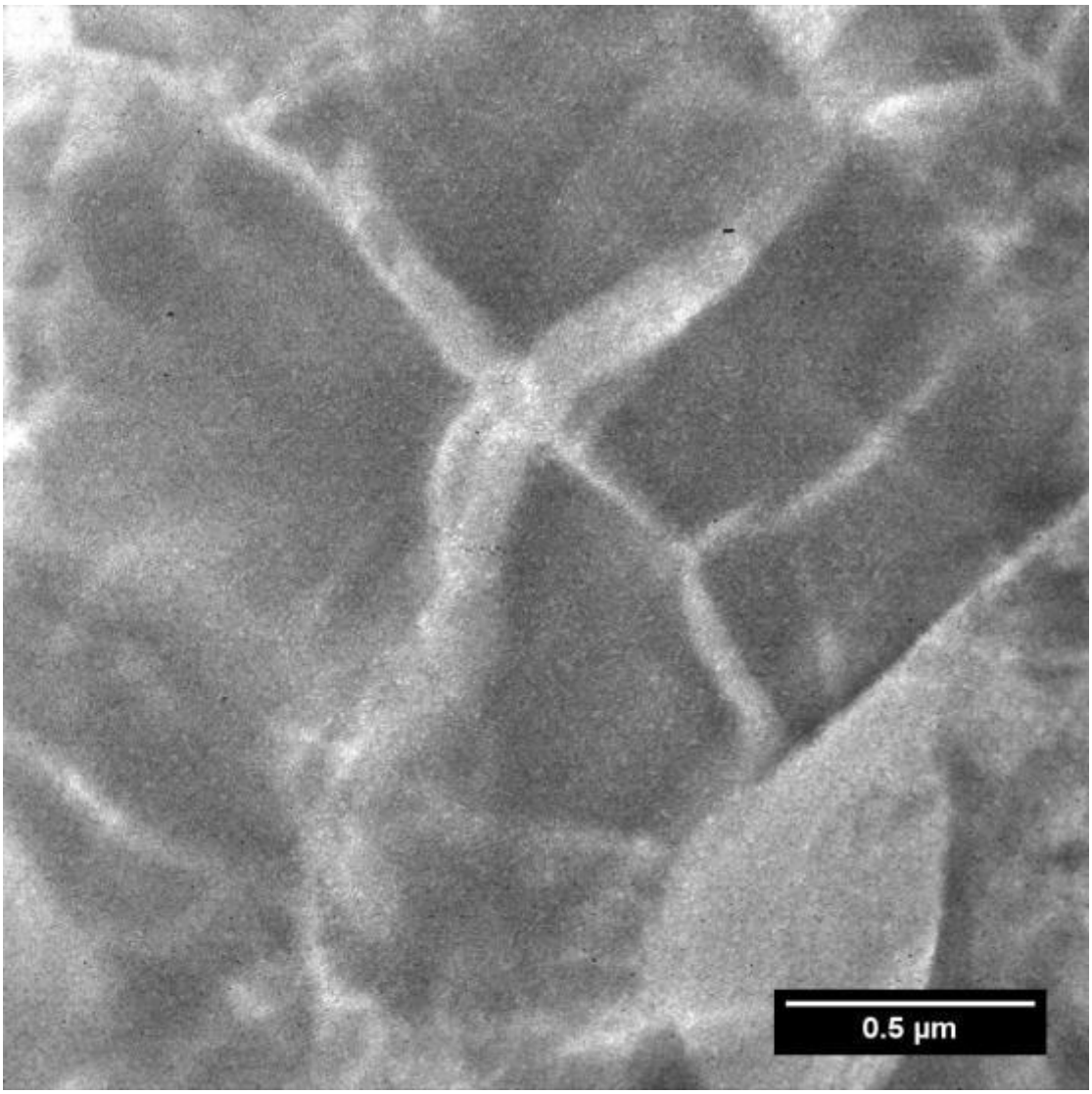

Figure 11.11: (during heating (black)). Interestingly, large PEG sheets were observed later on in the reaction. These sheets measured ~ 0.6 – 0.9 µm in length. The width of the sheets appeared to vary depending on visible fragmentation.

Most previously observed anatase crystals along (0 0 1) presented with well-defined edges, giving the crystals a square or rectangular appearance (in two dimensions). This crystal given in figure 11.12 appears to undergo inward and outward curvature (highlighted by the arrows). It is unlikely that this crystal grew in this manner as surface curvature increases the pressure and hence energy associated with anatase crystals[7]. The formation of this crystal is likely due to oriented attachment between three anatase crystals. As previously described, anatase crystals can undergo oriented attachment to nucleate rutile at the boundary between the crystals[8]. Additionally, surface curvature promoted the formation of rutile[7].

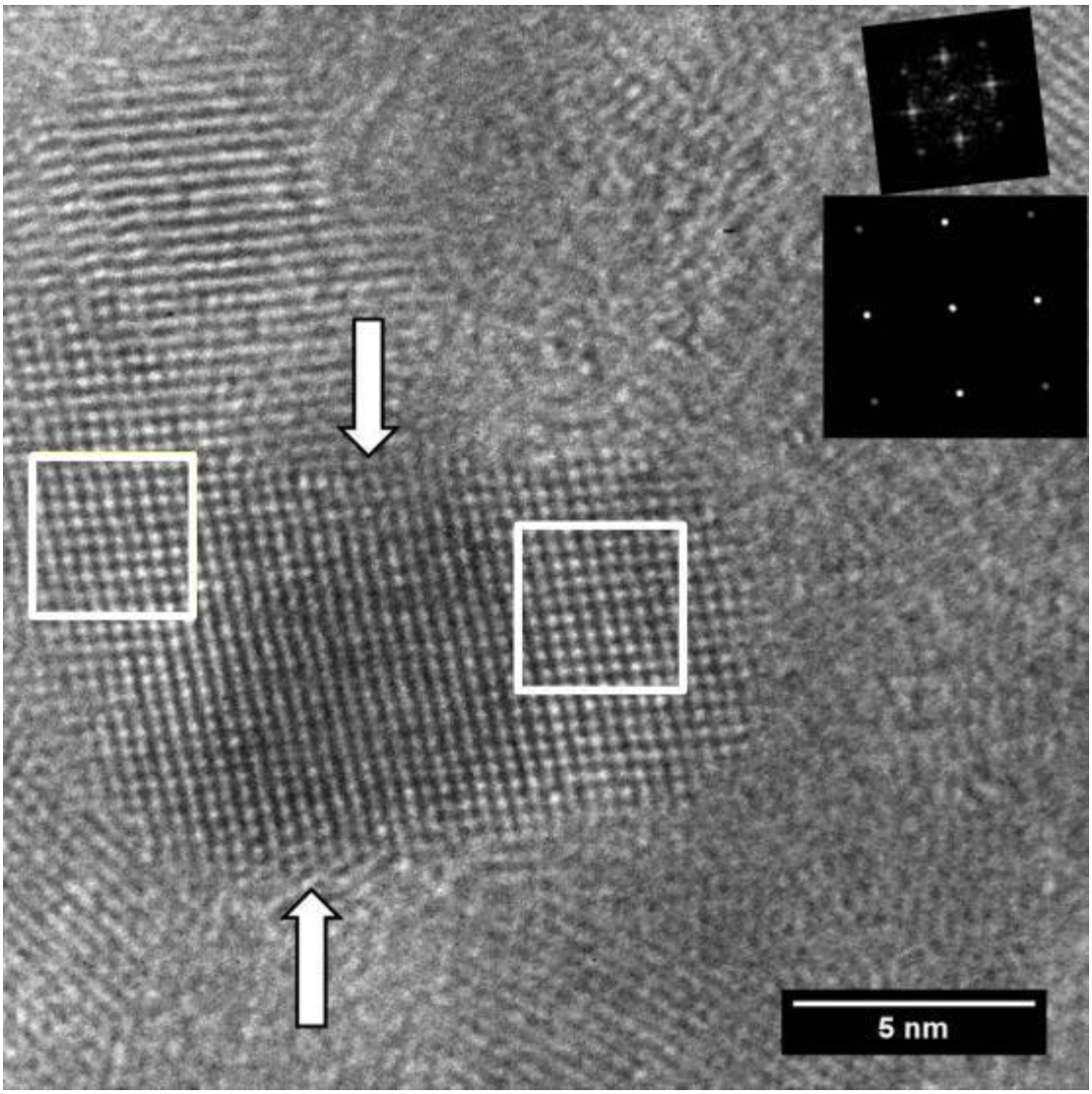

Figure 11.12: (during heating (black)). Most of the sample contained crystalline material. This image contains an interestingly shaped crystal in the (0 0 1) orientation.

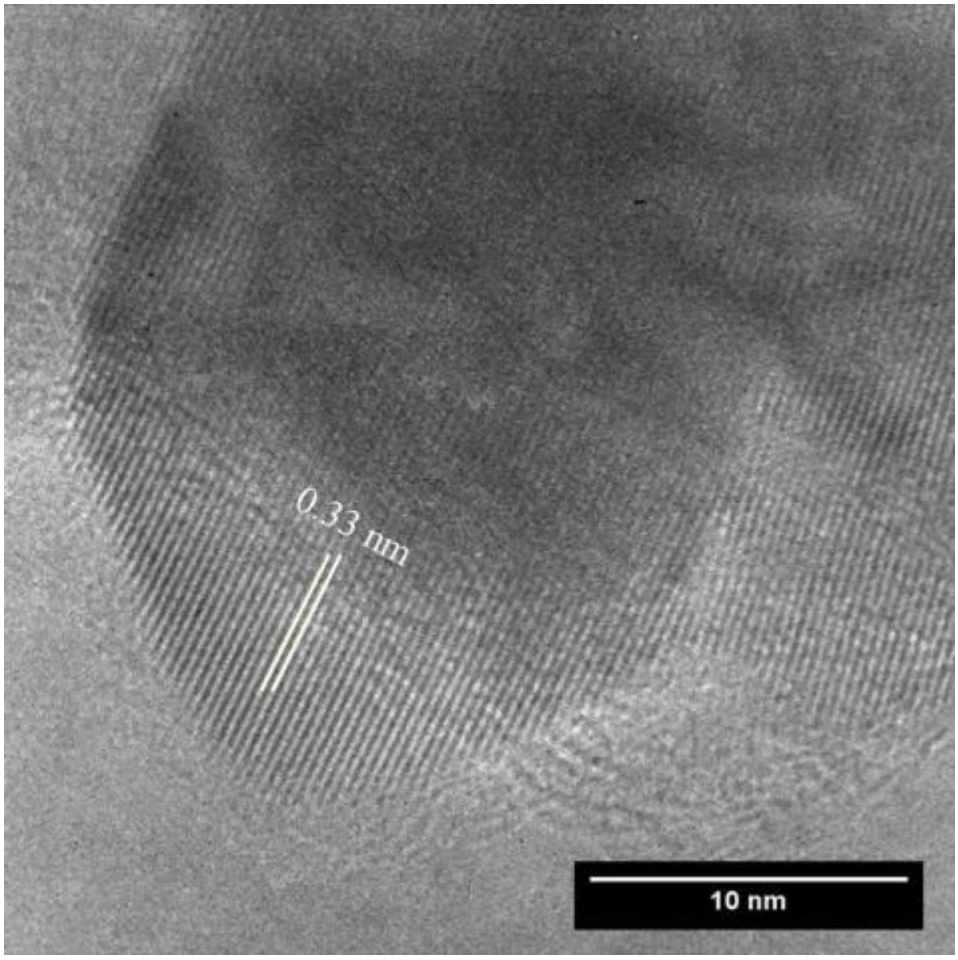

Figure 11.13: (during heating (black)). Anisotropic rutile crystals with tapered ends along [0 0 1] were observed. The lattice spacing of 0.33 nm is consistent with that previously observed for rutile crystals.

11.2.2 Aluminium rod generated molten drops

The production of low volume specimens in this experiment did not allow for the generation of XRD data. However, it did allow for the generation of TEM images that better revealed the association of PEG with metal ions forming nanoparticles as the reaction proceeded.

TEM images corresponding to samples synthesised using PEG of different molecular weights, sampled at various times during the reaction are given as follows:

- PEG 3000 g/mol after 1 hour: figures 11.14 – 11.17
- PEG 6000 g/mol after 1 hour: figures 11.18 and 11.19
- PEG 12000 g/mol after 1 hour: figure 11.20
- PEG 4000 g/mol after 3.5 hours: figures 11.21 – 11.23

- PEG 10000 g/mol during ignition: figures 11.24 – 11.28

Only TEM images that contain useful data are presented:

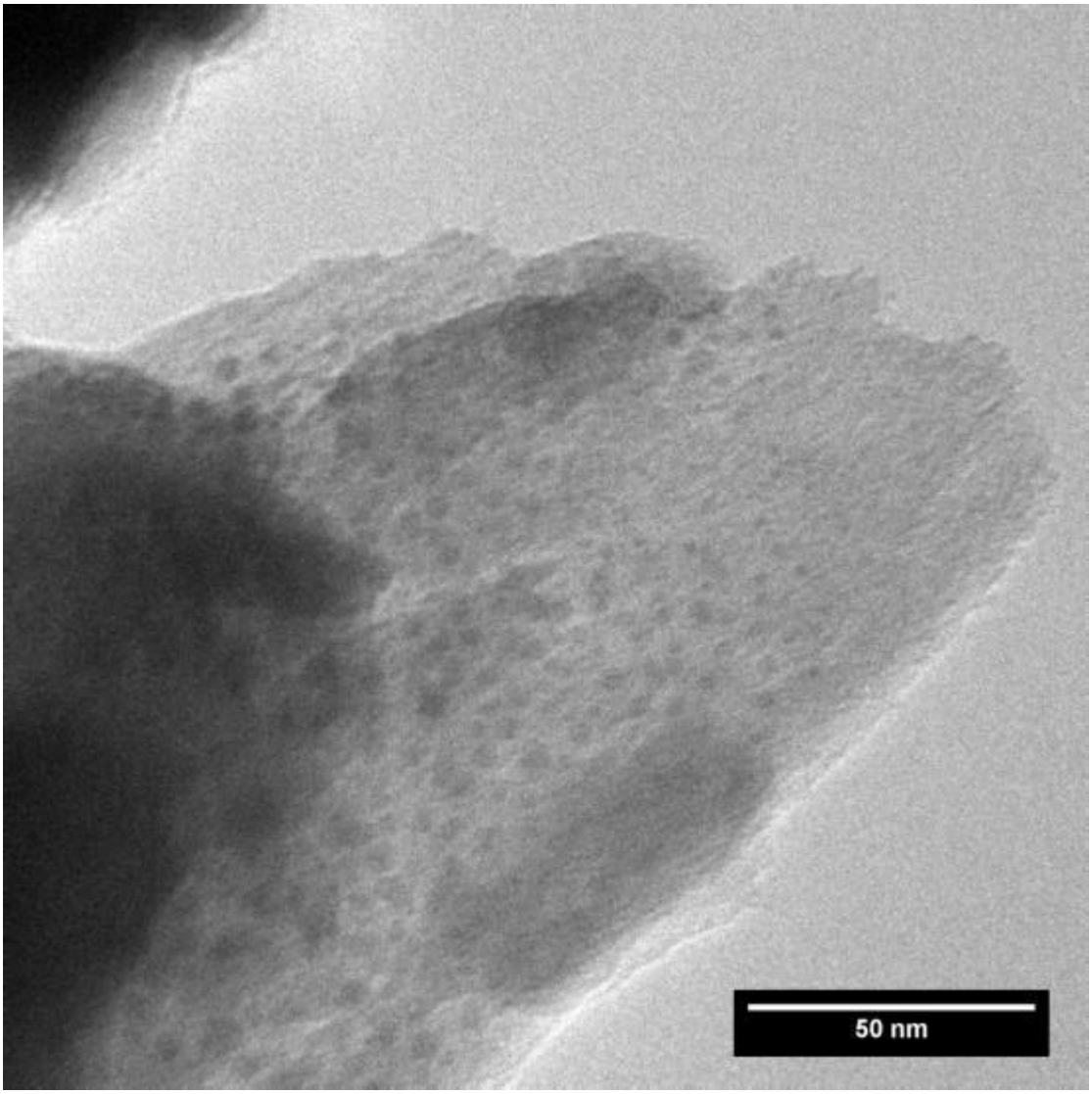

Figure 11.14: (PEG 3000 g/mol after 1 hour). A polymer fragment likely containing many small nanoparticles (represented by the darker dots within the polymer). The fragment measured ~ 130 nm across its width and > 200 nm in length.

From the observations in figure 11.15, it is possible that PEG sphere formation marks a point in the formation of polymer reaction chambers. The formation of polymer reaction chambers has been hypothesised throughout this study. The association of nucleated titania within the polymer reaction chambers was previously hypothesised in this study.

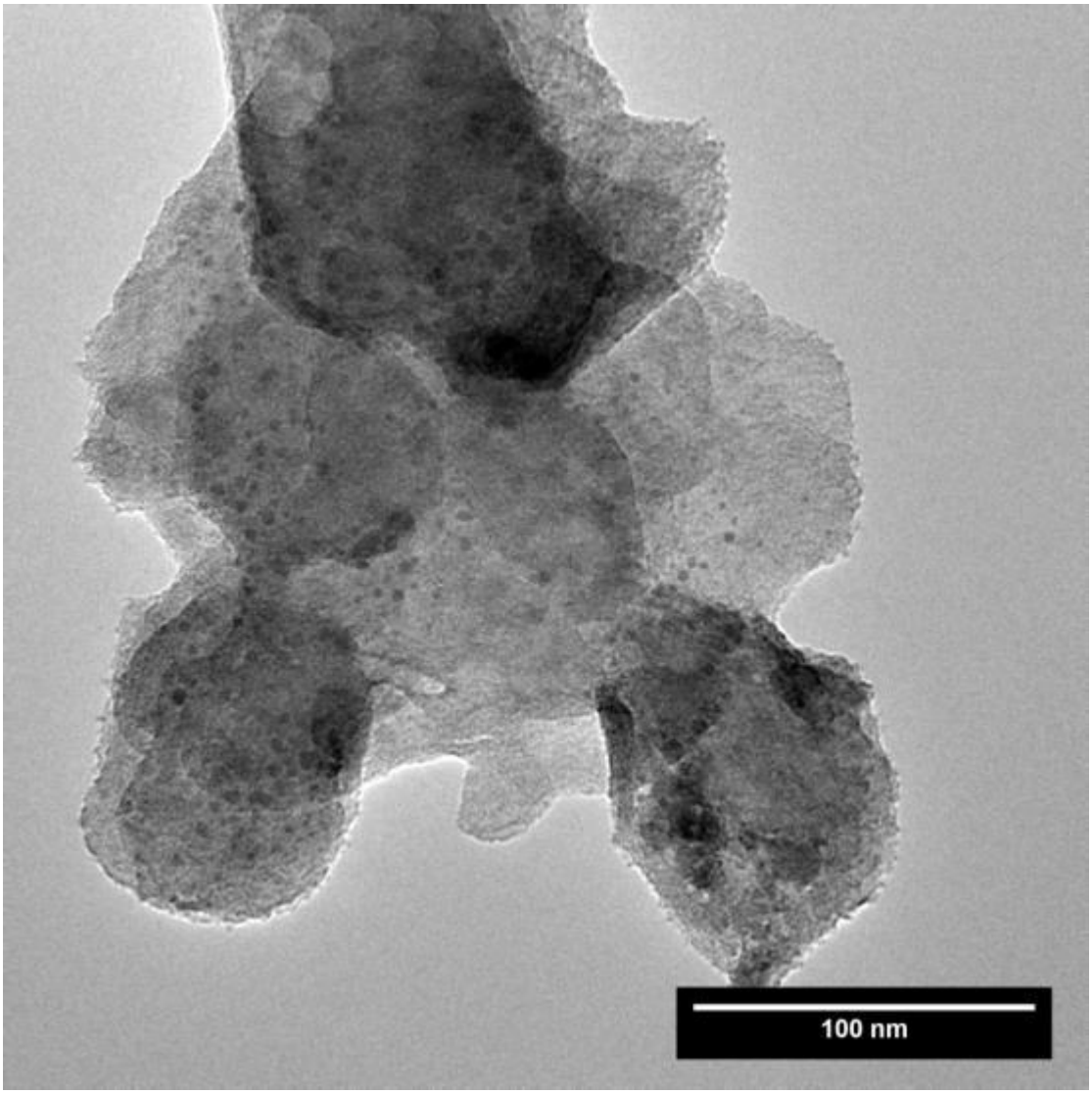

Figure 11.15: (PEG 3000 g/mol after 1 hour). Nearly spherical polymer fragment formations were observed. The structures measured ~ 80 nm in diameter. Darker regions within the polymer spheres (represented by dots) are indicative of the presence of titania nanoparticles.

The larger particles shown in figure 11.16 are evidence of coalescence. All particles and the aggregated sphere were contained within the polymer, as evidenced in the image. From chapter 5, PEG 3000 g/mol produced rutile as the major phase. Therefore, given its size, this structure could correspond to a rutile mesocrystal nucleation site. The lack of evident particle anisotropy suggests that this site was imaged early on in the mesocrystal formation process.

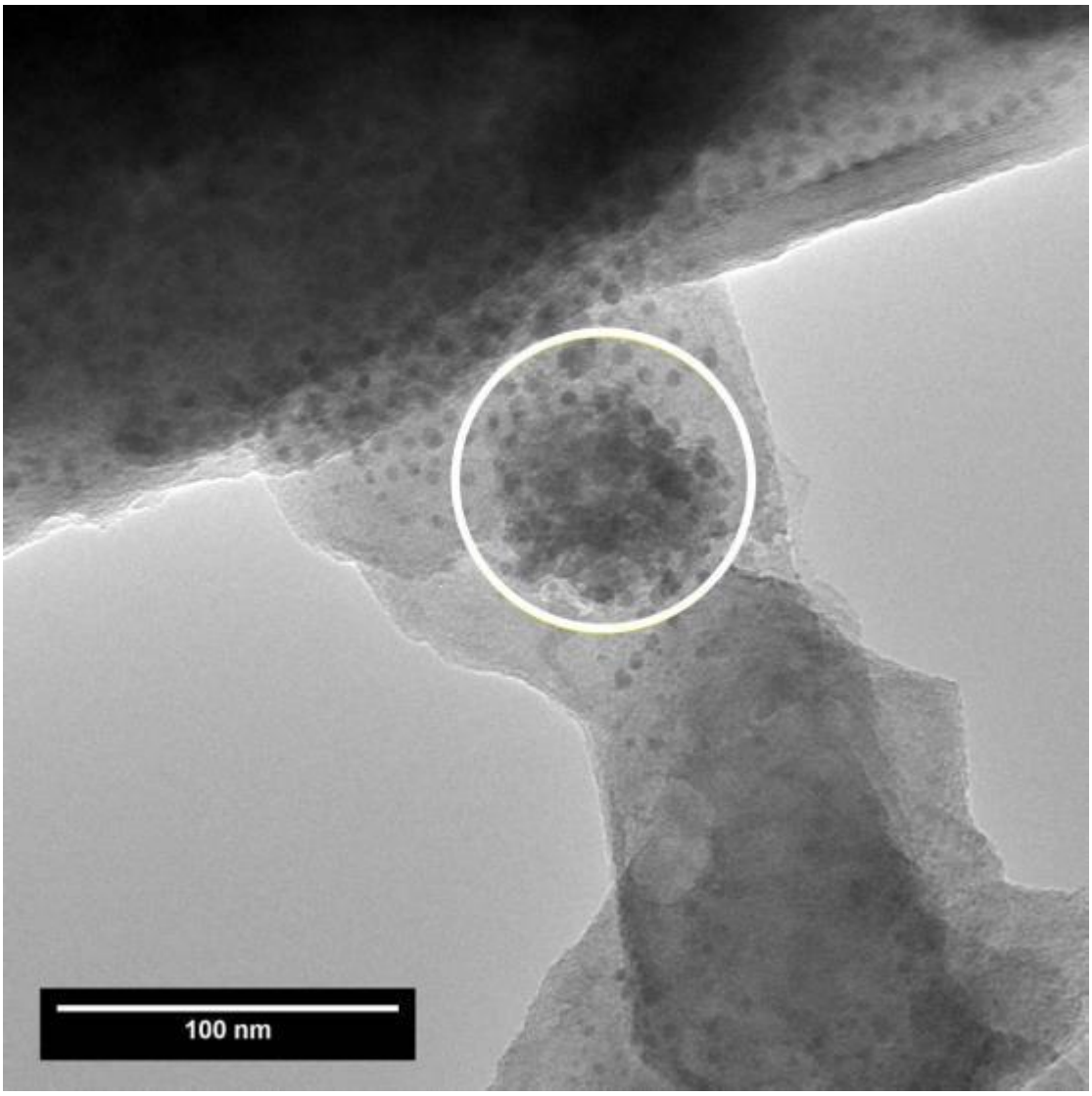

Figure 11.16: (PEG 3000 g/mol after 1 hour). Individual nanoparticles measured between 3 – 7 nm. Interestingly, some particles appeared to aggregate into a structure measuring > 60 nm across its width and length (contained within the circle). Distinct particles were observed at the edges of the structure, in contrast to the centre region of the structure that appeared to contain larger particles.

Care should be taken to not misinterpret the significance of the ‘tuning fork’ shaped structures given in figure 11.17. These structures were initially believed to be polymer sheets folding back on themselves. However, a polymer-free sample (appendix I) was imaged in a similar manner and also revealed the presence of these structures. This indicated that these structures corresponded to the holey carbon film breaking free from the copper grid and rolling on itself under the electron beam.

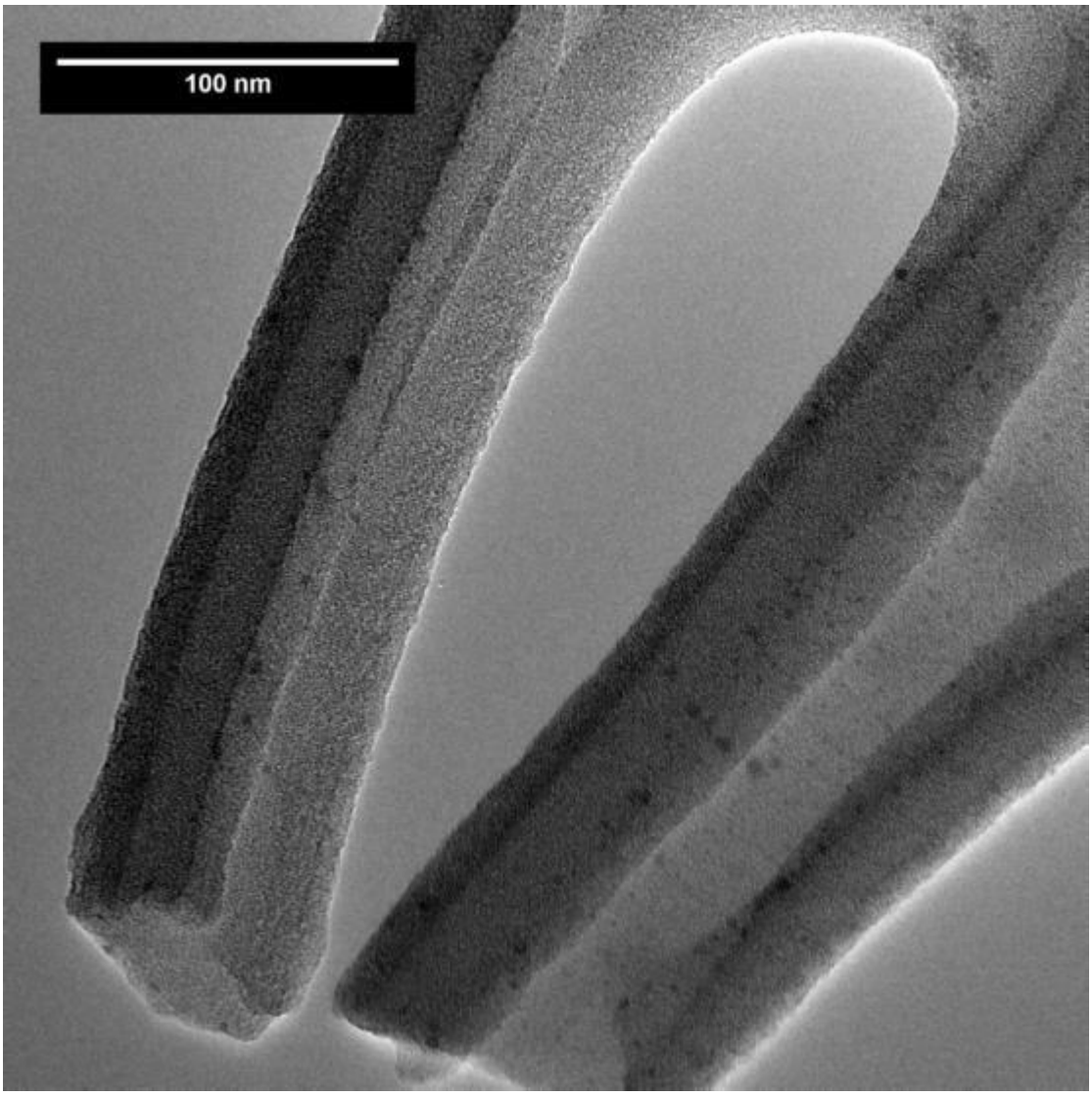

Figure 11.17: (PEG 3000 g/mol after 1 hour). “Tuning-fork shaped structures”.

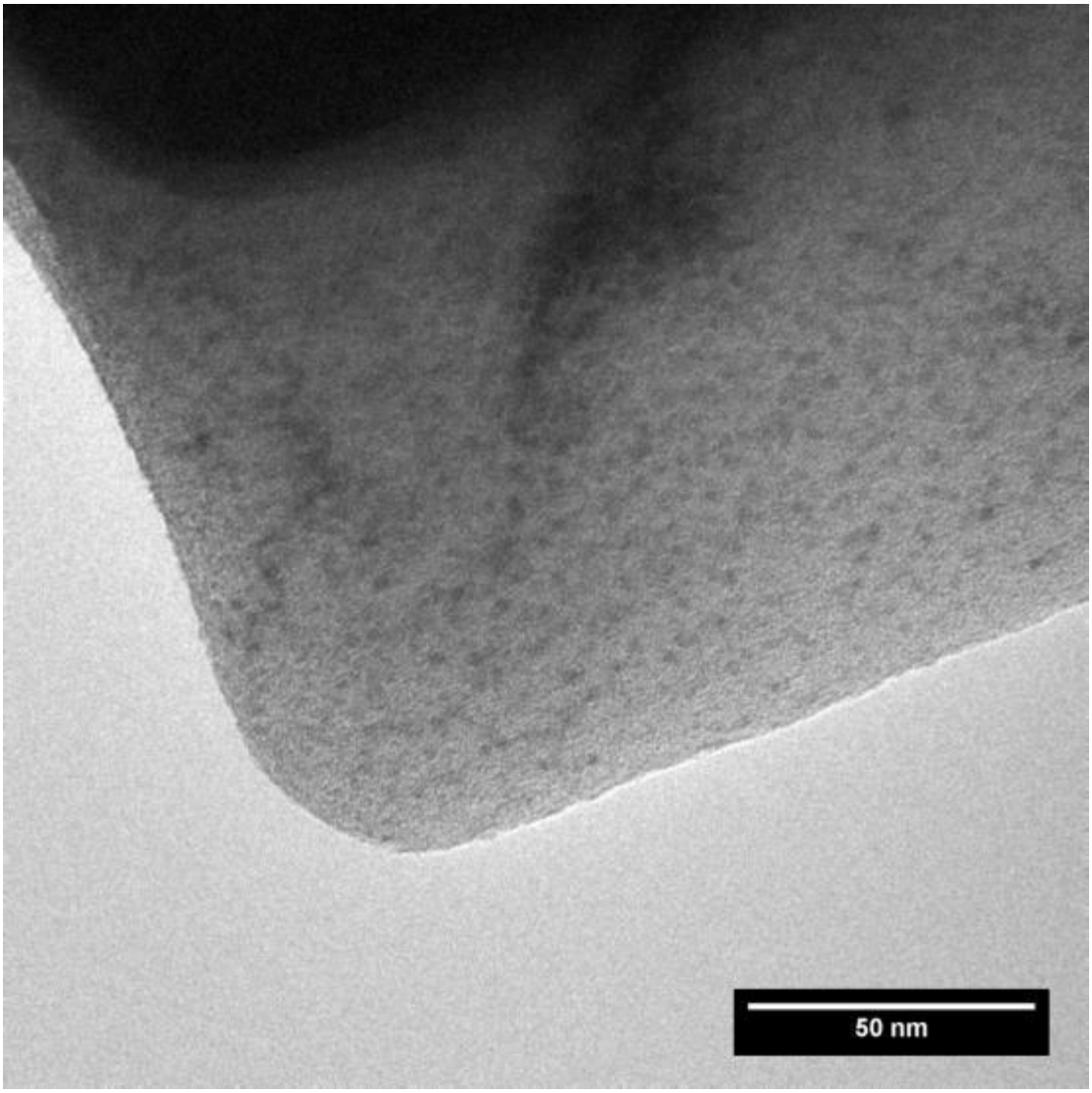

Figure 11.18: (PEG 6000 g/mol after 1 hour). Imaging this sample also revealed the presence of nanoparticles contained within polymer fragments after 1 hour of heating.

With reference to the superstructure shown in figure 11.19, from chapter 5, it was observed that PEG 6000 g/mol produced 91.8 % of rutile. Thus the presence of rutile mesocrystals in this sample was not unexpected. The large size of the mesocrystal is surprising given that this sample had been heated for 1 hour implying that the sample was not close to its flash point.

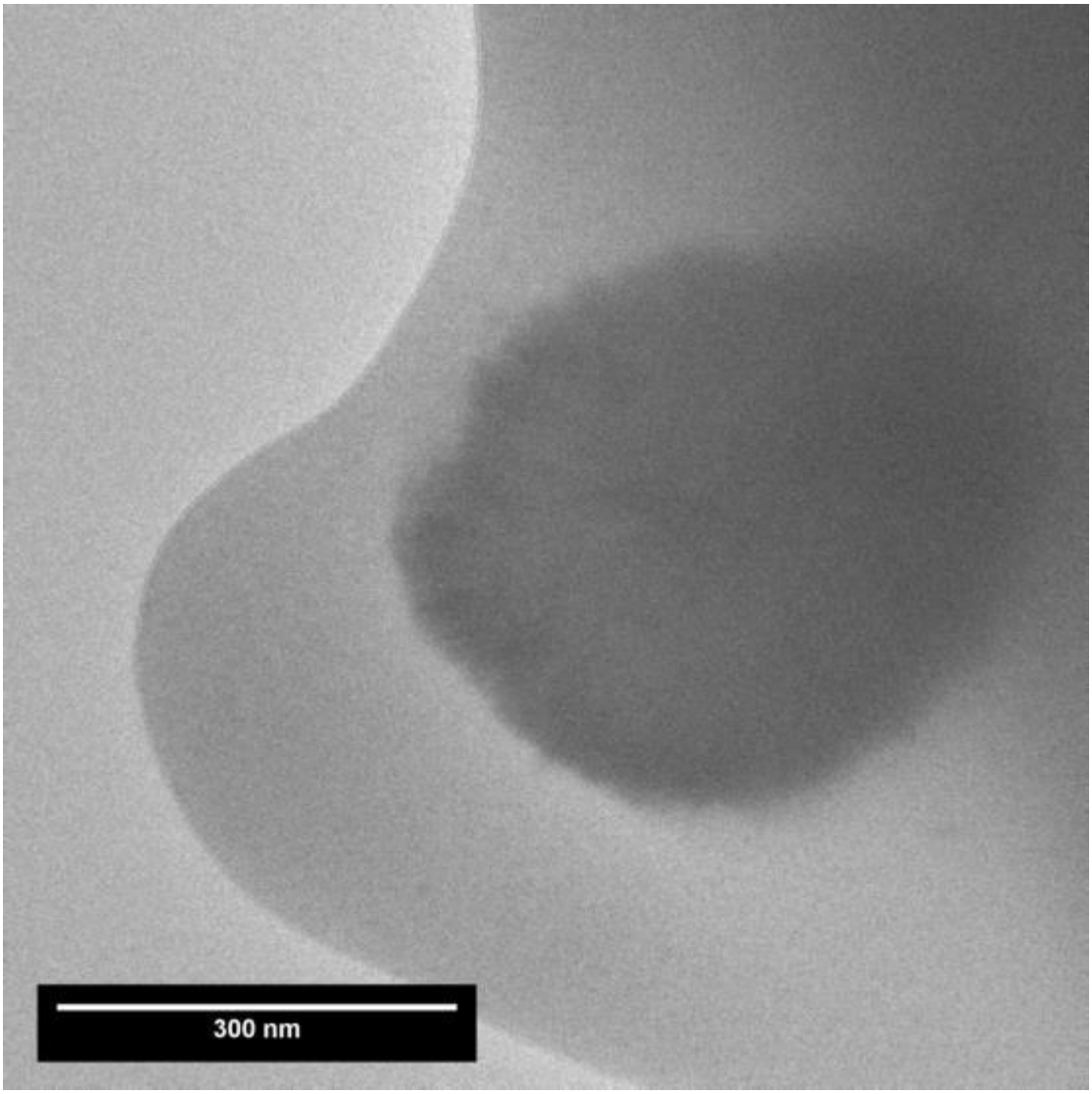

Figure 11.19: (PEG 6000 g/mol after 1 hour). The superstructure within the polymer (darker region of the image) is consistent with the formation of a rutile mesocrystal. The structure measured ~ 500 nm across its width and ~ 400 nm from top to bottom.

Imaging samples synthesised using longer PEG chains (as that exhibited in figure 11.20) posed a significant challenge. The volume of polymer in the sample and low dose conditions limited the ability of the electron beam to penetrate the specimen and obtain useful data.

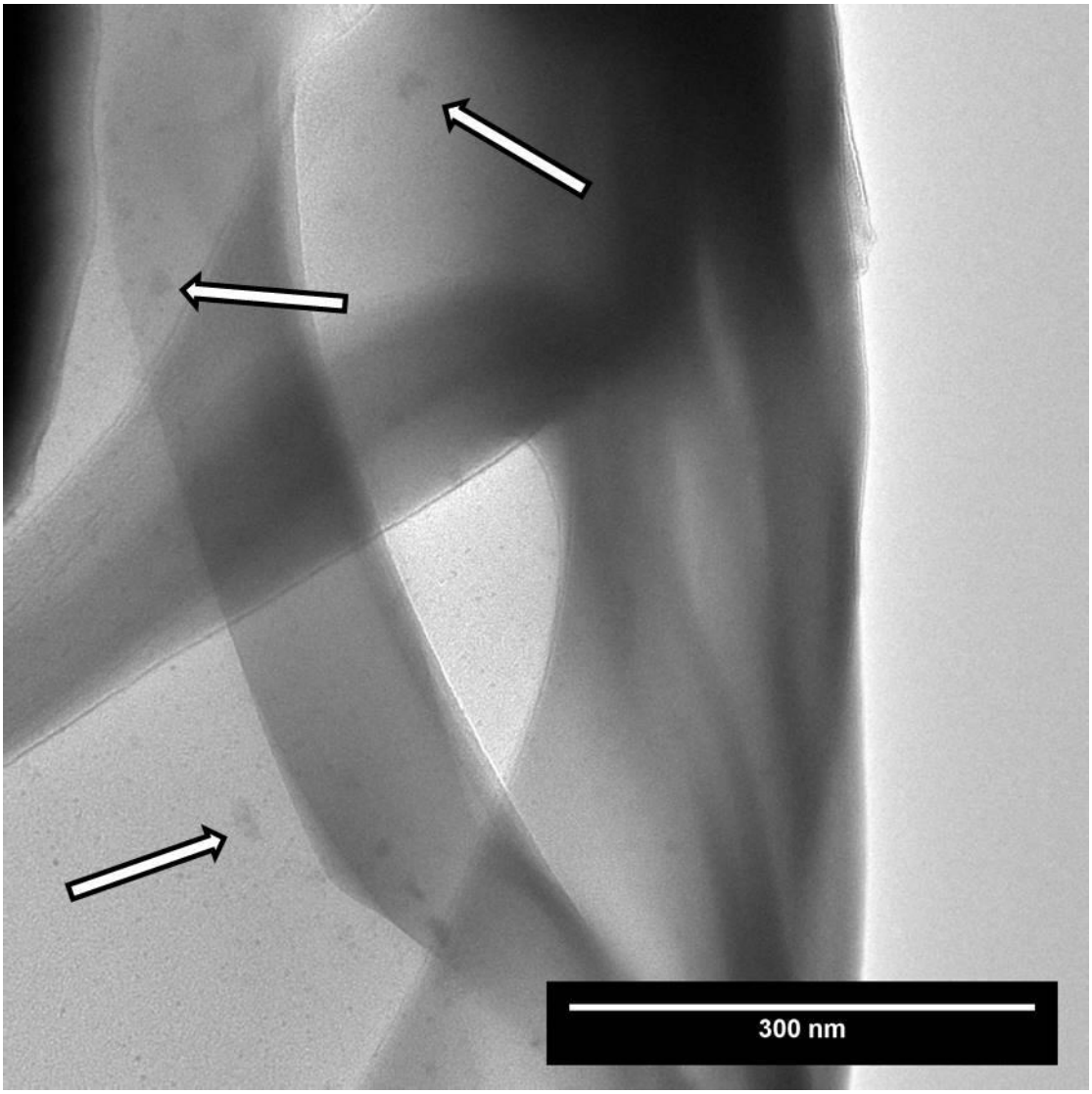

Figure 11.20: (PEG 12000 g/mol after 1 hour). This image shows the presence of nanoparticles (highlighted with arrows) associated with polymer fragments.

The presence of PEG in figure 11.21 is not unexpected. As previously observed, it is possible for PEG to be present within the sample close to the end point of ignition. It is believed that the presence of PEG controls the amounts of nucleated anatase and rutile, and explains why these amounts fluctuate post-calcination. Arrows point to high aspect ratio polymer sheets or fibres. The region contained within the circle was magnified and imaged. These images follow.

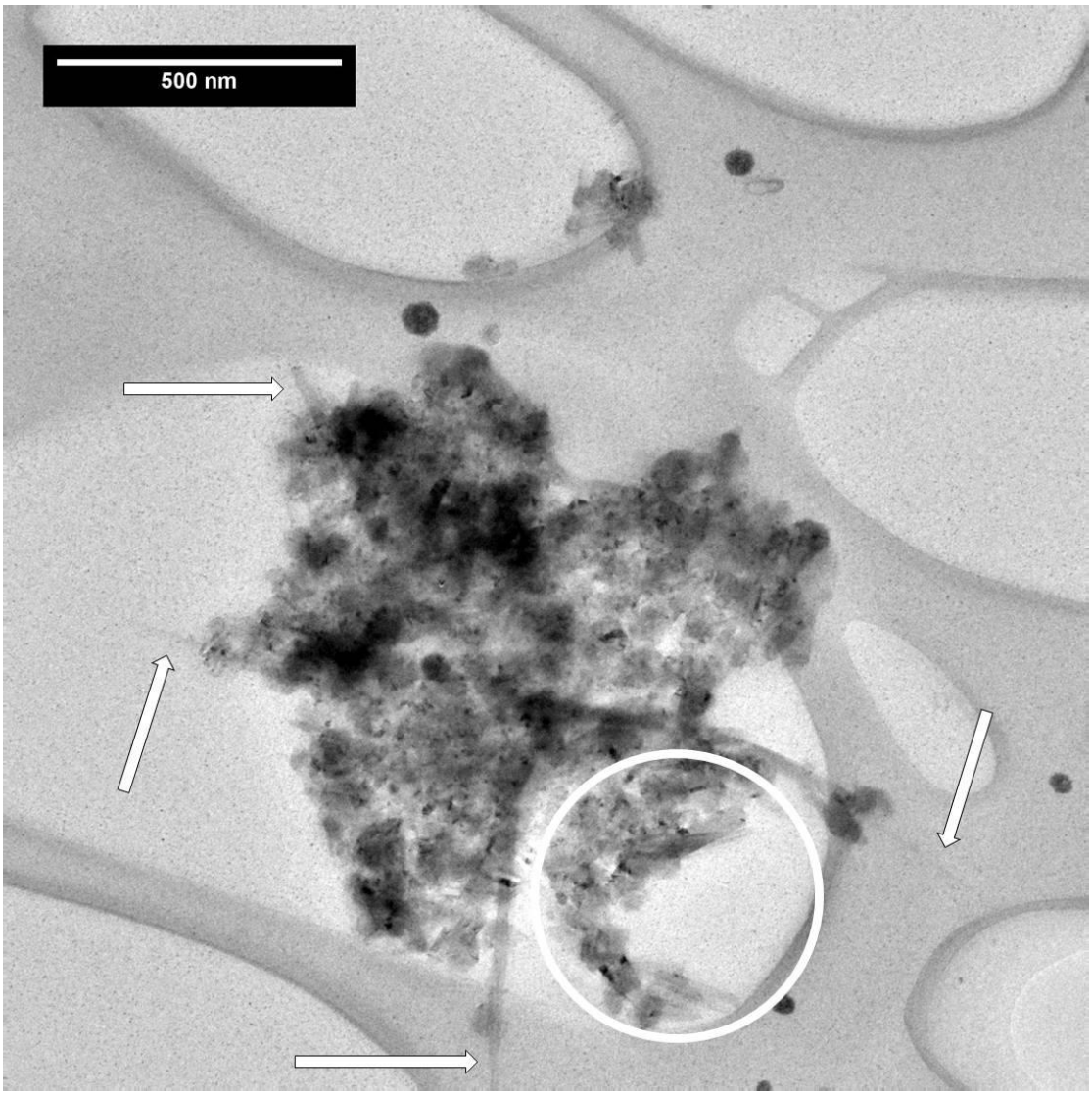

Figure 11.21: (PEG 4000 g/mol after 3.5 hours). The structure contained within the image measured ~ 1.2 µm across its length and width and is indicative of PEG (or carbon generated from PEG) aggregation.

The observations in figure 11.22 are consistent with the hypothesised mechanism of particle formation within reaction chambers using resin-gel synthesis.

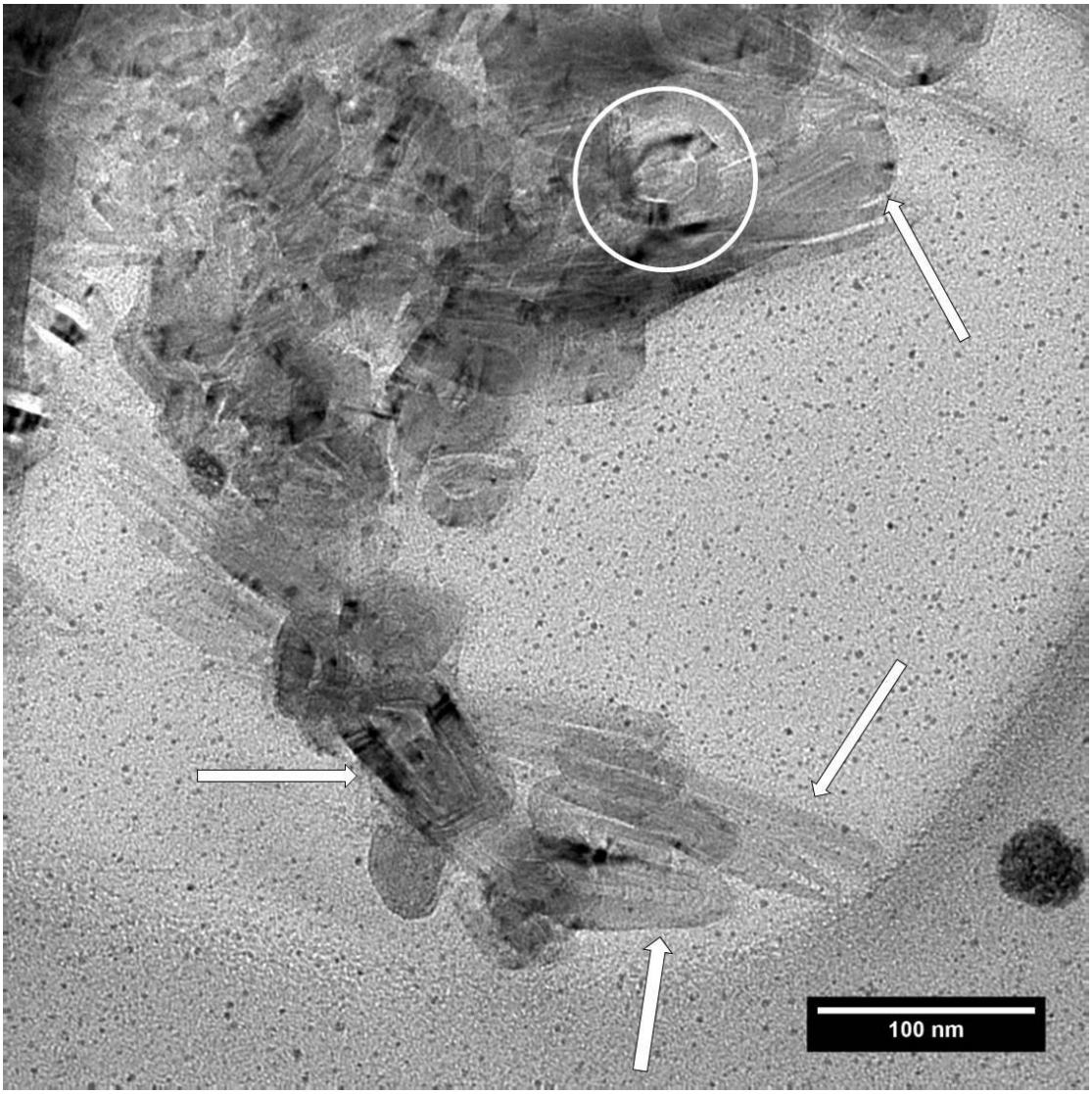

Figure 11.22: (PEG 4000 g/mol after 3.5 hours). This image represents PEG sheets (or carbon material generated from PEG) folding back on itself to create non-spherical reaction chambers. The light contrast of the central region of the chambers suggests that they are hollow or nearly hollow. As highlighted by arrows, the central hollow region of the chambers measured between 3 – 7 nm in width. The region contained with the circle was magnified and imaged. This image follows.

The intershell spacing of 0.326 nm highlighted in figure 11.23 is consistent with that documented for multi-walled carbon nanotubes[9]. Estimating the internal diameter is complicated by the presence of a smaller, crystalline, circular structure contained within the larger structure. Carbon was an expected product of the ignition. However, this is the first observation of shaped carbon material formed using resin-gel synthesis. It is possible that during later stages of the ignition, PEG degrades into shaped carbon materials that serve to protect the surfaces of nucleated titania, and hence serve as reaction chambers. It should be noted that toward the end of the reaction, most titania has already formed through the actions of heating and the interplay between the precursor molecules and PEG. Therefore, the effects of shaped carbon materials should not be present throughout the reaction.

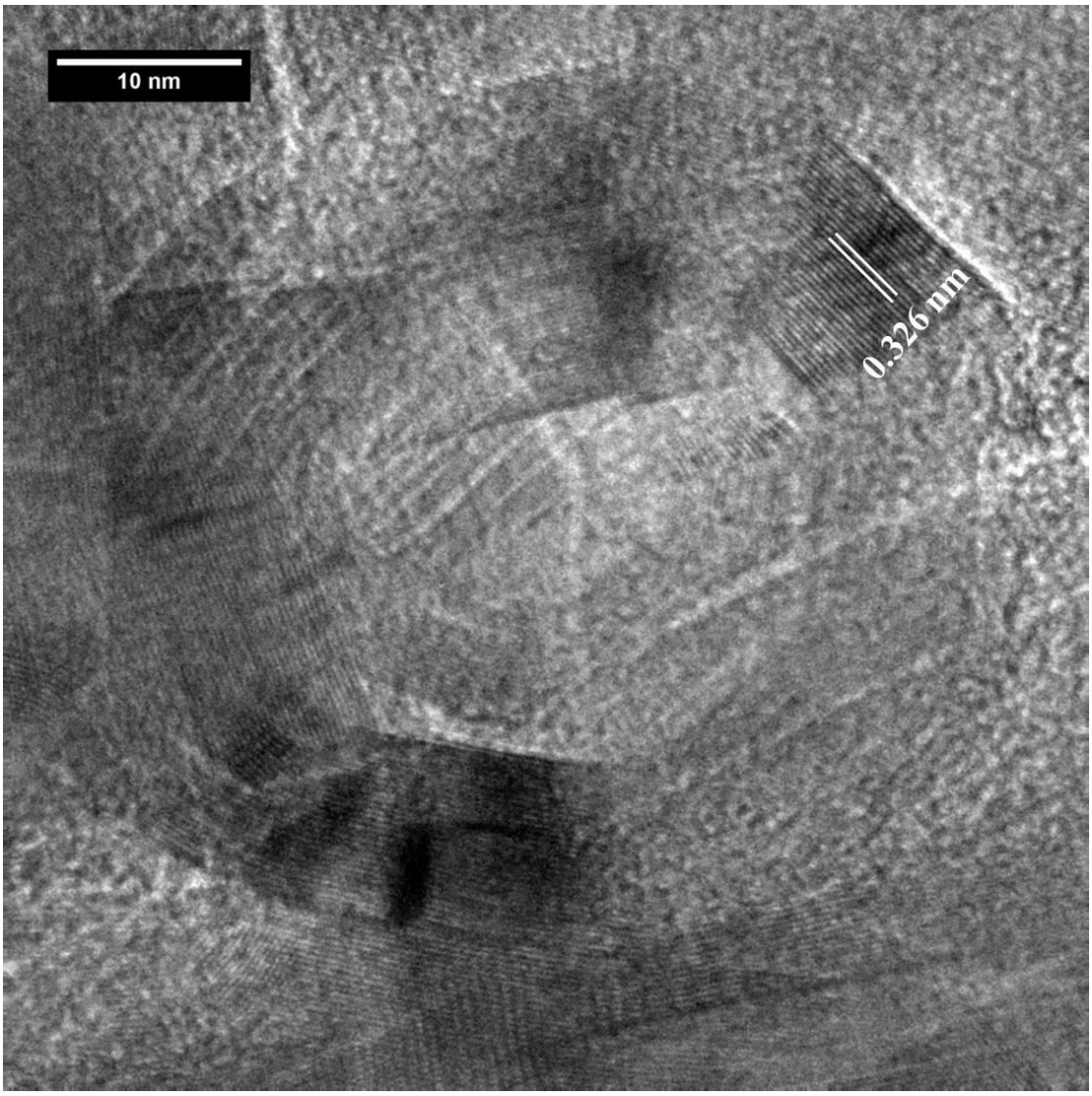

Figure 11.23: (PEG 4000 g/mol after 3.5 hours). Apparent formation of a circular reaction chamber. The intershell spacing measured 0.326 nm.

Based on previously obtained data on the tendency of rutile to form mesocrystals, it is likely that the superstructures given in figure 11.24 correspond to rutile aligned along [0 0 1]. It is possible that areas contained within the black circles represent rutile mesocrystal nuclei that would have developed into larger structures if the reaction was not stopped. Interestingly, the length of the anisotropic rods and diameter of the mesocrystals were similar. Given the propensity of rutile to coarsen along [0 0 1], it is likely that the rutile nucleating conditions influenced whether superstructures or rods are formed. These conditions were likely inflicted by the formation of polymer reaction chambers.

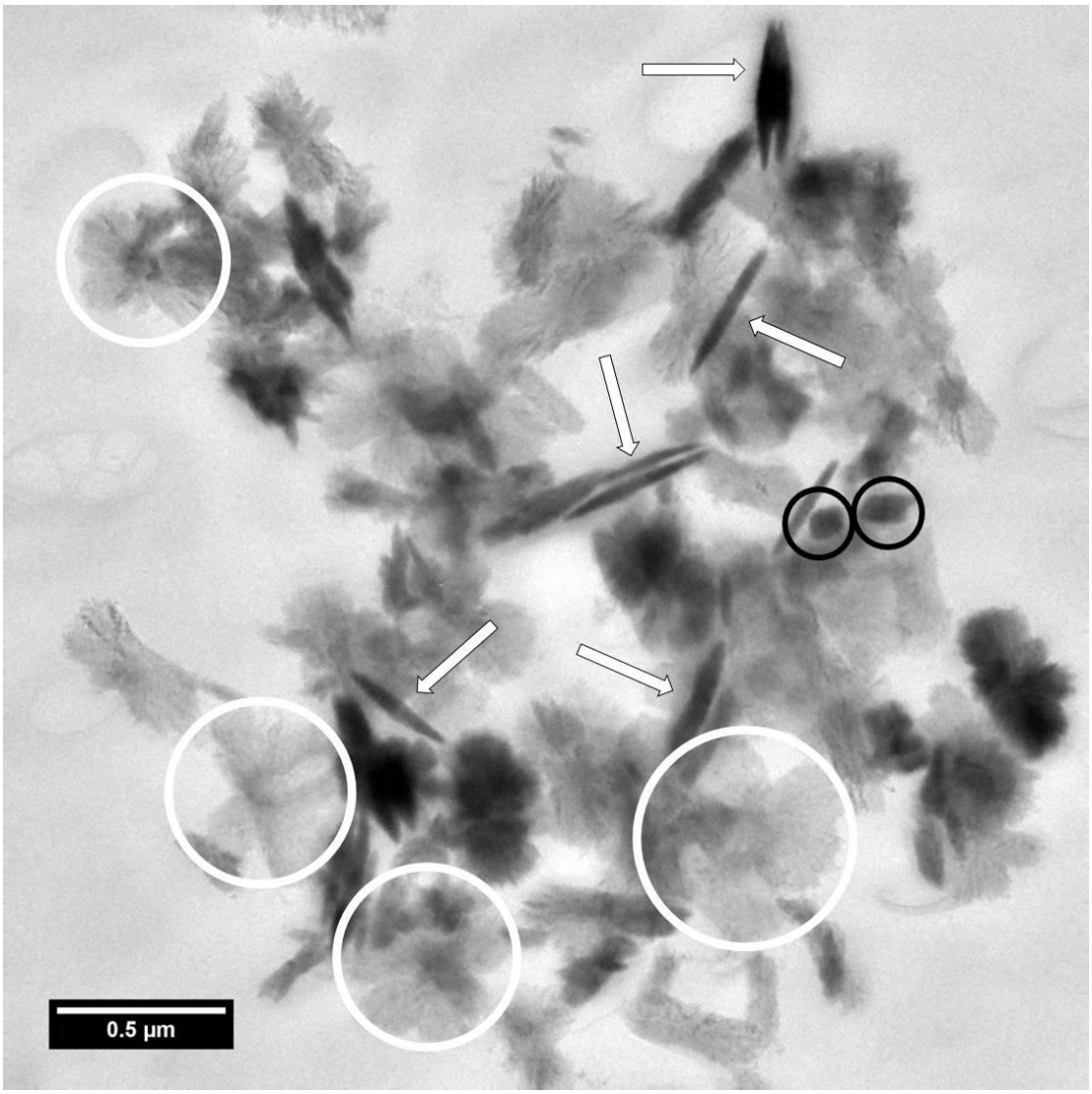

Figure 11.24: (PEG 10000 g/mol during ignition). This sample produced titania that aggregated into anisotropic rods (highlighted by arrows). Some of these rods arranged into hierarchical superstructures (highlighted by white circles). Black circles are indicative of smaller, more densely packed nanoparticles.

The proposed mechanism of rutile mesocrystal formation (figure 11.25) is anatase seed crystals that nucleate rutile. The rutile nucleus coarsens along [0 0 1] to form nanorods that extend radially outward from the centre of the assembly. A combination of polymer reaction chamber effects and oriented attachment is believed to catalyse the formation of mesocrystals of various sizes.

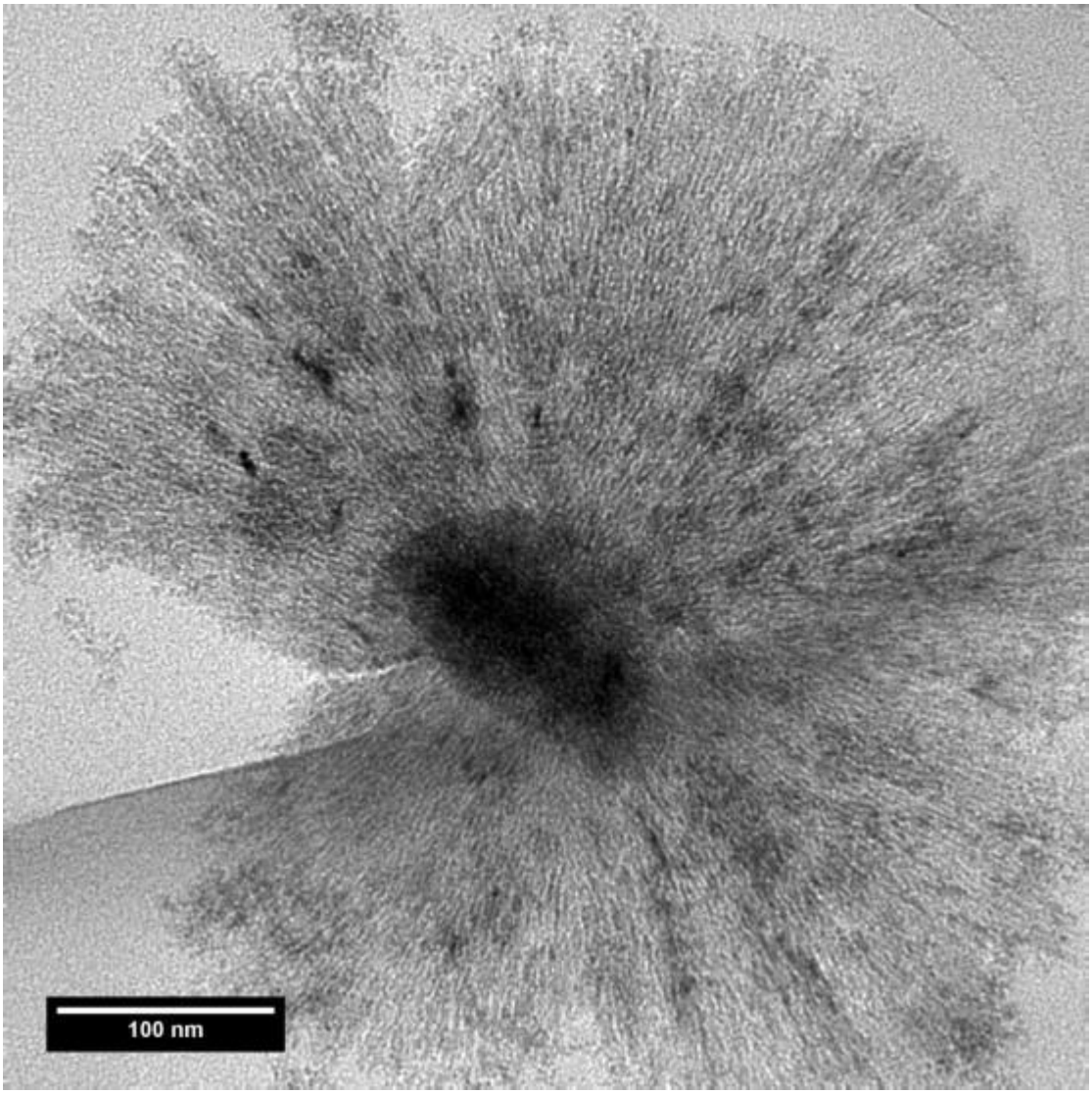

Figure 11.25: (PEG 10000 g/mol during ignition). Sparsely grown mesocrystal most likely comprised of rutile. The central region of this assembly is significantly denser than the outer rim. Additionally, the mesocrystal is imperfect as evidenced by the lack of nanorods present in the lower left part of the image.

Figure 11.26 was prepared by panoramically fitting two images corresponding to two parts of the structure without changing the aspect ratio. It is possible that within this superstructure, exist many reaction chambers of various sizes that govern the formation of titania nanomaterials

The nature of this polymer was curious given that the sample was obtained during ignition.

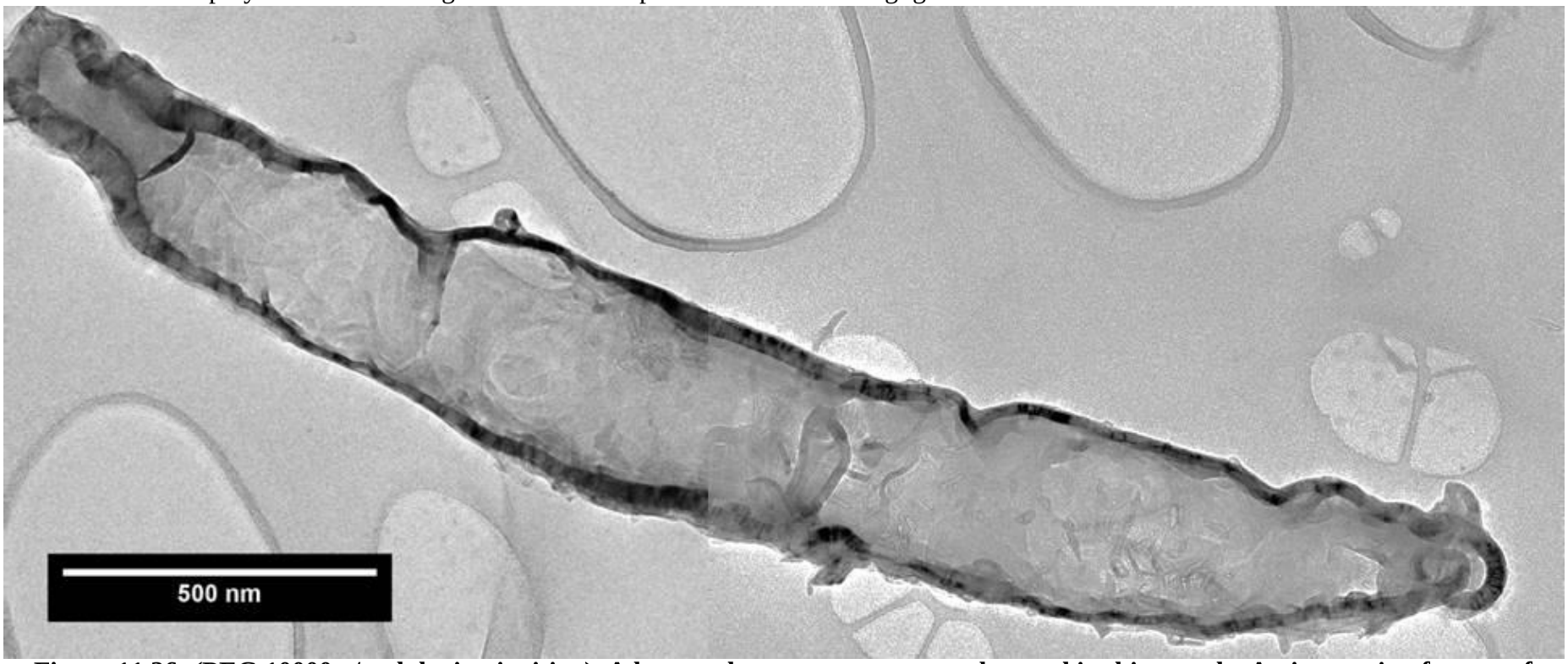

Figure 11.26: (PEG 10000 g/mol during ignition). A large polymer structure was observed in this sample. An interesting feature of this structure is the boundary that encloses it. Within the polymer, many different structures can be observed. The following images represent magnified sections of this structure.

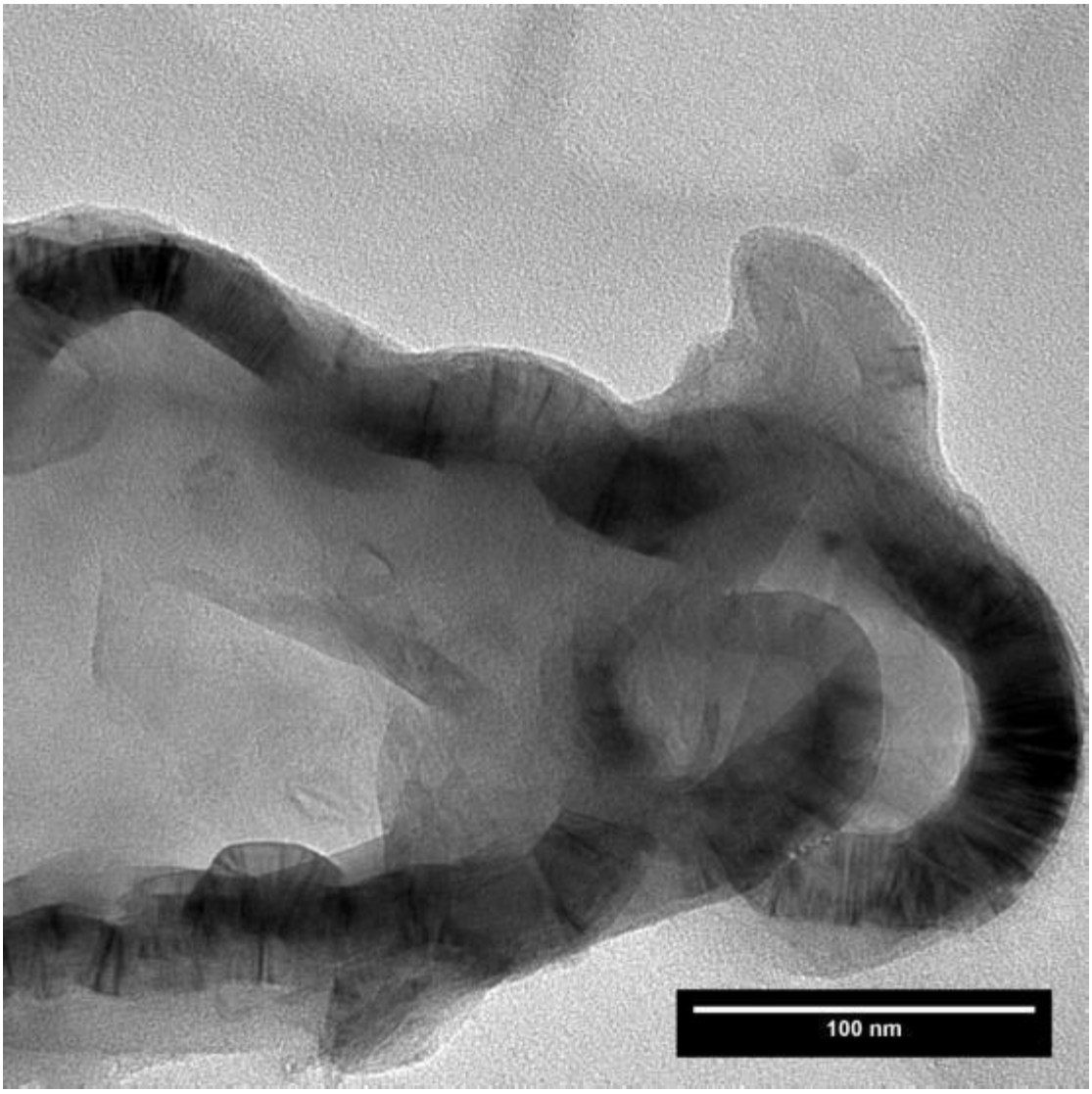

Figure 11.27: (PEG 10000 g/mol during ignition). A magnified image of the right hand side of the structure observed in figure 11.26. The outside boundary appears to loop causing the internal structure to change, and may be indicative of a polymer reaction chamber.

The similarity of internal components observed ion figures 11.21 and 11.28 suggests that both PEG and crystallised carbon generated from PEG play a role in the formation of titania nanoparticles using the resin-gel synthesis method.



Figure 11.28: (PEG 10000 g/mol during ignition). The internal components of this portion of the superstructure are similar to that observed in figure 11.21.

11.3 Conclusions

The facile methods employed in this study for the direct observation of the mechanism of resin-gel synthesis proved successful. Liquid N_2 induced quenching showed the presence of large polymer fragments with few associated nanoparticles. This was in contrast to the aluminium rod generated molten drops experiment that exhibited greater success at displaying the interactions between polymer fragments and nanoparticles. Additionally, the latter experiment produced better images on account of the lower sample volume employed in the experiment. This method also allowed for better precision with less sample wastage for each timed snapshot.

PEG and crystalline carbon formed interesting structures that existed as – or decomposed to form – reaction chambers. Various shaped PEG and/or carbon material such as sheets, superstructures, and spheres were observed. This experiment produced positive evidence of carbon material folding back on itself to form cavities. These cavities likely served as titania nucleation and protection sites. Despite both experiments failing to prove which type of structures resulted in the formation of anatase and rutile, they did provide visual evidence of the hypothesised reaction chambers that exist in various sizes.

Evidence of polymer fragments present late during the reaction progression elucidates why the amounts of anatase and rutile varied before and after calcination – as previously hypothesised.

Observed titania existed as nanorods, mesocrystals and aggregated nanoparticles. These findings are consistent with previously obtained TEM data in this study. This suggests that the experiment did not cause any abnormal results.

Imaging a sparsely grown rutile mesocrystal lent credibility to the developed hypothesis on their formation under the conditions of resin-gel synthesis.

11.4 References

1. Spurr, R. A. & Myers, H. Quantitative Analysis of Anatase-Rutile Mixtures with an X-Ray Diffractometer. *Analytical Chemistry* **29,** 760 – 762 (1957).

2. Ranade, M. R. *et al.* Energetics of nanocrystalline TiO2. *Proceedings of the National Academy of Sciences of the United States of America* **99,** 6476 – 6481 (2002).

3. Zhang, H., Finnegan, M. & Banfield, J. F. Preparing Single-Phase Nanocrystalline Anatase from Amorphous Titania with Particle Sizes Tailored by Temperature. *Nano letters* **1,** 81 – 85 (2001).

4. Zhang, H. & Banfield, J. F. Kinetics of Crystallization and Crystal Growth of Nanocrystalline Anatase in Nanometer-Sized Amorphous Titania. *Chemistry of Materials* **14,** 4145 – 4154 (2002).

5. Hocine, S. & Li, M.-H. Thermoresponsive self-assembled polymer colloids in water. *Soft Matter* **9,** 5839 – 5861 (2013).

6. Kakiuchi, K., Hosono, E., Imai, H., Kimura, T. & Fujihara, S. {1 1 1}-faceting of low-temperature processed rutile TiO2 rods. *Journal of Crystal Growth* **293,** 541 – 545 (2006).

7. Gribb, A. A. & Banfield, J. F. Particle size effects on transformation kinetics and phase stability in nanocrystalline TiO2. *American Mineralogist* **82,** 717 – 728 (1997).

8. Penn, R. L. & Banfield, J. F. Formation of rutile nuclei at anatase {112} twin interfaces and the phase transformation mechanism in nanocrystalline titania. *American Mineralogist* **84,** 871 – 876 (1999).

9. Kiang, C. H., Endo, M., Ajayan, P. M., Dresselhaus, G. & Dresselhaus, M. S. Size Effects in Carbon Nanotubes. *Physical Review Letters* **81,** 1689 – 1872 (1998).

Chapter 12: Conclusions

The facile, yet accepted working theory of resin-gel synthesis was that metal ions bond to a coordinating polymer. Segregation and precipitation of the metal ions were prevented by the polymer until resin ignition forced the formation of nanoparticles. Understanding the underlying mechanism and nuances of nanoparticle formation using resin-gel synthesis is imperative to harnessing its ability to form multi mixed metal oxides with varying stoichiometries. Due to the many tuneable parameters available in resin-gel synthesis, this technique has the advantage of affording control over particle size, shape, purity, morphology, and phase composition. The benefits of this technique can only be applied to other systems once the mechanism of nanoparticle formation is understood. Therefore, the primary goal of this investigation was to describe the mechanism of nanoparticle formation by altering various parameters and observing changes in TiO_2 crystalline phases and crystallite sizes. Studies were conducted in order to determine the effects of the type of polymer, solvent, acid, and metal ion precursor. Other parameter variations explored the effects of polymer chain length and stoichiometry, and variations in heating rates toward resin ignition. Finally, temporally controlled intermittent resin-gel syntheses were conducted in order to observe directly, the interaction between metal ions and resin components. A consequence of titania synthesis was the formation of rutile mesocrystals. Therefore, the formation mechanism for rutile mesocrystals under the conditions of resin-gel synthesis was described as a secondary aim.

12.1 Conclusion 1

Approaching a system as unknown as resin-gel synthesis, a few preliminary investigations were deemed necessary in order to obtain rudimentary information about PEG degradation and ideal synthesis conditions. To this end, TG analysis was performed on as-received PEG of various molecular weights. The results revealed that under oxidative conditions, the onset of decomposition occurred $\geq$ 175 °C with higher temperatures necessary for longer chain PEG. Given that all PEG samples had completely decomposed at 500 °C, the calcination temperature for the remainder of this study was ascertained. Subtle differences were observed in the degradation profiles of as-received and loaded PEG. This led to the development of a gas heating

ring and sand bath heating system to be employed for the conventional degradation of resins in the remainder of this study.

12.2 Conclusion 2

The second preliminary investigation involved systematically removing oxygen from each component in the system in an attempt to obtain optimum synthesis conditions for the conduction of all further resin-gel syntheses. The primary discovery was that TiO_2 formed in all samples containing at least one oxygen-containing component. This implied that all further investigations could be conducted under normal atmospheric conditions. Except for when oxygen was included in all reaction components, anatase was the preferred phase formed. The effects of an oxygen-containing (PEG) and an oxygen-free polymer (PEI) were also established: under the same atmospheric and solvent conditions, PEI favoured the formation of anatase compared with PEG that favoured rutile formation. TEM imaging of unignited samples revealed the presence of superstructures exhibiting short-range crystallinity. The composition of these structures suggested that they were decomposition products of the polymer.

12.3 Conclusion 3

Until now, the role of the solvent in resin-gel syntheses was assumed unimportant to the products formed. Therefore, a subsequent study was concerned with varying the type of solvent employed in the reaction and monitoring the titania products formed as a function of increasing PEG molecular weight. The results revealed that ethanol produced nearly phase pure anatase for certain PEG chain lengths (200 – 20000 g/mol). Anatase was produced as the majority phase when long chain PEG (35000 g/mol) was employed in the reaction. When water containing HNO_3 was used as the solvent, rutile was the preferred phase formed (by considering the average amount of rutile formed across all PEG molecular weights). Unlike for samples synthesised in ethanol, rutile formation was dependent on PEG molecular weight, when water containing HNO_3 was employed as the solvent. With good reproducibility, it was found that certain PEG chain lengths produced nearly phase pure rutile, compared with others that produced a mixture of polymorphs. This led to an up and down effect of the amount of rutile formed as a function of PEG chain length. Intriguingly, the amount of rutile formed displayed an inversely proportional relationship with the

average rutile crystallite size formed as a function of increasing PEG molecular weight. This inverse relationship was previously observed in literature for the formation of brookite as a function of time. However, its presence for rutile as a function of PEG molecular weight was a novel finding.

Based on the literature finding that PEG chain length affects metal ion coordination, and the PEG superstructures observed in the preliminary investigations, the concept of the formation of PEG reaction chambers was conceived. The formation of these chambers was used as a means to explain the up and down effect of the amount of rutile formed as a function of increasing PEG molecular weight observed in this study.

12.4 Conclusion 4

Following these findings, the rate of polymer degradation was increased by increasing the heating rate while keeping all other reaction parameters consistent. The primary aim was to develop further, the newly conceived model for nanoparticle formation using resin-gel synthesis. As expected, enhanced heating produced larger crystallites on average, than conventional heating. Under enhanced heating, the use of ethanol as a solvent produced nearly phase pure anatase independent of PEG of certain chain lengths (200 – 20000 g/mol). This implied that ethanol was a greater determinant of phase formation than heating rate. The amounts of anatase formed (and anatase crystallite size formed) were similar for PEG 35000 g/mol regardless of the heating rate used. When water containing HNO_3 was employed as the solvent under enhanced heating, the results obtained were significantly different to those obtained using conventional heating. Enhanced heating using water containing HNO_3 showed a clear dependence on the PEG chain length employed in the synthesis: low molecular weight PEG produced almost no rutile, medium molecular weight PEG produced a mixture of anatase and rutile, and high molecular weight PEG produced nearly phase pure rutile. Despite these differences, the amount of rutile formed was inversely proportional to its respective crystallite size – as previously observed with conventional heating.

12.5 Conclusion 5

A subsequent study aimed at lending credibility to the hypothesis that solvent components affect TiO_2 nucleation within polymer reaction chambers. Literature studies revealed that the use of citric acid favoured the formation of anatase over

rutile in sol-hydrothermal and hydrothermal processing. Citric acid served to cap nucleating anatase crystals, protecting and stabilising their surfaces, and inhibiting transformation into rutile. Thus, in this investigation, citric acid was added to water and a range of PEG molecular weights. The results revealed that the average amount of anatase formed across all samples equalled 99.6%. This result implied that solvent components were actively involved in crystal stabilisation within the polymer reaction chambers. This experiment proved that polymer chains coordinate to metal-hydroxyl complexes formed between metal ions and solvent components.

12.6 Conclusion 6

The next phase of this investigation concentrated on the impact of polymer concentrations in resin-gel synthesis, with the aim of further advancing the mechanism of nanoparticle formation. Altering the PEG concentration has the effect of changing the fuel to metal ion ratio, among other effects. Three ratios of metal ions to the number of PEG chains were employed. It was found that the ratio of Ti^{4+} : PEG in a (1 : 1), (1 : 0.5), and (1 : 0.1) ratio altered the amount and size of anatase and rutile crystallites formed. Since water containing HNO_3 was used as the solitary solvent, the effects of polymer concentration on rutile were scrutinised. For synthesis in a (1 : 1) and (1 : 0.5) ratio, similar amounts of rutile were formed for short and medium chain PEG. For long chain PEG, samples synthesised in a (1 : 0.5) ratio resulted in significantly more rutile formation than samples synthesised in a (1 : 1) ratio. The data also suggested that synthesis in a (1 : 0.1) ratio favoured the formation of rutile when long chain PEG was employed in the synthesis.

12.7 Conclusion 7

Subsequently, the interplay between polymer concentration and a rapid rate of degradation were investigated. The results obtained would be used to bridge any gaps in the current model for polymer degradation and particle formation using resin-gel synthesis. After synthesising samples across a range of PEG molecular weights in (1 : 1) and (1 : 0.5) ratios, the resins underwent spontaneous ignition in a pre-heated cast-iron vessel at 915 °C. The decrease in peak intensity in PXRD patterns for samples synthesised using long chain polymers in a (1 : 1) synthesis signalled the presence of undecomposed polymer within the TiO_2 samples. This finding was supported by the low thermal conductivity of PEG and the thermal protection afforded by hydrogen

bonded water molecules. When these two factors were added to the polymer reaction chamber model, they successfully accounted for the similarity in amounts of rutile formed using rapid and conventional heating of stoichiometrically synthesised TiO_2. The rate of polymer decomposition had a greater impact on crystallite size, compared with the amount of PEG in the mixture that had a greater impact on the amount of rutile formed.

12.8 Conclusion 8

The final parameter variation study was concerned with changing the metal ion precursor and observing changes in the amount and size of TiO_2 crystallites. Based on the steric effects of slightly larger solution components (ethanol and citric acid) favouring the formation of anatase, it was assumed that increasing the size of the ligands attached to the titanium ion precursor would also favour anatase formation. Therefore, the formation of anatase in this study would serve as a successful test for the developed mechanism. However, non-exclusive anatase formation would allow the mechanism to be modified and refined to include contributions from the formation of metal hydroxyl complexes and polymer coordination to these complexes.

The use of titanium (IV) oxysulfate produced anatase as the major phase with a dependence on PEG chain length that was different to all previously obtained data. This was due to the presence of sulphur species serving as directing agents and favouring the formation of anatase. Because the sulphur species were not as proficient as citrate ions at stabilising the anatase phase, anatase formation was dependent on the size of polymer reaction chambers set up during the reaction. Removing sulphur species from the solution by the addition of $BaSO_4$ to $TiOSO_4$ produced results that were similar to when $TiCl_4$ was employed as the precursor, proving that the precursor ligands influenced the formed phase as described. The PEG chain length dependence on the amount of anatase formed when titanium (IV) (triethanolaminato) isopropoxide and titanium (IV) 2-ethylhexyloxide was similar. Both precursors were comprised of ligands that somewhat inhibited polymer chains from coordinating to oxygen atoms on the precursors. A poor association between polymer chains and hydroxylated precursors reduced the protection and stabilisation effects afforded by reaction chambers and hence resulted in rutile transformation. Titanium (IV) isopropoxide formed similar amounts of anatase as a function of increasing PEG molecular weight as $TiCl_4$ in water containing HNO_3. Since the structures of the formed hydroxylated

species were similar, it was concluded that the presence of small carbon chain solvent remnants within the polymer reaction chambers favoured anatase formation. Titanium diisopropoxide bis(acetylacetonate) and titanium (IV) bis (ammonium lactato) dihydroxide formed phase pure and nearly phase pure anatase respectively. Since the structures of these two precursors differed from titanium (IV) isopropoxide, the mechanism of anatase formation was dependent on other factors. It was concluded that the large number of accessible oxygen sites on the hydroxylated precursors available for coordination to the polymer increased the protection and stabilisation effects afforded by the reaction chambers. The protection effect was amplified by the presence of stabilising ligands within the reaction chambers.

The summarised results obtained from this study revealed that all metal ion precursors favoured the formation of phase pure or near phase pure anatase. PEG chain length played a deciding factor in the amount of anatase formed only if the size and constituents of the precursors were sub-optimum. Crystallite size was significantly dependent on PEG chain length.

12.9 Conclusion 9

Finally, attempts were made at directly observing aspects of resin-gel synthesis under TEM. The methodology was crude and qualitative in nature but provided visual validity of the proposed mechanism of polymer reaction chamber with associated nanoparticle formation. The results from liquid N_2 quenched samples revealed the presence of polymer sheets later during heating. This finding explained the variation in the amounts of anatase and rutile formed pre- and post-calcination. The experiment also yielded evidence of crystals that had undergone oriented attachment. The aluminium rod generated molten drops experiments revealed many PEG generated reaction chambers with associated nanoparticles. These structures appeared to fold back on themselves forming cavities. Spherical cavities exhibited an intershell spacing equalling 0.326 nm. This is consistent with the literature obtained value for multi-walled carbon nanotubes and hence provided positive evidence that the observed structures were composed of carbon generated from PEG. Additionally, reaction chambers were found to exist within larger polymer structures, later on during the reaction.

12.10 Conclusion 10

Rutile mesocrystals exhibiting various morphologies were observed. Depending on the reaction conditions, they presented as variable sized structures with numerous rutile nanorods and sections within the mesocrystal. Individual nanorods were found to be single crystal in nature and pyramidically capped. This is consistent with literature findings of rutile mesocrystals.

With the understanding of nanoparticle formation, various parameters involved in resin-gel synthesis can be manipulated to fabricate bespoke materials. For example, the stoichiometry of a mixed metal oxide may be altered by selecting two different metal ion precursors: one that is oxygen deficient (or that contains large ligands) and one that has many available oxygen sites for association to the polymer and small ligands. The biased association and protection afforded by the polymer to the two different precursors will then control the amount of each metal present in the final material. In a similar manner, phase purity of a mixed metal oxide can be tailored by adjusting the solvent used in the synthesis. It is possible to form a predictable mixture of phases based on the contents of the solvent and size of the coordinating polymer. Finally, a plethora of different crystalline material can be fabricated by using the correct combination of each metal with an appropriate solvent, and then adding each of these solutions to a communal coordinating polymer.

Refer to appendix J for a thorough discussion on plausible explanations for all concluding remarks made in this chapter.

Chapter 13: Proposals for Further Studies Related to Resin-gel Synthesis

With a synthetic technique in its infancy, there is considerable room to improve understanding. A three-pronged approach should be taken to contextualise and expedite work concerning resin-gel synthesis:

1) increased parameter variation studies to provide more insights into the mode of operation
2) quantitative studies that precisely measure various occurrences during a typical resin-gel reaction
3) applying the resin-gel method to the synthesis of multi component oxides to produce functional materials that can be accommodated into the voids of current and future problems

13.1 Parameter Variation Studies

The type of parameter variation studies that can still be achieved is limited only by the extent of imagination. Some parameter variation studies that can follow include investigating the effects of a combination of two or more solvents with various dielectric constants. In a similar manner, the effects of a combination of two or more coordinating polymers (or co-block polymers) or molecular weights of the same polymer may yield interesting results. By extension, employing the use of a precursor containing different metal ions may lead to the formation of a material with exotic properties. With an appropriate combination of starting materials, it may be possible to form crystallites that exhibit different morphologies in different parts of the particle. This may eventually lead to the synthesis of striated or layered materials. Microwave radiation has not yet been employed as a heating source. Given that microwave heating creates localised hotspots within the reaction matrix, and that the formation of nanoparticles is predicated on the formation of polymer reaction chambers, the ability to synchronise heating to specific reaction chambers may result in the formation of interesting materials. The effects of varying the ratio of metal ions to polymer monomer units have not yet been investigated. The results of a similar study should provide interesting results regarding the binding capabilities of polymer units under different conditions. Additionally, the present investigation did not

consider the effects of varying the concentration of metal ions in the mixture. Depending on the interplay between polymer concentration and solvent type, the concentration of the metal ion precursor may serve as a vector of control for phase or crystallite size formed. Finally, the complete removal of oxygen from the system in a preliminary investigation in this study revealed the presence of hollow-shell structures. While this technique has not yet synthesised nitrides, sulphides, or carbides, it will be interesting to perform a complete investigation on the formation of products from an oxygen-deprived system. It is theoretically possible, as long as an appropriate coordinating solvent and metal ion is used, to form something other than an oxide using resin-gel synthesis.

13.2 Quantitative Studies

The present study used the results from several parameter variation studies to create and then refine the mechanism of particle formation. However, the experiments did not accommodate quantitative work. For example, investigating the differences in the rates of heat transfer between polymers of various molecular weights, stoichiometries, and metal loading concentrations will allow for better control over formed products. New insights may be gained from applying a model (such as the Flory-Huggins solution theory model) to calculate the enthalpy, entropy, and ultimately Gibbs free energy associated with polymer-polymer, polymer-solvent, and solvent-solvent interactions. A solid-state NMR investigation into pre-heated resin samples will potentially allow for the exact coordination between PEG and metal ion complexes to be established. The present study would have benefitted from VT-XRD analysis of polymer degradation. Therefore, a future study could be to understand the kinetics of polymer degradation and phase transformation during heating and possibly ignition. This technique combined with *in situ* HRTEM equipped with a hot stage will allow for continued monitoring of the reaction and provide accurate data on the formation of reaction chambers. Finally, Raman analysis on partially synthesised samples will reveal the quantity of crystallised carbon material in the presence of degraded, polymer-derived structures. This information can improve the understanding of how nanoparticles develop within polymer reaction chambers with different carbon contents.

13.3 Applications of Resin-gel Synthesis

As a final consideration, future work can be directed at harnessing the power of resin-gel synthesis. Indeed, at the University of the Witwatersrand, insights gained from this work have been applied to the resin-gel synthesis of beta alumina sheets for use in batteries. Other ongoing research at this institution is focussed on using this technique for the fabrication of quaternary mixed metal oxides for photovoltaic and photocatalytic applications. At the University of Cambridge, the quaternary oxide system Bi_2O_3-CeO_2-Nb_2O_5 was successfully synthesised in nanoparticulate form using resin-gel synthesis. This material could potentially possess interesting characteristics that will be of benefit in a given application. For example, in the case of high temperature superconductors, current materials incorporate the use of mixed metal oxides. Resin-gel synthesis may have the ability to more easily form these materials, or different materials that have not yet been created.

Appendix A. JCPDS Powder Patterns and PXRD and (HR)TEM Components

A.1. JCPDS Powder Patterns for Titanium Dioxide Polymorphs

Figures A.1, A.2 A.3 show the JCPDS data cards for rutile, anatase and brookite respectively[1]

82-0514 Quality: C
CAS Number:
Molecular Weight: 79.90
Volume[CD]: 61.51
Dx: 4.314 Dm:
Sys: Tetragonal
Lattice: Primitive
S.G.: $P4_2/mnm$ (136)
Cell Parameters:
a 4.508 b c 3.027
α β γ
I/Icor: 3.43
Rad: CuKa1
Lambda: 1.54060
Filter:
d-sp: calculated
ICSD # : 074532
Mineral Name:
Rutile

Ti O2
Titanium Oxide
Ref: Calculated from ICSD using POWD-12++, (1997)
Ref: Lacks, D.J., Gordon, R.G., Phys. Rev. B: Condens. Matter, 48, 2889 (1993)

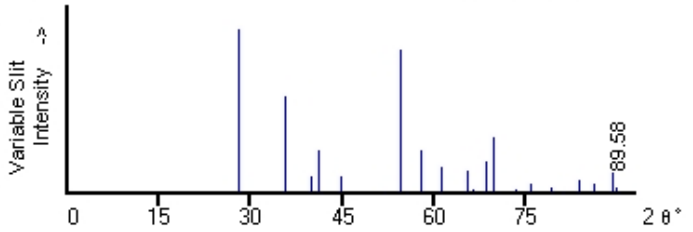

2θ	Int-v	h	k	l	2θ	Int-v	h	k	l	2θ	Int-v	h	k	l
27.968	100	1	1	0	61.188	14	0	0	2	76.063	1	3	2	0
35.700	58	1	0	1	65.415	12	3	1	0	79.050	2	2	1	2
39.967	9	2	0	0	66.214	1	2	2	1	83.607	7	3	2	1
41.089	25	1	1	1	68.584	18	1	1	2	86.235	5	4	0	0
44.926	9	2	1	0	69.823	32	3	0	1	89.154	12	2	2	2
54.655	86	2	1	1	73.350	2	3	1	1	89.584	2	4	1	0
57.803	25	2	2	0	75.620	4	2	0	2					

Figure A.1: JCPDS card for rutile.

84-1286 Quality: C
CAS Number:
Molecular Weight: 79.90
Volume[CD]: 135.93
Dx: 3.904 Dm:
Sys: Tetragonal
Lattice: Body-centered
S.G.: $I4_1/amd$ (141)
Cell Parameters:
a 3.782 b c 9.502
α β γ
I/Icor: 5.05
Rad: CuKa1
Lambda: 1.54060
Filter:
d-sp: calculated
ICSD # : 202243
Mineral Name:
Anatase, syn

Ti O2
Titanium Oxide
Ref: Calculated from ICSD using POWD-12++, (1997)
Ref: Burdett, J.K et al., J. Am. Chem. Soc., 109, 3639 (1987)

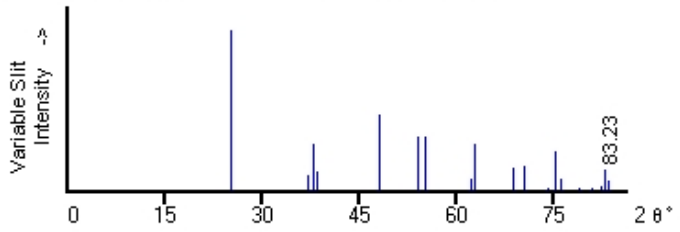

2θ	Int-v	h	k	l	2θ	Int-v	h	k	l	2θ	Int-v	h	k	l
25.325	100	1	0	1	62.165	6	2	1	3	78.754	0	2	0	6
36.989	9	1	0	3	62.750	28	2	0	4	80.860	1	0	0	8
37.841	28	0	0	4	68.842	13	1	1	6	82.236	2	3	0	3
38.601	11	1	1	2	70.346	14	2	2	0	82.759	13	2	2	4
48.074	46	2	0	0	74.155	1	1	0	7	83.232	5	3	1	2
53.952	33	1	0	5	75.129	24	2	1	5					
55.106	33	2	1	1	76.100	6	3	0	1					

Figure A.2: JCPDS card for anatase.

76-1937 Quality: C

CAS Number:

Molecular Weight: 79.90
Volume[CD]: 260.63
Dx: 4.072 Dm:

Sys: Orthorhombic
Lattice: Primitive
S.G.: Pbca (61)
Cell Parameters:
a 9.211 b 5.472 c 5.171
α β γ

I/Icor: 1.61
Rad: CuKa1
Lambda: 1.54060
Filter:
d-sp: calculated

ICSD # : 036411

Mineral Name:
Brookite

Ti O2
Titanium Oxide
Ref: Calculated from ICSD using POWD-12++, (1997)
Ref: Meagher, E.P., Lager, G.A., Can. Mineral., 17, 77 (1979)

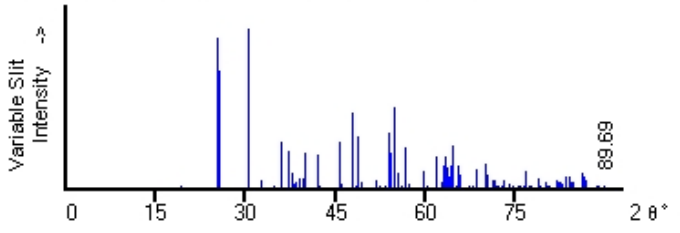

2θ	Int-v	h	k	l	2θ	Int-v	h	k	l	2θ	Int-v	h	k	l
19.257	0	2	0	0	49.462	4	1	2	2	64.656	26	1	2	3
25.255	93	2	1	0	51.854	4	4	2	0	65.197	1	4	3	0
25.578	73	1	1	1	52.556	0	2	2	2	65.642	14	6	1	1
30.679	100	2	1	1	53.225	2	4	0	2	65.806	8	2	3	2
32.705	4	0	2	0	54.031	34	2	3	0	67.289	0	2	2	3
34.667	0	0	0	2	54.202	21	1	3	1	67.968	0	4	3	1
36.052	29	1	0	2	55.020	50	4	2	1	68.539	12	0	4	0
37.147	23	0	2	1	55.507	9	5	1	1	70.130	15	3	3	2
37.805	9	3	1	1	56.010	1	4	1	2	70.298	8	4	1	3
38.231	3	2	2	0	56.842	25	1	1	3	71.247	5	0	4	1
38.455	3	1	2	1	57.449	3	3	2	2	71.402	4	6	0	2
39.086	5	4	0	0	59.670	11	2	1	3	71.570	5	3	2	3
39.749	6	1	1	2	60.234	1	6	0	0	71.684	3	5	2	2
39.957	21	2	0	2	61.784	19	3	3	1	71.946	1	2	4	0
42.172	20	2	2	1	61.784	19	5	0	2	72.091	1	1	4	1
42.560	1	4	1	0	62.818	3	6	1	0	72.930	1	6	2	1
43.373	1	2	1	2	63.141	13	1	3	2	73.148	4	0	0	4
45.846	29	3	0	2	63.423	19	5	2	1	73.782	1	6	1	2
46.197	2	4	1	1	63.766	13	0	2	3	73.984	3	1	0	4
47.840	47	3	2	1	63.887	7	4	2	2	74.601	0	2	4	1
48.399	1	0	2	2	64.211	9	3	1	3	75.567	0	5	3	1
48.932	32	3	1	2	64.332	14	5	1	2	75.997	0	4	3	2

Figure A.3: JCPDS card for brookite.

A.2. Powder X-ray Diffraction

A.2.1. Components of a PXRD

Two diffractometers with Bragg-Brentano geometry were employed in this study: 1) Bruker D2 Phaser (figure A.4) with a Cu Kα or Co Kα radiation source, a Ni Kβ filter, a 0.6 mm slit, secondary Söller slits at 2.5 °, a LynxEye™ detector, and a θ-θ goniometer. 2) Siemens D5000 with a Cu Kα radiation source, a forty-position automatic sample changer, variable aperture, stepping motor controlled incident- and diffracted-beam slits, a bent graphite crystal secondary monochromator, Söller slits at 2°, a scintillation counter, and a θ-2θ goniometer. This section shall discuss the need for and use of various components in a powder diffractometer and is largely based on Chapter 2: Experimental Setups (Cockcroft and Fitch) from Powder Diffraction: Theory and Practice (Dinnebier and Billinge)[2].

A.2.1.1. X-ray Source

X-rays are generated using a sealed X-ray tube. Electrons are emitted thermionically from the filament and are accelerated toward a metal anode inside the vacuum tube[3]. These collisions causes a series of electronic transitions in the target material instigating it to emit electromagnetic radiation as the electrons return to the ground state. A continuous spectrum of generated X-rays (Bremsstrahlung) exits the tube through beryllium windows. Figure A.5 shows a schematic of a typical X-ray tube and a photograph of an actual tube.

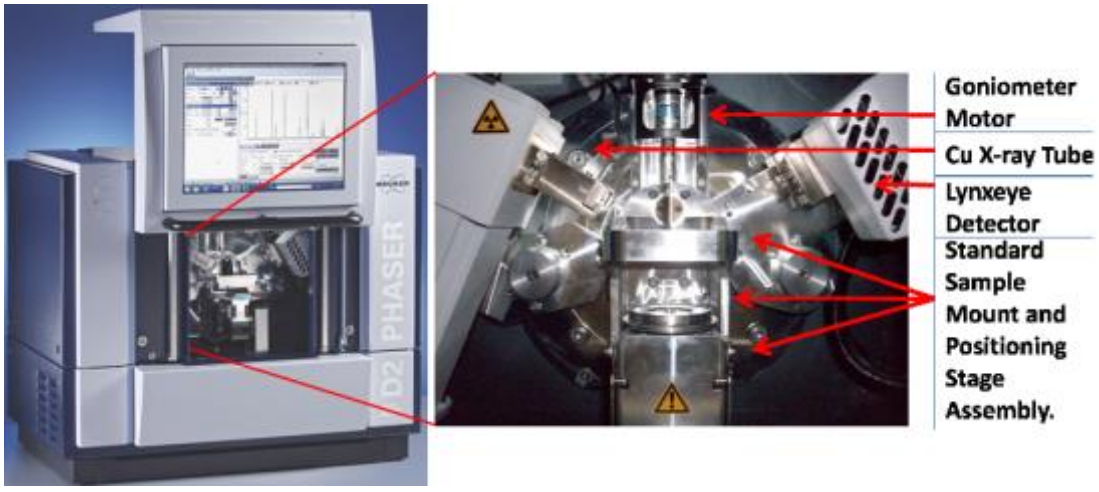

Figure A.4: (left) Bruker D2 Phaser diffractometer. (right) Internal mechanics of the D2 showing X-ray source, sample loading assembly and detector[4]. The source and detector rotate along the θ-θ goniometer respectively.

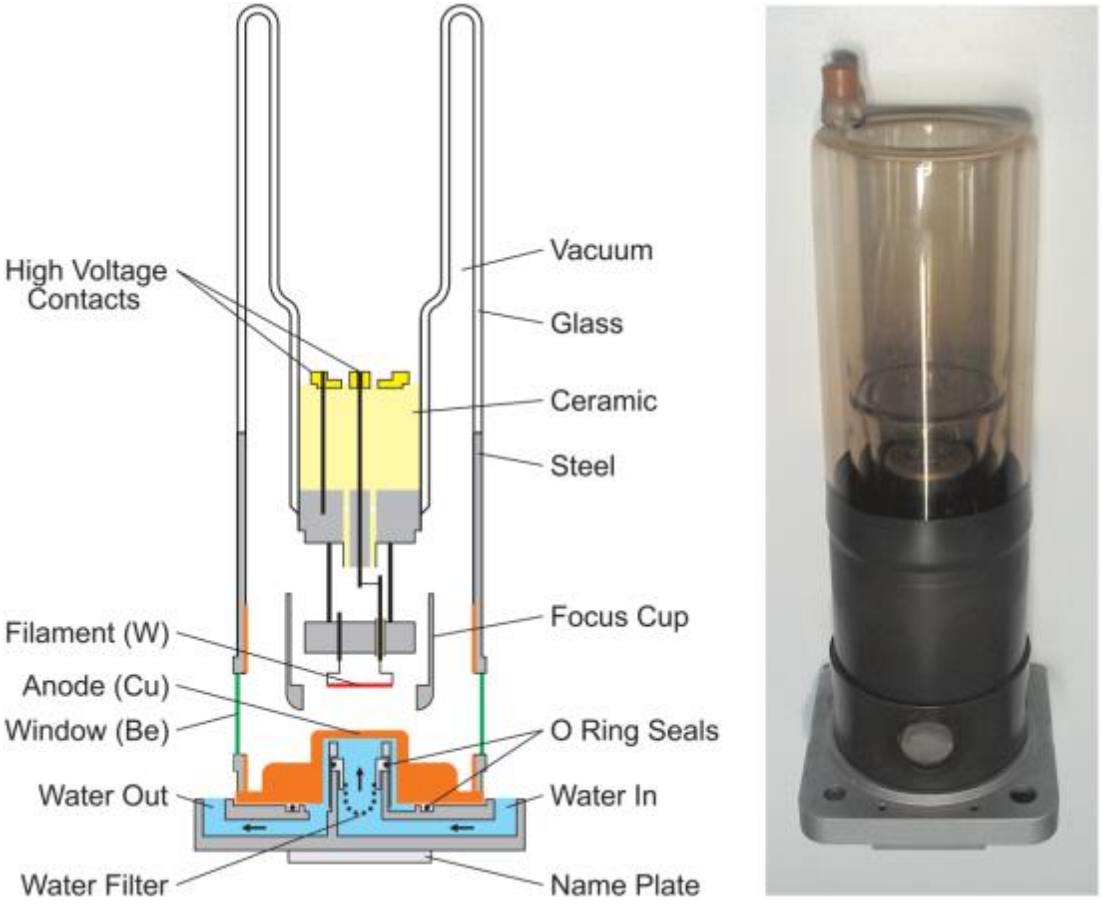

Figure A.5: (left) Schematic of a sealed X-ray tube. (right) Photograph of an actual X-ray tube[2].

The maximum energy lost can be tuned by employing different acceleration voltages and altering the source material. When the energy of accelerated electrons surpasses a threshold value, characteristic radiation peaks are superimposed onto the Bremsstrahlung as a result of the ejection of an electron from an inner electron shell of the atom. An electron from a higher energy level moves to fill the newly created vacancy and emits X-radiation with energy equivalent to the difference in energy between the two levels. This characteristic radiation is target material dependent and typically the required voltage to induce characteristic radiation is approximately 3.5 – 4 times the energy of the characteristic X-ray[3].

The characteristic wavelengths of generated X-rays used for analysis in this study were 1.54 Å (for Cu Kα) and 1.79 Å (for Co Kα). One of the reasons for Cu being a popular anode material in the generation of monochromatic radiation is due to its high thermal conductivity[3]. A full discussion on using Lorentzian functions to model the

peak shape of Kα radiation and understanding the asymmetry of different α lines can be found in the literature[5].

A.2.1.2. Filters

Once X-rays leave the tube and before they reach the sample, they must be filtered to select for the desired wavelength. When the target anode material is Cu, a thin, uniform sheet of Ni typically serves as the filter material. This is due to Ni having an absorption edge (1.488 Å) that is just lower than the energy of Cu Kβ X-rays (1.392 Å). Cu Kα X-rays do not possess sufficient energy to enable the Ni transition and therefore pass through the material with a low absorption rate.

A.2.1.3. Slits

Several slits (incident and detector beam Söller, divergence, anti-scatter, and receiving – figure A.6) are found at different positions within the beam path (figure A.7). Slits serve to collimate the incident and diffracted beam since diffractometers typically employ a line source of radiation[3]. The divergence slit determines the irradiated lengths on the sample by controlling the equatorial divergence of the incident beam[3]. Axial divergence is controlled by the incident and detector beam Söller slits. This is accomplished by the Söller slits by slicing the incident beam into a beam stack, each possessing low axial divergence[3]. By controlling equatorial divergence, the anti-scatter slit determines the observed length on the detector. The detector position is defined by the receiving slit[3].



Figure A.6: (left) A typical X-ray slit that is 0.3° in size. (right) Söller slits are composed of fine parallel foils[2].

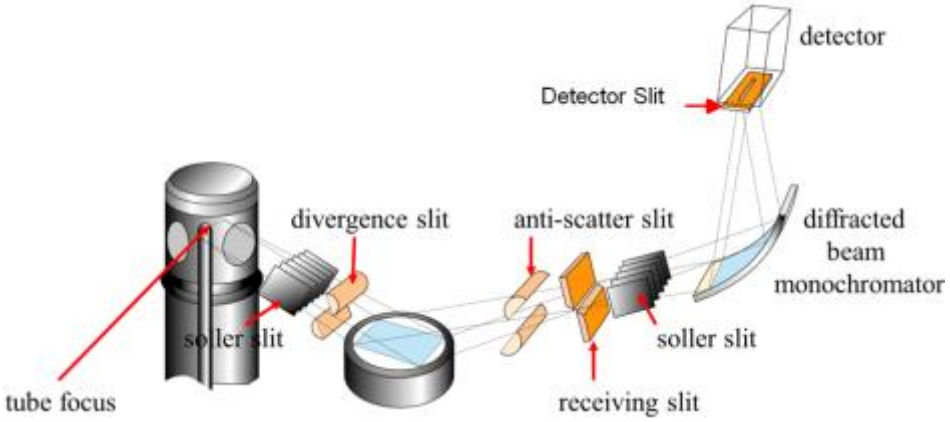

Figure A.7: Components of a powder diffractometer showing positions of the slits, sample and monochromator and detector in the beam path[6].

A.2.1.4. Sample Holders

Two instrument specific sample holders were employed in this study (figure A.8): in the D2 Phaser diffractometer, a flat-plate, shallow-well sample holder containing a zero-background Si crystal was used. In the D5000 diffractometer, fixed, non-rotating, flat-plate, shallow-well sample holders were used in a forty-position automatic sample changer. The primary benefit of employing flat-plate sample holders is that they are easy to fill. A Si crystal cut along planes that do not satisfy the Bragg equation provides a zero-background upon which the samples may be mounted. A disadvantage of using flat-plate sample holders is the procedure used to create a uniform sample surface height since flattening the sample can induce preferred orientation in some samples. Another disadvantage is the loss of sample by falling out of the sample holder while being rotated along the θ-2θ goniometer of the D5000. Flat-plate sample holders do not shield air-sensitive samples against the environment. To obtain a good, averaged powder pattern, the sample is typically spun about an axis normal to the flat-plate. The position of the sample in the path of the beam is given in figure A.7.



Figure A.8: Flat-plate, shallow-well sample holders. (left) Filled and unfilled Si zero-background sample holders used in the D2 Phaser. (right) Non-rotating sample holder used in the forty-position sample changer of the D5000.

A.2.1.5. Monochromators

Crystal monochromators serve two primary purposes: to produce highly monochromatic radiation and to form an intense convergent X-ray beam to improve the signal-to-background ratio of the diffraction pattern[3, 7]. These large, flat, thin, single crystals are placed in a particular orientation in the incident or diffracted beam such that one set of planes that diffract strongly is at the Bragg angle to the beam[7]. The Bragg angle is calculated for a desired wavelength. A monochromator placed in the path of the incident beam serves to eliminate diffracted Bremsstrahlung and other contamination radiations but does not prevent the detection of fluorescence from the sample[3]. Si, Ge, quartz, diamond and graphite are typically used materials for monochromators[2]. Separating $K\alpha_1$ from $K\alpha_2$ and $K\beta$ radiation has the effect of reducing overall intensity. To counter this effect, the crystal is curved[2]. The position of the monochromator in the path of the beam is given in figure A.7.

A.2.1.6. Detectors

Three classifications of detectors are point, linear, and area detectors (linear and area detectors are types of position sensitive detectors) that record the diffraction pattern in zero, one or two spatial dimensions respectively. Linear and area detectors can be fixed as opposed to point detectors that must be scanned in order to measure the diffraction pattern. The LynxEye™ detector is an example of a linear detector.

Linear detectors are classified as single or multiple anode devices that serve to measure the 2θ position of arrival of each X-ray. Single anode devices possess a wire

or blade contained in a gas-filled chamber. X-rays ionize the inert gas into an electron and ion pair. The generated electrons accelerate toward the anode which results in further ionization causing signal enhancement by gas amplification. A charge pulse is caused by the electrons interacting with the wire or blade at both ends. A comparison of the relative arrival time of the pulse at both ends of the wire or blade enables the position of the X-ray to be obtained. Quenching gas is added to the inert gas to reduce the dead time of the system. Higher count rates are possible due to multi-wire anodes such that each wire serves as an independent detector.

A.2.1.7. Goniometers

The goniometer is a mechanical device that provides precise movements to control the angles between the radiation source, sample, and detector[3]. In the D2 Phaser diffractometer, the goniometer keeps the sample fixed in position and rotates the X-ray tube and the detector along θ-θ. This is in contrast to the D5000 where the goniometer fixes the X-ray tube and rotates the sample and detector along θ-2θ. The goniometer path in relation to various components of the diffractometer is given in figure A.9.

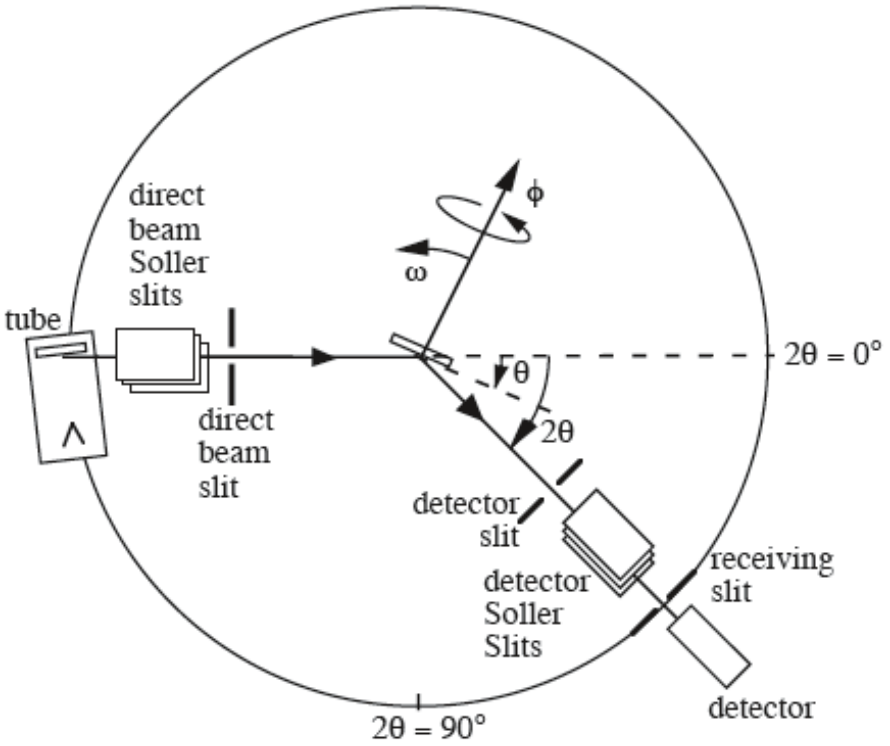

Figure A.9 Diagram of the goniometer path (defined by the circumference of the circle centred on the flat sample) in relation to some of the components of a θ-2θ diffractometer in Bragg-Brentano geometry[3].

A.2.2. PXRD Geometry

Of the two types of principle instrument geometries, reflection (i.e.: Bragg-Brentano – figures A.7 and A.9) and transmission, the former was employed in this study for both the D2 Phaser and the D5000 diffractometers. In reflection geometry, samples are mounted on flat-plate sample holders compared with transmission geometry in which the samples are mounted in glass capillaries or on tin foil. Reflection geometry diffractometers afford high diffracted beam intensity and good resolution by parafocussing the diffracted beam. After the beam interacts with the sample, the divergent, diffracted X-rays converge at a fixed distance from the sample. Diffraction peaks are not broadened by equatorial divergence in reflection geometry set-ups. A characteristic feature of Bragg-Brentano geometry is well-defined diffraction angles for finite slit widths[3].

A.3. Transmission Electron Microscopy

A.3.1 Components of a TEM

Several different transmission electron microscopes were employed in this study with the primary difference being the accelerating voltage. Routine, low resolution imaging was conducted using the FEI Tecnai T12 at 120 kV with a LaB6 source (figure A.10). High resolution imaging was conducted using an FEI Tecnai F20 at 200 kV with a field-emission gun, a JEOL JEM 2100 at 200 kV with a LaB6 source, and a JEOL 3011 at 300 kV, LaB6 source with Cs = 0.6 mm and Cc = 1.1 mm, and a 1 K camera (figure A.11).

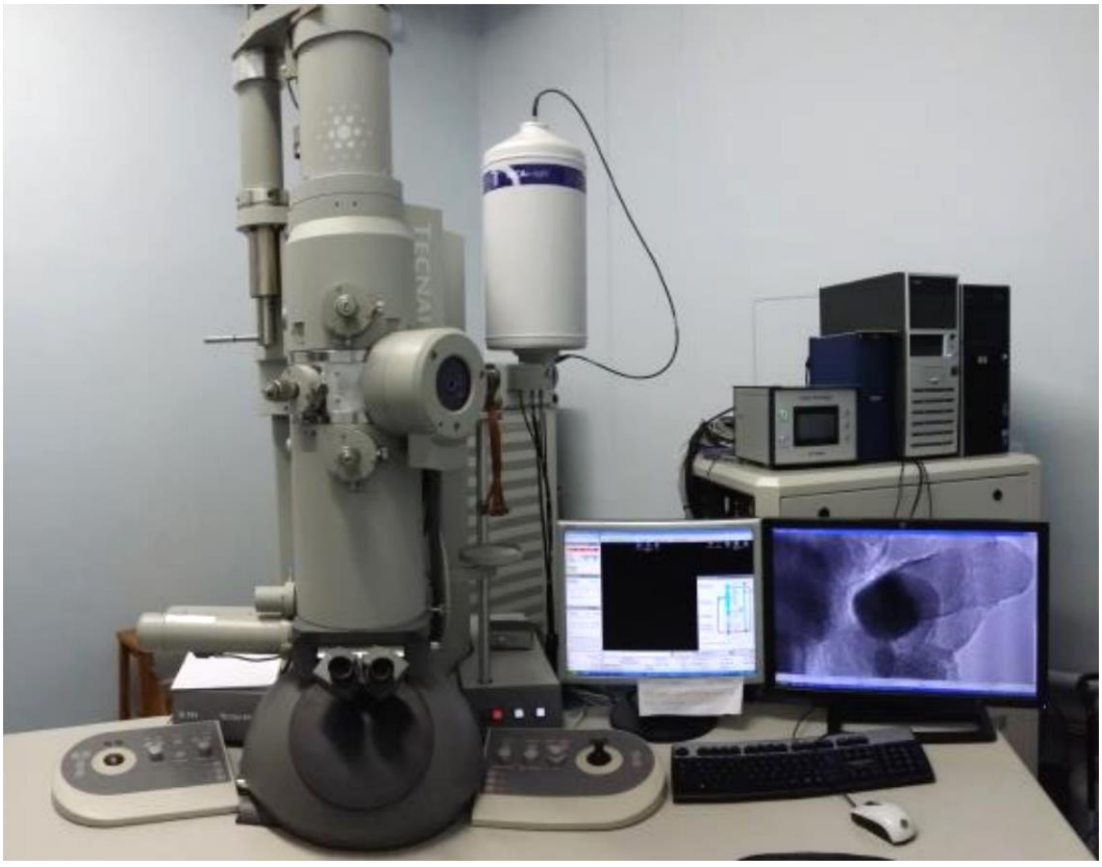

Figure A.10: FEI Tecnai T12 TEM based at the University of the Witwatersrand.



Figure A.11: JEOL 3011 HRTEM based at the University of Cambridge.

This section will focus on the electron gun, lenses, and apertures in a TEM. Other components necessary for TEM operation (detector, specimen holder, grids, pumps, etc.) will not be discussed. A cross-section schematic of the components in a typical TEM is given in figure A.12.

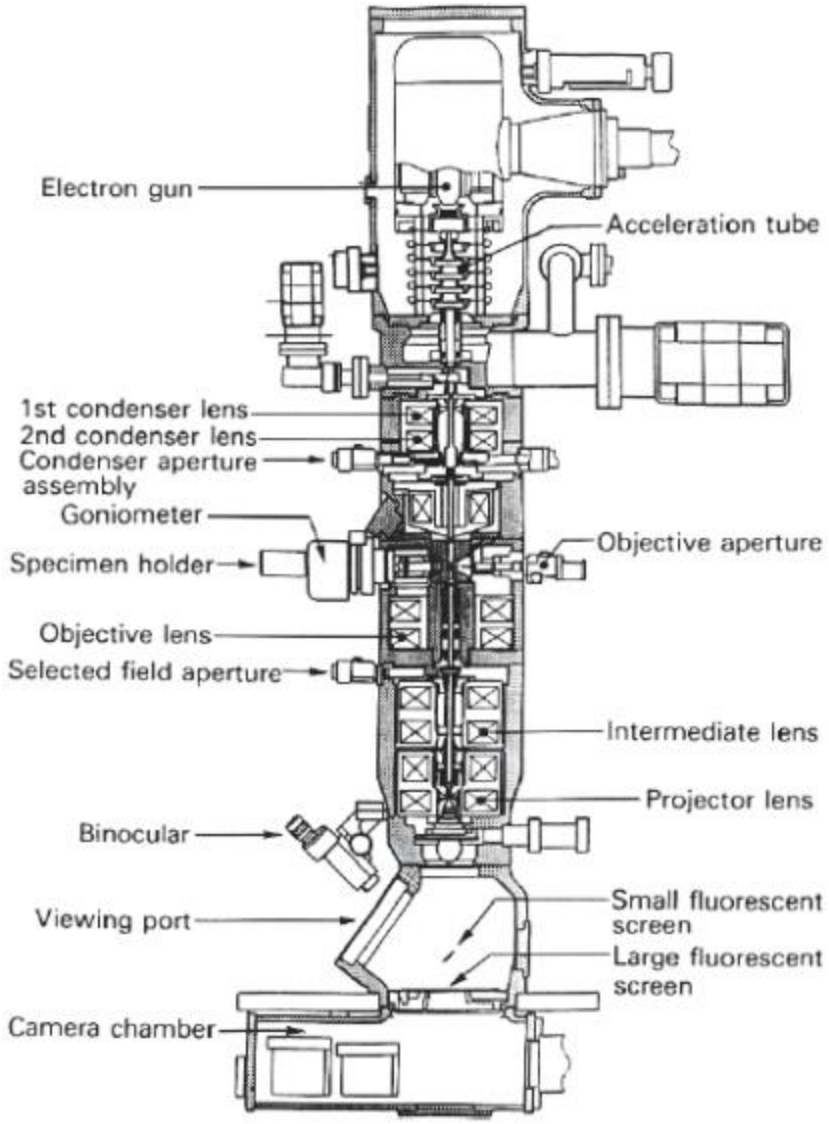

Figure A.12: Cross-section schematic of a typical TEM showing the major components in appropriate positions[3].

6.4.1.1 A.3.1.1 Electron Source

Thermionic and field-emission are the two types of electron sources available in TEM's. Electron guns function to focus the electrons emitted from the source. The gun design for thermionic emission is different to field-emission microscopes.

In thermionic emission, electrons are emitted after the source has been heated to a temperature above its work function. Preferred sources are those materials that

possess a high melting point or a low work function. W filaments have high melting points and LaB_6 crystals grown in the <1 1 0> orientation have a low work function that enhances emission. In the gun containing a LaB_6 source (figure A.13) the crystal functions as the cathode and the Wehnelt cylinder functions as the grid. The anode is at earth potential and a high voltage cable connects the cathode to the high voltage power supply. Additionally, the crystal is bonded to a metal wire filament that is heated causing thermionic emission. The generated electrons accelerate through the potential difference between the anode and cathode attaining the energy of the applied accelerating voltage. Applying a negative bias to the Wehnelt cylinder controls the electron beam and allows it to converge at the crossover point between the Wehnelt and the anode. This is an example of a self-biasing gun – as the emission current is increased, the Wehnelt bias is also increased.

In field-emission, electrons are produced when an electric field is applied across the source and anode. Field-emission is based on the principle that the strength of an electric field is increased at fine points and therefore applying a potential to a fine point decreases the work function. Preferred sources include materials that can be drawn out into a fine needle point and are mechanically strong to bear the stresses induced by strong electric fields. W needles grown in the <3 1 0> orientation have proven to be the best material for field-emission. Field-emission guns use the source (tip) as a cathode with two anodes. The first anode functions to create an intense electric field by being positively charged with respect to the tip. This charge produces the extraction voltage that causes electrons to be emitted from the tip. The second anode serves to accelerate the electrons to the applied accelerating voltage. The geometry of the anodes produce combined electric fields that act as an electrostatic lens which create a crossover point (figure A.14).

Field emission guns produce brighter and a more coherent beam than thermionic guns. LaB_6 affords more brightness, coherency and has a longer operating life than W.

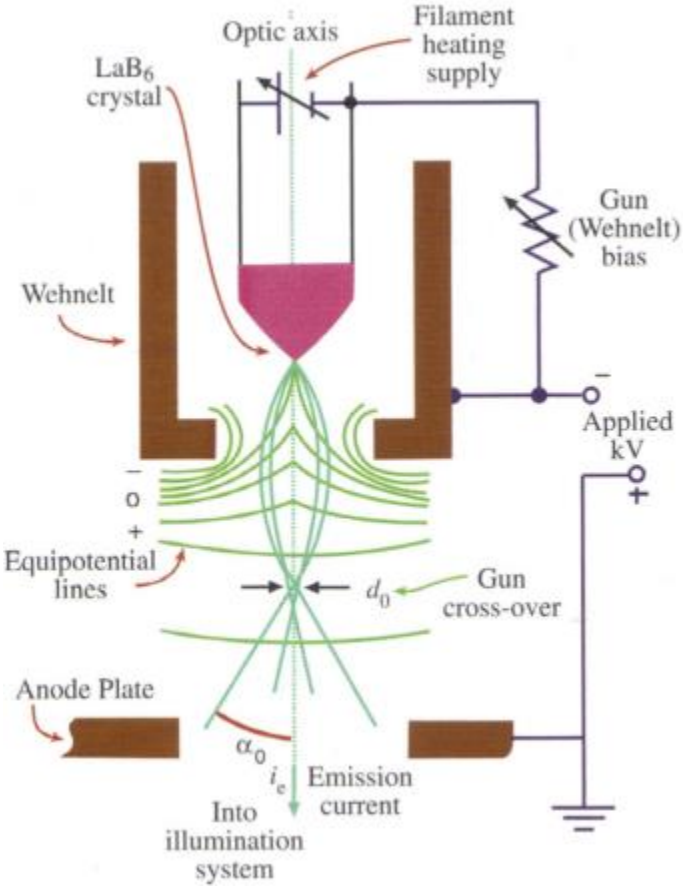

Figure A.13: Schematic of a thermionic emission gun. The convergence/divergence angle is given by α_0 and this is the true source for the lenses in the TEM[8].

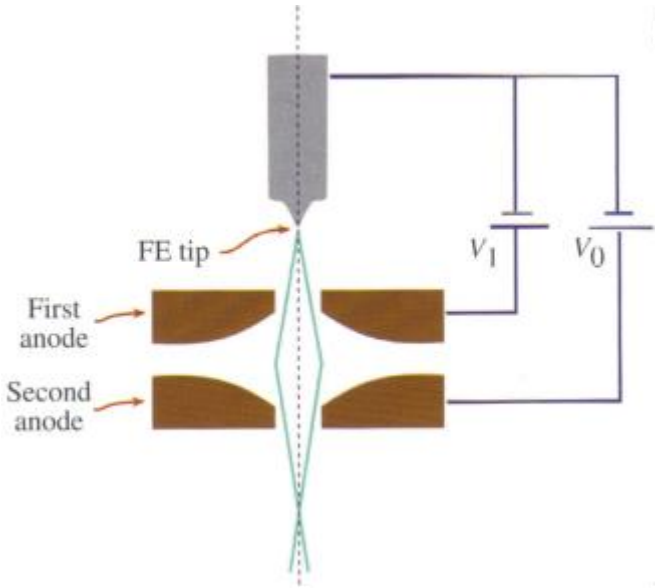

Figure A.14: Schematic of a field-emission gun. Notice how the two anode geometry creates a crossover point[8].

6.4.1.2 A.3.1.2 Lenses

While accelerating voltage determines the theoretical resolution that can be obtained using a TEM, imperfect electromagnetic lenses limit the achievable resolution of the microscope. Lenses are fixed in position in a TEM and functions such as changing focus, magnification, and beam intensity are controlled by changing the strength of the magnetic field within the lenses. Several lenses exist within the TEM – the first of which was discussed in section 1.3.2.3.1. While the gun creates an electrostatic lens, the subsequent lenses are based on magnetic field interactions with the incident beam.

A typically used TEM lens consists of a polepiece and a coil (figure A.15). The polepiece is a symmetrical cylinder made of a magnetic material such as iron with a bore drilled down the middle. Most lenses are composed of two polepieces separated by a gap. The performance of the lens is governed by the bore to gap ratio and the shape of the polepiece. The polepiece is surrounded by a coil of coper wire. When a current is passed through the coil, a magnetic field is generated in the bore. The trajectory of electrons travelling through the lens is controlled by varying the current in the coils and therefore varying the magnetic field imposed on the incident beam of electrons. Electrons follow a helical trajectory through the lens field.

While lenses limit the resolution of a TEM, they also allow for better depth of field and focus. Lenses suffer from spherical aberration, chromatic aberration and astigmatism.

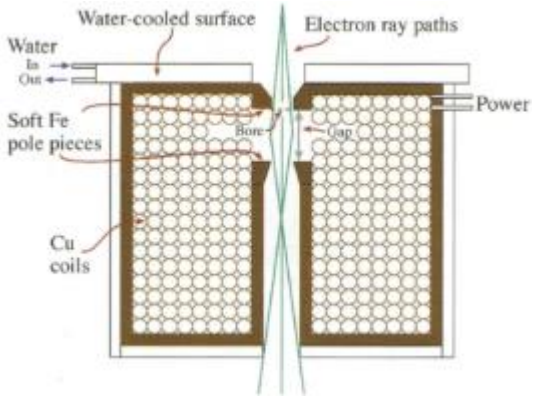

Figure A.15: Cross-section schematic of a TEM lens consisting of Fe polepieces surrounded by Cu coils[8].

6.4.1.3 A.3.1.3 Apertures

An aperture is a hole of a specific diameter punched in a metal sheet made from platinum or molybdenum. Apertures are used to limit the number of beams that pass

through lenses to those closer to the optic axis. This is in an attempt to reduce aberration. Apertures can be placed above, below or in the plane of the lens. They are also used to select different beams to form different images. An aperture in the objective lens allows for control over the image resolution formed by the lens, the depth of field and focus, the image contrast and the angular resolution of the diffraction pattern.

A.4. References

1. Franklyn, P. J. Hydrothermal Synthesis and Characterisation of Titania Nanoparticles. (University of the Witwatersrand, 2004).

2. Cockcroft, J. K. & Fitch, A. N. Experimental Setups. in *Powder Diffraction: Theory and Practice* (eds. Dinnebier, R. E. & Billinge, S. J. L.) (The Royal Society of Chemistry, 2008).

3. Fultz, B. & Howe, J. M. *Transmission Electron Microscopy and Diffraction of Materials*. (Springer-Verlag, 2008).

4. Barrett, D. H. A Stable High Temperature Gold Nano-Catalyst: Synthesis, Characterization and Application. (University of the Witwatersrand, 2012).

5. Deutsch, M. *et al.* X-Ray Spectrometry of Copper: New Results on an Old Subject. *Journal of Research of the National Institute of Standards and Technology* **109,** 75 – 98 (2004).

6. Elnaggar, A. M. Components of the Powder Diffractometer.

7. West, A. R. *Basic Solid State Chemistry*. (John Wiley and Sons Ltd, 1999).

8. Williams, D. B. & Carter, C. B. *Transmission Electron Microscopy: A Textbook For Materials Science*. (Springer Science+Business Media, LLC, 2009).

Appendix B. XRD Analysis of Control Samples

To reveal the effects of various reaction components on PEG, XRD analysis was performed on four different types of control samples: 1) as received PEG, 2) PEG loaded with a $TiCl_4$ solution, 3) homogenised PEG and 4) homogenised PEG with excess distilled H_2O. A final XRD analysis was performed on an empty Si zero-background sample holder. All analyses were achieved using a Bruker D2 Phaser diffractometer with Co Kα radiation between 10° – 60° 2θ. The instrument setup was described in chapter 5.

B.1 Unloaded PEG

This analysis would reveal the XRD patterns of as received PEG. PEG of various molecular weights (400, 4000 – 35000 g/mol, Aldrich) and (1000 – 1500 g/mol) were analysed as received. The XRD patterns generated from these samples follow in figure B.1. Figure B.1 shows that longer chain polymers exhibited greater crystallinity than shorter chain PEG. No peaks were evident from the sample synthesised using PEG 400 g/mol. This is likely due to PEG 400 g/mol existing as a viscous liquid. Peak misalignment is evident.

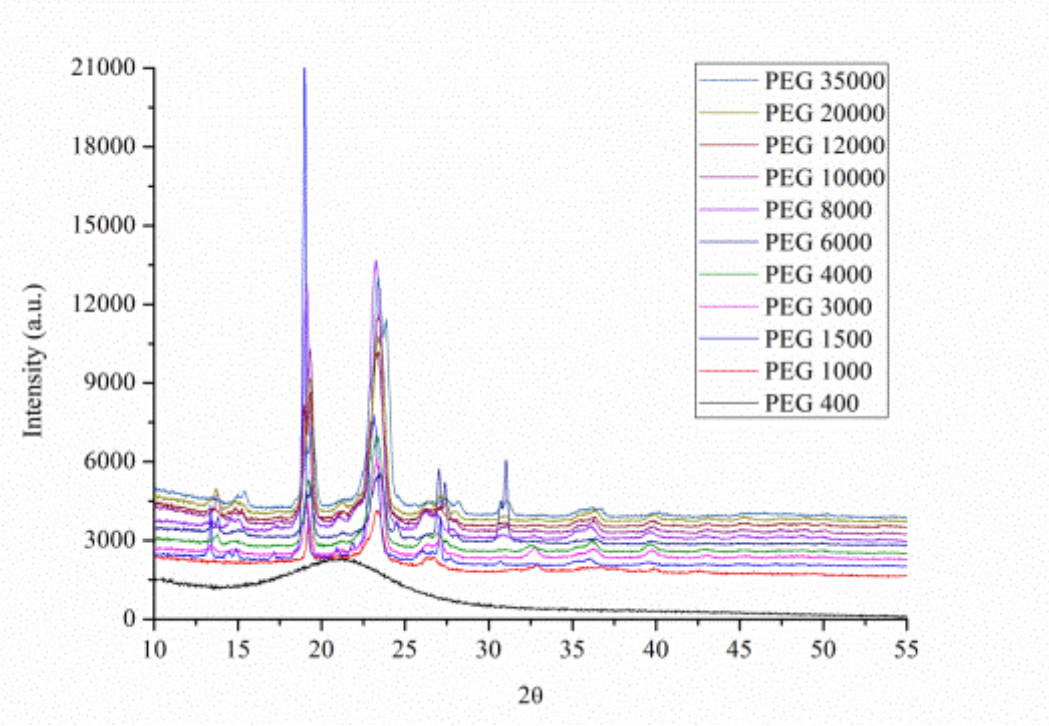

Figure B.1: XRD of unloaded PEG of various molecular weights.

B.2 PEG loaded with a $TiCl_4$ Solution

This analysis would reveal how the PEG XRD patterns are modified by the inclusion of a stoichiometric $TiCl_4$ solution. PEG of various molecular weights was loaded with a stoichiometric amount of $TiCl_4$ solution in a (Ti^{4+} : PEG = 1 : 0.5) ratio. Samples were synthesised, homogenised, and devoid of excess solvent as described in chapter 8. No further heat treatments were applied. Figure B.2 contains the XRD patterns generated from the loaded PEG samples. The sharper peaks in this this figure suggests that the addition of metal ions improved crystallinity of the polymer. This is particularly evident for the pair of doublet peaks at ca. 15° 2θ and ca. 27.5° 2θ. It should be noted that these polymers were melted to induce sample homogeneity. The effects of homogenising PEG on crystallinity will be explored later.

No peaks were observed at 25.325° 2θ and 27.968 ° 2θ – characteristics peaks corresponding to anatase (1 0 1) and rutile (1 1 0) respectively.

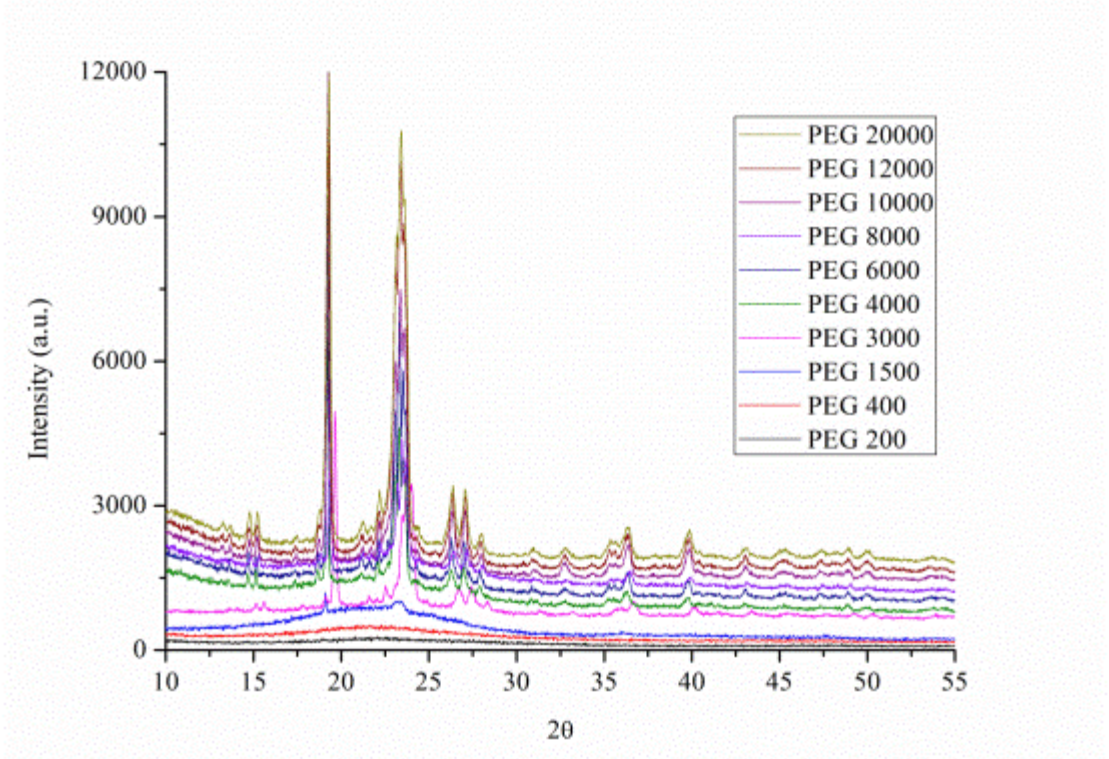

Figure B.2: XRD of loaded PEG of various molecular weights.

The following figures compare XRD patterns of loaded and unloaded PEG for specific PEG molecular weights.

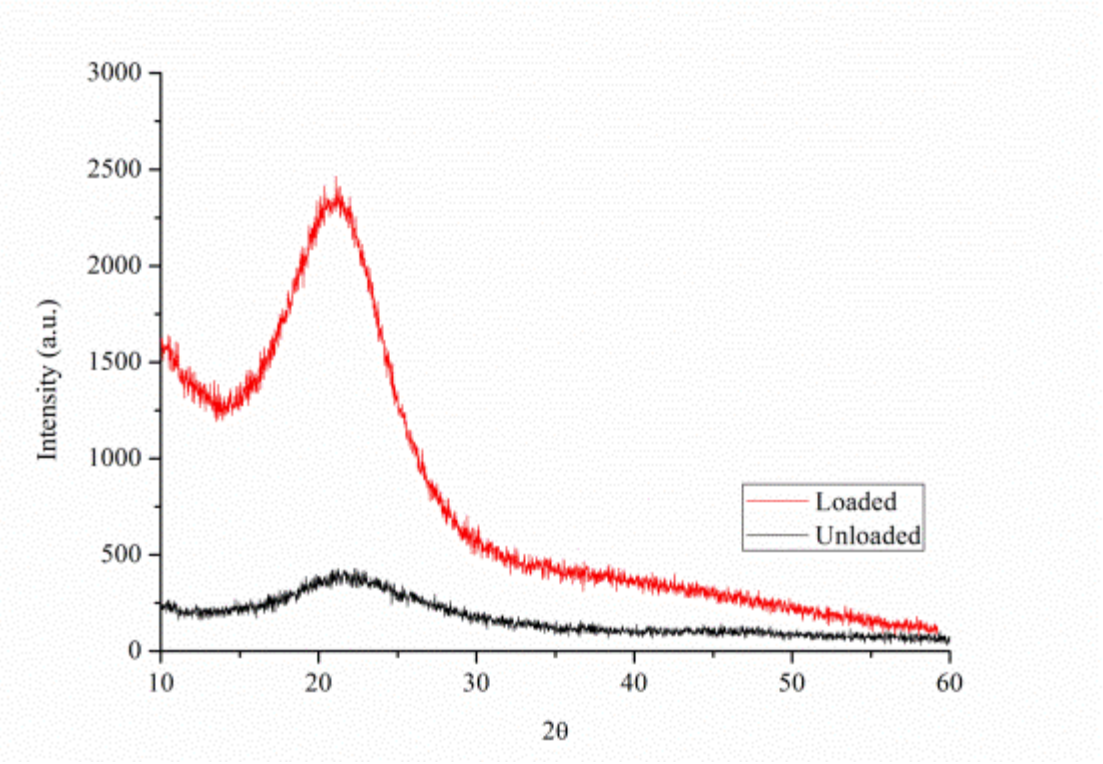

Figure B.3: XRD patterns for unloaded and loaded PEG 400 g/mol.

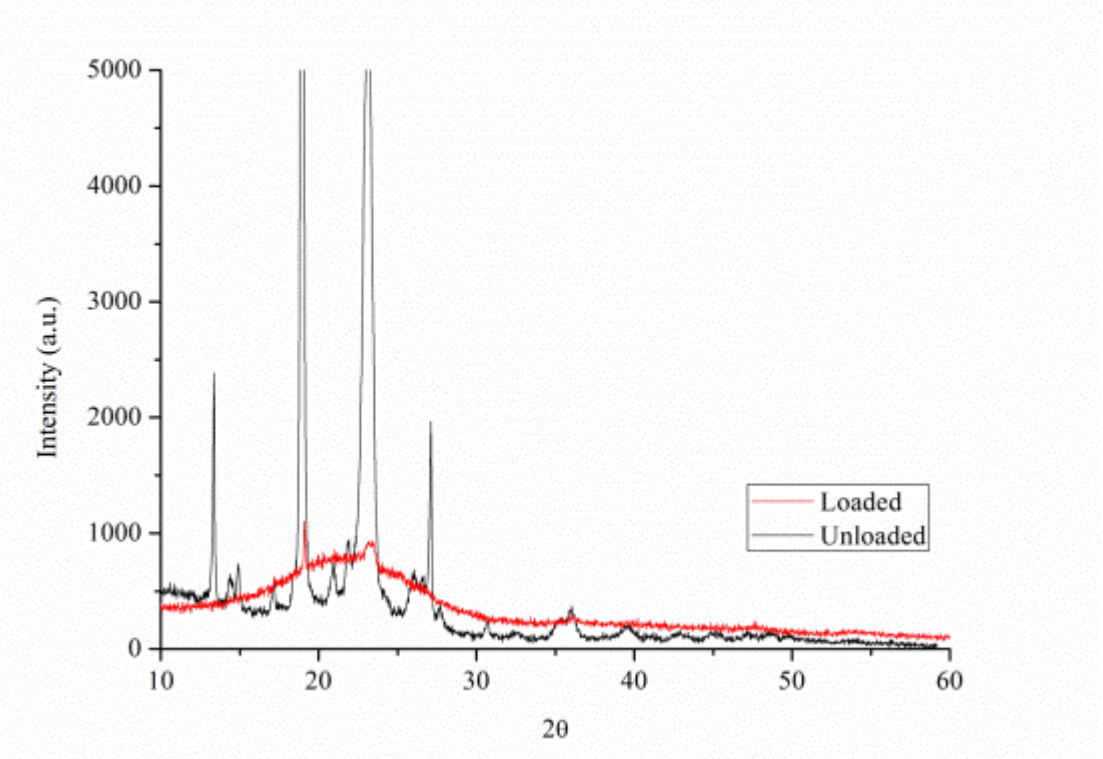

Figure B.4: XRD patterns for unloaded and loaded PEG 1500 g/mol.

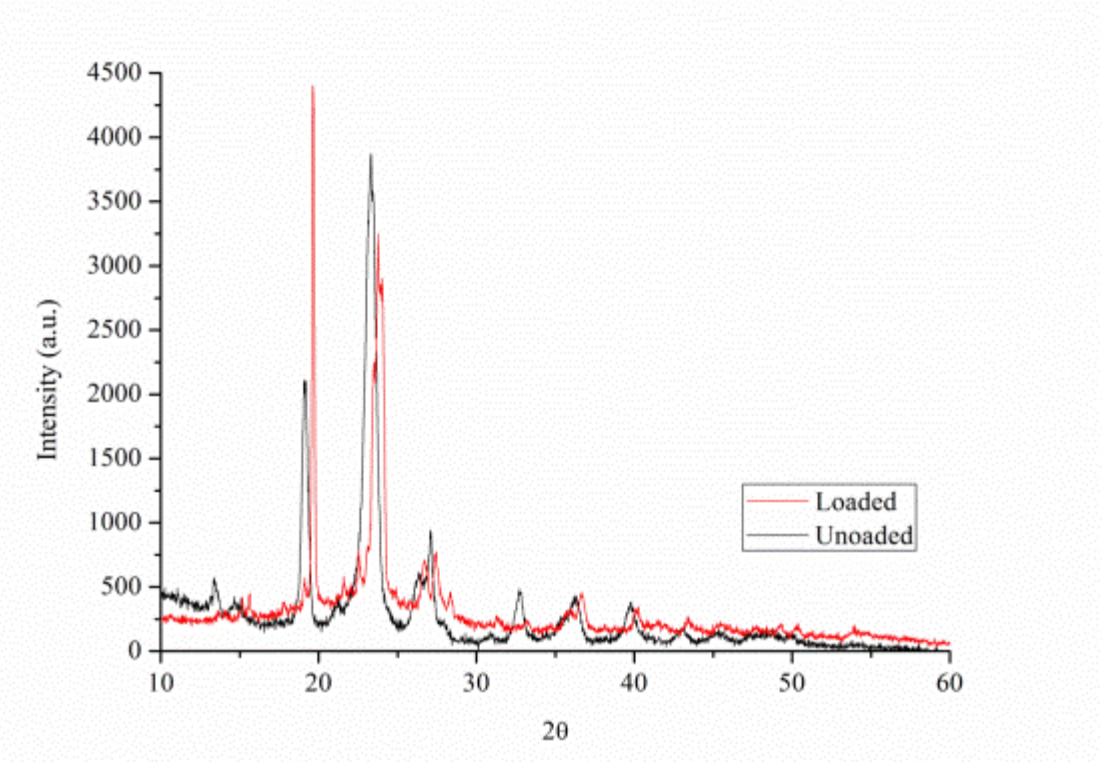

Figure B.5: XRD patterns for unloaded and loaded PEG 3000 g/mol.

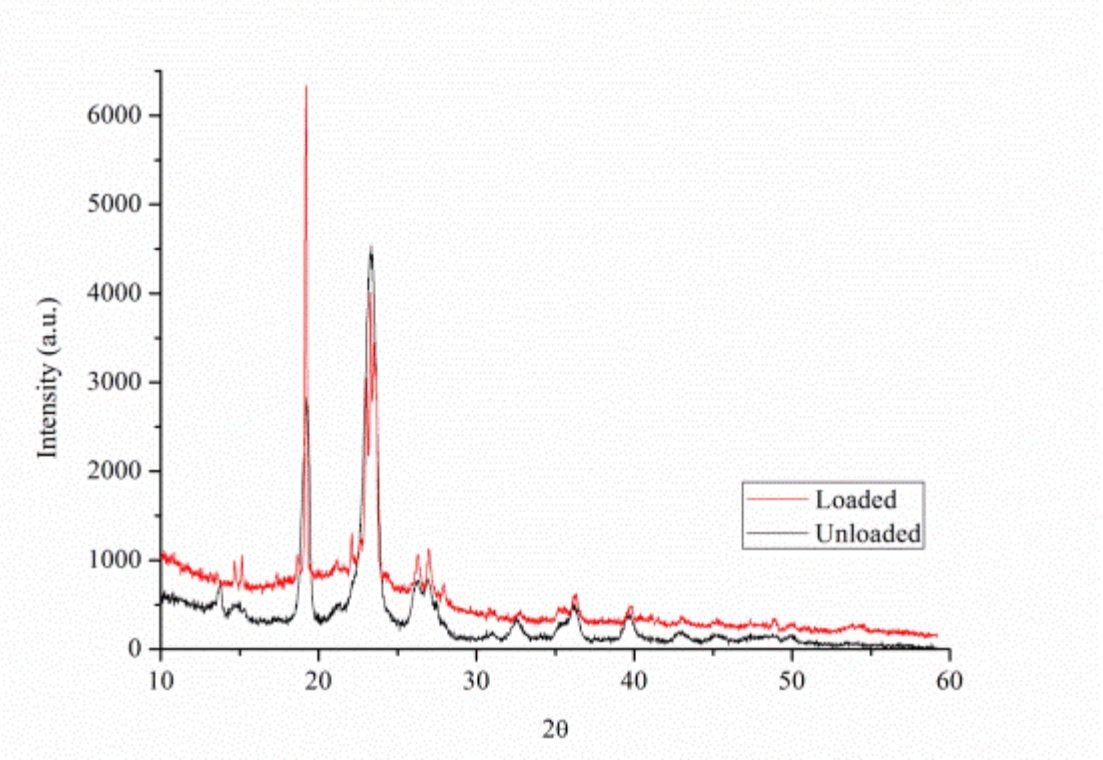

Figure B.6: XRD patterns for unloaded and loaded PEG 4000 g/mol.

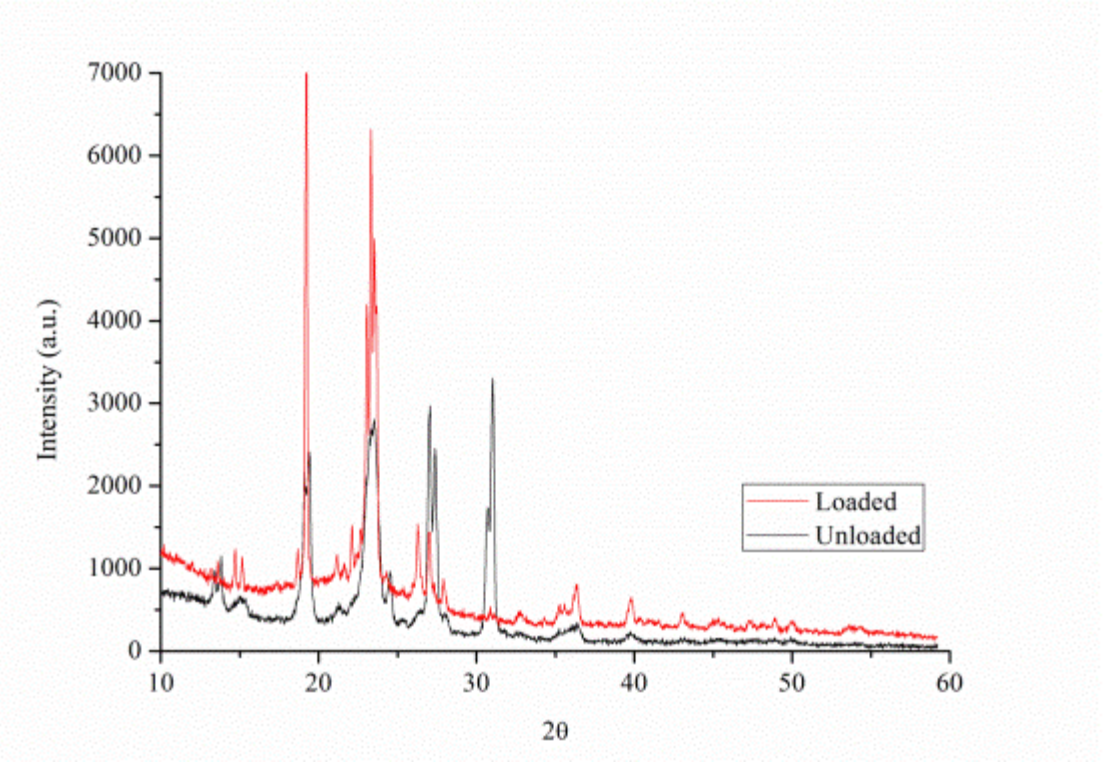

Figure B.7: XRD patterns for unloaded and loaded PEG 6000 g/mol.

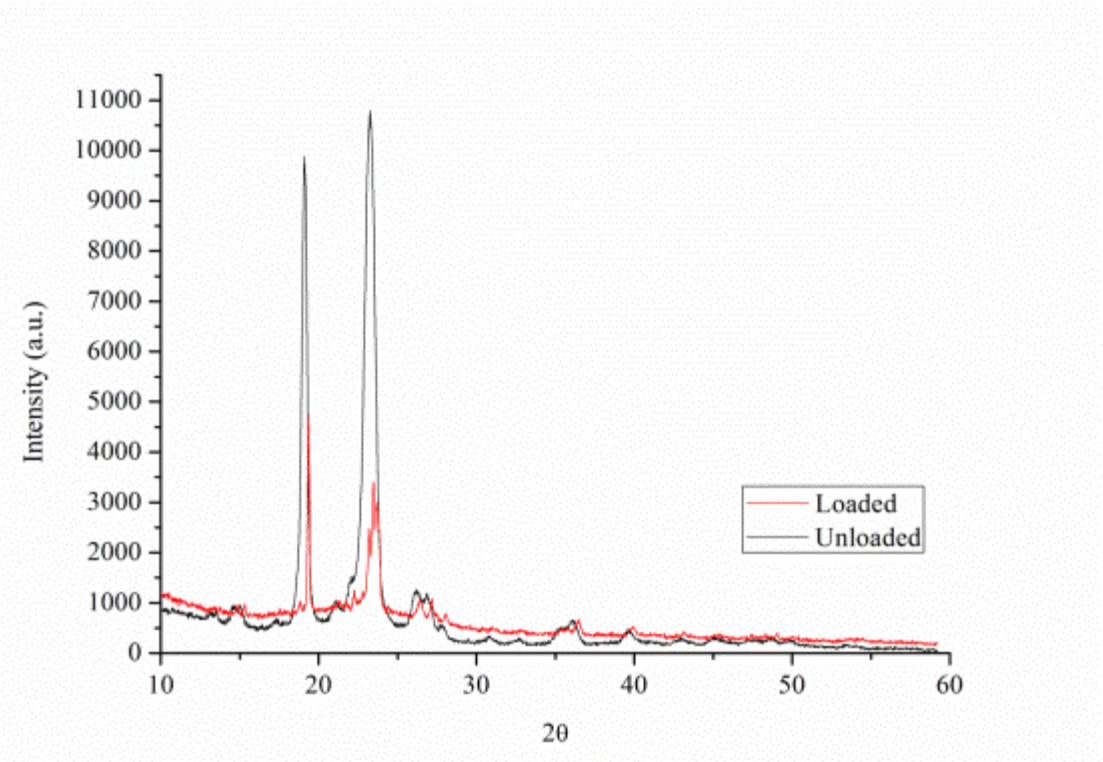

Figure B.8: XRD patterns for unloaded and loaded PEG 8000 g/mol.

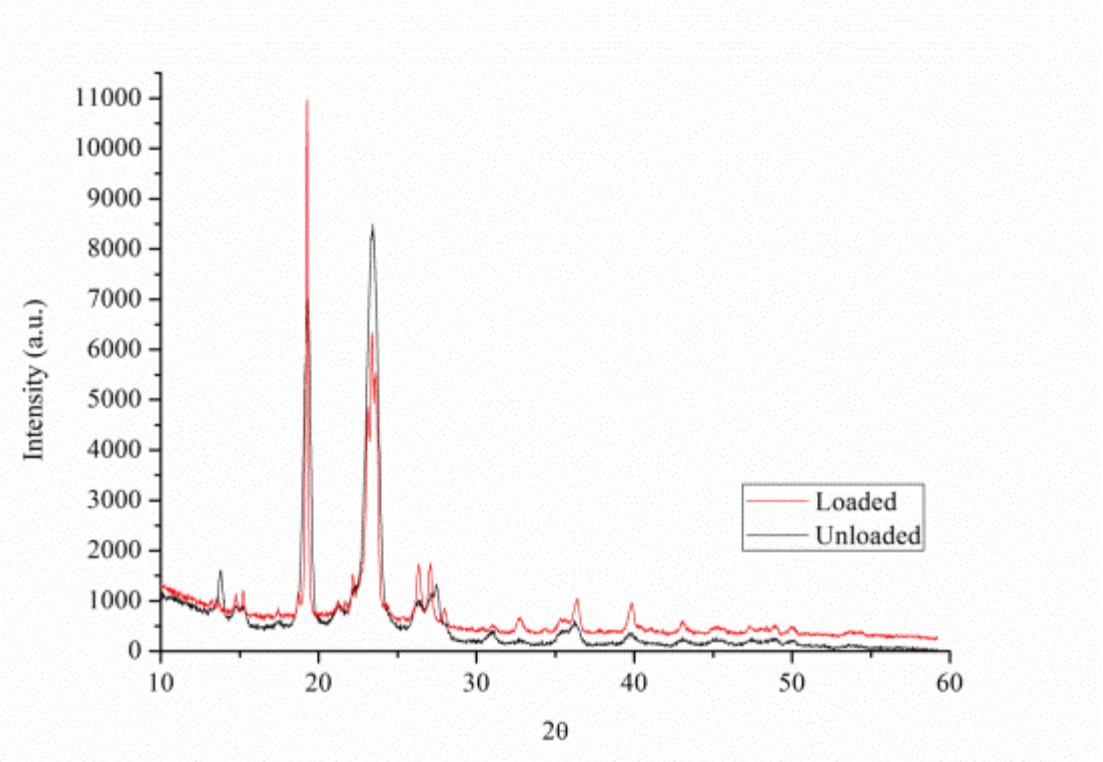

Figure B.9: XRD patterns for unloaded and loaded PEG 10000 g/mol.

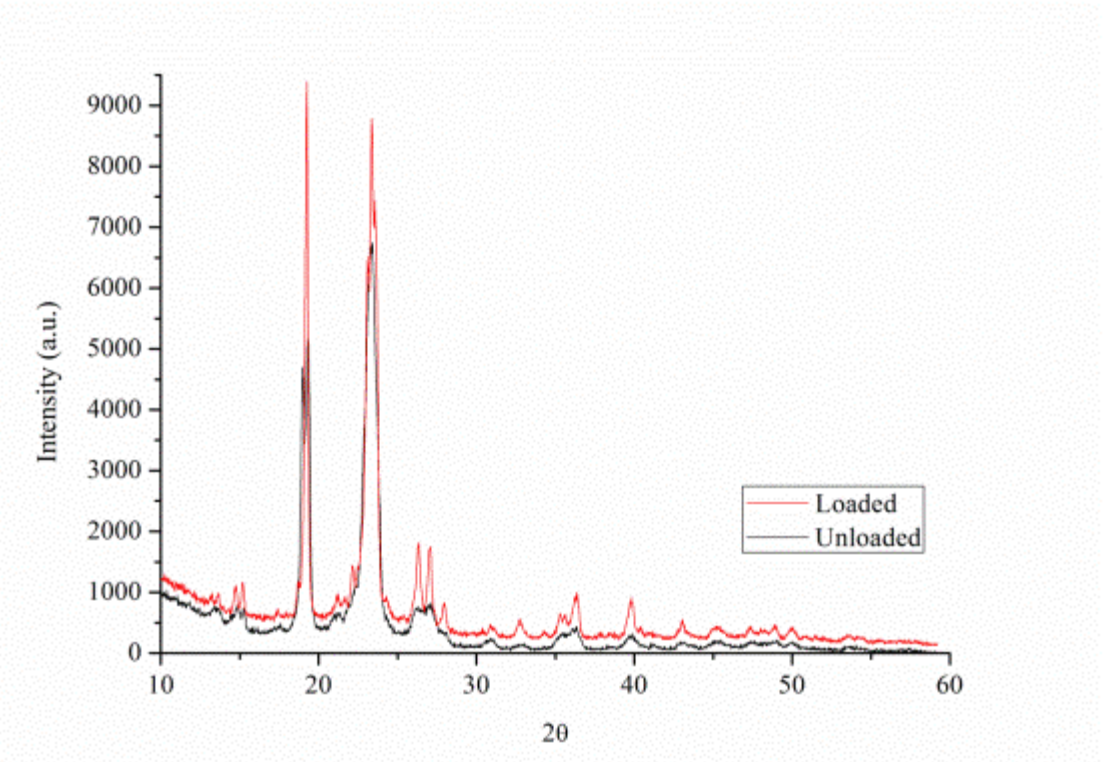

Figure B.10: XRD patterns for unloaded and loaded PEG 12000 g/mol.

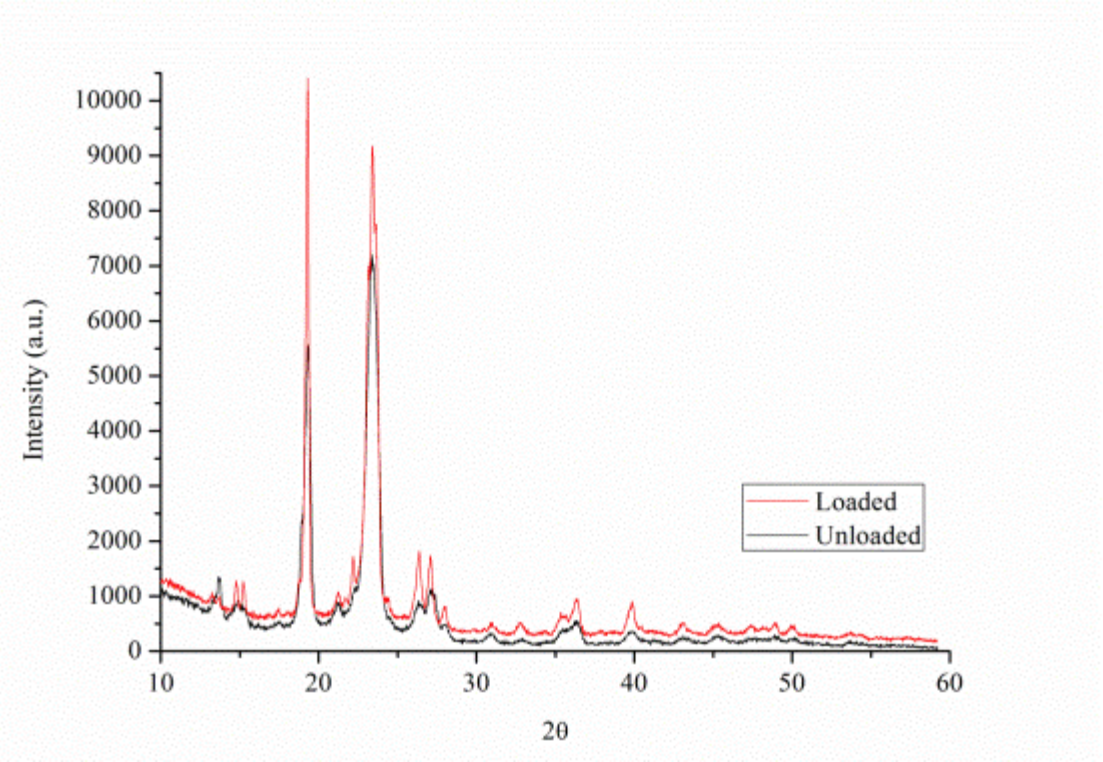

Figure B.11: XRD patterns for unloaded and loaded PEG 20000 g/mol.

B.3 Homogenised PEG

This analysis would reveal how heating and stirring to induce homogeneity affected the XRD pattern of PEG. Since the TGA degradation profiles for PEG of various molecular weights were fairly similar, it was deemed redundant to investigate the effects of PEG homogenisation on all available PEG molecular weights. Therefore, PEG 6000 g/mol (a polymer of intermediate chain length) was selected for this analysis.

Flakes of PEG 6000 g/mol were added to a beaker over a heater/stirrer. The polymer was heated and concurrently stirred using a glass rod until homogeneous. Analysis was effected after the polymer had cooled to room temperature and hardened into a solid mass.

Figure B.12 compares the XRD patterns generated for PEG 6000 g/mol analysed as received and analysed as homogenised flakes. From figure B.12, homogenisation affected PEG crystallinity. Some peaks (ca. 24° 2θ and 30.5° 2θ) that were present in the as received polymer were not present post-homogenisation. Other peaks such as the doublet at ca. 26 – 27° 2θ decreased in intensity and shifted in 2θ position post-homogenisation. Despite this, at higher 2θ values (> 32° 2θ), many peaks were present post-homogenisation that were absent in the as received polymer.

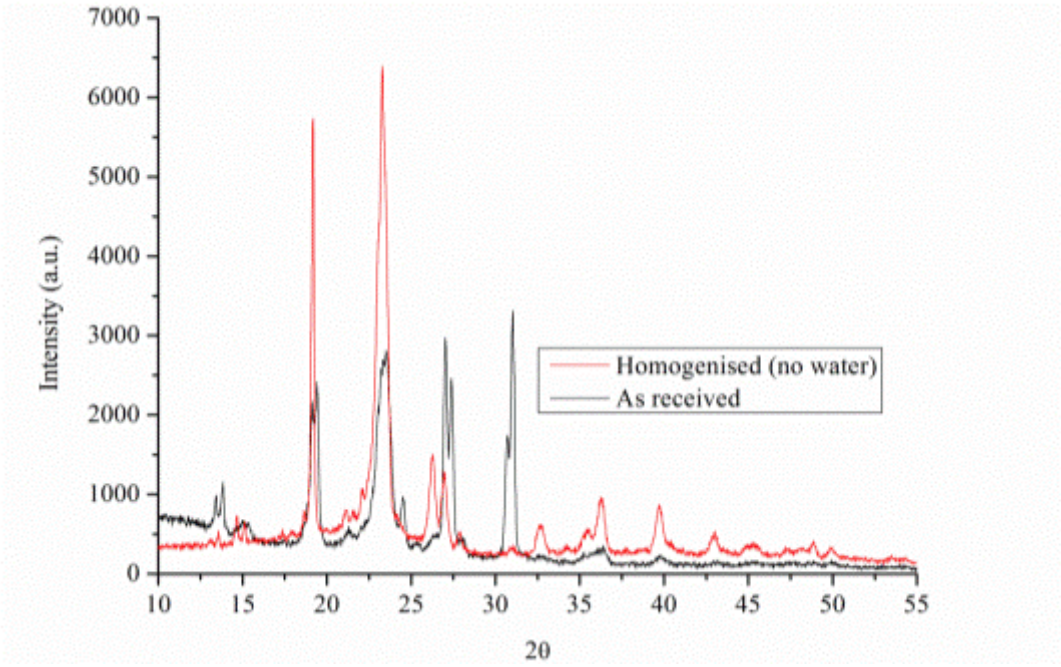

Figure B.12: Comparison of XRD patterns generated for as received and homogenised PEG 6000 g/mol.

B.4 Homogenised PEG with Excess Distilled H_2O

This analysis would reveal changes in the XRD pattern of PEG as a result of PEG homogenisation in excess distilled H_2O. Only PEG 6000 g/mol was selected for use in this analysis.

24.0 ml H_2O was added to 27.2406 g PEG 6000 g/mol. The mixture was heated and concurrently stirred to induce complete homogeneity. Thereafter, the mixture was left ca. 30 cm beneath 2 infrared light bulbs for a fortnight to effect complete solvent evaporation. Following this time, XRD analysis was conducted on the sample.

Figure B.13 compares the XRD patterns generated for PEG 6000 g/mol analysed as received, after homogenisation, and after solvent assisted homogenisation. PEG homogenisation in water does not appear to affect the position of any XRD peaks compared with homogenisation without water. After homogenising in water, the intensity of the peaks at ca. 18.5° 2θ and 23.5° 2θ increased compared with PEG homogenised without water.

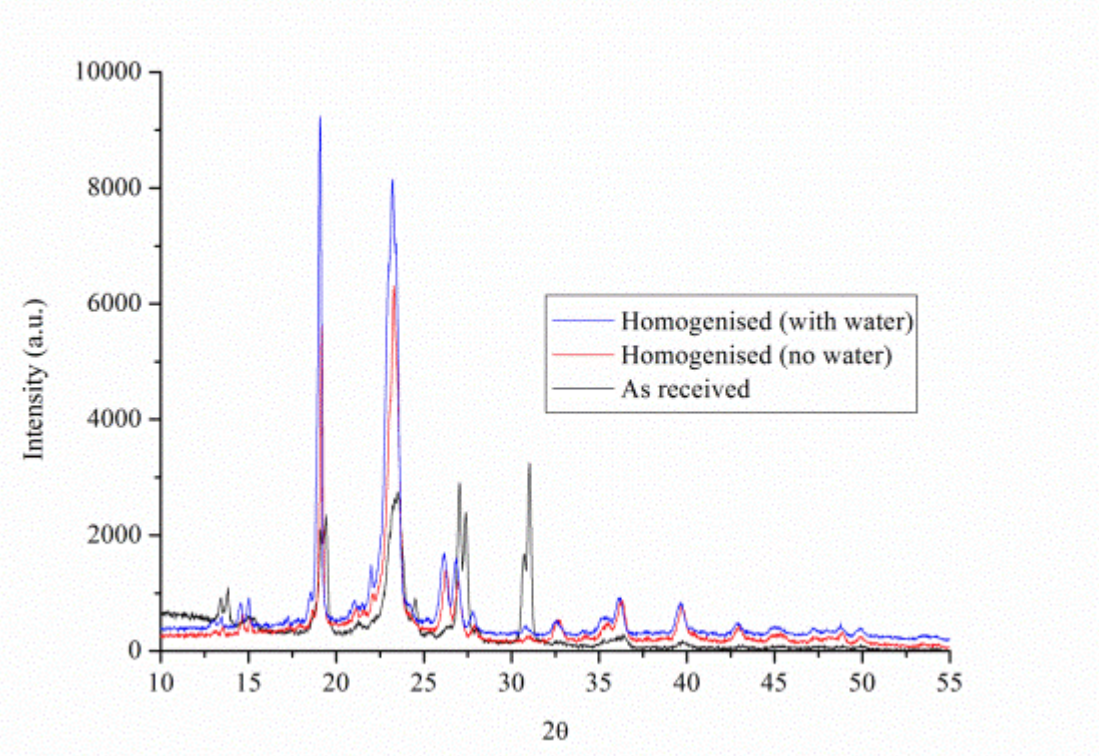

Figure B.13: Comparison of XRD patterns generated for as received, homogenised without water, and homogenised with water PEG 6000 g/mol.

B.5 Empty Zero-background Sample Holder

This analysis would reveal the XRD pattern from the zero-background sample holder used throughout this study. In doing so, any contributions from the zero-background sample holder to the XRD patterns of synthesised products can be ascertained.

Figure B.14 shows the XRD pattern collected from an empty Si zero-background sample holder. From this figure, no diffraction peaks were observed. This implies excellent sample holder performance for XRD analysis with synthesised samples.

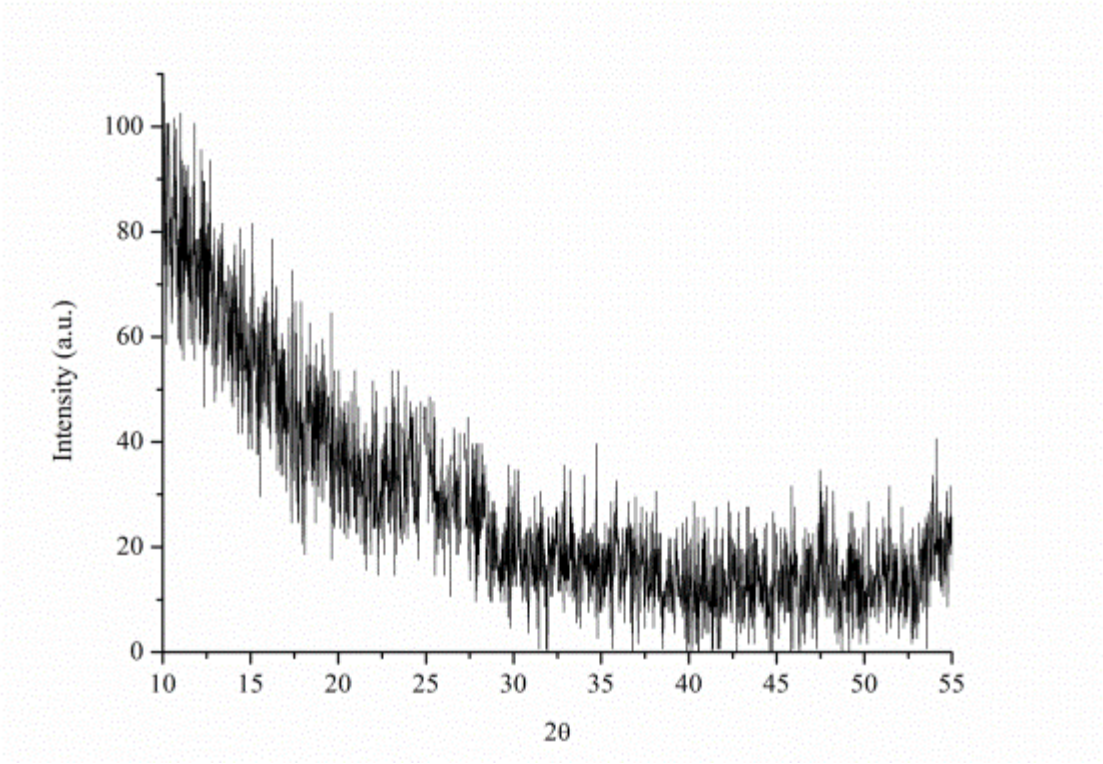

Figure B.14: XRD pattern generated from an empty Si zero-background sample holder.

Appendix C. Effects of Solvent and PEG Molecular Weight on Titania Polymorph and Crystallite Size Formation

The tables show all the raw data pertaining to chapter 5. The symbols in the tables are understood as follows:

EtOH	–	Ethanol
H_2O	–	Water
PEG	–	Polyethylene glycol (the molecular weight is given in the table)
OPEG	–	Calcined samples
%A	–	Amount of anatase formed
Ave%A	–	Average amount of anatase formed
Error%A	–	Error in %A = Standard deviation + 4% of the average anatase
%R	–	Amount of rutile formed
Ave%R	–	Average amount of rutile formed
Error%R	–	Error in %R = Standard deviation + 4% of the average rutile
As	–	Anatase crystallite size
AveAs	–	Average size of anatase crystallites
StdevAs	–	Standard deviation of the anatase crystallite size
Rs	–	Rutile crystallite size
AveRs	–	Average size of rutile crystallites
StdevRs	–	Standard deviation of the rutile crystallite size

EtOH																	
Sample ID	PEG	%A	%A	Ave%A	Error%A	%R	%R	Ave%R	Error%R	As (nm)	As (nm)	AveAs(nm)	StdevAs(nm)	Rs (nm)	Rs (nm)	AveRs(nm)	stdevRs(nm)
D2_00296/391	400	100	100	100	4	0	0	0	0	5.3	4.7	5.0	0.3	0	0	0	0
D2_00336/346	1000	100	100	100	4	0	0	0	0	4.7	4.8	4.8	0.1	0	0	0	0
D2_00347/348	1500	100	100	100	4	0	0	0	0	4.7	4.8	4.8	0.1	0	0	0	0
D2_00349/350	3000	100	100	100	4	0	0	0	0	3.8	3.5	3.7	0.1	0	0	0	0
D2_00352/354	4000	100	100	100	4	0	0	0	0	1.7	2.5	2.1	0.4	0	0	0	0
D2_00355/356	6000	100	100	100	4	0	0	0	0	4.2	3.9	4.1	0.2	0	0	0	0
D2_00357/358	8000	100	100	100	4	0	0	0	0	5.3	5.2	5.3	0.1	0	0	0	0
D2_00359/360	10000	100	100	100	4	0	0	0	0	7.4	4.9	6.2	1.2	0	0	0	0
D2_00361/362	20000	100	100	100	4	0	0	0	0	7.6	4.3	6.0	1.6	0	0	0	0
D2_00363/364	35000	84.492	72.19	78.341	9.28464	15.508	27.81	21.659	7.01736	11.3	8.6	9.9	1.4	32.0	27.9	29.9	2.1
	Average			97.8341	4.528464							5.2	0.5				
EtOH																	
Sample ID	OPEG	%A	%A	Ave%A	Error%A	%R	%R	Ave%R	Error%R	As (nm)	As (nm)	AveAs(nm)	StdevAs(nm)	Rs (nm)	Rs (nm)	AveRs(nm)	stdevRs(nm)
D2_00394/395	400	99.937	96.775	98.356	5.51524	0.063	3.225	3.225	1.71	16.2	13.9	15.0	1.2	0	0	0	0
D2_00396/397	1000	94.578	96.303	95.4405	4.68012	5.422	3.697	3.697	1.01038	21.7	21.7	21.7	0.0	0	0	0	0
D2_00398/399	1500	97.502	95.91	96.706	4.66424	2.498	4.09	4.09	0.9596	16.2	19.5	17.9	1.7	0	0	0	0
D2_00400/401	3000	100	100	100	4	0	0	0	0	17.7	14.6	16.1	1.6	0	0	0	0
D2_00402/403	4000	99.674	100	99.837	4.15648	0.326	0	0	0.163	11.4	12.9	12.2	0.8	0	0	0	0
D2_00404/405	6000	95.928	95.293	95.6105	4.14192	4.072	4.707	4.707	0.50578	17.7	16.2	16.9	0.7	0	0	0	0
D2_00406/407	8000	99.721	99.191	99.456	4.24324	0.279	0.809	0.809	0.29736	14.9	16.1	15.5	0.6	0	0	0	0
D2_00408/409	10000	94.773	89.865	92.319	6.14676	5.227	10.135	10.135	2.8594	28.0	24.5	26.3	1.7	0	0	0	0
D2_00410/419	20000	97.67	91.816	94.743	6.71672	2.33	8.184	8.184	3.25436	21.7	19.5	20.6	1.1	0	0	0	0
D2_00421/422	35000	77.831	65.708	71.7695	8.93228	22.169	34.292	34.292	7.43318	17.7	16.2	16.9	0.8	40.0	33.0	36.5	3.5
	Average			94.42375	5.3197							17.9	1.0				

H2O																	
Sample ID	PEG	%A	%A	Ave%A	Error%A	%R	%R	Ave%R	Error%R	As (nm)	As (nm)	AveAs(nm)	StdevAs(nm)	Rs (nm)	Rs (nm)	AveRs(nm)	stdevRs(nm)
D2_00365/366	400	67.444	64.262	65.853	4.22512	32.556	35.738	34.147	2.95688	4.7	5.6	5.1615	0.4406	0.0	0.0	0.0	0.0
D2_00367/368	1000	0.231	3.202	1.7165	1.55416	99.769	96.798	98.2835	5.41684	0.0	0.0	0	0	8.0	8.3	8.1	0.2
D2_00369/370	1500	10.193	3.718	6.9555	3.51572	89.807	96.282	93.0445	6.95928	0.0	0.0	0	0	5.3	6.9	6.1	0.8
D2_00371/372	3000	55.594	49.069	52.3315	5.35576	44.406	50.931	47.6685	5.16924	9.8	8.9	9.344	0.4101	16.8	15.6	16.2	0.6
D2_00373/374	4000	4.548	6.281	5.4145	1.08308	95.452	93.719	94.5855	4.64992	0.0	0.0	0	0	9.0	9.4	9.2	0.2
D2_00375/376	6000	15.066	9.684	12.375	3.186	84.934	90.316	87.625	6.196	0.0	0.0	0	0	6.1	7.7	6.9	0.8
D2_00377/378	8000	56.62	55.882	56.251	2.61904	43.38	44.118	43.749	2.11896	8.9	12.0	10.4487	1.5269	16.8	20.0	18.4	1.6
D2_00379/380	10000	6.806	1.037	3.9215	3.04136	93.194	98.963	96.0785	6.72764	0.0	0.0	0	0	5.6	9.0	7.3	1.7
D2_00386/387	20000	54.882	53.801	54.3415	2.71416	45.118	46.199	45.6585	2.36684	11.3	11.3	11.3273	0.0079	24.6	19.9	22.3	2.3
D2_00388/297	35000	23.245	12.503	17.874	6.08596	76.755	87.497	82.126	8.65604	9.8	9.3	9.5377	0.2135	12.7	11.4	12.1	0.7
	Average			27.7034	3.338036			72.2966	5.121764							11.8	1.0
H2O																	
Sample ID	OPEG	%A	%A	Ave%A	Error%A	%R	%R	Ave%R	Error%R	As (nm)	As (nm)	AveAs(nm)	StdevAs(nm)	Rs (nm)	Rs (nm)	AveRs(nm)	stdevRs(nm)
D2_00423/424	400	49.409	48.509	48.959	2.40836	50.591	51.491	51.041	2.49164	17.7	17.7	17.7	0.0	24.7	21.8	23.3	1.4
D2_00432/433	1000	1.808	1.645	1.7265	0.15056	98.192	98.355	98.2735	4.01244	0.0	0.0	0.0	0.0	24.6	28.2	26.4	1.8
D2_00434/435	1500	3.496	1.522	2.509	1.08736	96.504	98.478	97.491	4.88664	0.0	0.0	0.0	0.0	28.3	21.8	25.0	3.2
D2_00436/437	3000	52.288	56.727	54.5075	4.3998	47.712	43.273	45.4925	4.0392	21.7	21.7	21.7	0.0	28.3	24.7	26.5	1.8
D2_00438/439	4000	3.128	3.546	3.337	0.34248	96.872	96.454	96.663	4.07552	0.0	0.0	0.0	0.0	17.8	15.0	16.4	1.4
D2_00440/441	6000	6.988	5.051	6.0195	1.20928	93.012	94.949	93.9805	4.72772	0.0	0.0	0.0	0.0	16.3	17.8	17.0	0.7
D2_00442/443	8000	55.678	55.397	55.5375	2.362	44.322	44.603	44.4625	1.919	12.1	12.9	12.5	0.4	19.6	21.8	20.7	1.1
D2_00444/445	10000	1.101	1.172	1.1365	0.08096	98.899	98.828	98.8635	3.99004	0.0	0.0	0.0	0.0	21.8	19.6	20.7	1.1
D2_00446/447	20000	52.534	52.85	52.692	2.26568	47.466	47.15	47.308	2.05032	16.2	17.7	17.0	0.7	33.0	28.2	30.6	2.4
D2_00448/449	35000	20.626	20.998	20.812	1.01848	79.374	79.002	79.188	3.35352	12.9	13.8	13.4	0.5	21.8	19.6	20.7	1.1
	Average			24.72365	1.532496			75.27635	3.554604							22.7	1.6

Appendix D. Effects of an Enhanced Heating Rate on Titania Polymorph and Crystallite Size Formation

The tables show all the raw data pertaining to chapter 6. The symbols in the tables are understood as follows:

EtOH	–	Ethanol
H_2O	–	Water
PEG	–	Polyethylene glycol (the molecular weight is given in the table)
OPEG	–	Calcined samples
%A	–	Amount of anatase formed
Ave%A	–	Average amount of anatase formed
Error%A	–	Error in %A = Standard deviation + 4% of the average anatase
%R	–	Amount of rutile formed
Ave%R	–	Average amount of rutile formed
Error%R	–	Error in %R = Standard deviation + 4% of the average rutile
As	–	Anatase crystallite size
AveAs	–	Average size of anatase crystallites
StdevAs	–	Standard deviation of the anatase crystallite size
Rs	–	Rutile crystallite size
AveRs	–	Average size of rutile crystallites
StdevRs	–	Standard deviation of the rutile crystallite size

	EtOH																
Sample ID	PEG	%A	%A	Ave%A	Error%A	%R	%R	Ave%R	Error%R	As (nm)	As (nm)	AveAs(nm)	StdevAs(nm)	Rs (nm)	Rs (nm)	AveRs(nm)	stdevRs(nm)
D5_239/251	200	100.0	98.1	99.1	4.9	0.0	1.9	0.9	1.0	4.9	9.0	6.9	2.1	0	0	0	0
D5_240/252	400	99.5	99.4	99.5	4.0	0.5	0.6	0.5	0.0	5.7	7.7	6.7	1.0	0	0	0	0
D5_241/253	1000	100.0	100.0	100.0	4.0	0.0	0.0	0.0	0.0	7.2	7.7	7.5	0.3	0	0	0	0
D5_242/254	1500	98.0	99.5	98.8	4.7	2.0	0.5	1.2	0.8	12.1	13.7	12.9	0.8	0	0	0	0
D5_243/255	3000	95.3	94.2	94.8	4.3	4.7	5.8	5.2	0.8	10.3	14.6	12.5	2.1	0	0	0	0
D5_245/256	6000	96.9	97.2	97.1	4.0	3.1	2.8	2.9	0.3	8.7	10.9	9.8	1.1	0	0	0	0
D5_246/257	8000	100.0	100.0	100.0	4.0	0.0	0.0	0.0	0.0	9.4	10.9	10.1	0.7	0	0	0	0
D5_247/258	10000	100.0	100.0	100.0	4.0	0.0	0.0	0.0	0.0	6.0	9.4	7.7	1.7	0	0	0	0
D5_248/	12000	98.7	99.5	99.1	4.3	1.3	0.5	0.9	0.4	8.7	10.7	9.7	1.0	0	0	0	0
D5_249/	20000	100.0	99.9	100.0	4.0	0.0	0.1	0.0	0.0	10.3	11.4	10.9	0.6	0	0	0	0
D5_250/383	35000	80.5	82.6	81.5	4.3	19.5	17.4	18.5	1.8	9.0	9.9	9.4	0.4	0	0	0	0
	Average			97.2	4.2			2.8	0.5			9.5	1.1			0	0

	EtOH																
Sample ID	OPEG	%A	%A	Ave%A	Error%A	%R	%R	Ave%R	Error%R	As (nm)	As (nm)	AveAs(nm)	StdevAs(nm)	Rs (nm)	Rs (nm)	AveRs(nm)	stdevRs(nm)
D5_355/364	200	96.4	98.4	97.4	4.9	3.6	1.6	2.6	1.1	22.2	20.1	21.2	1.1	0	0	0	0
D5_356/365	400	92.3	94.3	93.3	4.7	7.7	5.7	6.7	1.3	24.8	20.1	22.5	2.3	0	0	0	0
D5_357/366	1000	99.3	97.7	98.5	4.7	0.7	2.3	1.5	0.9	24.8	20.1	22.5	2.3	0	0	0	0
D5_358/391	1500	99.6	99.0	99.3	4.3	0.4	1.1	0.7	0.4	20.1	20.1	20.1	0.0	0	0	0	0
D5_359/392	3000	97.9	98.5	98.2	4.2	2.1	1.5	1.8	0.4	18.4	22.2	20.3	1.9	0	0	0	0
D5____/393	6000	98.4	99.6	99.0	4.6	1.6	0.4	1.0	0.6	15.9	12.8	14.3	1.5	0	0	0	0
D5____/394	8000	99.0	97.6	98.3	4.6	1.0	2.4	1.7	0.7	25.0	22.2	23.6	1.4	0	0	0	0
D5____/395	10000	99.4	100.0	99.7	4.3	0.6	0.0	0.3	0.3	20.0	22.2	21.1	1.1	0	0	0	0
D5_361/	12000	96.6	97.8	97.2	4.5	3.4	2.2	2.8	0.7	18.4	20.8	19.6	1.2	0	0	0	0
D5_362/396	20000	98.7	99.6	99.1	4.4	1.3	0.4	0.9	0.5	18.4	20.1	19.2	0.9	0	0	0	0
D5_363/	35000	91.5	91.9	91.7	3.9	8.5	8.1	8.3	0.5	16.9	19.6	18.3	1.4	0	0	0	0
	Average			97.4	4.5			2.6	0.7			20.2	1.4			0	0

	H2O																
Sample ID	PEG	%A	%A	Ave%A	Error%A	%R	%R	Ave%R	Error%R	As (nm)	As (nm)	AveAs(nm)	StdevAs(nm)	Rs (nm)	Rs (nm)	AveRs(nm)	stdevRs(nm)
D5_282/294	200	100.0	100.0	100.0	4.0	0.0	0.0	0.0	0.0	6.0	4.8	5.4	0.6	0.0	0.0	0.0	0.0
D5_283/295	400	99.9	96.4	98.2	5.7	0.1	3.6	1.8	1.8	5.8	11.4	8.6	2.8	0.0	0.0	0.0	0.0
D5_284/296	1000	97.5	100.0	98.7	5.2	2.5	0.0	1.3	1.3	12.1	12.8	12.5	0.4	0.0	0.0	0.0	0.0
D5_285/297	1500	97.7	98.9	98.3	4.5	2.3	1.1	1.7	0.6	13.7	13.7	13.7	0.0	0.0	0.0	0.0	0.0
D5_286/298	3000	72.9	70.5	71.7	4.1	27.1	29.5	28.3	2.3	12.1	12.8	12.5	0.4	17.0	18.5	17.7	0.7
D5_287/299	4000	70.3	66.9	68.6	4.4	29.7	33.1	31.4	3.0	11.4	11.4	11.4	0.0	18.5	22.3	20.4	1.9
D5_288/318	6000	62.2	63.2	62.7	3.0	37.8	36.8	37.3	2.0	13.7	13.7	13.7	0.0	18.5	20.0	19.2	0.8
D5_289/319	8000	67.2	66.5	66.8	3.0	32.8	33.5	33.2	1.7	10.9	10.3	10.6	0.3	13.7	17.0	15.4	1.6
D5_290/320	10000	0.0	0.0	0.0	0.0	100.0	100.0	100.0	4.0	0.0	0.0	0.0	0.0	8.7	9.1	8.9	0.2
D5_291/321	12000	1.5	0.1	0.8	0.7	98.5	99.9	99.2	4.7	0.0	0.0	0.0	0.0	6.6	9.5	8.0	1.5
D5_292/322	20000	0.0	1.6	0.8	0.8	100.0	98.4	99.2	4.7	0.0	0.0	0.0	0.0	7.5	7.7	7.6	0.1
D5_293/323	35000	4.0	2.8	3.4	0.7	96.0	97.2	96.6	4.5	0.0	0.0	0.0	0.0	7.7	7.0	7.4	0.4
	Average			55.8	3.0			44.2	2.6			7.4	0.4			8.7	0.6

	H2O																
Sample ID	OPEG	%A	%A	Ave%A	Error%A	%R	%R	Ave%R	Error%R	As (nm)	As (nm)	AveAs(nm)	StdevAs(nm)	Rs (nm)	Rs (nm)	AveRs(nm)	stdevRs(nm)
D5_367/371	200	100.0	100.0	100.0	4.0	0.0	0.0	0.0	0.0	13.7	22.2	17.9	4.3	0.0	0.0	0.0	0.0
D5_368/380	400	98.5	97.5	98.0	4.4	1.5	2.5	2.0	0.6	20.1	22.2	21.2	1.1	0.0	0.0	0.0	0.0
D5_369/381	1000	99.9	99.0	99.5	4.5	0.1	1.0	0.5	0.5	16.9	18.4	17.6	0.7	0.0	0.0	0.0	0.0
D5_370/382	1500	99.3	91.5	95.4	7.7	0.7	8.5	4.6	4.1	22.2	18.4	20.3	1.9	0.0	0.0	0.0	0.0
D5_379/360	3000	72.5	74.7	73.6	4.0	27.5	25.3	26.4	2.2	16.9	16.9	16.9	0.0	22.3	20.2	21.3	1.1
D5_372/384	4000	64.4	61.6	63.0	3.9	35.6	38.4	37.0	2.9	16.9	14.6	15.8	1.2	22.3	28.2	25.3	2.9
D5_373/385	6000	65.0	66.0	65.5	3.1	35.0	34.0	34.5	1.9	20.1	16.9	18.5	1.6	28.2	24.7	26.5	1.7
D5_374/386	8000	68.9	68.8	68.8	2.8	31.1	31.2	31.2	1.3	20.1	15.7	17.9	2.2	20.2	20.2	20.2	0.0
D5_375/387	10000	0.2	1.3	0.7	0.6	99.8	98.7	99.3	4.5	0.0	0.0	0.0	0.0	20.2	17.0	18.6	1.6
D5_376/388	12000	0.2	0.3	0.3	0.1	99.8	99.7	99.7	4.0	0.0	0.0	0.0	0.0	20.2	15.4	17.8	2.4
D5_377/389	20000	0.4	0.2	0.3	0.1	99.6	99.8	99.7	4.1	0.0	0.0	0.0	0.0	17.0	15.7	16.4	0.6
D5_378/390	35000	0.4	1.3	0.8	0.4	99.6	98.7	99.2	4.4	0.0	0.0	0.0	0.0	20.2	18.5	19.3	0.9
	Average			55.5	3.0			44.5	2.5			12.2	1.1			13.8	0.9

Appendix E. Effects of Citric Acid on Titania Polymorph and Crystallite Size Formation

The tables show all the raw data pertaining to chapter 7. The symbols in the tables are understood as follows:

EtOH	–	Ethanol
H_2O	–	Water
PEG	–	Polyethylene glycol (the molecular weight is given in the table)
OPEG	–	Calcined samples
%A	–	Amount of anatase formed
Ave%A	–	Average amount of anatase formed
Error%A	–	Error in %A = Standard deviation + 4% of the average anatase
%R	–	Amount of rutile formed
Ave%R	–	Average amount of rutile formed
Error%R	–	Error in %R = Standard deviation + 4% of the average rutile
As	–	Anatase crystallite size
AveAs	–	Average size of anatase crystallites
StdevAs	–	Standard deviation of the anatase crystallite size
Rs	–	Rutile crystallite size
AveRs	–	Average size of rutile crystallites
StdevRs	–	Standard deviation of the rutile crystallite size

Sample ID	(1 : 1)																
	PEG	%A	%A	Ave%A	Error%A	%R	%R	Ave%R	Error%R	As (nm)	As (nm)	AveAs(nm)	StdevAs(nm)	Rs (nm)	Rs (nm)	AveRs(nm)	stdevRs(nm)
d2_017382/383	1000	99	98.1	98.5	4.4	1	1.9	1.5	0.5	10.2	10.2	10.2	0	0	0	0	0
d2_017384/385	1500	98.3	100	99.2	4.8	1.7	0	0.8	0.9	8.2	9.7	8.9	0.8	0	0	0	0
d2_017386/387	3000	100	99.7	99.9	4.1	0	0.3	0.1	0.2	15.4	18	16.7	1.3	0	0	0	0
d2_017388/389	4000	99.7	100	99.8	4.2	0.3	0	0.2	0.2	5.7	8.5	7.1	1.4	0	0	0	0
d2_017390/391	10000	100	100	100	4	0	0	0	0	6.6	8.5	7.6	0.9	0	0	0	0
d2_017394/395	12000	100	100	100	4	0	0	0	0	5.7	5.4	5.6	0.1	0	0	0	0
d2_017396/397	20000	100	100	100	4	0	0	0	0	4.1	5	4.6	0.4	0	0	0	0
	Average			99.6	4.2			0.4	0.2			8.7	0.7	0	0	0	0
	(1 : 1)																
	OPEG	%A	%A	Ave%A	Error%A	%R	%R	Ave%R	Error%R	As (nm)	As (nm)	AveAs(nm)	StdevAs(nm)	Rs (nm)	Rs (nm)	AveRs(nm)	stdevRs(nm)
d2_017422/423	1000	98.2	98	98.1	4	1.8	2	1.9	0.2	14.3	15.4	14.9	0.5	0	0	0	0
d2_017424/425	1500	98.9	100	99.5	4.5	1.1	0	0.5	0.6	24.3	21.8	23.1	1.2	0	0	0	0
d2_017426/427	3000	98.6	99.1	98.8	4.2	1.4	0.9	1.2	0.3	24.3	31.8	28	3.7	0	0	0	0
d2_017428/429	4000	99.6	99.6	99.6	4	0.4	0.4	0.4	0	21.8	19.7	20.8	1	0	0	0	0
d2_01742/433	10000	100	99.3	99.7	4.3	0	0.7	0.3	0.3	14.3	12.6	13.5	0.9	0	0	0	0
d2_017434/435	12000	98.6	99.2	98.9	4.2	1.4	0.8	1.1	0.3	16.6	16.6	16.6	0	0	0	0	0
d2_017436/437	20000	100	100	100	4	0	0	0	0	13.4	11.9	12.6	0.8	0	0	0	0
	Average			99.2	4.2			0.8	0.2			18.5	1.2			0	0

Appendix F. Effects of Polyethylene Glycol Molecular Weight and Stoichiometry on Titania Polymorph and Crystallite Size Formation

The tables show all the raw data pertaining to chapter 8. The symbols in the tables are understood as follows:

EtOH	–	Ethanol
H_2O	–	Water
PEG	–	Polyethylene glycol (the molecular weight is given in the table)
OPEG	–	Calcined samples
%A	–	Amount of anatase formed
Ave%A	–	Average amount of anatase formed
Error%A	–	Error in %A = Standard deviation + 4% of the average anatase
%R	–	Amount of rutile formed
Ave%R	–	Average amount of rutile formed
Error%R	–	Error in %R = Standard deviation + 4% of the average rutile
As	–	Anatase crystallite size
AveAs	–	Average size of anatase crystallites
StdevAs	–	Standard deviation of the anatase crystallite size
Rs	–	Rutile crystallite size
AveRs	–	Average size of rutile crystallites
StdevRs	–	Standard deviation of the rutile crystallite size

	(1:1)																
Sample ID	PEG	%A	%A	Ave%A	Error%A	%R	%R	Ave%R	Error%R	As (nm)	As (nm)	AveAs(nm)	StdevAs(nm)	Rs (nm)	Rs (nm)	AveRs(nm)	stdevRs(nm)
d2_12_748/749	200	6.6	8.0	7.3	1.0	93.4	92.0	92.7	4.4	0.0	0.0	0.0	0	9.8	11.6	10.7	0.9
d2_12_750/751	400	99.8	89.7	94.7	8.9	0.2	10.3	5.3	5.3	5.9	5.9	5.9	1E-04	0.0	0.0	0.0	0.0
d2_12_752/753	1500	87.5	92.7	90.1	6.2	12.5	7.3	9.9	3.0	9.3	7.6	8.4	0.8	0.0	0.0	0.0	0.0
d2_12_754/755	3000	18.4	19.0	18.7	1.0	81.6	81.0	81.3	3.5	0.0	0.0	0.0	0	7.2	7.2	7.2	0.0
d5_331/340	4000	8.8	9.3	9.0	0.6	91.2	90.7	91.0	3.9	0.0	0.0	0.0	0	6.4	7.0	6.7	0.3
d5_332/341	6000	8.9	7.4	8.2	1.1	91.1	92.6	91.8	4.4	0.0	0.0	0.0	0	6.6	7.0	6.8	0.2
d2_12_756/757	10000	24.1	23.2	23.7	1.4	75.9	76.8	76.3	3.5	0.0	0.0	0.0	0	8.7	9.6	9.1	0.4
d5_333/342	12000	66.1	52.6	59.4	9.2	33.9	47.4	40.6	8.4	5.0	5.1	5.1	0.1	10.0	10.4	10.2	0.2
d2_12_758/759	20000																
	Average			38.9	3.7			61.1	4.6			2.4	0.1			6.3	6.3

	(1:1)																
Sample ID	OPEG	%A	%A	Ave%A	Error%A	%R	%R	Ave%R	Error%R	As (nm)	As (nm)	AveAs(nm)	StdevAs(nm)	Rs (nm)	Rs (nm)	AveRs(nm)	stdevRs(nm)
d2_12_772/773	200	25.8	12.3	19.1	7.5	74.2	87.7	80.9	10.0	21.3	22.6	22.0	0.7	19.3	19.3	19.3	0.0
d2_12_774/775	400	97.7	99.8	98.8	5.0	2.3	0.2	1.2	1.1	21.3	19.1	20.2	1.1	0.0	0.0	0.0	0.0
d2_12_776/777	1500	93.5	91.8	92.7	4.6	6.5	8.2	7.3	1.1	20.2	20.2	20.2	0.0	21.5	19.2	20.4	1.1
d2_12_778/779	3000	9.4	12.3	10.9	1.9	90.6	87.7	89.1	5.0	14.7	13.6	14.1	0.5	18.3	18.3	18.3	0.0
d5_415/424	4000	2.2	1.4	1.8	0.5	97.8	98.6	98.2	4.3	0.0	0.0	0.0	0.0	18.5	18.7	18.6	0.1
d5_416/425	6000	0.9	0.9	0.9	0.0	99.1	99.1	99.1	4.0	0.0	0.0	0.0	0.0	17.0	16.7	16.9	0.1
d2_12_780/781	10000	13.5	10.0	11.7	2.2	86.5	90.0	88.3	5.3	10.3	10.9	10.6	0.3	17.5	17.5	17.5	0.0
d5_417/426	12000	35.7	40.7	38.2	4.0	64.3	59.3	61.8	5.0	12.1	12.6	12.4	0.3	24.9	24.7	24.8	0.1
d2_12_782/783	20000	44.7	50.3	47.5	4.7	55.3	49.7	52.5	4.9	9.0	10.0	9.5	0.5	18.4	18.3	18.4	0.0
	Average			35.7	3.4	64.1	64.5	64.3	4.5	12.1	12.1	12.1	0.4	17.3	17.0	17.1	0.2

	(0.5:1)																
Sample ID	PEG	%A	%A	Ave%A	Error%A	%R	%R	Ave%R	Error%R	As (nm)	As (nm)	AveAs(nm)	StdevAs(nm)	Rs (nm)	Rs (nm)	AveRs(nm)	stdevRs(nm)
d2_12_736/737	200	26.5	31.0	28.8	3.4	73.5	69.0	71.2	5.1	15.3	12.3	13.8	1.5	14.8	16.8	15.8	1.0
d2_12_738/739	400	84.5	84.0	84.3	3.6	15.5	16.0	15.7	0.9	7.3	9.5	8.4	1.1	0.0	0.0	0.0	0.0
d2_12_740/741	1500	100.0	100.0	100.0	4.0	0.0	0.0	0.0	0.0	6.9	7.4	7.2	0.3	0.0	0.0	0.0	0.0
d2_12_742/743	3000	50.7	45.1	47.9	4.7	49.3	54.9	52.1	4.9	8.1	10.9	9.5	1.4	9.6	12.4	11.0	1.4
d5_328/337	4000	60.2	54.3	57.2	5.3	39.8	45.7	42.8	4.7	11.4	8.3	9.9	1.6	13.7	9.5	11.6	2.1
d5_329/338	6000	7.7	3.0	5.4	2.6	92.3	97.0	94.6	6.1	0.0	0.0	0.0	0.0	8.3	8.7	8.5	0.2
d2_12_744/745	10000	7.5	4.7	6.1	1.7	92.5	95.3	93.9	5.2	0.0	0.0	0.0	0.0	6.9	7.6	7.3	0.3
d5_330/339	12000	20.4	16.7	18.6	2.6	79.6	83.3	81.4	5.1	0.0	0.0	0.0	0.0	9.9	8.3	9.1	0.8
d2_12_746/747	20000	18.9	16.0	17.5	2.1	81.1	84.0	82.5	4.7	0.0	0.0	0.0	0.0	8.3	8.3	8.3	0.0
	Average			40.6	3.3	58.2	60.6	59.4	4.1	5.4	5.4	5.4	0.6	8.0	7.9	7.9	0.6

	(0.5:1)																
Sample ID	OPEG	%A	%A	Ave%A	Error%A	%R	%R	Ave%R	Error%R	As (nm)	As (nm)	AveAs(nm)	StdevAs(nm)	Rs (nm)	Rs (nm)	AveRs(nm)	stdevRs(nm)
d2_12_760/761	200	40.2	44.8	42.5	4.0	59.8	55.2	57.5	4.6	24.0	27.6	25.8	1.8	21.5	20.3	20.9	0.6
d2_12_762/763	400	91.5	92.0	91.8	3.9	8.5	8.0	8.2	0.5	29.8	25.7	27.7	2.0	25.9	20.3	23.1	2.8
d2_12_764/765	1500	95.5	94.6	95.0	4.3	4.5	5.4	5.0	0.7	14.1	14.7	14.4	0.3	0.0	0.0	0.0	0.0
d2_12_766/767	3000	57.2	56.4	56.8	2.6	42.8	43.6	43.2	2.1	18.2	19.1	18.7	0.5	21.5	22.7	22.1	0.6
d5_412/421	4000	59.5	52.8	56.1	5.6	40.5	47.3	43.9	5.1	18.4	20.1	19.2	0.9	22.3	20.0	21.2	1.1
d5_413/422	6000	1.4	0.2	0.8	0.6	98.6	99.8	99.2	4.6	0.0	0.0	0.0	0.0	15.7	14.7	15.2	0.5
d2_12_768/769	10000	4.3	1.8	3.1	1.4	95.7	98.2	96.9	5.1	0.0	0.0	0.0	0.0	19.3	21.5	20.4	1.1
d5_414/423	12000	14.6	9.4	12.0	3.1	85.4	90.6	88.0	6.1	14.6	15.7	15.1	0.5	17.0	24.9	21.0	4.0
d2_12_770/771	20000	12.3	6.1	9.2	3.5	87.7	93.9	90.8	6.7	16.6	14.1	15.4	1.2	21.5	21.5	21.5	0.0
	Average			40.8	3.2	58.2	60.2	59.2	4.0	15.1	15.2	15.2	0.8	18.3	18.4	18.4	1.2

	(0.1:1)																
Sample ID	PEG	%A	%A	Ave%A	Error%A	%R	%R	Ave%R	Error%R	As (nm)	As (nm)	AveAs(nm)	StdevAs(nm)	Rs (nm)	Rs (nm)	AveRs(nm)	stdevRs(nm)
d5_325/334	4000	93.1	95.6	94.3	5.0	6.9	4.4	5.7	1.4	9.0	11.4	10.2	1.2	0.0	0.0	0.0	0.0
d5_326/335	6000	100.0	96.5	98.3	5.7	0.0	3.5	1.7	1.8	12.8	15.7	14.2	1.4	0.0	0.0	0.0	0.0
d5_327/336	12000	24.4	25.0	24.7	1.3	75.6	75.0	75.3	3.3	13.7	11.4	12.6	1.1	11.5	12.9	12.2	0.7
	Average			72.4	4.0			27.6	2.2			12.3	1.2			4.1	0.2
Sample ID	OPEG	%A	%A	Ave%A	Error%A	%R	%R	Ave%R	Error%R	As (nm)	As (nm)	AveAs(nm)	StdevAs(nm)	Rs (nm)	Rs (nm)	AveRs(nm)	stdevRs(nm)
d5_409/418	4000	99.8	99.1	99.4	4.3	0.2	0.9	0.6	0.3	18.4	24.8	21.6	3.2	0.0	0.0	0.0	0.0
d5_410/419	6000	97.8	96.3	97.0	4.6	2.2	3.7	3.0	0.9	22.2	24.8	23.5	1.3	0.0	0.0	0.0	0.0
d5_411/420	12000	26.5	25.7	26.1	1.4	73.5	74.3	73.9	3.3	20.1	22.2	21.2	1.1	24.9	22.3	23.6	1.3
	Average			74.2	3.4			25.8	1.5			22.1	1.9			7.9	0.4

Appendix G. Effects of Rapid Heating on Titania Polymorph and Crystallite Size Formation

The tables show all the raw data pertaining to chapter 9. The symbols in the tables are understood as follows:

EtOH	–	Ethanol
H_2O	–	Water
PEG	–	Polyethylene glycol (the molecular weight is given in the table)
OPEG	–	Calcined samples
%A	–	Amount of anatase formed
Ave%A	–	Average amount of anatase formed
Error%A	–	Error in %A = Standard deviation + 4% of the average anatase
%R	–	Amount of rutile formed
Ave%R	–	Average amount of rutile formed
Error%R	–	Error in %R = Standard deviation + 4% of the average rutile
As	–	Anatase crystallite size
AveAs	–	Average size of anatase crystallites
StdevAs	–	Standard deviation of the anatase crystallite size
Rs	–	Rutile crystallite size
AveRs	–	Average size of rutile crystallites
StdevRs	–	Standard deviation of the rutile crystallite size

	(1 : 1)																
Sample ID	OPEG	%A	%A	Ave%A	Error%A	%R	%R	Ave%R	Error%R	As (nm)	As (nm)	AveAs(nm)	StdevAs(nm)	Rs (nm)	Rs (nm)	AveRs(nm)	stdevRs(nm)
d2_12_796/797	1500	43.8	52.5	48.2	6.3	56.2	47.5	51.8	6.4	43.4	43.4	43.4	0.0	80.8	66.8	73.8	7.0
d2_12_798/799	3000	0.5	0.9	0.7	0.2	99.5	99.1	99.3	4.2	0.0	0.0	0.0	0.0	15.4	16.7	16.0	0.7
d2_12_800/801	6000	23.7	21.8	22.7	1.9	76.3	78.2	77.3	4.1	10.6	10.9	10.7	0.2	13.7	15.4	14.5	0.8
d2_12_802/803	10000	22.3	20.3	21.3	1.8	77.7	79.7	78.7	4.1	10.0	9.3	9.6	0.4	14.2	13.2	13.7	0.5
d2_12_804/805	12000	25.3	24.4	24.9	1.5	74.7	75.6	75.1	3.5	7.7	8.4	8.1	0.4	13.2	14.2	13.7	0.5
d2_12_806/807	20000	32.3	28.3	30.3	3.2	67.7	71.7	69.7	4.8	8.8	11.2	10.0	1.2	12.0	16.7	14.3	2.4
	Average			24.7	2.5			75.3	4.5			13.7	0.3			24.4	2.0
	(1 : 0.5)																
Sample ID	OPEG	%A	%A	Ave%A	Error%A	%R	%R	Ave%R	Error%R	As (nm)	As (nm)	AveAs(nm)	StdevAs(nm)	Rs (nm)	Rs (nm)	AveRs(nm)	stdevRs(nm)
d2_12_784/785	1500	57.7	60.0	58.9	3.5	42.3	40.0	41.1	2.8	29.7	31.1	30.4	0.7	56.6	58.8	57.7	1.1
d2_12_786/787	3000	0.3	0.0	0.2	0.2	99.7	100.0	99.8	4.2	0.0	0.0	0.0	0.0	17.5	12.4	15.0	2.6
d2_12_788/789	6000	7.7	7.4	7.5	0.5	92.3	92.6	92.5	3.9	9.8	10.3	10.0	0.3	14.8	14.2	14.5	0.3
d2_12_790/791	10000	27.6	27.6	27.6	1.1	72.4	72.4	72.4	2.9	10.3	11.5	10.9	0.6	16.7	18.3	17.5	0.8
d2_12_792/793	12000	65.2	63.3	64.3	3.5	34.8	36.7	35.7	2.4	9.7	9.8	9.7	0.0	24.2	24.1	24.2	0.0
d2_12_794/795	20000	13.7	8.6	11.2	3.0	86.3	91.4	88.8	6.1	7.8	6.6	7.2	0.6	15.4	16.7	16.0	0.7
	Average			28.3	2.0			71.7	3.7			11.4	0.4			24.2	0.9

Appendix H. Effects of Precursor Variation on Titania Polymorph and Crystallite Size Formation

The tables show all the raw data pertaining to chapter 10. The symbols in the tables are understood as follows:

EtOH	–	Ethanol
H_2O	–	Water
PEG	–	Polyethylene glycol (the molecular weight is given in the table)
OPEG	–	Calcined samples
%A	–	Amount of anatase formed
Ave%A	–	Average amount of anatase formed
Error%A	–	Error in %A = Standard deviation + 4% of the average anatase
%R	–	Amount of rutile formed
Ave%R	–	Average amount of rutile formed
Error%R	–	Error in %R = Standard deviation + 4% of the average rutile
As	–	Anatase crystallite size
AveAs	–	Average size of anatase crystallites
StdevAs	–	Standard deviation of the anatase crystallite size
Rs	–	Rutile crystallite size
AveRs	–	Average size of rutile crystallites
StdevRs	–	Standard deviation of the rutile crystallite size

	TiOxS																
Sample ID	OPEG	%A	%A	Ave%A	Error%A	%R	%R	Ave%R	Error%R	As (nm)	As (nm)	AveAs(nm)	StdevAs(nm)	Rs (nm)	Rs (nm)	AveRs(nm)	stdevRs(nm)
d2_14_1407/417	200	86.3	92.5	89.4	6.7	13.7	7.5	10.6	3.5	11.5	10.9	11.2	0.3	0.0	0.0	0.0	0.0
d2_14_1408/418	400	100.0	100.0	100.0	4.0	0.0	0.0	0.0	0.0	16.6	14.1	15.4	1.2	0.0	0.0	0.0	0.0
d2_14_1409/419	1500	95.2	97.1	96.1	4.8	4.8	2.9	3.9	1.1	15.3	13.6	14.5	0.8	0.0	0.0	0.0	0.0
d2_14_1410/420	3000	81.7	75.6	78.6	6.2	18.4	24.4	21.4	3.9	27.5	22.6	25.1	2.5	35.5	22.7	29.1	6.4
d2_14_1411/421	4000	83.5	74.9	79.2	7.4	16.5	25.1	20.8	5.1	17.4	18.2	17.8	0.4	17.5	32.4	24.9	7.5
d2_14_1412/422	6000	92.2	91.3	91.7	4.1	7.8	8.7	8.3	0.8	16.6	15.9	16.3	0.4	32.6	15.4	24.0	8.6
d2_14_1413/423	8000	95.6	98.4	97.0	5.3	4.4	1.6	3.0	1.5	14.1	14.2	14.1	0.0	0.0	0.0	0.0	0.0
d2_14_1414/2273	10000	80.0	81.6	80.8	4.0	20.0	18.4	19.2	1.6	13.6	20.2	16.9	3.3	20.3	16.7	18.5	1.8
d2_14_1415/425	12000	85.7	84.0	84.9	4.3	14.3	16.0	15.1	1.5	14.7	14.1	14.4	0.3	13.2	21.5	17.4	4.1
d2_14_2274/426	20000	51.8	50.4	51.1	2.7	48.2	49.6	48.9	2.7	19.1	14.1	16.6	2.5	25.8	29.9	27.9	2.0
	Average			84.9	4.9			15.1	2.2			16.2	1.2			14.2	3.0
	OTiClx																
Sample ID	OPEG	%A	%A	Ave%A	Error%A	%R	%R	Ave%R	Error%R	As (nm)	As (nm)	AveAs(nm)	StdevAs(nm)	Rs (nm)	Rs (nm)	AveRs(nm)	stdevRs(nm)
d2_15_2081/082	400	38.2	47.5	42.8	6.4	61.8	52.5	57.2	7.0	101.6	102.9	102.3	0.6	140.4	142.7	141.6	1.2

	Ti-isopro																
Sample ID	OPEG	%A	%A	Ave%A	Error%A	%R	%R	Ave%R	Error%R	As (nm)	As (nm)	AveAs(nm)	StdevAs(nm)	Rs (nm)	Rs (nm)	AveRs(nm)	stdevRs(nm)
d2_14_2270/280	200	91.6	96.7	94.1	6.3	8.4	3.3	5.9	2.8	19.1	13.6	16.4	2.7	0.0	0.0	0.0	0.0
d2_14_2271/281	400	95.0	100.0	97.5	6.4	5.0	0.0	2.5	2.6	20.2	12.7	16.5	3.8	0.0	0.0	0.0	0.0
d2_14_2272/282	1500	96.2	97.3	96.7	4.4	3.8	2.7	3.3	0.7	16.6	12.3	14.4	2.1	0.0	0.0	0.0	0.0
d2_14_1424/283	3000	95.1	99.5	97.3	6.1	4.9	0.5	2.7	2.3	13.6	13.6	13.6	0.0	0.0	0.0	0.0	0.0
d2_14_2288/284	4000	100.0	100.0	100.0	4.0	0.0	0.0	0.0	0.0	12.7	13.2	12.9	0.2	0.0	0.0	0.0	0.0
d2_14_2275/285	6000	95.3	96.8	96.1	4.6	4.7	3.2	3.9	0.9	14.7	12.7	13.7	1.0	0.0	0.0	0.0	0.0
d2_14_2276/286	8000	93.3	97.0	95.2	5.6	6.7	3.0	4.8	2.0	14.2	8.1	11.1	3.0	0.0	0.0	0.0	0.0
d2_14_2277/287	10000	94.1	96.4	95.2	5.0	5.9	3.6	4.8	1.4	17.4	9.5	13.4	3.9	0.0	0.0	0.0	0.0
d2_14_2278/1416	12000	87.0	85.7	86.3	4.1	13.0	14.3	13.7	1.2	19.1	15.3	17.2	1.9	29.9	17.5	23.7	6.2
d2_14_2279/289	20000	92.0	95.2	93.6	5.4	8.0	4.8	6.4	1.9	18.2	15.3	16.7	1.5	0.0	0.0	0.0	0.0
	Average			95.2	5.2			4.8	1.6			14.6	2.0			2.4	0.6

	TiEHOx																
Sample ID	OPEG	%A	%A	Ave%A	Error%A	%R	%R	Ave%R	Error%R	As (nm)	As (nm)	AveAs(nm)	StdevAs(nm)	Rs (nm)	Rs (nm)	AveRs(nm)	stdevRs(nm)
d2_14_2214/204	200	65.3	73.7	69.5	7.0	34.7	26.3	30.5	5.5	29.8	25.7	27.7	2.0	39.0	39.2	39.1	0.1
d2_14_2215/205	400	82.5	73.0	77.8	7.9	17.5	27.0	22.2	5.6	32.4	29.8	31.1	1.3	22.8	25.8	24.3	1.5
d2_14_2216/206	1500	41.1	38.5	39.8	2.9	58.9	61.5	60.2	3.7	21.3	24.1	22.7	1.4	22.8	19.3	21.0	1.8
d2_14_2217/207	3000	100.0	97.3	98.6	5.3	0.0	2.7	1.4	1.4	20.2	20.2	20.2	0.0	0.0	0.0	0.0	0.0
d2_14_2218/208	4000	94.9	99.1	97.0	6.0	5.1	0.9	3.0	2.3	20.2	17.4	18.8	1.4	0.0	0.0	0.0	0.0
d2_14_2219/209	6000	91.2	90.6	90.9	3.9	8.8	9.4	9.1	0.6	15.9	13.6	14.8	1.1	30.0	22.7	26.4	3.6
d2_14_2220/210	8000	94.8	95.5	95.2	4.1	5.2	4.5	4.8	0.5	14.1	11.9	13.0	1.1	0.0	0.0	0.0	0.0
d2_14_2221/211	10000	79.8	82.6	81.2	4.7	20.2	17.4	18.8	2.2	16.6	12.3	14.5	2.2	25.9	20.3	23.1	2.8
d2_14_2222/212	12000	26.6	31.0	28.8	3.3	73.4	69.0	71.2	5.0	16.6	12.3	14.5	2.2	21.5	17.5	19.5	2.0
d2_14_2223/213	20000	2.4	5.8	4.1	1.9	97.6	94.2	95.9	5.5	14.1	15.9	15.0	0.9	16.0	13.7	14.9	1.1
	Average			68.3	4.7			31.7	3.2			19.2	1.4			16.8	1.3

	TiAcAc																
Sample ID	OPEG	%A	%A	Ave%A	Error%A	%R	%R	Ave%R	Error%R	As (nm)	As (nm)	AveAs(nm)	StdevAs(nm)	Rs (nm)	Rs (nm)	AveRs(nm)	stdevRs(nm)
d2_14_2234/224	200	85.3	85.8	85.5	3.7	14.7	14.2	14.5	0.9	22.6	27.5	25.1	2.5	43.6	43.6	43.6	0.0
d2_14_2235/225	400	100.0	100.0	100.0	4.0	0.0	0.0	0.0	0.0	21.3	35.3	28.3	7.0	0.0	0.0	0.0	0.0
d2_14_2236/226	1500	100.0	100.0	100.0	4.0	0.0	0.0	0.0	0.0	18.2	17.4	17.8	0.4	0.0	0.0	0.0	0.0
d2_14_2237/227	3000	100.0	100.0	100.0	4.0	0.0	0.0	0.0	0.0	18.2	25.7	22.0	3.7	0.0	0.0	0.0	0.0
d2_14_2238/228	4000	100.0	100.0	100.0	4.0	0.0	0.0	0.0	0.0	18.2	16.6	17.4	0.8	0.0	0.0	0.0	0.0
d2_14_2239/229	6000	100.0	100.0	100.0	4.0	0.0	0.0	0.0	0.0	16.7	25.7	21.2	4.5	0.0	0.0	0.0	0.0
d2_14_2240/230	8000	99.1	99.9	99.5	4.4	0.9	0.1	0.5	0.4	13.6	14.1	13.9	0.2	0.0	0.0	0.0	0.0
d2_14_2241/231	10000	98.7	98.3	98.5	4.1	1.3	1.7	1.5	0.2	14.7	16.6	15.6	1.0	0.0	0.0	0.0	0.0
d2_14_2242/232	12000	95.9	92.1	94.0	5.6	4.1	7.9	6.0	2.1	15.9	17.4	16.7	0.7	0.0	0.0	0.0	0.0
d2_14_2243/2185	20000	89.3	93.6	91.5	5.8	10.7	6.4	8.5	2.5	15.3	18.2	16.7	1.5	81.5	20.3	50.9	30.6
	Average			96.9	4.4			3.1	0.6			19.5	2.2			9.5	3.1

	TiAmOH																
Sample ID	OPEG	%A	%A	Ave%A	Error%A	%R	%R	Ave%R	Error%R	As (nm)	As (nm)	AveAs(nm)	StdevAs(nm)	Rs (nm)	Rs (nm)	AveRs(nm)	stdevRs(nm)
d2_14_2161/174	200	100.0	100.0	100.0	4.0	0.0	0.0	0.0	0.0	17.4	15.9	16.7	0.7	0.0	0.0	0.0	0.0
d2_14_2162/175	400	100.0	100.0	100.0	4.0	0.0	0.0	0.0	0.0	19.2	16.7	17.9	1.3	0.0	0.0	0.0	0.0
d2_14_2163/176	1500	100.0	100.0	100.0	4.0	0.0	0.0	0.0	0.0	16.0	15.3	15.6	0.3	0.0	0.0	0.0	0.0
d2_14_2167/177	3000	100.0	100.0	100.0	4.0	0.0	0.0	0.0	0.0	16.7	15.9	16.3	0.4	0.0	0.0	0.0	0.0
d2_14_2168/178	4000	100.0	100.0	100.0	4.0	0.0	0.0	0.0	0.0	21.3	17.4	19.3	2.0	0.0	0.0	0.0	0.0
d2_14_2169/179	6000	100.0	100.0	100.0	4.0	0.0	0.0	0.0	0.0	17.4	13.6	15.5	1.9	0.0	0.0	0.0	0.0
d2_14_2170/180	8000	100.0	100.0	100.0	4.0	0.0	0.0	0.0	0.0	16.6	10.6	13.6	3.0	0.0	0.0	0.0	0.0
d2_14_2171/181	10000	100.0	100.0	100.0	4.0	0.0	0.0	0.0	0.0	17.4	11.6	14.5	2.9	0.0	0.0	0.0	0.0
d2_14_2172/182	12000	100.0	100.0	100.0	4.0	0.0	0.0	0.0	0.0	15.3	9.7	12.5	2.8	0.0	0.0	0.0	0.0
d2_14_2173/183	20000	100.0	100.0	100.0	4.0	0.0	0.0	0.0	0.0	12.7	10.9	11.8	0.9	0.0	0.0	0.0	0.0
	Average			100.0	4.0			0.0	0.0			15.4	1.6			0.0	0.0

	TiEApro																
Sample ID	OPEG	%A	%A	Ave%A	Error%A	%R	%R	Ave%R	Error%R	As (nm)	As (nm)	AveAs(nm)	StdevAs(nm)	Rs (nm)	Rs (nm)	AveRs(nm)	stdevRs(nm)
d2_14_2184/194	200	94.0	95.2	94.6	4.4	6.0	4.8	5.4	0.8	20.2	14.1	17.1	3.0	29.9	20.3	25.1	4.8
d2_14_2233/195	400	73.8	72.3	73.1	3.7	26.2	27.7	26.9	1.8	16.6	18.2	17.4	0.8	81.5	142.9	112.2	30.7
d2_14_2186/196	1500	95.4	84.7	90.1	9.0	4.6	15.3	9.9	5.8	18.2	15.9	17.1	1.1	29.9	66.8	48.4	18.5
d2_14_2187/197	3000	93.6	92.9	93.3	4.1	6.4	7.1	6.7	0.6	19.1	17.4	18.2	0.9	140.5	39.4	90.0	50.6
d2_14_2188/198	4000	91.9	90.0	91.0	4.6	8.1	10.0	9.0	1.3	19.1	18.2	18.6	0.5	35.5	32.4	33.9	1.5
d2_14_2189/199	6000	66.1	65.8	65.9	2.8	33.9	34.2	34.1	1.5	19.1	17.4	18.2	0.9	24.2	24.2	24.2	0.0
d2_14_2190/200	8000	94.6	90.2	92.4	5.9	5.4	9.8	7.6	2.5	13.6	20.2	16.9	3.3	19.3	27.7	23.5	4.2
d2_14_2191/201	10000	88.5	84.8	86.7	5.3	11.5	15.2	13.3	2.4	12.3	19.1	15.7	3.4	12.8	35.5	24.1	11.4
d2_14_2192/202	12000	92.2	96.0	94.1	5.6	7.8	4.0	5.9	2.1	11.9	18.2	15.0	3.1	27.7	32.5	30.1	2.4
d2_14_2193/203	20000	60.7	59.6	60.2	3.0	39.3	40.4	39.8	2.1	10.3	12.3	11.3	1.0	25.8	30.0	27.9	2.1
	Average			84.1	4.8			15.9	2.1			16.6	1.8			43.9	12.6

Appendix I. Attempts at Directly Observing Titanium Dioxide Formation Using Resin-gel Synthesis

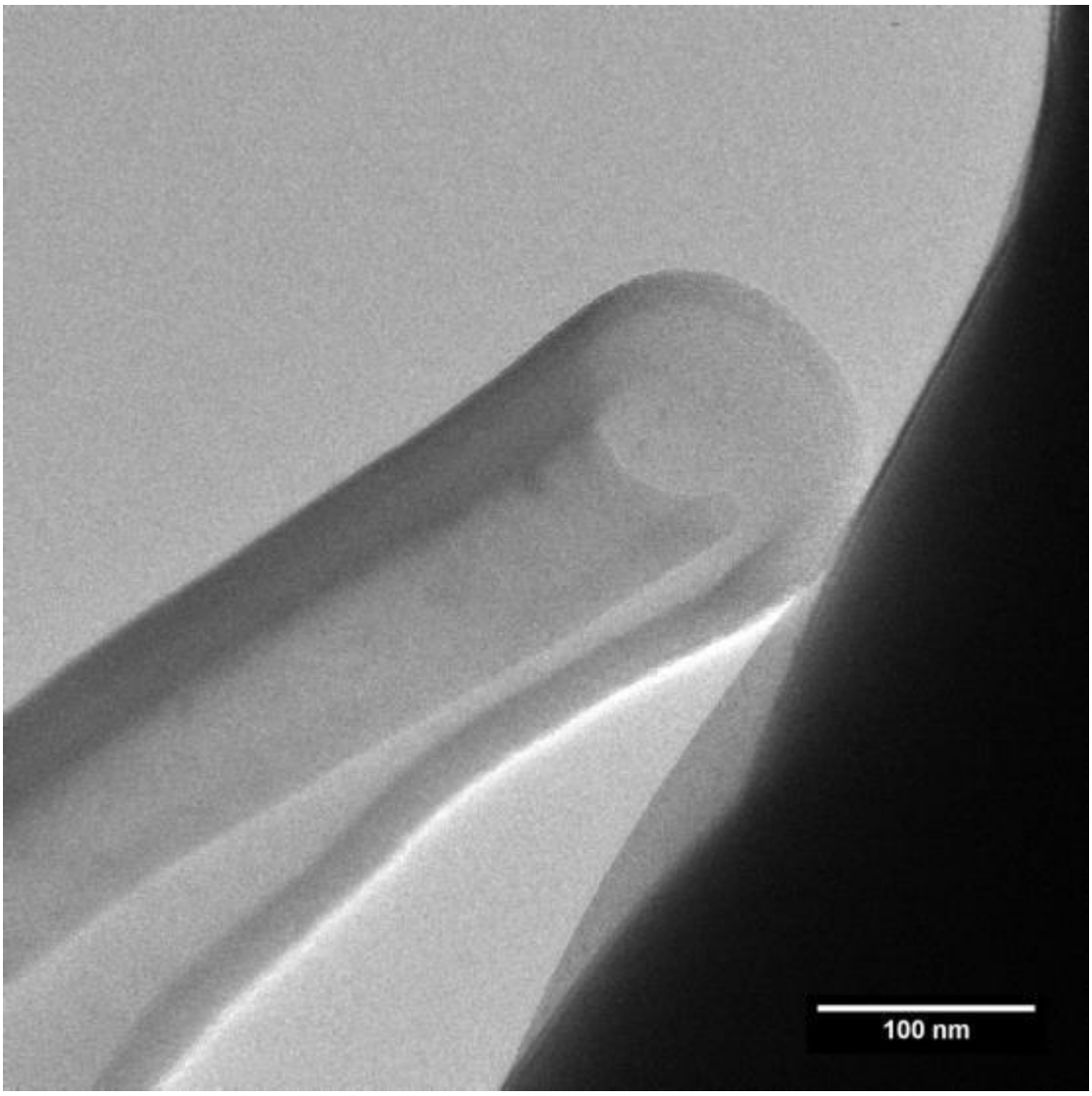

Figure I.1: This TEM image was obtained from a sample synthesised without any polymer. The wrapping effect of the holey carbon film is evident in the formation of this pseudo-superstructure.

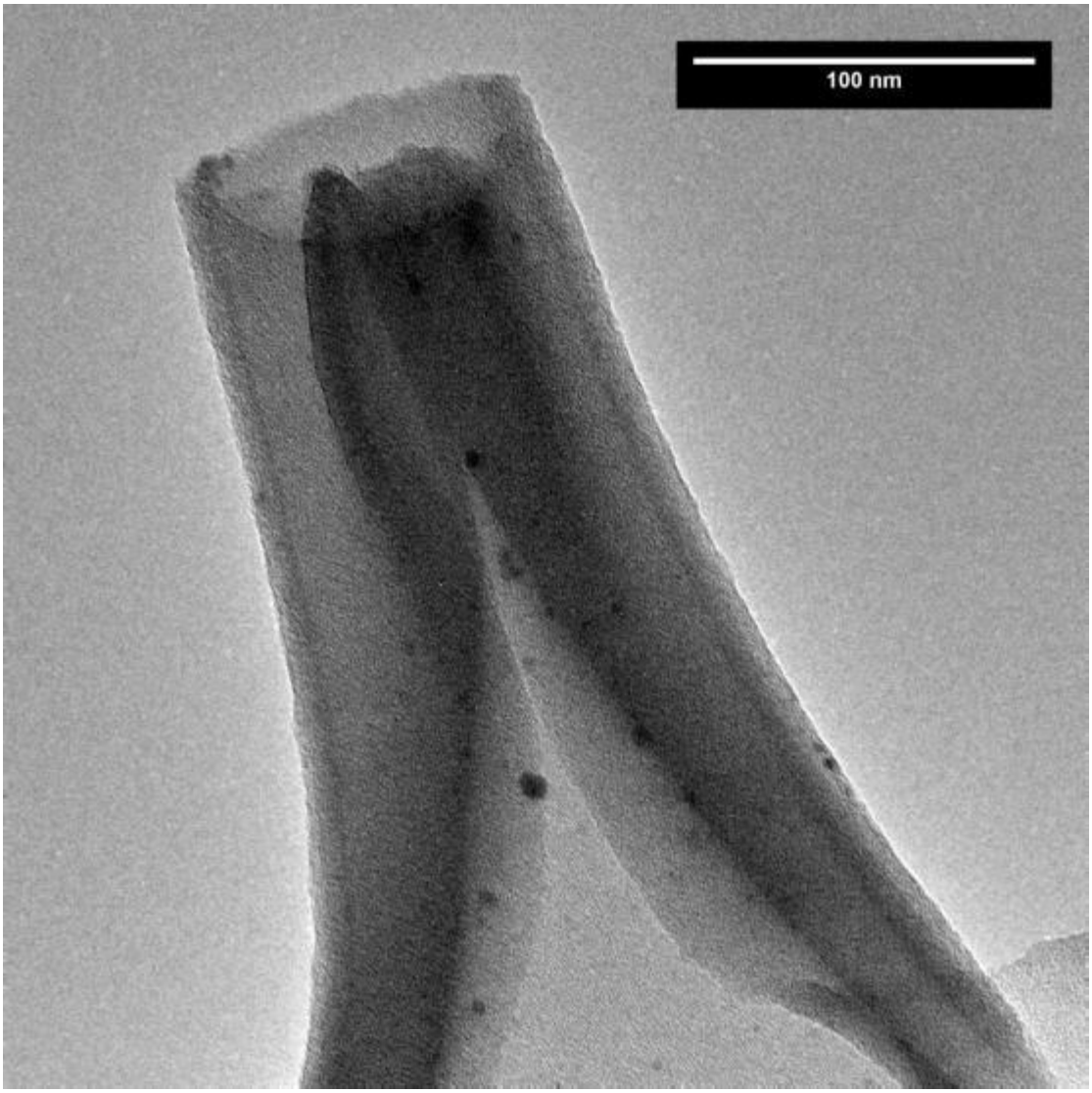

Figure I.2: Side profile view of the formation of a pseudo-superstructure. This structure was obtained from a sample synthesised without PEG and shows associated nanoparticles with the wrapped holey carbon film. Note that these structures occurred as a doublet giving rise to a 'tuning-fork' structure or individually as represented in this image.

Appendix J. Inference Based on Findings

Chapter 11 contains concluding remarks based on reproducible results obtained from this study. The purpose of this appendix is to aid in providing plausible explanations for the remarks in chapter 11. Since the discussion was developed over numerous parameter variation exercises, several hundred samples, several thousand data points, and discussed over many chapters, this appendix contains the entire discussion of particle formation using resin-gel synthesis in a convenient summary. It is intended to be read in conjunction with chapter 11.

Conclusion 2

With reference to the variation in phase formed between PEG and PEI, the absence of Ti_xN_y products from the sample containing PEI implied that metal ions did not coordinate to the nitrogen groups on PEI. The formation of anatase using PEI was likely due to the branched nature of the polymer that better protected the nucleated anatase phase from transformation into rutile. With reference to the superstructures exhibiting short-range crystallinity found in unignited samples, it was assumed that features such as loops, folds, and cavities within the polymeric superstructures could potentially serve as titania nucleation sites. This idea was developed with further parameter variation studies.

Conclusion 3

From the solvent variation experiment, and based on the thermodynamic stability of small anatase crystallites, it was gleaned that certain PEG chain lengths stabilised anatase and inhibited its transformation into rutile. Any transformation that occurred formed rutile crystallites that coarsened by taking up material from the matrix.

The formation of polymer reaction chambers was used to explain the pseudo-oscillation of the amount of rutile formed as a function of increasing PEG molecular weight according to the following hypothesis: PEG reaction chambers were formed from PEG that underwent chain scission at specific points (or multiples of specific points) during heating and ignition. Individual fragments then folded upon themselves leading to the formation of reaction chambers (loops, folds, and cavities). The sizes of the chambers were hypothesised as being critical to the formation of anatase, rutile, or a mixture of phases. If the reaction chambers were of a sufficiently large size to

protect and stabilise anatase, then small anatase crystallites would nucleate. Larger reaction chambers did not protect and stabilise anatase as effectively and allowed rutile to nucleate. This concept was refined and tested with subsequent studies.

The following was proposed to include the effects of the solvent in the proposed polymer reaction chamber model: hydroxylated metal ion complexes formed from the addition of $TiCl_4$ to both water and ethanol. The size of the solvent counter ions remaining after the formation of these complexes sterically stabilised these complexes. Ethanol produced larger counter ions than water. Larger counter ions better stabilised the anatase phase. According to the formation kinetics of titania, anatase is the first nucleated phase. Therefore, anatase was better stabilised in ethanol than in water. The combination of steric protection and stabilisation effects from the solvent counter ions and the polymer then governed the phase that formed.

Finally, it was hypothesised that the counter ions remaining from ethanol limited the number of hydrogen bonds that could be formed between the solvent and the polymer, compared with water. Since hydrogen bonds served to stabilise the structural integrity of the polymer, water better stabilised PEG than did ethanol. Thus, in ethanol, the PEG structure was less rigid and more conforming to the changing conditions during heating and ignition. This was advantageous to the formation of anatase that required intimate steric stabilisation from the polymer.

Conclusion 4

To explain the consistency in anatase mass percentage and crystallite size formed using PEG 35000 g/mol across heating rates, the following was proposed: in keeping with the reaction chamber mechanism, it was concluded that long chain polymers have a greater propensity to undergo chain entanglement. This had the effect of forming larger chambers that did not effectively stabilise the anatase phase, encouraging rutile transformation.

The effects of enhanced heating in study were rationalised by considering that for any given PEG chain length, enhanced heating caused faster polymer chain scission that occurred at better-defined points, forming chambers with a smaller size distribution. Consequently, short chain PEG formed smaller chambers as opposed to long chain PEG that formed larger chambers. The effects of the size of polymer chambers on crystallite stabilisation were described in the previous study.

Conclusion 5

A plausible explanation for the action of citric acid favouring the anatase phase and inhibiting transformation into rutile dealt with the stabilisation effect afforded by the larger counter ion remaining after the formation of metal-hydroxylated species. Citric acid has the ability to form numerous hydrogen bonds with the polymer, improving its structural integrity. As previously observed, this has the effect of favouring rutile formation. Given that anatase was produced nearly exclusively, crystallite capping and protection was a greater determinant of phase formation than PEG structure stabilisation. Since the average anatase crystallite size across all samples was 8.7 nm, it was inferred that the anatase to rutile phase transformation was inhibited by citric acid limiting anatase coarsening.

Conclusion 6

The results obtained from the PEG stoichiometry variation were modelled into the polymer reaction chamber hypothesis as follows: short chain polymers (200 g/mol) unlikely exhibited chain entanglement, forming reaction chambers that were sufficiently large to nucleate anatase and rutile but small enough that they did not undergo further decomposition to form smaller chambers. For this reason, anatase and rutile was formed in a (1 : 0.5) ratio. In a (1 : 1) ratio, the increased amount of polymer in the system resulted in longer and hotter ignitions, therefore increasing the amount of the more stable rutile phase formed. During decomposition longer chain PEG (400 – 1500 g/mol) formed longer chain fragments that were destabilised relative to PEG 200 g/mol chain fragments. Therefore, these destabilised longer fragments degraded into shorter chains that formed smaller reaction chambers. As previously discussed, smaller reaction chambers favour anatase formation. This was observed for (1 : 1) and (1 : 0.5) syntheses. Intermediate chain length (PEG 3000 – 6000 g/mol) also underwent degradation to form shorter chain fragments. However since the starting chains were longer than PEG 400 – 1500 g/mol, larger reaction chambers ensued. Larger chambers nucleate anatase and rutile. This was observed for the (1 : 0.5) synthesis but not for (1 : 1) synthesis. In a (1 : 1) synthesis, the number of polymer chains were doubled relative to (1 : 0.5) synthesis. Therefore, the volume of polymer present in the synthesis caused entanglement that led to the formation of larger chambers. Larger chambers favoured the formation of rutile. Finally, long chain PEG (10000 – 20000 g/mol) degraded to form large chambers that favoured rutile

formation. This was observed for the (1 : 0.5) synthesis. The decreased quantity of rutile formed in the (1 : 1) synthesis was explained by considering that the sheer volume of polymer in the system served to cause steric stabilisation of nucleated particles. This caused rutile transformation inhibition. For (1 : 0.1) synthesis, short chain PEG did not provide sufficient polymer to the system to form large chambers. Therefore, anatase was nucleated. Long chain PEG increased the amount of polymer in the system sufficiently to form larger reaction chambers and nucleate rutile.

The variation in results was explained by considering variations in PEG decomposition, chain entanglement, and steric entrapment due to high polymer concentrations. These factors were predicated on the formation of polymer reaction chambers. Hence, the developing hypothesis was modified to account for the effects of polymer concentration.

Conclusion 8

The mechanism of particle formation using resin-gel synthesis was modified to include the effects of various metal ion precursors as follows: hydroxylated precursors coordinate to PEG chains. The extent of this coordination is governed by the amount of accessible oxygen sites available on the precursor. If the precursor has sufficient sites for coordination to the polymer, the formed reaction chambers will be sufficiently small to protect and stabilise the nucleated anatase phase. Additionally, if the ligands attached to the metal ion are small, they do not sufficiently contribute to the stabilisation of anatase favouring rutile formation. If the ligands are too large, they inhibit polymer chains from engulfing the hydroxylated species, thus reducing polymer protection effects. When the ligands attached to the metal ion are of a fair size and possess sufficient accessible oxygen sites for association with polymer reaction chambers, anatase is nucleated. This provides the best combination of protection effects from the ligands and polymer for anatase nucleation.

Conclusion 10

The proposed formation for rutile superstructures is: several rutile seed crystals in close proximity to each other begin growing anisotropically along [0 0 1] (growth along [0 0 1] is a fundamental property of rutile). As the seed crystals impinge on each other, they fuse to form the nucleus of the mesocrystal. Nanorods continue to develop by taking up material from the solution, or via oriented attachment with nearby crystals.

The Grand Resin-gel Synthesis TiO_2 Particle Formation Hypothesis

Accounting for all of the parameters varied in this study, resin-gel synthesis forms TiO_2 in the following way: hydroxylated metal ion species are formed from the addition of metal ions to a hydroxyl-containing solvent. These species are protected and stabilised by remnants of solvent components. The size of the ligands attached to the metal ion precursor dictate the degree of protection and stabilisation afforded to the hydroxylated species, by the precursor. These complexes are further coordinated to polymer fragments that form reaction chambers of various sizes as degradation is encouraged. The number of available oxygen sites on the hydroxylated species governs the degree of association of the reaction chambers to the metal ion complexes. An intimate association between the reaction chambers and hydroxylated complexes increases the protection and stabilisation effects afforded by the reaction chambers. Additionally, the sizes of the polymer chambers are governed by the quantity of added PEG to the reaction mixtures, and to a lesser degree, the heating rate employed in the synthesis. As the reaction proceeds further, anatase is nucleated. If the combination of solvent components, precursor ligands, and association of reaction chambers of appropriate sizes is insufficient to stabilise anatase, rutile is nucleated. Rutile crystals grow anisotropically along [0 0 1]. Rutile mesocrystal growth is encouraged if the polymer chambers have degraded sufficiently, or if they are sufficiently large to accommodate these mesocrystals.